UNIVERSITY OF CALIFORNIA, SAN DIEGO

PROBABILISTIC PERFORMANCE-BASED OPTIMUM SEISMIC DESIGN OF SEISMIC ISOLATION FOR CALIFORNIA HIGH-SPEED RAIL PROTOTYPE BRIDGE

A dissertation submitted in partial satisfaction of the requirements for the degree

Doctor of Philosophy

in

Structural Engineering

by

Yong Li

Committee in charge:

Professor Joel P. Conte, Chair
Professor Ahmed-Waeil M. Elgamal
Professor Philip E. Gill
Professor Bo Li
Professor José I. Restrepo

2014

The dissertation of Yong Li is approved, and it is acceptable in quality and form for publication on microfilm:

Chair

University of California, San Diego

2014

DEDICATION

To my parents and sister

TABLE OF CONTENTS

SIGNATURE PAGE iii

DEDICATION iv

TABLE OF CONTENTS v

LIST OF FIGURES xiv

LIST OF TABLES xliii

ACKNOWLEDGEMENTS xliv

VITA xlvi

ABSTRACT OF THE DISSERTATION xlvii

CHAPTER 1 INTRODUCTION 1

1.1. Background and Motivation 1

1.2. The Evolution of Seismic Design Philosophy 3

1.3. Probabilistic Performance-based Earthquake Engineering (PBEE) 4

1.3.1. The rise of PEER PBEE methodology 5

1.3.2. Analysis steps in PBEE and applications research review 6

1.3.3. Extension of the PBEE methodology 6

1.3.4. Potential further development of PBEE for probabilistic performance-based optimum seismic design 7

1.4. The Advent of Earthquake Protection Technologies 8

1.4.1. Fundamental mechanism of seismic isolation 8

1.4.2. Isolator devices and related research review 9

1.4.3. Applications of seismic isolation to building and bridge structures 10

1.4.4. Need for optimal isolator design 11

1.5. Optimization in Structural Design 12
1.5.1. Literature review on structural optimization 13
1.5.2. Literature review on optimization for seismic isolation system 17
1.5.3. Limitations in current research and ideas for future development of probabilistic design optimization in this dissertation 20
1.6. Research Needs, Scope, and Objectives 21
1.7. Opportunities and Challenges 24
1.8. Organization of This Dissertation 26
References 29
CHAPTER 2 FRAMEWORK OF PROBABILISTIC PERFORMANCE-BASED OPTIMUM SEISMIC DESIGN (PPBOSD) 39
2.1. Introduction 39
2.2. Proposed PPBOSD Framework 41
2.3. Structural Model and Site Location 46
2.4. Forward PBEE Analyses 47
2.4.1. Probabilistic seismic hazard analysis (PSHA) 47
2.4.2. Probabilistic seismic demand analysis (PSDeA) 53
2.4.3. Probabilistic seismic damage analysis (PSDaA) 60
2.4.4. Probabilistic seismic loss analysis (PSLA) 65
2.5. Parametric PBEE Analyses 67
2.6. Inverse PBEE Analysis within PPBOSD Framework 69
2.7. Conclusions 74
Acknowledgement 75
References 75

CHAPTER 3 CALIFORNIA HIGH-SPEED RAIL (CHSR) PROTOTYPE BRIDGE DESIGN AND COMPUTATIONAL MODEL DEVELOPEMENT 78
3.1. Introduction 78
3.2. Description of the Bridge Design 80
3.3. Description of the Computational Model 84
3.4. Bridge Superstructure and Piers 86
3.4.1. Bridge deck and pier columns 86
3.4.2. Seismic isolators for connections between deck and pier 89
3.4.3. Slotted hinge joints for decks at interior expansion joints 90
3.5. Soil-Foundation-Structure-Interaction (SFSI) Modeling 94
3.5.1. Embankment-abutment component 96
3.5.2. Abutment shear key component 104
3.5.3. Pile foundation component 105
3.6. Track-Structure Interaction Modeling 111
3.6.1. Rail 111
3.6.2. Rail-structure connection 112
3.6.3. Rail boundary spring 114
3.7. Static and Dynamic Analysis of Abutment Substructure 118
3.8. Substructure Analysis of a Single Pier Column Founded on Pile Group Foundation for Static Hysteretic Behavior 122
3.9. Dynamic Analysis to Study Substructure Behavior Focusing on Multiple Support Excitation Considering the Depth-varied Ground Motion 128
3.9.1. Free field site response analysis 129

3.9.2. Damping (energy dissipation) 131
3.9.3. Earthquake loading (energy input) 136
3.9.4. Verification of multiple-support-excitation (displacement loading) for SDOF system and substructures 143
3.10. Technical Issues for Seismic Simulation of the CHSR Prototype Bridge 151
3.11. Conclusions 157
References 158
CHAPTER 4 SEISMIC SIMULATION OF CHSR PROTOTYPE BRIDGE FOCUSING ON DETERMINISTIC PERFORMANCE COMPARISON BETWEEN SEISMIC ISOLATED AND NON-ISOLATED BRIDGE 163
4.1. Introduction 163
4.2. Earthquake Selection, Scaling, and De-convolution 164
4.3. Investigation of Effects of Seismic Isolators on System Response 170
4.3.1. Seismic response comparison on OBE hazard level 171
4.3.2. Seismic response comparison on MCE hazard level 178
4.3.3. Comparison of seismic response distribution along the bridge for IB and NIB 180
4.4. Conclusions 184
CHAPTER 5 PROBABILISTIC PERFORMANCE EVALUATION OF SEISMIC ISOLATION FOR THE CHSR PROTOTYPE BRIDGE 186
5.1. Introduction 186
5.2. Ground Motions 188
5.2.1. Ground motion database 189

5.2.2. Probabilistic seismic hazard analysis 190
5.2.3. Ground motion selection 194
5.2.4. Ground motion scaling 196
5.2.5. Ground motion de-convolution for depth-varied displacements 197
5.3. Computational Models for Isolated Bridge (IB) and Non-isolated Bridge (NIB) 197
5.4. Probabilistic Seismic Demand Hazard Analysis: Stripe Method 198
5.4.1. Record-by-record comparison under OBE hazard level earthquakes. 198
5.4.2. Record-by-record comparison under MCE hazard level earthquakes 206
5.4.3. Conditional probabilistic demand hazard analysis using the stripe method 212
5.4.4. Unconditional demand hazard analysis 228
5.5. Probabilistic Seismic Demand Hazard Analysis: Cloud Method 239
5.5.1. Conditional PSDHA using cloud method 240
5.5.2. Probabilistic seismic demand hazard analysis 255
5.6. Comparison between the Stripe Method and the Cloud Method 256
5.7. Conclusions 268
CHAPTER 6 CLOUD COMPUTING FOR PARAMETRIC PROBABILISTIC ANALYSIS & OPTIMIZATION 270
6.1. Background and Motivation 270
6.2. Computing Demand Involved in PPBOSD 272
6.3. Development and Implementation of CBO Workflow 273
6.4. Computing Resources and Workflow Management Software used in CBO 276

6.4.1. Computing resources 276
6.4.2. Job management software 277
6.5. Application of CBO to 3D Parametric Study of Single Seismic Isolator 277
6.6. Conclusions 287
References 287
CHAPTER 7 PARAMETRIC PROBABILISTIC SEISMIC DEMAND ANALYSIS OF SEISMIC ISOLATED CHSR PROTOTYPE BRIDGE 289
7.1. Introduction 289
7.2. Structural Model and Design Variables 290
7.2.1. Seismic isolator parameters based on physical configuration 291
7.2.2. Seismic isolator parameters bounds considering operation loads of trains 292
7.2.3. Grids of seismic isolator parameters for parametric study 293
7.3. Earthquake Selection and Scaling, and De-convolution for Cloud Method 294
7.4. Probabilistic Parametric Performance Evaluation with Definition and Formulation of Risk Features 296
7.4.1. Risk features extracted from conditional demand hazard analysis 297
7.4.2. Risk features extracted from probabilistic seismic demand hazard analysis 300
7.5. Risk Feature Exploration 302
7.5.1. Risk feature exploration for conditional demand hazard analysis 303
7.5.2. Risk feature exploration for probabilistic seismic demand hazard analysis 330

7.5.3. Risk feature distribution along the bridge 360
7.5.4. Summary of risk feature values 368
7.6. Conclusions 375
CHAPTER 8 PROBABILISTIC PERFORMANCE-BASED OPTIMUM SEISMIC DESIGN OF CHSR PROTOTYPE BRIDGE 376
8.1. Introduction 376
8.2. Alternatives of Optimization Formulations in PPBOSD 378
8.2.1. Optimization with constraints considering different type of risk features 379
8.2.2. Optimization with constraints across different EDPs 380
8.2.3. Optimization with constraints across different hazard levels 382
8.2.4. Optimization with constraints across different hazard analysis steps 383
8.3. Probabilistic Performance-based Seismic Design Requirements for CHSR Bridges 385
8.3.1. EDPs of CHSR bridges used for probabilistic design constraints 386
8.3.2. Risk features and limiting values to define probabilistic design constraints 387
8.4. Formulations and Solutions of Structural Optimization Problems for the CHSR Prototype Bridge 388
8.4.1. Structural optimization for seismic performance of discretized hazard levels: conditional seismic demand hazard 388
8.4.2. Structural optimization for seismic performance of continuous hazard levels: the unconditional seismic demand hazard 402

8.4.3. Structural optimization for seismic performance based on the mean demand and variance demand 404
8.5. Optimum Design Evaluation..... 409
8.6. Conclusions..... 418
References..... 419
CHAPTER 9 CONCLUSIONS AND FUTURE WORK 420
9.1. Summary of Research Work..... 420
9.1.1. Implementation of PEER performance-based earthquake engineering (PBEE) methodology..... 421
9.1.2. Formulation and implementation of the proposed PPBOSD framework and application to a nonlinear SDOF system for illustration, verification and validation 422
9.1.3. Design, modeling, and seismic response simulation of CHSR prototype bridge considering track-structure interaction (TSI) and soil-foundation-structure-interaction (SFSI)..... 422
9.1.4. Deterministic and probabilistic performance evaluation of seismic isolation for the CHSR prototype bridge system..... 424
9.1.5. Cloud-based parametric probabilistic analysis and optimization framework 425
9.1.6. Probabilistic performance-based optimization of seismic isolation for the CHSR prototype bridge 426
9.2. Limitations of this Research Work 427
9.2.1. Pertinent sources of uncertainty to be considered in probabilistic performance evaluation 427

9.2.2. Definition of risk-based performance metrics in the context of the PEER PBEE methodology 428
9.2.3. Scalar intensity measure in probabilistic seismic hazard analysis and scalar EDP for demand hazard analysis and limit-state function formulation 428
9.2.4. Probabilistic seismic hazard accounting explicitly for near-fault ground motions 429
9.2.5. Optimization for probabilistic optimum seismic design of seismic isolation for CHSR prototype bridge 429
9.2.6. Finite element modeling and simulation 430
9.3. Recommendations for Future Research Work 431
APPENDIX A PASSIVE PRESSURE THEORY FOR ESTIMATING PILE CAP RESISTANCE AND ABUTMENT WALL RESISTANCE 433
APPENDIX B SOIL SPRING (p-y, t-z, q-z) FORMULATION SUMMARY AND PROPERTIES SPECIFICATION PROCEDURE 439

LIST OF FIGURES

Figure 1.1: Conceptual framework of the probabilistic performance-based earthquake engineering methodology by the Pacific Earthquake Engineering Research Center… 5
Figure 1.2: Configuration of seismic isolators: (a) lead rubber bearing from Dynamic Isolation System, Inc., and (b) friction pendulum from Earthquake Protection System, Inc.…..9
Figure 2.1: Humboldt Bay Middle Channel (HBMC) Bridge (Courtesy of Caltrans) 41
Figure 2.2: Forward PBEE analysis and inverse PBEE analysis for probabilistic performance-based seismic design/retrofit 42
Figure 2.3: Illustration of the motivation for probabilistic performance-based optimum seismic design (PPBOSD).....43
Figure 2.4: Probabilistic performance-based optimum seismic design (PPBOSD) framework45
Figure 2.5: Nonlinear single-degree-of-freedom (SDOF) bridge model.....46
Figure 2.6: Uniform hazard spectra of 30 different hazard levels.....50
Figure 2.7: Probabilistic seismic hazard curves 50
Figure 2.8: Probabilistic seismic hazard M−R de-aggregation for the site of study (Oakland) associated with hazard level of probability of exceedance of 2% in 50 years 52
Figure 2.9: The two main seismic faults to the selected site of study, Oakland, California 52
Figure 2.10: Conditional seismic demand hazard for EDP of displacement ductility.....57
Figure 2.11: Conditional seismic demand hazard for EDP of peak absolute acceleration.....57
Figure 2.12: Conditional seismic demand hazard for EDP of hysteretic energy dissipation 57
Figure 2.13: Probabilistic seismic demand hazard curve of displacement ductility (left) and its de-aggregation w.r.t. intensity measure (right) 59
Figure 2.14: Probabilistic seismic demand hazard curve of peak absolute acceleration (left) and its de-aggregation w.r.t. intensity measure (right).....59
Figure 2.15: Probabilistic seismic demand hazard curve of normalized hysteretic energy dissipation (left) and its de-aggregation of w.r.t. intensity measure (right) 59
Figure 2.16: Illustration of discrete damage measure 60

Figure 2.17: Fragility curves for limit-states of failure mode associated with displacement ductility....61
Figure 2.18: Fragility curves for limit-states of failure mode associated with peak absolute acceleration....62
Figure 2.19: Fragility curves for limit-states of failure mode associated with normalized hysteretic energy dissipated....62
Figure 2.20: Displacement ductility associated damage hazard de-aggregation for different limit states with respect to edp (left) and im (right)....64
Figure 2.21: Absolute acceleration associated damage hazard de-aggregation for different limit states with respect to edp (left) and im (right)....64
Figure 2.22: Normalized hysteretic energy dissipation associated damage hazard de-aggregation for different limit states with respect to edp (left) and im (right)....64
Figure 2.23: Multilayer Monte Carol (MCS) simulation for estimation of total loss hazard....67
Figure 2.24: Probabilistic demand hazard curves of displacement ductility....68
Figure 2.25: Probabilistic demand hazard curves of peak absolute acceleration....68
Figure 2.26: Probabilistic demand hazard curves of normalized hysteretic energy dissipation 68
Figure 2.27: Probabilistic loss hazard curves for system with different yield strengths....69
Figure 2.28: Illustration example for the proposed PPBOSD....70
Figure 2.29: Two-dimensional (2D) objective function plot....71
Figure 2.30: Optimization search history with 3D plot of the objective function for the PPBOSD illustration example....72
Figure 2.31: Optimization search history with contour of the objective function for the PPBOSD illustration example....73
Figure 2.32: The evolution of the probabilistic seismic demand hazard curves....73
Figure 2.33: The evolution of the probabilistic seismic loss hazard curves....74
Figure 3.1: The high-speed rail bridge system sketch....79
Figure 3.2: Isometric view of the CHSR Prototype Bridge....81
Figure 3.3: Schematic views of the CHSR Prototype Bridge....81
Figure 3.4: Abutment system for bridge supports at both ends: (a) longitudinal view, (b) transverse view....81

Figure 3.5: Superstructure, substructure, and superstructure-substructure connections: (a) transverse view, (b) longitudinal view for discontinuous joints, and (c) longitudinal view at continuous joints 82
Figure 3.6: Pile group foundation (2 × 2) for CHSR pier column 83
Figure 3.7: Pile group foundation (2 × 3) for CHSR abutments 83
Figure 3.8: Schematic view of the model for substructure and its connection with superstructure 87
Figure 3.9: Schematic view of a single span of the CHSR Prototype Bridge model 87
Figure 3.10: Schematic view of a single frame consisting of three continuous spans of the CHSR Prototype Bridge model 88
Figure 3.11: Pier column (a) fiber section discretization, (b) fiber material models for steel reinforcement, (c) concrete cover, and (d) concrete core 89
Figure 3.12: Distribution of axial forces in isolators and the layout of seismic isolators of group A (small) and group B (large) 90
Figure 3.13: Schematic view of the SHJ device in the segmental control strategy 92
Figure 3.14: Design details of the SHJ device in CHSR prototype bridge 92
Figure 3.15: Schematic view of the model of the connection between two adjacent bridge segments at interior expansion joints with SHJ devices 93
Figure 3.16: Schematic view of the model of SHJ devices between two adjacent bridge segments at interior expansion joints 93
Figure 3.17: Schematic view of abutment model in both longitudinal direction (left) and transverse direction (right) 98
Figure 3.18: The p-y backbone curve for abutment back-wall resistance predicted using the GHFD prediction model proposed by Khalili-Tehrani et al. (2010) and the Log-Spiral approach prosed by Mokwa et al. (2001) as validation 101
Figure 3.19: 3D schematic view of the abutment modeling 103
Figure 3.20: Smooth gap material mechanism (a) and comparison with bilinear (b) 104
Figure 3.21: Shear key model calibrated with experimental data (Unit 3A reported by Megally et al. 2001) 105
Figure 3.22: Pile foundation with soil layer properties 108
Figure 3.23: Fiber section discretization of piles (left), and pile section moment-curvature relationship (right) 108

Figure 3.24: Sketch of pile foundation modeling using dynamic p-y approach.....109
Figure 3.25: Soil spring (p-y) behaviors for a typical soil spring in upper layer of clay (a) and a typical soil spring in lower layer of sand (b).....109
Figure 3.26: Typical track slab system with direct fixation.....112
Figure 3.27: Schematic illustration of track-structure-interaction layer.....112
Figure 3.28: Elevation view for the Track-Structure-Foundation-Soil Interaction (TSFSI) system.....113
Figure 3.29: Infinite long track supported on bilinear fasteners.....115
Figure 3.30: Monotonic static pushover curve.....115
Figure 3.31: Elastic/Plastic zone of fasteners: (a) deformation in the fasteners, and (b) number of fasteners in the elastic and plastic zones.....116
Figure 3.32: Multiple Series-Parallel Spring (MSPS) model.....117
Figure 3.33: Cyclic push-over curve comparison between the physical substructure model and the MSPS (S-P) model.....118
Figure 3.34: Abutment substructure system considered for the hysteretic and dynamic behavior.....119
Figure 3.35: Force-displacement relationship of abutment resistance to bridge end.....119
Figure 3.36: Relative displacement of the abutment mass node with respect to free field ground.....120
Figure 3.37: Abutment backfill resistance during the earthquake loading.....121
Figure 3.38: Relative displacement of the bridge deck node with/without accounting for the abutment mass in longitudinal direction.....122
Figure 3.39: Model for single pier column founded on pile group foundation and the moment curvature relationship of the pier column and the pile.....123
Figure 3.40: Monotonic pushover curve of the single pier column with pile group foundation (in red) compared with rigid base (in blue).....124
Figure 3.41: The pier column deformation with contribution decompositions from foundation and column deformation at different time steps: (a)time step at limit state S_1, (b) time step at limit state S_2, and (c) ultimate time step.....125
Figure 3.42: Pile response profile corresponding to different time step during the monotonic pushover analysis: (a) pile deformation, (b) pile bending moment, and (c) pile shear force.....126

Figure 3.43: Force deformation in soil springs at different depths below the ground surface with markers corresponding to the limit states of the pier column bottom section defined in the monotonic pushover analysis 127
Figure 3.44: Cyclic pushover curve of the single pier column with pile group foundation (solid line) compared with rigid base (dashed line) 127
Figure 3.45: Force deformation relationship in soil springs at different depths below the ground surface under cyclic pushover analysis 128
Figure 3.46: Soil profile for the CHSR Prototype Bridge located at San Jose Site.....130
Figure 3.47: Soil shear modulus reduction curve (left) and damping curve (right) 131
Figure 3.48: Physical interpretation for Rayleigh Damping in uniform acceleration loading formulation (a) and multiple support displacement loading formulation (b) 142
Figure 3.49: SDOF system with stiffness proportional damping 144
Figure 3.50: SDOF system with mass proportional damping 144
Figure 3.51: Substructure models of the single pier column founded on pile group foundation modeled using dynamic p-y approach 145
Figure 3.52: Convergence study of time step on substructure system with stiffness proportional damping (2%) 146
Figure 3.53: Convergence study on the consistence of multiple supports excitation loading with uniform acceleration loading on substructure system with stiffness proportional damping (2%) 147
Figure 3.54: Convergence study on the consistence of MSE loading with uniform acceleration loading on substructure system with mass proportional damping (2%).....148
Figure 3.54: Convergence study on the consistence of MSE loading with uniform acceleration loading on substructure system with mass proportional damping (2%).....149
Figure 3.56: Radiation effect study on substructure system with both stiffness proportional and mass proportional Rayleigh damping (2%): earthquake ground motion scaled by 0.5 150
Figure 3.57: Radiation effect study on substructure system with both stiffness proportional and mass proportional Rayleigh damping (2%): earthquake ground motion unscaled…. 150
Figure 3.58: Convergence study on the consistence of MSE loading with uniform acceleration loading (MCE) on CHSR Bridge system with stiffness proportional damping (2%):

transversal displacement of deck over pier #5 (top plot) and transversal displacement of pier #5 top node (bottom plot) 152
Figure 3.59: Convergence study on the consistence of MSE loading with uniform acceleration loading (MCE) on CHSR Bridge system with stiffness proportional damping (2%): longitudinal displacement of deck over pier #5 (top plot) and longitudinal displacement of pier #5 top node (bottom plot) 153
Figure 3.60: Convergence study on the consistence of MSE loading with uniform acceleration loading (MCE) on CHSR Bridge system with mass proportional damping (2%): transversal displacement of deck over pier #5 (top plot) and transversal displacement of pier #5 top node (bottom plot) 153
Figure 3.61: Convergence study on the consistence of MSE loading with uniform acceleration loading (MCE) on CHSR Bridge system with mass proportional damping (2%): longitudinal displacement of deck over pier #5 (top plot) and longitudinal displacement of pier #5 top node (bottom plot) 154
Figure 3.62: Convergence study on the consistence of MSE loading with uniform acceleration loading (MCE) on CHSR Bridge system with both stiffness and mass proportional damping (2%): transversal displacement of deck over pier #5 (top plot) and transversal displacement of pier #5 top node (bottom plot) 155
Figure 3.63: Convergence study on the consistence of MSE loading with uniform acceleration loading (MCE) on CHSR Bridge system with both stiffness and mass proportional damping (2%): longitudinal displacement of deck over pier #5 (top plot) and longitudinal displacement of pier #5 top node (bottom plot) 155
Figure 3.64: Convergence study on the consistence of MSE loading with uniform acceleration loading (OBE) on CHSR Bridge system with both stiffness and mass proportional damping (2%): transversal displacement of deck over pier #5 (top plot) and transversal displacement of pier #5 top node (bottom plot) 156
Figure 3.65: Convergence study on the consistence of MSE loading with uniform acceleration loading on CHSR Bridge system with both stiffness and mass proportional damping (2%): longitudinal displacement of deck over pier #5 (top plot) and longitudinal displacement of pier #5 top node (bottom plot) 157
Figure 4.1: Geometric mean spectra comparison of the selected and scaled ground motion for MCE hazard level: (a) NGA#832, and (b) NGA#183.....166

Figure 4.2: Components spectra comparison of the selected and scaled ground motion for MCE hazard level: (a) NGA#823 (left), and (b) NGA#183.....167
Figure 4.3: Time histories of ground motion record (NGA#832, FP component, MCE) 168
Figure 4.4: Time histories of ground motion record (NGA#832, FN component, MCE).....168
Figure 4.5: Time histories of ground motion record (NGA#183, FP component, MCE) 169
Figure 4.6: Time histories of ground motion record (NGA#183, FN component, MCE).....169
Figure 4.7: Response spectra (5% damped) of NGA#832: (a) acceleration spectra, and (b) displacement spectra.....170
Figure 4.8: Force-deformation response of seismic isolator #3 over pier #1 and isolator #13 over pier #5 under (a) NGA#832 and (b) NGA#183.....171
Figure 4.9: Absolute acceleration of deck over pier #5 under (a) NGA#832 and (b) NGA#183 of OBE hazard level 172
Figure 4.10: Relative displacement of deck (w.r.t. pile cap) over pier #5 (a) NGA#832 and (b) NGA#183 of OBE hazard level.....172
Figure 4.11: Relative displacement of the top of pier #5 under (a) NGA#832 and (b) NGA#183 of OBE hazard level.....173
Figure 4.12: Total base shear force across all piers under (a) NGA#832 and (b) NGA#183 of OBE hazard level.....173
Figure 4.13: Total base shear force across all piers and bearings under (a) NGA#832 and (b) NGA#183 of OBE hazard level.....174
Figure 4.14: Total base shear force across all piers and bearings plus pounding force under (a) NGA#832 and (b) NGA#183 of OBE hazard level.....174
Figure 4.15: Relative translation of pile foundation cap under pier #5 w.r.t. free-field ground surface under (a) NGA#832 and (b) NGA#183 of OBE hazard level.....175
Figure 4.16: Pile Foundation response under (a) NGA#832 and (b) NGA#183 of OBE hazard level 176
Figure 4.17: Envelope of peak rail stress due to axial force under (a) NGA#832 and (b) NGA#183 of OBE hazard level.....177
Figure 4.18: Envelope of peak rail stress due to axial force and bending under (a) NGA#832 and (b) NGA#183 of OBE hazard level 178
Figure 4.19: Total base shear force across all piers under (a) NGA#832 and (b) NGA#183 of MCE hazard level.....179

Figure 4.20: Relative translation of pile foundation cap w.r.t. free-field ground surface under (a) NGA#832 and (b) NGA#183 of MCE hazard level.....179
Figure 4.21: Envelope of peak rail stress due to axial force and bending under (a) NGA#832 and (b) NGA#183 of MCE hazard level.....180
Figure 4.22: Comparison of the maximum deformation in the (a) longitudinal direction and (b) transverse directions of all isolators (bearings) 181
Figure 4.23: Comparison of the maximum absolute acceleration in the (a) longitudinal and (b) transverse directions of bridge deck.....182
Figure 4.24: Abutment gap pounding: (a) occurrence #, (b) pounding force.....182
Figure 4.25: Comparison of maximum pier column base shear force in the (a) longitudinal and (b) transverse directions 183
Figure 4.26: Comparison of (a) maximum normalized pile cap rotation and (b) maximum pile moment around the transverse direction.....183
Figure 4.27: Comparison of rail stresses (a) due to axial force and (b) due to both axial and bending.....184
Figure 5.1: Average shear wave velocity in the top 30 meters.....190
Figure 5.2: Hazard spectrum surface for downtown area of San Jose, California. 191
Figure 5.3: Probabilistic seismic hazard curves for both the IB and NIB 192
Figure 5.4: Probabilistic seismic hazard de-aggregation for San Jose (121.903W, 37.330N) at Sa (T = 1.0, ξ = 5%) for probability of exceedance of 2% in 50 years 193
Figure 5.5: Probabilistic seismic hazard de-aggregation for San Jose (121.903W, 37.330N) at Sa (T = 1.0, ξ = 5%) for probability of exceedance of 10% in 100 years 193
Figure 5.6: Probabilistic seismic hazard de-aggregation for San Jose (121.903W, 37.330N) at Sa (T = 1.0, ξ = 5%) for probability of exceedance of 50% in 50 years 193
Figure 5.7: Ground motions scaling for the stripe method to target 7 hazard levels: (a) IB, and (b) NIB 196
Figure 5.8: Comparison of absolute acceleration of bridge deck over pier #5 with mean value lines (IB: circular markers; NIB: triangular markers) 199
Figure 5.9: Comparison of RMS of absolute acceleration of bridge deck over pier #5 with mean lines (IB: circular markers; NIB: triangular markers).....199
Figure 5.10: Comparison of relative displacement of bridge deck over pier #5 w.r.t. ground surface with mean lines (IB: circular markers; NIB: triangular markers).....200

Figure 5.11: Deformation of seismic isolators over pier #5 with mean lines for IB model (with resultant displacement denoted by circular unfilled markers).....201
Figure 5.12: Comparison of relative displacement of top of pier #5 w.r.t. pile foundation cap with mean lines (IB: circular markers; NIB: triangular markers) 201
Figure 5.13: Comparison of peak base shear in pier column #5 with mean lines (IB: circular markers; NIB: triangular markers) 202
Figure 5.14: Comparison of total base shear force across all pier columns with mean lines (IB: circular markers; NIB: triangular markers) 202
Figure 5.15: Comparison of total horizontal reaction (total base shear force + pounding force) with mean lines (IB: circular markers; NIB: triangular markers) 203
Figure 5.16: Comparison of maximum pile cap translation of foundation under pier #5 with mean lines (IB: circular markers; NIB: triangular markers).....203
Figure 5.17: Comparison of maximum pile cap rotation of foundation under pier #5 with mean lines (IB: circular markers; NIB: triangular markers).....204
Figure 5.18: Comparison of maximum bending moment demand in piles of foundation under pier #5 with mean lines (IB: circular markers; NIB: triangular markers) 204
Figure 5.19: Comparison of maximum shear force demand in piles of foundation under pier #5 with mean lines (IB: circular markers; NIB: triangular markers) 205
Figure 5.20: Comparison of maximum rail stress at left abutment gap due to axial force (left) and transverse bending (right) with mean lines (IB: circular markers; NIB: triangular markers) 206
Figure 5.21: Comparison of maximum rail stress at interior expansion joint gap due to axial force (left) and transverse bending (right) with mean lines (IB: circular markers; NIB: triangular markers) 206
Figure 5.22: Comparison of absolute acceleration of bridge deck over pier #5 with mean value lines (IB: circular markers; NIB: triangular markers) 207
Figure 5.23: Comparison of RMS of absolute acceleration of bridge deck over pier #5 with mean lines (IB: circular markers; NIB: triangular markers).....208
Figure 5.24: Comparison of relative displacement of bridge deck over pier #5 w.r.t. field ground surface with mean lines (IB: circular markers; NIB: triangular markers)…….....208

Figure 5.25: Deformation of seismic isolators over pier #5 with mean lines for IB model (with resultant displacement denoted by circular unfilled markers).....209
Figure 5.26: Comparison of relative displacement of top of pier #5 w.r.t. field ground surface with mean lines (IB: circular markers; NIB: triangular markers) 209
Figure 5.27: Comparison of peak base shear in pier column #5 with mean lines (IB: circular markers; NIB: triangular markers) 210
Figure 5.28: Comparison of total shear force across all pier columns and abutment bearings with mean lines (IB: circular markers; NIB: triangular markers) 210
Figure 5.29: Comparison of total horizontal reaction force with mean lines (IB: circular markers; NIB: triangular markers) 211
Figure 5.30: Comparison of maximum pile cap translation of foundation under pier #5 with mean lines (IB: circular markers; NIB: triangular markers).....211
Figure 5.31: Comparison of maximum pile cap rotation of foundation under pier #5 with mean lines (IB: circular markers; NIB: triangular markers).....212
Figure 5.32: Comparison of maximum bending moment demand in piles of foundation under pier #5 with mean lines (IB: circular markers; NIB: triangular markers) 212
Figure 5.33: Comparison of maximum shear force demand in piles of foundation under pier #5 with mean lines (IB: circular markers; NIB: triangular markers) 212
Figure 5.34: Conditional PSDHA results with the stripe method for the absolute deck acceleration over pier #5 in long. dir. (x) for IB (left) and NIB (right).....215
Figure 5.35: Comparison of conditional probabilistic properties of demand for all seismic hazard levels (left) and conditional CCDF given representative seismic hazard level (right) on absolute deck acceleration over pier #5 in long. dir. (x). 215
Figure 5.36: Conditional PSDHA results: conditional PDF of absolute deck acceleration over pier #5 in trans. dir. for IB (left) and NIB (right).....215
Figure 5.37: Comparison of conditional probabilistic properties of demand for all seismic hazard levels (left) and conditional CCDF given representative seismic hazard level (right) on absolute deck acceleration over pier #5 in trans. dir. (y).....216
Figure 5.38: Comparison of conditional probabilistic properties of demand for all seismic hazard levels (left) and conditional CCDF given representative seismic hazard level (right) on relative deck displacement over pier #5 in long. dir. (x).....216

Figure 5.39: Comparison of conditional probabilistic properties of demand for all seismic hazard levels (left) and conditional CCDF given representative seismic hazard level (right) on relative deck displacement over pier #5 in trans. dir. (y) 216
Figure 5.40: Conditional PSDHA results: conditional PDF of isolator deformation over pier #5 in the long. dir. (x) and trans. dir. (y) for IB.....217
Figure 5.41: Comparison of conditional probabilistic properties of demand for all seismic hazard levels (left) and conditional CCDF given representative seismic hazard level (right) on isolator deformation over pier #5 in long. dir. (x) 217
Figure 5.42: Comparison of conditional probabilistic properties of demand for all seismic hazard levels (left) and conditional CCDF given representative seismic hazard level (right) on isolator deformation over pier #5 in trans. dir. (y) 218
Figure 5.43: Comparison of conditional probabilistic properties of demand for all seismic hazard levels (left) and conditional CCDF given representative hazard level (right) on pier column drift of pier #5 w.r.t. pile cap in long. dir. (x) 218
Figure 5.44: Comparison of conditional probabilistic properties of demand for all seismic hazard levels (left) and conditional CCDF given representative seismic hazard level (right) on pier column drift of pier #5 w.r.t. pile cap in trans. dir. (y).....218
Figure 5.45: Comparison of conditional probabilistic properties of demand for all seismic hazard levels (left) and conditional CCDF given representative seismic hazard level (right) on column base moment of pier #5 in long. dir. (x) 219
Figure 5.46: Comparison of conditional probabilistic properties of demand for all seismic hazard levels (left) and conditional CCDF given representative seismic hazard level (right) on column base moment of pier #5 in trans. dir. (y) 219
Figure 5.47: Comparison of conditional probabilistic PDF for column base moment and the relative end rotation of bottom element in pier #5 in the trans. dir. (y).....220
Figure 5.48: Comparison of conditional probabilistic properties of demand for all hazard levels (left) and conditional CCDF given representative hazard level (right) on column base shear force of pier #5 in long. dir. (x) 221
Figure 5.49: Comparison of conditional probabilistic properties of demand for all hazard levels (left) and conditional CCDF given representative hazard level (right) on column base shear force of pier #5 in trans. dir. (y).....221

Figure 5.50: Comparison of conditional probabilistic properties of demand for all hazard levels (left) and conditional CCDF given representative hazard level (right) on total base shear force in long. dir. (x) 222
Figure 5.51: Comparison of conditional probabilistic properties of demand for all hazard levels (left) and conditional CCDF given representative hazard level (right) on total base shear force in trans. dir. (y) 222
Figure 5.52: Comparison of conditional probabilistic properties of demand for all hazard levels (left) and conditional CCDF given representative hazard level (right) on pile cap displacement of foundation under pier #5 in long. dir. (x) 223
Figure 5.53: Comparison of conditional probabilistic properties of demand for all hazard levels (left) and conditional CCDF given representative hazard level (right) on pile cap displacement of foundation under pier #5 in trans. dir. (y) 223
Figure 5.54: Comparison of conditional probabilistic properties of demand for all hazard levels (left) and conditional CCDF given representative hazard level (right) on pile cap rotation of foundation under pier #5 in long. dir. (x) 224
Figure 5.55: Comparison of conditional probabilistic properties of demand for all hazard levels (left) and conditional CCDF given representative hazard level (right) on pile cap rotation of foundation under pier #5 in trans. dir. (y) 224
Figure 5.56: Comparison of conditional probabilistic properties of demand for all hazard levels (left) and conditional CCDF given representative hazard level (right) on bending moment of piles under pier #5 in long. dir. (x) 225
Figure 5.57: Comparison of conditional probabilistic properties of demand for all hazard levels (left) and conditional CCDF given representative hazard level (right) on bending moment of piles under pier #5 in trans. dir. (y) 225
Figure 5.58: Comparison of conditional probabilistic properties of demand for all hazard levels (left) and conditional CCDF given representative hazard level (right) on shear force of piles under pier #5 in long. dir. (x) 226
Figure 5.59: Comparison of conditional probabilistic properties of demand for all hazard levels (left) and conditional CCDF given representative hazard level (right) on shear force of piles under pier #5 in trans. dir. (y) 226

Figure 5.60: Comparison of conditional probabilistic properties of demand for all hazard levels (left) and conditional CCDF given representative hazard level (right) on rail stress at abutment expansion joint #1 due to axial force in long. dir. (x).....227
Figure 5.61: Comparison of conditional probabilistic properties of demand for all hazard levels (left) and conditional CCDF given representative hazard level (right) on rail stress at abutment expansion joint #1 due to bending in trans. dir. (y) 227
Figure 5.62: Comparison of conditional probabilistic properties of demand for all hazard levels (left) and conditional CCDF given representative hazard level (right) on rail stress at interior expansion joint #2 due to axial force in long. dir. (x).....228
Figure 5.63: Comparison of conditional probabilistic properties of demand for all hazard levels (left) and conditional CCDF given representative hazard level (right) on rail stress at interior expansion joint #2 due to bending in trans. dir. (y) 228
Figure 5.64: Probabilistic seismic demand hazard curve and de-aggregation of absolute deck acceleration over pier #5 in the long. dir. (x). 229
Figure 5.65: Probabilistic seismic demand hazard curve and de-aggregation of absolute deck acceleration over pier #5 in the trans. dir. (y).....230
Figure 5.66: Probabilistic seismic demand hazard curve of absolute deck acceleration over pier #5 in the long. dir. (left) and in the trans. dir. (right) 230
Figure 5.67: Probabilistic seismic demand hazard curve of relative deck displacement over pier #5 in the long. dir. (left) and in the trans. dir. (right) 231
Figure 5.68: Probabilistic seismic demand hazard curve and de-aggregation of isolator deformation over pier #5 231
Figure 5.69: Probabilistic seismic demand hazard curve of pier column drift of pier #5 w.r.t. pile cap in the long. dir. (left) and in the trans. dir. (right).....232
Figure 5.70: Probabilistic seismic demand hazard curve of column base moment of pier #5 in the long. dir. (left) and in the trans. dir. (right) 233
Figure 5.71: Probabilistic seismic demand hazard of column base shear force of pier #5 in the long. dir. (left) and in the trans. dir. (right) 233
Figure 5.72: Probabilistic seismic demand hazard curve of total base shear force in the long. dir. (left) and in the trans. dir. (right) 233
Figure 5.73: Probabilistic seismic demand hazard curve of total horizontal reaction force in the long. dir. (left) and in the trans. dir. (right) 234

Figure 5.74: Probabilistic seismic demand hazard curve comparison between total shear force and total horizontal reaction force in longitudinal dir. (x) 234
Figure 5.75: Probabilistic seismic demand hazard curve comparison between total shear force and total horizontal reaction force in transverse dir. (y).....235
Figure 5.76: Probabilistic seismic demand hazard curve of pile cap displacement of foundation under pier #5 in the long. dir. (left) and in the trans. dir. (right) 236
Figure 5.77: Probabilistic seismic demand hazard curve of pile cap rotation of foundation under pier #5 in the long. dir. (left) and in the trans. dir. (right) 236
Figure 5.78: Probabilistic seismic demand hazard curve of bending moment of piles under pier #5 in the long. dir. (left) and in the trans. dir. (right) 237
Figure 5.79: Probabilistic seismic demand hazard curve of shear force of piles under pier #5 in the long. dir. (left) and in the trans. dir. (right) 237
Figure 5.80: Probabilistic seismic demand hazard curve of rail stress at abutment expansion joint #1 due to axial force in the long. dir. (left) and in the trans. dir. (right) 238
Figure 5.81: Probabilistic seismic demand hazard curve of rail stress at interior expansion joint #2 due to axial force in long. dir. (left) and bending in trans. dir. (right).....238
Figure 5.82: Conditional PSDHA results: conditional PDF of absolute deck acceleration over pier #5 in long. dir. (x) for IB (left) and NIB (right) 242
Figure 5.83: Comparison of conditional probabilistic properties of demand for all hazard levels (left) and conditional CCDF for representative hazard level (right) on the absolute deck acceleration over pier #5 in long. dir. (x). 242
Figure 5.84: Conditional probabilistic demand hazard analysis results: conditional PDF of absolute deck acceleration over pier #5 in trans. dir. for IB (left) and NIB (right)242
Figure 5.85: Comparison of conditional probabilistic properties of demand for all hazard levels (left) and conditional CCDF given representative hazard level (right) on absolute deck acceleration over pier #5 in trans. dir. (y).....243
Figure 5.86: Comparison of conditional probabilistic properties of demand for all hazard levels (left) and conditional CCDF for representative hazard levels (right) on relative deck displacement over pier #5 in long. dir. (x).....243
Figure 5.87: Comparison of conditional probabilistic properties of demand for all hazard levels (left) and conditional CCDF given representative hazard level (right) on relative deck displacement over pier #5 in trans. dir. (y) 244

Figure 5.88: Conditional PSDHA results: conditional PDF of isolator deformation over pier #5 in long. dir. (left) and transverse dir. (right) for IB 244
Figure 5.89: Comparison of conditional probabilistic properties of demand for all hazard levels (left) and conditional CCDF given representative hazard level (right) on isolator deformation over pier #5 in long. dir. (x).....245
Figure 5.90: Comparison of conditional probabilistic properties of demand for all hazard levels (left) and conditional CCDF given representative hazard level (right) on isolator deformation over pier #5 in trans. dir. (y) 245
Figure 5.91: Comparison of conditional probabilistic properties of demand for all hazard levels (left) and conditional CCDF given representative hazard level (right) on pier column drift of pier #5 w.r.t. pile cap in long. dir. (x).....246
Figure 5.92: Comparison of conditional probabilistic properties of demand for all hazard levels (left) and conditional CCDF given representative hazard level (right) on pier column drift of pier #5 w.r.t. pile cap in trans. dir. (y).....246
Figure 5.93: Comparison of conditional probabilistic properties of demand for all hazard levels (left) and conditional CCDF given representative hazard level (right) on column base moment of pier #5 in long. dir. (x).....247
Figure 5.94: Comparison of conditional probabilistic properties of demand for all hazard levels (left) and conditional CCDF given representative hazard level (right) on column base moment of pier #5 in long. dir. (x).....247
Figure 5.95: Comparison of conditional probabilistic properties of demand for all hazard levels (left) and conditional CCDF given representative hazard level (right) on column base shear force of pier #5 in long. dir. (x) 248
Figure 5.96: Comparison of conditional probabilistic properties of demand for all hazard levels (left) and conditional CCDF given representative hazard level (right) on column base shear force of pier #5 in trans. dir. (y).....248
Figure 5.97: Comparison of conditional probabilistic properties of demand for all hazard levels (left) and conditional CCDF given representative hazard level (right) on total base shear force in long. dir. (x).....249
Figure 5.98: Comparison of conditional probabilistic properties of demand for all hazard levels (left) and conditional CCDF given representative hazard level (right) on total base shear force in trans. dir. (y) 249

Figure 5.99: Comparison of conditional probabilistic properties of demand for all hazard levels (left) and conditional CCDF given representative hazard level (right) on pile cap displacement of foundation under pier #5 in long. dir. (x) 250
Figure 5.100: Comparison of conditional probabilistic properties of demand for all hazard levels (left) and conditional CCDF given representative hazard level (right) on pile cap displacement of foundation under pier #5 in trans. dir. (y)..... 250
Figure 5.101: Comparison of conditional probabilistic properties of demand for all hazard levels (left) and conditional CCDF given representative hazard level (right) on pile cap rotation of foundation under pier #5 in long. dir. (x)..... 251
Figure 5.102: Comparison of conditional probabilistic properties of demand for all hazard levels (left) and conditional CCDF given representative hazard level (right) on pile cap rotation of foundation under pier #5 in trans. dir. (y) 251
Figure 5.103: Comparison of conditional probabilistic properties of demand for all hazard levels (left) and conditional CCDF given representative hazard level (right) on bending moment of piles under pier #5 in long. dir. (x)..... 252
Figure 5.104: Comparison of conditional probabilistic properties of demand for all hazard levels (left) and conditional CCDF given representative hazard level (right) on bending moment of piles under pier #5 in trans. dir. (y)..... 252
Figure 5.105: Comparison of conditional probabilistic properties of demand for all hazard levels (left) and conditional CCDF given representative hazard level (right) on shear force of piles under pier #5 in long. dir. (x)..... 253
Figure 5.106: Comparison of conditional probabilistic properties of demand for all hazard levels (left) and conditional CCDF given representative hazard level (right) on shear force of piles under pier #5 in trans. dir. (y) 253
Figure 5.107: Comparison of conditional probabilistic properties of demand for all hazard levels (left) and conditional CCDF given representative hazard level (right) on rail stress at abutment expansion joint #1 due to axial force in long. dir. (x)..... 254
Figure 5.108: Comparison of conditional probabilistic properties of demand for all hazard levels (left) and conditional CCDF given representative hazard level (right) on rail stress at abutment expansion joint #1 due to bending in trans. dir. (y) 254

Figure 5.109: Comparison of conditional probabilistic properties of demand for all hazard levels (left) and conditional CCDF given representative hazard level (right) on rail stress at interior expansion joint #2 due to axial force in long. dir. (x) 255
Figure 5.110: Comparison of conditional probabilistic properties of demand for all hazard levels (left) and conditional CCDF given representative hazard level (right) on rail stress at interior expansion joint #2 due to bending in trans. dir. (y) 255
Figure 5.111: Comparison of cloud method with stripe method in terms of conditional demand statistics and PDF of absolute acceleration of deck over pier #5 in longitudinal direction for NIB (left) and IB (right) 257
Figure 5.112: Comparison of cloud method with stripe method in terms of conditional CCDF on two hazard levels of absolute acceleration of deck over pier #5 in longitudinal direction for NIB (left) and IB (right) 257
Figure 5.113: Comparison of cloud method with stripe method in terms of unconditional probabilistic seismic demand hazard of absolute acceleration of deck over pier #5 in longitudinal direction for NIB (left) and IB (right) 257
Figure 5.114: Comparison of cloud method with stripe method in terms of conditional demand statistics and PDF of absolute acceleration of deck over pier #5 in transverse direction for NIB (left) and IB (right) 258
Figure 5.115: Comparison of cloud method with stripe method in terms of conditional CCDF on two hazard levels of absolute acceleration of deck over pier #5 in transverse direction for NIB (left) and IB (right) 258
Figure 5.116: Comparison of cloud method with stripe method in terms of unconditional probabilistic seismic demand hazard of absolute acceleration of deck over pier #5 in transverse direction for NIB (left) and IB (right) 259
Figure 5.117: Comparison of cloud method with stripe method in terms of conditional demand statistics and PDF of relative displacement of deck over pier #5 in longitudinal direction for NIB (left) and IB (right) 260
Figure 5.118: Comparison of cloud method with stripe method in terms of conditional CCDF on two hazard levels of relative displacement of deck over pier #5 in longitudinal direction for NIB (left) and IB (right) 260

Figure 5.119: Comparison of cloud method with stripe method in terms of unconditional probabilistic seismic demand hazard of relative displacement of deck over pier #5 in longitudinal direction for NIB (left) and IB (right) 260
Figure 5.120: Comparison of cloud method with stripe method in terms of conditional demand statistics and PDF of relative displacement of deck over pier #5 in transverse direction for NIB (left) and IB (right) 261
Figure 5.121: Comparison of cloud method with stripe method in terms of conditional CCDF on two hazard levels of relative displacement of deck over pier #5 in transverse direction for NIB (left) and IB (right) 261
Figure 5.122: Comparison of cloud method with stripe method in terms of unconditional probabilistic seismic demand hazard of relative displacement of deck over pier #5 in transverse direction for NIB (left) and IB (right) 262
Figure 5.123: Comparison of cloud method with stripe method in terms of conditional demand statistics and PDF of column base shear of pier #5 in longitudinal direction for NIB (left) and IB (right) 262
Figure 5.124: Comparison of cloud method with stripe method in terms of conditional CCDF on two hazard levels of column base shear force of pier #5 in longitudinal direction for NIB (left) and IB (right) 263
Figure 5.125: Comparison of cloud method with stripe method in terms of unconditional probabilistic seismic demand hazard of column base shear force of pier #5 in longitudinal direction for NIB (left) and IB (right) 263
Figure 5.126: Comparison of cloud method with stripe method in terms of conditional demand statistics and PDF of column base shear force of pier #5 in transverse direction for NIB (left) and IB (right) 264
Figure 5.127: Comparison of cloud method with stripe method in terms of conditional CCDF on two hazard levels of column base shear force of pier #5 in transverse direction for NIB (left) and IB (right) 264
Figure 5.128: Comparison of cloud method with stripe method in terms of unconditional probabilistic seismic demand hazard of column base shear force of pier #5 in transverse direction for NIB (left) and IB (right) 264

Figure 5.129: Comparison of cloud method with stripe method in terms of conditional demand statistics and PDF of maximum moment of piles under pier #5 in longitudinal direction for NIB (left) and IB (right) 265
Figure 5.130: Comparison of cloud method with stripe method in terms of conditional CCDF on two hazard levels of maximum moment of piles under pier #5 in longitudinal direction for NIB (left) and IB (right) 265
Figure 5.131: Comparison of cloud method with stripe method in terms of unconditional probabilistic seismic demand hazard of maximum moment of piles under pier #5 in longitudinal direction for NIB (left) and IB (right) 266
Figure 5.132: Comparison of cloud method with stripe method in terms of conditional demand statistics and PDF of maximum moment of piles under pier #5 in transverse direction for NIB (left) and IB (right) 266
Figure 5.133: Comparison of cloud method with stripe method in terms of conditional CCDF on two hazard levels of maximum moment of piles under pier #5 in transverse direction for NIB (left) and IB (right) 267
Figure 5.134: Comparison of cloud method with stripe method in terms of unconditional probabilistic seismic demand hazard of maximum moment of piles under pier #5 in transverse direction for NIB (left) and IB (right) 267
Figure 6.1: Cloud-based probabilistic optimization (CBO) workflow 274
Figure 6.2: Bilinear isolator design alternatives with a fixed post-yield stiffness ratio (left) and categories (right) 279
Figure 6.3: 4D plot of conditional median demand of absolute deck acceleration based on the single isolator model 280
Figure 6.4: Conditional median demand of absolute deck acceleration based on the single isolator model for seismic isolator with b = 0.0 280
Figure 6.5: Conditional median demand of absolute deck acceleration based on the single isolator model for seismic isolator with b = 0.05 281
Figure 6.6: Conditional median demand of absolute deck acceleration based on the single isolator model with b = 0. 10 281
Figure 6.7: 4D plot of conditional median demand of isolator deformation based on the single isolator model 282

Figure 6.8: Conditional median demand of isolator deformation based on the single isolator model with b = 0.0.....283
Figure 6.9: Conditional median demand of isolator deformation based on the single isolator model with b = 0.05.....283
Figure 6.10: Conditional median demand of isolator deformation based on the single isolator model with b = 0. 10.....284
Figure 6.11: 4D plot of conditional median demand of base shear force based on the single isolator model.....285
Figure 6.12: Conditional median demand of base shear force based on the single isolator model with b = 0.0.....285
Figure 6.13: Conditional median demand of base shear force based on the single isolator model with b = 0.05.....286
Figure 6.14: Conditional median demand of base shear force based on the single isolator model with b = 0. 10.....286
Figure 7.1: Earthquake selection and scaling for “cloud method” for the IB.....295
Figure 7.2: Earthquake selection and scaling for “cloud method” for the NIB.....295
Figure 7.3: Risk feature illustration in the context of conditional demand hazard.....298
Figure 7.4: Risk feature illustration in the context of seismic demand hazard.....300
Figure 7.5: Risk feature: conditional mean demand of absolute deck acceleration over pier #5 in the longitudinal direction at OBE hazard level 304
Figure 7.6: Risk feature: conditional mean demand of absolute deck acceleration over pier #5 in the transverse direction at OBE hazard level 305
Figure 7.7: Risk feature: conditional mean demand of relative deck displacement over pier #5 in the transverse direction at OBE hazard level 306
Figure 7.8: Risk feature: conditional mean demand of isolator deformation over pier #5 in the transverse direction at OBE hazard level 306
Figure 7.9: Risk feature: conditional mean demand of pier column drift of pier #5 w.r.t. pile cap in the longitudinal direction at OBE hazard level.....307
Figure 7.10: Risk feature: conditional mean demand of pier column drift of pier #5 w.r.t. pile cap in the transverse direction at OBE hazard level.....308
Figure 7.11: Risk feature: conditional mean demand of column base moment of pier #5 in the longitudinal direction at OBE hazard level 309

Figure 7.12: Risk feature: conditional mean demand of column base moment of pier #5 in the transverse direction at OBE hazard level 309
Figure 7.13: Risk feature: conditional mean demand of total base shear force in the longitudinal direction at OBE hazard level 310
Figure 7.14: Risk feature: conditional mean demand of total base shear force in the transverse direction at OBE hazard level.....310
Figure 7.15: Risk feature: conditional mean demand of pile cap displacement of foundation under pier #5 in the longitudinal direction at OBE hazard level.....311
Figure 7.16: Risk feature: conditional mean demand of pile cap displacement of foundation under pier #5 in the transverse direction at OBE hazard level.....311
Figure 7.17: Risk feature: conditional mean demand of pile cap rotation of foundation under pier #5 in the longitudinal direction at OBE hazard level.....312
Figure 7.18: Risk feature: conditional mean demand of pile cap rotation of foundation under pier #5 in the transverse direction at OBE hazard level.....312
Figure 7.19: Risk feature: conditional mean demand of bending moment of piles under pier #5 in the longitudinal direction at OBE hazard level 313
Figure 7.20: Risk feature: conditional mean demand of bending moment of piles under pier #5 in the transverse direction at OBE hazard level 313
Figure 7.21: Risk feature: conditional mean demand of shear force of piles under pier #5 in the longitudinal direction at OBE hazard level 314
Figure 7.22: Risk feature: conditional mean demand of shear force of piles under pier #5 in the transverse direction at OBE hazard level 314
Figure 7.23: Risk feature: conditional mean demand of rail stress at abutment expansion joint #1 due to axial at OBE hazard level.....316
Figure 7.24: Risk feature: conditional mean demand of rail stress at abutment expansion joint #1 due to bending in the transverse direction at OBE hazard level.....317
Figure 7.25: Risk feature: conditional mean demand of rail stress at interior expansion joint #2 due to axial at OBE hazard level.....317
Figure 7.26: Risk feature: conditional mean demand of rail stress at interior expansion joint #2 due to bending in the transverse direction at OBE hazard level.....318
Figure 7.27: Risk feature: conditional median demand of column base moment of pier #5 in the transverse direction at OBE hazard level 319

Figure 7.28: Risk feature: 95th percentile of conditional demand of column base moment of pier #5 in the transverse direction at OBE hazard level 319
Figure 7.29: Risk feature: conditional demand c.o.v. of column base moment of pier #5 in the transverse direction at OBE hazard level 320
Figure 7.30: Risk feature: conditional mean demand of absolute deck acceleration over pier #5 in the longitudinal direction at MCE hazard level.....322
Figure 7.31: Risk feature: conditional mean demand of absolute deck acceleration over pier #5 in the transverse direction at MCE hazard level.....322
Figure 7.32: Risk feature: conditional mean demand of relative deck displacement over pier #5 in the longitudinal direction at MCE hazard level.....323
Figure 7.33: Risk feature: conditional mean demand of relative deck displacement over pier #5 in the transverse direction at MCE hazard level.....323
Figure 7.34: Risk feature: conditional mean demand of column base moment of pier #5 in the longitudinal direction at MCE hazard level.....324
Figure 7.35: Risk feature: conditional mean demand of column base moment of pier #5 in the longitudinal direction at MCE hazard level.....324
Figure 7.36: Risk feature: conditional mean demand of total base shear force in the longitudinal direction at MCE hazard level.....325
Figure 7.37: Risk feature: conditional mean demand of total base shear force in the transverse direction at MCE hazard level.....325
Figure 7.38: Risk feature: conditional mean demand of pile cap displacement of foundation under pier #5 in the longitudinal direction at MCE hazard level 326
Figure 7.39: Risk feature: conditional mean demand of pile cap displacement of foundation under pier #5 in the transverse direction at MCE hazard level 327
Figure 7.40: Risk feature: conditional mean demand of pile cap rotation of foundation under pier #5 in the longitudinal direction at MCE hazard level 327
Figure 7.41: Risk feature: conditional mean demand of pile cap rotation of foundation under pier #5 in the transverse direction at MCE hazard level.....328
Figure 7.42: Risk feature: conditional mean demand of bending moment of piles under pier #5 in the longitudinal direction at MCE hazard level.....328
Figure 7.43: Risk feature: conditional mean demand of bending moment of piles under pier #5 in the transverse direction at MCE hazard level.....329

Figure 7.44: Risk feature: conditional mean demand of shear force of piles under pier #5 in the longitudinal direction at MCE hazard level.....329
Figure 7.45: Risk feature: conditional mean demand of shear force of piles under pier #5 in the transverse direction at MCE hazard level.....330
Figure 7.46: Parametric illustration of probabilistic seismic demand hazard curve of the absolute deck acceleration over pier #5 in the long. (left) and trans. (right) directions.....331
Figure 7.47: Risk feature: the unconditional demand of hazard level PE100 = 86% (i.e., RP = 50 yrs.) on the absolute deck acceleration over pier #5 in the long. dir.....332
Figure 7.48: Risk feature: the unconditional demand of hazard level PE100 = 10% (i.e., RP = 950 yrs.) on the absolute deck acceleration over pier #5 in the long. dir.....333
Figure 7.49: Risk feature: the unconditional demand of hazard level PE100 = 86% (i.e., RP = 50 yrs.) on absolute deck acceleration over pier #5 in the trans. dir. 333
Figure 7.50: Risk feature: the unconditional demand of hazard level PE100 = 10% (i.e., RP = 950 yrs.) on absolute deck acceleration over pier #5 in the trans. dir. 334
Figure 7.51: Parametric illustration of probabilistic seismic demand hazard curve of the relative deck displacement over pier #5 in the long. (left) and trans. (right) directions.....335
Figure 7.52: Risk feature: the unconditional demand of hazard level PE100 = 86% (i.e., RP = 50 yrs.) on relative deck displacement over pier #5 in the long. dir.....335
Figure 7.53: Risk feature: the unconditional demand of hazard level PE100 = 10% (i.e., RP = 950 yrs.) on relative deck displacement over pier #5 in the long. dir.....336
Figure 7.54: Risk feature: the unconditional demand of hazard level PE100 = 86% (i.e., RP = 50 yrs.) on relative deck displacement over pier #5 in the trans. dir.....336
Figure 7.55: Risk feature: the unconditional demand of hazard level PE100 = 10% (i.e., RP = 950 yrs.) on relative deck displacement over pier #5 in the trans. dir.....337
Figure 7.56: Parametric illustration of probabilistic seismic demand hazard curve of isolator deformation over pier #5 in the long. (left) and trans. (right) directions.....338
Figure 7.57: Risk feature: the unconditional demand of hazard level PE100 = 86% (i.e., RP = 50 yrs.) on isolator deformation over pier #5 in the long. dir.....338
Figure 7.58: Risk feature: the unconditional demand of hazard level PE100 = 10% (i.e., RP = 100 yrs.) on isolator deformation over pier #5 in the long. dir.....339

Figure 7.59: Risk feature: unconditional demand of hazard level PE100 = 86% (i.e., RP = 50 yrs.) on isolator deformation over pier #5 in the trans. dir. 339
Figure 7.60: Risk feature: unconditional demand of hazard level PE100 = 10% (i.e., RP = 950 yrs.) on isolator deformation over pier #5 in the trans. dir. 340
Figure 7.61: Parametric illustration of probabilistic seismic demand hazard curve of pier column drift of pier #5 w.r.t. pile cap in the long. (left) and trans. (right) directions… 341
Figure 7.62: Risk feature: unconditional demand of hazard level PE100 = 86% (i.e., RP = 50 yrs.) on pier column drift of pier #5 w.r.t. pile cap in the long. dir. 341
Figure 7.63: Risk feature: unconditional demand of hazard level PE100 = 10% (i.e., RP = 950 yrs.) on pier column drift of pier #5 w.r.t. pile cap in the long. dir. 342
Figure 7.64: Risk feature: unconditional demand of hazard level PE100 = 86% (i.e., RP = 50 yrs.) on pier column drift of pier #5 w.r.t. pile in the trans. dir. 342
Figure 7.65: Risk feature: unconditional demand of hazard level PE100 = 10% (i.e., RP = 950 yrs.) on pier column drift of pier #5 w.r.t. pile in the trans. dir. 343
Figure 7.66: Parametric illustration of probabilistic seismic demand hazard curve of column base moment of pier #5 in the long. (left) and trans. (right) directions 343
Figure 7.67: Risk feature: unconditional demand of hazard level PE100 = 86% (i.e., RP = 50 yrs.) on column base moment of pier #5 in the long. dir. 344
Figure 7.68: Risk feature: unconditional demand of hazard level PE100 = 10% (i.e., RP = 950 yrs.) on column base moment of pier #5 in the long. dir. 344
Figure 7.69: Risk feature: unconditional demand of hazard level PE100 = 86% (i.e., RP = 50 yrs.) on column base moment of pier #5 in the trans. dir. 345
Figure 7.70: Risk feature: unconditional demand of hazard level PE100 = 86% (i.e., RP = 50 yrs.) on column base moment of pier #5 in the trans. dir. 345
Figure 7.71: Parametric illustration of probabilistic seismic demand hazard curve of bending moment of piles under pier #5 in the long. (left) and trans. (right) directions 346
Figure 7.72: Risk feature: unconditional demand of hazard level PE100 = 86% (i.e., RP = 50 yrs.) on bending moment of piles under pier #5 in the long. dir. 346
Figure 7.73: Risk feature: unconditional demand of hazard level PE100 = 10% (i.e., RP = 950 yrs.) on bending moment of piles under pier #5 in the long. dir. 347

Figure 7.74: Risk feature: unconditional demand of hazard level PE100 = 86% (i.e., RP = 50 yrs.) on bending moment of piles under pier #5 in the trans. dir.....347
Figure 7.75: Risk feature: unconditional demand of hazard level PE100 = 10% (i.e., RP = 950 yrs.) on bending moment of piles under pier #5 in the trans. dir.....348
Figure 7.76: Parametric illustration of probabilistic seismic demand hazard curve of shear force of piles under pier #5 in the long. (left) and trans. (right) dir.....348
Figure 7.77: Risk feature: unconditional demand of hazard level PE100 = 86% (i.e., RP = 50 yrs.) on shear force of piles under pier #5 in the long. dir.....349
Figure 7.78: Risk feature: unconditional demand of hazard level PE100 = 10% (i.e., RP = 950 yrs.) on shear force of piles under pier #5 in the long. dir.....349
Figure 7.79: Risk feature: unconditional demand of hazard level PE100 = 86% (i.e., RP = 50 yrs.) on shear force of piles under pier #5 in the trans. dir.....350
Figure 7.80: Risk feature: unconditional demand of hazard level PE100 = 10% (i.e., RP = 950 yrs.) on shear force of piles under pier #5 in the trans. dir.....350
Figure 7.81: Parametric illustration of probabilistic seismic demand hazard curve for the rail stress at abutment expansion joint #1.....351
Figure 7.82: Risk feature: unconditional demand of hazard level PE100 = 86% (i.e., RP = 50 yrs.) on rail stress at abutment expansion joint #1 due to axial force.....351
Figure 7.83: Risk feature: unconditional demand of hazard level PE100 = 10% (i.e., RP = 950 yrs.) on rail stress at abutment expansion joint #1 due to axial force.....352
Figure 7.84: Risk feature: unconditional demand of hazard level PE100 = 86% on rail stress at abutment expansion joint #1 due to trans. bending.....352
Figure 7.85: Risk feature: unconditional demand of hazard level PE100 = 10% on rail stress at abutment expansion joint #1 due to trans. bending.....353
Figure 7.86: Parametric illustration of probabilistic seismic demand hazard curve of rail stress at abutment expansion joint #2.....354
Figure 7.87: Risk feature: unconditional demand of hazard level PE100 = 86% on rail stress at interior expansion joint #2 due to axial force.....354
Figure 7.88: Risk feature: unconditional demand of hazard level PE100 = 10% on rail stress at interior expansion joint #2 due to axial force.....355
Figure 7.89: Risk feature: unconditional demand of hazard level PE100 = 86% on rail stress at interior expansion joint #2 due to trans. bending.....355

Figure 7.90: Risk feature: unconditional demand of hazard level PE100 = 10% on rail stress at interior expansion joint #2 due to trans. bending 356
Figure 7.91: Risk feature: unconditional mean demand on isolator deformation of isolator #13 over pier #5 in the trans. dir. 357
Figure 7.92: Risk feature: unconditional demand c.o.v. on isolator deformation of isolator #13 over pier #5 in the trans. dir. 357
Figure 7.93: Risk feature: unconditional mean demand on column base moment of pier #5 in the trans. dir. 358
Figure 7.94: Risk feature: unconditional demand c.o.v. on column base bottom moment of pier #5 in the transverse direction 358
Figure 7.95: Risk feature: unconditional mean demand on rail stress due to transverse bending at interior expansion joint #2 359
Figure 7.96: Risk feature: unconditional demand c.o.v. on rail stress due to transverse bending at interior expansion joint #2 359
Figure 7.97: Distribution of mean demand on absolute deck acceleration along the bridge conditioned on OBE hazard level in the longitudinal direction (x dir.) for different yield strengths of seismic isolators 360
Figure 7.98: Distribution of absolute deck acceleration mean demand along the bridge conditioned on MCE hazard level in the longitudinal direction (x dir.) for different yield strengths of seismic isolators 361
Figure 7.99: Distribution of mean demand on relative deck displacement along the bridge conditioned on OBE hazard level in the longitudinal direction (x dir.) for different yield strengths of seismic isolators 362
Figure 7.100: Distribution of mean demand on relative deck displacement along the bridge conditioned on OBE hazard level in the longitudinal direction (x dir.) for different initial stiffness's of seismic isolators 363
Figure 7.101: Distribution of mean demand on relative deck displacement along the bridge conditioned on OBE hazard level in the transverse direction (y dir.) for different yield strengths of seismic isolators 364
Figure 7.102: Distribution of mean demand on relative deck displacement along the bridge conditioned on MCE hazard level in the transverse direction (y dir.) for different yield strengths of seismic isolators 365

Figure 7.103: Distribution of mean demand on isolator deformation along the bridge conditioned on OBE hazard level in the longitudinal direction (x dir.) for different yield strengths of seismic isolators.....366
Figure 7.104: Distribution of mean demand on isolator deformation along the bridge conditioned on OBE hazard level in the transverse direction (y dir.) for different yield strengths of seismic isolators.....367
Figure 7.105: Distribution of mean demand on pier bottom bending moment along the bridge conditioned on OBE hazard level in the transverse direction (y dir.) for different yield strengths of seismic isolators.....368
Figure 8.1: Optimization problem formulation alternative considering different risk features380
Figure 8.2: Optimization problem formulation alternative considering different EDPs.....381
Figure 8.3: Optimization problem formulation alternative considering different hazard levels….....383
Figure 8.4: Optimization problem formulation alternative considering different hazard analysis steps.....384
Figure 8.5: Structural optimization solution to the optimization problem formulated for probabilistic performance-based design on given seismic hazard level (i.e., OBE)….....393
Figure 8.6: Structural optimization solution to the optimization problem formulated for probabilistic performance-based design with constraints on OBE & MCE.....401
Figure 8.7: Structural optimization solution to the problem formulated for continuous hazard levels based on the unconditional seismic demand hazard with the objective function as the ALC of total base shear in the trans. dir. of the CHSR prototype bridge.....404
Figure 8.8: Structural optimization solution to the problem formulated to minimize the conditional mean demand with the constraints on conditional demand variance on OBE hazard level.....406
Figure 8.9: Structural optimization solution to the problem formulated to minimize the conditional mean demand with the constraints on conditional demand variance on OBE hazard level and other constraints 407

Figure 8.10: Structural optimization solution to the problem formulated to minimize the unconditional mean demand with the constraints on unconditional demand variance hazard level and other constraints 408
Figure 8.11: Structural optimization solution to the problem formulated to minimize the unconditional mean demand with the constraints on unconditional demand variance and other constraints.....409
Figure 8.12: Conditional median demand on all continuous seismic hazard levels (left) and conditional PDF of demand on OBE and MCE hazard level (right) for the EDP of the absolute acceleration at deck over pier #5 in the transverse direction.....410
Figure 8.13: Conditional CCDF of demand on OBE and MCE hazard level (left) and unconditional probabilistic seismic demand hazard curves for the EDP of the absolute acceleration at deck over pier #5 in the trans. dir.....411
Figure 8.14: Conditional median demand on all continuous seismic hazard levels (left) and conditional PDF of demand on OBE and MCE hazard level (right) for the EDP of the maximum deformation in the isolator over pier #5 in the long. dir.....411
Figure 8.15: Conditional CCDF of demand on OBE and MCE hazard level (left) and unconditional probabilistic seismic demand hazard curves for the EDP of the maximum deformation in the isolator over pier #5 in the long. dir.....412
Figure 8.16: Conditional median demand on all continuous seismic hazard levels (left) and conditional PDF of demand on OBE and MCE hazard level (right) for the EDP of the maximum deformation in the isolator over pier #5 in the trans. dir. 412
Figure 8.17: Conditional CCDF of demand on OBE and MCE hazard level (left) and unconditional probabilistic seismic demand hazard curves for the EDP of the maximum deformation in the isolator over pier #5 in the trans. dir. 412
Figure 8.18: Conditional median demand on all continuous seismic hazard levels (left) and conditional PDF of demand on OBE and MCE hazard level (right) for the EDP of the maximum bottom moment of pier #5 in the trans. dir. 413
Figure 8.19: Conditional CCDF of demand on OBE and MCE hazard level (left) and unconditional probabilistic seismic demand hazard curves for the EDP of the maximum bottom moment of pier #5 in the trans. dir.....414
Figure 8.20: Conditional median demand on all continuous seismic hazard levels (left) and conditional PDF of demand on OBE and MCE hazard level (right) for the EDP of

the maximum relative end rotation of bottom element of pier #5 in the trans. dir…. 414
Figure 8.21: Conditional CCDF of demand on OBE and MCE hazard level (left) and unconditional probabilistic seismic demand hazard curves for the EDP of the maximum relative element end rotation of bottom of pier #5 in the trans. dir.....415
Figure 8.22: Conditional median demand on all continuous seismic hazard levels (left) and conditional PDF of demand on OBE and MCE hazard level (right) for the EDP of the maximum total base shear across all columns in long. dir. 415
Figure 8.23: Conditional CCDF of demand on OBE and MCE hazard level (left) and unconditional probabilistic seismic demand hazard curves for the EDP of the maximum total base shear across all columns in longitudinal direction 416
Figure 8.24: Conditional median demand on all continuous seismic hazard levels (left) and conditional PDF of demand on OBE and MCE hazard level (right) for the EDP of pile moment under pier #5 in the trans. dir. 416
Figure 8.25: Conditional CCDF of demand on OBE and MCE hazard level (left) and unconditional probabilistic seismic demand hazard curves for the EDP of pile moment under pier #5 in the trans. dir. 416
Figure 8.26: Conditional median demand on all continuous seismic hazard levels (left) and conditional PDF of demand on OBE and MCE hazard level (right) for the EDP of rail stress at abutment gap #1 due to axial force and bending moments 417
Figure 8.27: Conditional CCDF of demand on OBE and MCE hazard level (left) and unconditional probabilistic seismic demand hazard curves for the EDP of rail stress at abutment gap #1 due to axial force and bending moments.....418

LIST OF TABLES

Table 2.1: Relevant parameters for postulated fragility curves.....61
Table 2.2: Seismic damage hazard of each damage state considered 63
Table 2.3: Repair cost distribution data for each damage state.....65
Table 3.1: Section properties for the CHSR prototype bridge box girder.....86
Table 3.2: Modeling properties for the SHJ adopted in CHSR Prototype Bridge.....94
Table 3.3: Rail-structure connection modeling properties 114
Table 4.1: Selected ground motions for deterministic study.....165
Table 5.1: Representative faults' close to San Jose site (From Caltrans ARS).....194
Table 5.2: Selected ground motions for CHSR Prototype Bridge.....195
Table 5.3: Conditional probability of limit states exceedance for column base moment of pier #5 in trans. dir. (y).....220
Table 5.4: Conditional probability of the limit states exceedance for relative end rotation of bottom element in pier #5 in trans. dir. (y).....220
Table 7.1: Lead rubber bearing isolator material properties 291
Table 7.2: Lead rubber bearing isolator engineering properties (from DIS Inc.).....292
Table 7.3: Properties range of bilinear isolators for parametric study 293
Table 7.4: Risk feature values based on conditional demand hazard on OBE.....369
Table 7.5: Risk feature values based on conditional demand hazard on MCE 371
Table 7.6: Risk features based on the derived PDF of unconditional seismic demand hazard characterized by probability exceedance in exposure time of 100 years.....373
Table 8.1: Summary of optimization results comparison with different objective functions for probabilistic performance-based design conditioned on OBE hazard level.....395
Table 8.2: Summary of optimization results comparison with different objective functions for probabilistic performance-based design conditioned on MCE hazard level 399

ACKNOWLEDGEMENTS

The author, as the principal investigator, would like to admit this research work, like any bridges or buildings in the engineering field, can never be completed without the support or help of other organizations or people.

This research is funded by the Department of Transportation in the State of California through Pacific Earthquake Engineering Research (PEER) Center. The generous support from the funding agency is graciously acknowledged.

I owe my special acknowledgements to, including but not limited to, my advisor as well as other committee members, engineering practitioners involved in this project, my colleagues and friends around, and my family members. I will take this opportunity to thank some of them in particular here.

Through the course of my Ph.D. program, Professor Joel P. Conte, as a knowledgeable mentor, has unceasingly encouraged and guided me on my way in the academic aspects, sharing me with research ideas, challenging me to solve some difficult problems, correcting my mistakes in my research work, and even typos in my papers and presentations. I would like to attribute my first and deepest thanks to him. His knowledge and attitude towards research ignited my passion for learning and research. Thank you for all your efforts and time, keeping me on the right track of my research for the past five years.

Also, I am indebted to my other committee members, Professor Ahmed-Waeil M. Elgamal, Professor Philip E. Gill, Professor Bo Li, and Professor José Restrepo. Your insightful advice and valuable comments have inspired me to dig deeper and look further in my research. Special thanks are to Professor Steve Mahin at University of California,

Berkeley, who has showed special interest in my research topic and has been invovled in serveral face-to-face meetings and conference calls.

Thank you to Thomas B. Jackson, Pang Yen Lin, Kongsak Pugasap at Parsons Brinckerhoff, Inc., who provided us the valuable help on the preliminary design of the California High-Speed Rail Prototype Bridge. Also, special thanks go to a senior engineer Roy A. Imbsen at Earthquake Protection System, Inc., who shared with us some insightful ideas on the seismic resistant design. All your assistance facilitated the progress of my research work.

Acknowledgement for the contribution of our colleagues also goes to Professor Andre R. Barbosa at Oregon State University regarding the understanding of PBEE methodology; Professor Quan Gu at Xiamen University in China for his hands on understanding the framework of OpenSees; Professor Scott J. Brandenberg at University of California, Los Angeles, and Professor Ross W. Boulanger at University of California, Davis, for their help on the modeling part of pile-structure-interaction in my research work.

All my friends, I would like thank you for keeping me company through my ups and downs these years. In the end, I would like to dedicate this dissertation to my parents and my sister. It is you who have made the journey of my Ph.D. life easier, thank you all for your unconditional love and supports. I have to say thanks to my loved girl whom I may have not met yet in the past five years. Thanks to everything in my life that does not kill me but makes me much stronger.

Chapter 2, in part, is currently being prepared for submission for publication of the material. Li, Yong; Conte, Joel P.; Gu, Quan, Gill, Philip E., “Framework for Probabilistic Performance-Based Optimum Seismic Design of Structures”. The dissertation author was the primary investigator and author of this material.

VITA

2014 Ph.D. in Structural Engineering, University of California, San Diego

2013 M.A. in Applied Mathematics, University of California, San Diego

2009 M.S. in Civil Engineering, Tsinghua University, Beijing, China

2006 B.S. in Civil Engineering, Beihang University, Beijing, China

ABSTRACT OF THE DISSERTATION

Probabilistic Performance-Based Optimum Seismic Design of Seismic Isolation for California High-Speed Rail Prototype Bridge

by

Yong Li

Doctor of Philosophy in Structural Engineering

University of California, San Diego, 2014

Professor Joel P. Conte, Chair

Over the last five decades, remarkable progress has been achieved in the field of earthquake engineering, especially in the following areas: seismic design philosophy, earthquake protective systems, seismic design and performance evaluation of structures, and theory of structural optimization. The progress achieved and products developed in these areas can be integrated to develop a desired computer-aided optimum structural design framework.

Accordingly, a probabilistic performance-based optimum seismic design (PPBOSD) framework is proposed and first illustrated and validated on a simplified single-degree-of-freedom (SDOF) bridge model optimized (i.e., rated) for a target seismic loss hazard curve.

The feasibility and optimality of seismic isolation is investigated for a California High-Speed Rail (CHSR) prototype bridge testbed using the proposed PPBOSD framework, balancing the beneficial and detrimental effects of seismic isolation for such a bridge. Towards this goal, a three-dimensional detailed nonlinear finite element model of the CHSR prototype bridge, including soil-pile-structure interaction and rail-structure interaction, is developed in *OpenSees*. The seismic response of the isolated bridge is compared to that of the corresponding non-isolated bridge both in deterministic and probabilistic terms. A comprehensive parametric probabilistic demand hazard analysis is carried out to investigate the effects of the seismic isolator properties on the seismic risk of the CHSR prototype bridge. To enable the computationally intensive probabilistic seismic response analyses, a cloud-based optimization framework was used integrating cloud computing resources with the high throughput computing in PPBOSD methodology. Furthermore, some well-posed practical optimization problems are formulated and investigated for seismic isolation in CHSR bridges.

In summary, the unique contributions and findings are summarized as follows: (1) A PPBOSD framework is proposed, illustrated, and validated using a nonlinear SDOF bridge model; (2) Compared to a non-isolated bridge, the seismic isolation increases the deck displacement and rail stress demands, while it reduces the seismic demand in the bridge substructure in both the deterministic and probabilistic sense; (3) A cloud-based computing platform is developed for PPBOSD to address the high computational cost; (4) The feasibility and optimality of seismic isolation for the prototype bridge is achieved using the PPBOSD framework, reaching various performance objectives considering the relevant sources of uncertainty.

CHAPTER 1

INTRODUCTION

1.1. Background and Motivation

In contrast to the design of mass-produced products in other engineering fields, the design and construction of products in the area of civil engineering—including structural and geotechnical engineering—are regulated by public laws (Ellingwood, 2000) because civil infrastructure facilities (e.g., bridges, buildings, and geotechnical systems) serve the fundamental needs of society at large. Consequently, civil infrastructure facilities are expected, but not guaranteed, to be designed to withstand demands imposed by their service requirements and by natural environmental events; therefore they are subject to evolving design codes, standards and other regulatory documents (Ellingwood, 2008). Essentially, high uncertainties in the demands and capacities of structural/geotechnical facilities, due to randomness inherent within the loads (e.g., highly variable wind and earthquake loads) as well as limited performance data available under repeatable circumstances, distinguish civil infrastructure design from other design projects.

Significant effort has been devoted to the enormous undertaking of updating design codes as better understanding of the hazards of loads/actions evolve, utilization of new structural systems and materials in practice, and the widespread availability of fast-advancing computing technologies for analysis (i.e., numerical analysis software and affordable

hardware). Based on a comprehensive literature review, this author has concluded that the goal of improving structural response field has focused primarily on the following three areas: (1) reframing the design philosophy; (2) introducing innovative materials and structural components into the design of traditional infrastructure systems; and (3) developing and implementing design approaches centered on response estimation and performance evaluation procedures (i.e., loads characterization and numerical structural modeling).

The design process is essentially a decision-making process. Old-fashioned design was performed through a manual trial-and-error approach, guided by a simplified design philosophy. Applying modern optimization techniques to structural design can accelerate the design process. Optimization becomes even more essential and necessary when an increasing number of conflicting or competing design constraints need to be satisfied to achieve a reliable, robust, and economic design. Furthermore, optimization is also ideal for design when an advanced reliability-based or risk-based design method is adopted, involving probabilistic performance evaluations at multiple hazard levels, because of the inherent complexity in the design process and the various sources of uncertainty affecting it. These uncertainties require more research and development before the practical implementation and realization of the attractive performance-based design philosophy using automated computer-aided design based on structural optimization and comparison of design alternatives is realized. Given the degree of uncertainty for structural response, design methodologies must evolve toward performance-based design and introduction of innovative performance-based technologies; judgment and intuition are insufficient to realize a design satisfying specified performance objectives.

Considering earthquake engineering methodologies for seismic design, the following four aspects are elaborated on below: (1) the seismic design philosophy; (2) the new technologies improving the seismic performance of structures; (3) the performance-based

seismic design/evaluation methodology; (4) the prospect of optimization for advanced seismic design. Integration of these four aspects will lead to more successful designs of civil infrastructure with improved seismic performance.

1.2. The Evolution of Seismic Design Philosophy

The philosophy of seismic design and analysis of civil structures has evolved from the safeguard against structural collapse and loss of lives (more specifically, safety standards that ensure that a structure successfully responds to minor earthquakes without damage, responds to moderate earthquakes with some nonstructural but without any structural damage; and responds to major earthquakes with structural damage but without collapse) to performance based seismic design (PBSD). Aimed at ensuring post-earthquake functionality, PBSD was developed in response to the substantial direct economic losses in earthquakes (e.g., $20 billion losses for the 1994 M6.7 Northridge earthquake). In that earthquake many structures suffered significant damage to structural and non-structural components and systems, as well as the significant indirect losses due to the post-earthquake malfunction and socio-economic turmoil, including business disruption, relocations expenses, and supply chain interruption. Correspondingly, seismic design philosophy has evolved from force-based design to performance-based design, with the basic concepts described in the SEAOC Vision 2000 document (SEAOC, 1995).

The advent of the performance-based design philosophy together with the highly uncertain nature of earthquake ground motions have brought the probabilistic performance-based seismic design (PBSD) to the forefront of seismic design in order to satisfy probabilistic performance criteria. A probabilistic performance objective (or criteria) consists of a performance level and an acceptable (or target) probability of exceedance of this performance level. A performance level is defined as a threshold value of a specified Engineering Demand

Parameter (EDP), e.g., maximum plastic hinge rotation of 1.5%, maximum peak interstory drift ratio of 2.0 percent, and peak roof acceleration of 0.8*g*. More generally, a performance level is defined as the exceedance of a limit-state, e.g., concrete spalling, bar buckling, and concrete crushing. The acceptable (or target) probability of exceedance is defined either as (i) conditional on a specified seismic hazard level (e.g., conditional on the occurrence of an earthquake with a given return period, or conditional on an earthquake ground motion intensity level with a given annual probability of exceedance) or (ii) unconditional (i.e., considering all earthquake ground motion intensity levels) over an exposure time (or reference time). Corresponding examples of a probabilistic performance objective for a bridge structure are: (i) the probability of a pier drift ratio exceeding 3.0 percent conditional on the occurrence of an earthquake ground motion with a return period of 100 years (i.e., an annual probability of exceedance of approximately 0.01) must not exceed 10 percent (0.10); or (ii) the annual probability of a pier (any pier of the bridge structure) drift ratio exceeding 3.0 percent must be less than 0.1 percent (0.001).

Probabilistic performance-based seismic design requires a probabilistic performance evaluation (or assessment) framework so that a structure can be designed to satisfy a set of probabilistic performance objectives (criteria) specified by the codes or defined by the owners or stakeholders of the structure.

1.3. Probabilistic Performance-based Earthquake Engineering (PBEE)

Randomness in structural loads and material properties, namely, the induced variability in demands placed on the structural system and capacity of the system to respond to and withstand those demands, are at the root of uncertain structural performance (i.e., serviceability, safety, resilience, and sustainability). Structural engineers have traditionally approached uncertainty and risk problems by applying a judgmental “factor of safety.” The

Load and Resistance Factor Design (LRFD) methodology represents the first attempt in the United States to implement a rational probabilistic approach to managing uncertainties in the building process in a structural design code (Ellingwood, 2000).

1.3.1. The rise of PEER PBEE methodology

The research community of PBSD recognizes that the seismic performance of the structure must be characterized in a probabilistic manner to explicitly account for uncertainties in seismic loading and structural modeling. Accounting for these uncertainties prompted the development of a well-modularized methodology, referred to as the PEER PBEE methodology. Originally proposed by Cornell and Krawinkler (2000), this methodology has been promoted and developed by the Pacific Earthquake Engineering Research (PEER) Center, as shown in Figure 1.1.

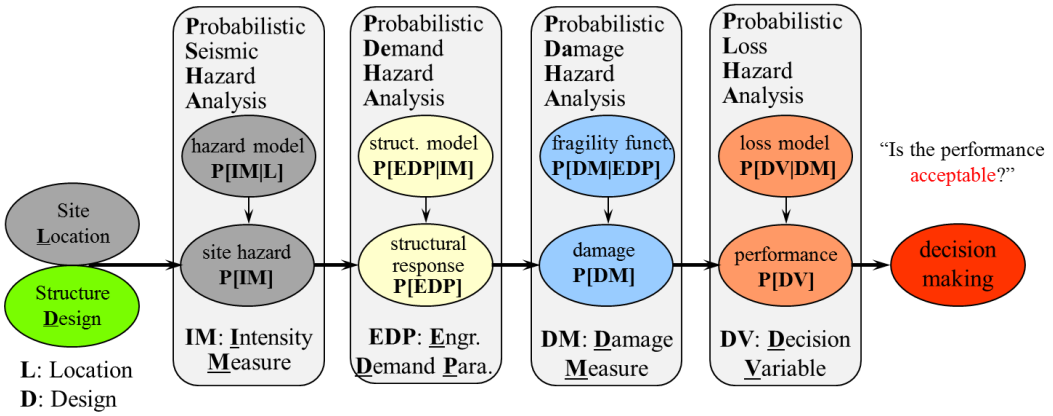

Figure 1.1: Conceptual framework of the probabilistic performance-based earthquake engineering methodology by the Pacific Earthquake Engineering Research Center

The objective of this methodology is to enable the quantitative assessment of risk in terms of probability imposed on a civil structure by future possible earthquakes, which involves the seismology, geotechnical and structural engineering, and construction or repair cost estimation. The main idea is to propagate the uncertainty related to the intensity of future

earthquakes through a mathematical model of the structure characterized by a number of uncertainties, all the way to a probabilistic estimate of structural performance with probabilistic capacity to the end of this procedure, using the total probability theorem.

1.3.2. Analysis steps in PBEE and applications research review

As shown in Figure 1.1, the PBEE methodology consists of four stages: (1) probabilistic seismic hazard analysis (PSHA) to characterize the intensity of future earthquakes affecting the site of the structure; (2) probabilistic seismic demand analysis of the structural and/or geotechnical system (referred to as probabilistic demand hazard analysis, PDeHA); (3) probabilistic seismic damage analysis (referred to as probabilistic damage hazard analysis, PDaHA); and (4) probabilistic seismic loss or consequence analysis (referred to as probabilistic loss hazard analysis, PLHA). The probabilistic properties of intermediate variables such as intensity measures (IMs), engineering demand parameters (EDPs), damage measures (DMs), and decision variables (DVs) are computed in the corresponding analysis stage.

In the last fifteen years, significant research efforts have been devoted to the development of the PEER PBEE methodology, summarized in a collection of publications (Cornell and Krawinkler 2000; Krawinkler 2002; Moehle 2003; Porter 2003; Krawinkler and Miranda 2004; Moehle and Deierlein 2004, Mosalam and Günay 2014). Applications of PBEE for probabilistic performance evaluation of various testbed structures can be found in Comerio (2005), Krawinkler (2005), Goulet et al. (2006), Kunnath (2006), Kunnath et al. (2006), Mitrani-Reiser et al. (2006), Zhang (2006), and Haselton et al. (2011).

1.3.3. Extension of the PBEE methodology

As the pioneering application and implementation of performance-based engineering (PBE) in earthquake engineering (Ellingwood 2001, Porter 2003), the well-established PBEE

framework has also been extended to other engineering fields. Representative examples are performance-based blast engineering (Hamburger and Whittaker 2003), performance-based fire engineering (Lamont and Rini 2008), performance-based wind engineering (Petrini 2009; Ciampoli and Petrini 2012), performance-based hurricane engineering (Barbato et al. 2013), and performance-based tsunami engineering (Riggs et al. 2008).

1.3.4. Potential further development of PBEE for probabilistic performance-based optimum seismic design

Due to the probabilistic nature of the methodology and the comprehensive background in earthquake engineering required by various analysis stages, the application of PBEE has received limited attention from practicing engineers beyond the academic arena. The adoption of PBEE in design practice requires the inversion of the available probabilistic performance-based assessment methodology into a practical probabilistic performance-based design methodology, with comparison of design alternatives and the possible addition of an optimization component/stage. Therefore, aiming at promoting the practical application of PBEE in seismic design optimization, significant efforts will be devoted in this dissertation to proposing, developing, and exercising the probabilistic performance-based optimum seismic design framework (PPBOSD) as an extension of PBEE for optimum seismic design. In this dissertation, performance evaluation will be performed using the PBEE methodology considering the uncertainties associated with the input earthquake ground motions only, i.e., excluding the uncertainties characterizing the structural and/or geotechnical systems (e.g., material and mechanical parameters), as the uncertainties in the earthquake ground motion usually outweighs the system uncertainties and thus control the uncertainties in the seismic response of the structure.

1.4. The Advent of Earthquake Protection Technologies

In the past twenty years, a broad range of seismic response modification devices or technologies for earthquake protection have witnessed a variety of applications in seismic design of structures, including seismic isolators, viscous and friction dampers, and re-centering technology (e.g. hybrid rocking systems). Among them, seismic isolation has played a prevailing role in passive control of seismic response and for damage mitigation in earthquake engineering practice. As concluded in the state-of-the-art reviews of seismic isolation (Buckle et al. 1990; Ahmadi 1995; Kelly 1997; Kunde and Jangid 2003; Deb 2004; Warn and Ryan 2012), seismic isolation is a promising cost-effective design and rehabilitation strategy for mitigating seismic damage at various hazard levels of ground motions in earthquake-prone regions.

1.4.1. Fundamental mechanism of seismic isolation

Seismic isolation aims to decouple a structure from the damaging actions of earthquakes: in the case of a building the isolators are placed below the foundation; for part of a structure in the case of a bridge deck where isolators are inserted between the bridge deck and the top of piers and abutments; or for non-structural components in the structure in the case of equipment where isolators are located between the equipment and the structure. Seismic isolation reduces the transmissibility of ground motion to the structural system through shifting the fundamental period of the isolated system from the fixed-base period of the structure and from the predominant period of the ground motion.

Apart from the aforementioned period elongation effect, another equally important contribution from seismic isolators is the added hysteretic energy dissipation caused by the nonlinear force-deformation behavior of the seismic isolators, thereby reducing the seismic energy transmitted into other structural components. However, an undesirable consequence of

using isolators is the increased seismic deformation demand concentrated at the isolation layer. Typically in response to this side effect, an additional energy dissipation capacity (i.e., supplemental damping) via a combination of velocity-dependent viscous dampers and/or deformation-dependent hysteretic dampers can be integrated with the isolators, if necessary, to control the deformation and achieve the desired behavior (Hwang 2005).

1.4.2. Isolator devices and related research review

A variety of isolation devices including elastomeric bearings (with or without lead core, see Figure 1.2 (a)), high-damping rubber, frictional or sliding bearings (see Figure 1.2 (b)), and roller bearings has been developed and widely used in practical applications for seismic protection of structures and non-structural components (Kelly 1997).

Figure 1.2: Configuration of seismic isolators: (a) lead rubber bearing from Dynamic Isolation System, Inc., and (b) friction pendulum from Earthquake Protection System, Inc.

The popularity of seismic isolation strategies in practice over the past few decades has prompted significant research efforts devoted to a variety of isolator devices in terms of theoretical, experimental, and analytical studies. The primary objective is to better understand the force-deformation behavior for high-fidelity modeling. Theoretical studies on friction pendulums or sliding isolation bearings can be found in the literature (Tsai et al. 2003; Fenz and Constantinou 2007). Experimental studies on rubber bearings (Kelly et al. 1987; Griffith

et al. 1988; Aiken et al. 1989; De la Llera and Lüders 2004) and friction pendulums (Tsai et al. 2005; Becker et al. 2011) have been published as well. Numerous analytical studies are available in the literature for rubber bearings (Koh and Kelly 1988; Kikuchi and Aiken 1997; IIzuka 2000; Hwang et al. 2002; Abrahamson and Mitchell 2003; Kikuchi et al. 2007; Kalpakidis et al. 2010; Kikuchi et al. 2010) and friction sliding bearings (Zayas et al. 1990; Almazan and De la Llera 2002, 2003; Tsai 2003; Mosqueda et al. 2004; Fenz and Constantinou 2008; Tsai and Lin 2009; Morgan and Mahin 2010; Tsai et al. 2010; Becker and Mahin 2012).

The literature places special emphasis on modeling of the coupling effects of axial and lateral behavior (including flexural and shear) of seismic isolators (Kelly et al. 1987; Koh and Kelly 1987; Griffith et al. 1988; Aiken et al. 1989; Kikuchi and Aiken 1997; Kelly 2003; Ryan et al. 2004, 2005). A variety of numerical models of seismic isolators with various capabilities have been proposed, implemented, and verified using experimental data, and then applied to modeling of seismic isolated structural systems.

The bilinear hysteretic model of the force-deformation behavior in the lateral direction of seismic isolators has been widely used for modeling structural systems equipped with seismic isolation. This simplified and robust model has proved to be a good approximation in most cases. Considering the high computational cost and the requirements for the numerical stability of the nonlinear structural analyses performed in this research on probabilistic optimization, the bilinear seismic isolator model will be adopted herein.

1.4.3. Applications of seismic isolation to building and bridge structures

Widespread applications of seismic isolation can be found in the design or retrofit of building and bridge structures. A historical survey on the seismic performance of actual isolated structures subjected to earthquakes further proved the benefits of seismic isolators

(Asher et al. 1997; Nagarajaiah and Sun. 2000, 2001; Matsagar and Jangid 2006). The seismic performance of isolated structures has also been evaluated through comparative analytical study of bridges (Hwang 1994; Sarrazin et al. 2012) and buildings (Nagarajaiah and Sun 2000) with and without seismic isolation. The observed behaviors of seismic isolated buildings and bridges in past earthquakes reported in the literature are consistent with their expected performance and the structures experienced little damage (Nagarajaiah and Sun 2000; Higashino 2006). In addition, the effects of structural flexibility (i.e., bridge pier and deck, building superstructure) on the seismic response of isolated bridges and buildings have been investigated (Kunde 2006; Jangid 2006), indicating that the seismic isolation system is dependent on the specific type of structure for which it is designed.

Preliminary seismic isolation design can be found in the 1986 “Yellow Book” of first document describing design requirements for seismic isolated buildings by the Structural Engineers Associated of Northern California (SEAONC 1986), the appendix of the Uniform Building Code (UBC 1997), the California’s Building Code (CBC), and the 1991 Standard by the American Association of State Highway and Transportation Officials (AASHTO) (Mayes et al. 1992). Other simplified design guidelines can also be found in the literature (Islam et al. 2011).These preliminary design guides do not guarantee the targeted performance. The highly nonlinear behavior of seismic isolators as well as the sensitivities of the structural response to the isolator properties, the dynamic properties of the structural system, and the input ground motions require performing a seismic performance evaluation and verification process.

1.4.4. Need for optimal isolator design

Consequently, the whole thrust of seismic isolation is to reduce the estimated damage under a certain seismic hazard level or the probability of a specified damage level, thus reducing repair costs. Maximizing the benefits of seismic isolation requires proper selection

and design of seismic isolation system, which depends on several factors. One factor is the site location, geology and seismology as wee as the local soil conditions, which determines the characteristics of future earthquake ground motions (e.g., earthquake amplitude and frequency content) at the site. Another factor is structure specific, i.e., the structural systems (buildings, bridges), the contents inside the building (e.g., newspaper printing press machines, piping, etc.), or the function of a structure (e.g., high-speed rail track). The subjectivity of the engineers, clients, or stakeholders in terms of the performance under various seismic hazard levels also plays a role in defining the performance objectives or targeted performance. Therefore, it is imperative that all these factors be considered when choosing a seismic isolation system; it is a trade-off between the benefits of the isolation system and its cost. The research reported herein studied the feasibility and optimality of applying seismic isolation for California high-speed rail (CHSR) bridges. The performance of seismic isolated and non-isolated bridges will be evaluated both deterministically and probabilistically to systematically investigate the beneficial and detrimental effects of seismic isolation on the seismic performance of a typical CHSR prototype bridge system.

1.5. Optimization in Structural Design

Structural optimization is a quest for excellence in design. It represents a yardstick against which feasible but non-optimal alternatives can be measured, but also may offer alternative solutions. It is a process whereby structural input data (geometry, loadings, and materials) are synthesized into optimal output via a mathematical operator, a functional feature that opens the door for approaches from system and control theories to be used for structural design optimization (Cohn 1991).

Current design strategies for mitigating seismic response are highly dependent on designers' intuition and experience and are largely trial-and-error; thus, the final design may

not achieve the performance objectives defined at different hazard levels. This problem is more obvious when the structural complexity increases by incorporating innovative devices (e.g., seismic isolators, supplemental dampers) into conventional designs, especially when uncertainties are accounted for using a probabilistic framework. Accordingly, an automated optimal design framework within a probabilistic performance evaluation context is urgently needed to satisfy the design performance objectives effectively and in some cases meet the stakeholders' own risk thresholds that are beyond minimum code requirements. As stated in the Vision 2000 Committee Report (1995), "Studies are needed to improve presently available methods for automatic optimal design satisfying simultaneously the requirements imposed by different performance levels (limit states) associated with the performance design objectives (design criteria)."

With the evolution of seismic design philosophies, the introduction of innovative earthquake protection systems, and the development of design and performance evaluation methodologies, the time is ripe to develop a framework in which seismic designs can be systematically improved or optimized. This is further enhanced by the rapid progress in computing and software engineering, as well as in the theoretical and computational aspects of optimization, and the growing applications of optimization in such fields as mechanical engineering and chemical engineering.

1.5.1. Literature review on structural optimization

According to Webster's Dictionary, optimization is the process or method for making something (design, system, decision) as fully perfect, functional, or effective as possible. The introduction of a formal structural optimization strategy into this process has witnessed great success in many industries. The theory of structural optimization has advanced considerably, as reported by state-of-the-art review papers in the structural optimization community

(Venkayya 1978; Barthelemy 1993; Cohn 1994; Cohn and Dinovitzer 1994; Wang 2005; Kang et al. 2006). Unfortunately, the structural engineering community has been rather slow in transferring research to engineering practice, although a variety of potential applications of structural optimization exist in the real word.

The various formulations proposed and developed for optimizations of problems encountered in different fields can be subdivided in three broad categories: (1) the direct approach formulated in the design variable space, also known as, the nested analysis and design (NAND) approach; (2) the simultaneous analysis and design (SAND) approach; and (3) the optimality criteria (OC) approach by Kirsch and Rozvany (1994). The NAND approach treats only structural design variables as optimization variables, while in the SAND approach, both design variables and state variables (e.g.., displacements) are treated as optimization variables. Reviews and comparisons of these alternative formulations can be found in the literature (Kirsch and Rozvany 1994; Arora and Wang 2005; Wang and Arora 2006).

In the literature, the OC approach has been widely used for deterministic structural optimization. Chan (2004) developed a novel computer-based optimization technique for wind-induced serviceability design of tall buildings using the optimality criteria method. Zou (2002, 2008) developed an optimal seismic performance-based design methodology for reinforced concrete buildings subjected to drift performance criteria, considering both elastic design based on response spectrum and linear time history analysis, and inelastic design based on nonlinear pushover analysis, to minimize the construction cost of RC buildings.

Unfortunately, the optimality criteria in the OC approach are highly dependent on the specific structural behavior and optimization objectives, which become impractical in a complex structural optimization—such as in the probabilistic performance based optimal seismic design under random dynamic earthquake loading. Despite its inefficiency (Kirsch

1981) in dealing with a problem with a large number of design variables and the lack of robustness of algorithms or non-existence of universal optimization algorithms, the advantage of the NAND approach is its generality for various types of structural optimization problems in which the model of a structural system serves as an implicit mathematical function.

Although uncertainty and optimality are two inherent features in structural design, they are typically ignored (Grierson et al. 2006) by only seeking a feasible design that satisfies the design constraints. Recently there has been increasing interest in combined problems of probabilistic optimal design, with the need illustrated by the comparison between deterministic and probabilistic optimization of structures (Beck and Gomes 2012).

Motivated by the thrust to use advanced numerical methods and optimization theory to develop a probabilistic optimum seismic design methodology, there has been considerable effort made in developing the theoretical framework and corresponding application examples. A significant amount of the past research on probabilistic optimization has focused on reliability-based optimization (Haukaas 2008; Jensen et al. 2010; Fragiadakis and Lagaros 2011). Another formulation that allows uncertainty to be taken into account explicitly is probabilistic performance-based or risk-based optimization, which is more general and practical for current design practice. The effects of uncertainties (e.g., the inherent variability/randomness in an ensemble of earthquake loads) were addressed by Austin et al. [1987(a), 1987(b)], who developed and tested a methodology for optimal probabilistic limit states design of seismic-resistant steel frames, which is the genesis of this thesis.

It is only after probabilistic performance evaluation approaches reached a mature state in seismic assessment that the studies on structural optimization began to expand. Based on the progress achieved in the conceptual probabilistic PBEE framework, considerable efforts have been directed toward seismic design optimization frameworks (Aktas et al. 2001;

Ellingwood and Wen 2005; Fragiadakis and Lagaros 2011; Rojas et al. 2011). Nevertheless, to the knowledge of the author, there are no existing efforts to incorporate the well-established PEER PBEE methodology, a fully probabilistic approach to performance evaluation, into structural optimization to develop a unified probabilistic performance-based optimum seismic design framework. The research reported herein consists in formulating and developing a unified probabilistic performance-based optimum seismic design (PPBOSD) framework and applying it first, for illustration purposes, to a simplified example in terms of loss hazard evaluated using the fully PBEE methodology. Then, a real-world application example is considered for the PPBOSD framework, consisting of a California high-speed rail (CHSR) prototype bridge.

Unsurprisingly, initial construction expense and lifetime cost (e.g., costs due to operation, maintenance, damage repair, failure consequences, etc.) are common conflicting/competing objectives for the design of civil infrastructural systems. Decision makers (e.g., engineers, owners, stakeholders) must strike a balance among competing objectives, which motivates the use of an optimization strategy. Thus life-cycle oriented design optimization has received much attention for cost-effective solutions among possible design candidates. Frangopol et al. (1997) performed life-cycle cost analysis for optimal maintenance planning of deteriorating bridges for life-time functionality. Considering the possible costs associated with seismic damage, minimization of life-cycle costs has also been investigated (Kohno 2000; Ang and Lee 2001; Kang et al. 2006). Instead of setting a single objective function in the optimization problem formulation, multiple competing objectives can be addressed using genetic algorithms in the Pareto optimal sense. Multi-objective optimization result in different optimal design alternatives with different trade-off decisions that affect the design (Cheng and Li 1996; Liu et al. 2003; Liu et al. 2004).

Design optimization for life-cycle costs of complex bridge systems requires verification based on extensive statistical economic data, thus, it is still impractical in most cases. In this research, no life-cycle costs optimization was performed. For the purpose of demonstrating the PPBOSD framework, postulated repair cost data was utilized to characterize the probabilistic seismic loss hazard for a simple, real-world inspired, academic example. In contrast, optimization of seismic isolation for the CHSR prototype bridge reported herein was performed only based on the second step of PBEE, i.e., probabilistic demand hazard analysis, highlighting the flexibility of the proposed framework in formulating optimization problems in terms of risk defined at any stage within the PBEE analysis process.

1.5.2. Literature review on optimization for seismic isolation system

As discussed in Section 1.4, given the benefits and costs of applying seismic isolation in a structure, an improved/optimum design method is desired to realize a more reliable and effective seismic isolation design. Research work related to optimum design of seismic isolators in building or bridge structures is specific and limited (Zhou et al. 1992; Park and Otsuka 1999; Jangid 2000; Jangid 2005; Jangid 2006; Hameed et al. 2008; Bucher 2011). Below is a brief overview of some of the most notable studies.

Park and Otsuka (1992) focused on one of the important parameters of seismic isolators (i.e., yield level) to determine the optimal yield force normalized to the total weight of the structure subjected to a single earthquake record scaled at various amplitudes. Using energy concept, they studied more than 1000 two degree-of-freedom (2DOF) models of regular short highway bridges considering pier flexibility. An optimal yield ratio (OYR) to achieve maximum RAE (ratio of energy absorbed by the isolator to the total seismic input energy over the duration of the earthquake) was proposed as a linear function of the earthquake amplitude.

Jangid (2000) optimized the friction coefficient of a sliding isolation system for minimum RMS top floor absolute acceleration of a linear multi-story shear type structure isolated by a sliding system at the base. The time-dependent equivalent linearization method for stochastic response under a non-stationary earthquake ground motion model (Kanai-Tajimi) of the 1940 El-Centro earthquake was adopted. The variation of the optimum friction coefficient of the sliding system when varying other system parameters was studied comprehensively.

Jangid (2005) investigated the optimal seismic isolator properties of a friction pendulum system (FPS) for multi-story buildings and bridges under the normal component of six recorded near-fault earthquake ground motions and the variation of the optimum parameters of the FPS under different structural system parameters. A bilinear spring was utilized to model the FPS characterized by two parameters (friction coefficient and the isolated period defined using the post yield stiffness). Closely related work was conducted by Jangid (2006) for lead-rubber bearings (LRBs), where a bilinear spring in parallel with a viscous damper was utilized to model the LRB characterized by four parameters (i.e., yield strength, yield displacement, post-yield stiffness, and viscous damping ratio). From the trends of the roof/deck total acceleration and the bearing deformation, it was concluded that the optimal yield strength of the seismic isolators under near-fault earthquake ground motions was found to be in the range of 0.05W to 0.15W for FPSs and 0.10W to 0.15W for LRBs. The optimal yield strength sought increased with stiffness of both the seismic isolators and the superstructure.

Buncher (2009, 2011) used a Pareto-type optimization approach for conflicting objectives (i.e., maximum structural displacement, residual isolator displacement, and mean plus three standard deviations of the maximum isolation deformation) to investigate an

SDOF/MDOF oscillator seismically isolated with a single friction pendulum (SFP) or a triple friction pendulum (TFP), including a comparison of the Pareto frontiers between the two types of devices. The earthquake excitation was modeled as a non-stationary random process (Kanai-Tajimi). Based on their performance when optimized, it was found that there is no clear preference between SFP and TFP.

A parametric study was conducted to investigate the effect of LRB isolators in the response of seismically isolated bridges subjected to ground motions with different characteristics (Hameed et al. 2008). In this paper, the characteristic strength, post-yield stiffness, and post-yield to initial stiffness ratio were varied to reduce the maximum isolator deformation or maximum isolator force, and appropriate ranges of parameters were recommended for preliminary design.

Optimal selection of seismic isolation design parameters plays a crucial role in mitigating bridge damage. Fragility method and genetic algorithms were utilized to search for optimal seismic isolation parameters (Huo and Alemdar 2013). It was found that the characteristic yielding strength and the post-yield stiffness of the bearings are crucial for seismic damage mitigation, but the pre-yield stiffness and several other hysteretic controlling constants are not influential.

Optimization of the seismic isolation system alone has been of interest in most of the research reported above, where the focus has been on determining the isolation parameters for best or targeted structural performance. Since the optimal isolation parameters depend strongly on the structural system parameters, an ideally integrated design optimization problem should be formulated for the optimal combination of structural system parameters and control system parameters (i.e., seismic isolation parameters). Very few attempts have been made in this area

(Cheng et al., 1996, Zou 2008) to optimize the structural system and seismic response modification devices simultaneously.

The seismic response of seismic isolated structures is typically analyzed through nonlinear time history analysis or by response spectrum analysis using a linearized method (Chopra 1995; Kelly 1997; UBC 1997). Due to the simplicity and sufficient accuracy inherent in the equivalent linear elastic method, Zou (2008) has attempted to automate isolator optimization by integrating spectrum analysis and design optimization. Unsurprisingly, nonlinear time history analysis is the most rigorous procedure for seismic response and has earned more popularity in seismic response prediction and has therefore earned popularity in isolator optimization (Park et al. 2002; Morgan and Mahin 2008; Yang et al. 2008; Islam et al. 2011; Zhao et al. 2011).

The beneficial effects of seismic isolation can be maximized through numerical optimization strategies. As presented in this research, the search for optimum seismic isolator parameters will be considered within the proposed PPBOSD framework as applied to CHSR prototype bridges.

1.5.3. Limitations in current research and ideas for future development of probabilistic design optimization in this dissertation

Despite recent advances, a wide gap exists between the state-of-the-art optimization theory and practical application to achieve optimal engineering design. The main limitations of the current research and potential research directions for future development of probabilistic design optimization can be outlined as follows.

(1) Instead of using fully nonlinear high-fidelity computational models of civil infrastructure systems, in most cases, simplified models have been employed for seismic response prediction in the optimization process for practical reasons. Recognizing that the

optimality in the design variable space also depends on other system properties not accounted for in simplified models, examples of which are soil-structure interaction effects, comprehensive computational models need to be used.

(2) Most structural optimization work has been conducted in the deterministic sense with structural and/or geotechnical systems subjected to one or a few earthquake ground motions. In view of the uncertainties associated with the seismic hazard and the record-to-record variability in the definition of the seismic input, the probabilistic quantification of the seismic risk must be considered in the formulation of the optimization problems.

(3) The optimization problems have not been formulated in a systematic performance-based evaluation framework with flexible selection of objectives and constraints functions to allow for different risk-taking preferences and free selection of the performance metrics.

(4) Few numerical optimization algorithms and few comprehensive parametric studies in the design variable space have been integrated into a unified probabilistic optimum design framework to perform structural optimization considering uncertainties.

In response to the above limitations, the research work presented herein will integrate advanced mechanics-based computational models of structural systems, probabilistic seismic performance evaluation, computational optimization tools, and cloud-based computing technology to develop a framework for probabilistic performance-based optimum seismic design.

1.6. Research Needs, Scope, and Objectives

A significant amount of the past research in earthquake-resistant design of civil structures has focused mainly on the following individual aspects of seismic design: (1) seismic design philosophy, (2) design and performance evaluation (deterministic, probabilistic) methodology including numerical modeling, (3) earthquake protection systems,

and (4) approaches to realize improved/optimum design. Unfortunately, there exist very limited research efforts and applications which integrate those four ingredients to develop a probabilistic performance-based optimum seismic design framework for structural systems with especially those equipped with earthquake protection devices and systems. There is a unique opportunity and an urgent need to develop a PPBOSD framework for earthquake-resistant structure systems.

To date, the PEER PBEE methodology has focused mainly on probabilistic performance assessment of a given structure at a given location with a specific seismic hazard condition, which can be referred to as forward probabilistic performance analysis or assessment. However, the design/retrofit of structural, geotechnical, and soil-foundation-structure-interaction (SFSI) systems requires an inverse PBEE analysis consisting of determining how to design or retrofit a system rated for specified risk-based seismic performance objectives (i.e., expressed in probabilistic terms), which can be realized through optimization in the context of current PBEE methodology. The ultimate goal of this research is to enable the application of the probabilistic performance evaluation tool of the PBEE methodology to seismic design, by extending the PBEE analysis methodology to the PPBOSD framework.

High-speed railway bridges and highway bridges play a crucial role in the socio-economic framework of modern society. As lifeline structures, they are a weak link in the transportation network due to their potential vulnerability to strong ground motion. Even aside from their socio-economic impact, the failure of bridges in the event of an earthquake will seriously hinder the post-earthquake relief and rehabilitation work. This makes the design of new bridges and retrofit of existing bridges extremely important, especially considering design

sustainability and resilience. Compared to the traditional bridge design, seismic isolation provides a promising alternative for the seismic design and retrofit of bridges.

The type of isolation system and tis design parameters will strongly depend on a number of factors, such as the specific bridge dynamic properties and the seismic hazard conditions at the site, risk-based performance objectives in terms of structural damage limit-states as well as decision limit-states (e.g., economic and social functionality requirement). Structural optimization must be used as a substitute to the current reliance on the engineering experience and intuition of designers, in order to more systematically and robustly obtain the optimal design solution. In this research, the PPBOSD framework will be applied to optimize the seismic isolation for a CHSR prototype bridge.

The key objective of the CHSR prototype bridge test-bed study is to first validate the feasibility of applying seismic isolation to CHSR bridges and then strive for the optimal effects of seismic isolation while striking a balance between conflicting effects such as: reducing the acceleration and force demand level at the expense of increasing the superstructure displacement (relative to the ground or pile cap) and rail stress demand level. The optimization necessary to select the proper design parameters for a specific structure located at a given site is complicated in that not all seismic isolation systems are beneficial to structures (Kelly, 1997). Therefore, the first task of this test-bed study consists of formulating a well-posed structural design optimization problem. This is essential before starting an optimization process that will yield meaningful and useful results.

The primary work reported here will include, but is not limited to, the optimization of isolators (e.g., elastomeric bearings, friction pendulum bearings) in the context of the PEER PBEE methodology, considering the system performance objectives under proper probabilistic design constraints. First of all, the following research tasks need to be completed: (1) propose

the conceptual framework for PPBOSD and implemented it by coupling the analysis software (e.g., OpenSees), probabilistic performance evaluation software (e.g., PBEE), high-throughput computing resources, and computational optimization tools (e.g., SNOPT) to deliver an automated integrated optimization software; (2) verify and validate the PPBOSD software framework; (3) select a test-bed bridge structure (i.e., CHSR prototype bridge) and develop a detailed and robust nonlinear finite element model for seismic response simulation and prediction; (4) deterministic and probabilistic performance evaluation of the CHSR prototype bridges with and without seismic isolation in order to investigate quantitatively the beneficial and detrimental effects of seismic isolation; (5) resolve the high computational demand issues confronted in the application of PPBOSD of large-scale structural systems such as the CHSR prototype bridge considered here; and (6) apply the proposed PPBOSD approach to the seismic isolated CHSR prototype bridge. Note that although optimal design in the framework of the PEER PBEE methodology is presented for seismic isolated bridges in this research, it can also be tailored to other structural types, including building structures and underground construction.

1.7. Opportunities and Challenges

The innovative aspect of this research work is the integration of resources for the purpose of extending the PEER PBEE methodology into a PPBOSD framework and applying it to the seismic isolation of a CHSR prototype bridge to improve its seismic performance. A PPBOSD approach aims to streamline the probabilistic performance-based optimum seismic design of structures for use in design and evaluation practice. The research reported herein details a computer-aided risk-based optimal seismic design approach in terms of probabilistic performance evaluation, embodied in the objective and constraint functions. The development of this unified optimal seismic design methodology will enable engineers to optimize

probabilistically the seismic performance of bridge structures based on PBEE principles. Such a methodology will allow designers and engineers to better explore the design space and provide them with confidence in the application of innovative devices such as seismic isolators to improve the seismic resilience of structures.

The present research integrates the following four components: (1) fully nonlinear 3D finite element modeling of a CHSR prototype bridge, (2) probabilistic performance evaluation of the bridge in the context of PBEE, (3) high throughput computing technology in the cloud, and (4) optimization problem formulation and solution.

The challenges tackled by the present research include:

(1) The finite element (FE) modeling

The comprehensive FE model of the CHSR Prototype Bridge developed in OpenSees is built up by integrating different modeling techniques for the various components of the bridge (e.g., bridge deck, bridge piers, seismic isolators, slotted hinge devices, shear keys, abutments, pile cap, pile foundations, surrounding soil, and rails). Soil-foundation-structure interaction and track-structure interaction are also included in the model of the bridge system, where the dynamic *p-y* approach for simulation of pile foundations is employed with multi-support seismic excitation. To obtain the depth-varying displacement histories at the far-field ends of the *p-y* springs, Shake91 (software for one dimensional site response analysis) is integrated with Matlab for de-convolution analysis of an ensemble of ground motions, a required pre-processing task for soil-foundation-structure interaction analysis. Overall, the FE modeling and simulation is a challenging integration of different modeling techniques developed, verified, and validated by the author or other researchers.

(2) Probabilistic performance evaluation

Probabilistic performance evaluation of a large and complex bridge system with and without seismic isolators is a challenging task by itself. In this research, probabilistic performance evaluation is performed according to the PBEE methodology, which is implemented into the proposed PPBOSD framework.

(3) High computational needs and computing resources

The high computational costs due to the computationally intensive parametric nonlinear time history analyses considering hundreds of seismic inputs and the large volume of simulated data pose a challenge to civil engineers with limited knowledge of computing technologies. To overcome this obstacle in this project, high throughput cloud computing is integrated into the proposed PPBOSD framework, taking advantage of the latest advances in computer science for engineering applications.

(4) Probabilistic structural optimization

The automation of the optimal seismic design and the selection of optimization algorithms is a complex tast. The academic research on optimization tends to tackle this task using an “algorithm-seeks-problem” approach, while the engineering need is quite the opposite, and requires a “problem-seeks-algorithm” approach. This opens a door to all optimization algorithms, including the brute-force optimization through parametric studies (Cohn 1993). Optimization using mathematical algorithms or tools such as SNOPT (Gill 2008) requires automation of the interaction between different software packages.

1.8. Organization of This Dissertation

This dissertation is organized as follows:

Chapter 1 serves as a background introduction to probabilistic performance based optimum design of seismic isolators for bridge structures; it includes literature review/survey in the following four related aspects: (1) evolution of seismic design philosophy; (2)

performance-based design and evaluation procedure (PBEE methodology); (3) earthquake protection systems with special emphassis on seismic isolation; and (4) structural optimization to systematically improve or optimize the initial design. The research motivation, scope, objectives, opportunities, and challenges are also summarized in Chapter 1.

The proposed PPBOSD framework is formulated in **Chapter 2**. Before it is applied to a large real-world system such as the CHSR prototype bridge considered in this research, it is first applied to a simplified nonlinear SDOF model (inspired from a detailed nonlinear FE bridge model) for illustration and verification purposes. This chapter also presents the PEER PBEE methodology (forward probabilistic seismic performance evaluation) and its implementation in the context of the simplified SDOF bridge model.

Structural optimization of seismic isolators for application to a CHSR prototype bridge is selected as a test-bed for the proposed PPBOSD framework. The design of a CHSR prototype bridge system and a numerical model thereof are presented in detail in **Chapter 3**. A fully three-dimensional (3D) nonlinear FE model of the CHSR prototype bridge is developed in OpenSees, accounting for soil-foundation-structure interaction and track-structure interaction. Furthermore, pertinent simulation and analysis techniques are investigated and validated using the nonlinear time history analysis method.

To better understand the seismic response behavior of the seismic isolated CHSR prototype bridge, two comparative studies are conducted between the seismic isolated bridge (IB) and the conventional non-isolated bridge (NIB). The deterministic and probabilistic studies are presented in Chapter 4 and 5, respectively.

In **Chapter 4**, two bi-directional horizontal ground motion records (far-field and near-field) are selected and scaled to the same hazard level for both the IB and NIB. These two ground motion records are scaled to the operating basis earthquake level (OBE) and the

maximum considered earthquake level (MCE), respectively. The seismic responses of the IB and NIB subjected to the two ground motions records scaled to these two hazard levels are compared to determine the beneficial and detrimental effects of using seismic isolation in CHSR bridges from a deterministic point of view.

Chapter 5 takes into account the randomness and uncertainties inherent in the site-specific seismic hazard and the record-to-record variability to perform probabilistic demand hazard analysis for different pertinent EDPs. Probabilistic performance evaluation of the seismic isolators is conducted through comparison of the computed demand hazard curves for the IB and NIB.

Chapter 6 discusses the extensive computational needs for the analyses required by the PPBOSD framework. A cloud-based optimization (CBO) workflow is developed, making use of high throughput computing (HPC) technology for distributed computing in cloud. The CBO workflow aims to orchestrate the complex and multi-stage scientific computations and data manipulations required for the probabilistic parametric/optimization analyses involved in the PPBOSD framework as applied to the CHSR prototype bridge.

Chapter 7 uses the CBO workflow platform developed in Chapter 6 and performs parametric probabilistic demand hazard analyses for the seismic isolated CHSR prototype bridge. Two types of seismic demand risk features are defined and presented with the associated parametric PBEE analysis results. A comprehensive analysis of the beneficial and detrimental effects of seismic isolation for the CHSR prototype bridge is carried out as a basis for the structural optimization problem formulations and solutions under the PPBOSD framework presented in **Chapter 8**.

Chapter 9 summarizes the main contributions and findings of the research reported herein. Areas of future research are recommended.

References

Abrahamson, E., and Mitchell, S. (2003). "Seismic response modification device elements for bridge structures development and verification." *Computers and Structures*, 81, 463–467.

Ahmadi, G. (1995). "Overview of base isolation, passive and active vibration control strategies for aseismic design of structures." *Scientia Iranica*, 2(2), 99-116.

Aiken, I. D., Kelly, J. M., and Tajirian, F. F. (1989). "Mechanics of low shape factor elastomeric seismic isolation bearings." *Report No. UCB/ EERC-89/13*, Earthquake Engineering Research Center, Univ. of California, Berkeley, California.

Aktas, E., Moses, F., and Ghosn, M. (2001). "Cost and safety optimization of structural design specifications." *Reliability Engineering and System Safety*, 73, 205 - 212.

Almazan, J., and De la Llera, J. (2002). "Analytical model for structures with frictional pendulum isolators." *Earthquake Engineering and Structural Dynamics*, 31, 305–332.

Almazan, J., and Llera, J. (2003). "Physical model for dynamic analysis of structures with FPS isolators." *Earthquake Engineering and Structural Dynamics*, 32, 1157–1184.

Ang, AH-S, and Lee, J-C. (2001). "Cost optimal design of R/C buildings." *Reliability Engineering and System Safety*, 73, 233–8.

Arora, J., and Wang, Q. (2005). "Review of formulations for structural and mechanical system optimization." *Structural and Multidisciplinary Optimization*, 30, 251–272.

Asher, J. W., Hoskere, S. N., Ewing, R. D., Mayes, R. L., Button, M. R., and Van Volkinburg, D. R. (1997). "Performance of seismically isolated structures in the 1994 Northridge and 1995 Kobe earthquakes." *Proceedings of Structures Congress*, vol. XV, ASCE, 1997.

Austin, M., Pister, K., and Mahin, S. A. (1987a). Probabilistic design of moment-resistant frames under seismic loading. *Journal of Structural Engineering*, 113(8), 1660 - 1677.

Austin, M., Pister, K., and Mahin, S. A. (1987b). Probabilistic design of earthquake-resistant structures. *Journal of Structural Engineering*, 113(8), 1642 - 1659.

Barbato, M., Petrini, F., Unnikrishnan V. U., and Ciampoli, M. (2013). "Performance-based hurricane engineering (PBHE) framework." *Structural Safety*, 45, 24 – 35.

Barthelemy, J. F. M., and Haftka, R. T. (1993). "Approximation concepts for opti- mum structural design—a review." *Structural Optimization*, 5, 129–144.

Beck, A., and Gomes, W. (2012). “A comparison of deterministic, reliability-based and risk-based structural optimization under uncertainty.” *Probabilistic Engineering Mechanics*, 28, 18–29.

Becker, T. C., and Mahin, S. A. (2012). “Experimental and analytical study of the bidirectional behavior of the triple friction pendulum isolator.” *Earthquake Engineering and Structural Dynamics*, 41, 355 – 373.

Bucher, C. (2009). “Probability-based optimal design of friction-based seismic isolation devices.” *Structural Safety*, 31(6), 500–507.

Bucher, C. (2011). “Optimal friction pendulum systems for seismic isolation.” *Proceedings of the 8th International Conference on Structural Dynamics*, EURODYN 2011, Leuven, Belgium, July 2011 (July), 4–6.

Buckle, I., and Mayes, R. (1990). “Seismic isolation: history, application, and performance-a world view.” *Earthquake Spectra*. 6(2), 161-201.

California Buildings Standards Commission (2001). “*California Building Code*.” Sacramento, California.

Chan, C., and Zou, X. (2004). “Elastic and inelastic drift performance optimization for reinforced concrete buildings under earthquake loads.” *Earthquake Engineering and Structural Dynamics*, December, 929–950.

Cheng, F. Y., and Li, D. (1996). “Multi-objective optimization of structures with and without control.” *J. Guid. Control Dyn.*, 19(2), 393–397.

Chopra A. K. (1995). *Dynamics of Structures: Theory and Applications to Earthquake Engineering*. Prentice-Hall: Englewood Cliffs, NJ.

Ciampoli, M., Petrini, F. (2012). “Performance-based Aeolian risk assessment and reduction for tall buildings.” *Probabilistic Engineering Mechanics*, 28:75–84.

Cohn, M. (1994). “Theory and practice of structural optimization.” *Structural and Multidisciplinary Optimization*, 31, 20–31.

Cohn, M., and Dinovitzer, A. (1994). “Application of structural optimization.” *Journal of Structural Engineering*, 120(2), 617-650.

Comerio, M. C., Ed. (2005). *PEER Testbed Study on a Laboratory Building: Exercising Seismic Performance Assessment*, Pacific Earthquake Engineering Research Center, PEER, Report No. PEER 2005/12.

Cornell, C., and Krawinkler, H. (2000). “Progress and challenges in seismic performance.” *PEER Center News*, 3(2).

Deb, S. (2004). “Seismic base isolation-an overview.” *Special Section: Geotechnics and Earthquake Hazards*, 87(10), 140-170.

Ellingwood, B. R. (2000). “LRFD: implementing structural reliability in professional practice.” *Engineering Structures*, 22(2), 106–115.

Ellingwood, B. R. (2001). “Acceptable risk bases for design of structures.” *Prog. Struct. Engng Mater.*, 3: 170–179.

Ellingwood, B.R. (2001). “Earthquake risk assessment of building structures.” *Reliability Engineering System Safety*, 74, 251–62.

Ellingwood, B. R. (2008). “Structural reliability and performance-based engineering.” *Proceedings of the ICE - Structures and Buildings*, 161(4), 199–207.

Ellingwood, B. R., and Wen, Y. (2005). “Risk-benefit-based design decisions for low-probability/high consequence earthquake events in Mid-America.” *Progress in Structural Engineering Materials*, 7, 56–70.

Fenz, D. M., and Constantinou, M. C. (2008). “Modeling triple friction pendulum bearings for response-history analysis.” *Earthquake Spectra*, 24(4), 1011–1028.

Fragiadakis, M., and Lagaros, N. D. (2011). “An overview to structural seismic design optimisation frameworks.” *Computers and Structures*, 89(11-12), 1155–1165.

Frangopol, D.M., Lin, K-Y, Estes, A. (1997). “Life-cycle cost design of deteriorating structures.” *Journal of Structural Engineering*, 123(10), 1390–1401.

Goulet, C., Haselton, C. B., Mitrani-Reiser, J., Deierlein, G. G., Stewart, J. P., and Taciroglu, E. (2006). “Evaluation of the seismic performance of a code-conforming reinforced-concrete frame building – part I: ground motion selection and structural collapse simulation.” *8th National Conference on Earthquake Engineering (100th Anniversary Earthquake Conference)*, San Francisco, CA, April 18–22.

Griffith, M. C., Kelly, J. M., Coveney, V. A., and Koh, C.-G. (1988). “Experimental evaluation of medium-rise structures subject to uplift.” *Report No. UCB/EERC-88/02*, Earthquake Engineering Research Center, University of California, Berkeley, California.

Günay S. and Mosalam, K. M. (2013). “PEER Performance-based earthquake engineering methodology, revisited.” *Journal of Earthquake Engineering*, 17(6), 829-858.

Hamburger, R.O., Whittaker, A. S. (2003). “Considerations in performance-based blast resistant design of steel structures.” *In: Proceedings of AISC-SINY symposium on resisting blast and progressive collapse*, Dec.4–5, 2003, NewYork, USA.

Hameed, A., Koo, M., Do, T. D., and Jeong, J. (2008). “Effect of Lead Rubber Bearing Characteristics on the Response of Seismic-isolated Bridges.” *KSCE Journal of Civil Engineering*, 12(3), 187–196.

Haselton, C. B., Liel, A. B. Deierlein, G. G., Dean, B. S., and Chou, J. H. (2011). "Seismic Collapse Safety of Reinforced Concrete Buildings: I. Assessment of Ductile Moment Frames," American Society of Civil Engineers, *Journal of Structural Engineering*, 137(4), 481-491.

Haukaas, T. (2008). "Unified reliability and design optimization for earthquake engineering." *Probabilistic Engineering Mechanics*, 23, 471 – 481.

Haukaas T., and Bohl A. (2009). "Comparison of approaches for performance-based earthquake engineering." *Workshop on Performance-based Engineering*, Villa Orlandi, Anacapri, Italy, 2-4 July.

Higashino, M., and Okamoto, S. (Eds) (2006). *Response control and seismic isolation of buildings*, Taylor and Francis, New York.

Huo, Y. L., and Alemdar, B. N. (2013). "Optimal Seismic Isolation Design for A Highway Bridge with Nonlinear Base Isolator Modeling." *7th National Seismic Conference on Bridges and* Highways, May 20-22, 2013, Oakland, CA.

Hwang, J., Sheng, L., and Gates, J. (1994). "Practical analysis of bridges on isolation bearings with bi-linear hysteresis characteristics." *Earthquake Spectra*, 10(4), 705 – 727.

Hwang, J. S., Wu, J. D., Pan, T. C., and Yang, G. (2002). "A mathematical hysteretic model for elastomeric isolation bearings." *Earthquake Engineering and Structural Dynamics*, 31, 771–789.

Hwang, J., and Tseng, Y. (2005). "Design formulations for supplemental viscous dampers to highway bridges." *Earthquake Engineering and Structural Dynamics*, 34, 1627–1642.

IIzuka, M. (2000). "A macroscopic model for predicting large-deformation behaviors of laminated rubber bearings." *Engineering Structures*, 22, 323-324.

Islam, A. B. M. S., Jameel, M., Uddin, M. A., and Ahmad, S. I. (2011). "Simplified design guidelines for seismic base isolation in multi-storey buildings for Bangladesh National Building Code (BNBC)." *International Journal of the Physical Sciences*, 6(23), 5467–5486.

Jangid, R. S. (2000). "Optimum frictional elements in sliding isolation systems." *Computers and Structures*, 76, 651–661.

Jangid R. S. (2005). "Optimum friction pendulum system for near-fault motions." *Engineering Structures*, 27, 349–59.

Jangid, R. S. (2006). "Optimum lead-rubber bearings for near-fault motions." *Engineering Structures*, 29(10), 2503-2513.

Jensen, H., Ferre, M., and Kusanovic, D. (2010) “Reliability-based synthesis of non-linear stochastic dynamical systems: a global approximation approach.” *International Journal of Reliability and Safety*, 4(3/4), 139-165.

Kalpakidis, I. V., Constantinou, M. C., and Whittaker, A. S. (2010). “Modeling strength degradation in lead – rubber bearings under earthquake shaking.” *Earthquake Engineering and Structural Dynamics*, 39, 1533–1549.

Kang, B., Park, G., and Arora, J. (2006). “A review of optimization of structures subjected to transient loads.” *Structural and Multidisciplinary Optimization*, 31, 81–95.

Kelly, J. M. (1997). *Earthquake-Resistant Design with Rubber*, Springer, Berlin.

Kelly, J. M. (2003). “Tension buckling in multilayer elastomeric bearings.” *J. Eng. Mech.*, 129(12), 1363–1368.

Kelly, J. M., Buckle, I. G., and Koh, C.-G. (1987). “Mechanical characteristics of base isolation bearings for a bridge deck model test.” *Report No. UCB/EERC-86/11*, Earthquake Engineering Research Center, University of California, Berkeley, California.

Kikuchi, M., Aiken, I. D. (1997). “An analytical hysteresis model for elastomeric seismic isolation bearings.” *Earthquake Engineering and Structural Dynamics*, 26, 215–231.

Kikuchi, M., Nakamura, T., and Aiken, I. (2010). “Three dimensional analysis for square seismic isolation bearings under large shear deformations and high axial loads.” *Earthquake Engineering and Structural Dynamics*, 39, 1513–1531.

Kikuchi, M., Yamamoto, S., and Aiken, I. (2007). “An analytical model for lead–rubber bearings under large deformations.” *Proceedings of the Eighth Pacific Conference on Earthquake Engineering*, December 5 -7, Singapore.

Kirsch, U. (1981). *Optimum structural design*, New York: McGrawHill.

Kirsch, U., and Rozvany, G. (1994). “Alternative formulations of structural optimization. Structural and Multidisciplinary Optimization.” *Structural Optimization*, 7, 32–41.

Koh, C.-G., and Kelly, J. M. (1987). “Effects of axial load on elastomeric isolation bearings.” *Report No. UCB/EERC-86/12*, Earthquake Engineering Research Center, University of California, Berkeley, California.

Koh, C.G., Kelly, J. M. (1988). “A simple mechanical model for elastomeric bearings used in base isolation.” *Int. J. Mech Sci.* 30, 933-943.

Kohno, M., and Collins, K. R. (2000). “Merging life-cycle cost analysis and performance-based design of steel buildings.” *Research report UMCEE 00/06*, Department of Civil and Environmental Engineering, University of Michigan, Ann Arbor, MI, 2000.

Krawinkler, H. (2002). “A General Approach to Seismic Performance Assessment.” *International Conference on Advances and New Challenges in Earthquake Engineering*, Hong Kong.

Krawinkler, H., and Miranda, E. (2004). “Performance-based earthquake engineering.” *In Earthquake Engineering, From Engineering Seismology to Performance-Based Engineering, edited by Y. and Bertero, V.V., Bozorgnia*, CRC Press.

Krawinkler, H., and Miranda, E. (2004). “Performance-based Earthquake Engineering.” *in Earthquake Engineering: from Engineering Seismology to Performance-based Engineering*, eds. Y. Bozorgnia and V. V. Bertero (CRC Press, Boca Raton, FL), Ch. 9.

Krawinkler, H., (Ed.) (2005). *Van Nuys Hotel Building Testbed Report: Exercising Seismic Performance Assessment*, Pacific Earthquake Engineering Research Center, PEER, Report No. PEER 2005/11.

Kunde, M. C., and Jangid, R. S. (2003). “Seismic behavior of isolated bridges: A-state-of-the-art review.” *Electronic Journal of Structural Engineering*, 3, 140–170.

Kunde, M. C., and Jangid, R. S. (2006). “Effects of pier and deck flexibility on the seismic response of the isolated bridges.” *Journal of Bridge Engineering*, 11,109–121.

Kunnath, S. K. (2006). *Application of the PEER PBEE Methodology to the I-880 Viaduct*, Pacific Earthquake Engineering Research Center, PEER, Report No. 2006/10.

Kunnath, S. K., Larson, L., and Miranda, E. (2006). “Modeling considerations in probabilistic performance-based seismic evaluation: case study of the I-880 viaduct,” *Earthquake Engineering and Structural Dynamics*, 35(1), 57–75.

Lamont, S., and Rini, D. (2008). “*Performance-based structural fire engineering for modern building design*.” *Struct Congr 2008*:1–12.

Liu, M., Burns, S. A., and Wen, Y. K. (2003). “Optimal seismic design of steel frame buildings based on life cycle cost considerations.” *Earthquake Engineering and Structural Dynamics*, 32(9), 1313–1332.

Liu, M., Wen, Y. K., and Burns, S. A. (2004). “Life cycle cost oriented seismic design optimization of steel moment frame structures with risk-taking preference.” *Engineering Structures*, 26(10), 1407–1421.

Liu, M., and Frangopol, D. M. (2005). “Bridge annual maintenance prioritization under uncertainty by multiobjective combinatorial optimization.” *Computer-Aided Civil Infrastructure Engineering*, 20(5), 343–53.

Llera, J. D. la, and Lüders, C. (2004). “Analysis, testing, and implementation of seismic isolation of buildings in Chile.” Earthquake Engineering and Structural Dynamics, 33, 543–574.

Matsagar, V., and Jangid, R. (2006). “Seismic response of simply supported base-isolated bridge with different isolators.” *International Journal of Applied Science and Engineering*, 53–69.

Mayes, R., and Buckle, I. (1992). “AASHTO seismic isolation design requirements for highway bridges.” *Journal of Structural Engineering*, 118(1), 284–304.

Mitrani-Reiser, J., Haselton, C. B., Goulet, C., Porter, K. A., Beck, J., and Deierlein, G. G. (2006). “Evaluation of the seismic performance of a code-conforming reinforced-concrete frame building - part II: loss estimation.” *8th National Conference on Earthquake Engineering (100th Anniversary Earthquake Conference)*, San Francisco, California, April 18–22.

Moehle, J. P. (2003). “A framework for performance-based earthquake engineering.” *Proceedings of ATC-15-9 Workshop on the Improvement of Building Structural Design and Construction Practices*, Maui, HI, June.

Moehle, J. P. and Deierlein, G. G. (2004). “A framework for performance-based earthquake engineering.” *Proceedings of 13th World Conference on Earthquake Engineering*, Paper No 679, Vancouver, Canada.

Moehle J. P., Stojadinovic B., Der Kiureghian A., and Yang T. Y. (2005). “Application of PEER performance-based earthquake engineering methodology.” *Research Digest No. 2005-1*, Pacific Earthquake Engineering Research Center, University of California, Berkeley, CA.

Morgan, T. A., and Mahin, S. A. (2008). “The optimization of multi-stage friction pendulum isolators for loss mitigation considering a range of seismic hazard.” *The 14th World Conference on Earthquake Engineering*, October 12 – 17, Beijing, China

Morgan, T. A., and Mahin, S. A. (2010). “Achieving reliable seismic performance enhancement using multi-stage friction pendulum isolators.” *Earthquake Engineering and Structural Dynamics*, 39(13), 1443–1461.

Mosalam, K. M. and Günay, S. (2014). “Seismic performance evaluation of high voltage disconnect switches using real-time hybrid simulation: I. System development and validation.” *Earthquake Engineering & Structural Dynamics*, 43(8), 1205–1222.

Mosqueda, G., Whittaker, A. S., Fenves, G. L. (2004). “Characterization and modeling of friction pendulum bearings subject to multiple components of excitation.” *Journal of Structural Engineering*, 130(3), 433–442.

Nagarajaiah, S., Sun, X. (2000). “Response of base isolated USC hospital building in Northridge earthquake.” *Journal of Structural Engineering*, 126, 1177–1186.

Nagarajaiah, S., Sun, X. (2001). “Base isolated FCC building: Impact response in Northridge earthquake.” *Journal of Structural Engineering*, 127, 1063–1074.

Park, J. and Otsuka, H. (1999). “Optimal yield level of bilinear seismic isolation devices.” *Earthquake Engineering and Structural Dynamics*, 28, 941-955.

Park, K.-S., Jung, H.-J., and Lee, I.-W. (2002). “A comparative study on aseismic performances of base isolation systems for multi-span continuous bridge.” *Engineering Structures*, 24(8), 1001–1013.

Petrini, F. (2009). A probabilistic approach to Performance-Based Wind Engineering (PBWE). *Ph.D. dissertation*. Rome, Italy: University of Rome “LaSapienza", 2009.

Porter, K. A. (2003). “An overview of PEER’s performance-based earthquake engineering methodology.” *Conference on Applications of Statistics and Probability in Civil Engineering (ICASP9)*, Civil Engineering Risk and Reliability Association (CERRA), San Francisco, California, July 6–9.

Riggs, H. R., Robertson, I. N., Cheung, K. F., Pawlak, G., Young, Y. L., and Yim, S. C. S. (2008). “Experimen-tal simulation of tsunami hazards to buildings and bridges. *In:Proceedings of the 2008 NSF engineering research and innovation conference*. Jan 7 - 10, Knoxville, USA.

Rojas, H., Foley, C., and Pezeshk, S. (2011). “Risk-Based Seismic Design for Optimal Structural and Nonstructural System Performance.” *Earthquake Spectra*, 27(3), 857–880.

Ryan, K. L., Kelly, J. M., and Chopra, A. K. (2004). “Experimental observation of axial-load effects in isolation bearings.” *Proc., 13th World Conference on Earthquake Engineering*, Paper No. 1707, Canadian Association for Earthquake Engineering, Vancouver, British Columbia, Canada.

Ryan, K. L., Kelly, J. M., and Chopra, A. K. (2005). “Nonlinear model for lead–rubber bearings including axial-load effects.” *Journal of Engineering Mechanics*, 131(12), 1270–1278.

Sarrazin, M., Moroni, O., Neira, C., and Venegas, B. (2012). “Performance of bridges with seismic isolation bearings during the Maule earthquake, Chile.” *Soil Dynamics and Earthquake Engineering*, 1–15.

SEAOC (1995). *Vision 2000 - A Framework for Performance Based Earthquake Engineering*. Vol. 1, California.

Structural Engineers Association of Northern California - SEAONC (1986), *Tentative Seismic Isolation Design Requirements*. San Francisco, California.

Tsai, C., Chiang, T., and Chen, B. (2003). “Finite element formulations and theoretical study for variable curvature friction pendulum system.” *Engineering Structures*, 25, 1719–1730.

Tsai, C., and Lin, Y. (2009). “Mechanical Characteristics and Modeling of Multiple Trench Friction Pendulum System with Multi-intermediate Sliding Plates.” *Proc. of World Academy of Science, Engineering and Technology*, 50, 343–360.

Tsai, C., Lin, Y., and Su, H. (2010). "Characterization and modeling of multiple friction pendulum isolation system with numerous sliding interfaces." *Earthquake Engineering and Structural Dynamics*, 39, 1463–1491.

Tsai, C., Lu, P., Chen, W., and Chiang, T. (2008). "Finite element formulation and shaking table tests of direction-optimized-friction-pendulum system." *Engineering Structures*, 30, 2321–2329.

Tsai, C., Chiang, T., and Chen, B. (2005). "Experimental evaluation of piecewise exact solution for predicting seismic responses of spherical sliding type isolated structures." *Earthquake Engineering and Structural Dynamics*, 34, 1027–1046.

UBC (1997). *Uniform Building Code*, International Council of Building Code Officials.

Venkayya, V. (1978). "Structural optimization: a review and some recommendations." *International Journal for Numerical Methods in Engineering*, 13, 203–228.

Wang, Q., and Arora, J. (2006). "Alternative formulations for structural optimization: an evaluation using frames." *Journal of Structural Engineering*, December, 1880–1889.

Warn, G. P., and Ryan, K. L. (2012). "A Review of Seismic Isolation for Buildings: Historical Development and Research Needs." *Buildings*, 2(4), 300–325.

Yang, F., Zhong, T., and Xia, H. (2008). "Optimization study on the design parameters of seismic isolated bearing for railway bridges." *The 14th World Conference on Earthquake Engineering*, October 12-17, Beijing, China.

Zayas, V., Low, S., and Mahin, S. A. (1990). "A simple pendulum technique for achieving seismic isolation." *Earthquake Spectra*, 6, 317–334.

Zhang, Y. (2006). "Probabilistic structural seismic performance assessment methodology and application to an actual bridge-foundation-ground system." Ph.D. dissertation, Univ. of California, San Diego, San Diego.

Zhang, Y., Conte, J. P., Yang, Z., Elgamal, A., Bielak, J., and Acero, G. (2008). "Two-dimensional nonlinear earthquake response analysis of a bridge-foundation-ground system." *Earthquake Spectra*, 24(2), 343 – 386.

Zhao, G., Zhao, J., and Zhang, X. (2011)." Optimization of Large-tonnage Lead Rubber Bearing for Highway Bridge." *Applied Mechanics and Materials*, 71-78, 3832–3836.

Zhou, F. L., Kelly, J. M., Fuller, K. N. G., and Pan, T. C. (1992). "Optimal design of seismic isolation for multistoried buildings." *Proceedings of the World Conference on Earthquake Engineering*, Madrid, Spain.

Zou, X. K. (2002). “Optimal seismic performance-based design of reinforced concrete buildings.” *Ph.D. sissertation*, Hong Kong Univ. of Science and Technology, Hong Kong, P.R. China.

Zou, X. K. (2008). “Integrated design optimization of base-isolated concrete buildings under spectrum loading.” *The Journal of Structural Multidisc Optimization*, 36, 493- 507.

CHAPTER 2

FRAMEWORK OF PROBABILISTIC PERFORMANCE-BASED OPTIMUM SEISMIC DESIGN (PPBOSD)

2.1. Introduction

The seismic design process involves lots of sources of uncertainties, including seismic loadings (e.g., seismic hazard for a given site characterized by the randomness in the intensity measure and the record-to-record variation), the mathematical models (e.g., finite element model) with certain assumptions for response simulation, and the construction materials and so on. It is important to recognize, identify, and quantify these uncertainties inherent in the performance evaluation and therefore in the performance-based design.

In the deterministic design approach adopted in current practice, load factors and resistance factors are employed to account for the uncertainties in the loads applied and the structural capacity respectively implicitly. In the field of structural reliability and integrated risk assessment and management, systematic and quantitative approaches are essential to structural design for public safety. Consequently, a new-generation design method to consider the uncertainty explicitly is expected to make the probabilistic design more transparent.

A probabilistic performance assessment procedure is required, and the well-established Probabilistic Performance-Based Earthquake Engineering Methodology (PBEE) methodology addresses this this need in the area of earthquake engineering. The state-of-the-art PBEE methodology has been accepted as a paradigm for probabilistic performance evaluation of structures.

The PBEE methodology, developed under the auspice of the Pacific Earthquake Engineering Research (PEER) Center in the last fifteen years, is implemented mainly for risk assessment of the existing or newly designed structural system. It consists of four analytical steps to quantify the seismic hazard, structural response, structural damage and seismic loss in a probabilistic manner. The principal idea of PBEE is to propagate the uncertainties originating from earthquake ground motions to the uncertainties in structural response, seismic damage and relevant seismic loss, considering other relevant uncertainties during the procedure.

PBEE provides the foundation of probabilistic seismic performance evaluation for given structures, referred to as forward PBEE analysis herein, while it needs to be inverted for performance-based design (i.e., inverse PBEE analysis). Furthermore, a risk-based optimum seismic design framework is desired for computer-aided optimum design/retrofit in order to minimize the seismic risk to structural system. The time is ripe to promote the concept of automated design process in structural optimization for decision-making in risk management instead of using trial and error approaches in the design, especially considering the advancement of the computing resources and optimization capabilities. Accordingly, a probabilistic performance-based optimum seismic design (PPBOSD) framework is proposed in the context of the PBEE methodology.

This research work stands at the intersection of the research and practice. For illustration and validation purposes, the proposed PPBOSD framework is first exercised on a simplified nonlinear single-degree-of-freedom (SDOF) bridge model optimized (i.e., rated) for a target seismic loss hazard curve. The nonlinear SDOF model employed herein is calibrated based on the longitudinal behavior of the Humboldt Bay Middle Channel (HBMC, shown in Figure 2.1) Bridge developed in *OpenSees*.

Figure 2.1: Humboldt Bay Middle Channel (HBMC) Bridge (Courtesy of Caltrans)

Based on the nonlinear SDOF bridge model, the forward PBEE analysis is presented comprehensively with the application of all four steps of PBEE to show the complete methodology, followed by several PBEE analyses for a perturbation of system parameters. An optimization problem is proposed, formulated, and solved under the PPBOSD framework in order to illustrate and validate the systematic and standardized inverse PBEE analysis approach. The proposed methodology opens a new door to extend the PEER PBEE methodology to use optimization for assisting decision-making in risk management and to apply the promising methodology to practical problems in the field of structural engineering.

2.2. Proposed PPBOSD Framework

As an essential component of the PPBOSD framework, the PEER PBEE methodology consists of four stages for a given structural design located at a specific site location (see

Figure 2.2). They include four analytical steps, i.e., probabilistic seismic hazard analysis, probabilistic seismic demand hazard analysis, probabilistic structural damage hazard analysis, and probabilistic seismic loss hazard analysis. Each step is associated with the characterization of probabilistic properties of such intermediate output variables as ground motion Intensity Measure (IM), Engineering Demand Parameter (EDP), Damage Measure (DM), and Decision Variable (DV) respectively.

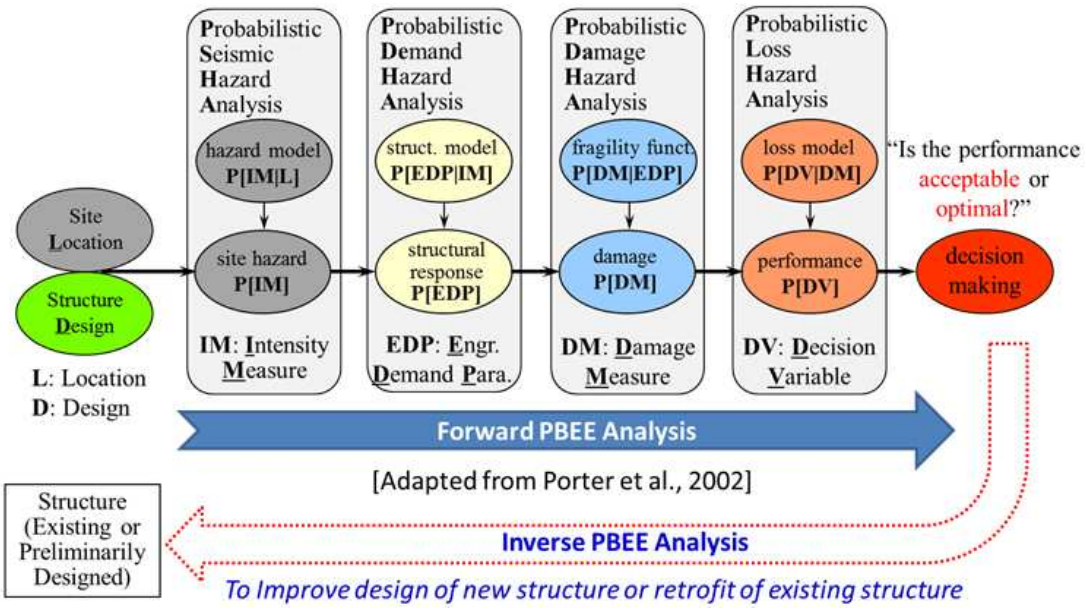

Figure 2.2: Forward PBEE analysis and inverse PBEE analysis for probabilistic performance-based seismic design/retrofit

Forward PBEE analysis with a perturbation in structural parameters performed in this research will expose how the PBEE analysis results will change as a function of structural system parameters. As observed from the perturbation analysis, different seismic demand/damage/loss curves can be obtained by varying the structural parameters (SP) of **x**. A schematic plot of the variation of demand/loss hazard curves is exhibited in Figure 2.3 to illustrate the motivation for PPBOSD.

The hazard curve #1 represents the seismic risk characterized by the probability of EDP/DV exceeding a threshold value in a life exposure period for a civil system with initial design parameters **x**. To improve the current design, there are three possible possibilities. Ideally it is desirable to update the initial design parameters of **x** aiming at reducing seismic risk across all hazard levels, to reach the hazard curve #4. Given the practical design constraints, if the hazard curve #4 is not reachable, the structure can either be designed to reduce the seismic risk at lower hazard levels at the cost of increasing the seismic risk at higher hazard levels, e.g., reaching the design hazard curve #2; or the other way around, e.g., reaching the design hazard curve #3.

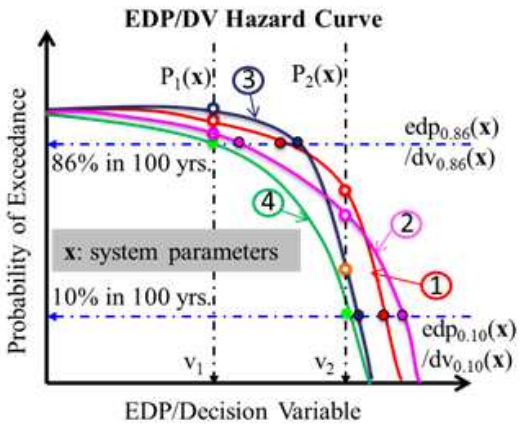

Figure 2.3: Illustration of the motivation for probabilistic performance-based optimum seismic design (PPBOSD)

In essence, an inverse problem inherent is confronted here, which implies the underlying motivation of the need for probabilistic performance-based optimum seismic design/retrofit. To address the issues of updating the initial design or retrofit, trial-and-error approach has been widely used to tackle the inverse problem in the deterministic design by experienced senior engineers. While in the context of probabilistic performance-based design of complex structural system, intuition and experience fail to easily guarantee a feasible or

optimal design. Therefore, the probabilistic performance-based optimum seismic design (PPBOSD) framework, as illustrated in Figure 2.4, is proposed and implemented through wrapping an optimization layer outside the forward PBEE analysis procedure, to form a closed iterative loop for structural optimization.

The PPBOSD framework mainly consists of four components: probabilistic model development, probabilistic performance evaluation, definition of design objectives, and decision analysis. Among them, the first two components have been weaved together to form the current PEER PBEE methodology. The following is a summary of some exclusive attractive features and advantages unique to this general framework proposed here.

(1) Herein, seismic hazard will be the only hazard considered, even though the proposed framework can be easily extended for a decision-making framework when more natural hazards are accounted for in the proposed framework.

(2) The independent components embedded in the formulation of the PEER PBEE methodology is extracted and exposed as probabilistic model development, on which considerable research can be carried out independently to promote the PBEE methodology.

(3) An optimization layer for decision making is wrapped outside the forward PBEE analysis (i.e., probabilistic performance evaluation). The updating process for optimal design can either resort to rigorous numerical optimization tools (i.e., SNOPT), or brutal force method based on grid-based parametric analysis using high-throughput and cloud-computing technologies to address the high computing need required.

(4) The modularized PPBOSD framework is proposed using objective-oriented optimization in the context of PBEE analysis to realize an expected performance target. Objectives need to be defined quantitatively in terms of demand hazard, damage hazard,

and/or decision hazard for performance objectives (e.g., serviceability, safety, resiliency, and sustainability).

As an extension of the PBEE methodology, the proposed PPBOSD framework marks a major advance in the approach to implementing probabilistic performance-based design (PBD) by updating the initial design or retrofitting the existing structure using optimization techniques. Using the PPBOSD framework, the structural design parameters (**x**) of the civil system can be optimized for different purposes, to serve specific objectives of the structural designers and analysts in the stages of seismic demand and damage analysis, or of the stakeholders and owners of the civil system in the stage of seismic loss analysis. The probabilistic performance objectives are explicitly stated and all pertinent sources of uncertainty are included in the analysis procedure in this framework.

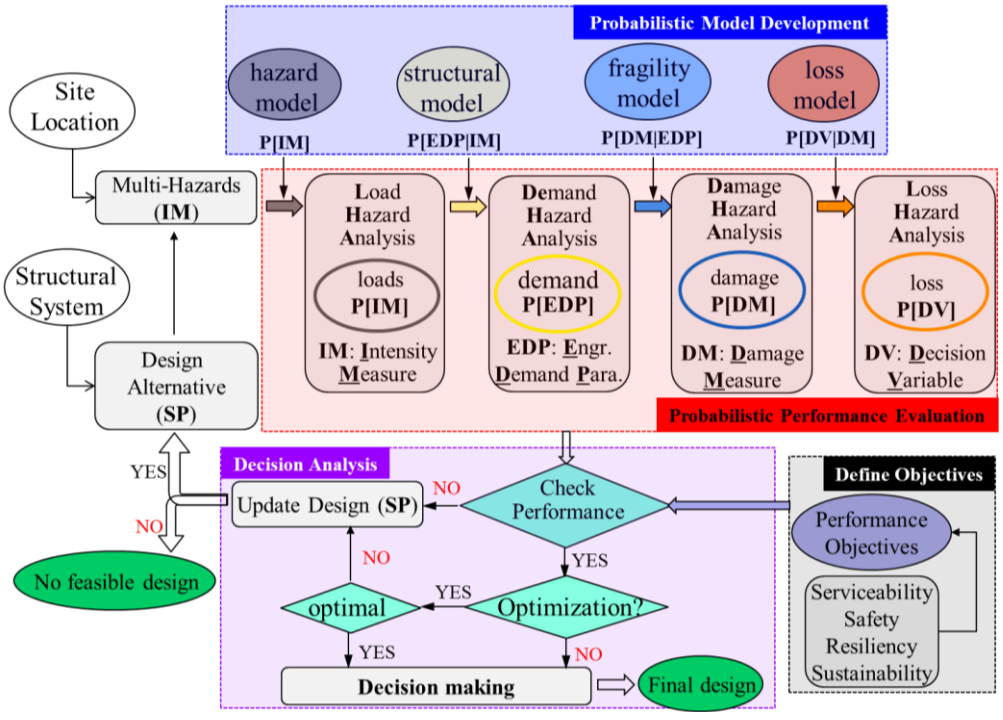

Figure 1.4: Probabilistic performance-based optimum seismic design (PPBOSD) framework

For illustration and validation purposes, the above PPBOSD framework is exercised on a nonlinear single-degree-freedom (SDOF) bridge model optimized (i.e., rated) for a target seismic loss hazard curve, and possible optimization candidates are proposed for further analysis.

2.3. Structural Model and Site Location

For the forward PBEE and inverse PBEE analysis, a structure and site location to be selected and tested is the main input into the PBEE methodology and the PPBOSD framework. To develop and explore the PPBOSD framework, the nonlinear SDOF model is calibrated from the longitudinal force-deformation behavior of the Humboldt Bay Middle Channel (HBMC) Bridge, matching the initial period of the bridge model in the longitudinal direction. The nonlinear hysteretic behavior is modeled using the Menegotto-Pinto material model with the main parameters listed in Figure 2.5. This nonlinear SDOF model is utilized for seismic response simulation and prediction.

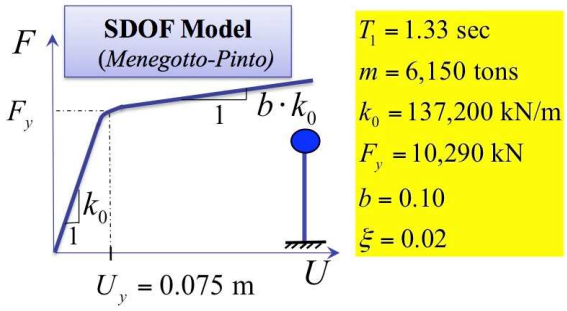

Figure 2.5: Nonlinear single-degree-of-freedom (SDOF) bridge model

The seismic hazard was obtained for the site location, Oakland (37.803N, 122.287W), and NEHRP soil type class C-D, with the average shear wave velocity in the top 30 meters of soil medium, Vs_{30}, as 360m/s. In this research, the probabilistic seismic hazard analysis is carried out based on this site location and soil condition selected.

2.4. Forward PBEE Analyses

According to the Total Probability Theorem (TBT), the PEER PBEE methodology breaks down the seismic risk procedure into four successive steps. In each step, the probabilistic characterization of the aforementioned intermediate output variables of IM, EDP, DM, and DV (see Figure 2.4) is implemented respectively. The mathematical model for risk analysis in the PBEE methodology is written as (Porter et al. 2002)

$$\nu_{DV}(dv) = \iiint G\langle dv|dm,edp,im\rangle \cdot \left|dG\langle dm|edp,im\rangle\right| \cdot \left|dG\langle edp|im\rangle\right| \cdot \left|d\nu_{IM}(im)\right| \tag{2.1}$$

In which, $\nu_X(x)$ denotes the mean annual rate of occurrence of events $\{X > x\}$, $G\langle x|y\rangle = P(X > x|Y = y)$ denotes the conditional complementary cumulative distribution function (CDF) of a random variable X given a random variable $Y = y$, and $d\nu_{IM}(im) = \nu_{IM}(im) - \nu_{IM}(im + dim)$. In practice, "one-step" forward dependence is assumed in the probability propagation process, i.e., $G\langle dm|edp,im\rangle = G\langle dm|edp\rangle$ and $G\langle dv|dm,edp,im\rangle = G\langle dv|dm\rangle$, thus Equation (2.1) is reduced to

$$\nu_{DV}(dv) = \iiint G\langle dv|dm\rangle \cdot \left|dG\langle dm|edp\rangle\right| \cdot \left|dG\langle edp|im\rangle\right| \cdot \left|d\nu_{IM}(im)\right| \tag{2.2}$$

The integration of the above needs to characterize $\nu_{IM}(im)$ first, which refers to as the mean annual rate of earthquake ground motion intensity measure IM exceeding the threshold value im. It is to be obtained in the step of probabilistic seismic hazard analysis illustrated below.

2.4.1. Probabilistic seismic hazard analysis (PSHA)

Pioneered by the theoretical framework developed by Cornell (1968), Probabilistic Seismic Hazard Analysis (PSHA) has become the most accepted approach for assessing the

site-specific seismic hazard risk (McGuire 1995, Kramer 1996, Shome et al. 1998, Luco and Cornell 2002, Petersen et al. 2008). PSHA is the first step of the PEER PBEE methodology, corresponding to the procedure to obtain the probabilistic properties of an intensity measure (IM) for earthquake ground motions. Probabilistic seismic hazard is characterized by the quantification of the uncertainties in the ground motion IM in terms of the mean annual rate (MAR), $\nu_{IM}(im) = \nu_{IM}(IM > im)$, or the probability of exceedance (PE) for an exposure time. In a given site location, the contribution of all possible causative seismic sources ($N_{sources}$) is integrated using the total probability theorem, with mainly the following assumptions: (1) the occurrence of an earthquake from one source is independent of the occurrence of earthquakes from other sources; (2) Given the occurrence of an earthquake from a specific source i, the magnitude (M_i) and source-to-site distance (R_i) are statistically independent; (3) the Poisson random occurrence model is assumed for the occurrence of earthquake. The mathematical model for PSHA can be formulated as

$$\nu_{IM}(im) = \sum_{i=1}^{N_{sources}} \nu_i \int_{R_i} \int_{M_i} P\left[IM > im \middle| M_i = m, R_i = r\right] f_{M_i}(m)\, f_{R_i}(r)\, dm\, dr \tag{2.3}$$

In which ν_i is the mean annual rate (MAR) of occurrence of earthquakes with magnitudes greater than a lower bound threshold value, m_0, from seismic source *i*. $f_{M_i}(m)$ and $f_{R_i}(r)$ denote the probability density functions (PDF) to characterize the uncertainties for the magnitude (M_i) and source-to-site distance (R_i) respectively, conditional to an earthquake with magnitude greater than the predefined lower bound from seismic source *i*.

Regarding to the term $P\left[IM > im \middle| M_i = m, R_i = r\right]$ inside the integration, several studies have been performed for different IMs and locations around the world. The term is given by a ground motion prediction equation (GMPE), or “attenuation relation”, developed

by applying statistical regression analyses to seismic data recorded or derived from recordings. For sites in the western U.S. where the selected site is located, three Next Generation of Attenuation models, i.e., Boore–Atkinson 2008, Campbell–Bozorgnia 2008, and Chiou–Youngs 2008, are used for the PSHA.

Among a family of earthquake ground motion intensity measures, e.g., peak ground motion acceleration (PGA), peak ground velocity (PGV), Arias Intensity (AI), and elastic spectral acceleration (PSA) for a certain period and damping ratio, a statistically efficient and sufficient predictor needs to be selected. According to the correlation studies by Cornell and his co-workers (Shome et al. 1998, Luco and Cornel 2002), a 5% damped elastic spectral acceleration associated with the fundamental period (T_1) of structural system $S_a\left(T_1, \xi = 5\%\right)$ is the best alternative and is now widely utilized, e.g., as the United States Geological Survey (USGS) publicly available PSHA results. In this study, the USGS PSHA tool (USGS 2008 Interactive De-aggregations, http://earthquake.usgs.gov/hazards/) is used to generate the probabilistic seismic hazard curve for the test-bed structure located at the selected site of study. Uniform hazard spectra of 30 hazard levels, ranging from lowest hazard level (50% in 30 years) to highest hazard level (1% in 200 years), are obtained as shown in Figure 2.6. Figure 2.7 displays the probabilistic seismic hazard curves, with the spectra values IM_i at the fundamental period of our structure (T = 1.33 sec) corresponding to 30 different hazard levels characterized as mean annual rate MAR_i, annual probability of exceedance APE_i, or probability of exceedance in 50 years $PE50_i$ for $i = 1, 2, \cdots, 30$.

To get an analytical expression for the seismic hazard curve, the data points $(IM_i,\ PE50_i)$ are fitted using a least square optimization to a nonlinear function such as the CCDF of a lognormal random variable, namely:

$$\min_{\theta_1,\ \theta_2} \sum_{i=1}^{np} \left[g(IM_i,\ \theta_1,\ \theta_2) - PE50_i \right]^2 \tag{2.4}$$

The nonlinear function to be fitted is

$$g(im,\ \theta_1,\ \theta_2) = 1 - \Phi\left(\frac{\ln im - \theta_1}{\theta_2} \right) \tag{2.5}$$

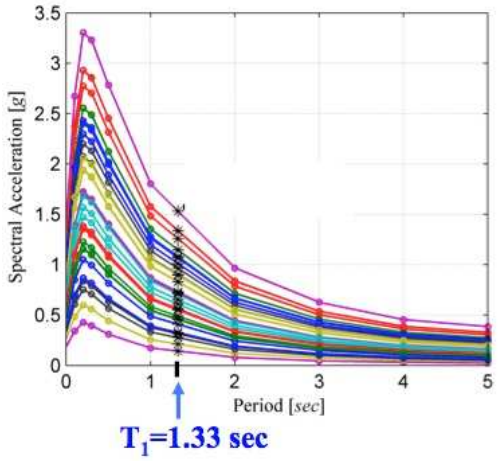

Figure 2.6: Uniform hazard spectra of 30 different hazard levels

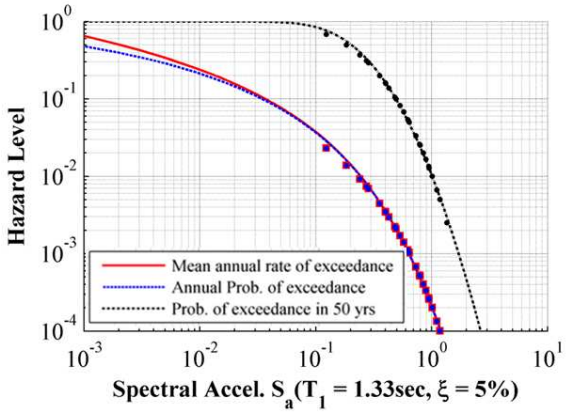

Figure 2.7: Probabilistic seismic hazard curves

After the nonlinear fitting, the analytical probabilistic seismic hazard curve is presented in Figure 2.7 in terms of mean annual rate of exceedance (MAR), annual probability of exceedance (APE), and probability of exceedance in 50 years (PE50) respectively. The probabilistic seismic hazard curve is to be convolved with the conditional probabilistic seismic demand hazard curve in the next step of PBEE analysis to get the probabilistic seismic demand hazard curve.

Besides the probabilistic seismic hazard curve obtained, any seismic hazard point on the hazard curve can be de-aggregated with respect to source-to-site distance and magnitude. It shows more insights into the contributory magnitude and source-to-site distance bins of earthquake events and they are used as a guide to select the site-specific ground motions for the second step of the PBEE analysis.

Figure 2.8 shows the probabilistic seismic hazard de-aggregation of the spectral acceleration at a period of 1.0sec, the closest value to the period of interest among the available de-aggregation results, corresponding to a hazard level with a probability of exceedance of 2% in 50 years. Obviously, there exist two modes here. The higher mode corresponds to the contribution of the Hayward Fault to the east of Oakland, while the lower mode is mainly the contribution from the San Andreas Fault to the west. Based on geological and seismological conditions (i.e., fault mechanism as strike-slip), the M-R de-aggregation of probabilistic seismic hazard results (i.e., $5.9 < M < 7.3$, $9 < R < 40$km), and local site condition (e.g., Vs30), 146 horizontal ground motion components are selected out of 3551 in the PEER NGA Database for the seismic demand hazard estimation.

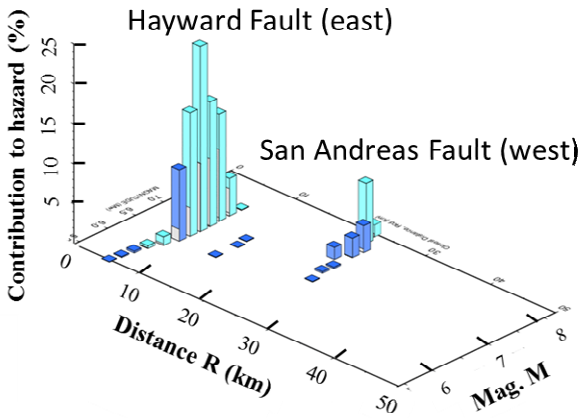

Figure 2.8: Probabilistic seismic hazard M−R de-aggregation for the site of study (Oakland) associated with hazard level of probability of exceedance of 2% in 50 years

Figure 2.9: The two main seismic faults to the selected site of study, Oakland, California

2.4.2. Probabilistic seismic demand analysis (PSDeA)

The second step of the PEER PBEE methodology, the probabilistic seismic demand analysis (PSDeA), estimates the probabilistic properties of the seismic demand imposed on the structure by future earthquake ground motions for a set of engineering demand parameters (*EDPs*). Examples are computing the mean annual rate of *EDP* (e.g., displacements, deformations, induced internal forces or stresses, etc.) exceeding a threshold value edp, $\nu_{EDP}(edp)$, denoted as the probabilistic seismic demand hazard curve. This probabilistic seismic demand hazard curve characterized by the mean annual rate of exceedance can also be converted to probability of exceedance in an exposure life time (e.g., for 100 years, denoted as PE100) assuming Poisson process. Aiming at characterizing the seismic risk in terms of seismic demand to structures, PSDeA can be accomplished with two steps: (i) Compute the conditional probabilistic demand for given hazard level, $P\left[EDP \middle| IM = im\right]$, and (ii) Convolve the conditional probability of demand analysis results $P\left[EDP \middle| IM = im\right]$ with the seismic hazard curve already obtained in the first step of the PBEE analysis. Then, the TPT for a continuous random variable IM leads to the following equation (2.6) for probabilistic seismic demand hazard curve

$$\nu_{EDP}(edp) = \int_{IM} P\left[EDP > edp \middle| IM = im\right] \left| d\nu_{IM}(im) \right| \tag{2.6}$$

(1) Probabilistic response analysis conditioned on IM

The first step of the PSDeA is to find out the probability distribution of EDP given a certain IM associated with a specific seismic hazard level, which could be addressed through several alternative approaches like the cloud method, and the stripe method. Basically, it is to establish a statistical model to predict the structural response, EDP, based on the given earthquake ground motion intensity measure IM.

In this study, the cloud method employs the large sample of selected ground motions spanning a wide range of earthquake intensity levels. The ground motions are not scaled to specific hazard levels and the conditional probability can be estimated over continuous range of IMs. In this method, the ground motions are either unscaled or scaled by the same factors to excite the structure to the stage of structure response of interest, if the sample size of selected ground motions is small. Here, a series of nonlinear dynamic analyses are performed using the structural model developed in OpenSees, subjected to the ensemble of actual earthquake ground motion records selected. Response data set, consisting of pairs of IM values and the associated EDP values, $(edp_i,\ im_i)$, is generated through the finite element simulations and used for statistical inference analysis.

In order to determine $\mathrm{P}[\ln EDP \mid IM = im]$ from n pairs of observations $(edp_i,\ im_i)$, a linear regression analysis could be performed based on the data sample. The theoretical background behind the cloud method is summarized as follows.

An identity can be written as

$$\begin{aligned} \ln EDP \mid IM &= E[\ln EDP \mid IM] + (\ln EDP \mid IM - E[\ln EDP \mid IM]) \\ &= E[\ln EDP \mid IM] + e \mid IM \end{aligned} \tag{2.7}$$

where the error term $e = \ln EDP - E[\ln EDP]$ is a random variable with conditional mean $E[e \mid IM] = 0$ and conditional variance $Var[e \mid IM] = Var[\ln EDP \mid IM]$. Given a linear relationship between logarithms of these two variables (i.e., $\ln EDP$ and $\ln$ IM) often provides a reasonable estimate of the mean value of $\ln EDP$ (Baker, 2005), the mean function $E[\ln EDP \mid IM]$ is assumed to have a linear relationship

$$E[\ln EDP \mid IM] = a_0 + a_1 \ln IM \tag{2.8}$$

Equivalently,

$$\ln EDP \mid IM = a_0 + a_1 \ln IM + e \mid IM \tag{2.9}$$

Furthermore, it is often assumed that the distribution of $e \mid IM$ does not depend on IM at all, thus, $e \mid IM$ can be reasonably replaced by e

$$\ln EDP \mid IM = a_0 + a_1 \ln IM + e \tag{2.10}$$

Equation (2.10) is a simple linear statistical regression model between $\ln EDP$ and $\ln IM$, in which $\ln EDP$ is the response variable, $\ln IM$ is the predictor and parameters a_0 and a_1 will be estimated as $\hat{a}_0$ and $\hat{a}_1$ respectively through linear regression analysis based on transformed data set $(\ln edp_i,\ \ln im_i)$. The third parameter to characterize the simple linear regression model is the variance of the error term $Var[e]$,

$$Var[e] = Var[\ln EDP \mid IM] = \sigma^2 \tag{2.11}$$

Consequently, the mean value of $\ln EDP$ given a specified IM of value im is introduced via the linear relationship,

$$\mathrm{E}[\ln EDP \mid IM = im] = \hat{a}_0 + \hat{a}_1 \ln im \tag{2.12}$$

and the variance of e is estimated as

$$\hat{S}^2 = \frac{\sum_{i=1}^{n} \left(ln\ edp_i - \left(\hat{a}_0 + \hat{a}_1 \ln im_i \right) \right)^2}{n-2} \tag{2.13}$$

Combining the assumption that the random event $\{\ln EDP \mid IM = im\}$ should conform to a normal distribution approximately, which is coinciding with the restrictive assumption that the random error (e) conforms to a zero mean normal distribution, the probabilistic properties of event $\{\ln EDP \mid IM = im\}$ can be fully represented through the complementary cumulative function (CCDF).

$$G_{EDP|IM}[edp \mid im] = P[EDP > edp \mid IM = im] = 1 - \Phi\left(\frac{\ln edp - \left(\hat{a}_0 + \hat{a}_1 \ln im \right)}{\hat{S}}\right) \tag{2.14}$$

in which Φ is the CDF of standard normal distributed random variable.

The conditional demand hazard analysis results using the cloud method are presented in Figure 2.10 to Figure 2.12, including the cloud plot of the data sample points, the regressed linear relationship of the predicted mean of the event $\{\ln EDP \mid IM = im\}$ with respect to $\ln IM$, and the probabilistic distribution of EDP conditional to IM for three hazard levels commonly used (i.e., probability of exceedance of 50% in 50 years, 10% in 50 years, and 2% in 50 years). In this study, three representative EDPs are selected to investigate the structural response: the displacement ductility, the peak absolute acceleration, and the normalized hysteretic energy dissipated (a good damage indicator for "cumulative damage", interpreted as "cumulative ductility") defined respectively as follows

$$\mu_d = \underset{0 < t < t_d}{Max}\left(\frac{u(t)}{U_y}\right) \tag{2.15}$$

$$A_{Abs.} = \underset{0 < t < t_d}{Max}\left(\frac{\ddot{u}(t)+\ddot{u}_g(t)}{g}\right) \tag{2.16}$$

$$E_H = \frac{\int_0^{t_d} R(t)du(t) - E_E}{F_y U_y} \tag{2.17}$$

in which, $\ddot{u}_g(t)$ and t_d are the ground motion acceleration and duration of the earthquake input respectively; F_y and U_y are the yield force and yield displacement of the nonlinear SDOF model respectively; $u(t)$, $\ddot{u}(t)$, and $R(t)$ are the displacement, acceleration, and resisting force histories respectively; μ_d, $A_{Abs.}$, E_E, and E_H are the displacement ductility, peak absolute acceleration, elastic energy, and hysteretic energy dissipation of the nonlinear SDOF model.

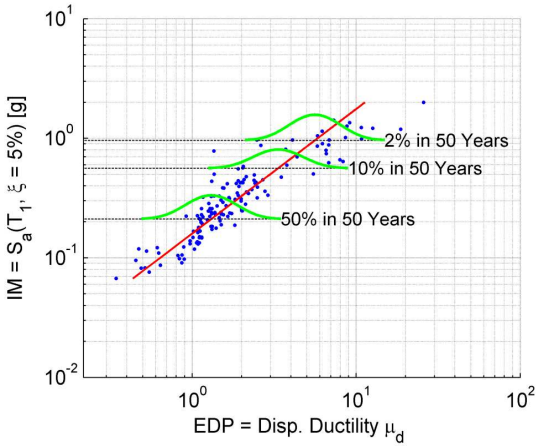

Figure 2.10: Conditional seismic demand hazard for EDP of displacement ductility

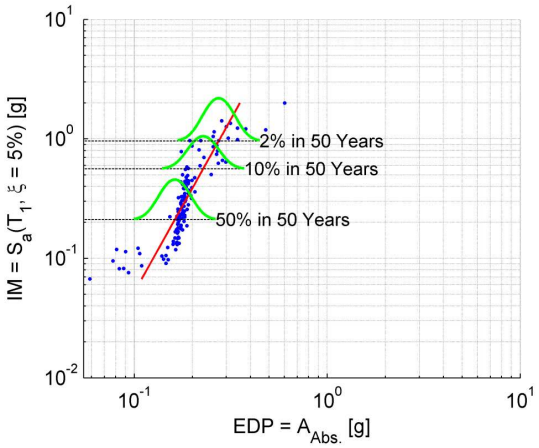

Figure 2.11: Conditional seismic demand hazard for EDP of peak absolute acceleration

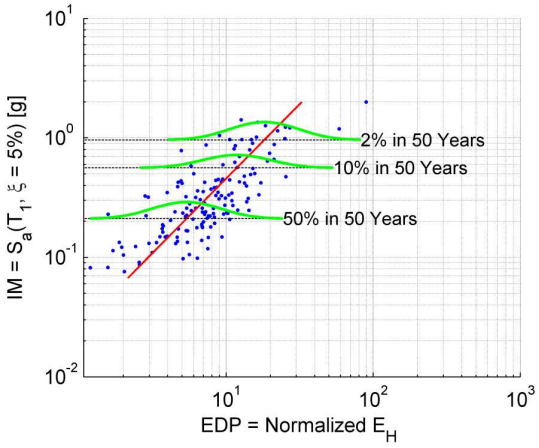

Figure 2.12: Conditional seismic demand hazard for EDP of hysteretic energy dissipation

It is observed that the linear inference model based on linear regression for the EDPs of displacement ductility and normalized hysteretic energy works well, but the assumptions for the cloud method for the EDP of deck acceleration is violated here.

(2) Unconditional probabilistic seismic demand analysis

After obtaining the probabilistic seismic hazard results, $\nu_{IM}(im) = \nu_{IM}(IM > im)$, and the conditional probabilistic seismic demand hazard analysis results $P[EDP > edp \mid IM = im]$, the convolution in Equation (2.6) results in the demand hazard curves associated with the interested EDPs, as shown in Figure 2.13 to Figure 2.15.

Additional insight into the distribution of ground motion intensities contributing to exceedance of a given structural response level (i.e., the relative contributions of bins of Δim_i to $\nu_{EDP}(edp)$), is provided by the de-aggregation of the seismic demand hazard, computed as follows

$$\begin{aligned} \nu_{EDP}(edp) &= \int_{IM} P\left[EDP > edp \middle| IM\right] \left| \frac{d\nu_{IM}(im)}{dim} \right| dim \\ &= \sum_i P\left[EDP > edp \middle| IM\right] \left| \frac{d\nu_{IM}(im_i)}{dim_i} \right| \cdot \Delta im_i \end{aligned} \tag{2.18}$$

The above integrand is referred to as the de-aggregation with respect to intensity measure *im* of demand hazard at *edp*, and indicates the contribution weight of each Δim_i to the event $\{EDP > edp\}$. Figure 2.13 to Figure 2.15 (right columns) present the de-aggregation results for the seismic demand hazard points as denoted on the probabilistic seismic demand hazard curves of displacement ductility, peak absolute acceleration, and normalized hysteretic energy dissipation respectively. As noticed from the de-aggregation results, with the increase of EDP level, the de-aggregation curves shift towards higher values of IM, which implies that more contribution to larger EDPs is from ground motions of higher intensity levels.

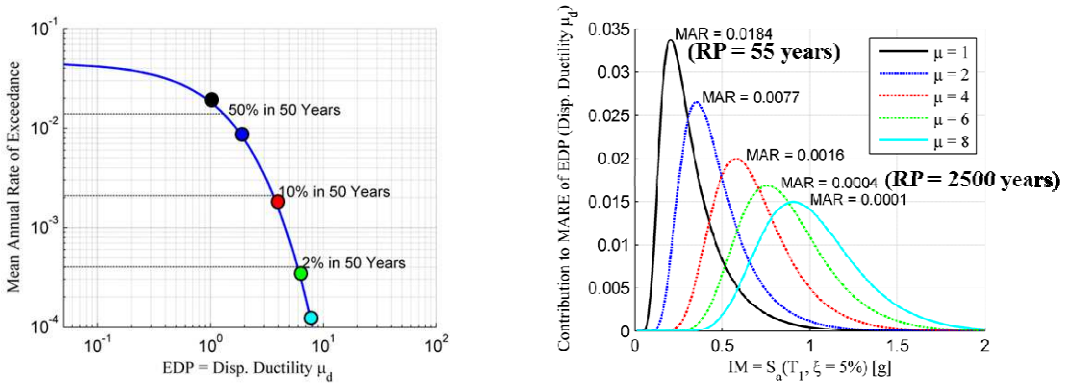

Figure 2.13: Probabilistic seismic demand hazard curve of displacement ductility (left) and its de-aggregation w.r.t. intensity measure (right)

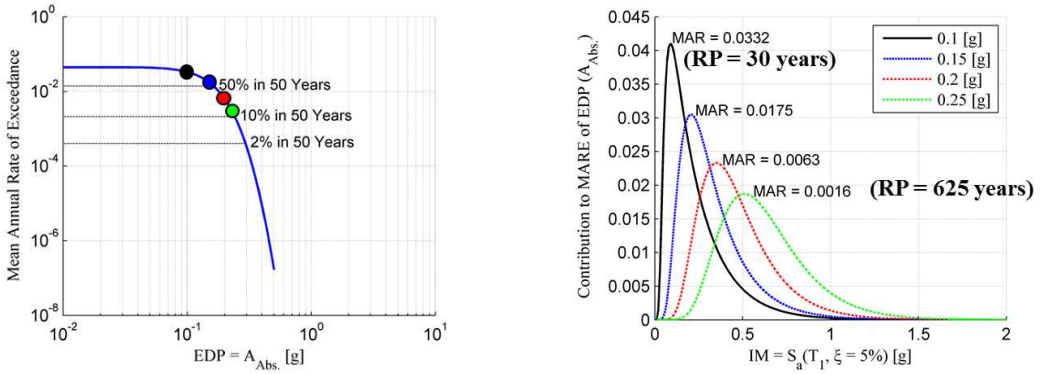

Figure 2.14: Probabilistic seismic demand hazard curve of peak absolute acceleration (left) and its de-aggregation w.r.t. intensity measure (right)

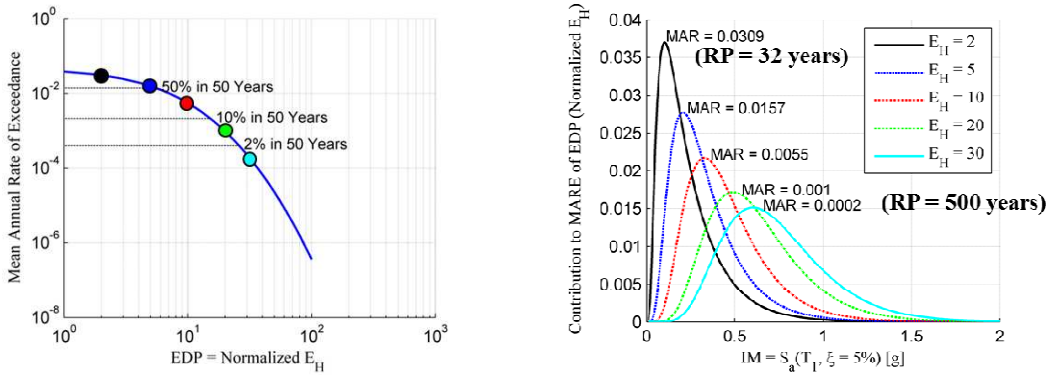

Figure 2.15: Probabilistic seismic demand hazard curve of normalized hysteretic energy dissipation (left) and its de-aggregation of w.r.t. intensity measure (right)

2.4.3. Probabilistic seismic damage analysis (PSDaA)

The third step of the PEER PBEE methodology, the probabilistic seismic damage hazard analysis evaluates probabilistically the seismic damage hazard for a structure. In practice, for each failure mode of a structure, a set of discrete damage states (DS) is defined to quantify the damage. The damage states of structures are defined as exceeding a certain limit-state (*LS*) for a failure mode as illustrated in Figure 2.16.

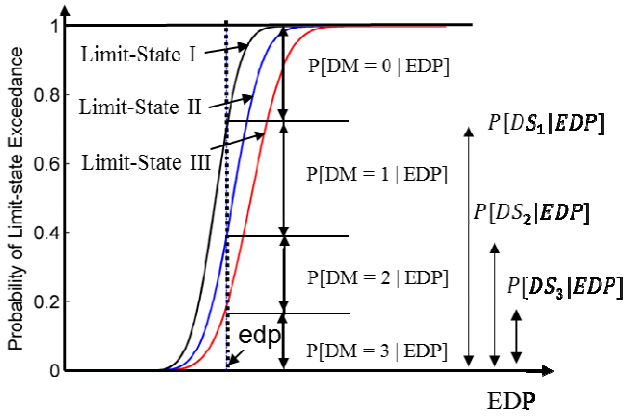

Figure 2.16: Illustration of discrete damage measure

The damage hazard, ν_{DS_k}, is characterized by the mean annual rate of the k-th limit state exceedance, i.e., event $\{DM \geq ls_k\}$, which can be computed as the following convolution using the TPT.

$$\nu_{DS_k} = \int_{EDP} P\left[DM \geq ls_k \mid EDP = edp\right] \left| d\nu_{EDP}(edp) \right| \tag{2.19}$$

The conditional probability $P\left[DM \geq ls_k \mid EDP = edp\right]$ is traditionally called fragility analysis or probabilistic capacity analysis, which is to model/quantify the uncertainties in the capacity of the structures. The only way to develop the fragility function is to perform a statistical model assessment by comparing analytical and/or empirical capacity models with

experimental data either in the field or in the laboratory (Gardoni et al 2002). Here, the fragility curves associated with three EDPs adopted in this study are postulated and parameterized by assuming the ratio of measured-to-predicted capacity as indicated in Table 2.1, and the corresponding fragility curves are shown in Figure 2.17 to Figure 2.19.

Table 2.1: Relevant parameters for postulated fragility curves

Associated EDP	Limit-states	Predicted Capacity	Measured-to-predicted capacity ratio (Normal distributed)	
			Mean	c.o.v
Displacement Ductility	I	$\mu = 2$	1.095	0.201
	II	$\mu = 6$	1.124	0.208
	III	$\mu = 8$	1.254	0.200
Peak Absolute Acceleration [g]	I	$A_{Abs.} = 0.10$	0.934	0.128
	II	$A_{Abs.} = 0.20$	0.952	0.246
	III	$A_{Abs.} = 0.25$	0.973	0.265
Normalized Hysteretic Energy Dissipated	I	$E_H = 5$	0.934	0.133
	II	$E_H = 20$	0.965	0.140
	III	$E_H = 30$	0.983	0.146

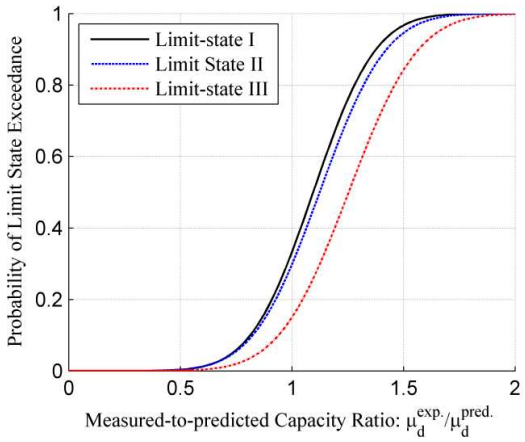

Figure 2.17: Fragility curves for limit-states of failure mode associated with displacement ductility

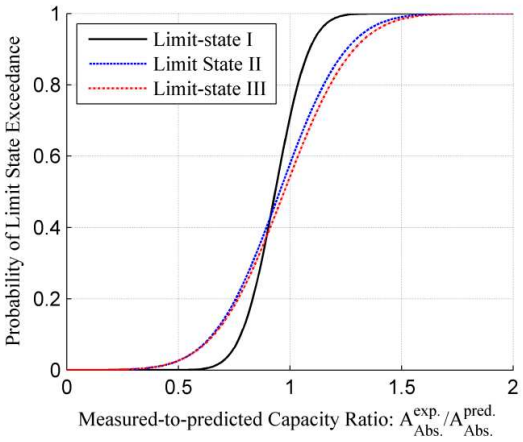

Figure 2.18: Fragility curves for limit-states of failure mode associated with peak absolute acceleration

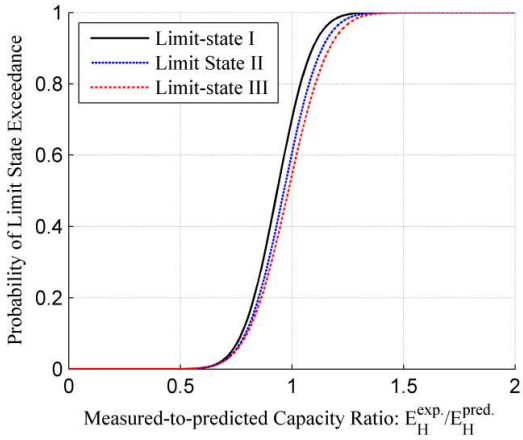

Figure 2.19: Fragility curves for limit-states of failure mode associated with normalized hysteretic energy dissipated

By convolution of the fragility curves with the demand hazard curves, the seismic damage hazard results associated with the corresponding EDPs, in terms of MAR of limit state exceedance, are summarized in Table 2.2. The return period of limit state exceedance (RP) as

well as probability of exceedance in 50 years (PE50) is appended as well assuming the Poisson process of the event of limit state exceedance.

Table 2.2: Seismic damage hazard of each damage state considered

Failure Associated EDP	Limit-states	MAR	RP	PE50
Displacement Ductility	I ($\mu_d = 2$)	0.0394	26 years	86%
	II ($\mu_d = 6$)	0.0288	35 years	76%
	III ($\mu_d = 8$)	0.0231	44 years	68%
Peak Absolute Acceleration [g]	I ($A_{Abs} = 0.1g$)	0.0349	29 years	82%
	II ($A_{Abs} = 0.2g$)	0.0104	96 years	41%
	III ($A_{Abs} = 0.25g$)	0.0048	208 years	21%
Normalized Hysteretic Energy Dissipated	I ($E_H = 5$)	0.0171	58 years	57%
	II ($E_H = 20$)	0.0012	833 years	6%
	III ($E_H = 30$)	0.0003	3330 years	1.5%

Similar to the de-aggregation conducted for the probabilistic seismic demand hazard with respect to the IM, the de-aggregation of damage hazard with respect to EDP and IM can be performed as well to investigate the relative contribution of EDP bins $\Delta(edp)_i$ and IM bins $\Delta(im)_i$ to the damage hazard ν_{DS_k} as follows

$$\nu_{DS_k} = \sum_i P\left[DM > ls_k \mid EDP = edp_i\right] \frac{\left|d\nu_{EDP}(edp_i)\right|}{\Delta(edp)_i} \Delta(edp)_i \tag{2.20}$$

$$\nu_{DS_k} = \sum_i P\left[DM > ls_k \mid EDP\right] \left| \int_{IM} dP\left[EDP > edp \mid IM\right] \right| \frac{\left|d\nu_{IM}(im_i)\right|}{\Delta(im)_i} \Delta(im)_i \tag{2.21}$$

De-aggregation results with respect to IM and EDPs are presented in Figure 2.20 to Figure 2.22, and the same trend is observed that the de-aggregation curves shift forward with higher IM or EDPs for severer damages. De-aggregation exposes the relative contributions of different IM or EDP bins to the damage hazard.

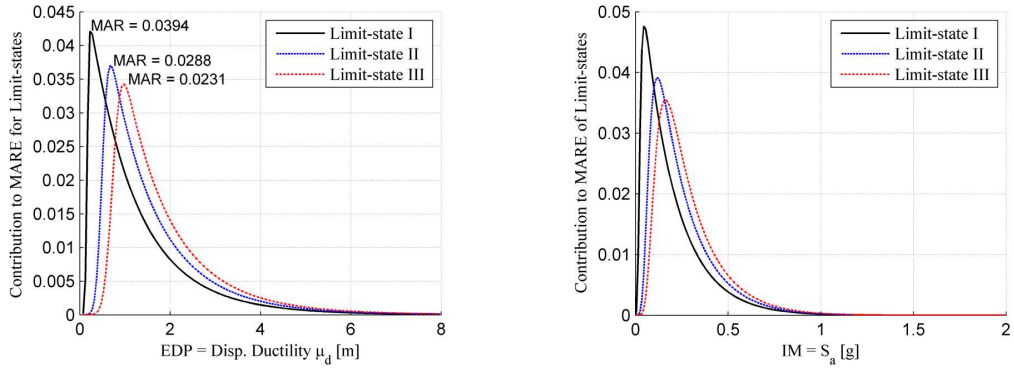

Figure 2.20: Displacement ductility associated damage hazard de-aggregation for different limit states with respect to edp (left) and im (right)

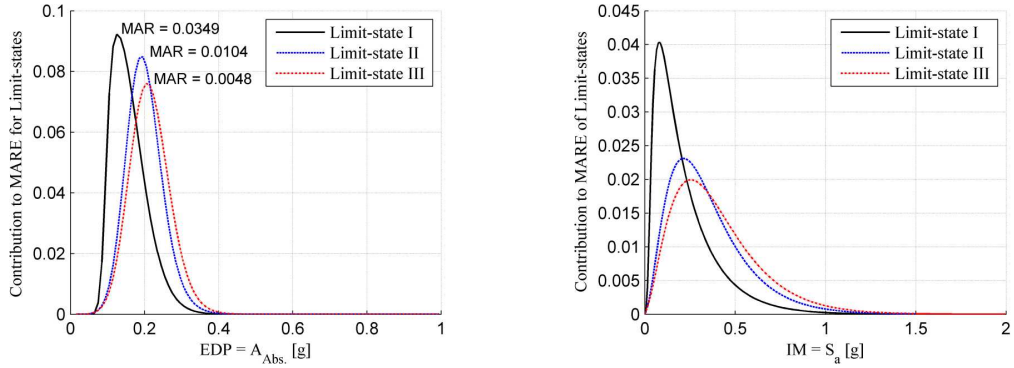

Figure 2.21: Absolute acceleration associated damage hazard de-aggregation for different limit states with respect to edp (left) and im (right)

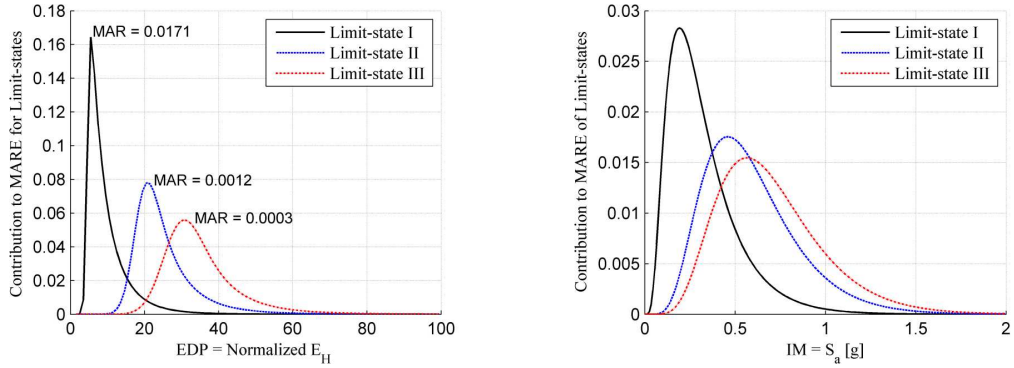

Figure 2.22: Normalized hysteretic energy dissipation associated damage hazard de-aggregation for different limit states with respect to edp (left) and im (right)

2.4.4. Probabilistic seismic loss analysis (PSLA)

The objective of probabilistic seismic loss analysis, as the final stage of PBEE methodology, is to predict the probabilistic properties of decision variable (DV) to imply the direct or indirect loss due to the damage to the structure. In this study, DV is chosen to be the total annual repair cost (L_T) to restore the structure after the earthquake, which is assumed to be the summation of the cost (L_j) of each damaged component j. The component-wise loss hazard curve for the possibly damaged component j with relevant EDP is obtained in the form of mean annual rate of cost exceeding specified cost levels as Equation (2.22).

$$\nu_{L_j}(l) = \int_{DM} P\left[\left(L_j > l\right) | DM\right] \left| d\nu_{DM} \right| = \sum_{k=1}^{nls_j} P\left[\left(L_j > l\right) | DM\right] \left| \nu_{DS_k^{[j]}} - \nu_{DS_{k+1}^{[j]}} \right| \tag{2.22}$$

The repair cost distribution term $P\left[\left(L_j > l\right) | DM\right]$ needs to be determined from statistical inference of repair cost data related to a certain failure mode. In this study, the repair/replacement cost for the failure associated the three EDPs is assumed to be normally distributed with postulated mean and coefficient of variation listed in Table 2.3.

Table 2.3: Repair cost distribution data for each damage state

Failure Associated EDP	Limit-states	Repair/Replacement Cost (Normal distributed)	
		Mean ($)	c.o.v.
Displacement Ductility	I	146,500	0.12
	II	246,400	0.25
	III	350,000	0.32
Peak Absolute Acceleration [g]	I	55,000	0.11
	II	100,000	0.20
	III	500,000	0.28
Normalized Hysteretic Energy Dissipated	I	55,650	0.13
	II	110,000	0.22
	III	520,000	0.28

Since the total loss is the summation of each component loss defined as above, computation of total loss hazard requires an n-fold integration of the joint PDF of the component losses, which is prohibitive, if not impossible, to obtain. Therefore the loss hazard is estimated using multilayer Monte Carlo Simulation (MCS) herein, which is a simple and powerful technique for approximating complicated and multi-fold integration at the cost of expensive computation. This technique is straightforward and able to incorporate and propagate the uncertainties in all random variables involved in the structural seismic economic loss analysis, including such random variable as the occurrence of earthquake, IM, EDP, and DM. Figure 2.23 shows the procedure for one simulation.

First, the number of earthquake in one year is randomly generated according to the Poisson occurrence model and the IM is simulated as a random variable with the probabilistic properties derived from PSHA. For a given IM level, an ensemble of EDPs is then generated according to the joint PDF of EDPs, constructed using the NATAF model based on the estimated correlation coefficients of *EDPs* and their marginal probability distributions. The damage measure DM and loss L_j for each component is generated from the fragility curves and PDF of repair cost respectively. Eventually, the total loss in the summation of all components' repair cost is simulated. Empirical cumulative distribution function (CDF) of the total repair cost can be obtained by repeating the above multi-layer MCS procedure a large number of times (say 100,000), thus the total loss hazard curve is obtained, as shown later in the section of the parametric PBEE analysis.

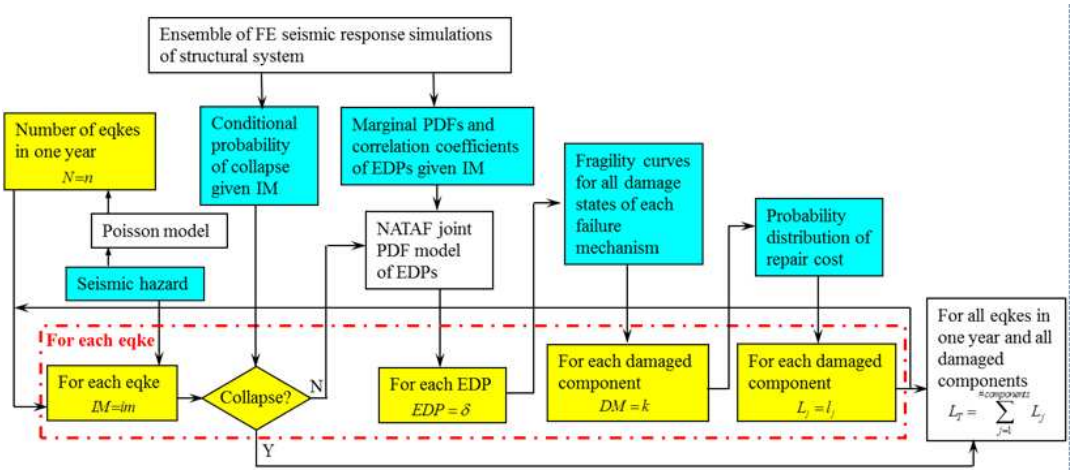

Figure 2.23: Multilayer Monte Carol (MCS) simulation for estimation of total loss hazard

2.5. Parametric PBEE Analyses

In the context of the PEER PBEE methodology, a perturbation analysis is performed in order to expose how the PBEE analysis results will change as a function of the system parameters. Five types of perturbations are considered in this study, for variations in the yield strength, the hardening ratio, the stiffness, the mass, and both stiffness and mass with a constant period. The demand hazard curves and total loss hazard curves are presented for two representative groups selected here: Figure 2.24 to Figure 2.27 for systems with 25% less or 25% more of yield strength (F_y) and for systems with 25% less or 50% more of initial stiffness (k_0).

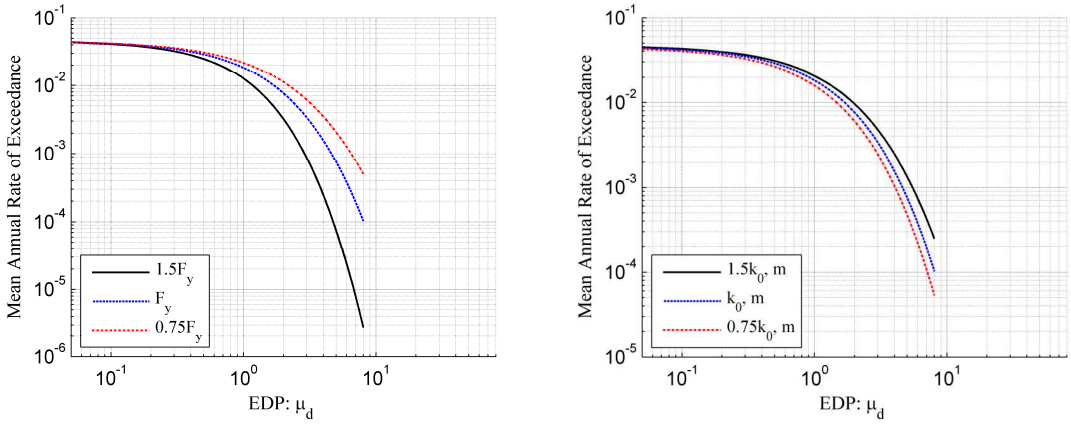

Figure 2.24: Probabilistic demand hazard curves of displacement ductility

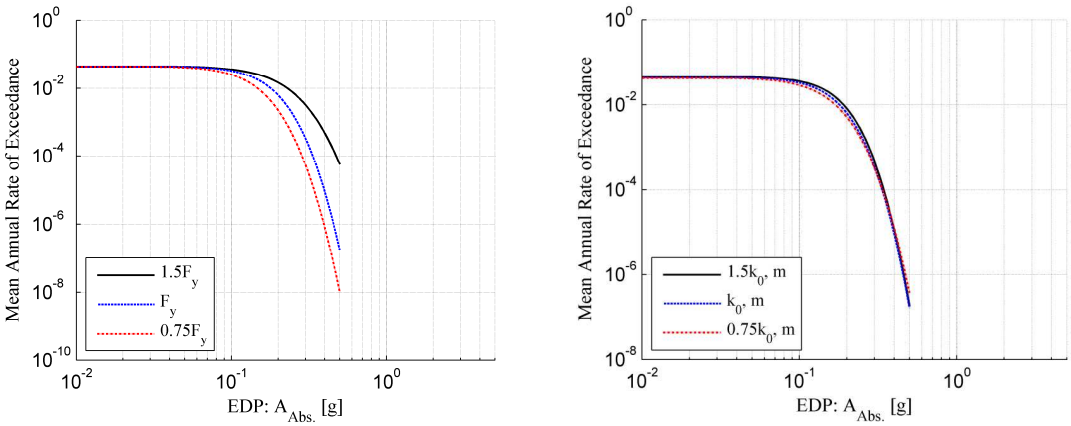

Figure 2.25: Probabilistic demand hazard curves of peak absolute acceleration

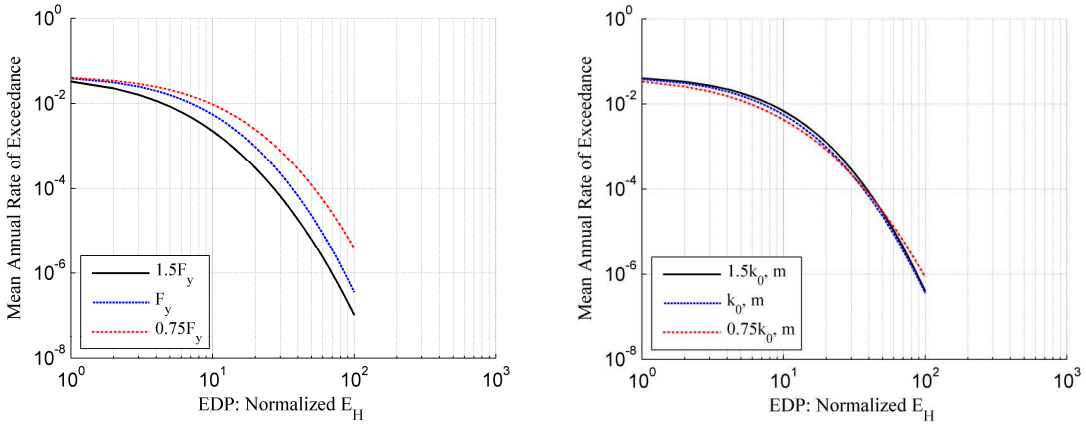

Figure 2.26: Probabilistic demand hazard curves of normalized hysteretic energy dissipation

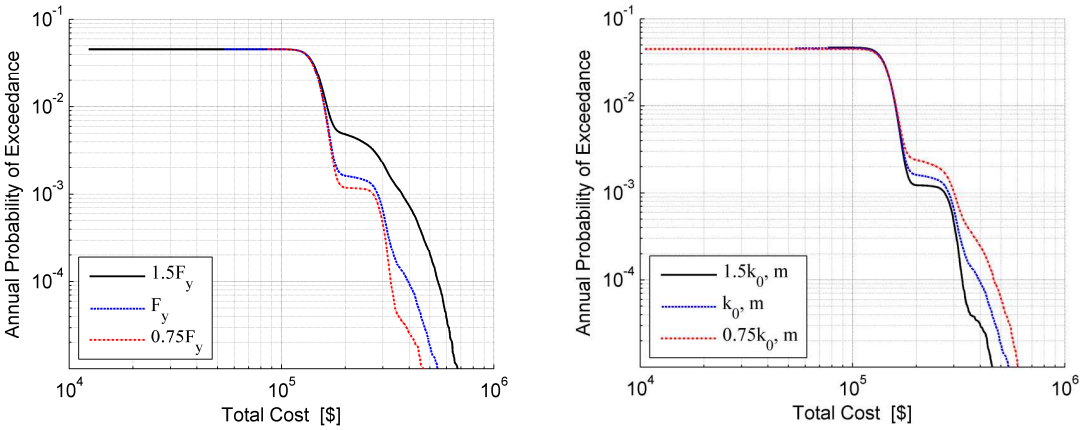

Figure 2.27: Probabilistic loss hazard curves for system with different yield strengths

It is observed that the probabilistic seismic demand hazard curves and loss hazard curves change with the increase or decrease of the yield strength and stiffness. Inspired by the sensitivity study of the PBEE analysis results shown above, it is natural to explore a methodology, the PPBOSD framework, using inverse PBEE analysis to design the structure with a target performance characterized in terms of the probabilistic demand hazard, probabilistic damage hazard, or probabilistic loss hazard.

2.6. Inverse PBEE Analysis within PPBOSD Framework

After observing how the loss hazard change as a function of the structural parameters, the stakeholder or owner may be interested to know whether a structure can be designed to achieve an expected performance probabilistically, e.g., reaching a targeted or desired probabilistic loss hazard curve. To tackle the problem of inverse PBEE analysis, the PPBOSD resorts to optimization techniques, instead of using traditional trial-and-error method by sweeping certain groups of system parameters for PBEE analysis, i.e., the intimidating “blind” search for target probabilistic seismic performance.

For illustration and validation purposes of the proposed PPBOSD framework to address the inverse PBEE problem, the simplified nonlinear SDOF bridge model is optimized

to achieve a target loss hazard curve, as illustrated in Figure 2.28. In order to set up a feasible optimization problem (i.e., to solve a well-posed problem for illustration and validation), the target loss hazard is chosen as the probabilistic loss hazard for a set of A-Priori selected design parameters. It is expected to find the optimum design parameters, as the A-Priori selected design parameters, using the proposed PPBOSD framework starting with another initial design.

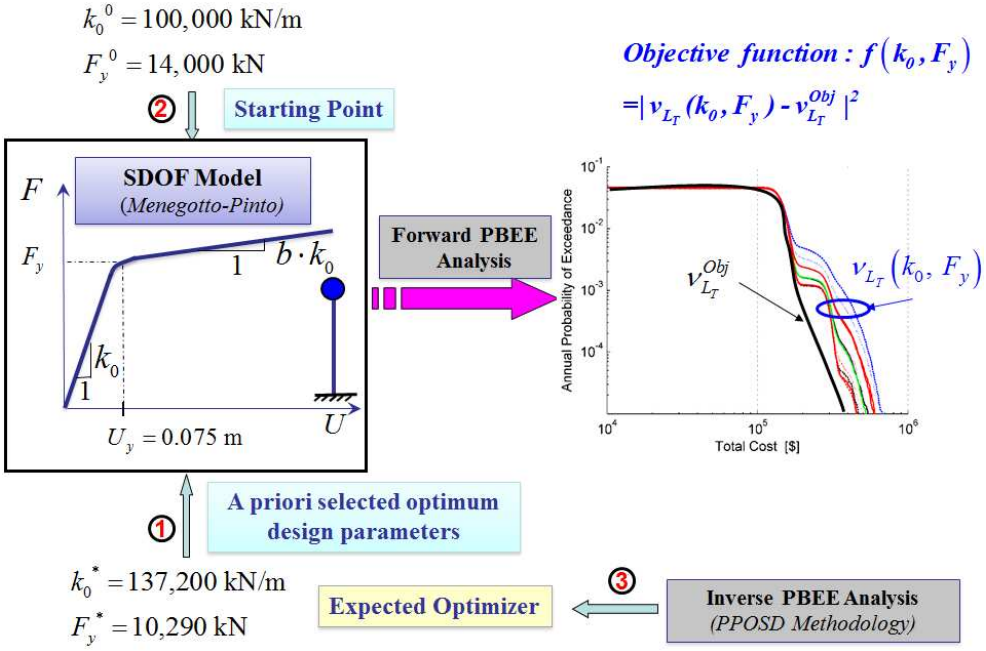

Figure 2.28: Illustration example for the proposed PPBOSD

The mathematical formulation of the optimization problem is stated in Equation(2.23), with the implicit objective function as sum square error (SSR) of the difference between our loss hazard curve and the target loss hazard curve.

$$\begin{aligned} &\underset{\{k_0, F_y\}}{Minimize} \quad f(k_0, F_y) = | v_{L_T}(k_0, F_y) - v_{L_T}^{Obj} |^2 \\ &subject\ to: \\ &\qquad 80,000 \le k_0 \le 187,200 \ \ (\text{kN/m}) \\ &\qquad 6,290 \le F_y \le 15,290 \ \ (kN) \end{aligned} \tag{2.23}$$

For the objective function with two design variables, 1089 parametric PBEE analyses are carried out to plot the 2D objective function as shown in Figure 2.29, using the cloud-based parametric PBEE analysis workflow developed under high throughput computing resources.

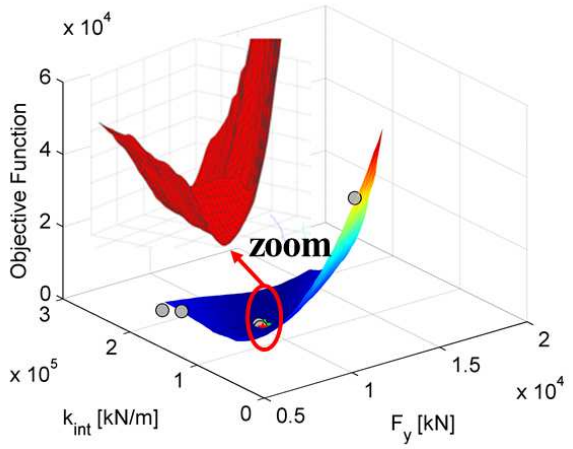

Figure 2.29: Two-dimensional (2D) objective function plot

In this study, the optimization problem is solved by OpenSees-SNOPT within the PPBOSD framework. OpenSees-SNOPT, an extended framework of OpenSees, is previously developed by linking of OpenSees (an existing software framework for nonlinear FE analysis) and SNOPT (a state-of-the-art software package for high-dimensional nonlinear constrained optimization). SNOPT (Sparse Nonlinear Optimizer) is a software package for solving large-scale nonlinear constrained optimization problems using sequential quadratic programming (SQP) algorithms. The optimization results are presented in Figure 2.30 to Figure 2.31.

Figure 2.30 shows the 3D objective function plot with the expected optimizer and the initial starting point. The target loss hazard curve and corresponding demand hazard curve for the initial point in the optimization process are shown in Figure 2.32 and Figure 2.33, which is

vastly different from the target. After 6 major iterations, the probabilistic loss hazard curves reached the target loss hazard at the corresponding optimal design with optimizer $(k_0^{end} = 135{,}774 \text{ kN/m}, F_y^{end} = 10{,}038 \text{ kN})$, which is close to the expected ideal optimizer $(k_0^{*} = 137{,}200 \text{ kN/m}, F_y^{*} = 10{,}290 \text{ kN})$ with error of 1% in the initial stiffness and 2% in the yield strength. The promise and applicability to solve such type of inverse PBEE problem is successfully demonstrated and validated using the well-posed illustrative application example herein. The PPBOSD framework is expected to be able to be applied to more complex and practical problems in the field of civil engineering.

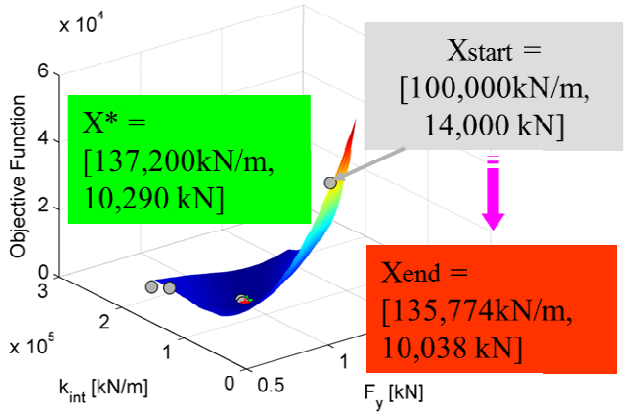

Figure 2.30: Optimization search history with 3D plot of the objective function for the PPBOSD illustration example

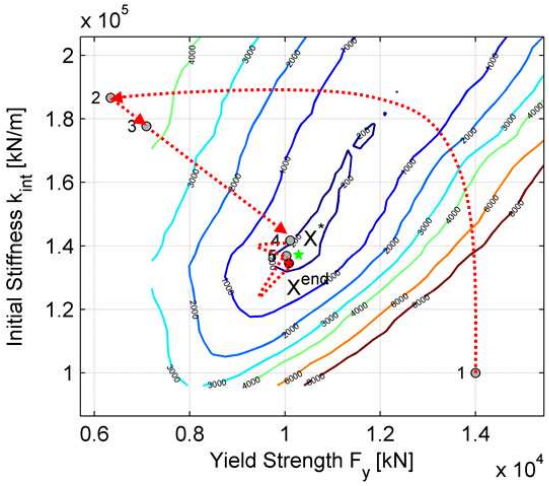

Figure 2.31: Optimization search history with contour of the objective function for the PPBOSD illustration example

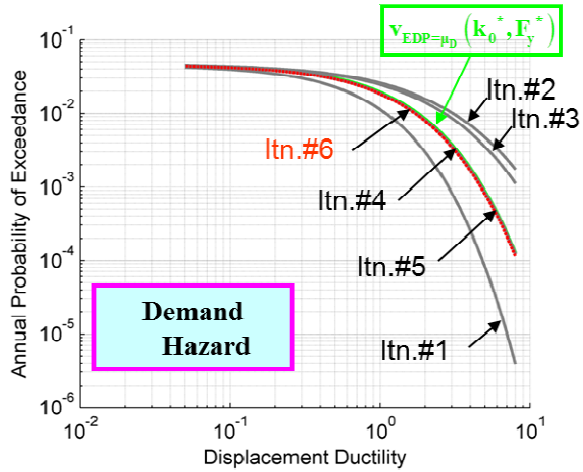

Figure 2.32: The evolution of the probabilistic seismic demand hazard curves

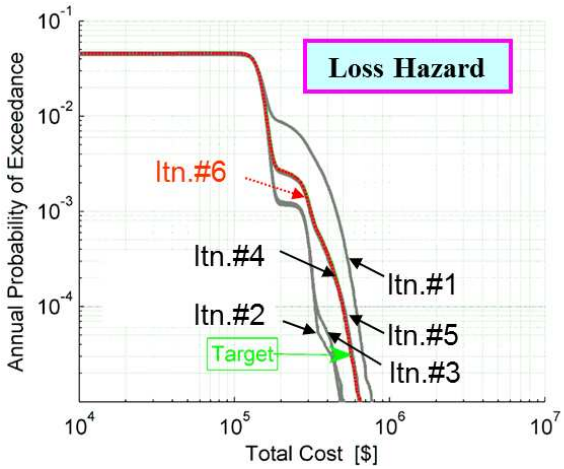

Figure 2.33: The evolution of the probabilistic seismic loss hazard curves

2.7. Conclusions

In the context of the well-established PEER Probabilistic Performance-based Earthquake Engineering (PBEE) Methodology, a probabilistic Performance-based Optimum Seismic Design (PPBOSD) framework is proposed. As an extension of conventional forward PBEE analysis, an optimization layer is wrapped outside the forward PBEE analysis to address the inverse PBEE problem, i.e., to design the structure with a target performance. All the four steps of PBEE methodology are implemented as a probabilistic seismic performance evaluation procedure, including a application example over simplified nonlinear SDOF bridge model. The parameter perturbation analysis exposed that the PBEE analysis results are sensitive to the structural design parameters, which implied the potential application of PPBOSD framework for probabilistic performance-based design. For illustration purpose, a nonlinear SDOF bridge model is redesigned within the proposed PPBOSD framework in the sense that the probabilistic seismic loss hazard curve reached a target loss hazard curve. The validation of the proposed PPBOSD framework based on the nonlinear SDOF bridge model

revealed the promising applicability of the proposed PPBOSD to solve real engineering problem for optimum probabilistic performance-based seismic design.

Acknowledgement

This chapter, in part, is currently being prepared for submission for publication of the material. Li, Yong; Conte, Joel P.; Gu, Quan, Gill, Philip E., "Framework for Probabilistic Performance-Based Optimum Seismic Design of Structures". The dissertation author was the primary investigator and author of this material.

References

Abrahamson, N. A., and Silva, W. J. (1997). "Empirical response spectral attenuation relations for shallow crustal earthquake." *Seismological Research Letter*, 68(1), 94-109.

Bazzurro, P., and Cornell, C. A. (1994). "Seismic hazard analysis of nonlinear structures. I: Methodology. II: Application." *Journal of Structural Engineering, ASCE*, 120(11), 3320-3365.

Bazzurro, P., and Cornell, C. A. (1999). "Disaggregation of seismic hazard." *Bulletin of the Seismological Society of America*, 89(2), 501-520.

Benjamin, J., and Cornell, C. A. (1970). *Probability, statistics and decision for civil engineers*, McGraw-Hill, New York.

Bozorgnia, Y., Crouse, C. B., Hamburger, R. O., Klemencic, R., Krawinkler, H., Malley, J., Moehle, J. P., Naeim, F., and Stewart, J. P. (2009). "Guidelines for seismic design of tall buildings." *Tall Buildings Initiative*, Pacific Earthquake Engineering Research Center.

Caltrans (2002). "Humboldt Bay bridges seismic substructure retrofit." <http://www.dot.ca.gov/ dist1/d1projects/humbaybridges> (November 29, 2005).

Campbell, K. W. and Bozorgnia, Y. (2007). "Campbell-Bozorgnia NGA ground motion relations for the geometric." Pacific Earthquake Engineering Research Center, University of California, Berkeley: PEER.

Conte, J. P., Pandit, H, Stewart, J. P., and Wallace, J. W. (2003). "Ground motion intensity measures for performance-based earthquake engineering." *Proceedings of the 9th International Conference on Applications of Statistics and Probability in Civil Engineering (ICASP9)*, 2, 1465-1472, July 6-9, San Francisco, CA, USA.

Cornell, C. A. (1968) “Engineering seismic risk analysis.” *Bulletin of the Seismological Society of America*, 58(5), 1583-1606.

Deierlein, G. G., Krawinkler, H., and Cornell, C. A. (2003). “A framework for performance-based earthquake engineering.” *Proceedings of the 2003 Pacific Conference on Earthquake Engineering*.

Gardoni, P., Mosalam, K. M., Der Kiureghian, A. (2002). “Probabilistic capacity models and fragility estimates for reinforced concrete columns based on experimental observations.” *Journal of Engineering Mechanics*, 128(10), 1024-1038.

Gu, Q., Barbato, M., and Conte, J.P. (2012). “OpenSees-SNOPT Framework for Finite-Element-Based Optimization of Structural and Geotechnical Systems.” *Journal of Structural Engineering*, 137(6), 822-834.

Kramer, S. L. (1996). *Geotechnical Earthquake Engineering*. Prentice-Hall.

Krawinkler, H. (2002). “A General Approach to Seismic Performance Assessment.” *International Conference on Advances and New Challenges in Earthquake Engineering.* Hong Kong.

Krawinkler, H., and Miranda, E. (2004). “Performance-based earthquake engineering.” *In Earthquake Enginering, From Engineering Seismology to Performance-Based Engineering*, edited by Y. and Bertero, V.V.; Bozorgnia. CRC Press.

Liu, P.L., and Der Kiureghian, A. (1986). “Multivariate distribution models with prescribed marginals and covariances.” *Probabilistic Engineering Mechanics*, 1(2), 105-112.

Luco, N., and C. A. Cornell (2007). “Structure-specific scalar intensity measures for near-source and ordinary earthquake ground motions.” *Earthquake Spectra*, 23(2), 357-392.

McKenna, F., and Fenves, G. L. (2001). *The OpenSees command language manual, version 1.2*, Pacific Earthquake Engineering Research Center, University of California at Berkeley.

Moehle, J, and Deierlein, G. G. (2004). “A framework methodology for performance-based earthquake engineering.” *Proceedings, 13th World Conference on Earthquake Engineering*, 1–6 August (CD-ROM), Vancouver, Canada

Petersen, Mark D., Frankel, Arthur D., Harmsen, Stephen C., Mueller, Charles S.,Haller, Kathleen M., Wheeler, Russell L., Wesson, Robert L., Zeng, Yuehua,Boyd, Oliver S., Perkins, David M., Luco, Nicolas, Field, Edward H., Wills,Chris J., and Rukstales, Kenneth S. (2008). “Documentation for the 2008 Update of the United States National Seismic Hazard Maps.” *U.S. Geological Survey Open-File Report 2008–1128*, 61.

Porter, K. A., Beck, J. L., and Shaikhutdinov, R. V. (2002). “Sensitivity of building loss estimates to major uncertain variables.” *Earthquake Spectra*, 18(4), 719-743.

Shome, N., Cornell, C.A., Bazzurro, P., and Carballo, J. E. (1998). “Earthquakes,records, and nonlinear responses.” *Earthquake Spectra*, 14(3), 469-500.

Zhang, Y., Conte, J. P., Yang, Z., Elgamal, A., Bielak, J., Acero, G. (2008). “Two-dimensional nonlinear earthquake response analysis of a bridge-foundation-ground system.” *Earthquake Spectra*, 24(2), 343 – 386.

CHAPTER 3

CALIFORNIA HIGH-SPEED RAIL (CHSR) PROTOTYPE BRIDGE DESIGN AND COMPUTATIONAL MODEL DEVELOPEMENT

3.1. Introduction

To meet ever-growing demands on California transportation infrastructure, the California High-Speed Rail (CHSR) Project is underway inspired by the successful high-speed train systems worldwide. The CHSR alignments, initially running from San Francisco to Los Angeles via the Central Valley and later extending to Sacramento and San Diego, will be supported on viaducts or bridges besides the roadbed due to the topography. Unfortunately, because of the California tectonics, some supporting bridge structures of some branches will be located in high seismicity regions, including major seismic faults such as San Andreas and Calaveras faults. Therefore, seismic risk is a critical concern to the CHSR project in California, and higher seismic performance is required considering the target high-speed train service and continuity of operation requirements under small earthquakes. Seismic isolation system (Naeim et al.1999, Skinner et al. 1993), which decouples the bridge substructure and superstructure to some extent, elongating the structure's period and adding energy dissipation

capability in the form of hysteretic damping, are considered to be a promising strategy to achieve the pursued target seismic performance levels.

Considering the social-economic functions of the CHSR system, as sketched in Figure 3.1, an optimal seismic isolator design for CHSR bridges based on advanced structural modeling, seismic response simulation and performance evaluation are of significant importance to guarantee the dedicated high-speed train services after earthquakes. In this research, these issues are investigated with a focus on evaluating the effects of seismic isolation for a CHSR prototype bridge. A detailed three-dimensional (3D) nonlinear finite element (FE) model of this bridge is developed using *OpenSees* (Mckenna 1997). This FE model will be used to simulate seismic response of the bridge and to evaluate its seismic performance when subjected to earthquake ground motions of different seismic hazard levels. Accordingly, a comprehensive FE model with high fidelity is expected to be established. Towards this goal, a detailed 3D nonlinear FE model of the CHSR prototype bridge, including soil-pile-structure interaction and rail-structure interaction, is developed.

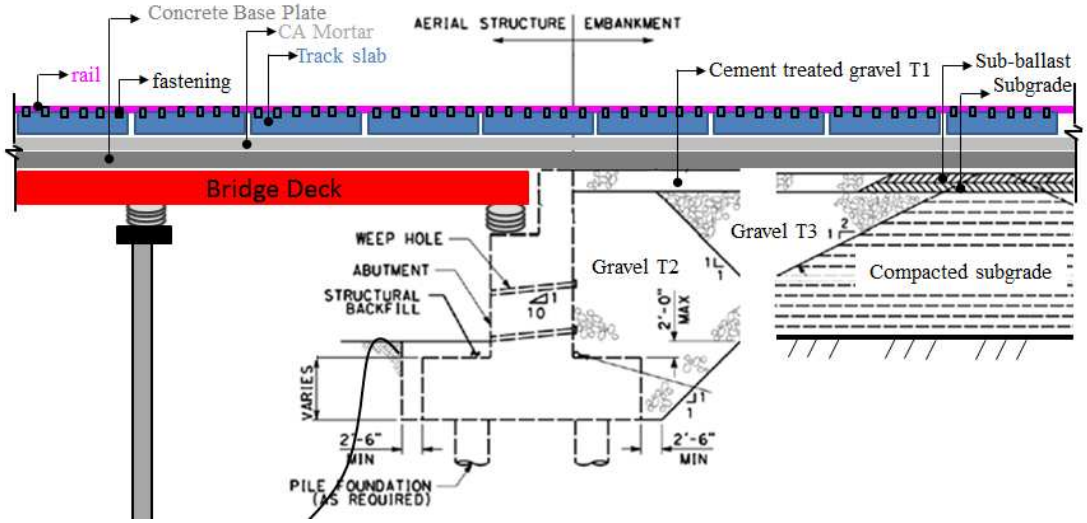

Figure 3.1: The high-speed rail bridge system sketch

3.2. Description of the Bridge Design

With the support of Parsons Brinckerhoff (PB), which is assisting the State of California in planning, designing, and managing the construction of the CHSR system, a prototype bridge design was selected for this study, which focuses on the feasibility and optimization of isolation systems in the context of the CHSR Project.

The prototype bridge, as shown in Figure 3.2, is straight, consisting of three 330.0ft long and 48.0ft tall frames (3 spans 110.0ft each) with two interior structural expansion joints between the central and the two end frames. The elevation view and plan view of the bridge is presented in Figure 3.3. The bridge superstructure, a post-tensioning single-cell box girder, with dimensions of 42.0ft wide at the top, 17.5ft wide at the bottom, and 9.5ft high, is resting on eight single-column piers/bents in the middle and on two seat-type abutments at both ends (see Figure 3.4). The pier columns of circular cross-section with diameter 8.0ft are of identical height, 35.0ft, measured from the top of the pile cap to the top surface of the pier head (see Figure 3.5). The abutments and pier columns are founded on a system, consisting of two types of pile group foundations with cast-in-place drilled shafts, namely a rigidly-capped pile group with 2×2 vertical piles for foundations supporting the eight pier columns (Figure 3.6) and a rigidly-capped pile group with 2×3 vertical piles for foundations supporting the abutments (Figure 3.7). All the piles are 120.0ft long with a constant circular section in diameter of 6.5ft.

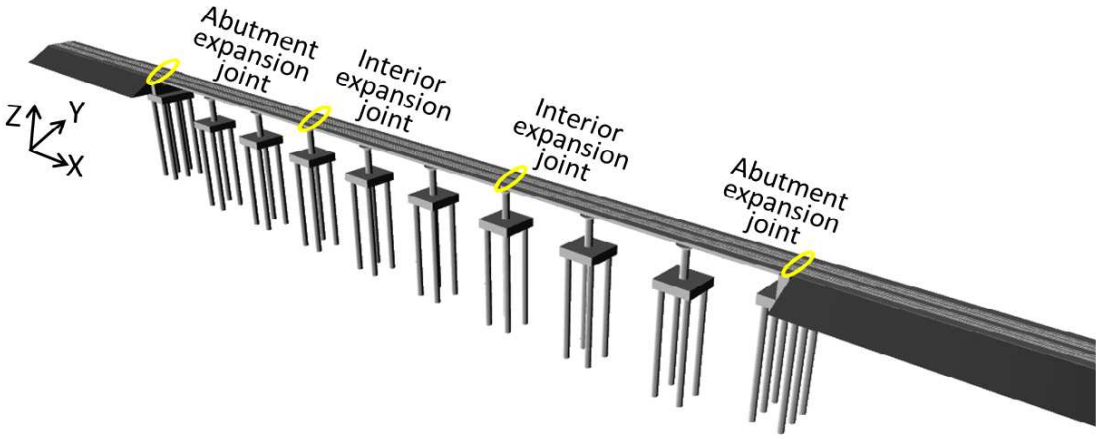

Figure 3.2: Isometric view of the CHSR Prototype Bridge

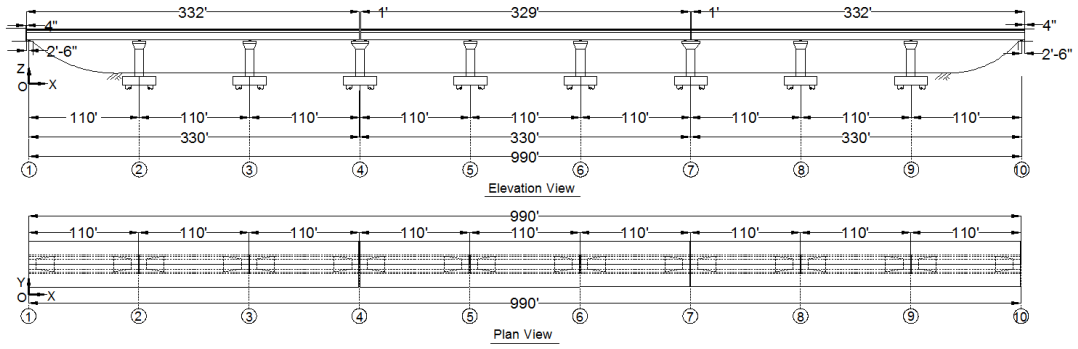

Figure 3.3: Schematic views of the CHSR Prototype Bridge

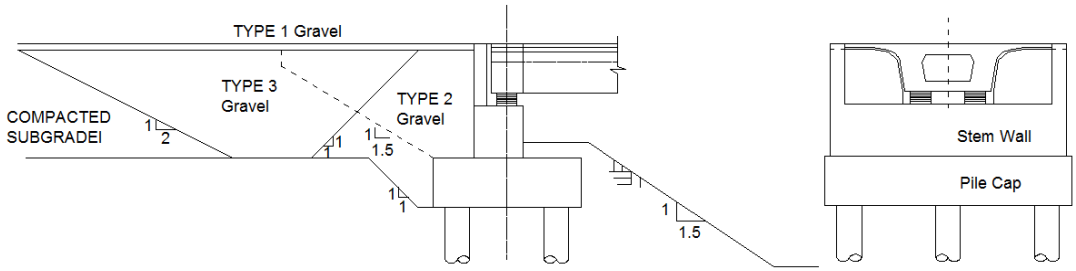

(a) (b)

Figure 3.4: Abutment system for bridge supports at both ends: (a) longitudinal view, (b) transverse view

In order to mitigate the high seismic risk of the bridge structure and the supported track system, seismic isolation together with a segmental displacement control strategy (slotted hinge joints) are integrated into the design of the bridge system. The superstructure and bridge pier columns are decoupled to a degree by one pair of uni-directional isolators (aligned transversally) at the abutments (i.e., isolated in the longitudinal direction whereas the transverse displacement of the deck relative to the abutment is restrained by the exterior shear keys), one pair of omni-directional isolators on top of each pier at continuous joints illustrated in Figure 3.4, and two pairs of omni-directional isolators on top of each pier at interior expansion joints as displayed in Figure 3.5. Also, to maintain the continuity of the transversal displacement of the bridge deck at interior expansion joints, a pair of slotted hinge joint (SHJ) devices is installed across each interior expansion joint to constrain the relative transverse displacement of adjacent bridge segments, while allowing relative longitudinal displacements of the two adjacent frames to accommodate deformations due to creep, shrinkage, and thermal expansion/contraction.

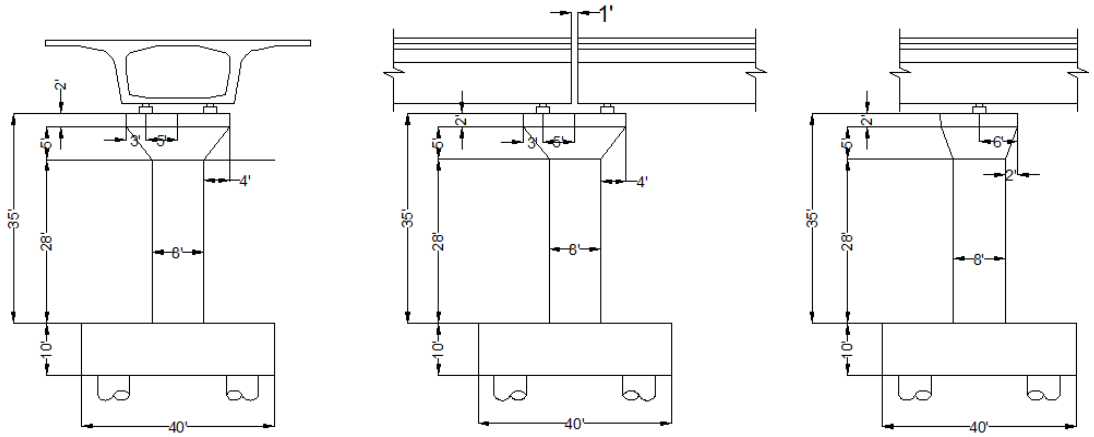

Figure 3.5: Superstructure, substructure, and superstructure-substructure connections: (a) transverse view, (b) longitudinal view for discontinuous joints, and (c) longitudinal view at continuous joints

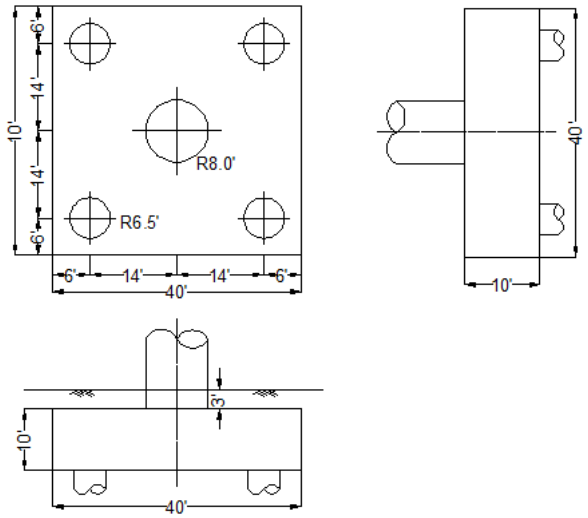

Figure 3.6: Pile group foundation (2 × 2) for CHSR pier column

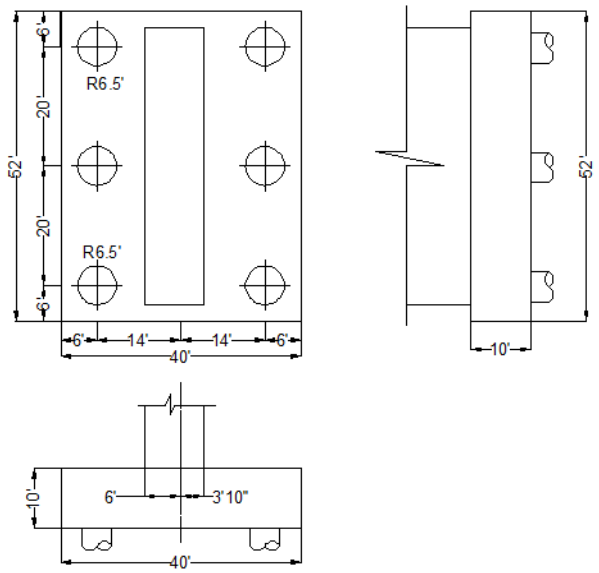

Figure 3.7: Pile group foundation (2 × 3) for CHSR abutments

The non-ballasted tracks are used in the CHSR prototype bridge and track with two continuous welded rails (CWR) are adopted because of its unique advantages especially as train speed increases, thanks to the lower maintenance cost compared to conventional non-

welded tracks with rails connected by joints to allow for thermal variations. The penalty for non-welded tracks is the care for maintenance-intensive joints beside its negative effect on track geometry, rails, sleepers, and fastenings, especially as speed increases. In a typical non-ballasted track system consisting of several layers (see Figure 3.1), the rails are attached to the track base (bridge deck or subgrade beyond the bridge) with direction fixation fasteners across the track slab (California High-speed Rail Authority 2012, Petrangeli 2008).

More details about the design and behavior of the superstructure/substructure components, including the seismic isolators, SHJ devices, pile foundations, abutment systems, and rail-structure connections, will be presented later together with a description of the modeling aspects of these components.

3.3. Description of the Computational Model

Probabilistic performance-based seismic assessment requires the development of high-fidelity and computationally efficient models for nonlinear dynamic time history analyses. The significant ingredients of modeling and simulation for such analyses are incorporated including, but not limited to, the structure system, the track system, the abutment embankment and pile foundation system. A 3D nonlinear FE model of the CHSR prototype bridge considering track-structure interaction (TSI) and soil-structure interaction (SSI) is implemented to predict the seismic response of the bridge and track system. The implementation of the 3D FE model of the bridge takes advantage of the current modeling capabilities of the *OpenSees* framework, including the library of existing element and material models, as well as its flexibility and extensibility in terms of implementing new elements. For the structures above ground level, elastic beam-column elements and nonlinear beam-column elements with fiber sections associated with uniaxial material models are used to model the bridge deck, pier columns, and rails, while zero-length elements associated with uniaxial

material models are used to model the local joints components (i.e., the abutment gaps, interior expansion joints, seismic isolators as connection between bridge deck and pier columns, and connections between rails and structures). Dynamic p-y approach, which considers a series of nonlinear soil springs with dashpot to represent the soil resistance, is used to model the pile group foundations for piers and abutments.

A general description of the FE model is presented below, before elaborating the details of each component of the complete FE model. The model of a single pier and its connection to the deck, as well as the connection between the deck and the rails are shown in Figure 3.8. Figure 3.9 schematically describes how the rails and the deck are connected along one span of the bridge. A deck segment refers to the deck portion of a frame (i.e., three continuous spans of bridge deck) as shown in Figure 3.10. At the expansion joint, the adjacent segments of the bridge are connected through a pair of SHJ devices. The rails are modeled as elastic beam elements and are continuous across the interior and abutment expansion joints, since continuous welded rails (CWR) are used in the CHSR for lower maintenance costs. To model the connections of the track (two rails) system to the box-girder deck through direct fixation fasteners, and the connections between the deck and the top of the piers or abutments through the seismic isolator bearings, a suite of linear elastic beam-column elements with exceedingly stiff (quasi-rigid) properties are used herein to define the rigid offsets.

The coordinates system used to define the model and analysis is shown in the plan view and elevation view (Figure 3.3). Axis x refers to the longitudinal direction of the bridge, y to the transverse direction of the bridge, and z to the vertical direction. For convenience, the abutments and piers are numbered and identified with tags as abutment 0, pier 1, and so on to abutment 9 from left to right.

3.4. Bridge Superstructure and Piers

To guarantee a desired level of accuracy of the seismic response simulation and performance evaluation, an analytical nonlinear FE model of the CHSR Prototype Bridge is developed in *OpenSees* considering different sources of nonlinearities in the bridge structures, i.e., material nonlinearities (concrete and steel bars), gap effects present in the expansion joints, hysteretic behavior in the special devices (seismic isolators and slotted hinge joints), and geometric nonlinearities (P-Δ effect) which is accounted directly in the analysis algorithm.

3.4.1. Bridge deck and pier columns

Typical section of the post-tensioned box girder as bridge deck for double track non-ballasted aerial structures is adopted, and the bridge deck is designed to remain linear elastic as capacity protected component. Therefore, it is reasonable to model the superstructure as equivalent linear elastic beam-column elements with the section properties reported in Table 3.1. Fourteen linear elastic beam-column elements are used instead of a single element for each span in order to account for its section variation at the end diaphragm of each span and for future modeling of its connection with the track system. The bridge deck masses are assigned with lumped translational and the rotational masses at all deck nodes and are computed based on the concrete density of 155pcf and the contributing volume. Also, additional equivalent mass from dead loads of approximately 9.4klf is assigned as well, accounting for the track system (i.e., cable vaults, derailment walls, OCS poles, OCS pole foundations, barriers, noise wall, rail and fasteners, electrification, system cables, etc.).

Table 3.1: Section properties for the CHSR prototype bridge box girder

Section	Area A (in^2)	Major Moment of Inertia I_z (in^4)	Minor Moment of Inertia I_y (in^4)	Torsion Constant J (in^4)	Polar Moment I_p (in^4)
Middle	12,848	1.82e8	2.18e7	4.33e7	2.07e8
End	22,434	2.22e8	3.24e7	7.02e7	2.56e8

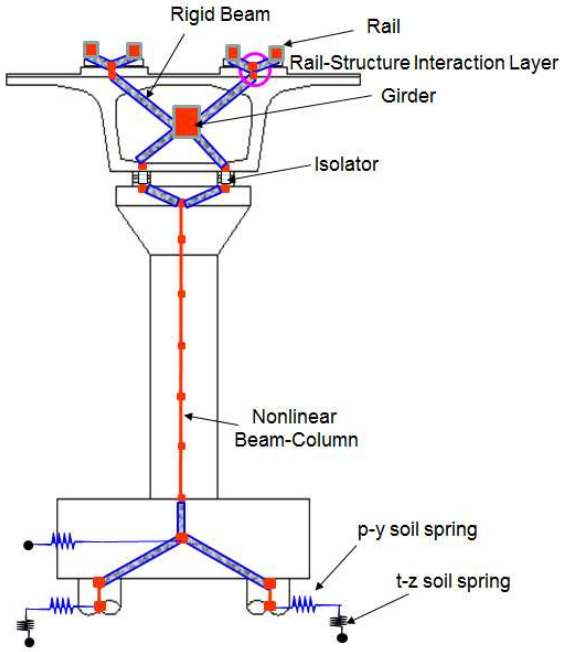

Figure 3.8: Schematic view of the model for substructure and its connection with superstructure

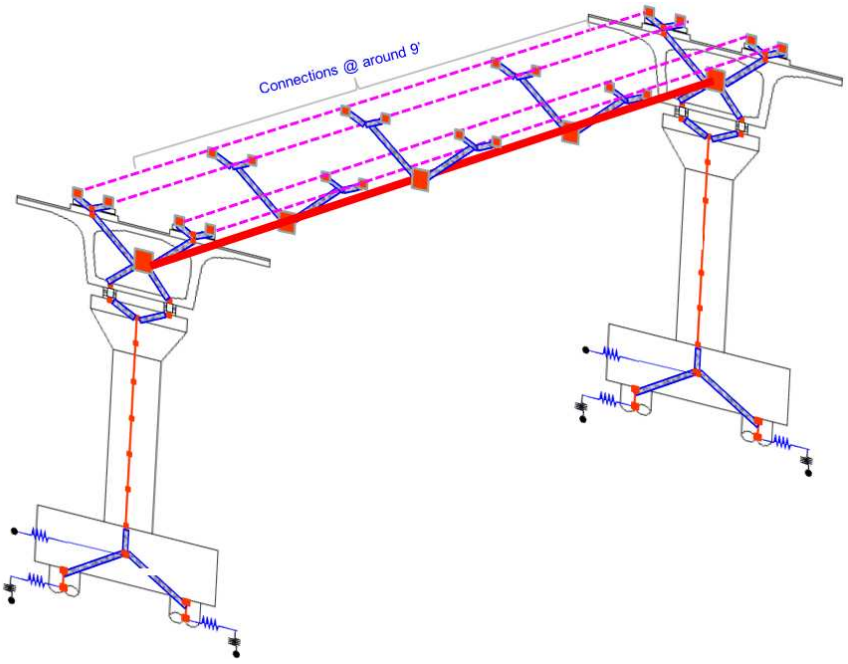

Figure 3.9: Schematic view of a single span of the CHSR Prototype Bridge model

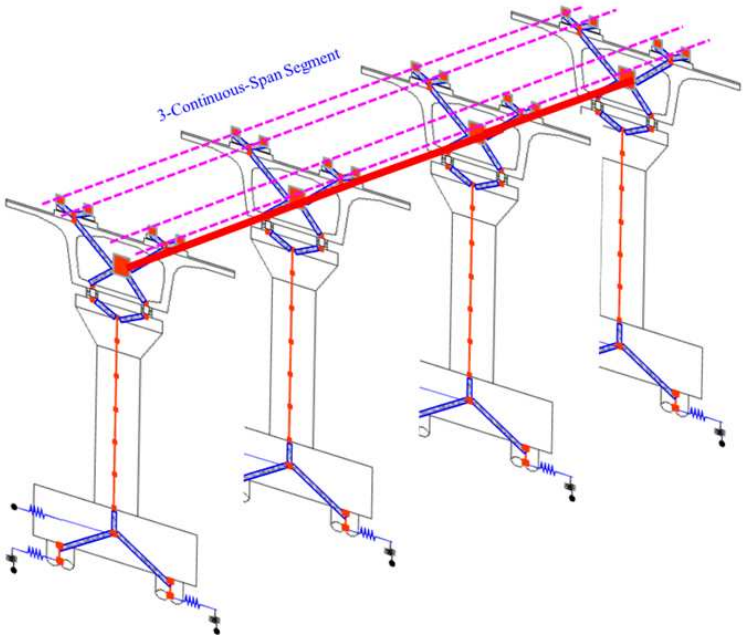

Figure 3.10: Schematic view of a single frame consisting of three continuous spans of the CHSR Prototype Bridge model

The bridge piers are modeled using nonlinear inelastic beam-column elements with nonlinear fiber sections and five Gauss-Lobatto integration points. The cross sections are discretized into small fibers with specific nonlinear uniaxial material models to represent the uni-axial stress-strain hysteretic behavior (Figure 3.11). Uniaxial concrete01, concrete02, and steel02 material are used for unconfined concrete in cover layers, confined concrete in the core areas, and reinforcing steel respectively. The mass of the pier column is distributed along the pier column height but lumped at all nodes.

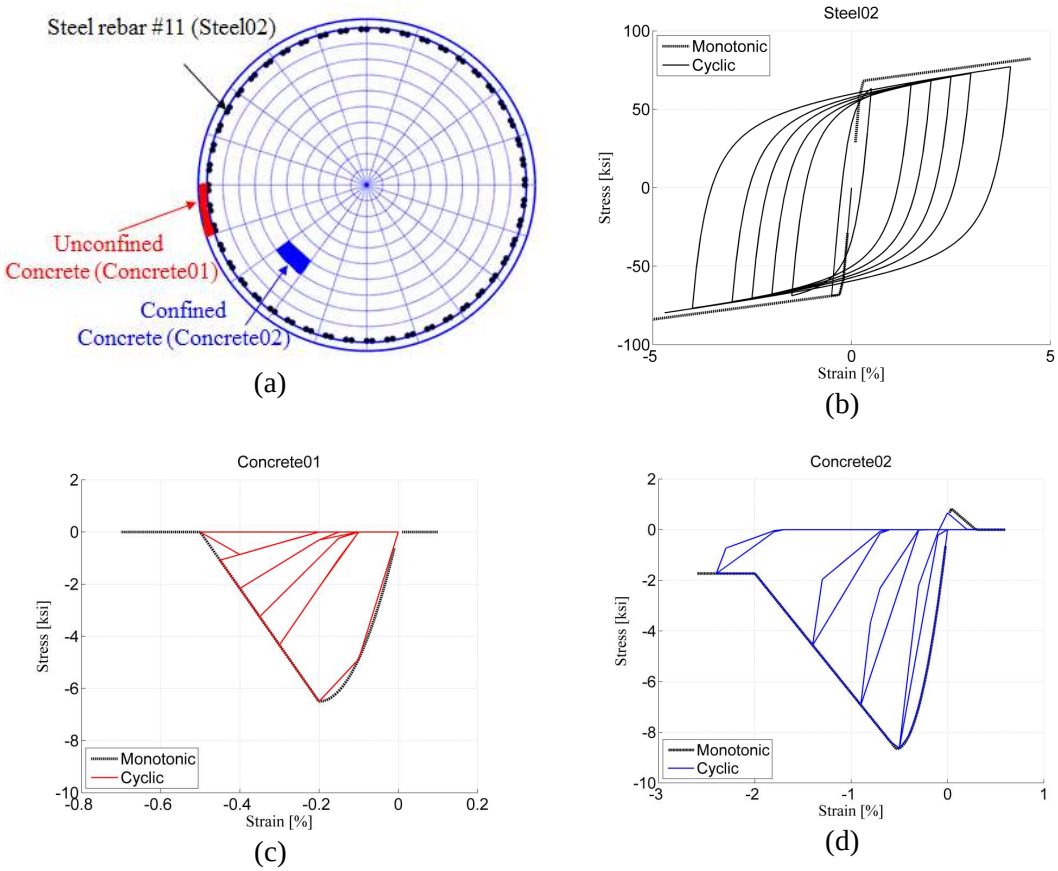

Figure 3.11: Pier column (a) fiber section discretization, (b) fiber material models for steel reinforcement, (c) concrete cover, and (d) concrete core

3.4.2. Seismic isolators for connections between deck and pier

Two groups of seismic isolators (i.e., isolator group A, and B) are used in the CHSR prototype bridge because the axial forces under vertical design loads in the seismic isolators located at the expansion joints and at the abutments are nearly half of the axial forces in those isolators located at the continuous joints. Isolator group A refers to the isolators with smaller axial forces and isolator group B refers to the isolators with larger axial forces (Figure 3.12). Since the objective of the analytical model is to study the feasibility and optimality of the seismic isolation, no particular models of specific isolators (such as, elastomeric bearing, lead

rubber bearing (LRB), single/double/triple friction pendulum bearding (FPB), high damping rubber bearing (HDP)) has been pre-selected herein.

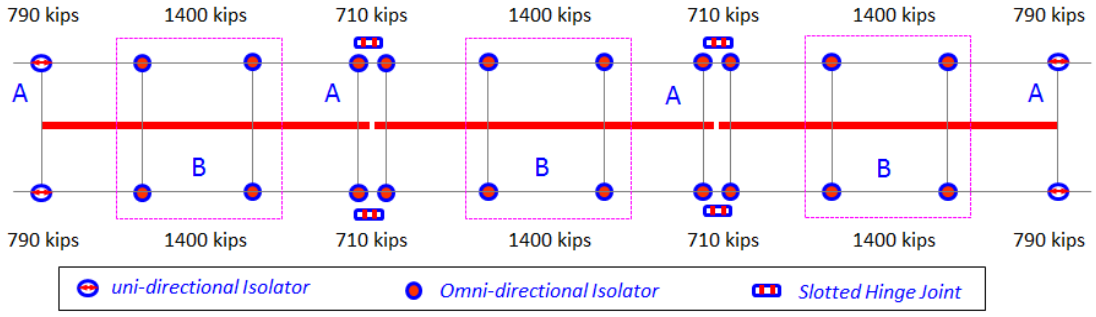

Figure 3.12: Distribution of axial forces in isolators and the layout of seismic isolators of group A (small) and group B (large)

Therefore, the idealized bilinear force-deformation characteristics representing a generic seismic isolation bearing are considered for optimization purposes. Each seismic isolator is modeled as a zero-length element with two uncoupled bilinear inelastic materials for horizontal lateral behavior: one in the longitudinal direction and the other in the transverse direction of the bridge. A preliminary design of the generic isolators is used as a starting point for the optimization procedure presented later. After the optimal force-deformation characteristics are obtained, a detailed design for a specific type of seismic isolator can be conducted in order to achieve the desired properties and characteristics.

3.4.3. Slotted hinge joints for decks at interior expansion joints

The bridge deck is broke into three seismic isolated segments because of the existence of designed interior expansion gaps. Instead of leaving alone the free relative movement of the adjacent deck segments resting on seismic isolators, a pair of SHJ devices is incorporated in the design to implement the segmental displacement control in the transversal direction and to serve as a fuse in the longitudinal direction of the bridge. At each of the two interior expansion

joints, a pair of SHJ devices is installed between the two adjacent end diaphragms of the bridge superstructure. The SHJ devices are vertically located at the height of the shear center of the box girder cross-section and at the outermost positions in the transverse direction. The SHJ device is composed of three steel plates with an elliptical hole which are tied together through a shear pin with cap plates (Figure 3.13). The inclusion of SHJ devices allows the relative movement of the end plates to a certain limit along the major axis (the longitudinal direction of the bridge) but constrains the relative movement of the end plates along the minor axis (the transverse direction of the bridge) with a finite stiffness.

Instead of considering a rigorous model of the SHJ device, each device is modeled as a zero-length element (Figure 3.15) with a gap-hook elastic-perfectly-plastic (EPP) spring in the longitudinal direction, an EPP spring with a tiny gap (0.0625in) between the slot and hold springs in the transverse direction, and an EPP spring vertical direction (Figure 3.16). The properties of these springs will be provided later.

The longitudinal gap/hook size is designed to be 2.0in on both compression and tension sides, respectively, to accommodate free deformation of the deck segments under creep, shrinkage, and temperature changes. In addition, gap elements with an elastic impact spring to model the potential pounding between adjacent deck segments are included (Figure 3.17) to limit the longitudinal compressive deformation of the SHJ devices, which cannot be larger than the expansion joint gap size. Even though these impact spring elements will most likely not be activated, they are still inserted in the FE model of the bridge to consider the possibility of large deformations of the SHJ connections during long return period (high seismic hazard) earthquakes.

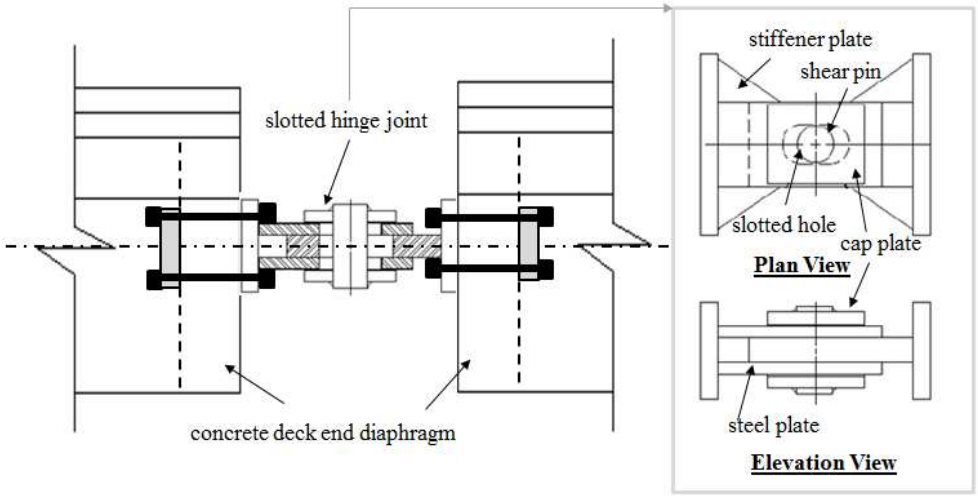

Figure 3.13: Schematic view of the SHJ device in the segmental control strategy

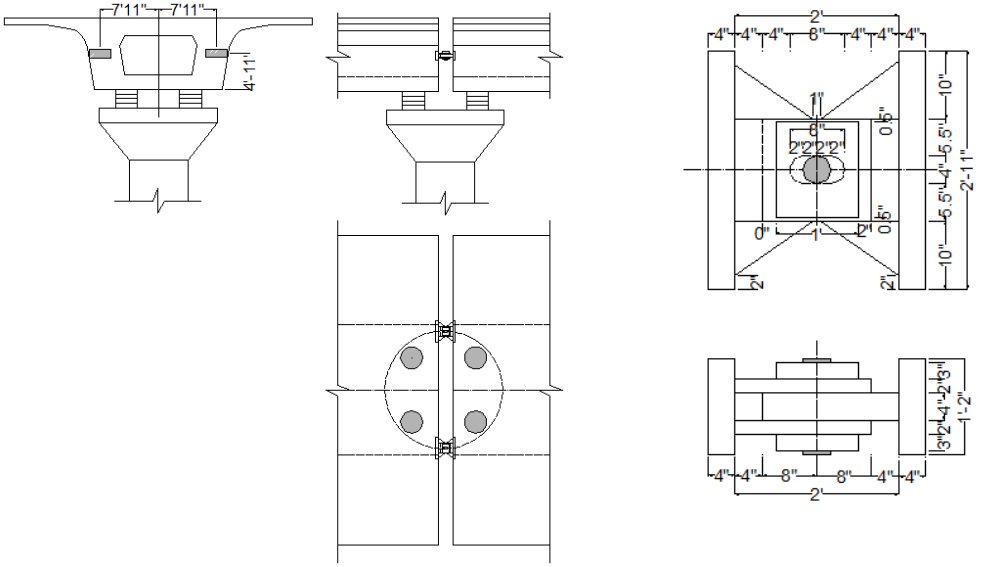

Figure 3.14: Design details of the SHJ device in CHSR prototype bridge

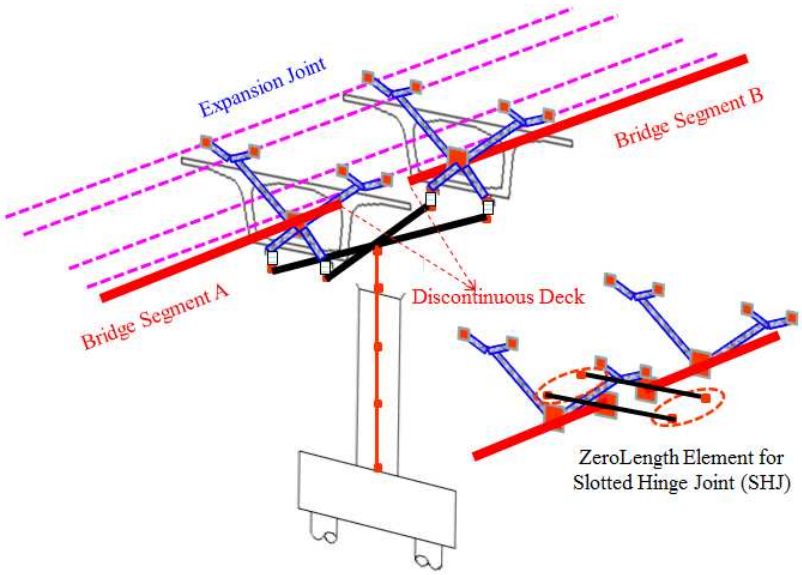

Figure 3.15: Schematic view of the model of the connection between two adjacent bridge segments at interior expansion joints with SHJ devices

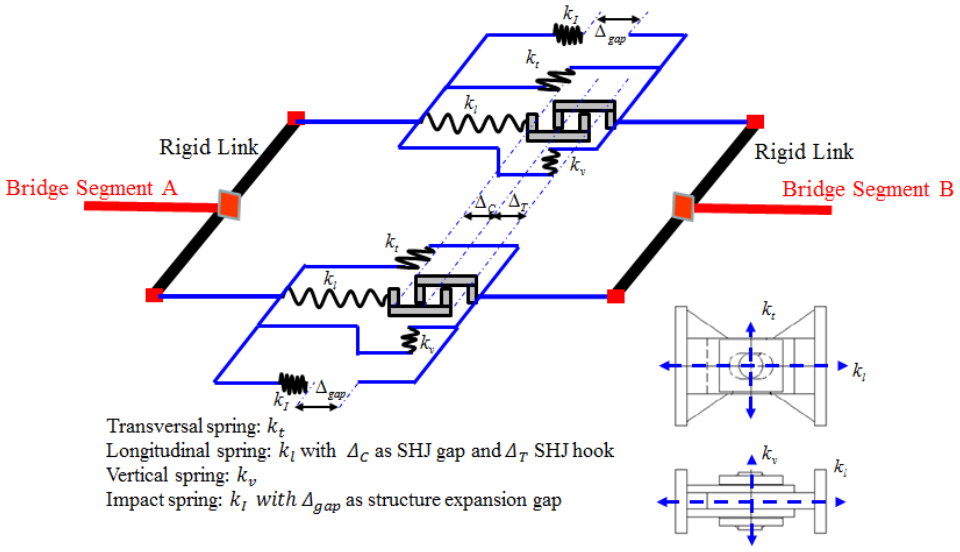

Figure 3.16: Schematic view of the model of SHJ devices between two adjacent bridge segments at interior expansion joints

The material specification for structural steel plates is ASTM A36, with yield strength of 36ksi when thickness is less than 8.0in, and the geometric dimensions of the SHJ design is shown in Figure 3.14. The estimated properties for the springs in the SHJ model are summarized in Table 3.2.

Table 3.2: Modeling properties for the SHJ adopted in CHSR Prototype Bridge

	Bilinear hysteretic spring	Gap size (in)	Initial stiffness (kips/in)	Yield strength (kips)
longitudinal	k_l	2.0	11,000	2,160
transversal	k_t	0.0625	9,200	228.5
vertical	k_v	0.0	36,800	914.0

3.5. Soil-Foundation-Structure-Interaction (SFSI) Modeling

Considering the significance of soil-foundation-structure-interaction (SFSI) effects observed in past studies, a robust and faithful fully nonlinear model is required to be established with appropriate consideration of SFSI. This need is enhanced by the necessary estimation of the seismic response of the bridge structure subjected to earthquake ground motions of a wide range of intensities in the context of PBEE. The effects of seismic isolation and SFSI act and react upon each other in terms of bridge response subjected to earthquake ground motions. This is explained that fact that seismic isolation tends to decrease the inertial effects in SFSI because of the reduction in force demand to the bridge substructure, whereas accounting for SSI could change the efficiency of seismic isolation. Therefore, SFSI needs to be incorporated into the FE model of CHSR Prototype Bridge, considering that a wide range of seismic isolation properties will be considered during the optimization process for the ultimate objective of optimum seismic design of CHSR Prototype Bridge in this research.

Dynamic SFSI, which addresses the effect of local soil conditions on the dynamic response of structures (buildings, highway over-crossing, river bridges, railway viaducts, and particularly nuclear power plants) subjected to earthquake ground motions, has been the

subject of considerable research interest. Various analytical and numerical approaches have been developed to tackle this problem for a better understanding and predicting the seismic response of structures accounting for SFSI. Consequently, considerable research results have greatly benefitted the practical engineering (Novak 1991).

After a comprehensive literature review on SFSI, three families of analysis methods for SFSI utilized in research and practical communities are summarized here: (1) modeling soil as continuum media using FE method (Kuhlemeyer 1979, Angelides and Roesset 1980, Randolph 1981, Faruque and Desai 1982), the finite difference method (FLAC), or the boundary element method (Sanchez-Sesma 1982, Sen et al. 1985); (2) modeling the soil resistance using a suite of nonlinear soil springs, referred to as dynamic p-y approach, stemming from the assumption of beam on a nonlinear Winkler foundation (BNWF) methods for shallow foundations (Harden et al., 2009, Raychowdhury 2009, Brandenberg 2005) and pile foundations (Wang 1998, Boulanger et al. 1999, Curras et al. 2001); (3) using equivalent linear springs and dash-pots derived from the impedance function based on the assumption that the soil is linear elastic or viscoelastic medium (Mylonakis et al. 2006, Luco et al. 1971).

Among these three approaches, approach (1) to model soil continuum media as the three-dimensional nonlinear domain is a more rigorous manner, but it is very demanding computationally for large civil engineering applications. Furthermore, a formidable computational work will be involved for parametric and optimization studies, where a significant number of nonlinear time history analyses needs to be performed (e.g., optimum seismic design of CHSR Prototype Bridge in the probabilistic performance-based earthquake engineering framework).

The widely used approach (3) is considered to be the most simplified and acceptable in practice for a single run situation, but it may not work well for this project with earthquakes

of a wide range of intensity levels for probabilistic performance evaluation. Compared to approaches (1) and (3), dynamic p-y approach is computationally attractive in engineering practice as a simplified approach, especially for seismic response estimation of bridge systems compared to 3D discretization of continuum approaches (Abghari and Chai 1995, Christopher and Pedro 2011). Although this modeling approach represents a simplification of the true behavior of soil, it does capture some critical state behavior of soil-pile interaction, like the nonlinearities in the soil and the piles.

For the CHSR Prototype Bridge system, an appropriate modeling approach for pile foundation and abutment system will be adopted and elaborated in detail to account for the SSI effects in the following sections.

3.5.1. Embankment-abutment component

Bridge abutment refers to the structure upon which the ends of a bridge rest. In terms of functionality, abutments are designed to provide vehicular and pedestrian access to the bridge, to withstand any loads directly applied or distributed from the bridge ends. Abutment consist of the stem wall to support the bridge deck, the back-wall with depth sufficient to accommodate the bridge deck depth, and wing walls to retain the backfill in between. Typically, abutments are considered and designed as retaining structures backed with embankment with local backfill right behind the back-wall. Wing walls are usually designed as conventional retaining walls to retain the abutment backfills and are expected to yield or fail during a major seismic event.

Measurements and observations of seismic response of bridge structures during earthquakes have shown the predominant role of abutments. The flexibility of the embankment-abutment system drastically affects the seismic response of the bridge system. Thus, the characterization of the inherently nonlinear stiffness of the abutment backfill system

is required for an appropriate boundary for the bridge to account for interaction between bridge superstructure and the abutment-embankment system.

Based on a thorough literature review on the abutment modeling and bridge abutment interaction analysis, applications of the three families of analysis approaches for SFSI aforementioned are summarized here. In view of the tremendous and demanding computational work in the dynamic performance evaluation of the bridge structures, the advanced two-dimensional (2D) or 3D continuum FE modeling is seldom utilized (Elgamal 2008, Zhang 2009), except for the purpose of modeling validation of simplified approaches or for investigation of the mechanisms of backfill failure (Kotsoglou 2007, Shamsabadi 2007). The equivalent linear spring with a linear dashpot derived from impedance function of soil domain was utilized to model and compare the instrumented bridge response (Zhang 2002a, 2002b). Nonlinear spring (p-y) to represent the resistance from the backfill or embankment to the bridge deck has been the most widely accepted approach accounting for abutment bridge interaction. These nonlinear springs have been calibrated from the field tests or 3D FE modeling (Romstad et al. 1995, Maroney et al. 1990, Gadre et al. 1998, Shamsabadi et al. 2007, Stewart et al. 2007).

For the ultimate objective of the model of CHSR Prototype Bridge, i.e., probabilistic performance evaluation and optimization later, the nonlinear spring (p-y) approach is adopted here. This approach will approximately represent the backfill resistance to the bridge deck as a function of the mobilized displacement of the abutment wall.

Model Description

The CHSR Prototype Bridge is supported on seat type abutments at both ends as shown in Figure 3.4, with a pair of seismic isolators to support the bridge deck. For seat type abutment adopted, only translational springs are deemed necessary to represent the supports

stiffness against the bridge deck from the abutments on both ends of the bridge and energy absorption through hysteresis. The embankment-backfill-abutment system is modeled using nonlinear springs longitudinally and transversally in an uncoupled manner.

In the longitudinal direction of the bridge, the support to the bridge deck is idealized by a mechanism with two parallel force paths. One path is to transmit the force from bridge deck through the seismic isolators to the stem wall, and then to soil behind the stem wall and the pile foundation, which is the only mechanism when abutment expansion gap is open. The other path is transmitting the force from bridge deck to the abutment back wall and backfill, and then to the embankment after the abutment expansion gap is closed. Nonlinear springs (p-y) in series with gap elements to represent the abutment gap will be used to simulate the resistance from the backfill.

In the transverse direction, the shear key to lock the relative displacement of bride deck with respect to the abutment stem wall provides the support to the bridge deck. Such a design aims to realize the uni-directional seismic isolation strategy in the longitudinal direction of bridge.

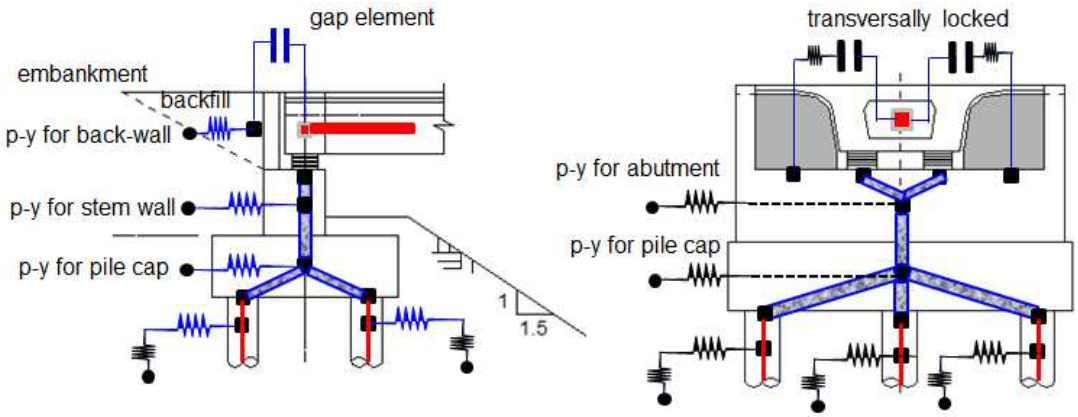

Figure 3.17: Schematic view of abutment model in both longitudinal direction (left) and transverse direction (right)

Calibration of Properties for Longitudinal Springs

In the longitudinal direction, a simplified elastic-perfectly-plastic (EPP) force-deformation relationship is prescribed by Caltrans for the estimation of abutment-backfill soil capacity and stiffness. The soil properties of backfill are not explicitly considered as the backfill behind modern highway bridge abutments usually satisfy AASHTO or State specifications with regard to typical compaction and soil type. In contrast, the CHSR abutment with atypical backfill properties with special treatment calls for a realistic representation of backfill resistance considering its properties explicitly.

A considerable amount of theoretical (Duncan et al. 2001, Siddharthan et al. 1994), experimental (Gadre et al. 1998, Romstad et al. 1995, Maroney et al. 1990) and numerical work (Sextos et al. 2008) has been carried out to characterize the force-displacement relationships up to the point of passive failure in the backfill for the backbone curve in the abutment backfill resistance in longitudinal direction. Shamsabadi et al. (2007) summarized all the field test data for a variety of abutments, i.e., a full scale abutment cyclic experiment with silty sand backfill in UCLA (Stewart et al., 2007), a full scale abutment cyclic test with clay in UC Davis (Romstad et al. 1995, Maroney et al. 1994), and concluded that the force-displacement curve is approximately hyperbolic with a verification through continuum FE modeling. A simple Hyperbolic Force-Displacement (HFD) relationship is proposed by Shamsabadi et al. (2007) as follows by curve fitting to the load displacement data derived from LSH modeling.

$$\bar{F}(y) = \frac{Cy}{1+Dy}, C = 2\bar{K}_{50} - \frac{\bar{F}_{ult}}{y_{\max}}, D = \frac{\bar{K}_{50}}{\bar{F}_{ult}} - \frac{1}{y_{\max}} \tag{3.1}$$

where,

$\bar{F}(y)$: abutment force per unit width of the wall corresponding to a displacement y

$\bar{K}_{50} = \frac{\bar{F}_{ult}}{2y_{50}}$: average abutment stiffness

$\bar{F}_{ult}$: maximum abutment force per unit width of the wall

y_{50}: displacement at 50% of the maximum abutment force capacity

The above HFD model involves parameters C and D depending on the soil properties and stem wall implicitly. Based on this work, an extended HFD equation (EHFD) was suggested by Shamsabadi et al. (2010) to account for the height effect explicitly. The EHFD model was validated using 3D numerical modeling and field tests results and validated using published measurements from several field and laboratory tests (i.e., two full-scaled field tests performed by Rollins and Cole 2006, and the centrifuge test at Rensselaer Polytechnic Institute by Gadre and Dobry 1998). Furthermore, to explicitly account for the physical properties of soil and geometrical dimensions of abutment wall, a closed-form relationship for the Generalized Hyperbolic Force-Displacement (GHFD) backbone curve prediction model was proposed by Khalili-Tehrani et al. (2010). The generalized predictive model is obtained by regression after performing extensive parametric studies for abutment wall with backfill using EHFD model. Consequently, GHFD model, accounting backfill properties explicitly, is used to derive a nonlinear spring with hyperbolic backbone curve representing the abutment back-fill resistance in CHSR Prototype Bridge.

The abutment back-fill soil employed in the CHSR Prototype Bridge is 3% cemented (by weight) well-graded gravel with low permeability. Under earthquake loading which is considered as un-drained condition, the passive resistance is governed by an un-drained strength of the soil. The abutment back-fill can be modeled as soil with zero friction angle and improved cohesion c = 50psi after Abramson (2001) and these soil properties are used to estimate the passive assistance force displacement relationship.

The backfill soil parameters, specified above for CHSR bridge abutments, are used to derive the backbone curve in Figure 3.18 based on the GHFD prediction model developed for usual highway bridge abutments. The appropriateness of using GHFD is verified using the Log Spiral formulation for passive soil pressure in PYCAP (Mokwa et al. 2001) herein as validation. It is found that the GHFD prediction agrees well with the rigorous estimation from Log Spiral (LS) Passive Pressure Theory (Figure 3.18). Thus, the predictive backbone curve is considered to be rational to represent the abutment back-fill resistance spring.

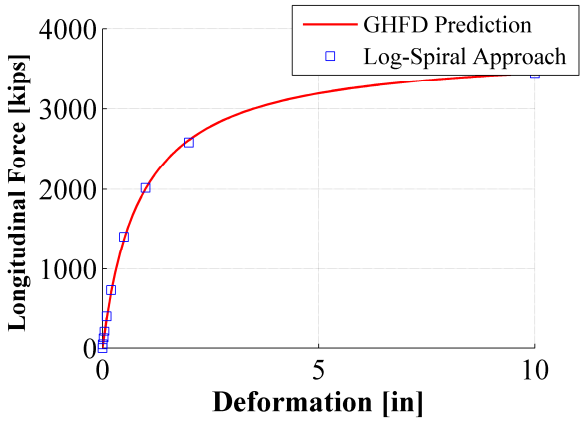

Figure 3.18: The p-y backbone curve for abutment back-wall resistance predicted using the GHFD prediction model proposed by Khalili-Tehrani et al. (2010) and the Log-Spiral approach prosed by Mokwa et al. (2001) as validation

The hyperbolic spring formulated in *OpenSees*, which was calibrated based on the static and dynamic test of abutment back-wall (Wilson et al. 2006, Shamsabadi et al. 2007, and Duncan et al. 2001), is used with the derived hyperbolic backbone curve to represent the cyclic behavior of backfill with energy dissipation. An element associated with this hyperbolic spring is combined in series with another element associated with a gap material model to simulate the abutment backfill support to the bridge deck. This allows the internal node in between to be assigned with a nodal mass considering the abutment back-wall and mobilized back-fill wedge mass in the dynamic analysis in the longitudinal direction of the bridge.

Similarly, the Log Spiral theory is adopted to calibrate the p-y springs representing the passive pressure (see Appendix A) in the longitudinal direction from surrounding soil against the abutment stem wall and the pile cap. The modeling of the pile foundation for abutment follows closely the modeling approach for pile foundation under piers as explained in the next section.

Calibration of Properties for Transverse Springs

Compared with studies on the longitudinal behavior of the abutment-embankment systems, limited studies have been carried out on the transverse behavior of the abutment. Typically for highway bridges, the abutment shear keys provide the transverse stiffness and capacity of the abutment to the bridge and neglect the flexibility of the embankment.

To account for the transverse flexibility of abutment system, Wilson et al. (1990) proposed an equivalent linear spring to represent the transverse stiffness of a monolithic abutment system based on linear elastic plane strain analysis of shear wedge model with a typical trapezoidal-shaped embankment cross section. Using the shear wedge model proposed by Wilson et al. (1990), the kinematic response function and dynamic stiffness (stiffness and damping) in transverse direction of the bridge were developed by Zhang et al. (2002) using equivalent linear elastic analysis. Compared to previous approaches, which are based on linear or equivalent linear estimation, Maroney et al. (1994) proposed a nonlinear spring with backbone curve modified from the longitudinal resistance backbone curve accounting for the wing-wall effectiveness coefficient and backfill participation coefficient (Mackie et al. 2006, Lu et al. 2011). This approximation was supported by the observation that similar dynamic stiffness in longitudinal and transverse directions were derived based on equivalent linear elastic analysis of the shear wedge model for embankments of two existing bridges by Zhang et al. (2002). Consistent with the modeling of longitudinal behavior, nonlinear spring (p-y)

approach is adopted here to represent the transverse resistance from the backfill between wing walls. The transverse support from the pile foundation is represented implicitly from the modeling of pile group foundation which will be introduced later on. After assembling the longitudinal and transversal modeling supports to the bridge on the abutments, the analytical model for abutment is implemented as illustrated Figure 3.19.

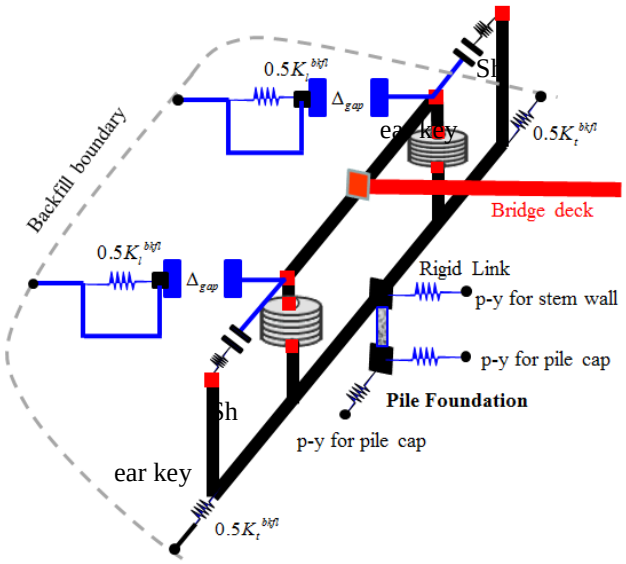

Figure 3.19: 3D schematic view of the abutment modeling

To avoid the steep change of stiffness of bilinear transition at the engagement of gap, formulation of the macro "smooth" gap material, making use of the existing fiber material models in *OpenSees* by paralleling several springs with different gaps but the same initial stiffness and yield displacement, is used and implemented in *OpenSees* for modeling purpose. The arrangement of the springs is presented in Figure 3.20 for a smooth transition from $\Delta(1-\alpha)$ to $\beta\Delta=(\alpha+1)\Delta$ instead of sharp change of stiffness at original gap Δ.

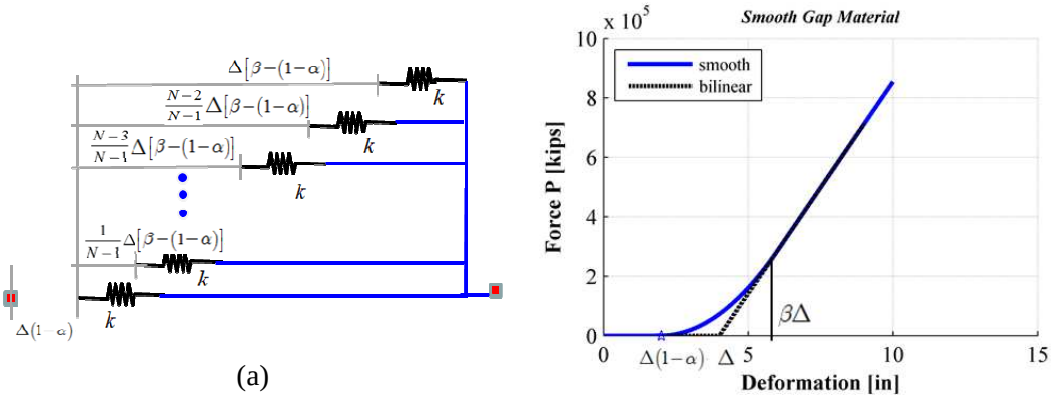

(a) (b)

Figure 3.20: Smooth gap material mechanism (a) and comparison with bilinear (b)

The properties of the N sub-springs are derived as follows,

$$\begin{aligned} \Delta_i &= \Delta(1-\alpha) + \Delta(\beta+\alpha-1)\frac{(i-1)}{N-1},\ i=1,2,\ldots,N \\ k_i &= k = K/N,\ i=1,2,\ldots,N \\ f_{yi} &= k\left(\frac{F_y}{K} + \Delta - \Delta_i\right),\ i=1,2,\ldots,N \end{aligned} \tag{3.2}$$

where Δ_i, k_i, f_{yi}, are the initial gap, initial stiffness, and yield strength of i-th sub-spring respectively, and Δ, K, F_y, are the initial gap, initial stiffness, and yield strength of bilinear spring respectively. The smoothness of the gap, which is more realistic, is intended to reduce possible numerical problems such as convergence issues.

3.5.2. Abutment shear key component

In the CHSR project, the transverse stiffness transition from the bridge to the embankment is of great concern to mitigate the potential damage on continuous welded rail. Ideally, rigid shear keys are expected so that the concept of ideal uni-directional seismic isolators at the abutment can be implemented to allow isolation only in longitudinal direction of the bridge and to maintain the continuity of the transverse stiffness transition. While from

the practical point of view, minimal allowable construction gap 0.5in is left between the bridge deck and shear keys, and the shear keys for CHSR Prototype Bridge are designed with limited shear capacity of 1125kips. Thus a rational modeling of the shear key behavior is required in the CHSR Prototype Bridge model.

A shear key model is developed using existing uniaxial material models available in *OpenSees*, i.e., a parallel of two uniaxial bilinear springs with different initial gaps and different permissible maximum deformations. This shear key model is calibrated with the hysteretic force-displacement behavior of experimental data (Megally et al. 2001) as shown in Figure 3.21. A scaled force-displacement curve of shear key (Test Unit 3A reported by Megally et al. 2001), by factor of 4.6 for force and factor 2.15 for displacement, is established as the analytical model for a shear key component in CHSR. Besides, an initial gap of 0.5in is included in series to account for the gap between the bridge deck and the shear key.

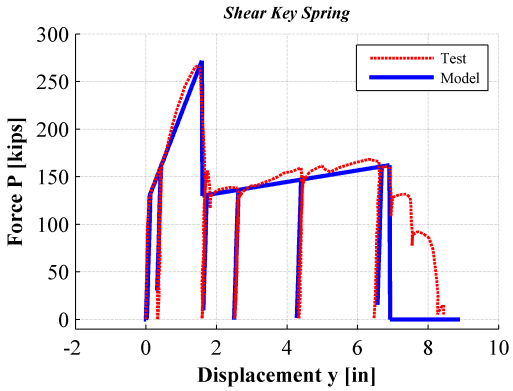

Figure 3.21: Shear key model calibrated with experimental data (Unit 3A reported by Megally et al. 2001)

3.5.3. Pile foundation component

It is well known that the seismic excitation transmitted to the base of a pile-supported structure is different (usually smaller) from the free-field motion, because of the dynamic interaction between the foundation and surrounding soil (Mylonakis et al. 2002). In addition,

the inertial force from the bridge structure excites the pile foundation. Thus soil-pile-structure interaction (SPSI) effect needs to be considered for an accurate evaluation of the dynamic response of whole bridge system under earthquake loading, especially when the earthquake ground motion intensity is relative high.

There are different approaches to account for SSI, each of them with the featured advantages and limitations aforementioned. One alternative to model SSI effects for pile group supported structures is the well-established and versatile p-y approach based on the Winkler assumption, which was argued analytically that the error inherent is not significant by Vesic (1961) for lateral loaded pile in static loading cases. Trochanis et al. (1991) showed that simulation results via BNWF approach agreed well with static load test data and 3D finite element analysis using Bouc-Wen soil pile p-y elements. Based on the confidence in the modeling strategy after a comprehensive understanding of the quantification of strength and stiffness evolution with deformation, p-y approach has been widely used in practice as well due to its simplicity and capabilities to capture most of the nonlinearities (API 2000, JRA 2002).

Applicability, validity, and reliability of dynamic p-y (BNWF) approach has been extended to shallow foundations and piles foundations under earthquake loading and has been validated using full-scale field experiments or laboratory tests, i.e., shaking table tests and centrifuge results, or rigorous 3D FE continuum modeling and simulation (Raychowdhury 2009, Boulanger et al. 1999, Curras 2001, Huo 2011, Zhao 2011).

In the formulation for BNWF, the soil medium is approximated by a series of closely spaced independent soil springs. The resistance of surrounding soils to flexible piles embedded in arbitrarily layered soil deposits is modeled by three sets nonlinear springs. Two set of uncoupled lumped lateral nonlinear springs (referred to as p-y springs) and one set of

vertical springs (referred to as t-z springs) independently attached to the pile at discrete locations along the pile. Another vertical spring (denoted as q-z spring) at the pile tip is attached to represent tip resistance. The resistance of these nonlinear springs against piles is a function of pile deflection at the corresponding point, and they are modeled realistically to reproduce the force-deformation relationship referred to as p-y (t-z, q-z) curves with due consideration on the effects of gapping, side friction, and passive or active soil pressure.

To estimate the lateral dynamic stiffness and radiation damping of flexible piles, a p-y model is conceptualized as consisting of elastic, plastic, and gap components in series as well as radiation damping modeled by a dashpot in parallel with the elastic component developed by Boulanger et al. (1999). It is implemented as a uniaxial material *Pysimple1* in *OpenSees* in terms of a system of mathematical expressions capable to capture the experimental results with satisfactory engineering accuracy when its parameters are well calibrated. To account for radiation damping, a dashpot is also attached to rationally represent the boundary conditions of pile foundation system, namely the dynamic soil reaction against piles and radiation energy dissipation.

For the CHSR Prototype Bridge model developed in *OpenSees*, the pile foundation component (Figure 3.22) is modeled using the well-established dynamic p-y approach herein to account for SSI effects. The pile shafts are modeled as nonlinear beam column elements with fiber sections (Figure 3.23). The piles are supported by a series of p-y springs and t-z springs along its depth, and q-z springs at each pile tip to represent the bearing capacity of piles (Figure 3.24). The lateral nonlinear p-y soil spring formulation as proposed by Boulanger et al. (1999) is adopted in this numerical model, with hysteretic relationships for two typical soil springs, namely clay and sand (Figure 3.25). The formulation is briefly summarized in Appendix B.

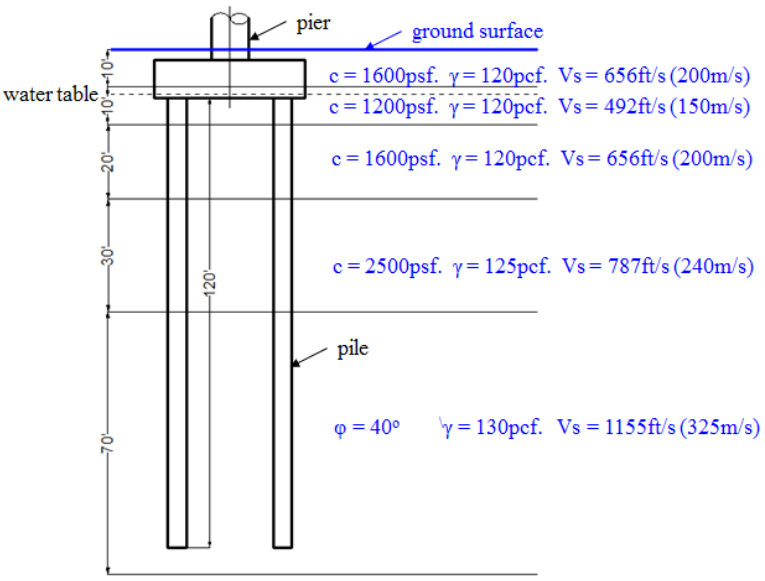

Figure 3.22: Pile foundation with soil layer properties

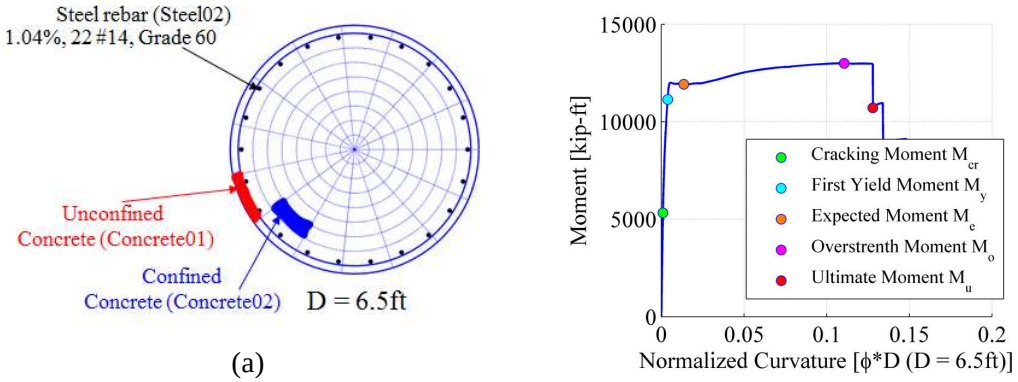

Figure 3.23: Fiber section discretization of piles (left), and pile section moment-curvature relationship (right)

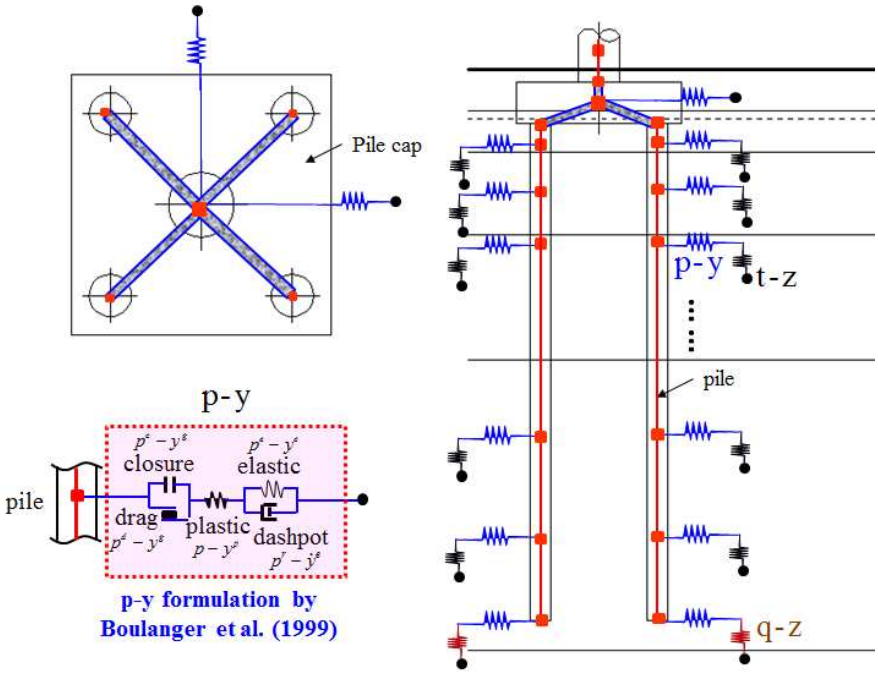

Figure 3.24: Sketch of pile foundation modeling using dynamic p-y approach

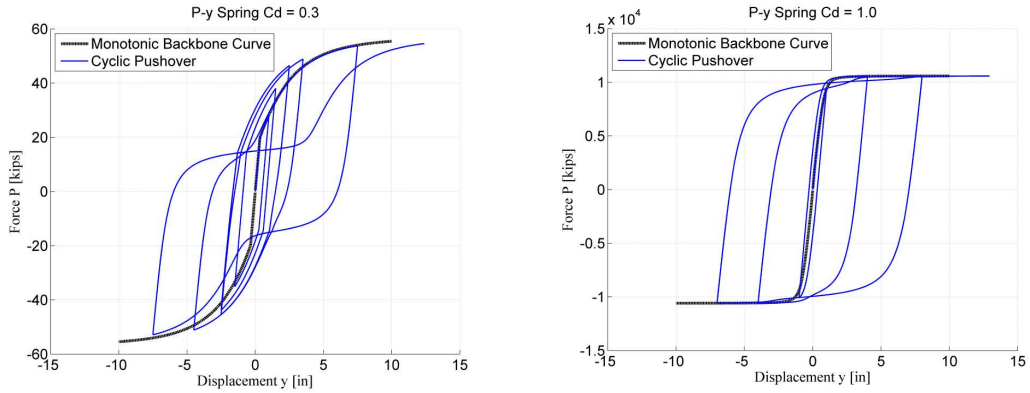

(a) (b)

Figure 3.25: Soil spring (p-y) behaviors for a typical soil spring in upper layer of clay (a) and a typical soil spring in lower layer of sand (b)

In practice, the specification of the ultimate capacity and displacement are of particular importance. All p-y curves are defined following the recommendations proposed based on the analysis of the results of full-scale experiments and the validation of numerical modeling. Thus, the key parameters in the nonlinear springs are estimated from the fundamental soil properties, following the well-developed and widely-adopted baseline procedures for p-y approach summarized in Appendix B.

In the context of dynamic SFSI analysis subjected to earthquakes or rotating machines, stress waves will be generated in the underlying or surrounding soil around the foundation when the foundation moves against the soil and transmitted to far field soil. Recalling the mechanism of damping for energy loss, radiation damping (geometric damping) is conceptualized to characterize the dissipation of energy carried away by the spreading outward of out-going stress waves. To directly evaluate the effects of radiation damping using realistic simple models is important in our model.

In the p-y formulation, a linear dashpot is implemented in parallel with the elastic component of the p-y spring, and then in series with the gap component and plastic component (Wang et al. 1998, Boulanger et al. 1999). The dashpot value is determined based on the recommendation by Gazetas G. et al. (1984), in which wave propagation idealizations in 1D elastic cylinder was made to gain insight of the nature of radiation damping and used to estimate the pile radiation damping (Boulanger et al. 1999). Detailed procedure is documented in Appendix B.

Compared to the flexible pile and the nonlinear soil springs, the pile cap is considered to be essentially rigid and modeled using exceedingly stiff (quasi-rigid) beam column elements to account for the geometric offset. Nonlinear soil springs are included to consider the soil resistance to pile cap using the passive pressure theory. Due to overlapping stress

fields of closely spaced piles and their mutual effects among the pile shafts, an average p-multiplier 0.7 is applied to the capacity of p-y springs in light of the limitation as recommended by Boulanger et al. (1999) based on the centrifuge test and numerical verification.

3.6. Track-Structure Interaction Modeling

According to Seismic Design Criteria for the CHST project, track-structure-interaction analysis is essential for the performance evaluation of bridges or aerial supporting structures in the high-speed rail system. A comprehensive model to simulate the track-structure-interaction analysis under earthquake excitation requires explicit modeling of rails and connection between rails and the bridge structure. A minimum finite length of explicit modeling of the track system beyond the bridge ends needs also to be included for better accounting for the boundary conditions of tracks on bridges. Also, at the cut of rail extension at the finite length, a nonlinear longitudinal spring, denoted as rail boundary spring, needs to be added at each rail end to represent the longitudinal support of infinitely long rail supported on track slab.

3.6.1. Rail

In practical design, stresses generated under Operating Basis Earthquake (OBE) need to be checked with the allowable axial rail stress (i.e., ±14.0ksi when no temperature stress is included and ±23.0ksi otherwise). Thus the performance of the rail in the track system is a crucial concern in seismic performance evaluation for OBE hazard levels. To investigate the rail stress imposed from the longitudinal and transverse deformation during the earthquake events, rails are explicitly modeled as elastic beam-column elements in the comprehensive numerical model for track-structure interaction analysis. All four lines of rails are continuous over the whole bridge as well as the rail extensions beyond the abutment. The material and section properties for rails of type 141RE in AREMA are utilized.

3.6.2. Rail-structure connection

The non-ballasted tracks are connected to the track base (bridge deck or subgrade beyond the bridge) with direction fixation fasteners (California High-speed Rail Authority, 2012; Petrangeli, 2008), as shown in Figure 3.26. A series of coupling springs on a per track basis to represent pairs of fasteners are included in the prototype bridge model (see Figure 3.27 and Figure 3.28). Figure 3.28 presents the elevation view of the modeling scheme used for the full track-structure-foundation-soil-interaction (TSFSI) system in the longitudinal direction.

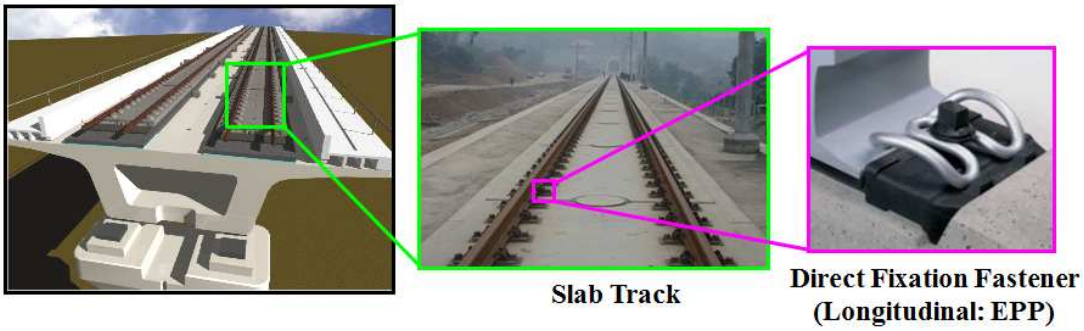

Figure 3.26: Typical track slab system with direct fixation

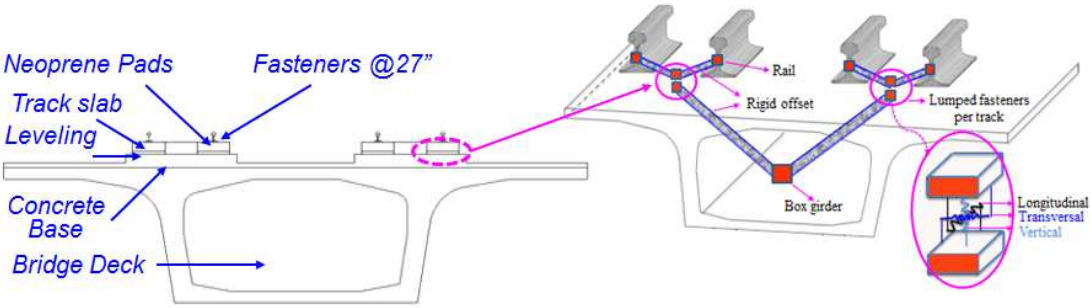

Figure 3.27: Schematic illustration of track-structure-interaction layer

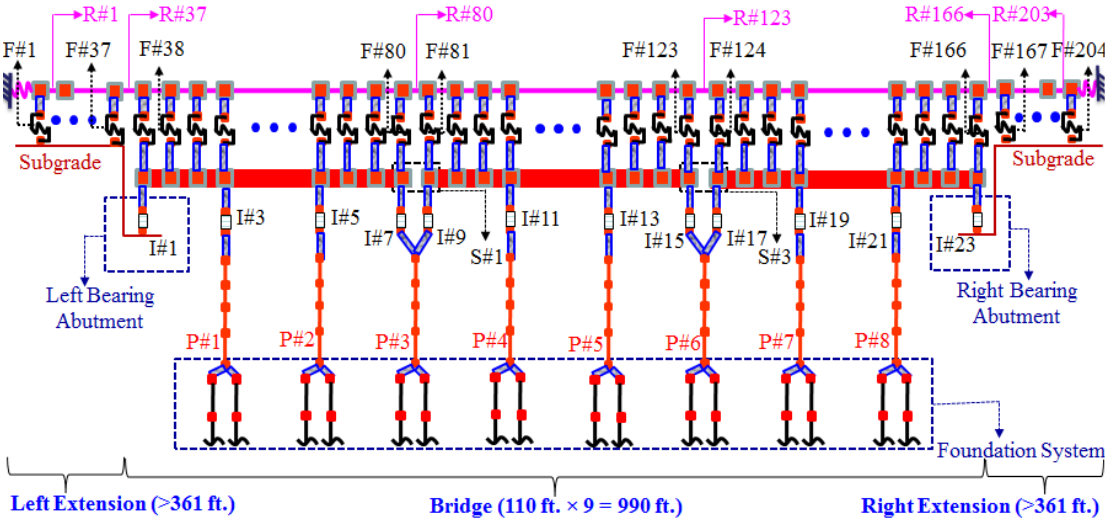

Figure 3.28: Elevation view for the Track-Structure-Foundation-Soil Interaction (TSFSI) system

In the Track-Structure interaction model, rail-structure interaction elements discretized and lumped every 7.9ft are adopted to idealize the connection system between rail and deck. This resulted in fourteen fastener elements per span consistent with the fastener spacing modeling requirements specified in the CHST project design criteria (CHSRA, 2012). In the vertical and transverse directions, the rail fastener elements are modeled as linear elastic springs per foot of track (two rails) with stiffness of 4,000kips/ft/ft and 450kips/ft/ft, respectively. In the longitudinal direction, the fasteners for non-ballasted track are represented by bi-linear inelastic coupling springs with parameters depending on the vertical load (none or train) acting on the rails as reported in Table 3.3. These bilinear springs characterize the resistance from the bridge deck to the track. The nonlinear behavior of the fasteners allows slippage of the rail relative to the track support structure. Based on the CHST project design criteria, no extra dampers are incorporated across the interaction layer between the rail track and the bridge deck.

Table 3.3: Rail-structure connection modeling properties

Direction	Material Type	Stiffness per Foot of Track (kips/ft/ft)	Yield Displ. (in)	Actual Fastener Spacing (in)	Modeling Requirement
Longitudinal	EPP	60(120)*	0.02	27	(1) # of Springs per Span ≥10
Transversal	Elastic	450	-	27	
Vertical	Elastic	4000	-	27	(2) Spacing ≤10 feet

*Note: Inside the parentheses is the value used for the loaded case.

3.6.3. Rail boundary spring

To appropriately model the boundary conditions of the track system on top of the bridge structure, the rails and coupling fasteners are extended a distance of 361ft from the face of the abutment into the embankment (or natural ground) at both ends of the bridge and modeled explicitly as elastic beams supported on coupling fasteners. Also, a horizontal boundary spring, representing the rail-fastener system behavior beyond the extension, is included to simulate the resistance against the rail extension in the longitudinal direction of the bridge.

The CHST design criteria suggest that an elastic-perfectly plastic spring should be specified at the end of the track (two rails) with a stiffness of 24,200kips/ft and a strength capacity of 40.3kips. However, the boundary spring needs to be verified to remain elastic throughout the track-structure interaction analysis; otherwise the extension of the rails and coupling fasteners beyond the bridge must be elongated. An important limitation of this practical approach is that the properties of the rail boundary spring are dependent on the rail and rail fixation properties.

To avoid unnecessary check during the analysis and repeated analysis after elongating the extension of the rails, a physical nonlinear spring model with perfectly captured behavior

is proposed here after a thorough study of the structural behavior of the resistance from an infinitely long rails supported on bilinear fasteners.

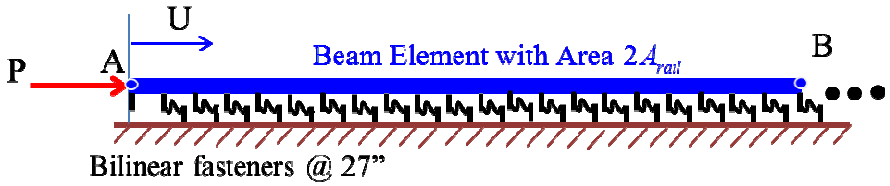

Figure 3.29: Infinite long track supported on bilinear fasteners

A substructure model of an infinitely long rails supported on bilinear fasteners is implemented to study the slippage behavior of rails on top of the track supporting structure (Figure 3.29), where the end of the rails is not stressed so that the finite length behavior mimics the infinite length behavior. The two rails for a track are condensed with an equivalent area, and the bilinear coupling fasteners with the prescribed properties are spaced with practical space. A monotonic static pushover analysis is carried out to better understand the behavior.

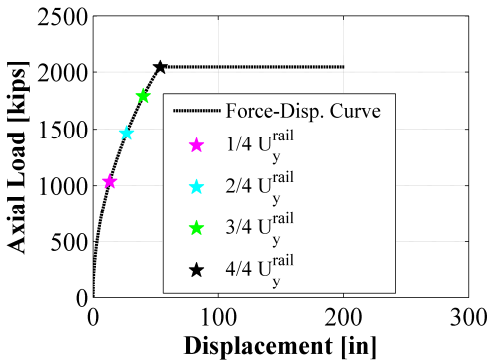

Figure 3.30: Monotonic static pushover curve

Figure 3.30 shows the monotonic static pushover curve, behaving initially until the first yield of fastener closest to the loading end. The stiffness decreases as the deformation increases, because more and an increasing number of fasteners become plastic.

The deformation distribution across all the fasteners is sketched in Figure 3.31 at 4 different states corresponding 25%, 50%, 75%, and 100% of the yield displacement of the rail. With the increase of load applied, more fasteners will be activated and more fasteners will enter plastic state to form the plastic zone/region denoted by the shaded area in Figure 3.31(a).

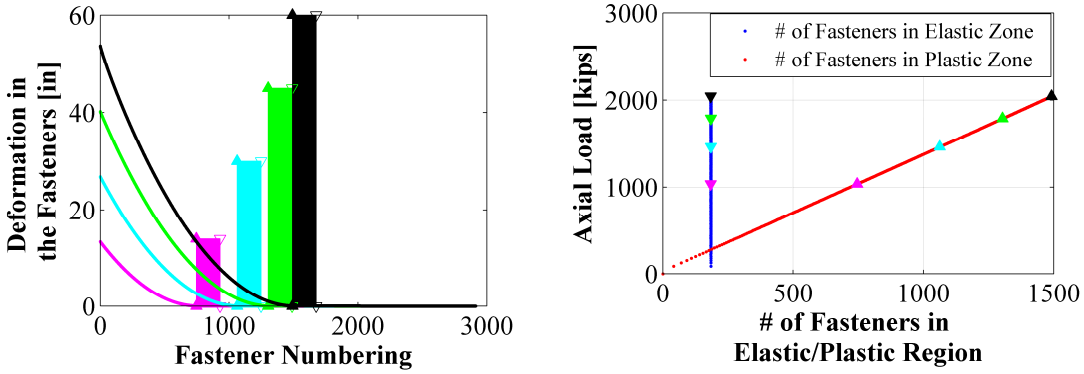

Figure 3.31: Elastic/Plastic zone of fasteners: (a) deformation in the fasteners, and (b) number of fasteners in the elastic and plastic zones

The number of fasteners in the elastic state to form the elastic zone/region is tracked and presented in Figure 3.31(b). The number of fasteners in the elastic region keeps invariant after a certain load level, whereas the number of fasteners in the plastic region keeps growing as the number of activation fasteners increases.

The described mechanism indicated in the static monotonic pushover analysis of the rail extension substructure here is similar to the bond slip of steel rebar in concrete. Thus a macro material, denoted as multiple-series-parallel-spring (MSPS) model, is developed via a systematic way combination of parallel and series springs as shown in Figure 3.32, whose

properties can be estimated readily by the properties of the rails and bilinear fasteners specified in Equation (3.3). Without any numerical calibration, the macro material behavior will behave almost exactly the way of the substructure model built up as shown in the cyclic pushover analysis (Figure 3.33). Thus a two-node element with this macro material can replace the substructure model with a significant reduction of the model size in terms of degrees of freedom.

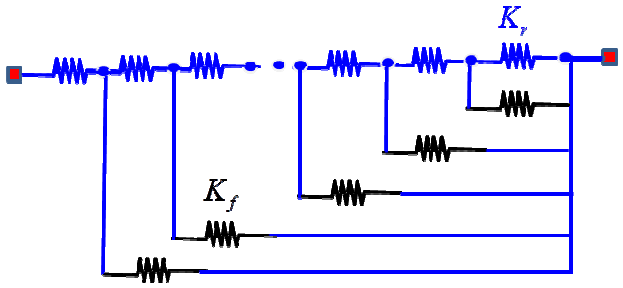

Figure 3.32: Multiple Series-Parallel Spring (MSPS) model

$$
\begin{aligned}
K_r &= \frac{E_{rail}\left(2A_{rail}\right)}{n_{lumped}\,l_{space}} \\
F_r^{\,y} &= f_{rail}\left(2A_{rail}\right) \\
K_f &= n_{lumped}\,k_{fastener} \\
F_f^{\,y} &= n_{lumped}\,f_{fastener}^{\,y}
\end{aligned}
\tag{3.3}
$$

where,

n_{lumped} = number of fasteners to be lumped

l_{space} = fastener space in practice

K_r = initial stiffness of the spring for the rails with length $n_{lumped}\,l_{space}$

$F_r^{\,y}$ = yield strength of the spring for the rails with length $n_{lumped}\,l_{space}$

K_f = initial stiffness of the spring for the lumped fasteners

F_f^y = yield strength of the spring for the lumped fasteners

E_{rail} = Young's modulus for the rail

A_{rail} = area of rail section

f_{rail} = yield stress of the rail

$k_{fastener}$ = initial stiffness of the bilinear fasteners

$f_{fastener}^y$ = yield strength of the bilinear fasteners at 0.02in

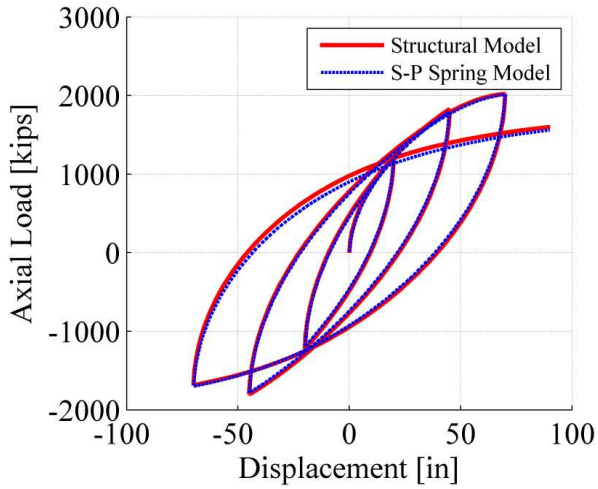

Figure 3.33: Cyclic push-over curve comparison between the physical substructure model and the MSPS (S-P) model

3.7. Static and Dynamic Analysis of Abutment Substructure

A static pushover analysis is performed on the abutment substructure shown in Figure 3.34, in order to investigate the abutment resistance behavior to the bridge end through seismic isolators resting on the abutment stem wall before the abutment gap is closed, and then the abutment back fill behind the abutment back-wall once the abutment gap is engaged.

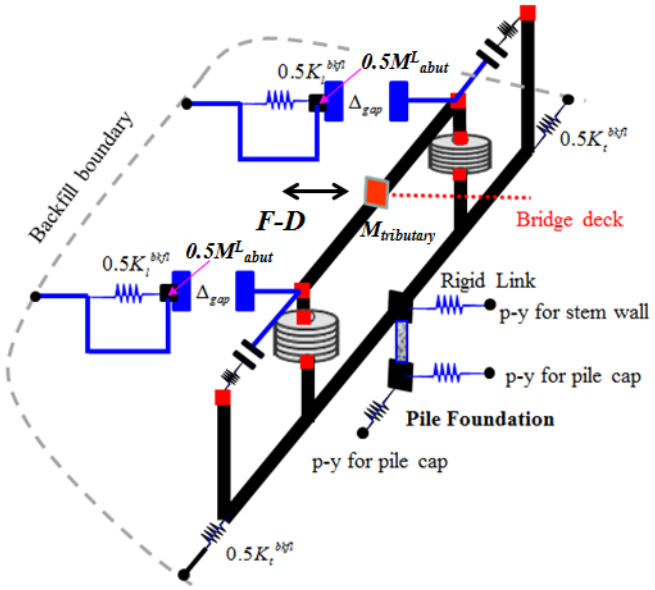

Figure 3.34: Abutment substructure system considered for the hysteretic and dynamic behavior

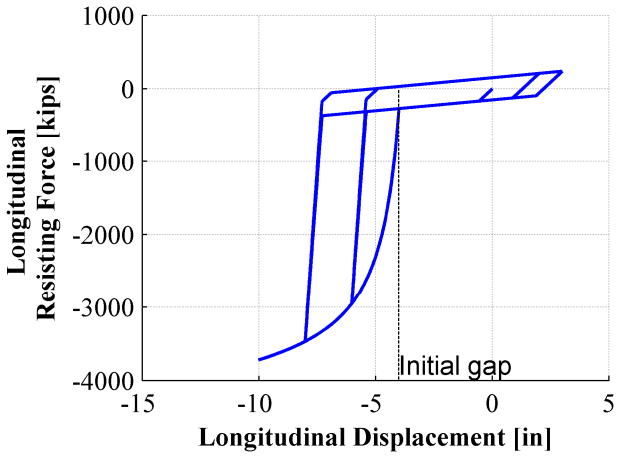

Figure 3.35: Force-displacement relationship of abutment resistance to bridge end

Figure 3.35 illustrates the hysteretic behavior of the abutment system resistance to the bridge superstructure. Before the abutment gap is closed, the stiffness of the abutment support is mainly from the seismic isolators. When the relative displacement is large enough to close the abutment gap, there is a steep stiffness increase due to the contribution of abutment back-

wall backfill system. Also, it is noticed that the abutment gap will increase due to the plastic (residual) deformation of the abutment.

A dynamic time history analysis is carried out to investigate the dynamic behavior of the abutment system with a tributary mass from the bridge deck lumped at the supporting node of the abutment system (a representative node of bridge end) with vibration frequency of 0.94Hz. In contrast, the vibration frequency of in the embankment-abutment system accounting for the backfill resistance and abutment mass, indicated by the abutment mass node, is as high as 8.8Hz. As illustrated in Figure 3.36, the abutment vibrates with a high frequency (around 8.8Hz) when the abutment gap is not closed under earthquake ground motion. In contrast, the abutment remains in place if the abutment mass is neglected, unless there is an impact between the bridge superstructure and the abutment during the earthquake. The impact will mobilize the backfill, and plastic (residual) deformation will occur, thus leading to an increase of the gap as shown in Figure 3.36. The abutment backfill resistance displacement relationship is presented in Figure 3.37 to show the effect of abutment mass.

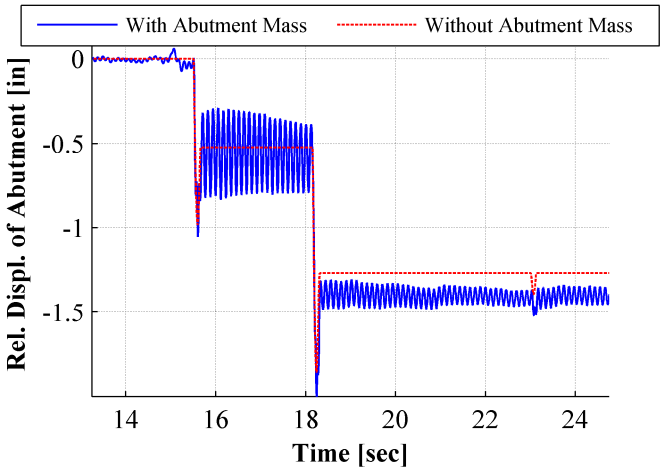

Figure 3.36: Relative displacement of the abutment mass node with respect to free field ground

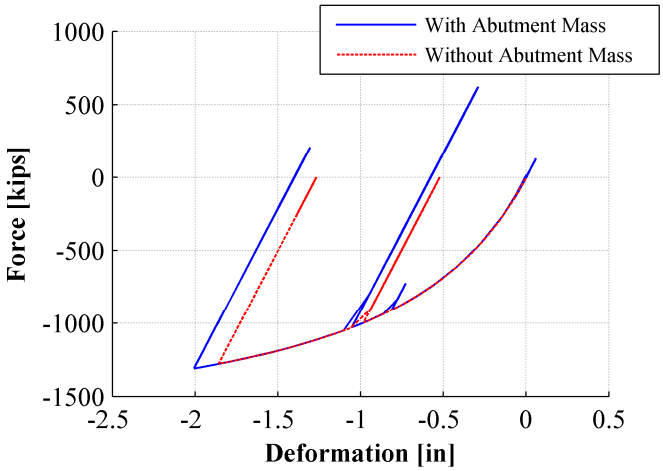

Figure 3.37: Abutment backfill resistance during the earthquake loading

The relative displacement of the abutment support node is presented in Figure 3.38. The displacement towards the abutment is relatively smaller due to the impact between the abutment and bridge deck with due consideration of the earthquake loading asymmetry. Furthermore, the inclusion of the abutment mass in the longitudinal direction does not affect the bridge deck end response much because the impact between the abutment and bridge deck is not frequent during the earthquake loading due to the existence of the abutment gap. The abutment mass effect is expected to be more predominant when a smaller gap for seat-type abutment or the integrated abutment system is used.

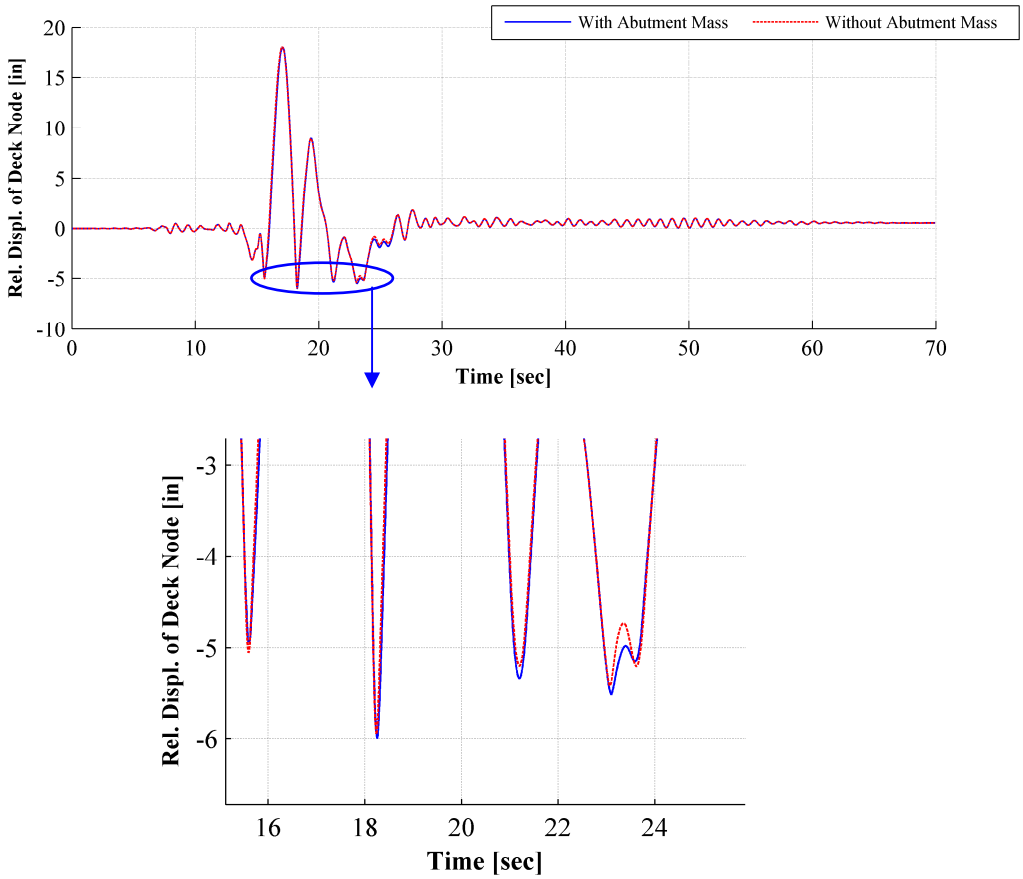

Figure 3.38: Relative displacement of the bridge deck node with/without accounting for the abutment mass in longitudinal direction

3.8. Substructure Analysis of a Single Pier Column Founded on Pile Group Foundation for Static Hysteretic Behavior

The p-y approach is used to investigate the hysteretic behavior of the substructure consisting of a single pier column founded on the pile group foundation by a quasi-static pushover analysis. Capacity analysis based on the model is shown in Figure 3.39, including the section capacity analysis results (moment-curvature relationship) of pier column and pile respectively.

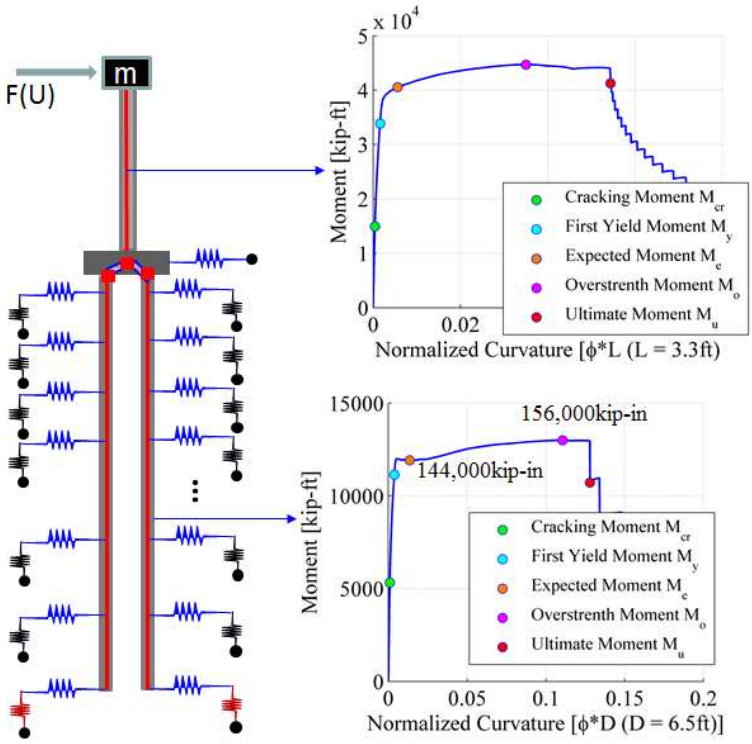

Figure 3.39: Model for single pier column founded on pile group foundation and the moment curvature relationship of the pier column and the pile

Figure 3.40 shows the monotonic pushover curve of the substructure of pier column with flexible pile group foundation and the rigid base case as reference. The inclusion of the flexibility of the pile group reduces the stiffness but the ultimate force capacity is not affected as the force capacity is dominated by the pier column and the pile foundation is capacity-protected component. The limit states corresponding to the onset of concrete cracking, the onset of concrete cover spalling, deep concrete cover spalling, crushing of confined concrete core, first yield of reinforcing steel bar, and the tensile strain of 1% for steel bar are specified based on the bottom section of the pier column. The sources of displacement of the pier column consist of the translation of the pile group foundation, the rotation of the pile group foundation, and the deformation of the pier column itself, as illustrated in Figure 3.41.

Initially, the flexibility of the pile group foundation plays a relatively smaller contribution when the pile column starts to reach its capacity.

The pile response (i.e., pile lateral deformation, pile bending moment, pile shear force) and force deformation relationship for soil springs at different depth are presented in Figure 3.42 and Figure 3.43. Compared to the pile moment capacity curve (see Figure 3.42), the maximum moment demand in piles are still around 30% of the capacity when the pier column reaches its capacity. As noticed in Figure 3.43, more and more soil springs are activated or in plastic stage when the load from pier column increases (i.e., from limit state S_1 to limit state C_4).

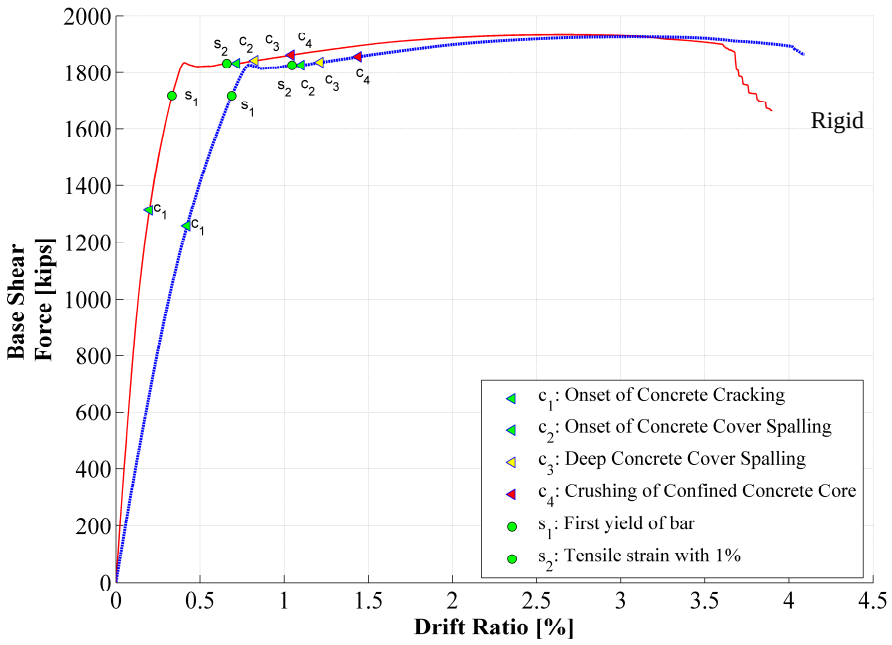

Figure 3.40: Monotonic pushover curve of the single pier column with pile group foundation (in red) compared with rigid base (in blue)

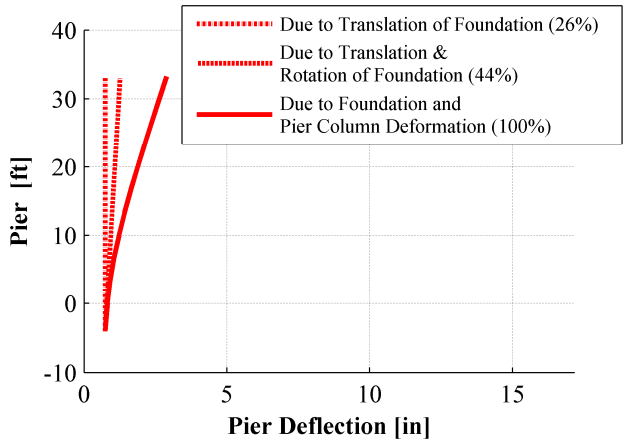

(a)

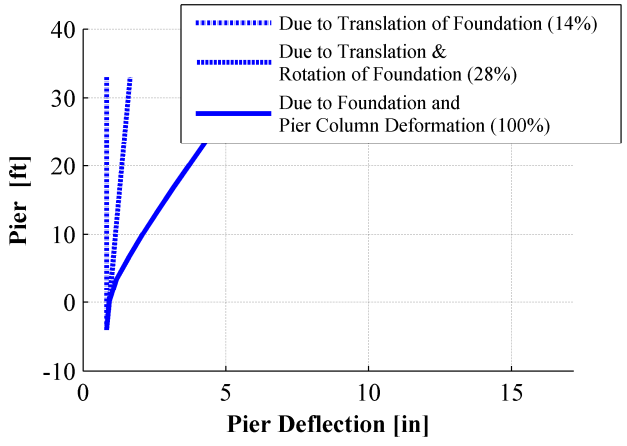

(b)

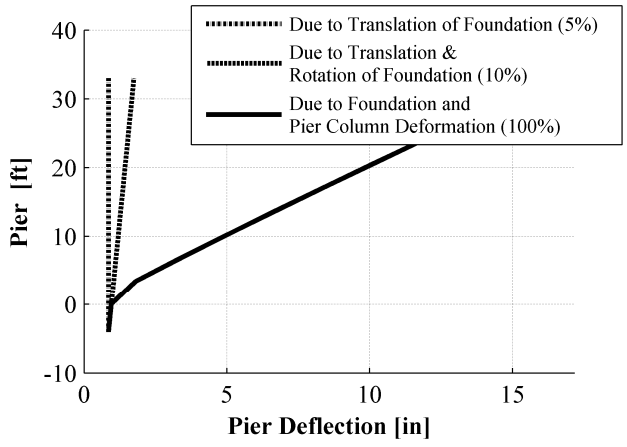

(c)

Figure 3.41: The pier column deformation with contribution decompositions from foundation and column deformation at different time steps: (a)time step at limit state S_1, (b) time step at limit state S_2, and (c) ultimate time step

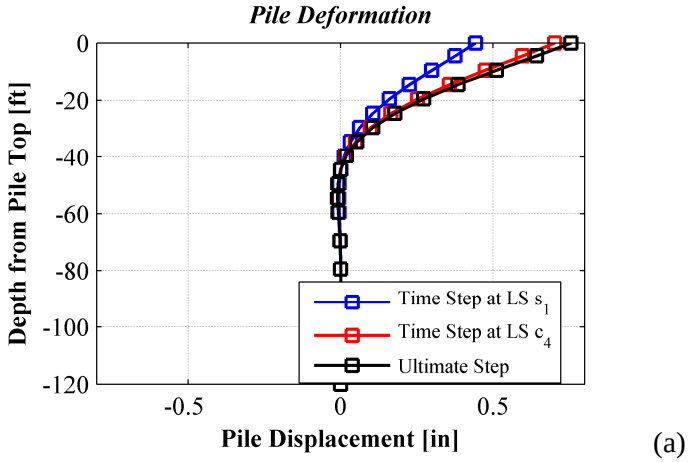

(a)

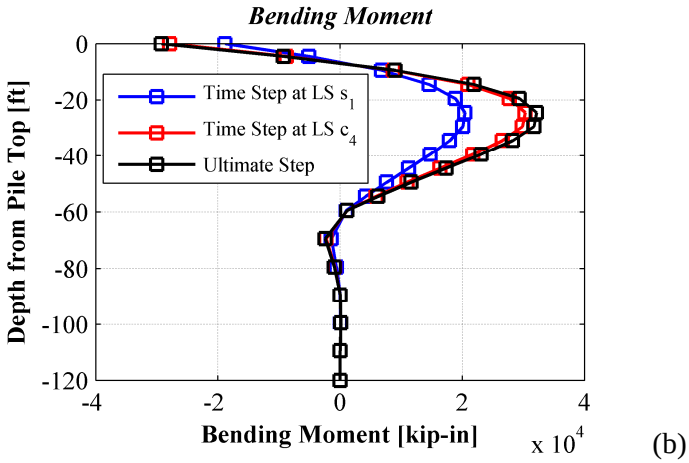

(b)

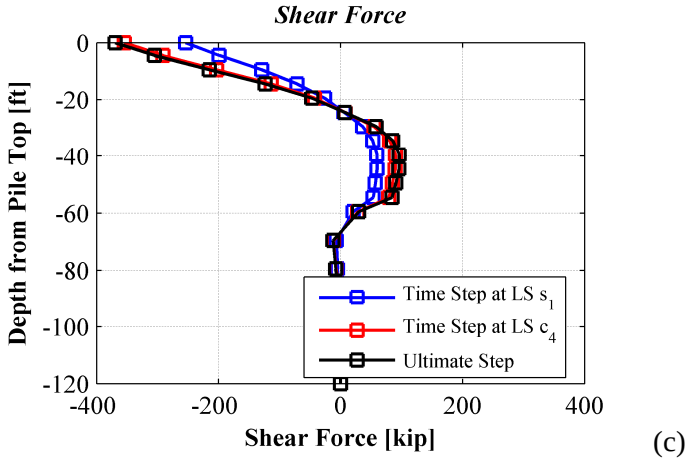

(c)

Figure 3.42: Pile response profile corresponding to different time step during the monotonic pushover analysis: (a) pile deformation, (b) pile bending moment, and (c) pile shear force

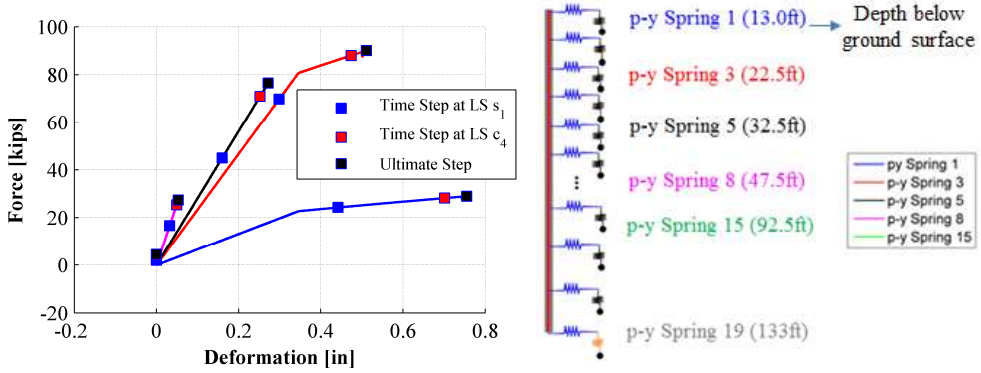

Figure 3.43: Force deformation in soil springs at different depths below the ground surface with markers corresponding to the limit states of the pier column bottom section defined in the monotonic pushover analysis

The cyclic pushover curve of the substructure is shown in Figure 3.44. The corresponding force-deformation relationships of soil springs at different depths are followed in Figure 3.45. The reduction in stiffness of the substructure due to the effect of the flexibility of pile group foundation leads to the tendency of "narrowing" of the hysteretic loops compared to the rigid base model.

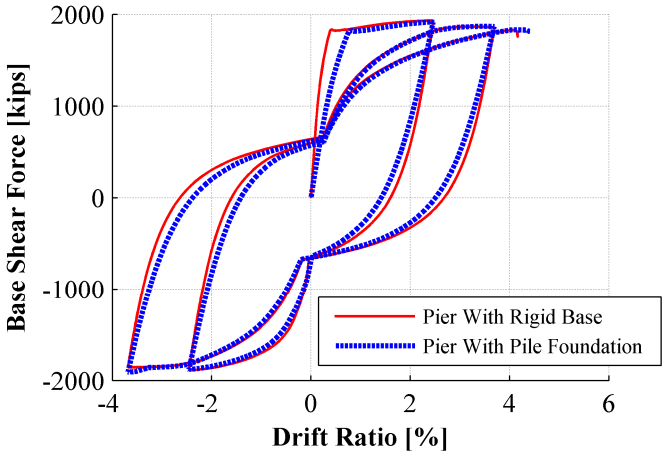

Figure 3.44: Cyclic pushover curve of the single pier column with pile group foundation (solid line) compared with rigid base (dashed line)

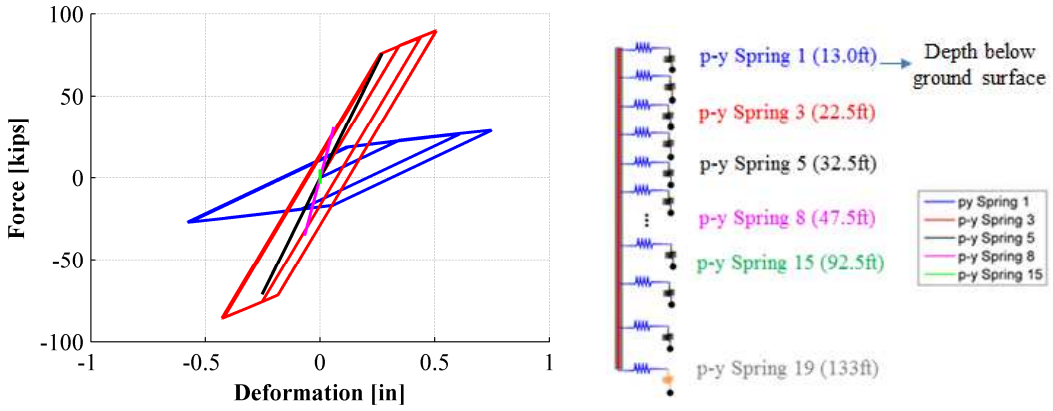

Figure 3.45: Force deformation relationship in soil springs at different depths below the ground surface under cyclic pushover analysis

3.9. Dynamic Analysis to Study Substructure Behavior Focusing on Multiple Support Excitation Considering the Depth-varied Ground Motion

Each pile-foundation-soil system is primarily excited by vertically propagating seismic shear waves (S-waves) from the ground motion records. Therefore, the displacement time series at the far-field ends of p-y springs need to be characterized correspondingly in the dynamic BNWF approach for the seismic simulation. The design motion known as the seismic waves at a specific ("control") point is taken at the ground surface as usual, which are selected and scaled based on the uniform hazard spectrum obtained from site-specific probabilistic seismic hazard analysis. A de-convolution analysis needs to be performed to generate the depth-varied ground motion from the prescribed free-field motion at the ground surface.

Multiple-support-excitation (MSE) has to be adopted for numerical analysis when different displacement loadings need to be prescribed for the supports along the depth of the foundation piles. In view of the possible numerical issues involved as stated in Wilson (1995) on multiple-support-excitation, multiple support displacement loading analysis technique is investigated and verified by the theoretic derivation and convergence study herein. The two

main issues are: (1) the additional damping introduced when mass proportional damping is used in Rayleigh Damping formulation due to the rigid body motion of the structure, and (2) the inaccuracy inherent in displacement loading compared to the "piece-wise linear" acceleration loading applied with cubic displacement implicitly. With reliable numerical analysis techniques verified, the investigation of depth-variation effect in soil-pile-structure interaction is studied.

3.9.1. Free field site response analysis

The location for this CHSR Prototype Bridge under investigation is selected to be in downtown San Jose in California, with a typical soil profile provided by Caltrans, which was consistent with the profile found in Asten (2007) for a site on 12th Street of San Jose in terms of shear wave velocity. The representative soil stratum (Figure 3.46) is comprised of three layers of silt clay overlaid on a stiff clay layer and an underlying layer of sandy gravel. The actual soil profile considered here is slightly idealized in that the layering for soil around all pile groups is assumed to be the same and uniform, with soil properties in each layer depicted in Figure 3.47.

For a site with known layered soil profile and the prescribed surface ground motion, a wave-propagation analysis is necessary to perform the free field site response analysis in order to estimate the ground motion at varied depths along the pile group foundation. Several computer programs are available for the site response analysis (convolution and de-convolution analysis). Examples are programs for linear or equivalent linear analysis in the frequency domain (i.e., Shake91 in a dos version, ProShake with user-friendly interface), and programs for linear or nonlinear analysis using hyperbolic backbone coupled with extended unload-reload Masing rules for soils in the time domain (i.e., DESRA, DMOD, DeepSoil, and TESS). Among them, the computer program, SHAKE91, is commonly used for conducting

equivalent linear seismic response analyses of a semi-infinite horizontally layered soil deposits overlying a uniform half-space subjected to vertically propagating shear waves in the frequency domain. In SHAKE91, the soil profile is idealized as a system of homogeneous, viscous-elastic sub-layers, with the strain-compatible properties obtained through an iterative procedure to account for the nonlinearity of soil in terms of modulus reduction and damping amplification (Idriss et al. 1972). Thus, here the well-established equivalent linear analysis in SHAKE91 is carried out for the de-convolution accounting for the shear modulus reduction and damping increase in multiple layers of soil medium (Figure 3.47) subjected to earthquake ground motions.

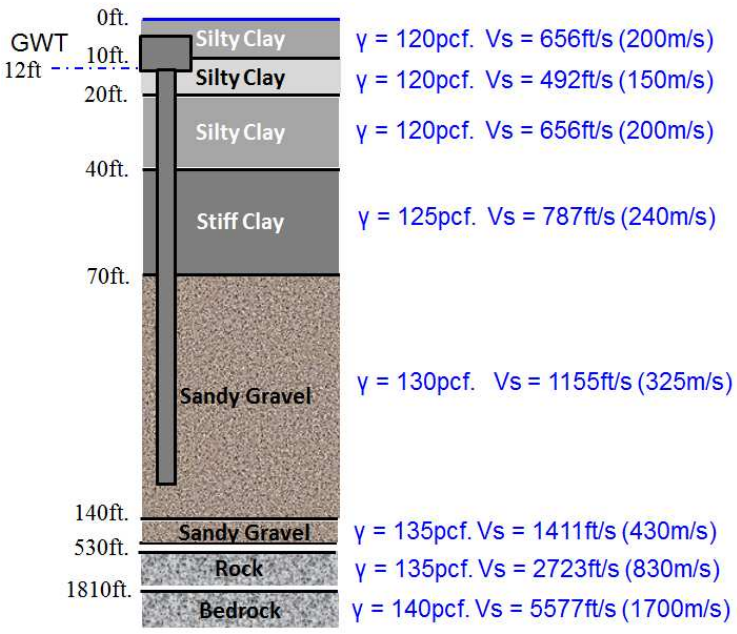

Figure 3.46: Soil profile for the CHSR Prototype Bridge located at San Jose Site

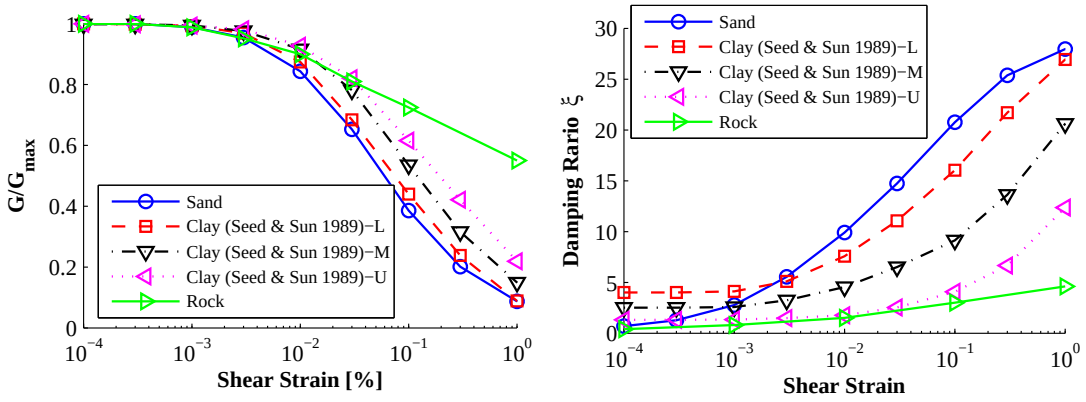

Figure 3.47: Soil shear modulus reduction curve (left) and damping curve (right)

3.9.2. Damping (energy dissipation)

The dynamic computational model, to simulate the vibration of civil structures subjected to dynamic loads such as earthquake ground motions, involves of the excitation loadings, formulation of mass matrix, stiffness matrix or the static resistance due to deformation, and the damping matrix accounting for the energy dissipation property. From the energy point of view, it is associated correspondingly with the energy input to the system domain modeled from outside of the system, the energy taking into the structure in the form of kinematic energy, potential energy and the hysteretic energy dissipations, and the other energy dissipation mechanisms of the explicitly modeled system to the surroundings.

As a crucial ingredient in structural dynamic response simulation, damping is the energy dissipation property in structures. According to the energy dissipation resources or mechanism, damping includes (1) material damping in the materials associated with irreversible transition of mechanical energy to thermal energy, (2) structural damping (assembled structures at their contact surfaces and interfaces), and (3) radiation damping or geometric damping accounting for energy radiation into surrounding medium due to finite domain modeling. In a numerical model for nonlinear structural analysis, the energy

dissipation is commonly accounted in those three aspects respectively. In addition to the hysteretic material energy dissipation considered implicitly in the nonlinear material models, the damping in the structure is commonly modeled approximately as the linear viscous type due to its mathematical convenience and its coincidence to achieve sufficient accuracy, i.e., a proper general structural damping model (i.e., Rayleigh damping).

The commonly used Rayleigh Damping model is formulated as a linear combination of the stiffness matrix and mass matrix with two free parameters to control the damping as shown in Equation (3.4). Two special cases are stiffness proportional only Rayleigh damping and mass proportional only Rayleigh damping.

$$[C] = \alpha[M] + \beta[K] \tag{3.4}$$

For better illustration of the stiffness proportional damping, mass proportional damping, and full Rayleigh damping used for investigation of the multiple support displacement loading, a brief summary about the formulation of Rayleigh damping and some derivatives are presented here.

According to the orthogonal properties of vibration modes for a linear system, the effective modal mass M_n and stiffness matrices K_n defined in terms of the n-th mode shape vector $\{\varphi\}_n$ are

$$M_n = \{\varphi\}_n^T [M] \{\varphi\}_n, \; K_n = \{\varphi\}_n^T [K] \{\varphi\}_n \tag{3.5}$$

We can express the n-th effective modal damping matrix C_n as follows

$$C_n = \{\varphi\}_n^T [C] \{\varphi\}_n = \alpha M_n + \beta K_n \tag{3.6}$$

By rewriting C_n in terms of effective damping ratio ζ_n

$$C_n = 2\zeta_n \omega_n M_n \tag{3.7}$$

where the effective damping ratio ζ_n for nth mode is

$$\zeta_n = \frac{\alpha}{2\omega_n} + \frac{\beta\omega_n}{2} \tag{3.8}$$

In which ω_n is the circular frequency for nth mode as below

$$\omega_n^2 = K_n / M_n \tag{3.9}$$

Usually, since the above assumption about the Rayleigh damping only involves two free parameters, it is natural to specify the damping ratios at two frequencies to determine these two parameters α and β, forming a linear system of two equations to solve for these two parameters. The calibration of the damping model refers to choosing the two parameters so that specific amounts of modal damping are achieved. The regular way to construct Rayleigh damping for a conventional structural system is as follows

$$\frac{1}{2}\begin{bmatrix} 1/\omega_i & \omega_i \\ 1/\omega_j & \omega_j \end{bmatrix}\begin{Bmatrix} \alpha \\ \beta \end{Bmatrix} = \begin{Bmatrix} \zeta_i \\ \zeta_j \end{Bmatrix} \tag{3.10}$$

And the two parameters can be solved as:

$$\begin{Bmatrix} \alpha \\ \beta \end{Bmatrix} = \frac{2\omega_i\omega_j}{\omega_j^2 - \omega_i^2}\begin{bmatrix} \omega_j & -\omega_i \\ -\dfrac{1}{\omega_j} & \dfrac{1}{\omega_i} \end{bmatrix}\begin{Bmatrix} \zeta_i \\ \zeta_j \end{Bmatrix} \tag{3.11}$$

If the same damping ratio ζ is prescribed at two frequencies, Equation (3.11) is reduced to

$$\begin{Bmatrix} \alpha \\ \beta \end{Bmatrix} = \frac{2\zeta}{\omega_i + \omega_j}\begin{Bmatrix} \omega_i\omega_j \\ 1 \end{Bmatrix} \tag{3.12}$$

With the determination of two parameters, i.e., the mass coeffecient and the stiffness coeffecient, the damping matrix can be formulated as follows

$$[C] = [C_M] + [C_K] = \alpha[M] + \beta[K] \tag{3.13}$$

The damping ratio as a function of frequencies is shown in Equation (3.14), which implies higher damping ratio assigned outside the frequency range $\left[\omega_i,\ \omega_j\right]$

$$\zeta(\omega) = \zeta_M + \zeta_K = \frac{\alpha}{2\omega} + \frac{\beta}{2}\omega = \frac{2\omega_i\omega_j}{\omega_j^2 - \omega_i^2}\left(\frac{1}{2\omega}\left(\omega_j - \omega_i\right) + \frac{\omega}{2}\left(-\frac{1}{\omega_j} + \frac{1}{\omega_i}\right)\right)\zeta \tag{3.14}$$

From the mathematical points of veiw, to solve for the two free parameters, there some special derivatives/extentions to regular application of Rayleigh damping, i.e., (i) under-determined Rayleigh damping model and (ii) over-determined Rayleigh damping model. In case (i), damping ratio only specified at one frequency, leading to an under-determined linear equation system with infinite number of solutions for the two free parameters. In case (ii), damping ratios are specified at more than two frequencies, leading to a over-determined linear equation system with no solution in the exact sense, but least square solution can be obtained from the pseduo-inverse problem.

For the under-determined Rayleigh damping in case (i), the governing equation is

$$\zeta_n = \frac{\alpha}{2\omega_n} + \frac{\beta\omega_n}{2} \tag{3.15}$$

There are infinit number of solutions to Equation (3.15) for α and β, i.e., application of Rayleigh damping to a numerical model of single-degree-freedom (SDOF) system, as shown in Equation (3.16) and Equation (3.17). Only one damping ratio at fundamental mode is prescribed to solve for the two parameters in Equation(3.17), and infinite number of solutions exist for the under-determined system. The Rayleigh damping model is proved to work on condition that Equation (3.15) is satisfied.

$$\begin{aligned} &m\ddot{u}(t) + c\dot{u}(t) + ku(t) = 0 \\ &i.e.,\ \ddot{u}(t) + 2\zeta\omega\dot{u}(t) + \omega^2 u(t) = 0 \end{aligned} \tag{3.16}$$

$$\begin{aligned} c &= \alpha m + \beta k \\ &= m\alpha + \beta\omega^2 m \\ &= 2m\omega\left(\frac{\alpha}{2\omega} + \frac{\beta}{2}\right) \\ &= 2m\omega\zeta \end{aligned} \tag{3.17}$$

where m, c, and k defines the mass, damping, and stiffness of a linear SDOF system; $u(t)$, $\dot{u}(t)$, and $\ddot{u}(t)$ are the relative displacement, velocity, and acceleration of the linear SDOF system.

For over-determined Rayleigh damping in case (ii),

$$\begin{pmatrix} \zeta_1 \\ \zeta_2 \\ \dots \\ \zeta_n \end{pmatrix} = \begin{pmatrix} \frac{1}{2\omega_1} & \frac{\omega_1}{2} \\ \frac{1}{2\omega_2} & \frac{\omega_2}{2} \\ \dots & \\ \frac{1}{2\omega_n} & \frac{\omega_n}{2} \end{pmatrix} \begin{pmatrix} \alpha \\ \beta \end{pmatrix} = W \begin{pmatrix} \alpha \\ \beta \end{pmatrix} \tag{3.18}$$

And two coefficients can be solved as

$$\begin{pmatrix} \alpha \\ \beta \end{pmatrix} = \left(W^T W\right)^{-1} W^T \begin{pmatrix} \zeta_1 \\ \zeta_2 \\ \dots \\ \zeta_n \end{pmatrix} \tag{3.19}$$

Constant damping ratio is preferred for all modes of interests, being consistent with the observations made from field data, which indicates modal damping ratios for modes of interest are fairly constant for a given structure. The above over-determined Rayleigh damping model tends to approach close damping ratio to the selected modes of interest as much as possible. Spurred by this same motivation, a convenient procedure is also proposed by John (2005) aiming at achieving a near-constant value of damping for all modes whose frequencies fall in the range from ω_i to ω_j.

Instead of using both the stiffness and mass proportional Rayleigh damping (i.e., full Rayleigh damping model), there are another two derivatives of Rayleigh damping, i.e., stiffness proportional Rayleigh damping shown in Equation (3.20), and mass proportional Rayleigh damping shown in Equation (3.21).

$$[C] = [C_K] = \beta [K],\ \beta = \frac{2\zeta_n}{\omega_n} \tag{3.20}$$

$$[C] = [C_M] = \alpha [M],\ \alpha = 2\zeta_n \omega_n \tag{3.21}$$

The derived formulations for Rayleigh damping model, as well as the extension such as mass proportional Rayleigh damping, and stiffness proportional Rayleigh damping are considered for the theoretical study and numerical investigation of multiple-support-excitation (displacement loading).

Regarding to the damping formulation in CHSR prototype bridge, Rayleigh damping is applied to the superstructure and substructure system except the isolation system in between. To properly account for the energy dissipation of an isolated bridge structure, the system damping matrix will be assembled from the independently constructed damping matrices of superstructure and substructure system as recommended by Chopra (2007). This is because the energy dissipation associated in the isolator units is already explicitly modeled in terms of the hysteretic energy dissipation (Hall, 2005). For the CHSR prototype bridge model with foundation modeled using the dynamic p-y approach, appropriate energy-absorbing foundation materials/elements are utilized as illustrated in the foundation modeling.

3.9.3. Earthquake loading (energy input)

The earthquake loading (energy input) can be applied (1) as equivalent inertial force when uniform ground acceleration imposed, or (2) using the artificial big mass method via applying equivalent force at the supporting nodes as a convenient way accommodated by many commercial computer programs, and (3) the displacement loading method at the

supporting nodes in the way like foundation settlement. For these three formulations, the first approach can only be implemented for uniform excitation and all the response is calculated with respect to a reference frame moving together with the ground, referred to as uniform excitation. Herein, the first and third approach is investigated and compared for dynamic response simulation under earthquake loading.

Uniform excitation formulation, which assumes all the supports have identical excitation prescribed, is based on the relative-displacement formulation in that the effective earthquake loading is applied in terms of equivalent “inertial” forces proportional to the spatial distribution of mass and relative displacement (velocity and acceleration) response with respect to supports is computed. It has been widely implemented and used in many software packages and it works very well to solve certain appropriate problems.

On the other side, multiple-support-excitation (MSE), which prescribes possibly uneven absolute displacement loading at the supports, arises for several situations. They include, but not limited to, seismic response analysis considering the earthquake spatial variation for large span structures like long bridges or pipe line systems due to horizontal wave propagation and local site conditions, dynamic response simulation considering vertical variation for deep foundations due to vertical wave propagation, hybrid simulation and substructure approaches. In this CHSR Prototype Bridge study, depth-varied ground displacement will be prescribed and multiple supports excitation will be used for dynamic analysis.

Under uniform excitation loading, the Rayleigh damping matrix formulated is considered to be rational because it damps the vibration of the structure relative to its base motion. While in the case of MSE formulation, the appropriateness of the Rayleigh damping matrix formulation needs to be verified before depth-variation along the piles is included for

the SFSI analysis for the CHSR Prototype Bridge. Theoretical study on linear or nonlinear dynamic system is performed to gain more insight into the damping problem in the formulation of multiple supports displacement loading first.

The mathematical formulation of the multi-support excitation on a linear dynamic system is

$$\begin{pmatrix} M_{ss} & M_{sb} \\ M_{bs} & M_{bb} \end{pmatrix} \begin{pmatrix} \ddot{U}_s^{\,t} \\ \ddot{U}_b \end{pmatrix} + \begin{pmatrix} C_{ss} & C_{sb} \\ C_{bs} & C_{bb} \end{pmatrix} \begin{pmatrix} \dot{U}_s^{\,t} \\ \dot{U}_b \end{pmatrix} + \begin{pmatrix} K_{ss} & K_{sb} \\ K_{bs} & K_{bb} \end{pmatrix} \begin{pmatrix} U_s^{\,t} \\ U_b \end{pmatrix} = \begin{pmatrix} 0 \\ F_b \end{pmatrix} \tag{3.22}$$

in which,

$\ddot{U}_s^{\,t}$: total acceleration of DOFs of the structure (non-support) nodes

$\dot{U}_s^{\,t}$: total velocity of DOFs of the structure (non-support) nodes

$U_s^{\,t}$: total velocity of DOFs of the structure (non-support) nodes

$\ddot{U}_b^{\,t}$: total acceleration of DOFs of the support nodes

$\dot{U}_b^{\,t}$: total velocity of DOFs of the support nodes

$U_b^{\,t}$: total velocity of DOFs of the support nodes

F_b : reaction force required to prescribe the displace loading

$\begin{pmatrix} M_{ss} & M_{sb} \\ M_{bs} & M_{bb} \end{pmatrix}$: mass matrix of the system

$\begin{pmatrix} C_{ss} & C_{sb} \\ C_{bs} & C_{bb} \end{pmatrix}$: damping matrix formulated for the dynamic system

$\begin{pmatrix} K_{ss} & K_{sb} \\ K_{bs} & K_{bb} \end{pmatrix}$: stiffness matrix for the linear dynamic system

For the well-defined problem above, the associated force F_b at the base supports associated with the prescribed displacement are unknown, but can be solved after unknown

total superstructure displacement U_s^t is obtained. And then the problem above is solved in the following way completely.

$$\begin{aligned} M_{ss}\ddot{U}_s^t + C_{ss}\dot{U}_s^t + K_{ss}U_s^t &= -M_{sb}\ddot{U}_b - C_{sb}\dot{U}_b - K_{sb}U_b \\ F_b &= M_{bb}\ddot{U}_b + C_{bb}\dot{U}_b + K_{bb}U_b + M_{bs}\ddot{U}_s^t + C_{bs}\dot{U}_s^t + K_{bs}U_s^t \end{aligned} \tag{3.23}$$

If lumped mass is considered as the usual case, the coupling terms in the mass matrix are zero matrices, $M_{sb} = 0$, then the first equation above is reduced to:

$$M_{ss}\ddot{U}_s^t + C_{ss}\dot{U}_s^t + K_{ss}U_s^t = -C_{sb}\dot{U}_b - K_{sb}U_b \tag{3.24}$$

In order to verify the above absolute displacement formulation in multiple-support-excitation, a benchmark problem is defined to be the trivial case when all the supports have the identical displacement movement. It is desired to achieve the same solution based on multiple-support-excitation and uniform excitation.

The universally acknowledged uniform excitation formulation is defined in terms of relative displacement as below

$$M_{ss}\ddot{U}_s^t + C_{ss}\dot{U}_s + K_{ss}U_s = 0 \tag{3.25}$$

in which

$\ddot{U}_s^t$: total acceleration of DOFs of the structure nodes

$\dot{U}_s$: the relative velocity of DOFs of the structure nodes with respect to the supports

U_s: the total velocity of DOFs of the structure nodes

Introducing the following Equation (3.26), into Equation (3.24)

$$\ddot{U}_s^t = \ddot{U}_s + L_s\ddot{U}_g,\ \ddot{U}_g = \left[\ddot{u}_{gx}\ \ddot{u}_{gy}\ \ddot{u}_{gz}\right]^T \tag{3.26}$$

in which L_s is the influence matrix, Equation (3.26) is reduced to

$$M_{ss}\ddot{U}_s + C_{ss}\dot{U}_s + K_{ss}U_s = -M_{ss}L_s\ddot{U}_g \tag{3.27}$$

For the benchmark problem, identical excitation is prescribed for all supports in each direction for multiple-support-excitation,

$$\ddot{U}_b = L_b \ddot{U}_g, \quad \ddot{U}_s^{\,t} = \ddot{U}_s + L_s \ddot{U}_g \tag{3.28}$$

Substitute Equation (3.28) into Equation (3.27), the following identity is desired,

$$\begin{aligned} &M_{ss}\left(\ddot{U}_s + L_s\ddot{U}_g\right) + C_{ss}\left(\dot{U}_s + L_s\dot{U}_g\right) + K_{ss}\left(U_s + L_s U_g\right) \\ &= -M_{sb}L_b\ddot{U}_g - C_{sb}L_b\dot{U}_g - K_{sb}L_b U_g \end{aligned} \tag{3.29}$$

Furthermore, the above equation leads to

$$\begin{aligned} M_{ss}\ddot{U}_s + C_{ss}\dot{U}_s + K_{ss}U_s = &-M_{ss}L_s\ddot{U}_g - M_{sb}L_b\ddot{U}_g \\ &-\left(C_{ss}L_s + C_{sb}L_b\right)\dot{U}_g - \left(K_{ss}L_s + K_{sb}L_b\right)U_g \end{aligned} \tag{3.30}$$

Realizing that

$$\left(K_{ss}L_s + K_{sb}L_b\right) = \begin{bmatrix} K_{ss} & K_{sb} \end{bmatrix}\begin{bmatrix} L_s \\ L_b \end{bmatrix} = 0 \tag{3.31}$$

Equation (3.30) is reduced to

$$M_{ss}\ddot{U}_s + C_{ss}\dot{U}_s + K_{ss}U_s = -M_{ss}L_s\ddot{U}_g - M_{sb}L_b\ddot{U}_g - \left(C_{ss}L_s + C_{sb}L_b\right)\dot{U}_g \tag{3.32}$$

Comparing Equation (3.32) and Equation and then enforcing these two systems with equivalence, Equation (3.27) is obtained as the sufficient and necessary condition to get consistent results for this benchmark problem using these two approaches, i.e., using uniform acceleration excitation and multiple support displacement loading.

$$-M_{sb}L_b\ddot{U}_g - \left(C_{ss}L_s + C_{sb}L_b\right)\dot{U}_g = 0 \tag{3.33}$$

After introducing the assumption that cross mass terms between supports' degree-of-freedoms and the structures' degree-of-freedoms is zero, which is not uncommon, the necessary and sufficient condition for consistency of Equation (3.33), then becomes

$$-\left(C_{ss}L_s + C_{sb}L_b\right)\dot{U}_g = 0 \tag{3.34}$$

When classical Rayleigh damping matrix is employed for both systems formulated in the uniform acceleration excitation loading and multiple support displacement loading respectively, more insight can be obtained related to the mass proportional part and stiffness proportional part of Rayleigh damping formulation demonstrated in Equation (3.35).

$$\begin{aligned} &\left(\left(\alpha M_{ss}+\beta K_{ss}\right)L_s+\left(\alpha M_{sb}+\beta K_{sb}\right)L_b\right)\dot{U}_g=0 \\ &\Leftrightarrow\left(\alpha\left(M_{ss}L_s+M_{sb}L_b\right)+\beta\left(K_{ss}L_s+K_{sb}L_b\right)\right)\dot{U}_g=0 \\ &\Leftrightarrow\alpha\left(M_{ss}L_s+M_{sb}L_b\right)\dot{U}_g=0 \end{aligned} \tag{3.35}$$

It is shown that the mass proportional damping part violates the necessary and sufficient condition derived previously, while the stiffness proportional damping part obeys the consistent rule automatically. This problematic issue in mass proportional damping part in multiple-support-excitation is enhanced from the physical interpretation as illustrated in Figure 3.48. The coefficients in the stiffness proportional damping coefficients represent a set of linear viscous dampers that interconnect the degrees of freedom in an arrangement parallel to the structural stiffness. The diagonal entries of mass-proportional damping represent a set of linear viscous dashpots that connect each degree of freedom to the moving support for uniform excitation, and to the fixed reference system for multiple-support-excitation. Consequently, the Rayleigh damping formulation for multiple support displacement loading in terms of the total velocity is problematic and non-physical. This is because when the structure moves rigidly with respect to the fixed reference system, damping forces are generated in the structure, due to the total velocity of the structure nodes accounting for the support velocity (i.e., the relative velocity with respect the fixed reference frame).

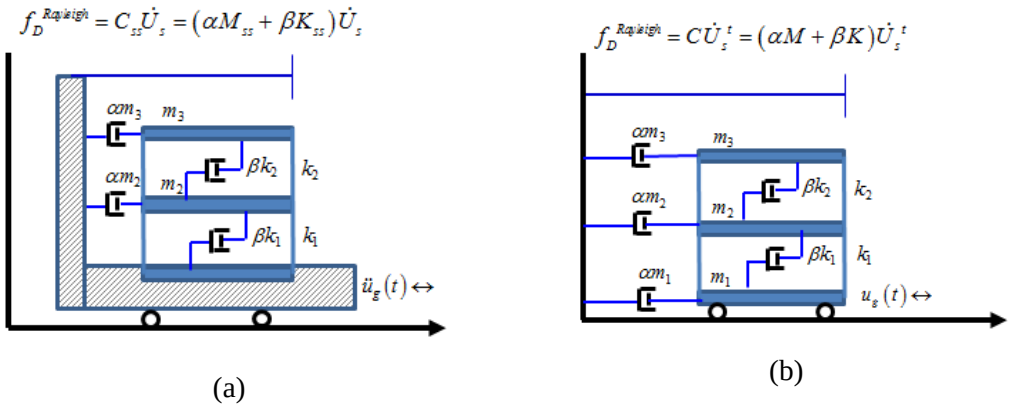

(a) (b)

Figure 3.48: Physical interpretation for Rayleigh Damping in uniform acceleration loading formulation (a) and multiple support displacement loading formulation (b)

Regarding to the nonlinear dynamic system with governing equation in Equation (3.36), similar flow of reasoning can be presented.

$$\begin{pmatrix} M_{ss} & M_{sb} \\ M_{bs} & M_{bb} \end{pmatrix}\begin{pmatrix} \ddot{U}_s^t \\ \ddot{U}_b \end{pmatrix} + \begin{pmatrix} C_{ss} & C_{sb} \\ C_{bs} & C_{bb} \end{pmatrix}\begin{pmatrix} \dot{U}_s^t \\ \dot{U}_b \end{pmatrix} + \begin{pmatrix} R_s\left(U_s^t, U_b\right) \\ R_b\left(U_s^t, U_b\right) \end{pmatrix} = \begin{pmatrix} 0 \\ F_b \end{pmatrix} \tag{3.36}$$

Thus the first equation of can be rearranged as below,

$$M_{ss}\ddot{U}_s + C_{ss}\dot{U}_s + R_s\left(U_s^t, U_b\right) = -M_{ss}L_s\ddot{U}_g - M_{sb}L_b\ddot{U}_g - \left(C_{ss}L_s + C_{sb}L_b\right)\dot{U}_g \tag{3.37}$$

Compared to the governing equation of nonlinear dynamic system in Equation (3.38) for the formulation of uniform acceleration loading,

$$M_{ss}\ddot{U}_s + C_{ss}\dot{U}_s + R_s\left(U_s\right) = -M_{ss}L_s\ddot{U}_g \tag{3.38}$$

and realizing that the static resorting force satisfies the following identity in Equation (3.39)

$$R_s\left(U_s^t, U_b\right) = R_s\left(U_s\right) \tag{3.39}$$

the same necessary and sufficient condition as stated in Equations (3.33), (3.34), and (3.35) is attained for application of multiple-support-excitation to nonlinear dynamic system. The two

formulations will arrive at the same solution for the benchmark problem if and only if this condition is guaranteed.

Based on the theoretical derivation above, it is reasonable to expect the stiffness proportional Rayleigh damping (*i.e.*, $\beta = 0$) is going to achieve consistent results for uniform acceleration loading and multiple support displacement loading with identical excitation, while not for mass proportional damping or complete Rayleigh damping (i.e., based on both the stiffness and mass proportional parts). This is verified through numerical investigation using a single-degree-of-freedom (SDOF) system and a substructure of a single pier column founded pile group foundation. Based on further investigation of damping issues and multiple-support-excitation for the CHSR Prototype Bridge, appropriate simulation technique will be selected as a comprise for the inherent issues in Rayleigh damping model when multiple-support-excitation is required in this research.

3.9.4. Verification of multiple-support-excitation (displacement loading) for SDOF system and substructures

To reveal the drawback of full Rayleigh damping model with multiple-support-excitation formulation as discovered in previous section through theoretical study, a linear elastic SDOF system is used first to compute the elastic displacement spectra of Earthquake NGA#180 (Imperial Valley-06, California, 1979) using uniform acceleration loading and multiple support displacement loading. The mass proportional or stiffness proportional Rayleigh damping with the same damping ratio (5%) can be applied based on the fundamental period as explained before. As observed in Figure 3.49, when stiffness proportional Rayleigh damping is used, the displacement spectra obtained from these two formulations are exactly the same. By contrast, when mass proportional Rayleigh damping is used, the discrepancy exists for the two formulations of earthquake loading, as shown in Figure 3.50.

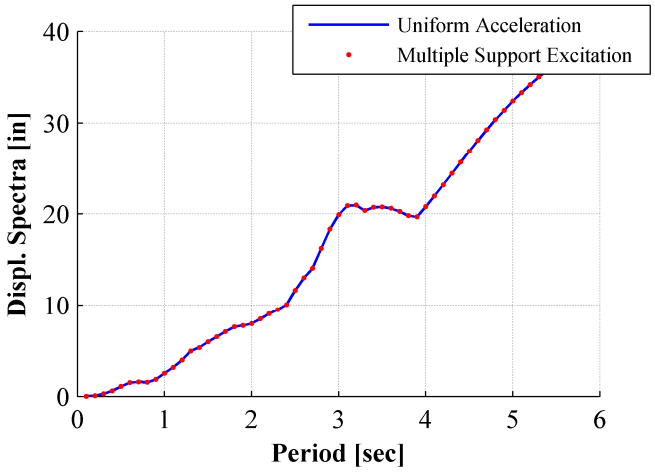

Figure 3.49: SDOF system with stiffness proportional damping

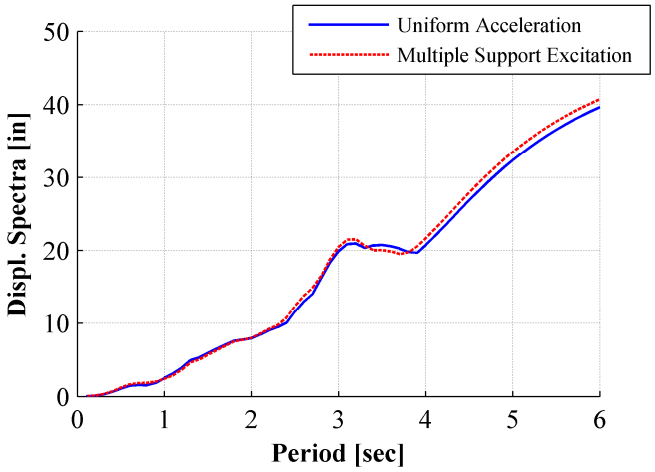

Figure 3.50: SDOF system with mass proportional damping

After the above illustration with a SDOF system, a similar investigation is carried out further based on a complex model with more excitation supports. The seismic response of substructure of a single pier column founded on pile group foundation subjected to Earthquake NGA1505 (Chi-Chi, Taiwan 1999) is simulated using both the uniform acceleration loading (see Figure 3.51a) and the multiple support displacement loading (see Figure 3.51b).

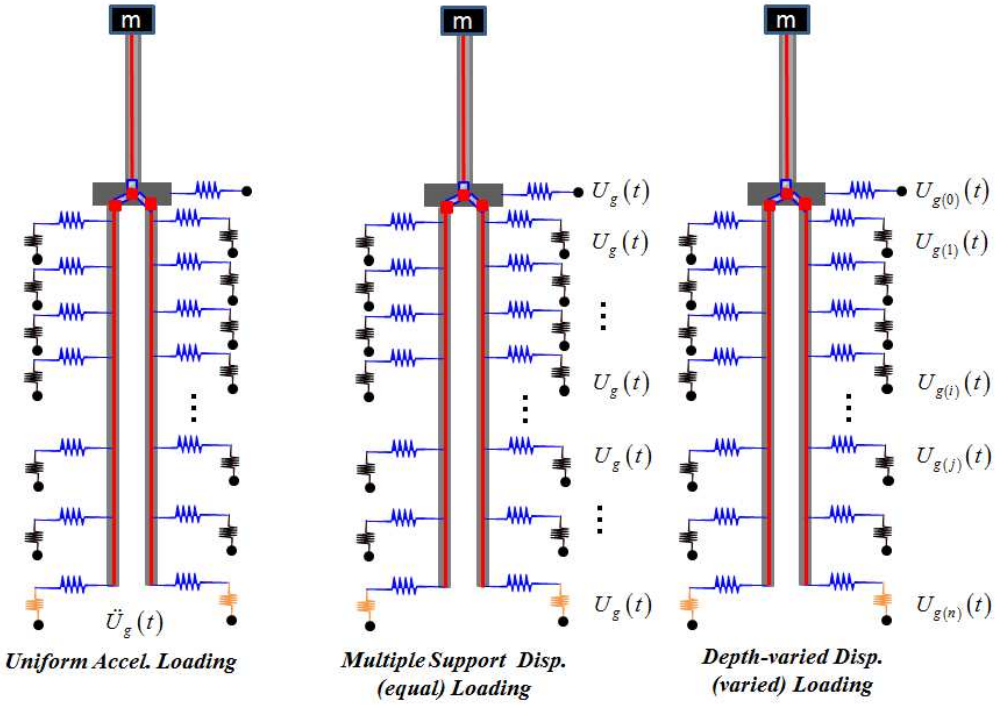

(a) (b) (c)

Figure 3.51: Substructure models of the single pier column founded on pile group foundation modeled using dynamic p-y approach

In the case shown in Figure 3.51b, the far-ends of soil springs are prescribed with identical ground displacement time series. Apart from the verification for inconsistence of multiple supports displacement loading with uniform excitation loading, more insights are observed regarding to the inaccuracy of multiple supports displacement loading compared to acceleration loading. Furthermore, the soil-foundation-structure effects (i.e., the depth-variation ground motion input) is exposed by comparative study between identical displacement loading (in the case of Figure 3.51b) and depth-varied displacement loading (in the case of Figure 3.51c) using multiple-support-excitation, as well as the case of rigid foundation.

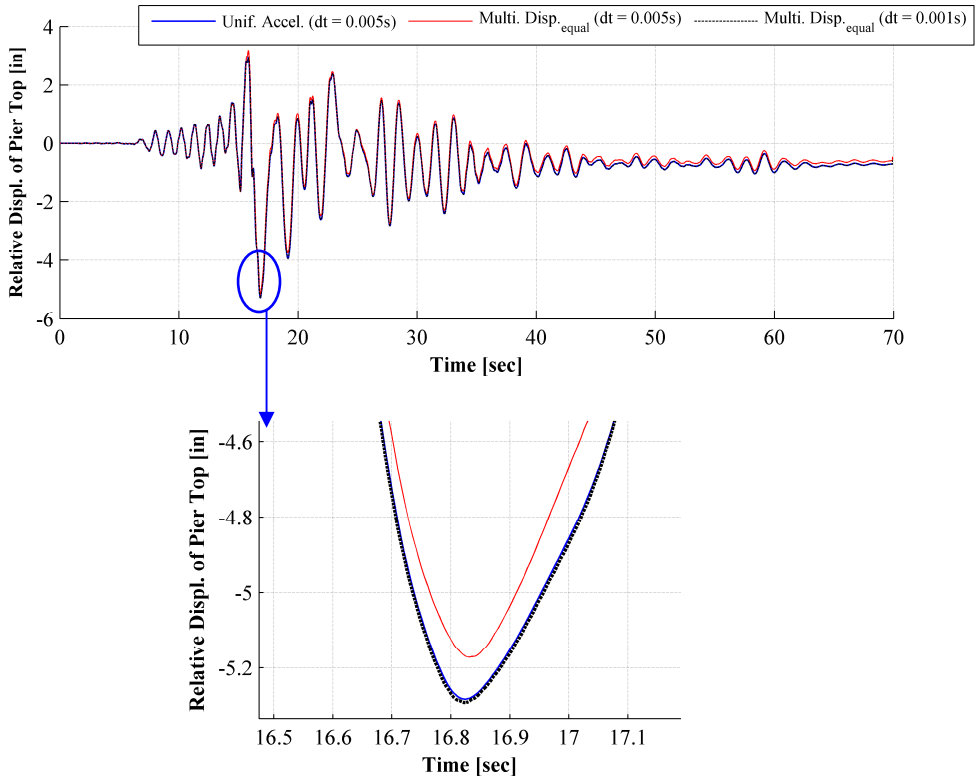

Figure 3.52: Convergence study of time step on substructure system with stiffness proportional damping (2%)

Aiming at investigating the inaccuracy of multiple supports displacement loading compared to acceleration loading, Figure 3.52 presents the comparison with the uniform acceleration loading with analysis time step 0.005sec, the multiple supports displacement loading (identical for all supports) with analysis time step 0.005sec and 0.001sec respectively. Since 2% stiffness proportional Rayleigh damping is applied to the first mode for the substructure, it is expected to achieve the same result for the uniform acceleration loading and the multiple-support displacement loading (identical for all supports), as proved theoretically, illustrated using the SDOF system, and further verified in the substructure system and the CHSR prototype bridge system later. While for the multiple-support displacement loading formulation, a much smaller time step (0.001sec) is required to achieve the same accuracy as

the uniform acceleration loading formulation with time step (0.005sec) as shown in Figure 3.52.

Consequently, time step of 0.001sec is used later on for multiple support displacement loading and time step 0.005sec is used for the uniform acceleration loading analysis of the substructure in order to eliminate the possible inaccuracy.

Figure 3.53, Figure 3.54, and Figure 3.55 present the analysis results of the models with stiffness proportional Rayleigh damping, with mass proportional Rayleigh damping, and with both stiffness and mass proportional Rayleigh damping respectively.

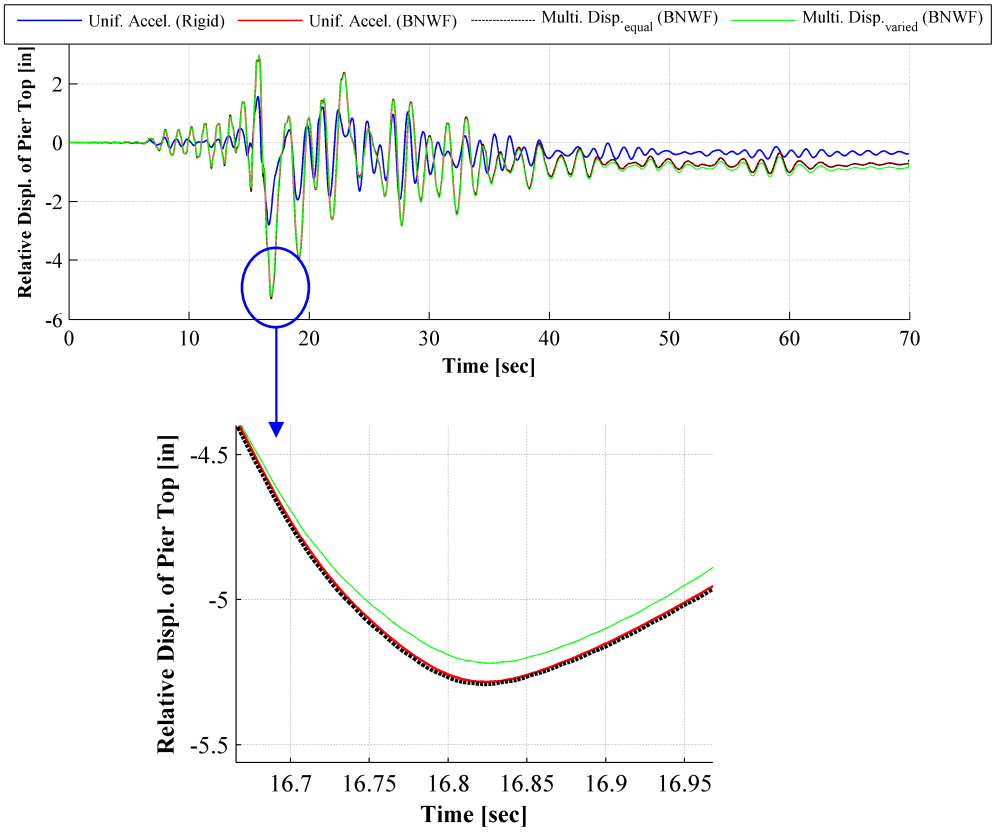

Figure 3.53: Convergence study on the consistence of multiple supports excitation loading with uniform acceleration loading on substructure system with stiffness proportional damping (2%)

As revealed in Figure 3.53, when the stiffness proportional Rayleigh damping is imposed, the multiple-support displacement loading with identical displacement arrives at the same results as the uniform acceleration loading, i.e., the two formulations are consistent (see Figure 3.53). As concluded before, this consistency is violated if mass proportional Rayleigh damping is included, (see Figure 3.54 and Figure 3.55).

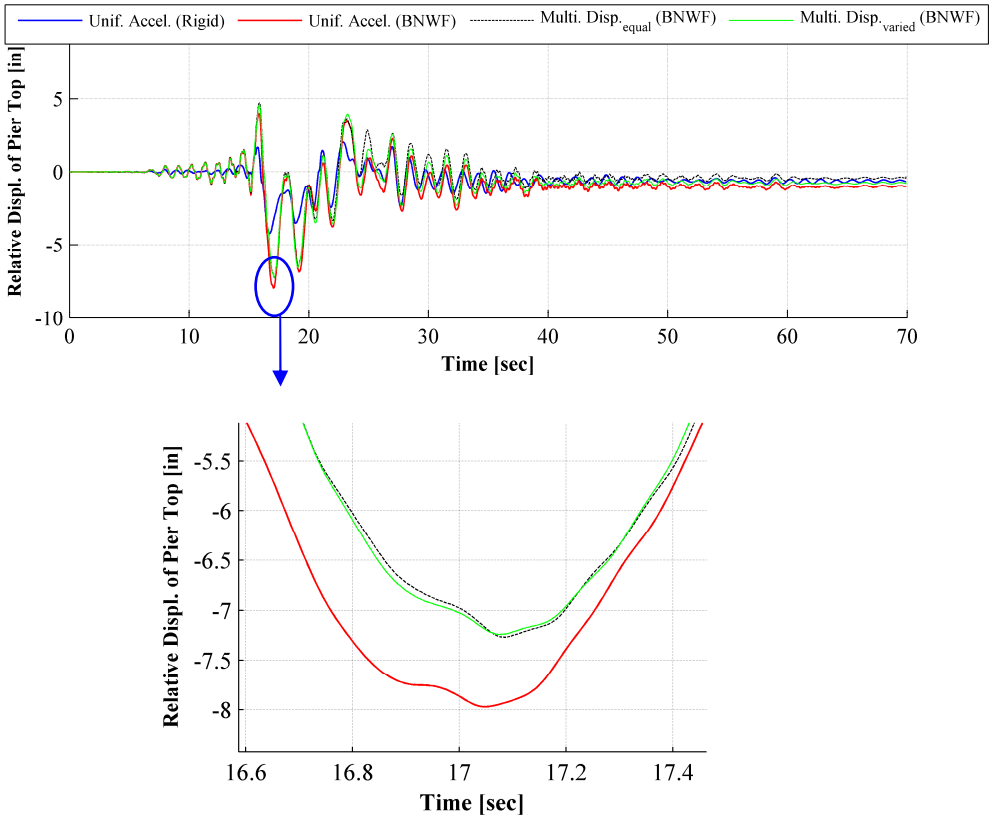

Figure 3.54: Convergence study on the consistence of MSE loading with uniform acceleration loading on substructure system with mass proportional damping (2%)

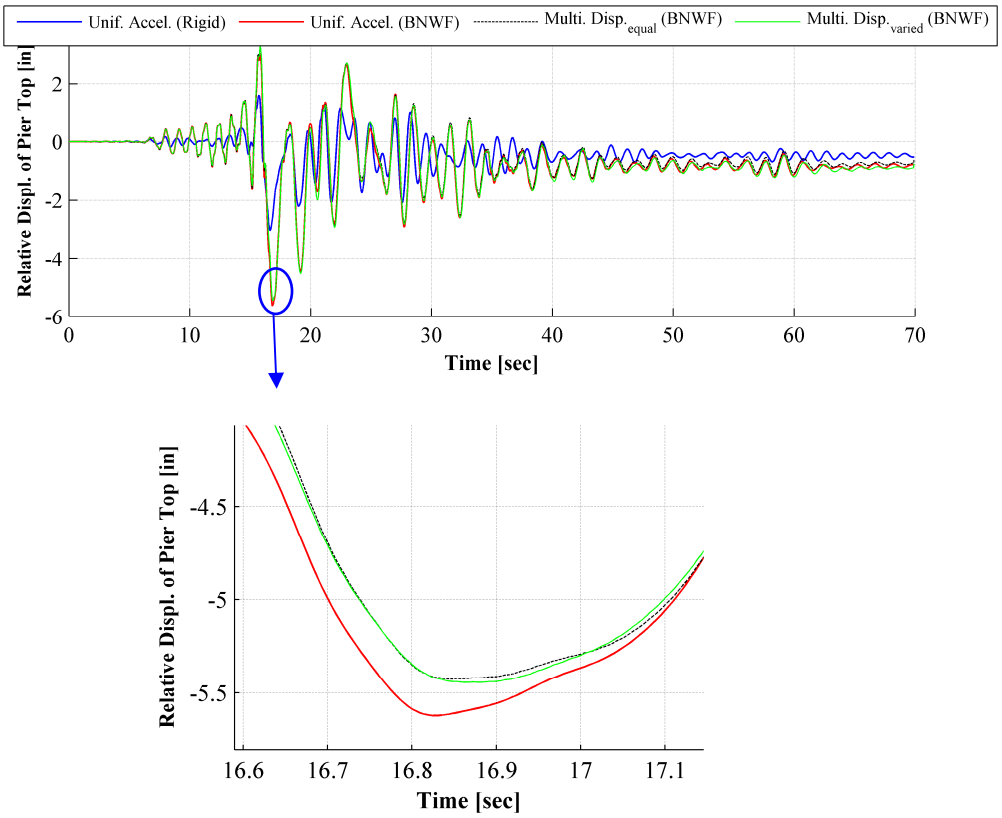

Figure 3.55: Convergence study on the consistence of MSE loading with uniform acceleration loading on substructure system with mass proportional damping (2%)

Based on the comparison among the rigid based single pier column model, the substructure of pile group founded single pier column neglecting the depth-variation of the ground motion, and the substructure accounting for the depth-variation of the ground motion, it is obvious that it is essential to account for the flexibility of the foundation, as the inertial effects in SFSI is significant here. In contrast, the depth-variation of the ground displacement does not play as a significant role as the flexibility of the foundation for this substructure and earthquake loading, and further study will be carried out on the CHSR prototype bridge in the coming section.

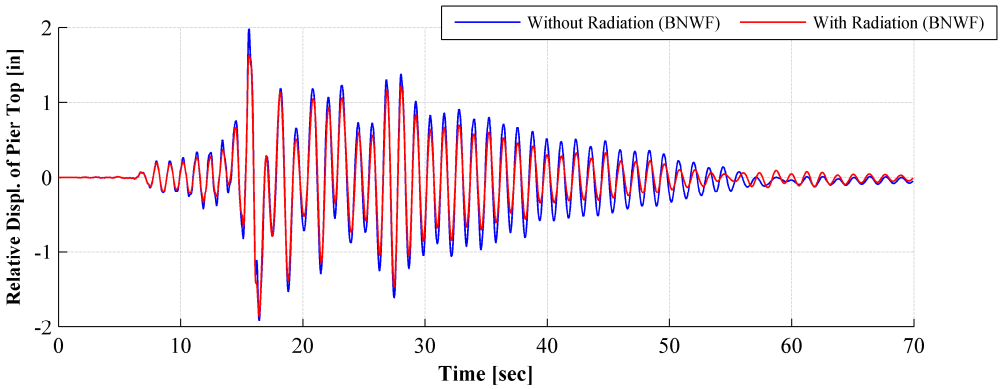

Figure 3.56: Radiation effect study on substructure system with both stiffness proportional and mass proportional Rayleigh damping (2%): earthquake ground motion scaled by 0.5

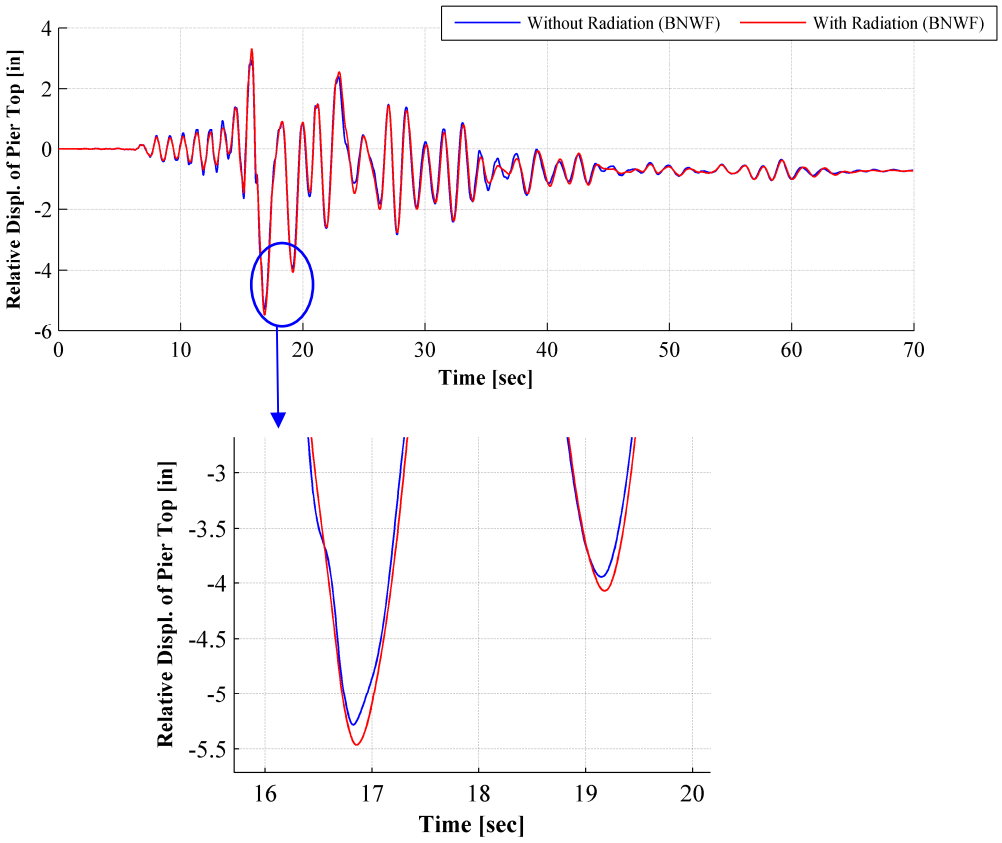

Figure 3.57: Radiation effect study on substructure system with both stiffness proportional and mass proportional Rayleigh damping (2%): earthquake ground motion unscaled

Figure 3.56 and Figure 3.57 present the effects of radiation damping on the substructure response. It is noticed that the radiation damping reduces the structure response as expected, and the reduction is more prominent especially when the earthquake intensity level is lower. This is because when the soil surrounding the piles involves more plastic deformation and less energy will be dissipated in terms of radiation. This effect is captured through the dynamic p-y modeling approach in that the dashpot is paralleled with the elastic component of the soil springs in formulation of soil springs.

3.10. Technical Issues for Seismic Simulation of the CHSR Prototype Bridge

Considering the technical issues confronted in the seismic simulation of CHSR Prototype Bridge, a parallel study for further verification of the foregoing observations is performed before diving into investigation of the seismic response of the CHSR Prototype Bridge. Three analysis approaches are employed here to study the seismic response under Earthquake NGA1505 (Chi-Chi, Taiwan 1999), the uniform acceleration loading (referred to as Approach I), multiple-support displacement loading neglecting the depth-variation of ground displacement along piles (referred to as Approach II), and multiple-support displacement loading accounting for the depth variation (referred to as Approach III). Consistent results regarding to the issues of MSE with Rayleigh damping are observed. For brevity, representative results are presented as follows.

Figure 3.58 to Figure 3.63 present the transversal and longitudinal displacement of pier #5 and the deck relative to the ground surface, when different Rayleigh damping models are applied (i.e., stiffness proportional, mass proportional, and both stiffness and mass proportional Rayleigh damping) subjected to Earthquake NGA1505 (Chi-Chi, Taiwan 1999) scaled to MCE hazard level. It illustrates the consistency of approaches I and II for stiffness proportional damping model and inherent inconsistency between approaches I and II for mass

proportional damping. Thus, the conclusion based on rigorous theoretical derivation and substructure verification is further enhanced for the CHSR Prototype Bridge, as follows:

(1) When stiffness proportional damping is applied to the CHSR prototype bridge, approaches I and II are consistent and perfectly equivalent as expected (see Figure 3.58 and Figure 3.59).

(2) When mass proportional damping is applied, inconsistency occurs (see Figure 3.60 and Figure 3.61). The inconsistency between approach I and approach II for the mass-proportional damping leads to a discrepancy in the longitudinal response as big as around 10% (shown in Figure 3.61).

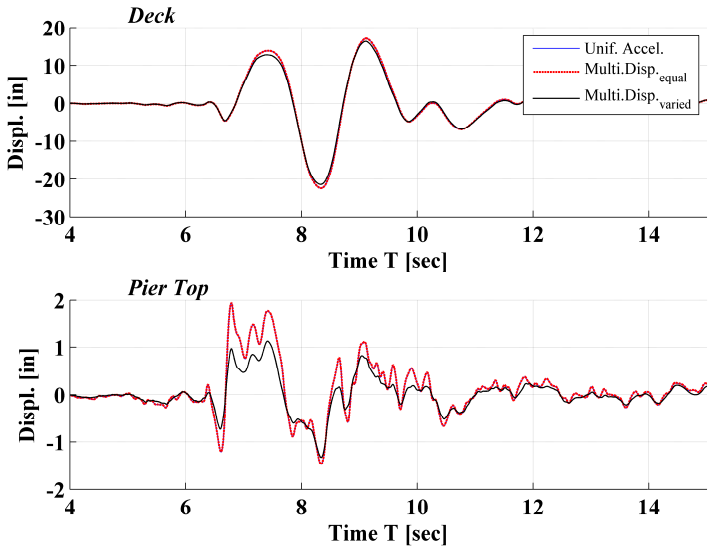

Figure 3.58: Convergence study on the consistence of MSE loading with uniform acceleration loading (MCE) on CHSR Bridge system with stiffness proportional damping (2%): transversal displacement of deck over pier #5 (top plot) and transversal displacement of pier #5 top node (bottom plot)

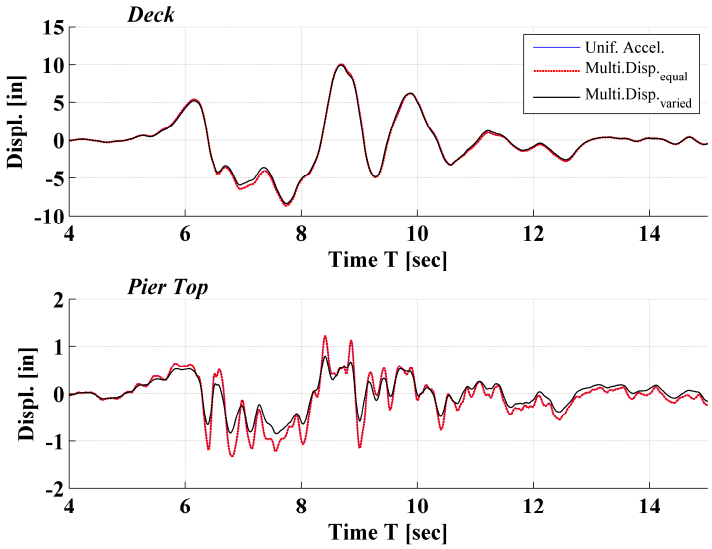

Figure 3.59: Convergence study on the consistence of MSE loading with uniform acceleration loading (MCE) on CHSR Bridge system with stiffness proportional damping (2%): longitudinal displacement of deck over pier #5 (top plot) and longitudinal displacement of pier #5 top node (bottom plot)

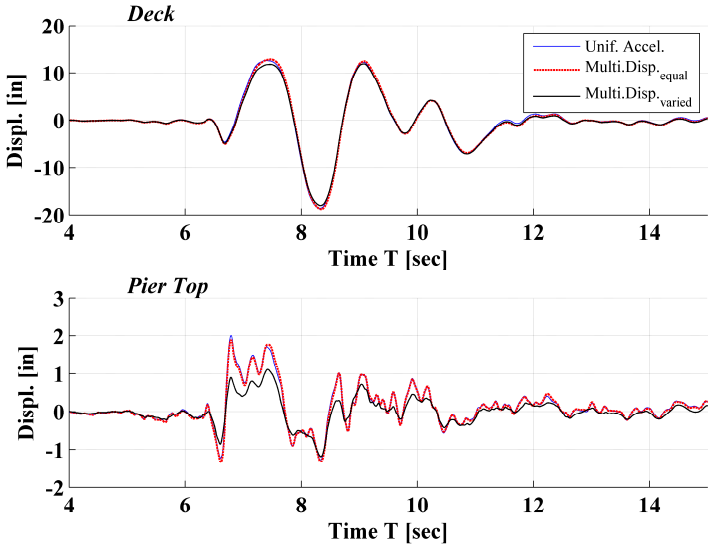

Figure 3.60: Convergence study on the consistence of MSE loading with uniform acceleration loading (MCE) on CHSR Bridge system with mass proportional damping (2%): transversal displacement of deck over pier #5 (top plot) and transversal displacement of pier #5 top node (bottom plot)

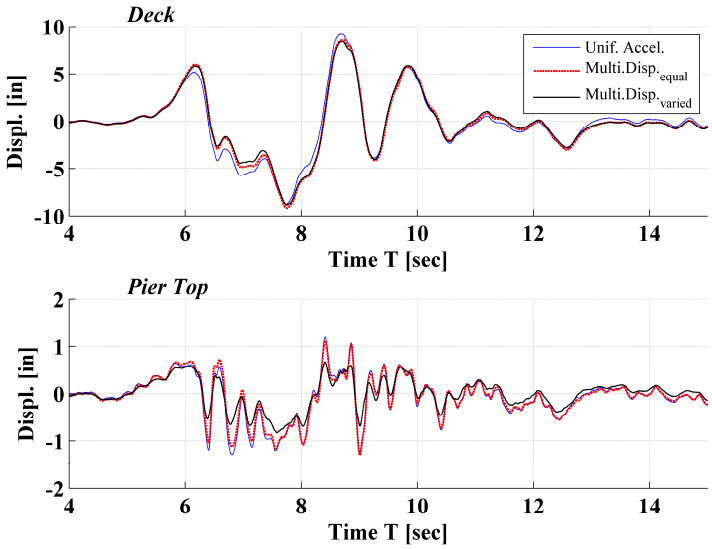

Figure 3.61: Convergence study on the consistence of MSE loading with uniform acceleration loading (MCE) on CHSR Bridge system with mass proportional damping (2%): longitudinal displacement of deck over pier #5 (top plot) and longitudinal displacement of pier #5 top node (bottom plot)

(3) Since it is ideal to impose nearly constant damping among the modes of interest, a combination of stiffness and mass proportional damping (i.e., full Rayleigh damping) is preferred. Accordingly, even though mass proportional damping is detrimental to the accuracy of multiple-support-excitation, Rayleigh damping based on first mode (transversal) frequency and sixth mode (longitudinal) frequency is adopted for the seismic response prediction of the CHSR prototype bridge as a comprise. Investigation of the cost of comprise (i.e., inconsistency) for a combination of stiffness and mass proportional Rayleigh damping is carried out (see Figure 3.62 and Figure 3.63). The discrepancy between approach I and approach II still exists but is small within a tolerance error of 5%.

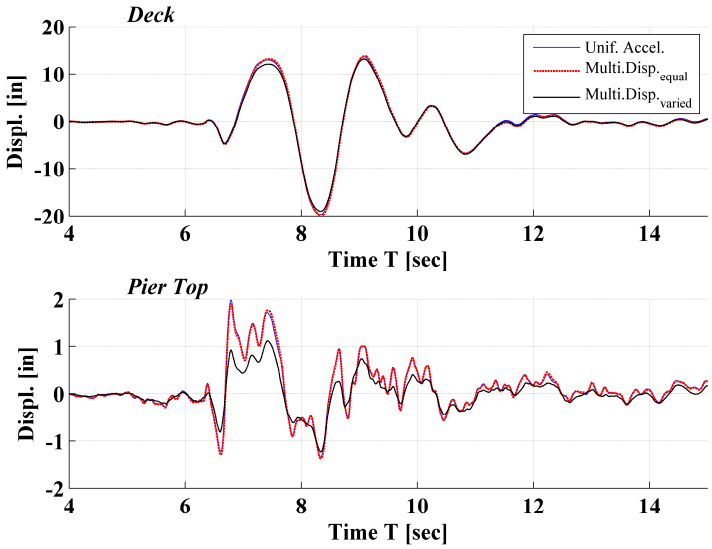

Figure 3.62: Convergence study on the consistence of MSE loading with uniform acceleration loading (MCE) on CHSR Bridge system with both stiffness and mass proportional damping (2%): transversal displacement of deck over pier #5 (top plot) and transversal displacement of pier #5 top node (bottom plot)

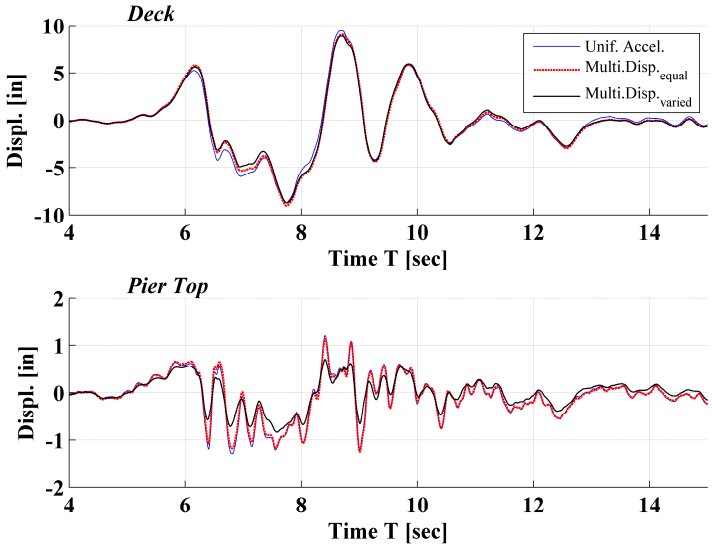

Figure 3.63: Convergence study on the consistence of MSE loading with uniform acceleration loading (MCE) on CHSR Bridge system with both stiffness and mass proportional damping (2%): longitudinal displacement of deck over pier #5 (top plot) and longitudinal displacement of pier #5 top node (bottom plot)

Apart from the investigation of consistency or inconsistency between approach I and approach II as shown above, the difference between approach II and approach III is more obvious for MCE hazard level earthquake excitations. Parallel results with for OBE hazard level earthquake excitations are followed in Figure 3.64 and Figure 3.65. The effects of depth-variation of ground displacement inputs from site response are negligible for deck response, while they play a significant role in the response of pier top displacements, especially for the MCE hazard levels where the soil structure interaction are significant in terms of kinematics of piles to modify the foundation motion input to the structure.

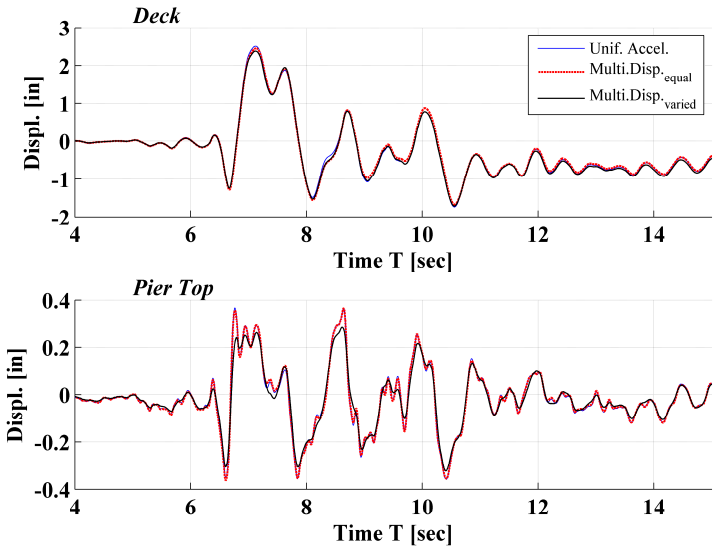

Figure 3.64: Convergence study on the consistence of MSE loading with uniform acceleration loading (OBE) on CHSR Bridge system with both stiffness and mass proportional damping (2%): transversal displacement of deck over pier #5 (top plot) and transversal displacement of pier #5 top node (bottom plot)

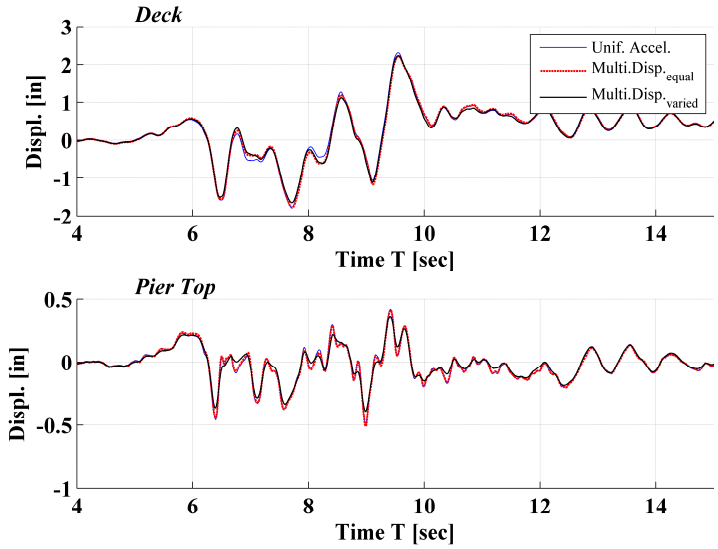

Figure 3.65: Convergence study on the consistence of MSE loading with uniform acceleration loading on CHSR Bridge system with both stiffness and mass proportional damping (2%): longitudinal displacement of deck over pier #5 (top plot) and longitudinal displacement of pier #5 top node (bottom plot)

3.11. Conclusions

In this chapter, a 9-span California High-Speed Rail (CHSR) prototype bridge is selected as a testbed study, with pertinent design description summarized for the purpose of numerical modeling. An advanced three-dimensional (3D) finite element (FE) model was developed in the open source object-oriented software framework of OpenSees, making use of the existing and developed modeling and simulation capabilities. In this complex bridge system model, both Soil-Foundation-Structure-Interaction (SFSI) and Track-Structure-Interaction (TSI) are accounted for at a system-level performance simulation. SFSI is considered using the dynamic p-y approach for pile group foundation and multiple nonlinear springs for the resistance from abutments to deck. TSI is accounted for by using series of closely-spaced nonlinear springs to represent the track-structure connection layer. The structural and geotechnical modeling is elaborated with the detailed modeling and certain

calibration of such components as the nonlinear substructure, elastic superstructure, bilinear seismic isolators, slotted hinge joint devices, abutment backfill, shear keys, pile foundations, and rail boundary springs. Static pushover analyses were performed on substructure components (i.e., abutments modeled using multiple springs, single pier founded on pile foundation modeled using p-y approach) to understand the cyclic hysteretic behavior of the components. Pertinent simulation and dynamic analysis techniques (i.e., multiple-support-excitation with Rayleigh damping model) are investigated theoretically and numerically, aiming at more reliable seismic response simulation and prediction for the CHSR Prototype Bridge. A sufficient and necessary condition for damping models were derived analytically in order to achieve the same solution for the benchmark problem proposed using the uniform excitation and multiple-support-excitation formulations. Following the analytical derivation, the Rayleigh damping model, consisting of both the mass proportional and stiffness proportional damping, turns to be problematic for multiple-support-excitation (MSE) formulation due to the mass proportional part. This is further verified by a response spectra analysis based on a linear SDOF system, nonlinear time history analysis of a substructure and CHSR Prototype Bridge. Soil-pile-structure-interaction needs to be included for realistic and reliable seismic response simulation under earthquake ground motions of a wide range of intensities. Accordingly, MSE approach needs to be adopted with full Rayleigh damping model for the seismic simulation of CHSR Prototype Bridge with acceptable comprise, notwithstanding the contaminating effects of mass proportional Rayleigh damping.

References

Abramson, L. W., Lee, T. S., Sharma S., and Boyce, G. M. (2001). *Slope Stability and Stabilization Methods*. Wiley, 2d Edition. New York.

American Petroleum Institute (API) (1993). *Recommended practice for planning, designing and constructing fixed offshore platforms – Working stress design*. 20th Edition, American Petroleum Institute, Washington, DC.

Aviram, A., Mackie, K. and Stojadinovic, B. (2008a). "Guidelines for Nonlinear Analysis of Bridge Structures in California," *Technical Report 2008/03*, Pacific Earthquake Engineering Research Center, University of California, Berkeley.

Aviram, A., Mackie, K.R., and Stojadinovic, B. (2008b). "Effect of Abutment Modeling on the Seismic Response of Bridge Structures," *Earthquake Engineering and Engineering Vibration*, 7(4), 395-402.

Boulanger, R.W., Curras, C.J., Kutter, B.L., Wilson, D.W., and Abghari, A. (1999). "Seismic soil-pile-structure interaction experiments and analysis." *Journal of Geotechnical and Geo-environmental Engineering*, 125(9),750-759

Boulanger, R.W., Kutter, B.L., Brandenberg S. J., Singh P., Chang D. (2003). "Pile foundations in liquefied and laterally spreading ground during earthquakes: centrifuge experiments and analyses." *Rep. No. UCD/CGM-03/01*, Center for Geo-technique Modeling, Dept. of Civil and Environmental Engineering, University of California, Davis, California.

Brandenberg, S. J. (2005). "Behavior of Pile Foundations in Liquefied and Laterally Spreading Ground." *Ph.D. dissertation*. University of California, Davis, California.

Caltrans SDC. (2010). *Caltrans Seismic Design Criteria*, California Department of Transportation, Sacramento, California.

California High-speed Rail Authority (CHSRA). (2012). *California High-speed Train Project Design Criteria*, San Francisco, California.

Curras, C., Boulanger, R., Kutter, B. L., and Wilson, D. W. (2001). "Dynamic experiments and analyses of a pile-group-supported structure." *Journal of geotechnical and Geoenvironmental Engineering*, 127(7), 585–596.

Duncan, J. M., and Mokwa, R. L. (2001). "Passive earth pressures: theories and tests." *Journal of Geotechnical and Geoenvironmental Engineering*, 127(3), 248-257.

Dash, S., Bhattacharya, S., Blakeborough, A., & Hyodo, M. (2008). "PY Curve to model lateral response of pile foundations in liquefied soils." *The 14th World Conference of Earthquake Engineering*, October 12-17, Beijing, China

Elgamal, A., Yan, L., Yang, Z., & Conte, J. (2008). "Three-dimensional seismic response of Humboldt Bay bridge-foundation-ground system." *Journal of Structural Engineering*, 1165–1176.

Gadre, A.D. and Dobry, R. (1998). “Centrifuge modeling of cyclic lateral response of pile cap systems and seat-type abutments in dry sand.” *Rep. MCEER-98-0010,* Rensselaer Institute, Civil Engineering Dept., Troy, N.Y..

Gazetas, G., and Dobry, R. (1984). “Simple Radiation Damping Model for Piles and Footings.” *Journal of Engineering Mechanics*, 110(6), 937–956.

Gazetas, G., & Dobry, R. (1984). “Horizontal Response of Piles in Layered Soils.” *Journal of Geotechnical Engineering*, 110(1), 20–40.

Harden, C., & Hutchinson, T. (2009). “Beam-on-nonlinear-Winkler-foundation modeling of shallow, rocking-dominated footings.” *Earthquake Spectra*, *25*(2), 277–300.

Huo, Y. L. (2011). “Highway Bridge Seismic Assessment and Improvement Analysis with Fragility Function Method.” *Ph.D., dissertation*, University of California, Los Angeles, California.

Japanese Road Association (JRA) (2002). *Specifications for Highway Bridges*. Japan Road Association, Preliminary English Version, prepared by Public Works Research Institute (PWRI) and Civil Engineering Research Laboratory (CRL), Japan, November.

Khalili-Tehrani P., Taciroglu E., and Shamsabadi A. (2010) “Backbone Curves for Passive Lateral Response of Abutment Walls with Homogeneous Backfills.” *Soil Foundation Structure Interaction*, Chapter 19, 149-154.

Khalili-Tehrani P., Shamsabadi A., Stewart J. P., and Taciroglu E. (2012) “Physically Parameterized Backbone Curves for Passive Lateral Response of Abutment Walls with Homogeneous Backfills.” *To be submitted to ASCE Journal of Geotechnical and Geoenvironmental Engineering*.

Kotsoglou, A., and Pantazopoulou, S. (2007). “Bridge–embankment interaction under transverse ground excitation.” *Earthquake Engineering and Structural Dynamics*, 36(12), 1719–1740.

Lu, J., Mackie, K.R., and Elgamal, A. (2011). BridgePBEE: *OpenSees* 3D Pushover and Earthquake Analysis of Single-Column 2-span Bridges, *User Manual*, Beta 1.0.

Luco, J., & Westmann, R. (1971). “Dynamic response of circular footings.” *Journal of the engineering mechanics Devision.* 1381-1395.

Maroney B. H. and Chai Y. H. (1994). “Seismic Design and Retrofitting of Reinforced Concrete Bridges,” Proceedings of 2nd International Workshop, Earthquake Commission of New Zealand, Queenstown, New Zealand.

Matlock, H. (1970). “Correlations for design of laterally loaded piles in soft clay.” *Proceedings of the 2nd Annual Offshore Technology Conference*, Houston, Texas, 577-594.

Mokwa, R. L. and Duncan, J. M. (2001). Experimental evaluation of lateral-load resistance of pile caps. *ASCE Journal of* Geotechnical *and Geoenvironmental Engineering*, 127 (2), 185-192.

Mcgann, C. R., Arduino, P., Asce, M., & Mackenzie-helnwein, P. (2012). *Simplified Procedure to Account for a Weaker Soil Layer in Lateral Load Analysis of Single Piles*, (September), 1129–1137.

Mckenna F. T. (1997) "Object-oriented finite element programming: frameworks for analysis, algorithms and parallel computing." *Ph.D., dissertation*, University of California, Berkeley, California.

Mylonakis, G., Asce, M., and Gazetas, G. (2002). "Kinematic pile response to vertical p-wave seismic excitation." 28(10), 860–867.

Mylonakis, G., Nikolaou, S., & Gazetas, G. (2006). "Footings under seismic loading: Analysis and design issues with emphasis on bridge foundations." *Soil Dynamics and Earthquake Engineering*, *26*, 824–853.

Naeim F., Kelly J. M. (1999). *Design of Seismic Isolated Structures from Theory to Practice*. John Wiley & Sons, New York.

Novak, M. (1991). "Piles under dynamic loads." *Proceedings of the Second International Conference on Recent Advances in Geo-technology*, Engineering and Soil Dynamics, vol. III. St Louis.

Petrangeli M., Tamagno C., and Tortolini P. (2008). "Numerical Analysis of Track-Structure Interaction and Time Domain Resonance." *Journal of Rail and Rapid Transit*, 345-353.

Petuskey A. (2011). "Superstructure Isolation Strategies for California High-Speed Rail Viaducts," *M.Eng. thesis*, University of California, Berkeley, California.

Priestley, M.J.N., Seible, F., and Calvi, M. (1996). *Seismic Design and Retrofit of Bridges*, John Wiley and Sons, New York, NY.

Raychowdhury, P., & Hutchinson, T. (2009). "Performance evaluation of a nonlinear Winkler-based shallow foundation model using centrifuge test results." *Earthquake Engineering & Structural Dynamics*,38(5), 679–698.

Rollins, K. M. and Cole, R. T., (2006). "Cyclic Lateral Load Behavior of a Pile Cap and Backfill" *Geotechnical and Geoenvironmental Engineering*, 132 (9), 1143-1153.

Reese, L.C. 1997. Analysis of laterally loaded piles in weak rock. Journal of *Geotechnical and Geoenvironmental Engineering*, 123(11),1010-1017

Shamsabadi, A., Rollins, K. M., and Kapuskar, M. (2007). "Nonlinear soil-abutment-bridge structure interaction for seismic performance-based design." *Journal of Geotechnical and Geoenvironmental Engineering*, 133(6), 707-720.

Skinner, R. I., Robinson, W. H. and McVerry, G. H. (1993). *An Introduction to Seismic Isolation*. John Wiley & Sons, New York.

Shamsabadi, A. (2007). "Three-dimensional nonlinear seismic soil-abutment-foundation-structure interaction analysis of skewed bridges." *Ph.D. dissertation*, University of Southern California, Los Angeles, California.

Siddharthan, R., El-Gamal, M., and Maragakis, E. A. (1994). "Investigation of performance of bridge abutments in seismic regions." *Journal of Structural Engineering*, 120(4), 1327-1346.

Sextos A., Mackie K., Stojadinnovic B., and Taskari O. (2008). "Simplified p-y relationships for modeling embankment-abutment systems of typical California bridges." *The 14th World Conference on Earthquake Engineering*, October 12-17, Beijing, China.

Trochanis, A. M., J. Bielak, and P. Christiano (1991). "Three-dimensional nonlinear study of piles." *Journal of Geotechnical Engineering*, 117(3), 429-447

Vesic, A. S., (1961). "Beams on elastic subgrade and the Winkler's hypothesis." *Proceedings of the 5th International Conference on Soil Mechanics and Foundation Engineering (ICSMFE)*, Paris. pp. 845-850.

Wilson, D. W. (1998). "Soil-pile-superstructure interaction in soft clay and liquefiable sand." *Rep. No. UCD/CGM-98/04*, Center for Geo-technique Modeling, Dept. of Civil and Environmental Engineering, University of California, Davis, California.

Wilson P., and Elgamal, A. (2006). "Large scale measurement of lateral earth pressure on bridge abutment back-wall subjected to static and dynamic loading." *Proceedings of the New Zealand Workshop on Geotechnical Earthquake Engineering*, University of Canterbury, Christchurch, New Zealand, 307-315.

Wilson, J., and Tan, B. (1990). "Bridge abutments: formulation of simple model for earthquake response analysis." *Journal of Engineering Mechanics*, 116(8), 1828–1837.

Zhang, Y., Conte, J., Yang, Z., and Elgamal, A. (2008). "Two-dimensional nonlinear earthquake response analysis of a bridge-foundation-ground system." *Earthquake Spectra*, 24(2), 343–386.

Zhang, J., and Makris, N. (2002a). "Kinematic response functions and dynamic stiffnesses of bridge embankments." *Earthquake Engineering & Structural Dynamics*, 31(11), 1933–1966.

Zhang, J., and Makris, N. (2002b). "Seismic response analysis of highway overcrossings including soil–structure interaction." *Earthquake engineering & structural dynamics*, 31(11), 1967–1991.

Zhao, M. X. (2011). "Response of bridges to lateral spreading and earthquake shaking." *Ph.D., dissertation*, University of California, Los Angeles, California.

CHAPTER 4

SEISMIC SIMULATION OF CHSR PROTOTYPE BRIDGE FOCUSING ON DETERMINISTIC PERFORMANCE COMPARISON BETWEEN SEISMIC ISOLATED AND NON-ISOLATED BRIDGE

4.1. Introduction

Based on the three-dimensional (3D) detailed nonlinear finite element (FE) model of the CHSR Prototype Bridge developed in OpenSees, including soil-foundation-structure interaction and rail-structure interaction, dynamic time history analysis of CHSR Prototype Bridge is carried out subjected to earthquake ground motion excitation. The dynamic behavior of the complex bridge system is investigated under operating based hazard level earthquakes (OBE) and maximum considered earthquakes (MCE).

Aiming to study the feasibility and optimality of seismic isolation in the CHSR prototype bridge system, the effects of seismic isolation are analyzed by comparing the simulated response of the bridge with and without seismic isolation (i.e., isolated and non-isolated bridge) and the corresponding track system behavior. Compared to the CHSR

Prototype Bridge as designed and modeled previously, the comparable non-isolated bridge has rigid pier-deck connections and non-isolation bearing pads at the abutments to support the bridge ends. In addition, the expansion joints gap at abutment is 1.0in for non-isolated bridge (NIB) 4.0in, which serves as a seismic gap for the isolated bridge (IB).

The seismic response of IB and NIB subjected to the same earthquake ground motion (i.e., based on certain single earthquake scenario) is compared, which is denoted as deterministic performance comparison in this chapter. It serves as a contrast to the probabilistic performance comparison in terms of statistics and hazard presented in next chapter. Both beneficial and detrimental effects of seismic isolation are observed in the deterministic comparison. It is found that the introduction of isolators into the CHSR bridge system significantly reduces the force demand in the bridge piers and thus the foundation, and tends to decrease the deck acceleration. However, it could increase the deck displacement and the stresses in the rails.

4.2. Earthquake Selection, Scaling, and De-convolution

To have a convincing investigation of the pros and cons of seismic isolation system for the CHSR bridge system with tracks attached above, a reasonably fair comparison is performed between the IB and NIB systems based on a single earthquake scenario. To guarantee a reasonably fair comparison, it is desirable to have the single earthquake input with the intensity measures for the IB and NIB that corresponds to the same hazard level, i.e., being associated with the same annual probability or mean annual rate of exceedance. The seismic performance of seismic isolation can be evaluated under the selected earthquake record in a consistent seismic hazard sense.

To evaluate the seismic performance of the IB and NIB under single earthquake scenario in a consistent seismic hazard sense, two ground motion records are selected out of

3182 records from PEER Ground Motion Database (BETA, http://peer.berkeley.edu/) which correlates well with the target spectrum for the period range of interest after scaling. The period range of interest spans the first transverse and longitudinal modes of both the non-isolated and isolated bridge. The target spectrum is selected to be the uniform hazard spectrum at maximum considerable earthquake (MCE) hazard level with return period of 950 years obtained from web application of USGS PSHA Tool (USGS Interactive De-aggregation 2008, http://geohazards.usgs.gov/) The detailed information for these two selected ground motion records is presented in Table 4.1, including the NGA sequence number, earthquake event name, recorded station name, recorded date, moment magnitude, peak ground acceleration (PGA), scale factors for both MCE and OBE hazard levels, and the pulse impulse indicator. Based on the quantitative classification of near-fault ground motions using wavelet analysis (Baker, 2007), earthquake (NGA#183, also denoted as EQ2) is identified as a pulse like ground motion with indicator of 1.0 for fault-normal (FN) direction, while the other earthquake (NGA#832, also denoted as EQ2) is not considered to be near fault.

Table 4.1: Selected ground motions for deterministic study

on comparison of isolated and non-isolated bridges on single earthquake scenario

NGA #	Earthquake	Station	Year	Magnitude	PGA (g)	Scale Factor (OBE)	Scale Factor (MCE)	Pulse Indicator (FP-FN)
183	Imperial Valley	El Centro Array #8	1979	M6.53	0.54	0.54	1.88	0.00-1.00
832	Landers	Amboy	1992	M7.28	0.13	1.28	4.40	0.01-0.00

Seismic response of CHSR Prototype Bridge is investigated subjected to the ground motion record of NGA#832 and NGA#183 (representative ground motion with near fault

effects). To study the seismic performance under different hazard levels, the ground motion records are scaled to OBE and MCE levels respectively.

To match the target spectra for OBE and MCE, the ground motion records are scaled to match the target spectra over the range of period of interests (0.4sec – 1.3sec), and optimal scale factors are obtained by minimizing the discrepancy between the target spectra and the scaled spectra in the log-scale. As shown in Figure 4.1, the spectra of the scaled ground motion records are well correlated with the target during the period range of interest, and the residual error characterized by the ratio of the area marked as green and the area below the spectra is around 5%- 6%. Thus both earthquake ground motion records can be considered approximately to be of the same hazard level for IB and NIB, which enables a fair comparison between the seismic response of IB and NIB.

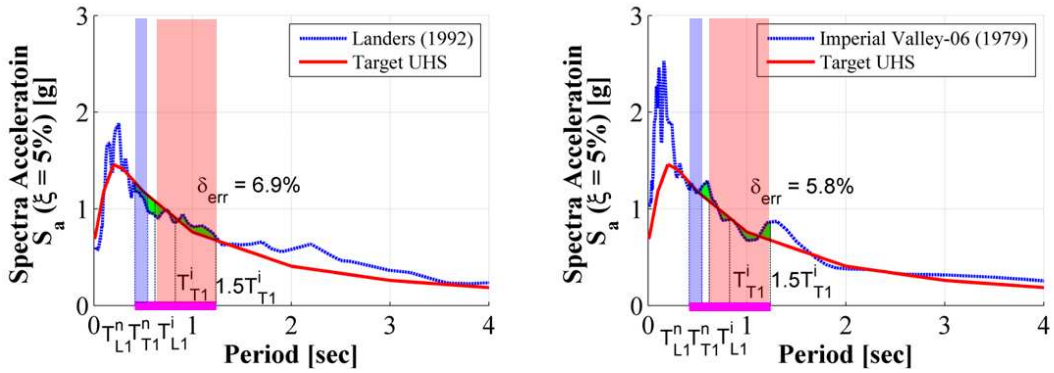

(a) (b)

Figure 4.1: Geometric mean spectra comparison of the selected and scaled ground motion for MCE hazard level: (a) NGA#832, and (b) NGA#183

Geometric mean spectra, as the intensity measure in the uniform hazard spectra from USGS, are used for the spectrum matching. The spectral value for each component still agrees well with the target spectrum with slightly larger difference over the period range of interest. The time histories of these two ground motions scaled for MCE hazard level with both

components (i.e., fault normal and fault parallel) are displayed here. Considering the alignment of the designed bridge and the contributory seismic faults, fault normal (FN) component is applied in the transverse direction of the bridge, and fault parallel (FP) component in the longitudinal direction of the bridge.

Dynamic p-y approach is utilized in the finite element model developed for the CHSR Prototype Bridge in Chapter 3 to account for the soil-foundation-structure-interaction (SFSI). Site response analysis as the first step of SFSI using p-y approach is required to derive the depth-varied ground motions through de-convolution analysis. As introduced in last chapter, de-convolution analysis is carried out for the selected ground motions to generate the corresponding displacement histories to be prescribed as seismic input at the far-ends of p-y springs along the depth of the piles. Depth-varied multiple-support excitation analysis is carried out for the seismic simulation of the CHSR Prototype Bridge.

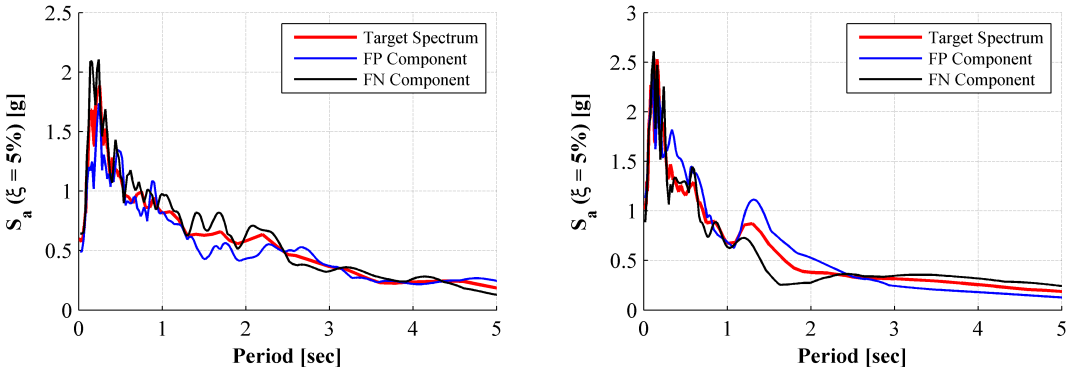

(a) (b)

Figure 4.2: Components spectra comparison of the selected and scaled ground motion for MCE hazard level: (a) NGA#823 (left), and (b) NGA#183

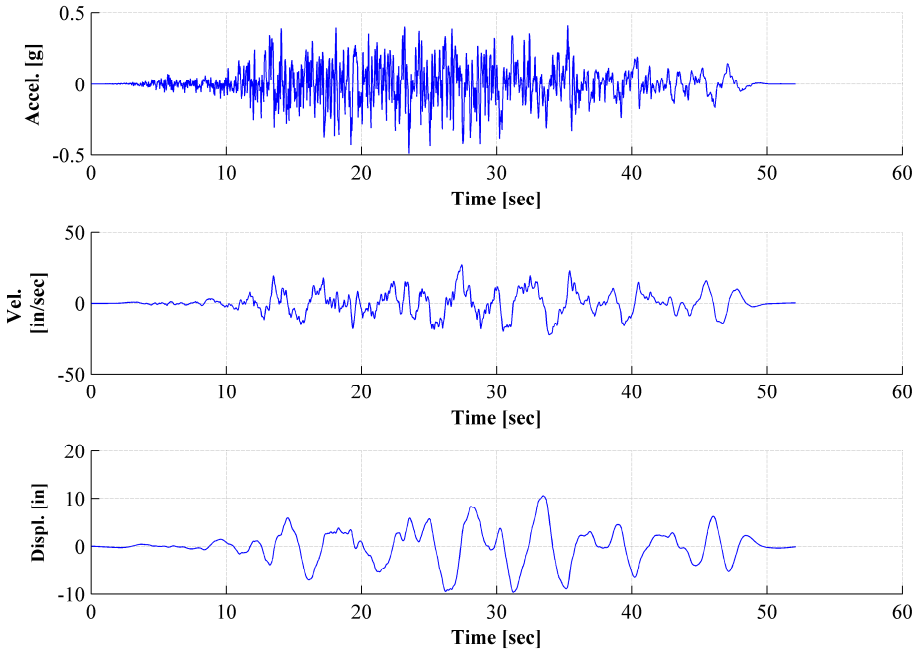

Figure 4.3: Time histories of ground motion record (NGA#832, FP component, MCE)

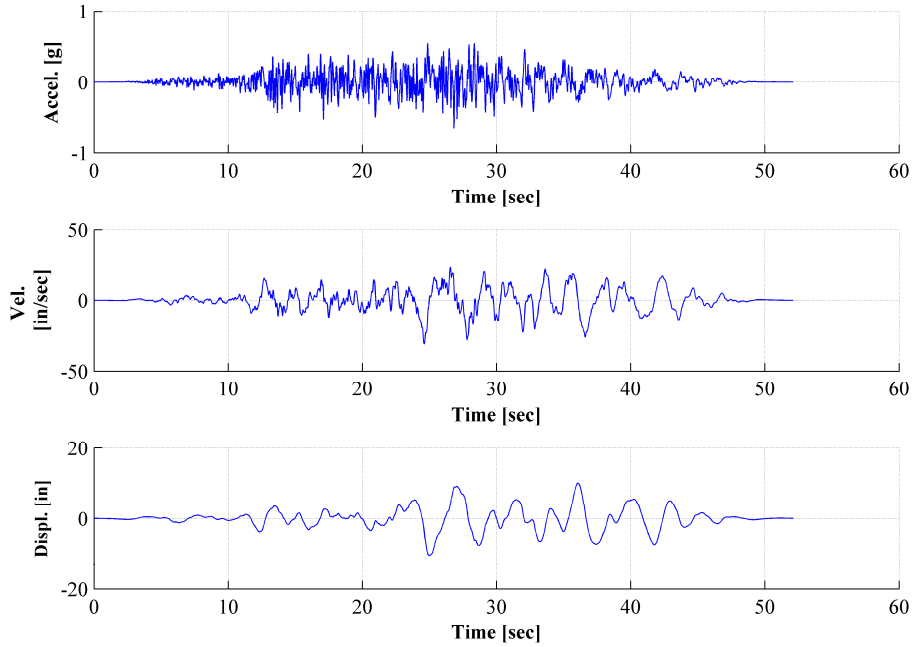

Figure 4.4: Time histories of ground motion record (NGA#832, FN component, MCE)

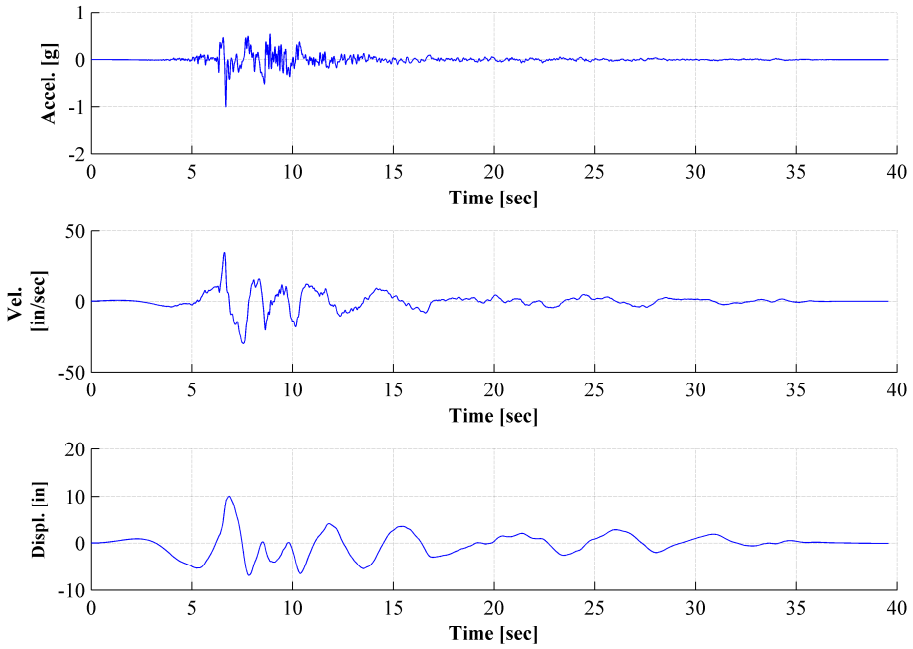

Figure 4.5: Time histories of ground motion record (NGA#183, FP component, MCE)

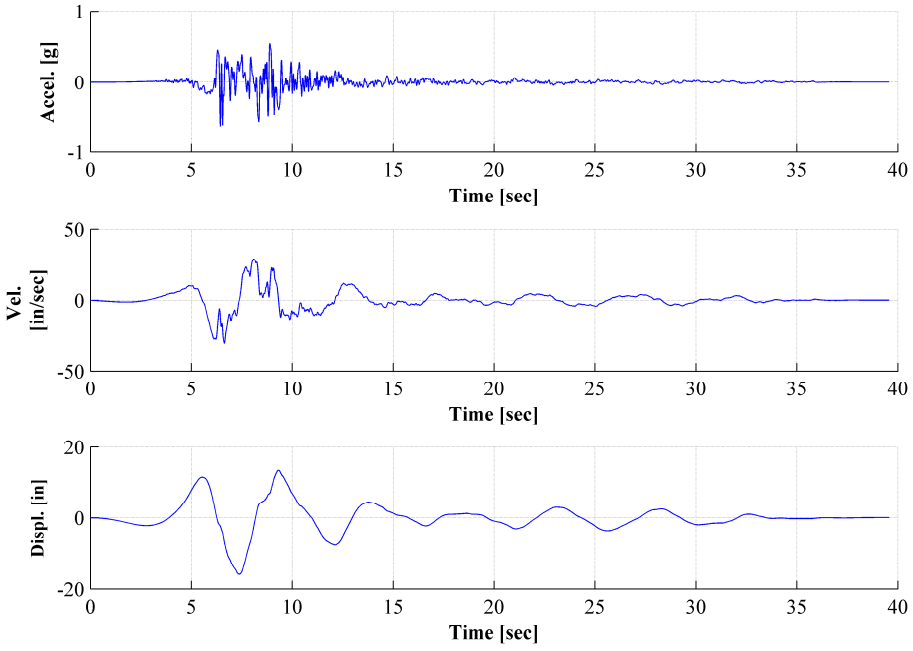

Figure 4.6: Time histories of ground motion record (NGA#183, FN component, MCE)

4.3. Investigation of Effects of Seismic Isolators on System Response

The elastic response spectra (i.e., acceleration spectra and displacement spectra) of the ground surface motion NGA#832 at OBE hazard level corresponding to the longitudinal and transverse direction of the bridge, i.e., the FP and FN components, are presented in Figure 4.7.

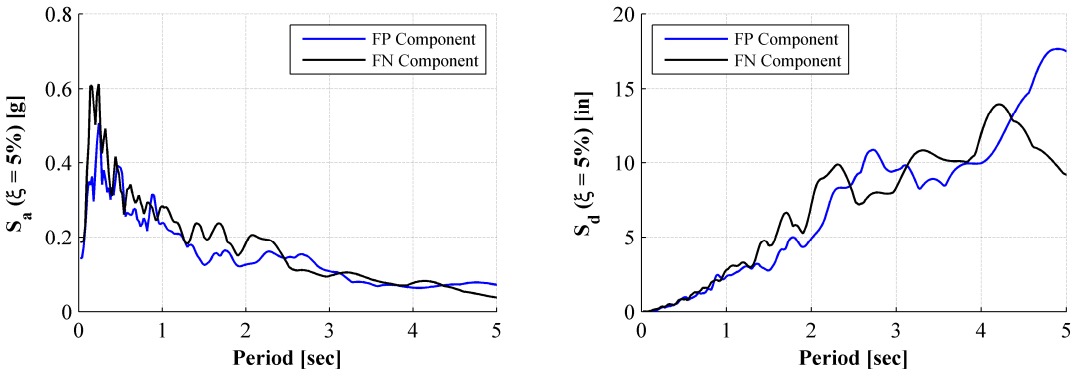

(a) (b)

Figure 4.7: Response spectra (5% damped) of NGA#832: (a) acceleration spectra, and (b) displacement spectra

The force-deformation response of representative seismic isolators I#3 seated on top of bridge pier #1 and I13 on #5 is presented in Figure 4.8. Circular marker indicates the residual deformation in the seismic isolators. The maximum deformation of I#13 is about 1.8in (1.7in) along the transverse direction and 0.9in (1.2in) along the longitudinal direction for NGA832 (NGA #183) under OBE hazard level ground motions. On the OBE hazard level, the seismic isolators yield and experience a residual deformation, and the resulting period elongation and supplemental energy dissipation take effects as so-called isolation effects. It is worth noting that the longitudinal deformations of all seismic isolators supporting the bridge deck are approximately of the same amplitude, while the transverse deformation of seismic isolators in the middle of the bridge is larger than those close to the abutments. This is due to the locking effects of shear keys at abutments in transverse direction, and correspondingly the

hysteretic energy dissipation close to the abutments is relatively smaller than those isolators in the intermediate spans.

The seismic isolator behavior under MCE events is also included in Figure 4.8. It is noticed that the deformation in the transverse direction corresponding to the lower mode is smaller than the deformation in the longitudinal direction. This is because the displacement spectra of the FP component has a much larger spectra value in the period range from 1.2sec to 2.4sec, and seismic isolation elongation under MCE hazard level can shift the structural periods to this range.

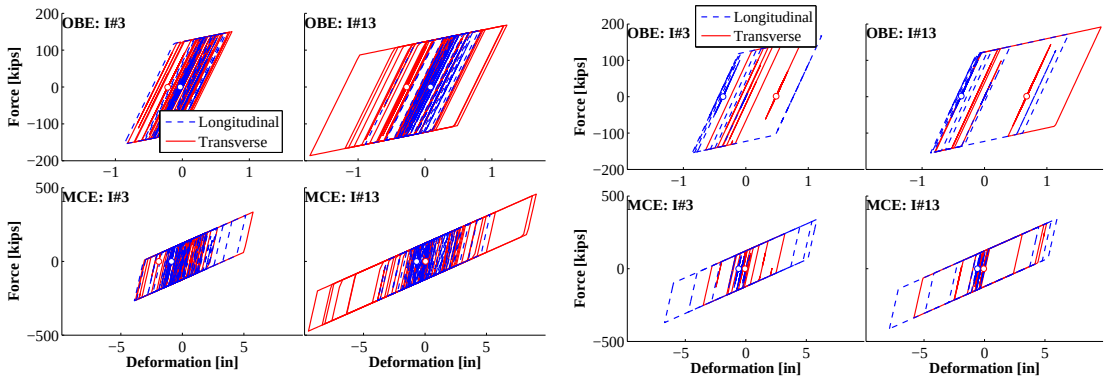

Figure 4.8: Force-deformation response of seismic isolator #3 over pier #1 and isolator #13 over pier #5 under (a) NGA#832 and (b) NGA#183

4.3.1. Seismic response comparison on OBE hazard level

The absolute acceleration time histories of bridge deck are presented in Figure 4.9. Under OBE hazard level ground motion excitation, the peak acceleration in the bridge deck tends to decrease due to the decoupling effects of seismic isolators between bridge piers and bridge deck, especially in the longitudinal direction. The effectiveness of seismic isolation on absolute acceleration is reduced in transverse direction is because the inclusion of the tiny gap between the bolt and hole within SHJ devices for IB leads to additional increase of

acceleration in terms of high frequency contents (spikes). This was observed by the comparison between the acceleration simulated when the tiny gap is included or not in the model.

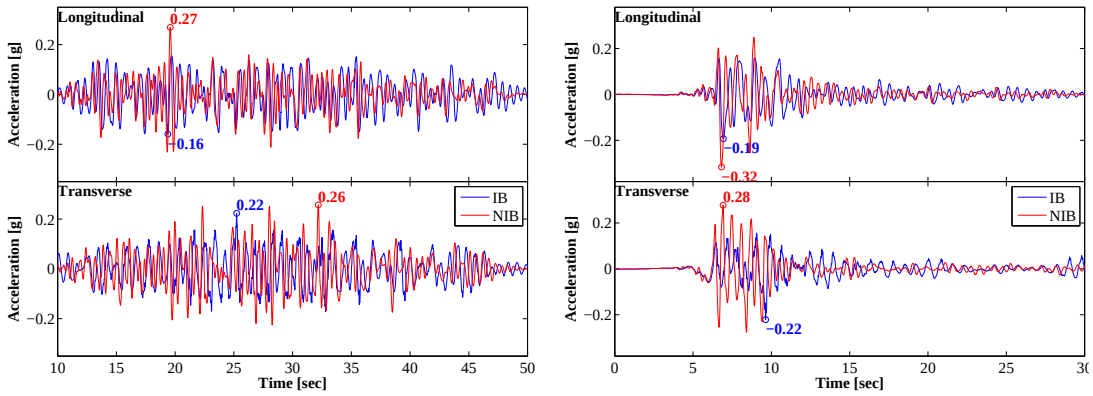

(a) (b)

Figure 4.9: Absolute acceleration of deck over pier #5 under (a) NGA#832 and (b) NGA#183 of OBE hazard level

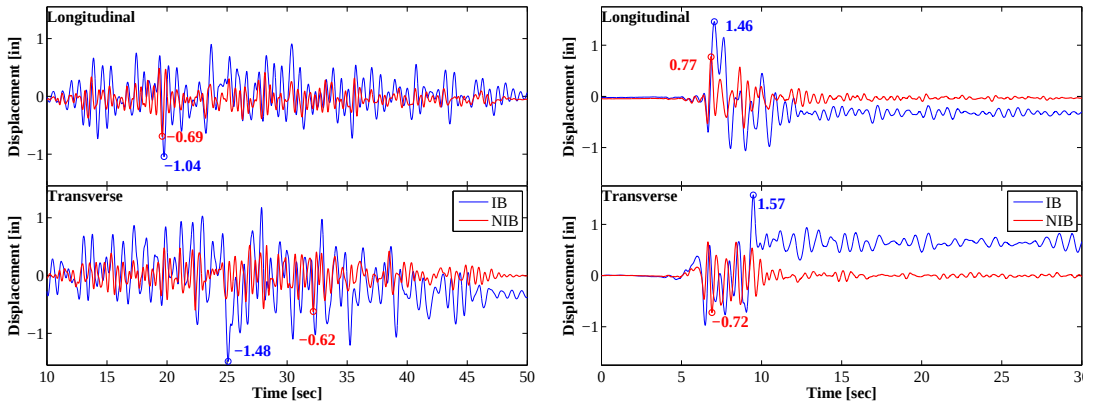

(a) (b)

Figure 4.10: Relative displacement of deck (w.r.t. pile cap) over pier #5 (a) NGA#832 and (b) NGA#183 of OBE hazard level

As illustrated in the comparative results of the relative displacement of bridge deck shown in Figure 4.10 and the pier top with respect to the pile cap in Figure 4.11, the pier top displacement is reduced by around 50% at the cost of increasing the relative deck

displacement. The increase of relative displacement in the bridge deck is mainly due to the deformation concentrated in the seismic isolators. In addition, more frequency contents with longer periods are observed from the deck displacement time history in IB, which is due to the elongation effect of seismic isolators.

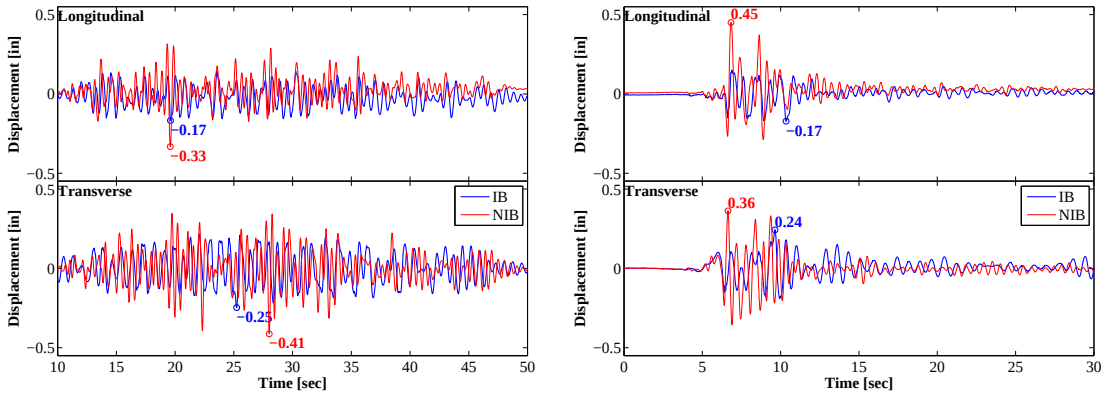

(a) (b)

Figure 4.11: Relative displacement of the top of pier #5 under (a) NGA#832 and (b) NGA#183 of OBE hazard level

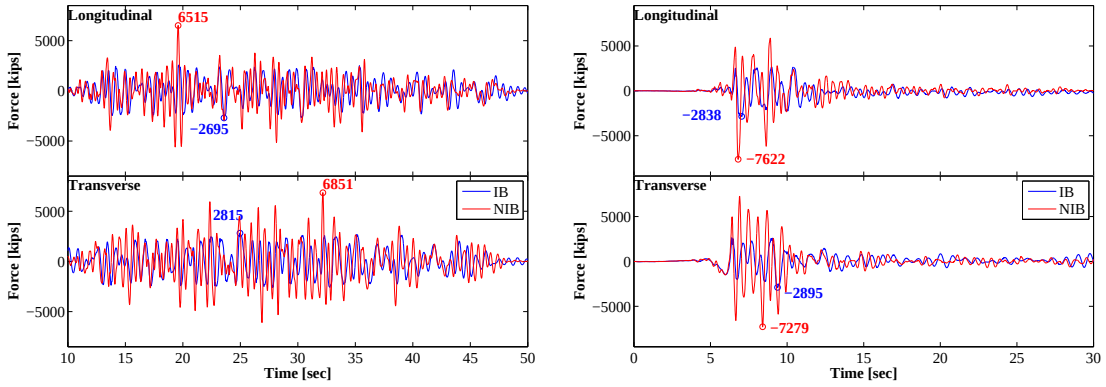

(a) (b)

Figure 4.12: Total base shear force across all piers under (a) NGA#832 and (b) NGA#183 of OBE hazard level

As displayed in Figure 4.12, the total base shear force across all pier columns for the bridge system is consequently highly reduced with seismic isolation. The similar reduction effect is observed with the comparison of total base shear force across all piers and bearings in Figure 4.13 and Figure 4.14 when pounding force is included as well.

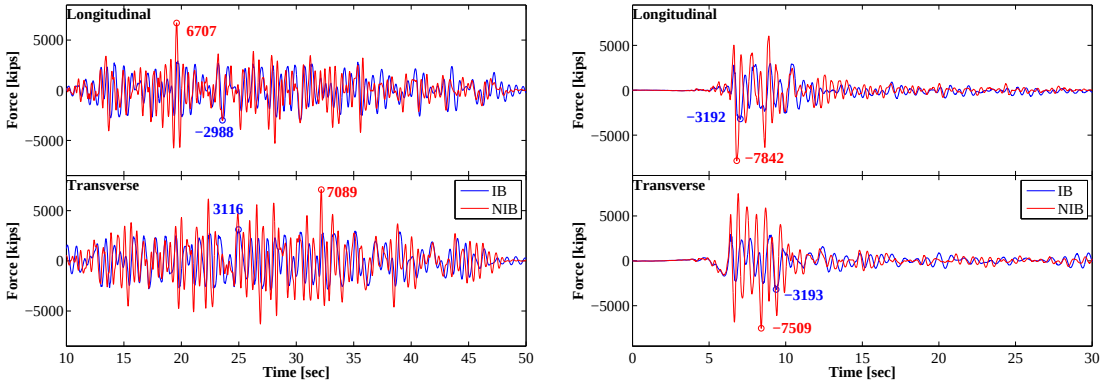

(a) (b)

Figure 4.13: Total base shear force across all piers and bearings under (a) NGA#832 and (b) NGA#183 of OBE hazard level

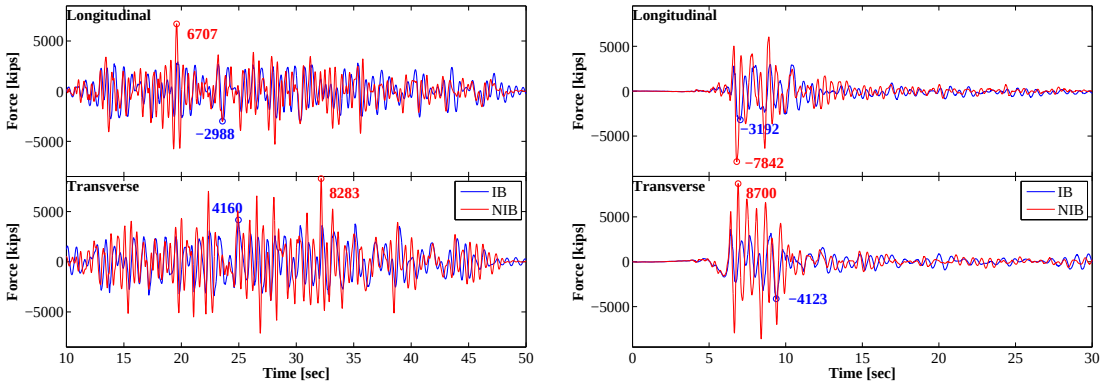

(a) (b)

Figure 4.14: Total base shear force across all piers and bearings plus pounding force under (a) NGA#832 and (b) NGA#183 of OBE hazard level

As an indicator of the soil-foundation interaction effect, the relative translation of pile foundation cap under pier #5 w.r.t. the free-field ground surface is shown in Figure 4.15 for

the comparison between IB and NIB. It implies that the less soil-structure interaction effects can be observed when seismic isolation is adopted in CHSR Prototype Bridge.

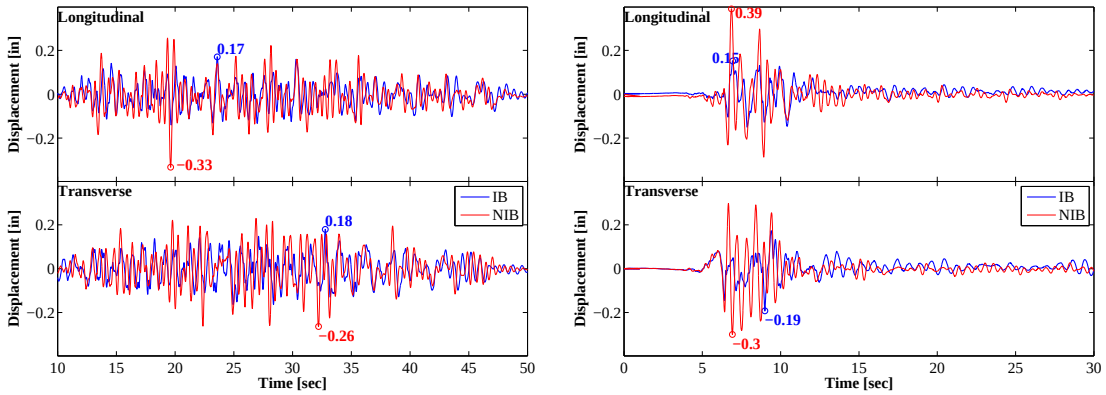

(a) (b)

Figure 4.15: Relative translation of pile foundation cap under pier #5 w.r.t. free-field ground surface under (a) NGA#832 and (b) NGA#183 of OBE hazard level

Figure 4.16 presents the comparison of the seismic response envelopes of the pile group foundation under pier #5: the deformation envelope of soil springs (p-y), the bending moment envelope in pile, and the shear force envelope in pile, as well as the cyclic hysteresis of a typical soil (p-y) spring. As implied from the total base shear force demand for the IB and NIB, the seismic demand on the pile group foundation is smaller due to the incorporation of seismic isolation. Under OBE hazard level ground motion, maximum moment demand (3,500kip-ft) is still smaller than the cracking moment (5,200kip-ft) obtained from the capacity analysis of pile section, and the soil spring located at the cap-pile-connection, to represent the horizontal soil resistance, is still in elastic range. It is worth noting that the seismic demands on the piles are mainly for the top 70ft segment, which is mainly from the inertial effects from the superstructure. The demands for the deeper zone of the piles mainly due to the kinematic effects are relatively small.

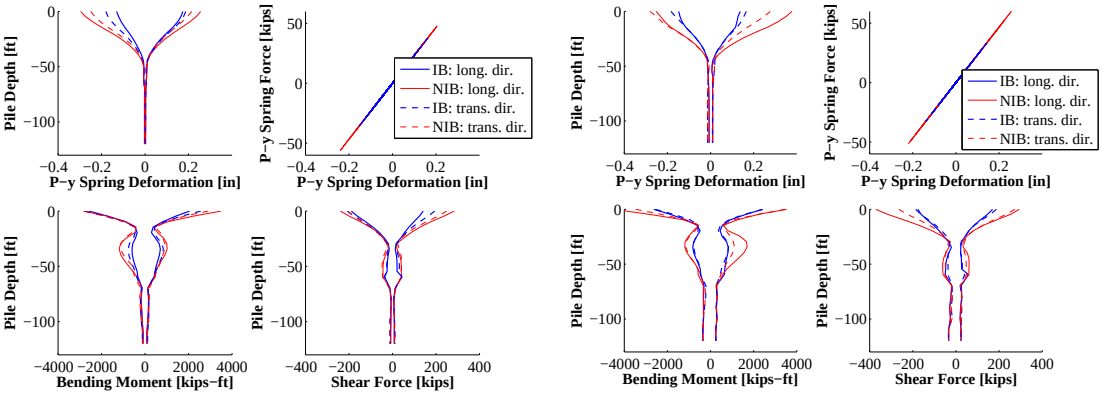

(a) (b)

Figure 4.16: Pile Foundation response under (a) NGA#832 and (b) NGA#183 of OBE hazard level

The rail stresses generated in the rails under an OBE hazard level earthquake are of great concern to the CHST Project authority. Therefore, it is important to examine the effects of the seismic isolators on the stresses in the rails. Figure 4.17 to Figure 4.18 show the envelope of the peak rail stresses generated during the OBE hazard level earthquakes considered here over all rail elements composing the outside-most rail line of the double track system. The normal stress in rails can be generated by three mechanisms, i.e., (a) the axial force P in the rail, referred to as axial stress (mainly due to the longitudinal seismic response of the bridge), (b) the bending of the rail in the horizontal plane Mz, referred to as stress due to transverse bending (mainly due to the transverse seismic response of the bridge), and (c) the bending of the rail in the vertical plane My, referred to as stress due to vertical bending (mainly due to the vertical seismic response of the bridge). The peak stress envelopes due to combined effect of all three mechanisms are presented respectively in Figure 33.

It is observed that: (1) the peaks of the stress envelope along the rail occur at the abutment and interior expansion joints, thus critical location of track for rail stress is the neighborhood of rail at the expansion joints; (2) the peaks of the stress envelope along the rail

are larger and spikier at the abutment joints, especially for the stress due to transverse bending and vertical bending; (3) at the abutment gaps, the rail stress due to axial force is increased obviously due to increase of deck displacement for IB compared to NIB; In contrast, at the interior expansion joints, new peaks of rail stress envelopes are generated for IB because of the relative deck displacement between adjacent frames; (4) the dominant mechanism to the rail stress is the transverse bending, and the rail stress due to transverse bending is around the same for IB and NIB due to the existence of shear key gaps at the abutments. The axial rail stress at OBE hazard level earthquakes here (i.e., 10.5ksi) is limited to be less than the allowable rail stress 14.0ksi, and the total normal stress (i.e., 38.0ksi) less than 59.0ksi.

In conclusion, the incorporation of the seismic isolators in the design of CHSR Bridge is detrimental to the rails, especially for the rails around the expansion joints. The vulnerable part of rail lies in the neighborhood of abutment gap, because the rail stress concentration is critical for both isolated and non-isolated bridge system due to the discontinuity of track transition in the transverse direction from the bridge to the roadbed.

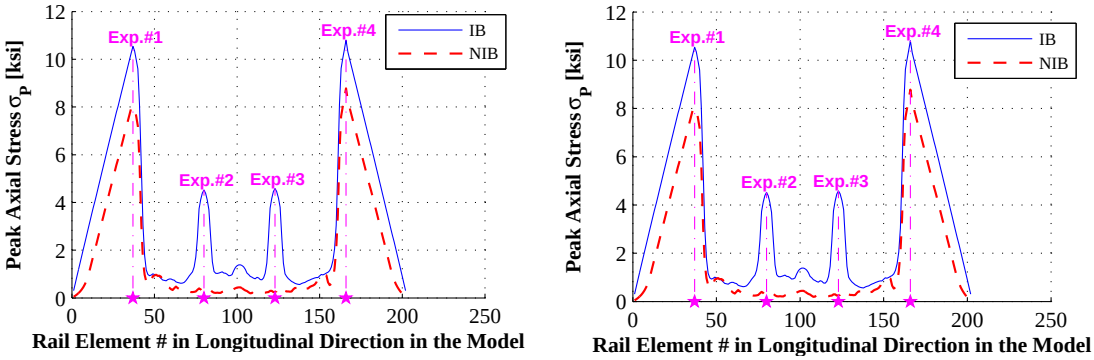

(a) (b)

Figure 4.17: Envelope of peak rail stress due to axial force under (a) NGA#832 and (b) NGA#183 of OBE hazard level

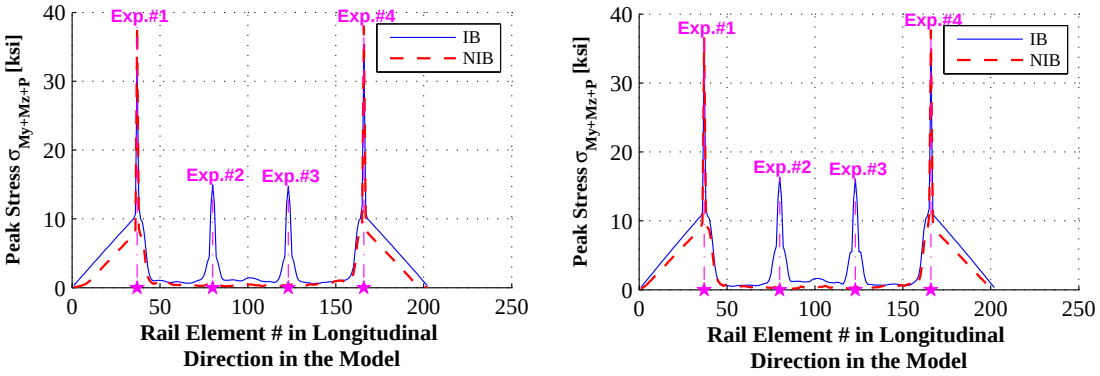

Figure 4.18: Envelope of peak rail stress due to axial force and bending under (a) NGA#832 and (b) NGA#183 of OBE hazard level

4.3.2. Seismic response comparison on MCE hazard level

Similar beneficial and detrimental effects of seismic isolation can be observed through parallel comparison of the seismic response of IB and NIB subject to MCE hazard level ground motions. Selected results are presented herein.

Under MCE hazard level earthquake ground motions, the resulting period elongation and energy dissipation in seismic isolators becomes more significant, and thus the total base shear force are reduced around two thirds as displayed in Figure 4.19. Compared to the OBE hazard level earthquake excitation, the reduction in the total base shear forces of seismic isolators is more significant under MCE hazard level. The pile cap translation with respect to the free-field ground surface in Figure 4.20 shows a remarkable difference between IB and NIB, which shows that seismic isolation can significantly reduce the soil-structure interaction under higher intensity level earthquake events.

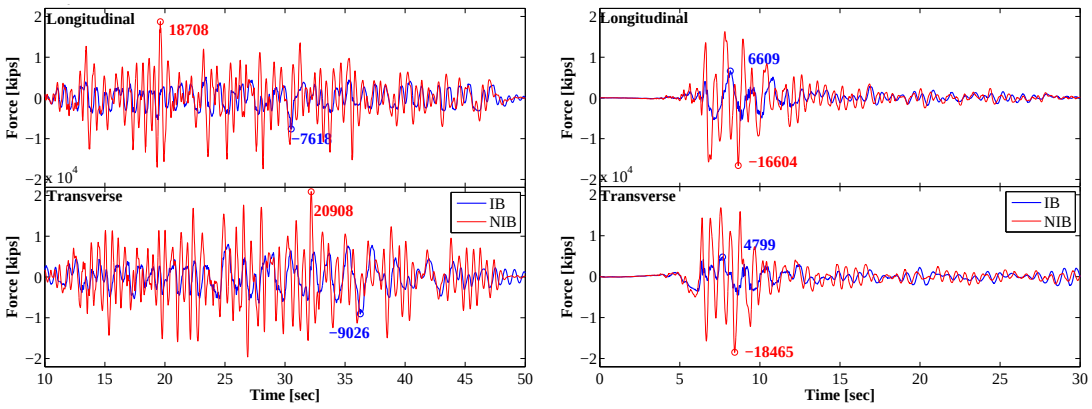

(a) (b)

Figure 4.19: Total base shear force across all piers under (a) NGA#832 and (b) NGA#183 of MCE hazard level

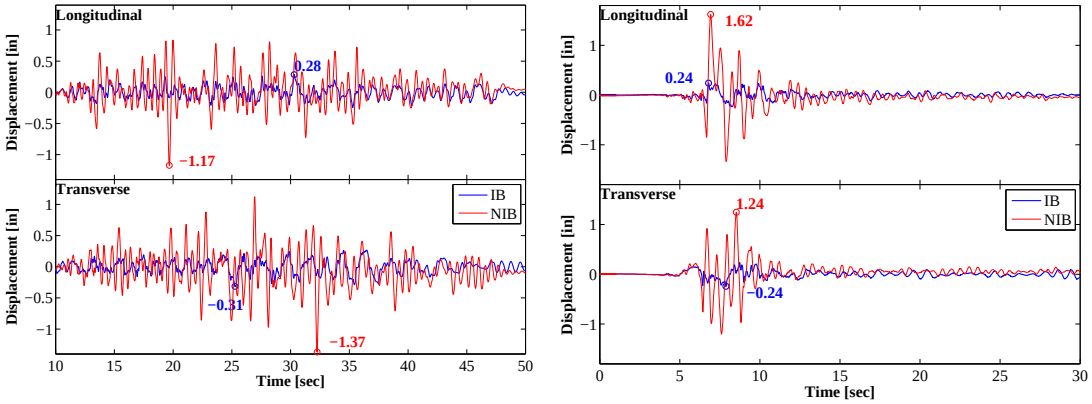

(a) (b)

Figure 4.20: Relative translation of pile foundation cap w.r.t. free-field ground surface under (a) NGA#832 and (b) NGA#183 of MCE hazard level

Comparison of local response quantities (i.e., the moment curvature relationship of the bottom section in pier #5) are presented in Figure 4.21(a), which implies that the pier column remains elastic for IB while it enters inelastic range for NIB. The pile foundation response under MCE of earthquake record NGA #832 is summarized in Figure 4.21(b).

The similar effects of seismic isolation as in the case of OBE are observed here. Seismic demand on the pile group foundation is smaller in IB compared to NIB, and the

reduction effects are more significant due to the higher level of shaking intensity. Under MCE hazard level ground motion, the maximum moment demand (10,800kip-ft) on piles in NIB is around the first yield moment (11,200kip-ft, defined as the moment corresponding to the first bar yield in the pile section). This implies that the piles are still in the elastic zone but close to enter the plastic zone. For NIB under MCE, more nonlinearity is observed in the typical soil spring located at the cap-pile-connection to represent the horizontal soil resistance. Under MCE hazard level ground motion excitation, seismic demands for the deeper zone of the piles are not negligible, because of the kinematic effects of the piles subjected to the depth-varied ground displacements obtained from the site response analysis.

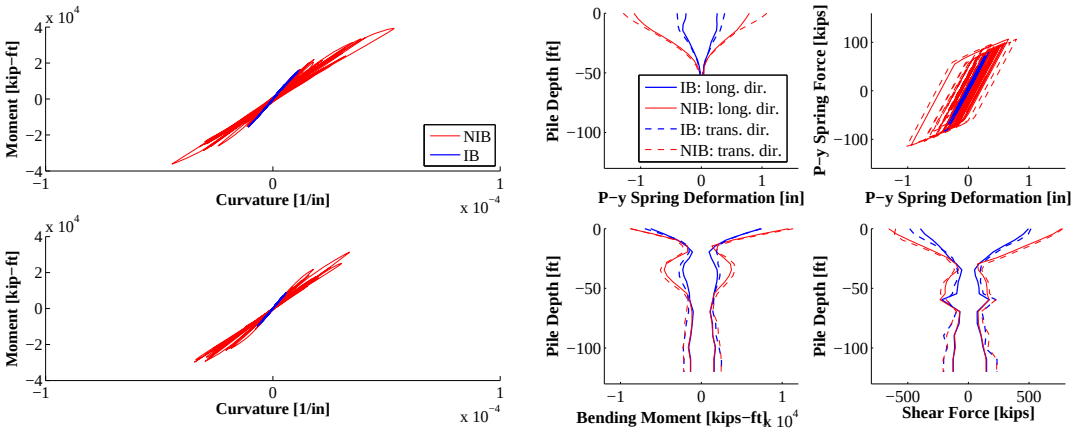

Figure 4.21: Envelope of peak rail stress due to axial force and bending under (a) NGA#832 and (b) NGA#183 of MCE hazard level

4.3.3. Comparison of seismic response distribution along the bridge for IB and NIB

Figure 4.22 shows the comparison of the maximum deformations in the longitudinal and transverse directions of isolators (bearings) for IB and NIB. The total bar height represents the response value under MCE event and the lower part represents the response value under OBE event. The maximum deformations of isolators along the bridge are almost the same for

IB in the longitudinal direction and show the first mode shape in the transverse direction. The counterpart in NIB is zero except that the non-isolation elastomeric bearings above abutments are deformed.

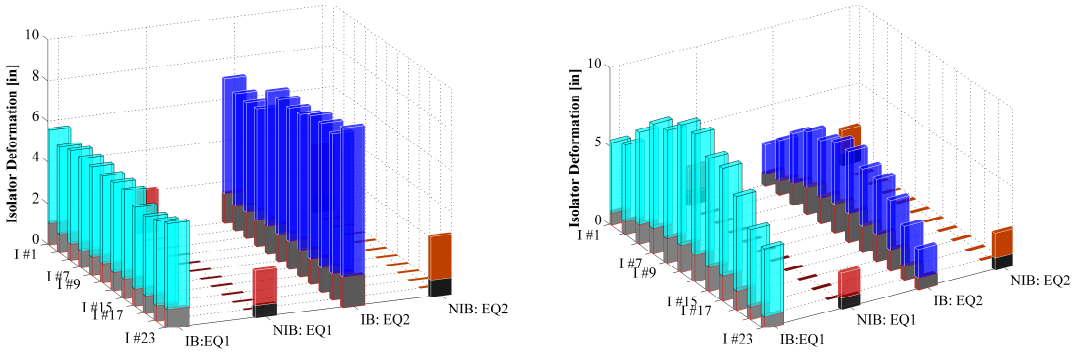

(a) (b)

Figure 4.22: Comparison of the maximum deformation in the (a) longitudinal direction and (b) transverse directions of all isolators (bearings)

Figure 4.23 shows the comparison of the maximum absolute accelerations for IB and NIB. For both earthquakes under OBE and MCE hazard levels, the acceleration reduction effect of seismic isolation is demonstrated clearly through the comparison between IB and NIB. It is also observed from the deck accelerations in the longitudinal direction for MCE events, the simulated acceleration of the side deck is relative higher than the middle or the other side frame. This is because the abutment gap pounding (e.g., the higher deck acceleration above pier #8 under EQ1 for IB corresponds to the pounding at right abutment, i.e., AG #3 and #4), and the higher acceleration is more correlated with the maximum pounding force than the pounding momentum or occurrence of pounding shown in Figure 4.24.

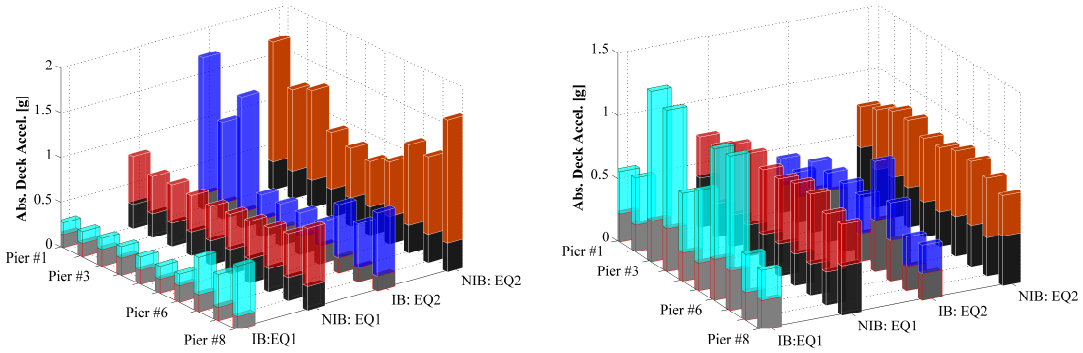

(a) (b)

Figure 4.23: Comparison of the maximum absolute acceleration in the (a) longitudinal and (b) transverse directions of bridge deck

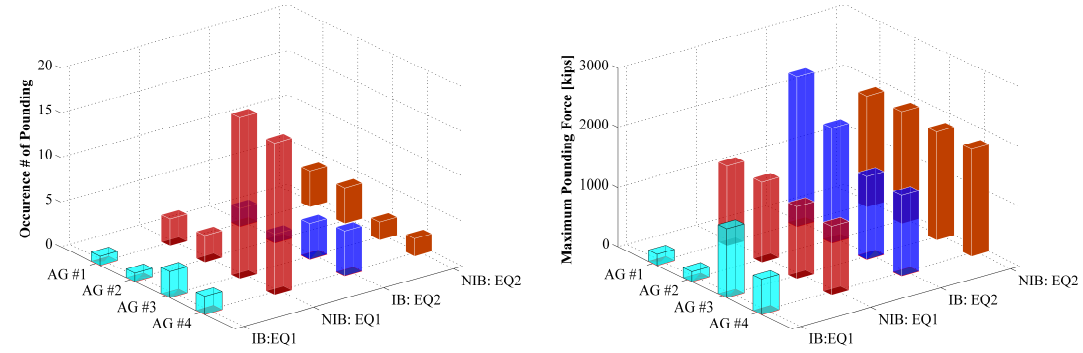

(a) (b)

Figure 4.24: Abutment gap pounding: (a) occurrence #, (b) pounding force

Figure 4.25 shows the distribution comparison of pier column base shear force, which indicates the reduction effect of seismic isolation on force demand on pier columns, which is significantly reduced especially under MCE hazard level events. It is also interesting to notice that the force distribution effect of seismic isolators on pier columns in the transverse direction: the distribution pattern can be adjusted by the installation of seismic isolators in between bridge deck and pier columns.

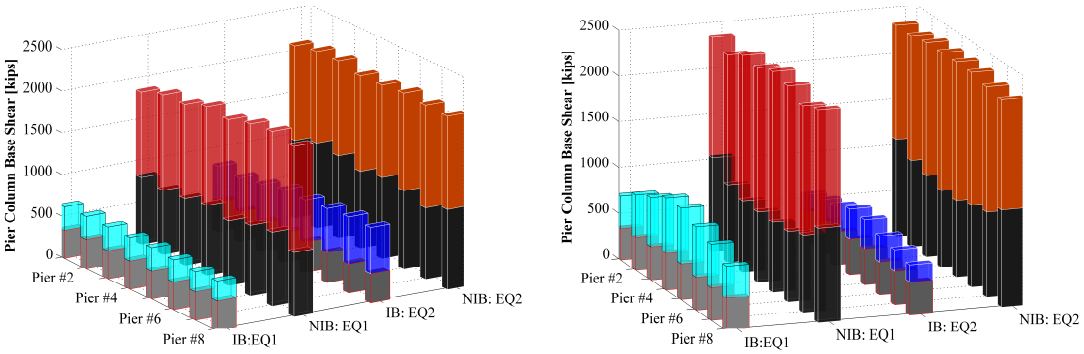

(a) (b)

Figure 4.25: Comparison of maximum pier column base shear force in the (a) longitudinal and (b) transverse directions

Figure 4.26 shows the comparison of pile foundation response. It is shown that the seismic isolation efficiently reduced the pile cap rotation for and the pile moment under both OBE and MCE events.

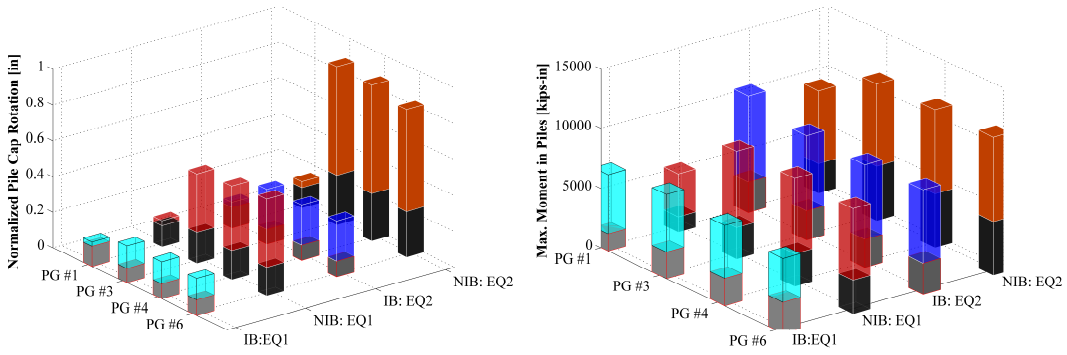

(a) (b)

Figure 4.26: Comparison of (a) maximum normalized pile cap rotation and (b) maximum pile moment around the transverse direction

Figure 4.27 shows the detrimental effect of seismic isolation in terms of imposing higher stress demand on rails especially at the vulnerable locations, i.e., expansion joints. The

stress demands due to axial and bending behavior at the abutment gaps are high for both IB and NIB, because the transverse continuity broken by the shear key gaps dominated the rail stress.

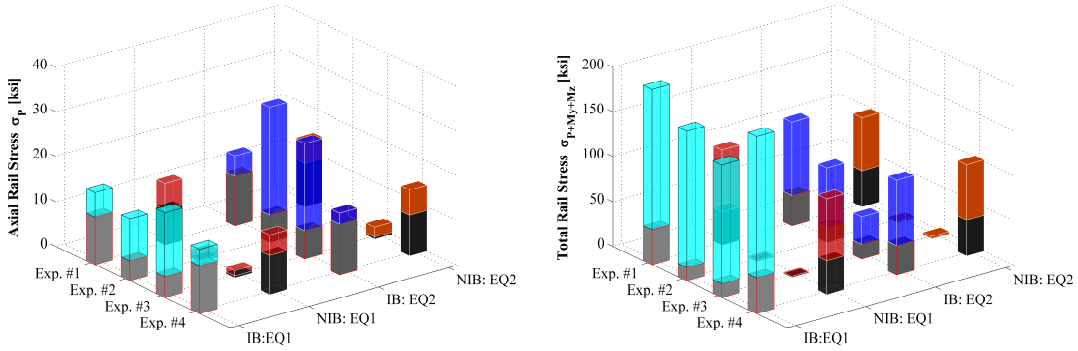

(a) (b)

Figure 4.27: Comparison of rail stresses (a) due to axial force and (b) due to both axial and bending

4.4. Conclusions

Based on the fully nonlinear three-dimensional (3D) finite element (FE) model of the selected California High-Speed Rail (CHSR) Prototype Bridge presented in Chapter 3, seismic simulations are carried out in this chapter to understand the dynamic behavior of the bridge under earthquake ground motions with different hazard levels, Operating Basis Earthquake (OBE) and Maximum Considered Earthquake (MCE). Two types of earthquake ground motions, non-pulse like representing far-field conditions and pulse-like ground motion representing near fault conditions are considered. Focusing on the comparispm between the seismic response of seismic isolated bridge (IB) and non-isolated bridge (NIB), the beneficial and detrimental effects of seismic isolation to the CHSR Prototype Bridge are investigated in terms of the bridge structure, pile foundation, and track response. Consistent observations are

observed and can be summarized as follows: (1) introduction of seimsic isolation can effeciently decrease the deck acceleration for earthquakes of high intensity level if spikes due to pounding and/or impact are not considered; (2) the bridge deck displacement increases, largely concentrated in seismic isolators, while the pier top drift decreases; (3) seismic demand on the substructures (i.e., bottom moment/curvature, total base shear force) is reduced by more than 50%, especially for large earthquakes (i.e., MCE); (4) the seismic isolation is beneficial for the foundation (i.e., pile cap displacement/rotation, pile moment/shear), leading to lower cost for construction of pile group foundation; (5) rail stress increases due to larger deck displacement, espcially for the bending stress caused by the transverse movement of the bridge, and the critical locations of rail failure lies in the neighborhood of abument gaps and interior expansion joints; (6) axial rail stress under OBE is still lower than the allowable rail sterss specified in the design criteria, even when seismic isolation is considered. The deterministic performance evalutation of the seismic isolations in the CHSR Prototype Bridge carried out in this chapter indicates the feasibility using seismic isolation. A further probabilsitic evaluation will be followed in next Chapter.

CHAPTER 5

PROBABILISTIC PERFORMANCE EVALUATION OF SEISMIC ISOLATION FOR THE CHSR PROTOTYPE BRIDGE

5.1. Introduction

In Chapter 4, the seismic simulations were carried out on the CHSR Prototype Bridge with and without seismic isolation (i.e., IB and NIB respectively), focusing on the performance evaluation of seismic isolation under a single earthquake scenario. The beneficial and detrimental effects of seismic isolation on the CHSR Prototype Bridge were then explored and demonstrated from a deterministic point of view. In this Chapter, a probabilistic performance evaluation of the seismic isolation in the CHSR Prototype Bridge is performed to determine the feasibility of seismic isolation for the CHSR bridges.

Sources of uncertainty in engineering safety problems can be classified into two major groups: aleatory variability and epistemic uncertainty, which are well-known concepts and terms widely used in seismic risk analysis. Aleatory variability is the natural or inherent randomness in a physical phenomenon, such as the time of occurrence and magnitude of future earthquakes in a region, and the record-to-record variability (e.g., amplitude, phase, and

duration of ground motion records). Epistemic uncertainty is the scientific uncertainty in the modeling process of the physical phenomenon due to limited understanding and experimental data, which can be reduced with larger sample size and using better models.

In the risk assessment of civil structures for seismic design and performance evaluation, a considerable number of uncertainties arise from the modeling and simulation process, including uncertainties associated with the seismic excitation. For example, uncertainties are inherent with events of a specified structural limit-state (i.e., thresholds of structural behavior) exceedance for a structural system subjected to future earthquake ground motions. In view of the sweeping uncertainties in the occurrence of earthquakes and record-to-record variability, in this research, the probabilistic seismic performance evaluation of the CHSR Prototype Bridge is limited to the uncertainties in the seismic excitations. Thus, a deterministic model for the CHSR Prototype Bridge without model uncertainties is employed to propagate the uncertainties in the seismic loading to the structural response with probabilistic quantification. Although the focus is placed on the uncertainties in earthquake loadings, the integrated framework developed and tested for probabilistic performance evaluation and optimization in the context of PBEE will be adapted to include other uncertainties easily as pointed out in Chapter 2.

In the context of the PEER PBEE methodology, the probabilistic seismic hazard analysis accounts for the uncertainties in the intensity measures (IMs) of earthquakes though probabilistic seismic hazard curve. The disaggregation of the probabilistic seismic hazard guides the ground motion selection, and the record-to-record variability among the selected ground motions is considered in the conditional demand hazard analysis. The record-to-record variability is reflected in the conditional probability of a certain engineering demand parameters (EDP) given a hazard level of earthquake ground motions. It is worth noting that

due to limited number of records available or selected as well as the mathematical model adopted (e.g., cloud method, stripe method), the epistemic uncertainties are also in the estimated conditional demand hazard analysis. In the second step of PBEE, i.e., probabilistic seismic demand hazard analysis, a convolution of the conditional demand hazard analysis results with the seismic hazard curve leads to the probabilistic demand hazard curve, compounding both the uncertainties in the seismic loadings (i.e., seismic hazard characterized by IM and record-to-record variability).

A comparison of the probabilistic performance of the IB and NIB configurations of the CHSR Prototype Bridge is also evaluated focusing on the probabilistic seismic demand hazard analysis. The uncertainties in the seismic loading is propagated to the structural demand (state) variables, i.e., EDPs such as the absolute deck acceleration, relative deck displacement, pier drift, pier column base moment/curvature, total base shear force, pile foundation translation/rotation, pile moment/shear, rail stress, etc.. The record-to-record comparison as well as conditional probabilistic demand comparison given a certain hazard level, and the probabilistic demand comparison are presented in this chapter, showing the beneficial and detrimental effects of seismic isolation on CHSR Prototype Bridge.

5.2. Ground Motions

As introduced in the formulation and implementation of the PBEE methodology in Chapter 2, after the site-specific probabilistic seismic hazard analysis, an ensemble of earthquake ground motions is selected to perform seismic simulations on the CHSR Prototype Bridge system based on the disaggregation of seismic hazard for the selected site and structural system. A brief introduction is presented here on the ground motion database, the probabilistic seismic hazard analysis, and a probability estimation of pulse-like ground motions for the selected site.

5.2.1. Ground motion database

The PEER Ground Motion Database (PGMD) includes metadata for a large set of ground motions recorded worldwide of shallow crustal earthquakes in active tectonic regions. This database is still under development in phase two as NGA-West2 following the NGA project (2003-2005), which was built from the PEER Strong Motion Database (1997-2000), containing 1557 records in as-recorded orientations from 143 earthquakes from tectonically active regions. The PEER NGA Database (2003-2005), includes 3551 records from 173 earthquakes, with magnitudes ranging from M4.3 to M7.9, more extensive meta-data, and some corrections to information in the original database. The database was used to develop the 2008 NGA (i.e., Next Generation ground motion Attenuation models) Ground Motion Prediction Equations (GMPEs), later adopted by USGS for development of the national/regional seismic hazard maps for deterministic analysis.

The latest PEER Ground Motion Database Beta Version (PGMD-beta) contains 3182 three-component records (369 records were excluded from the PEER NGA Database). In PGMD-beta, fault parallel (FP) and fault normal (FN) components, besides as-recorded orientations, are provided with pulse-like flag available for strike-normal and strike-parallel orientations.

At sites close to active faults, the fault-normal direction can experience significantly larger intermediate- and long-period ground motions than the fault-parallel direction. Thus for the selected site for the CHSR Prototype Bridge, the application angle of the two ground motion components over the simulated structure should be distinguished. Consequently, only earthquake ground motions with known FP and FN components are selected from the latest database of PGMD-beta.

5.2.2. Probabilistic seismic hazard analysis

To assess the seismic hazard at a specific site, the Probabilistic Seismic Hazard Analysis (PSHA), originally proposed and developed by Cornell (1968), aims to characterize the earthquake intensity measure (IM) probabilistically, e.g., the MAR curve of IM. The PSHA is based on the Total Probability Theorem (TPT), accounting for the uncertainties inherent in the earthquake ground shaking, including the time of occurrence, the Magnitude, the source-to-site distance, and the resulting IM of interest. Further development and implementation has been accomplished by other researchers in this field (e.g., Kramer 1996, Shome et al. 1998, Baker 2011, Luco and Cornell 2002, Field et al. 2003), and several analytical tools are now available, such as OpenSHA (Field et al. 2003), the web application PSHA tool (USGS 2008 Interactive De-aggregations, http://earthquake.usgs.gov/hazards/) developed by the U.S. Geological Survey (USGS). In this research, the USGS PSHA tool is adopted to obtain the probabilistic seismic hazard analysis results including the deaggregation.

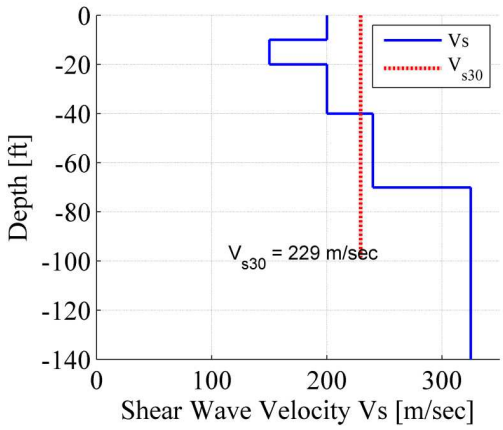

Figure 5.1: Average shear wave velocity in the top 30 meters

For the given site location and soil condition of the CHSR Prototype Bridge, described in Chapter 4, featured with the average shear wave velocity in the top 30 meters (Vs_{30}, see in Figure 5.1), the USGS tool provides the 5% damped spectral acceleration at 10 periods (i.e.,

0.0sec, 0.1sec, 0.2sec, 0.3sec, 0.5sec, 1.0sec, 2.0sec, 3.0sec, 4.0sec, and 5.0sec) corresponding to 30 different seismic hazard levels ranging from a probability of exceedance of 50% in 30 years to 1% in 200 years. In terms of return period, the hazard range is from 43 years to 19900 years.

Based on the PSHA results, the hazard spectrum surface for the downtown area in San Jose, California, is presented in Figure 5.2. The Intensity Measure IM = Sa(T, ξ=5%) can then be determined for a given hazard level and period of the structural system (T). Uniform hazard spectrum for a certain fixed hazard level (e.g., 950 years) can be obtained, and the probabilistic hazard curve using the intensity measure, IM = Sa (T, ξ = 5%), can be obtained for a given period (T) to determine the intensity measure. For example, the probabilistic seismic hazard curves for IB and NIB systems using the 5% damped spectral acceleration at their fundamental periods as intensity measure are shown in Figure 5.3, which includes the 7 hazard levels to be considered in the analysis.

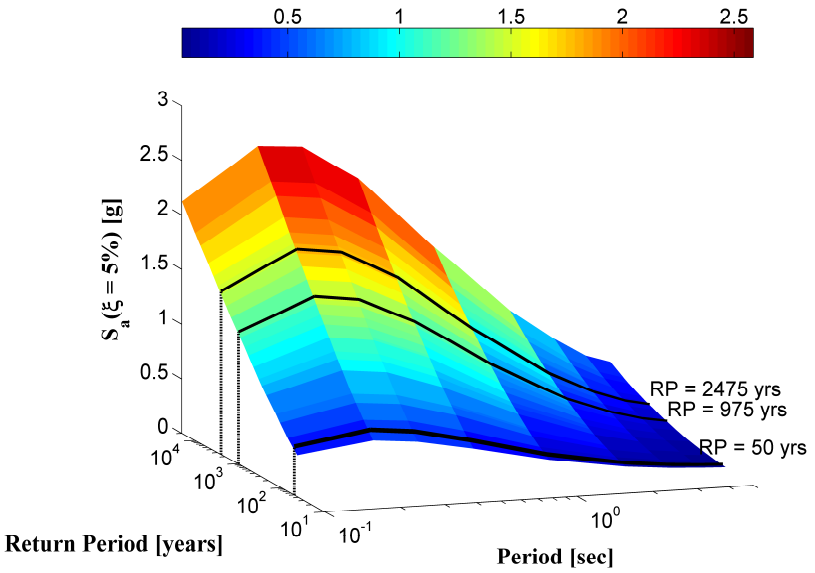

Figure 5.2: Hazard spectrum surface for downtown area of San Jose, California.

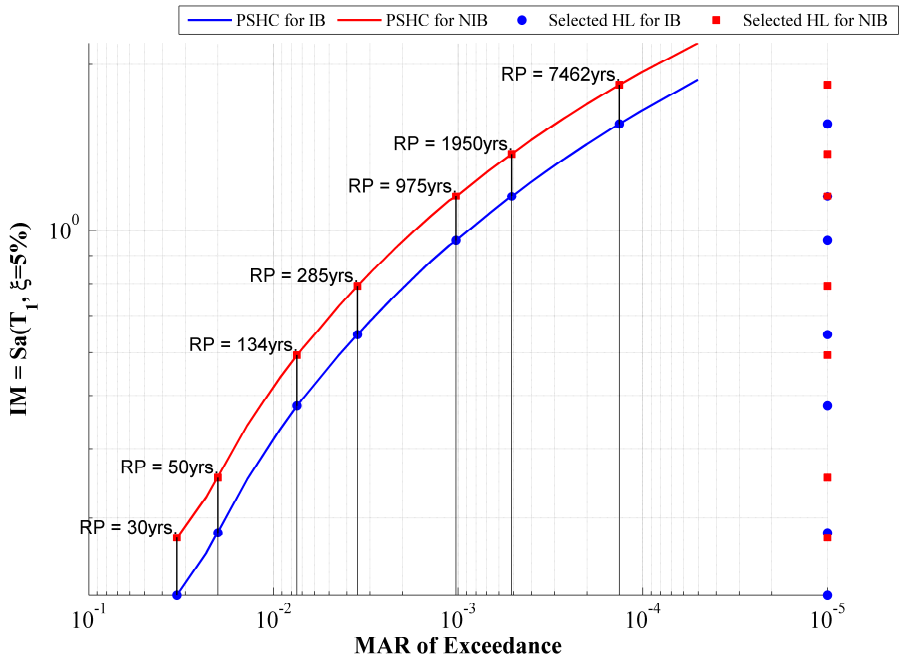

Figure 5.3: Probabilistic seismic hazard curves for both the IB and NIB

Figure 5.4 to Figure 5.6 present the de-aggregation results of the seismic hazard points at T = 1.0sec with return periods (RPs) of 2475, 950, and 43 years respectively. The bins in the bar plots represent the contribution to the seismic hazard based on the source-to-site distance and magnitude of the seismic events. From the de-aggregation results, the main contribution to the seismic hazard comes from earthquakes with magnitudes between 6.0 and 8.0, and a source-to-site distance in the range between 0 and 20km, which is consistent with the distance to the faults nearby, as illustrated in Table 5.1. Figure 5.6 shows that for lower hazard levels, earthquakes of smaller magnitude have a more significant contribution to the seismic hazard.

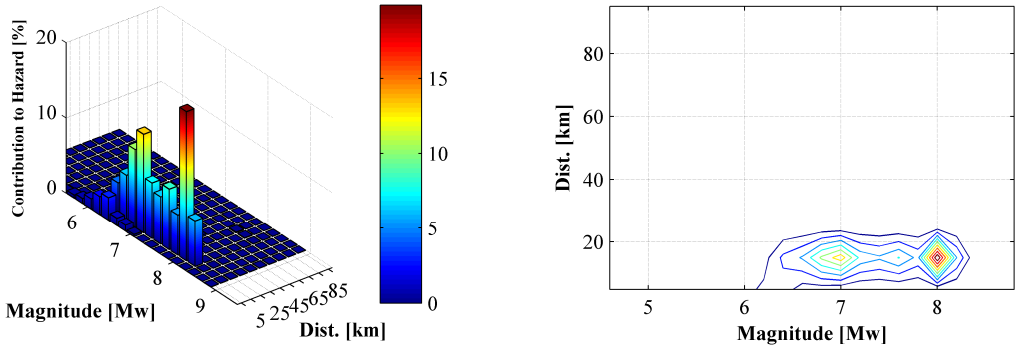

Figure 5.4: Probabilistic seismic hazard de-aggregation for San Jose (121.903W, 37.330N) at Sa (T = 1.0, ξ = 5%) for probability of exceedance of 2% in 50 years

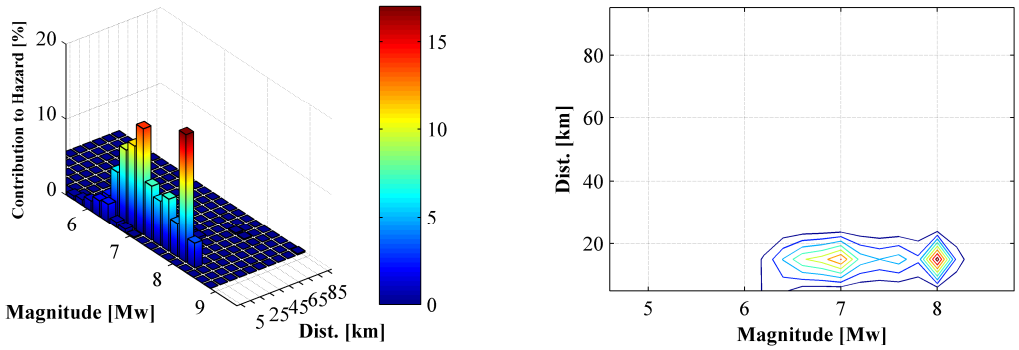

Figure 5.5: Probabilistic seismic hazard de-aggregation for San Jose (121.903W, 37.330N) at Sa (T = 1.0, ξ = 5%) for probability of exceedance of 10% in 100 years

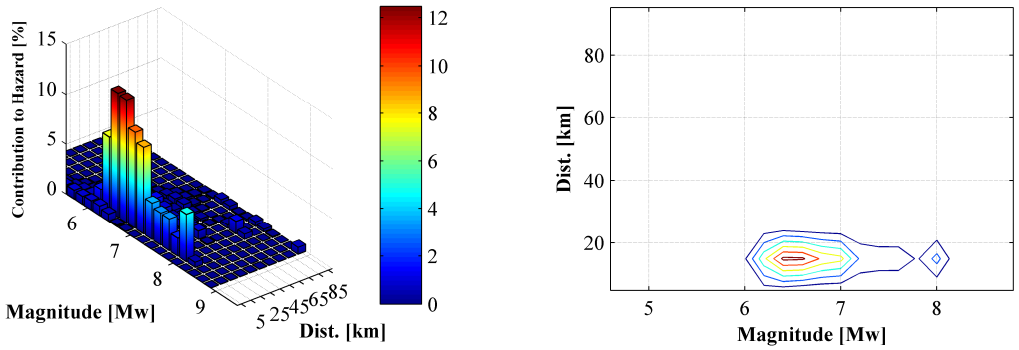

Figure 5.6: Probabilistic seismic hazard de-aggregation for San Jose (121.903W, 37.330N) at Sa (T = 1.0, ξ = 5%) for probability of exceedance of 50% in 50 years

Based on the de-aggregation results, a set of 40 ground motions were selected for the analysis following the selection procedure described in Baker et al. (2011). The selected ground motions were scaled to capture the system's performance over a wide range of earthquake intensity levels, in order to increase the amount of data for a seismic demand statistics' prediction. The scaling strategies are described in the following section depending on the approach for the conditional demand hazard analysis (stripe method or cloud method).

Table 5.1: Representative faults' close to San Jose site (From Caltrans ARS)

Fault #.	Fault	Site to fault Distance
1	Silver Creek	2.82km
2	Cascade fault	6.09km
3	San Andreas (Santa Cruz Mts.)	17.88km
4	San Andreas (Peninsula)	19.40km
5	Hayward (Southern extension)	10.38km
6	Monte Vista-Shannon	8.82km
7	Hayward (South)	17.21km
8	Calaveras (Central)	14.41km
9	Calaveras (North)	16.40km
10	Sargent fault (northwestern section)	21.93km

5.2.3. Ground motion selection

An appropriate set of ground motions, with two horizontal components for each record, is selected from the PEER Ground Motion Database (beta version) based on the probabilistic seismic hazard analysis results. The metadata of the selected ground motion records are listed in Table 5.2, including the NGA number, occurrence year, event name, station name, magnitude, and Campbell Distance provided in the database of PGMD-beta, as well as the pulse indicator based on the quantitative classification of near-fault ground motions using wavelet analysis (Baker, 2007).

Table 5.2: Selected ground motions for CHSR Prototype Bridge

NO.	NGA #	Event Name	Year	Station	Mag.	Camp. Dist. R (km)	Pulse Flag	
							FP	FN
1	126	Gazli, USSR	1976	Karakyr	6.80	5.46	0	0
2	180	Imperial Valley-06	1979	El Centro Array #5	6.53	4.82	0	1
3	181	Imperial Valley-06	1979	El Centro Array #6	6.53	3.49	1	1
4	182	Imperial Valley-06	1979	El Centro Array #7	6.53	3.59	1	1
5	723	Superstition Hills-02	1987	Parachute Test Site	6.54	3.53	0	1
6	779	Loma Prieta	1989	LGPC	6.93	3.88	1	0
7	821	Erzican, Turkey	1992	Erzincan	6.69	4.38	1	1
8	825	Cape Mendocino	1992	Cape Mendocino	7.01	6.96	1	0
9	879	Landers	1992	Lucerne	7.28	3.71	0	1
10*	982	Northridge-01	1994	Jensen Filter Plant	6.69	5.43	0	1
11	983	Northridge-01	1994	Jensen Filter Plant Gen.	6.69	5.43	0	1
12	1004	Northridge-01	1994	LA - Sepulveda VA Hosp.	6.69	8.44	0	0
13	1044	Northridge-01	1994	Newhall - Fire	6.69	5.92	0	0
14	1045	Northridge-01	1994	Newhall - W Pico Canyon	6.69	5.48	1	1
15	1063	Northridge-01	1994	Rinaldi Receiving	6.69	6.50	1	1
16	1084	Northridge-01	1994	Sylmar - Converter	6.69	5.35	0	1
17*	1085	Northridge-01	1994	Sylmar - Converter East	6.69	5.19	0	1
18	1086	Northridge-01	1994	Sylmar - Olive View	6.69	5.30	0	1
19	1087	Northridge-01	1994	Tarzana - Cedar Hill A	6.69	15.6	0	0
20	1106	Kobe, Japan	1995	KJMA	6.90	3.23	0	0
21*	1119	Kobe, Japan	1995	Takarazuka	6.90	3.00	0	1
22	1120	Kobe, Japan	1995	Takatori	6.90	3.45	0	1
23	1176	Kocaeli, Turkey	1999	Yarimca	7.51	5.31	1	0
24	1244	Chi-Chi, Taiwan	1999	CHY101	7.62	15.4	0	1
25	1492	Chi-Chi, Taiwan	1999	TCU052	7.62	5.00	0	0
26	1503	Chi-Chi, Taiwan	1999	TCU065	7.62	6.72	0	1
27	1504	Chi-Chi, Taiwan	1999	TCU067	7.62	6.54	0	0
28	1505	Chi-Chi, Taiwan	1999	TCU068	7.62	5.62	1	1
29	1507	Chi-Chi, Taiwan	1999	TCU071	7.62	5.14	0	0
30	1509	Chi-Chi, Taiwan	1999	TCU074	7.62	13.4	0	0
31	1517	Chi-Chi, Taiwan	1999	TCU084	7.62	11.2	0	0
32	1529	Chi-Chi, Taiwan	1999	TCU102	7.62	7.74	1	1
33	1549	Chi-Chi, Taiwan	1999	TCU129	7.62	6.96	0	0
34	1595	Chi-Chi, Taiwan	1999	WGK	7.62	15.4	1	0
35	1602	Duzce, Turkey	1999	Bolu	7.14	12.4	1	0
36	1605	Duzce, Turkey	1999	Duzce	7.14	6.59	1	0
37	2114	Denali, Alaska	2002	TAPS Pump Station #10	7.90	3.75	1	0
38	1197	Chi-Chi, Taiwan	1999	CHY028	7.62	8.72	0	0
39	183	Imperial Valley-06	1979	El Centro Array #8	6.53	5.61	0	1
40	832	Landers	1992	Amboy	7.28	69.3	0	0

Since the PSHA results did not explicitly account for the near fault ground motion hazard, the ground motion selection algorithm adopted here did not require the proportion of pulse-like ground motions either. The ground motions records were selected with 50% (20 out of 40) categorized as pulse-like type in the fault-normal direction, and 35% (14 out of 40) categorized as pulse-like type in the fault-parallel direction.

Since the longitudinal direction of CHSR Prototype Bridge is parallel with most near-faults, the rotated ground motion components are used for seismic simulation input. The FP and FN components are applied as the longitudinal and transverse excitations respectively without considering the excitation angles.

5.2.4. Ground motion scaling

The ground motions are usually scaled by a factor for two reasons: to scale the ground motions to match a target intensity measure (IM) value, $S_a(T_1,\ \xi = 5\%)$, as used in stripe method; or to scale ground motions to expand the sample size for other intensity range of interest, as used in the "cloud" method.

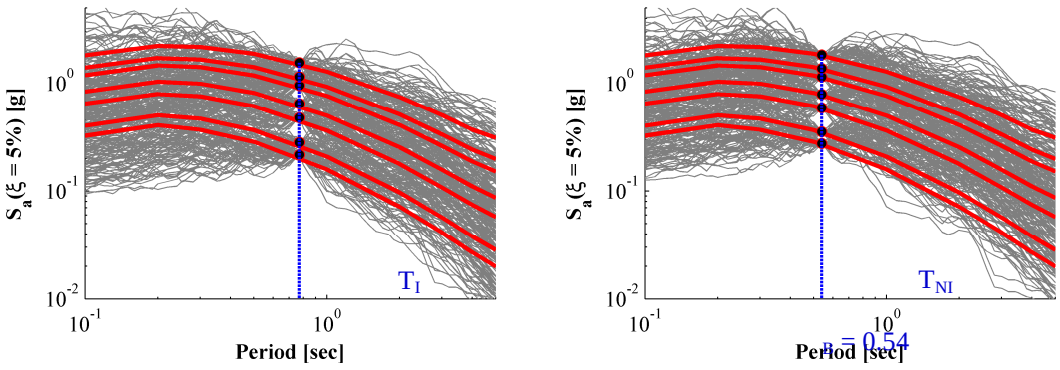

(a) (b)

Figure 5.7: Ground motions scaling for the stripe method to target 7 hazard levels: (a) IB, and (b) NIB

Both stripe and “cloud” methods are used in the probabilistic demand hazard analysis for the CHSR Prototype Bridge. In the stripe method, the ground motions are scaled to match a target IM value for both IB and NIB models at seven hazard levels with return periods as 30 years, 50 years, 134 years, 285 years, 975 years, 1950 years and 7462 years, as presented in Figure 5.7.

5.2.5. Ground motion de-convolution for depth-varied displacements

For the dynamic p-y approach used to account for soil-foundation-structure interaction (SFSI), the free field displacement histories are required to be prescribed at the free (i.e., far-field) ends of all the p-y springs at different depth along the piles. Site response analysis is well known to quantify the site effects on the ground motions. Thus instead of using identical ground motion inputs as the free field ground surface motion, a de-convolution analysis is necessary to account for the site effects to obtain the depth-varied ground motions.

A one-dimensional site response analysis is usually employed to account for the ground motion variation along the depth of piles. Using the computer software SHAKE91, all scaled ground motions are prescribed as the free field ground surface motion for the layered soil profile, and de-convolved to obtain the depth-varied ground displacement time series for the seismic inputs in multiple-support-excitation.

5.3. Computational Models for Isolated Bridge (IB) and Non-isolated Bridge (NIB)

To investigate the effect of seismic isolation in the CHSR Prototype Bridge in terms of the probabilistic seismic performance, instead of a single earthquake scenario, the same computational models (IB and NIB) from the deterministic comparison in Chapter 4 are used in the analysis. The IB is the finite element (FE) model for the CHSR Prototype Bridge with seismic isolators placed between the bridge piers/abutment stem-walls and the bridge deck. The NIB is FE model corresponding to the comparative bridge without seismic isolation

system, where the single-column piers and bridge deck are rigidly connected and the bridge deck is supported on non-isolated elastomeric bearing pads at the abutments.

5.4. Probabilistic Seismic Demand Hazard Analysis: Stripe Method

The stripe method is first employed to estimate the probabilistic characterization of the structural response (i.e., various EDPs). The seismic simulations of the CHSR Prototype Bridge models (IB and NIB) are carried out for an ensemble of 280 ground motions, with intensity measures (IM) corresponding to seven hazard levels.

Before performing the probabilistic or statistical analysis of the seismic response over a continuous range of hazard levels, further insight into the seismic isolation effects is obtained from a record-by-record comparison of the system performance for a given hazard level in terms of various EDPs (i.e., structural response, foundation response, and rail response). The comparison results between IB and NIB for two representative hazard levels (i.e., OBE and MCE) are presented to illustrate the seismic response of the system individually subjected to relatively small earthquakes and strong earthquakes.

5.4.1. Record-by-record comparison under OBE hazard level earthquakes

The seismic response of the IB and NIB subjected to 40 ground motions scaled to the targeted OBE hazard level are compared individually.

Structural Response

Figure 5.8 shows the absolute acceleration of the bridge deck over pier #5 in both the longitudinal direction and transverse direction of the bridge. From the mean values of the absolute acceleration, the seismic isolation reduced the deck acceleration in the longitudinal and transverse direction by 32% to 27% respectively. While the deck acceleration of IB in the longitudinal direction is always smaller than in NIB, for transverse direction, six out of the

forty cases show a higher acceleration due to the impacts in transverse direction in the SHJ devices at interior expansion joints.

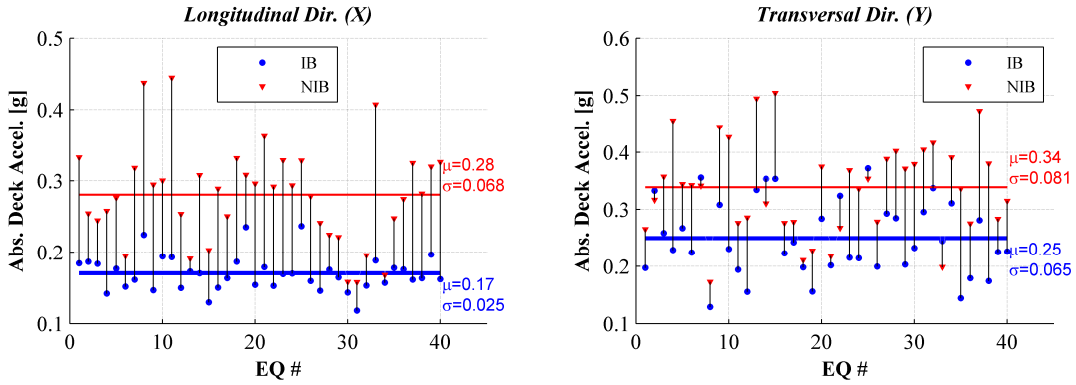

Figure 5.8: Comparison of absolute acceleration of bridge deck over pier #5 with mean value lines (IB: circular markers; NIB: triangular markers)

Besides the maximum absolute deck acceleration, the root mean square (RMS) of the absolute acceleration time history is presented in Figure 5.9, showing the beneficial effects of seismic isolation to the overall acceleration level on the bridge deck, except the spiky acceleration of high-frequency due to the closing of gaps in the bridge in a few earthquakes.

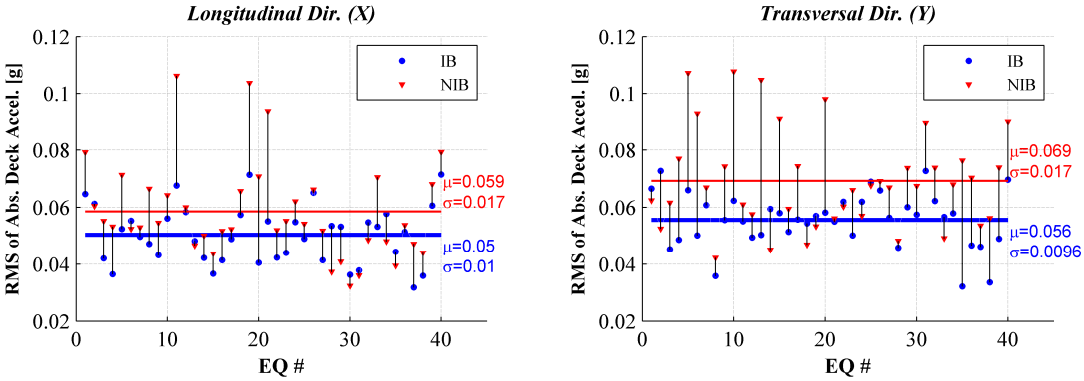

Figure 5.9: Comparison of RMS of absolute acceleration of bridge deck over pier #5 with mean lines (IB: circular markers; NIB: triangular markers)

Figure 5.10 presents the relative displacement of the deck over pier #5 with respect to the ground surface. For NIB the displacement consists of the contribution of foundation rotation, foundation translation, and pier column deflection. In contrast, the displacement of the deck for IB is primarily due to the deformation of the seismic isolator with a smaller contribution of the three mechanisms in the case of NIB. The seismic isolation increases the deck displacement in both the longitudinal and transverse direction by 80% and 170% on average respectively. The displacement demand on the pier columns and foundations is decreased as shown later, protecting the substructure system of CHSR prototype bridge.

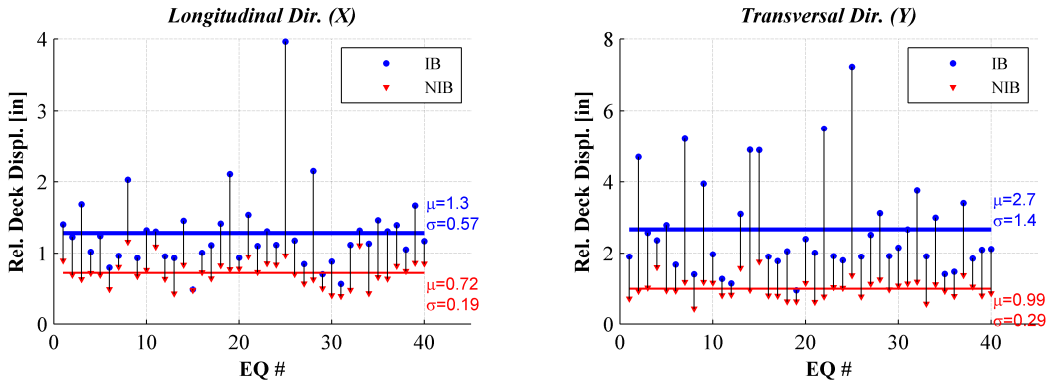

Figure 5.10: Comparison of relative displacement of bridge deck over pier #5 w.r.t. ground surface with mean lines (IB: circular markers; NIB: triangular markers)

Figure 5.11 shows the deformation concentrated in the seismic isolator over pier #5 in the longitudinal and transverse directions respectively compared to the resultant deformation. It is observed that the deformation of seismic isolator is about the same magnitude of the deck displacement in both directions, and the resultant deformation is only slightly bigger than the deformation in transverse direction. The resultant deformation in the seismic isolator over pier #5 is dominated by the deformation component in transverse direction, while this depends on the location of seismic isolators in that the seismic isolators close to the bridge ends experience more deformation in the longitudinal direction.

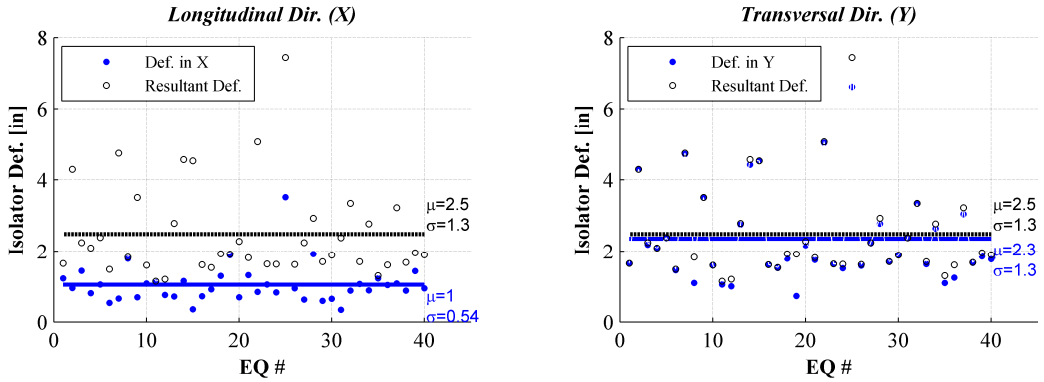

Figure 5.11: Deformation of seismic isolators over pier #5 with mean lines for IB model (with resultant displacement denoted by circular unfilled markers)

Figure 5.12 shows the beneficial effect of seismic isolation on the displacement demand of pier column top with respect to the pile cap. On average, the displacement demand on pier column is around 60% smaller for IB compared to NIB for the OBE hazard level.

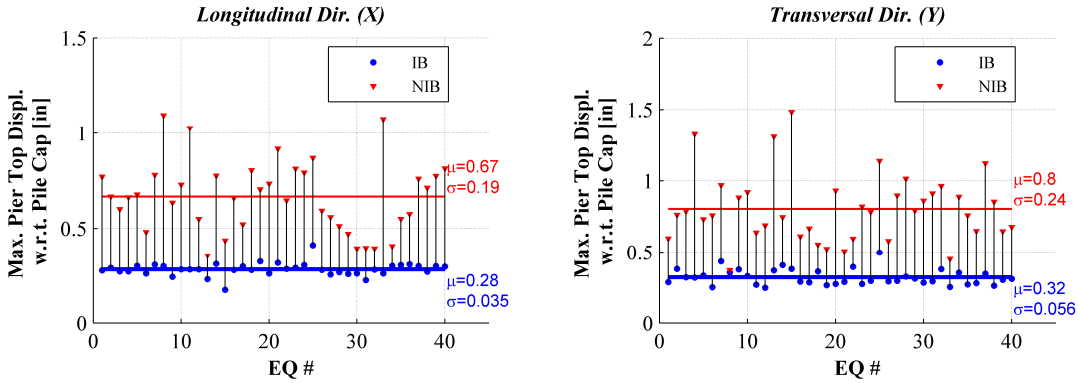

Figure 5.12: Comparison of relative displacement of top of pier #5 w.r.t. pile foundation cap with mean lines (IB: circular markers; NIB: triangular markers)

Consistent with the displacement demand on the substructure of the bridge, Figure 5.13 displays the base shear demand on the pier column in the longitudinal and transverse directions. From the comparison of the seismic response under OBE between IB and NIB, the seismic isolation system reduces the base shear force demand on pier column #5 by 50% on

average. Furthermore, the seismic isolation highly reduces the variation (uncertainties) in the force demand, which is beneficial for the reliability of bridge structures.

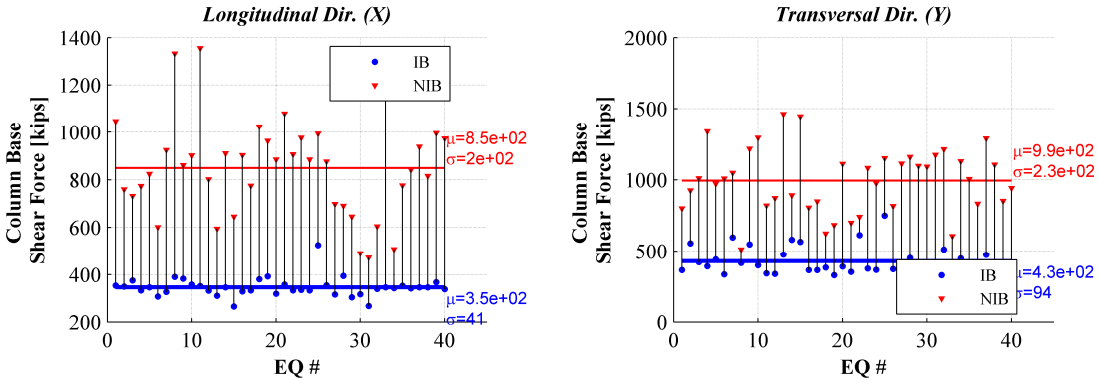

Figure 5.13: Comparison of peak base shear in pier column #5 with mean lines (IB: circular markers; NIB: triangular markers)

Besides the force demand on the single pier column #5 above, the total base shear force across all pier columns and the total horizontal reaction force to the bridge structure (total base shear force plus pounding forces at abutment gaps) comparison is presented in Figure 5.14 to Figure 5.15. As expected, the force demand on the entire bridge system is reduced by more than 60% on average by the seismic isolation system in IB, which reduces the force demand on the bridge substructure system.

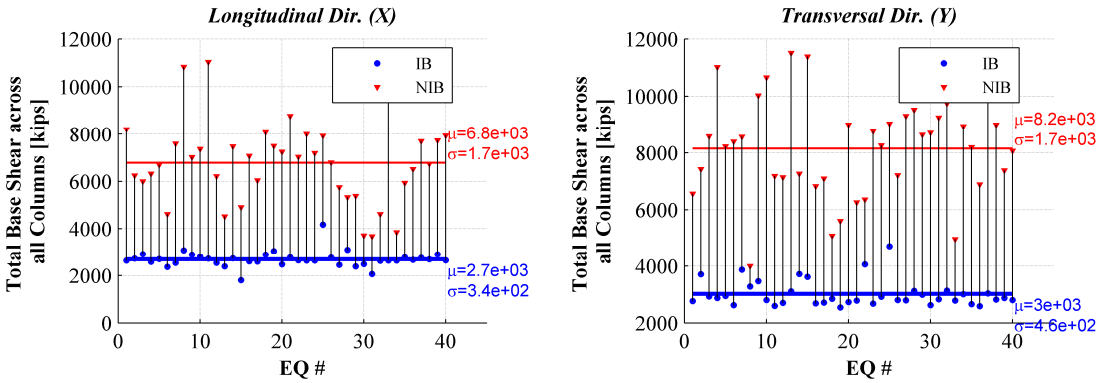

Figure 5.14: Comparison of total base shear force across all pier columns with mean lines (IB: circular markers; NIB: triangular markers)

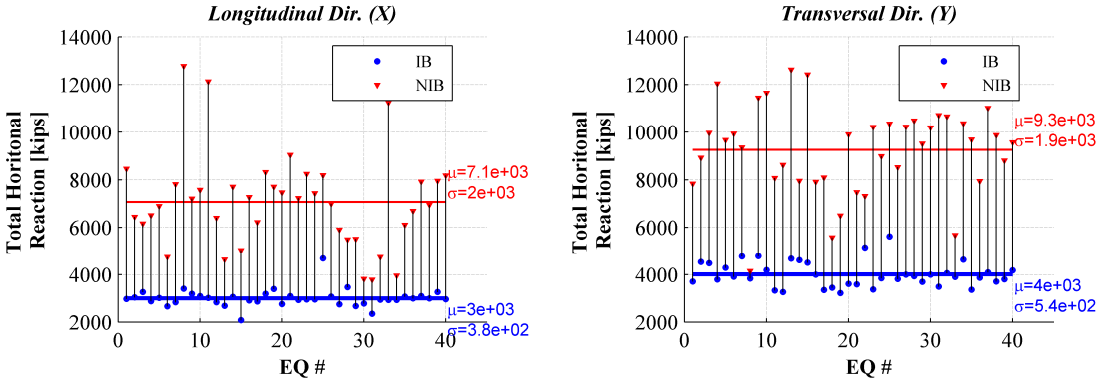

Figure 5.15: Comparison of total horizontal reaction (total base shear force + pounding force) with mean lines (IB: circular markers; NIB: triangular markers)

Foundation Response

Similar to the force demand on bridge pier columns, a reduction in the demand on the foundation system is also expected. Figure 5.16 and Figure 5.17 show the pile cap translation and normalized pile cap rotation (i.e., the equivalent pier top drift due to this rotation) of pile foundation under pier #5 respectively. The displacement demand on the pile group in IB is around 50% of the demand in NIB.

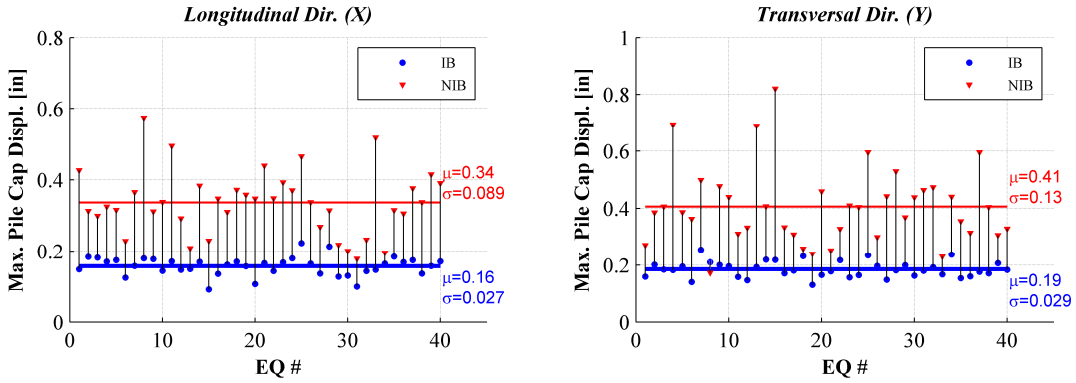

Figure 5.16: Comparison of maximum pile cap translation of foundation under pier #5 with mean lines (IB: circular markers; NIB: triangular markers)

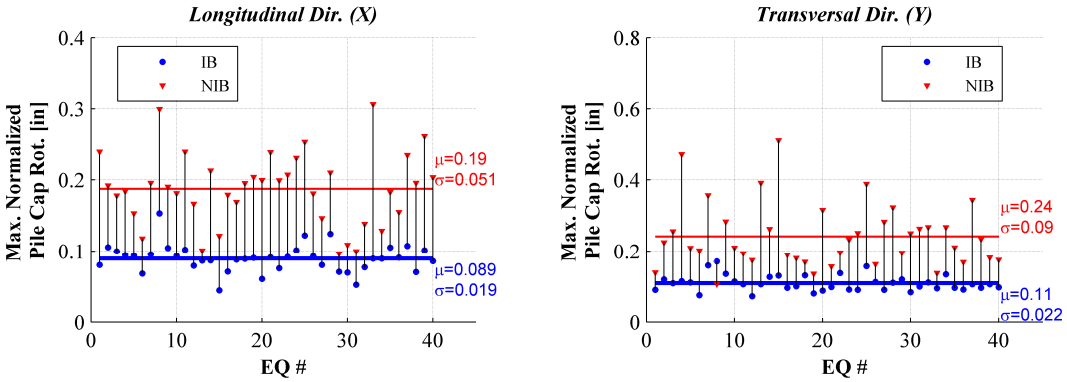

Figure 5.17: Comparison of maximum pile cap rotation of foundation under pier #5 with mean lines (IB: circular markers; NIB: triangular markers)

Figure 5.18 and Figure 5.19 compare maximum bending moment and shear force demand in piles under pier column #5 for OBE hazard level earthquakes. The introduction of seismic isolation into the CHSR Bridge shows a reduced effect in reducing the demand over the piles compared to the results obtained for the piers. This could be explained as only the inertial effect is reduced by the isolation system but not the kinematic effect in the soil-pile-structure interaction effect.

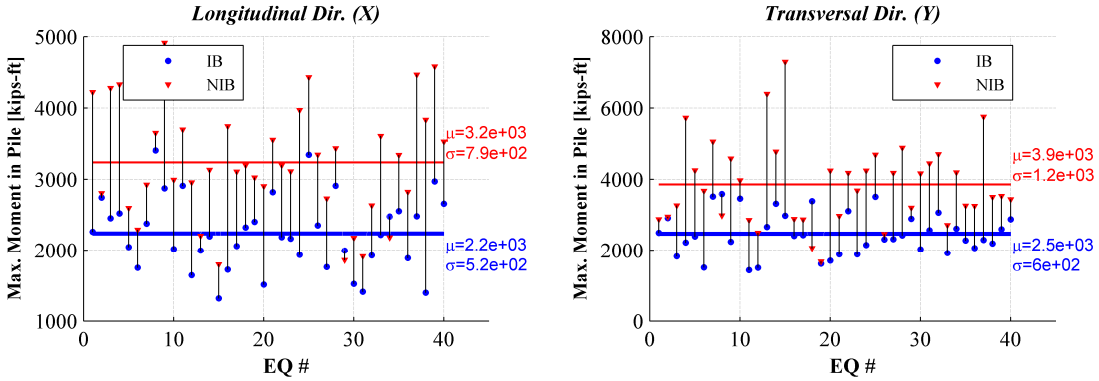

Figure 5.18: Comparison of maximum bending moment demand in piles of foundation under pier #5 with mean lines (IB: circular markers; NIB: triangular markers)

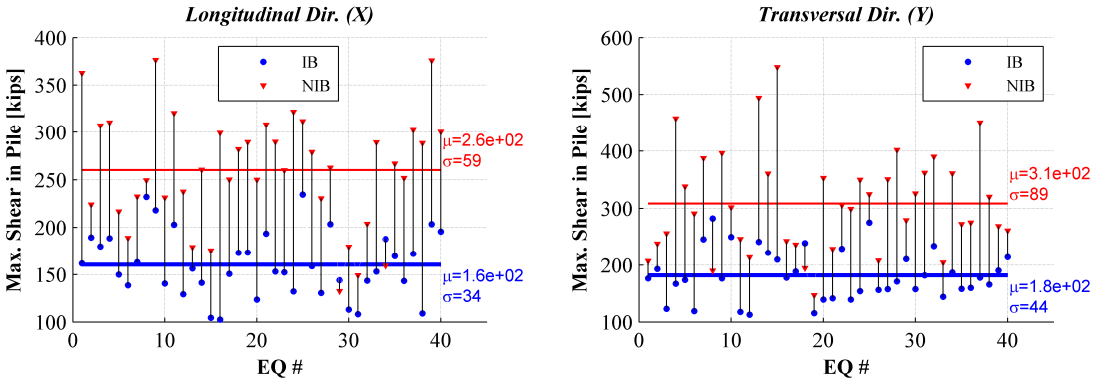

Figure 5.19: Comparison of maximum shear force demand in piles of foundation under pier #5 with mean lines (IB: circular markers; NIB: triangular markers)

Track Response

As observed from seismic simulation results, the most vulnerable rail segments lie in the neighborhood of expansion joints (i.e., abutment gap joints and interior expansion joints). The maximum rail stress generated at the left abutment gap and interior expansion joint, due to the axial force in the longitudinal direction and the transverse bending (i.e., bending around the vertical axis) are presented in Figure 5.20 and Figure 5.21. At the abutment gap, the rail stress is around 50% larger in the bridge with seismic isolation, but still smaller than the allowable rail stress on average. The rail stress due to transverse bending remains the same due to the shear key gap. Herein the abutment shear key gap is designed to be the minimum allowable construction gap, which needs to be minimized in the design. At the interior expansion joint, the detrimental effects caused by the seismic isolation to the rail stress is pronounced.

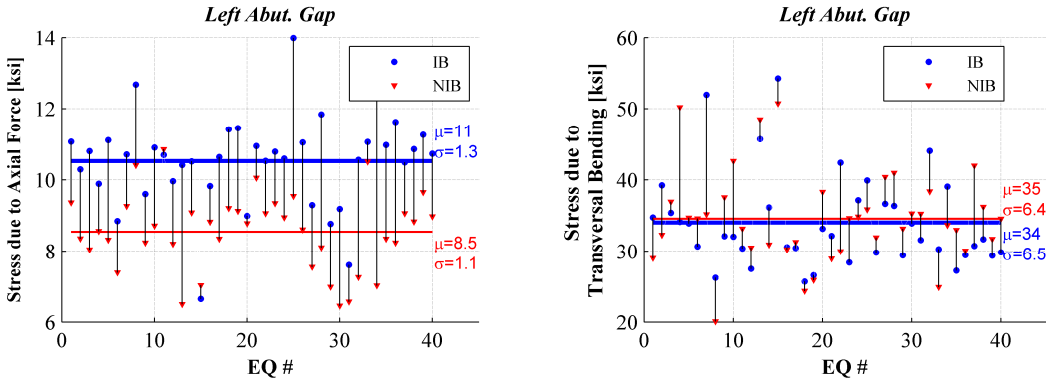

Figure 5.20: Comparison of maximum rail stress at left abutment gap due to axial force (left) and transverse bending (right) with mean lines (IB: circular markers; NIB: triangular markers)

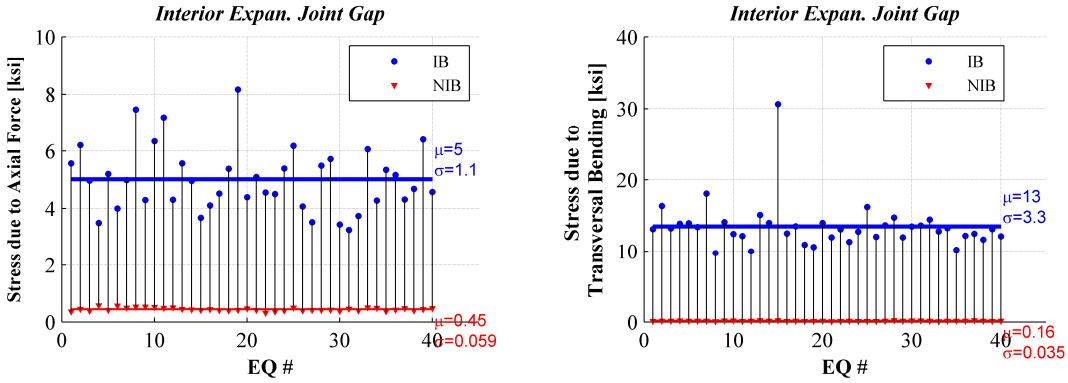

Figure 5.21: Comparison of maximum rail stress at interior expansion joint gap due to axial force (left) and transverse bending (right) with mean lines (IB: circular markers; NIB: triangular markers)

5.4.2. Record-by-record comparison under MCE hazard level earthquakes

As the intensity measure (IM) increases, the dynamic mechanisms in the CHSR Bridge differs from the response under lower hazard level ground motion excitations (e.g., OBE) due to higher contribution of non-linear effects, such as material nonlinearity, contact nonlinearity, and even geometric nonlinearities in the model). Therefore, the parallel results under excitations of MCE hazard level earthquakes are presented as follows.

Structural Response

Due to the pounding in the longitudinal direction within the SHJ devices under ground motion excitations of higher intensity levels, precious seismic simulations have shown spiky acceleration noise of high frequency component. Figure 5.22 presents the absolute deck acceleration of the bridge deck over pier #5 under MCE hazard level ground motion excitations. Unlike OBE, some of the acceleration response for IB is even higher than the NIB under MCE level earthquakes due to the occurrence of pounding. On average, however, the acceleration demand for IB is still smaller than NIB for this hazard level, as in only six out of forty records the peak acceleration in IB is higher than in NIB. This fraction grows as the hazard level goes up.

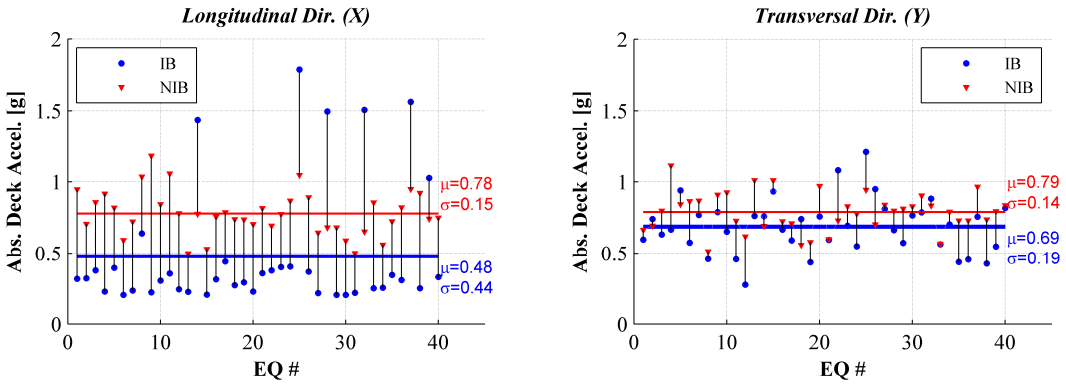

Figure 5.22: Comparison of absolute acceleration of bridge deck over pier #5 with mean value lines (IB: circular markers; NIB: triangular markers)

Instead of filtering out the high frequency acceleration spikes due to pounding in the cloud computing for ensemble analysis, the RMS of the acceleration time series is another way to evaluate the acceleration reduction effect of seismic isolation. Figure 5.23 shows the RMS of the absolute deck acceleration in both the longitudinal and transverse directions, which implies that the acceleration level for IB is lower more than the OBE case.

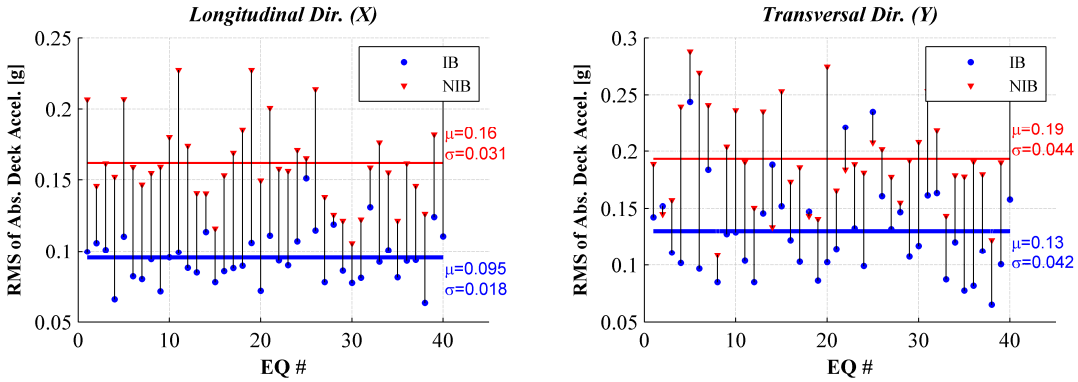

Figure 5.23: Comparison of RMS of absolute acceleration of bridge deck over pier #5 with mean lines (IB: circular markers; NIB: triangular markers)

The deck displacement is increased by 100% and 200% on average in the longitudinal and transverse directions respectively, compared to the 80% and 170% in the OBE hazard level.

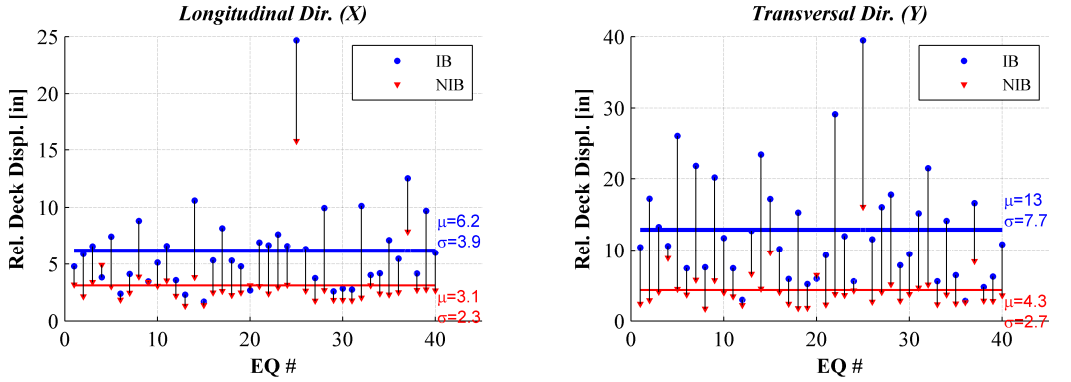

Figure 5.24: Comparison of relative displacement of bridge deck over pier #5 w.r.t. field ground surface with mean lines (IB: circular markers; NIB: triangular markers)

Figure 5.25 shows the deformation concentrated in the seismic isolator over pier column #5 in both the longitudinal and transverse directions with the resultant deformation. Similar to the OBE case, the difference from the resultant deformation and transverse deformation in this seismic isolator is less than 10%.

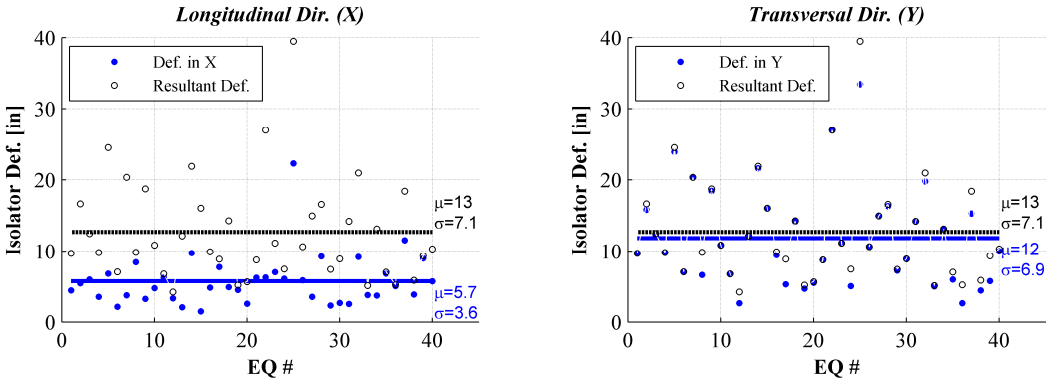

Figure 5.25: Deformation of seismic isolators over pier #5 with mean lines for IB model (with resultant displacement denoted by circular unfilled markers)

Figure 5.26 displays the displacement demand at pier #5 top under MCE earthquakes. The displacement demand on the pier column is reduced by around 80% compared to 60% for the OBE hazard level. The mitigation effect of seismic isolation is more pronounced in reducing the displacement demand on pier column for higher intensity level earthquakes.

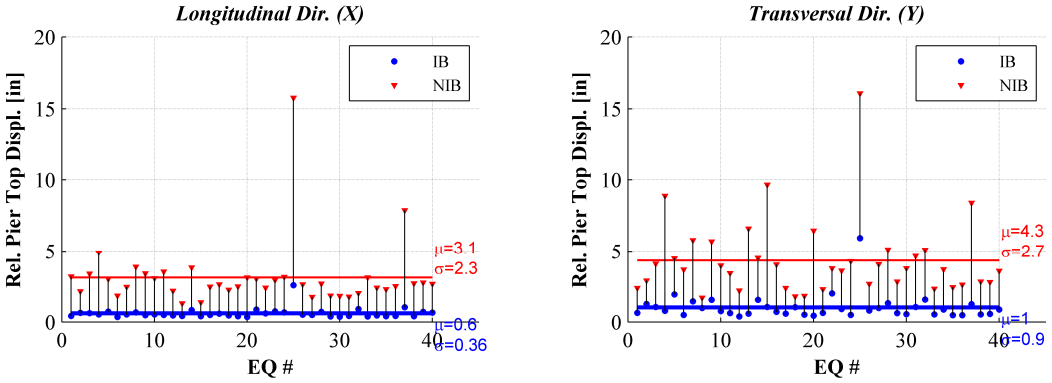

Figure 5.26: Comparison of relative displacement of top of pier #5 w.r.t. field ground surface with mean lines (IB: circular markers; NIB: triangular markers)

Correspondingly, the seismic isolation reduces the force demand on pier columns as shown in Figure 5.27. The shear force is reduced around 50% - 66% by the introduction of seismic isolation into the system.

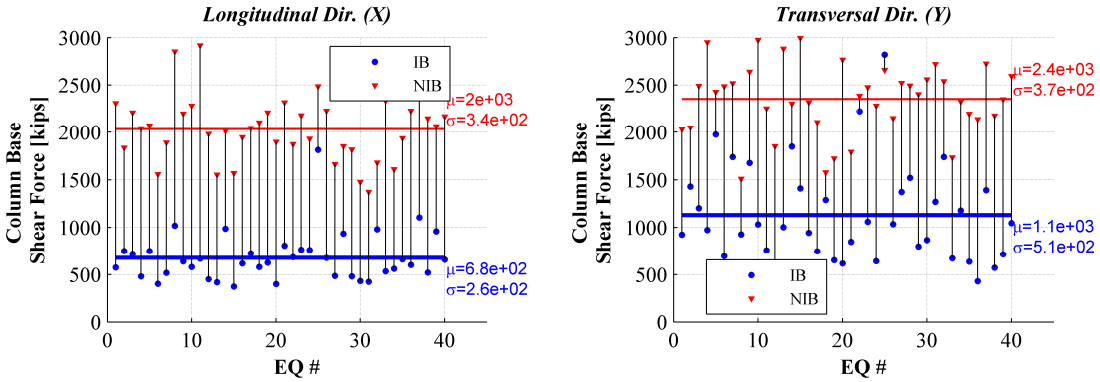

Figure 5.27: Comparison of peak base shear in pier column #5 with mean lines (IB: circular markers; NIB: triangular markers)

Figure 5.28 to Figure 5.29 show the force demand on the system in terms of the total shear force across all pier columns and abutment bearings, and the total horizontal reaction force including the pounding force. It is observed that more pounding force is activated at the abutments in the longitudinal direction under MCE level excitations compared to the OBE case for both NIB and IB based on the difference when pounding force is included or not.

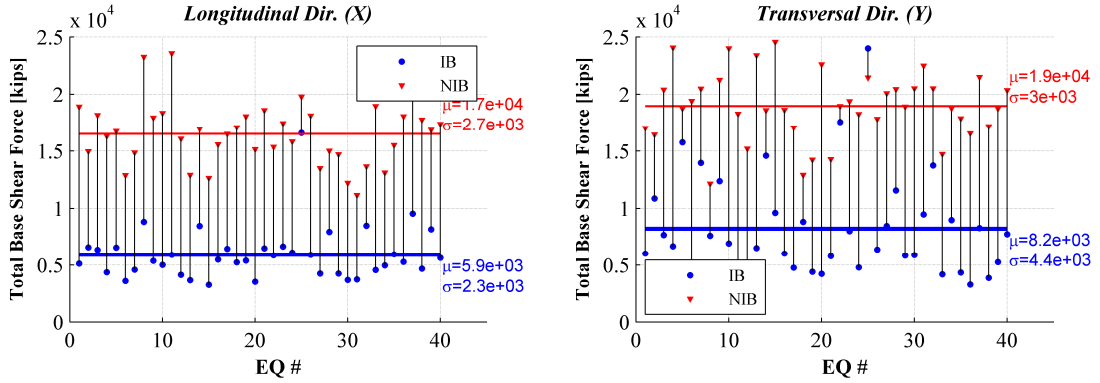

Figure 5.28: Comparison of total shear force across all pier columns and abutment bearings with mean lines (IB: circular markers; NIB: triangular markers)

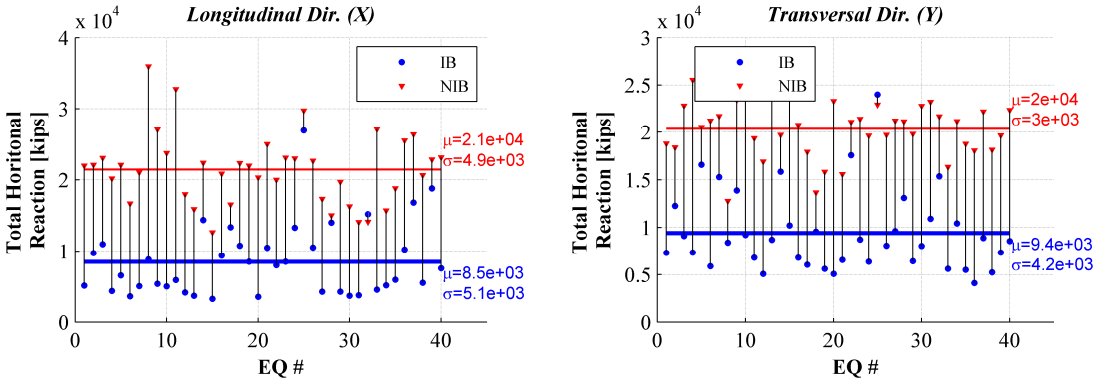

Figure 5.29: Comparison of total horizontal reaction force with mean lines (IB: circular markers; NIB: triangular markers)

Foundation Response

The seismic demand on the pile foundation under MCE hazard level earthquakes is presented in Figure 5.30 to Figure 5.33. The seismic isolation proves its beneficial effects by reducing the seismic demand on pile foundation, especially on the pile group foundation cap displacement demand. Given the higher dependence of the force demand over the piles on the kinematics of the depth-varied ground motions for MCE hazard level earthquakes, the seismic isolation is not as efficient in reducing the force demand in piles as for the OBE hazard level.

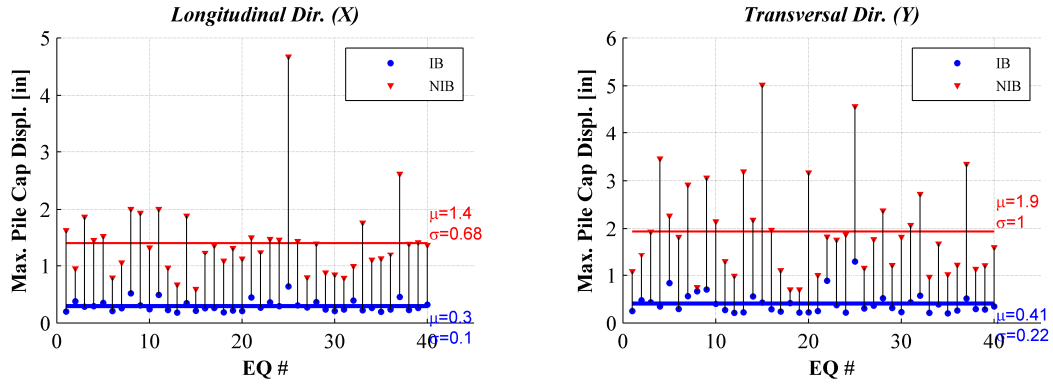

Figure 5.30: Comparison of maximum pile cap translation of foundation under pier #5 with mean lines (IB: circular markers; NIB: triangular markers)

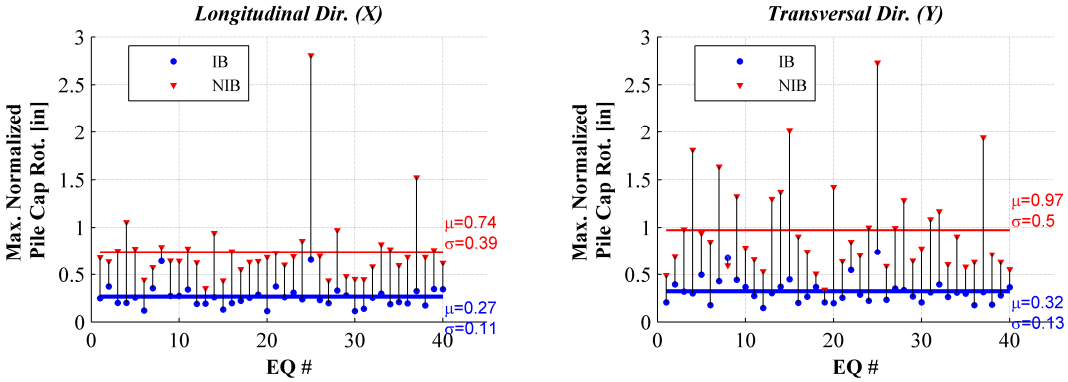

Figure 5.31: Comparison of maximum pile cap rotation of foundation under pier #5 with mean lines (IB: circular markers; NIB: triangular markers)

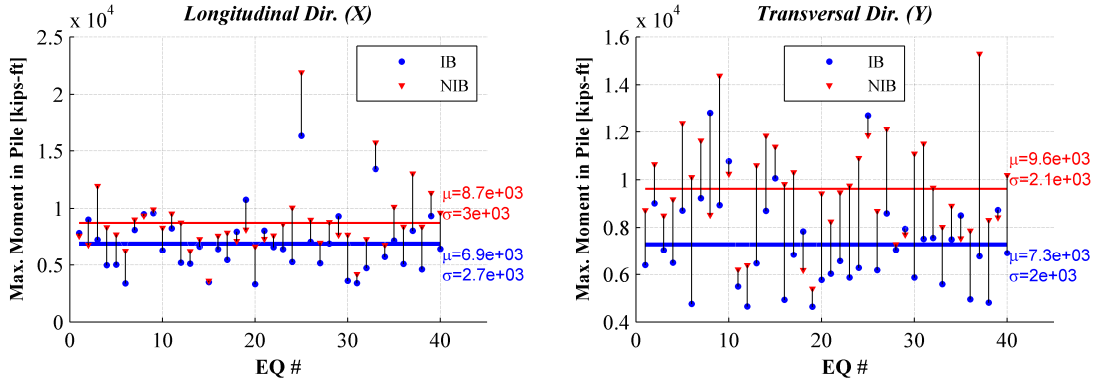

Figure 5.32: Comparison of maximum bending moment demand in piles of foundation under pier #5 with mean lines (IB: circular markers; NIB: triangular markers)

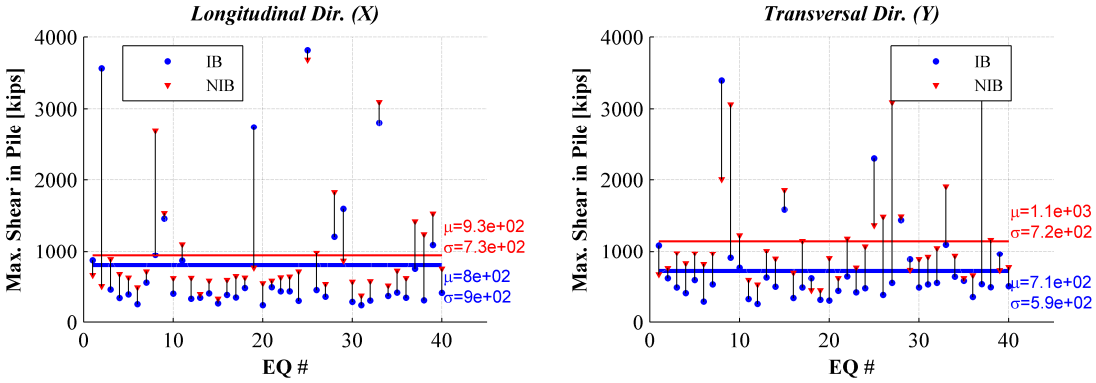

Figure 5.33: Comparison of maximum shear force demand in piles of foundation under pier #5 with mean lines (IB: circular markers; NIB: triangular markers)

5.4.3. Conditional probabilistic demand hazard analysis using the stripe method

In the stripe method, a data sample of EDPs for seven given seismic hazard levels is generated through the nonlinear dynamic analysis under 40 ground motion records, with IM fixed at the corresponding seismic hazard level. A lognormal distribution for the probability distribution of an EDP is fitted using the nonlinear least square method at each stripe level, with an estimation of the mean and variance of $\ln(EDP \mid IM = im)$. The statistics (mean and variance) of $\ln(EDP \mid IM = im)$ at other hazard levels are predicted by linear interpolation and extrapolation.

Based on the assumption of log normal distribution of the EDPs, the exponential of the mean of $\ln(EDP \mid IM = im)$ is the median of the EDP, then the logarithm of the median of the EDP, denoted by η_{EDP}, is the mean of $\ln(EDP \mid IM = im)$. The variance of $\ln(EDP \mid IM = im)$ is denoted by $\sigma_{\ln(EDP)}$, and $\mu_{\ln(EDP|IM=im)} \pm \sigma_{\ln(EDP)}$ stands for the 16th and 84th percentile respectively as plotted to show the dispersion around the mean for a given seismic hazard or IM level together with the PDF in the Conditional probabilistic seismic hazard analysis results.

The spectral acceleration with 5% damping ratio corresponding to the fundamental mode period of the CHSR Prototype Bridge Structure, $S_a(T_1, \xi = 5\%)$, is used as the intensity measure (IM) in the PBEE framework herein. Due to the fundamental period difference in CHSR Prototype Bridge with or without seismic isolators, denoted as Isolated Bridge (IB) and Non-Isolated Bridge (NIB), the same IM value represents different hazard levels for IB and NIB. The conditional probabilistic properties (i.e., mean, dispersion, and PDF) for all seismic hazard levels, as well as the conditional complementary cumulative probability distribution (CCDF) of the EDP to characterize the probability of EDP exceeding a certain threshold value, is also presented for IB and NIB. The probabilistic performance

conditioned on a given seismic hazard level is first investigated for comparison for all different kinds of EDPs for both IB and NIB.

Structural Response

Figure 5.34 presents the conditional probabilistic seismic demand hazard analysis (PSDHA) results of the absolute deck acceleration over pier #5 in the longitudinal direction using the Stripe Method for both the IB and NIB. The conditional mean and variance for 7 different discretized hazard levels are estimated through a log-normal distribution fitting for EDP sample at each hazard level. The conditional mean and variance for other hazard levels are estimated by linear interpolation and extrapolation. As observed from the stripe analysis results of the absolute deck acceleration in IB, a new phase of structural behavior is displayed with higher acceleration values after the increasing seismic hazard level reaches the 975 years return period (i.e., around MCE). The engaged pounding in the SHJ devices in the longitudinal direction at interior expansion joints can be attributed for this phenomenon.

Even though the accounted pounding effects may lead to artificial spiky accelerations, the seismic isolation can still reduce the acceleration level efficiently. This is observed from the comparison of the conditional mean and percentiles ($\mu_{\ln(EDP|IM=im)} \pm \sigma_{\ln(EDP)}$) of IB and NIB shown in Figure 5.35 (left), as well as the PDF of the EDP conditioned on two hazard levels (i.e., OBE and MCE). The acceleration reduction effect of seismic isolation is easily observed from the probabilistic point of view.

The complementary CDF (CCDF) of absolute acceleration of deck over pier #5 with the empirical CCDF marked with solid dots are shown in Figure 5.35 (right). The log-normal fitting works well except for large tail effects due to the pounding-induced acceleration.

Similar observations can be made from the transverse acceleration of IB and NIB, as summarized in Figure 5.36 and Figure 5.37.

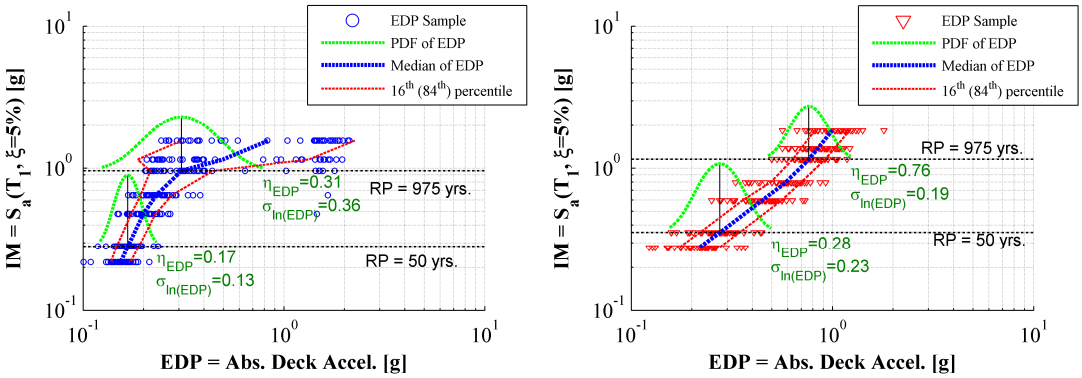

Figure 5.34: Conditional PSDHA results with the stripe method for the absolute deck acceleration over pier #5 in long. dir. (x) for IB (left) and NIB (right)

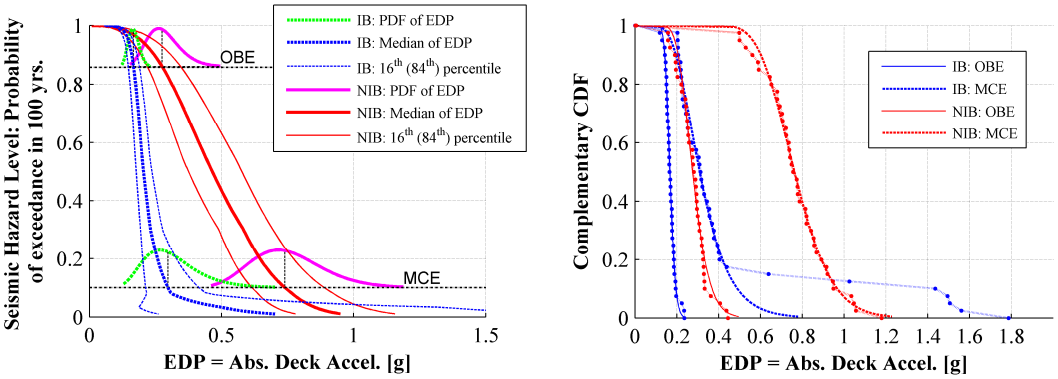

Figure 5.35: Comparison of conditional probabilistic properties of demand for all seismic hazard levels (left) and conditional CCDF given representative seismic hazard level (right) on absolute deck acceleration over pier #5 in long. dir. (x).

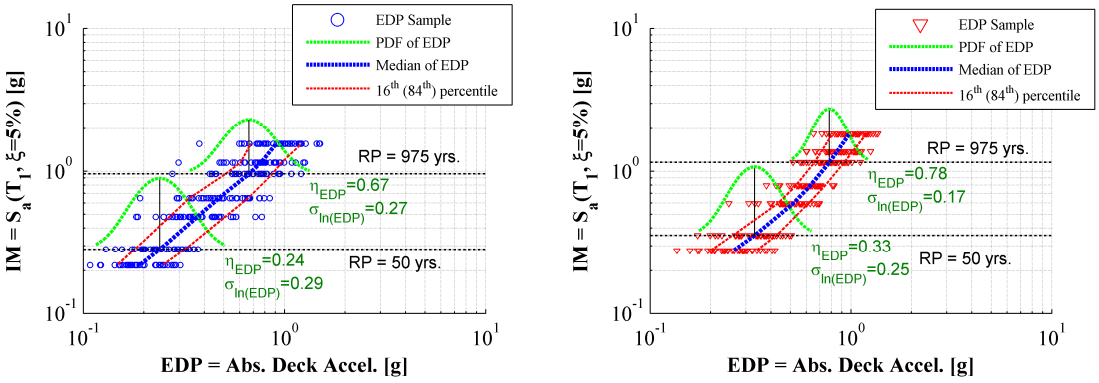

Figure 5.36: Conditional PSDHA results: conditional PDF of absolute deck acceleration over pier #5 in trans. dir. for IB (left) and NIB (right)

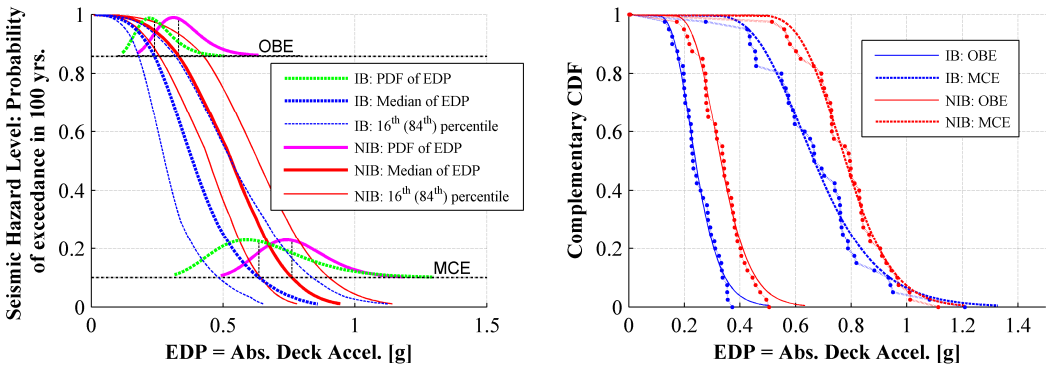

Figure 5.37: Comparison of conditional probabilistic properties of demand for all seismic hazard levels (left) and conditional CCDF given representative seismic hazard level (right) on absolute deck acceleration over pier #5 in trans. dir. (y)

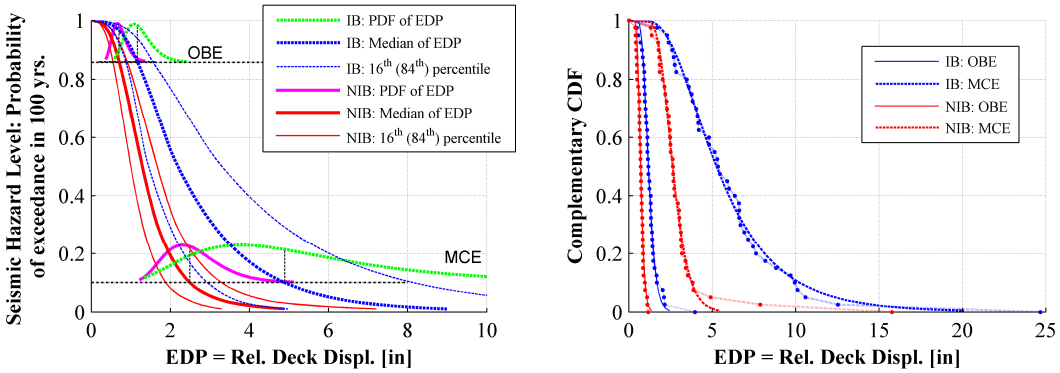

Figure 5.38: Comparison of conditional probabilistic properties of demand for all seismic hazard levels (left) and conditional CCDF given representative seismic hazard level (right) on relative deck displacement over pier #5 in long. dir. (x)

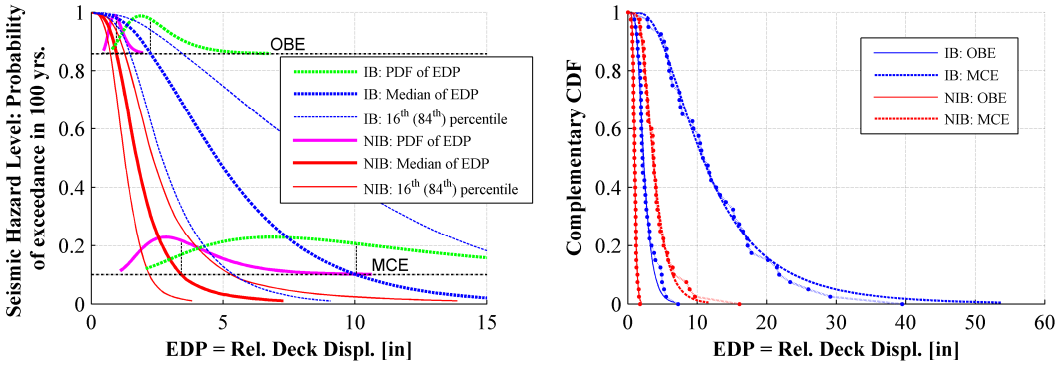

Figure 5.39: Comparison of conditional probabilistic properties of demand for all seismic hazard levels (left) and conditional CCDF given representative seismic hazard level (right) on relative deck displacement over pier #5 in trans. dir. (y)

Figure 5.38 (Figure 5.39) shows the conditional PSDHA results for the relative deck displacement over pier #5 in the longitudinal (transverse) direction. The imposed seismic risk of the deck displacement is much higher for IB than NIB due to the flexible behavior of seismic isolation layer between the bridge deck and pier columns/abutments.

In IB model with seismic isolations, the deformation concentrated in seismic isolators tends to be of interest to bridge engineers. Figure 5.40 to Figure 5.42 display the conditional PSDHA results of the seismic isolator on top of pier column #5 in the longitudinal and transverse directions respectively.

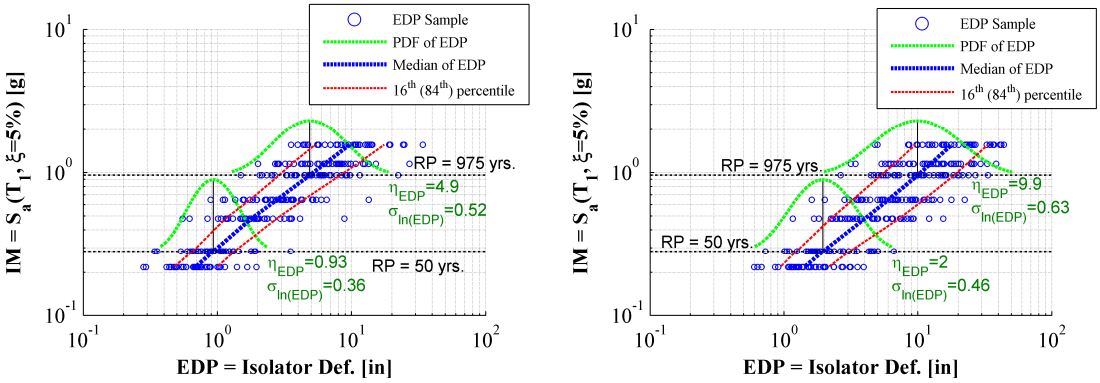

Figure 5.40: Conditional PSDHA results: conditional PDF of isolator deformation over pier #5 in the long. dir. (x) and trans. dir. (y) for IB

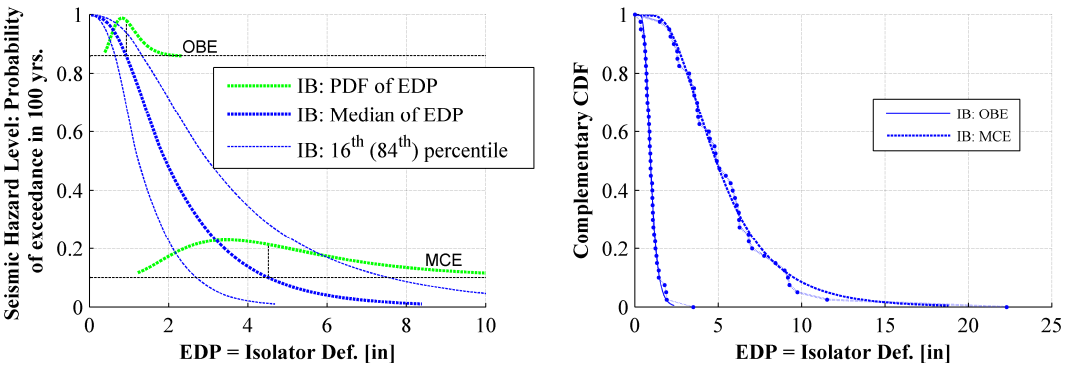

Figure 5.41: Comparison of conditional probabilistic properties of demand for all seismic hazard levels (left) and conditional CCDF given representative seismic hazard level (right) on isolator deformation over pier #5 in long. dir. (x)

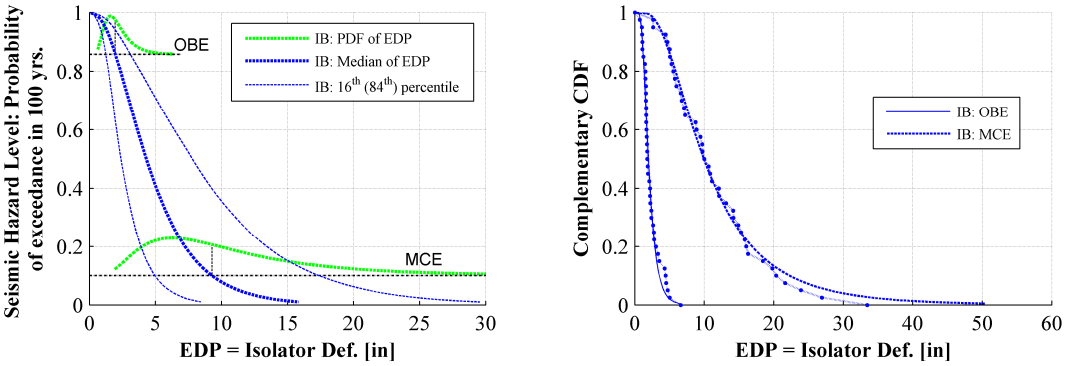

Figure 5.42: Comparison of conditional probabilistic properties of demand for all seismic hazard levels (left) and conditional CCDF given representative seismic hazard level (right) on isolator deformation over pier #5 in trans. dir. (y)

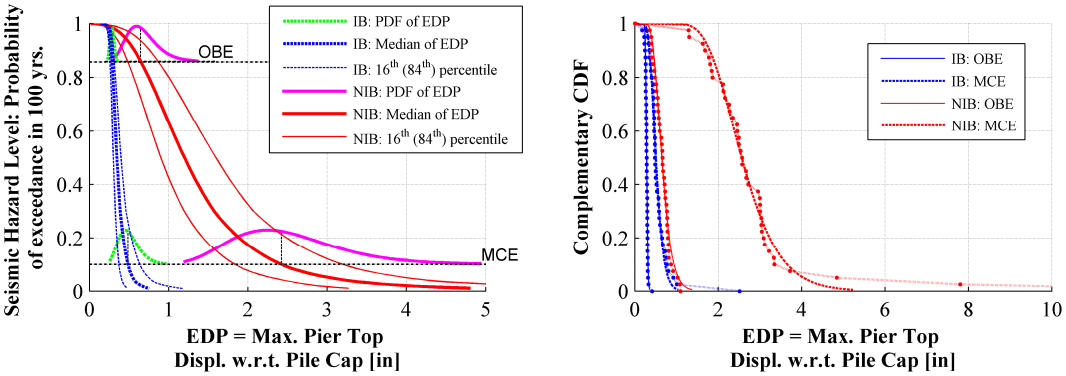

Figure 5.43: Comparison of conditional probabilistic properties of demand for all seismic hazard levels (left) and conditional CCDF given representative hazard level (right) on pier column drift of pier #5 w.r.t. pile cap in long. dir. (x)

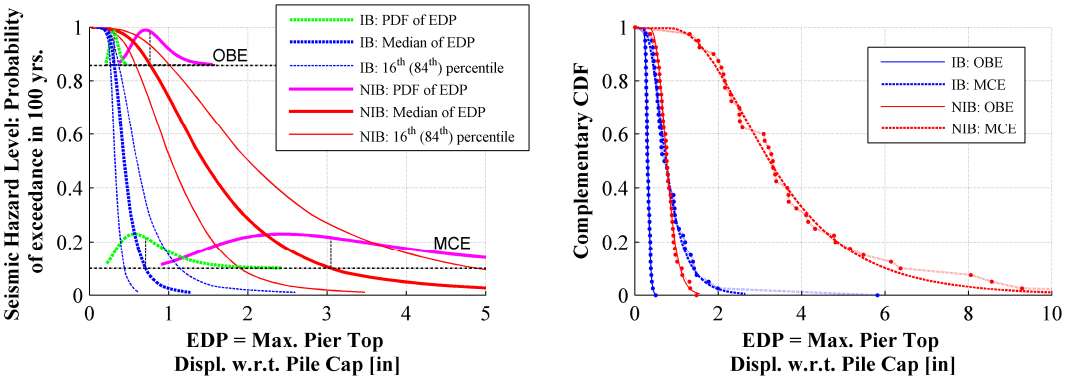

Figure 5.44: Comparison of conditional probabilistic properties of demand for all seismic hazard levels (left) and conditional CCDF given representative seismic hazard level (right) on pier column drift of pier #5 w.r.t. pile cap in trans. dir. (y)

Figure 5.43 and Figure 5.44 present the conditional PSDHA results of the column drift of pier #5 w.r.t. pile cap in the longitudinal direction and transverse direction. Consistent with the results from the record-by-record comparison, the seismic isolation highly reduces the seismic risk of displacement demand on the pier columns.

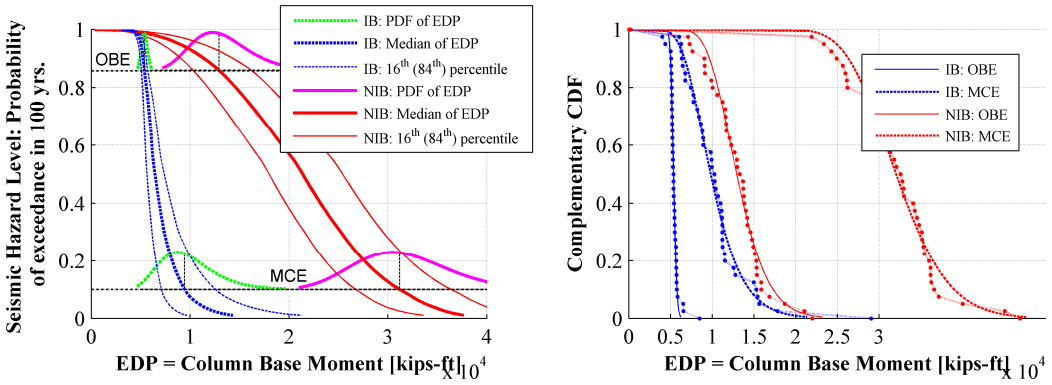

Figure 5.45: Comparison of conditional probabilistic properties of demand for all seismic hazard levels (left) and conditional CCDF given representative seismic hazard level (right) on column base moment of pier #5 in long. dir. (x)

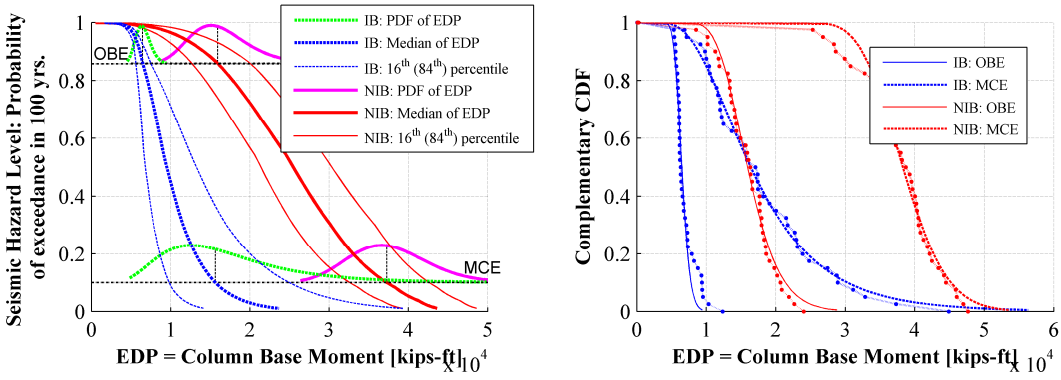

Figure 5.46: Comparison of conditional probabilistic properties of demand for all seismic hazard levels (left) and conditional CCDF given representative seismic hazard level (right) on column base moment of pier #5 in trans. dir. (y)

The conditional PSDHA results for the column base moment of pier #5 in the longitudinal and transverse directions are presented in Figure 5.45 and Figure 5.46 respectively. The seismic isolation shows to be a promising seismic risk mitigation strategy

from a probabilistic point of view after taking into account the uncertainties in the earthquake ground motions.

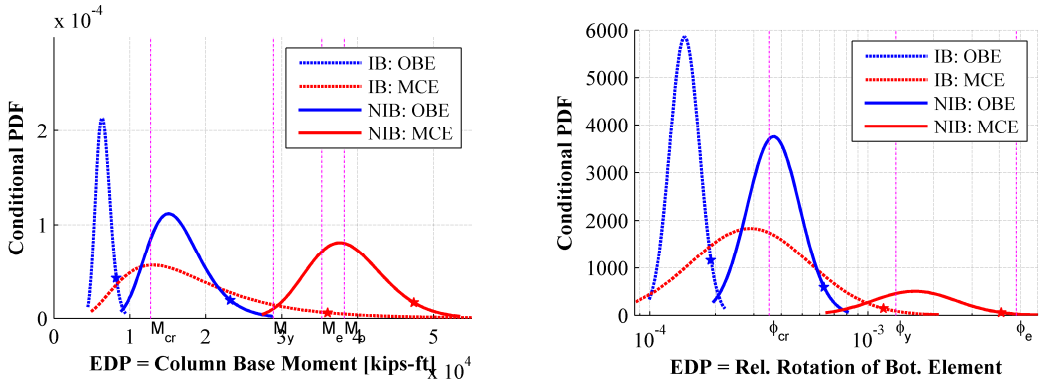

Figure 5.47: Comparison of conditional probabilistic PDF for column base moment and the relative end rotation of bottom element in pier #5 in the trans. dir. (y)

Table 5.3: Conditional probability of limit states exceedance for column base moment of pier #5 in trans. dir. (y)

	M_{cr} = 1.5e4 (kips-ft)	M_y = 3.4e4 (kips-ft)	M_e = 4.15e4 (kips-ft)	M_o = 4.5e4 (kips-ft)
IB: OBE	0%	0%	0%	0%
IB: MCE	58%	6.4%	2.6%	1.8%
NIB: OBE	60.2%	0.05%	0.002%	0.0003%
NIB: MCE	100%	81.9%	26.7%	10.6%

Table 5.4: Conditional probability of the limit states exceedance for relative end rotation of bottom element in pier #5 in trans. dir. (y)

	φ_{cr} = 0.0415 %	φ_y = 0.158 %	φ_e = 0.563%	φ_o = 3.5%
IB: OBE	0%	0%	0%	0%
IB: MCE	52%	1.8%	0.2%	0%
NIB: OBE	44%	0%	0%	0%
NIB: MCE	99.98%	70%	0.87%	0%

Figure 5.47 shows the comparison of conditional probabilistic PDF for column base moment and the relative end rotation of bottom element in pier #5, and the conditional

probability of the limit states exceedance in transverse direction is summarized in Table 5.3. The significant risk reduction effect of seismic isolation is observed from the conditional demand on pier column #5.

Figure 5.48 and Figure 5.49 further demonstrates the advantage of seismic isolation to reduce the seismic risk of shear force demand on the pier columns in terms of base shear force. The conditional PSDHA results of total base shear force are presented in Figure 5.50 and Figure 5.51.

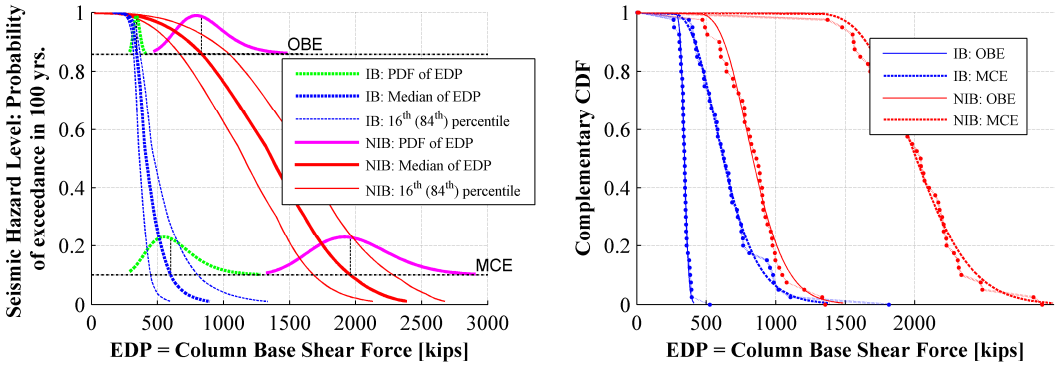

Figure 5.48: Comparison of conditional probabilistic properties of demand for all hazard levels (left) and conditional CCDF given representative hazard level (right) on column base shear force of pier #5 in long. dir. (x)

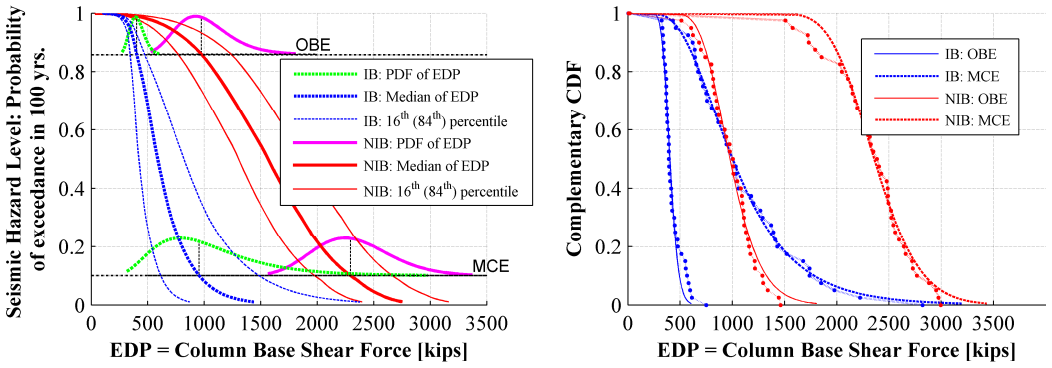

Figure 5.49: Comparison of conditional probabilistic properties of demand for all hazard levels (left) and conditional CCDF given representative hazard level (right) on column base shear force of pier #5 in trans. dir. (y)

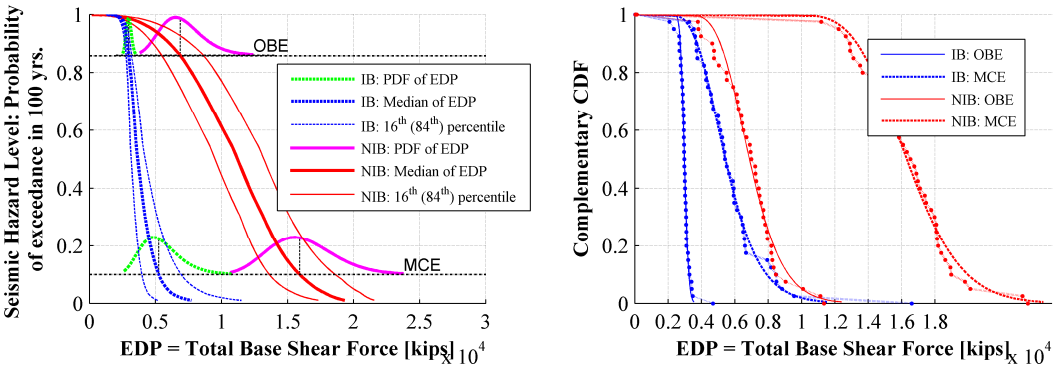

Figure 5.50: Comparison of conditional probabilistic properties of demand for all hazard levels (left) and conditional CCDF given representative hazard level (right) on total base shear force in long. dir. (x)

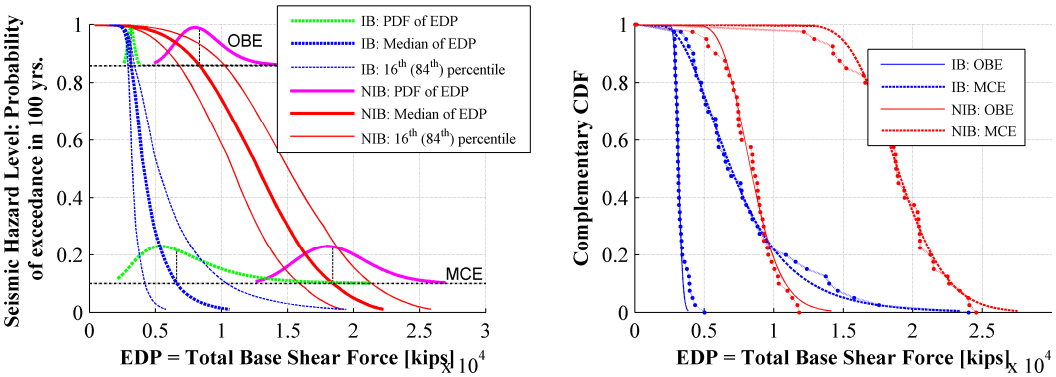

Figure 5.51: Comparison of conditional probabilistic properties of demand for all hazard levels (left) and conditional CCDF given representative hazard level (right) on total base shear force in trans. dir. (y)

Figure 5.52 and Figure 5.53 show the conditional PSDHA results of the pile cap displacement of the foundation under pier #5 in the longitudinal direction and the transverse direction of the bridge.

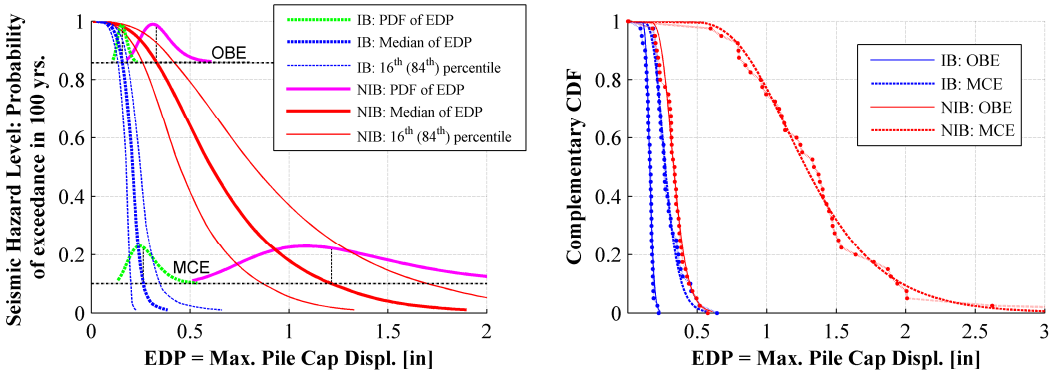

Figure 5.52: Comparison of conditional probabilistic properties of demand for all hazard levels (left) and conditional CCDF given representative hazard level (right) on pile cap displacement of foundation under pier #5 in long. dir. (x)

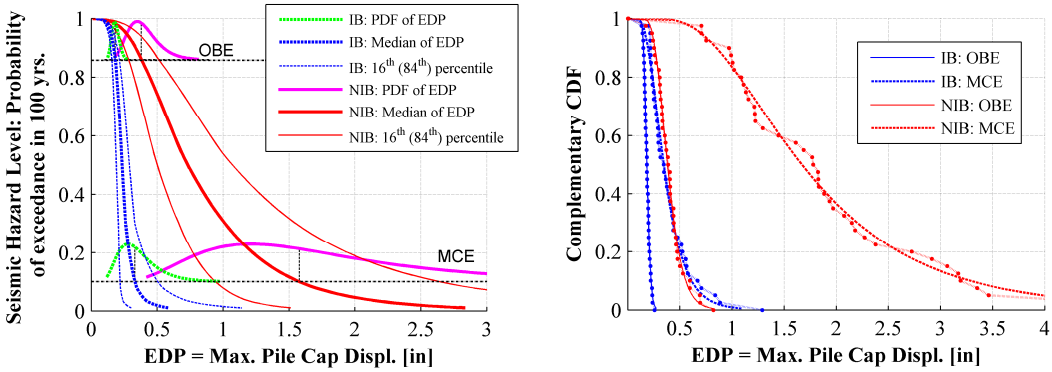

Figure 5.53: Comparison of conditional probabilistic properties of demand for all hazard levels (left) and conditional CCDF given representative hazard level (right) on pile cap displacement of foundation under pier #5 in trans. dir. (y)

Figure 5.54 shows the conditional PSDHA results of pile cap rotation of foundation under pier #5 in longitudinal direction of the bridge. Figure 5.55 shows the conditional PSDHA results of pile cap rotation of foundation under pier #5 in transverse direction of the bridge.

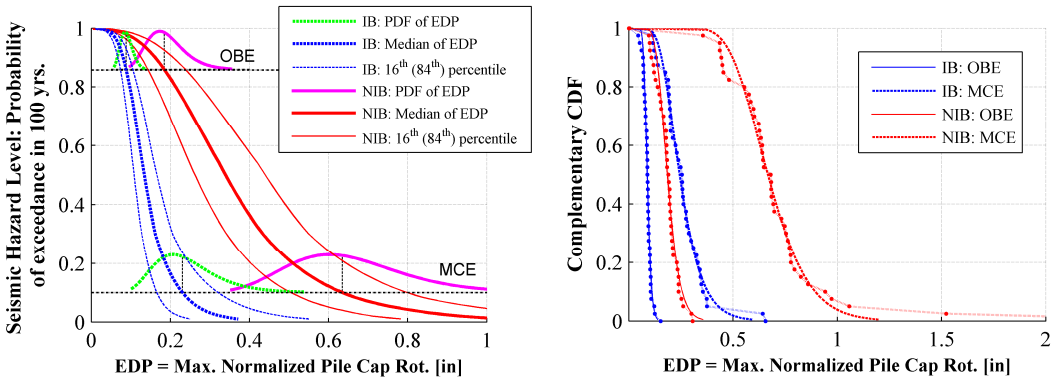

Figure 5.54: Comparison of conditional probabilistic properties of demand for all hazard levels (left) and conditional CCDF given representative hazard level (right) on pile cap rotation of foundation under pier #5 in long. dir. (x)

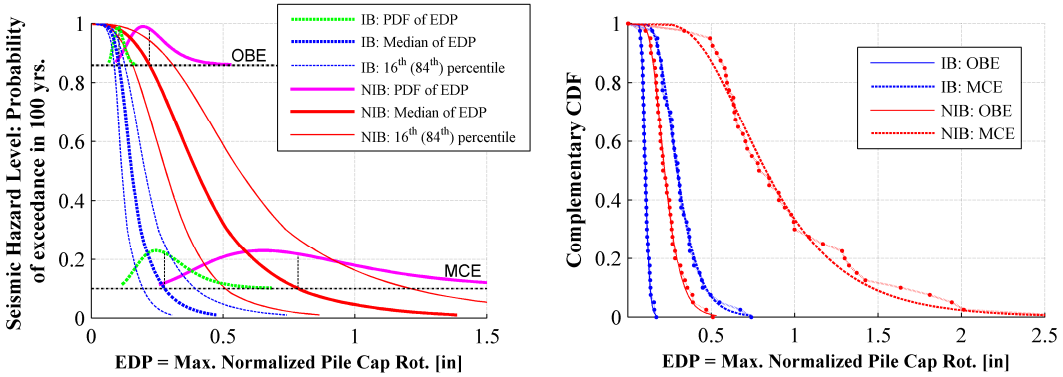

Figure 5.55: Comparison of conditional probabilistic properties of demand for all hazard levels (left) and conditional CCDF given representative hazard level (right) on pile cap rotation of foundation under pier #5 in trans. dir. (y)

Figure 5.56 shows the conditional PSDHA results of bending moment of piles under pier #5 in longitudinal direction of the bridge. Figure 5.57 shows the conditional PSDHA results of bending moment of piles under pier #5 in transverse direction of the bridge.

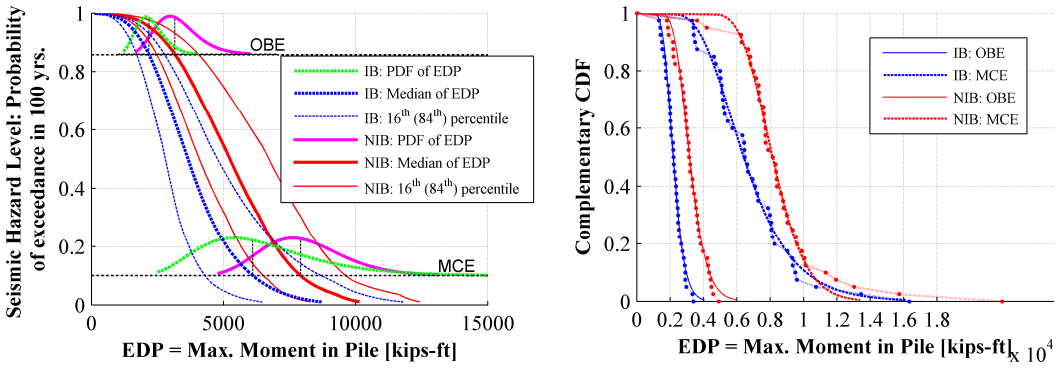

Figure 5.56: Comparison of conditional probabilistic properties of demand for all hazard levels (left) and conditional CCDF given representative hazard level (right) on bending moment of piles under pier #5 in long. dir. (x)

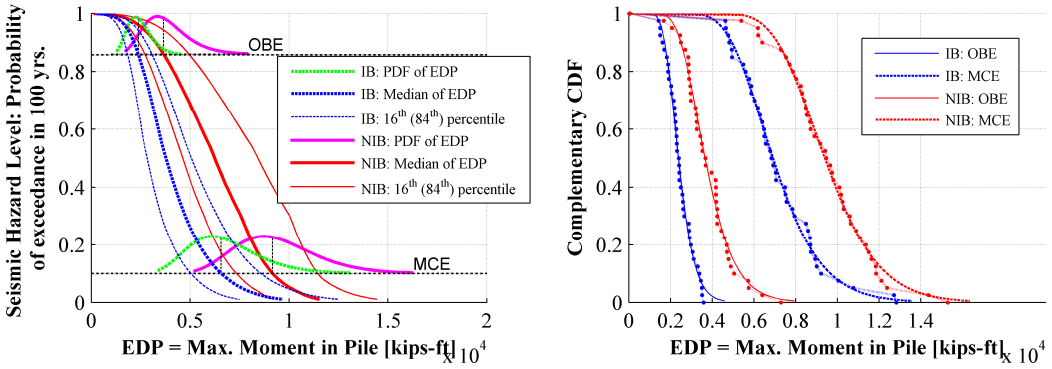

Figure 5.57: Comparison of conditional probabilistic properties of demand for all hazard levels (left) and conditional CCDF given representative hazard level (right) on bending moment of piles under pier #5 in trans. dir. (y)

Figure 5.58 shows the conditional PSDHA results of the shear force of the piles under pier #5 in the longitudinal direction of the bridge. Figure 5.59 shows the conditional PSDHA results of the shear force of the piles under pier #5 in the transverse direction of the bridge.

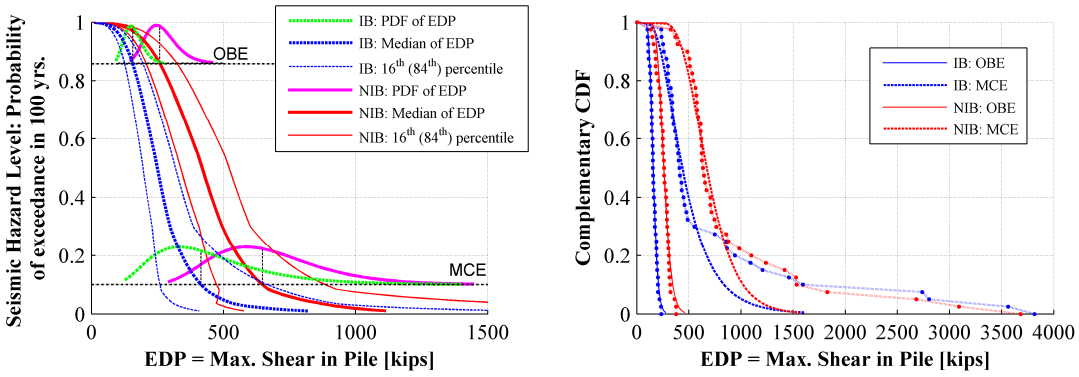

Figure 5.58: Comparison of conditional probabilistic properties of demand for all hazard levels (left) and conditional CCDF given representative hazard level (right) on shear force of piles under pier #5 in long. dir. (x)

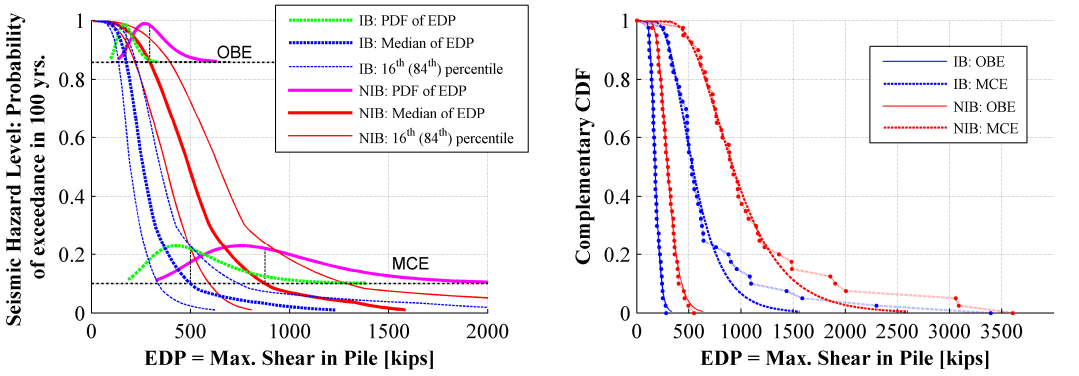

Figure 5.59: Comparison of conditional probabilistic properties of demand for all hazard levels (left) and conditional CCDF given representative hazard level (right) on shear force of piles under pier #5 in trans. dir. (y)

Seismic Risk to Track

Figure 5.60 shows the conditional PSDHA results of the rail stress at the abutment expansion joint #1 due to axial force in the longitudinal direction of the bridge. Figure 5.61 shows the conditional PSDHA results of rail stress at abutment expansion joint #1 due to the bending in transverse direction of the bridge.

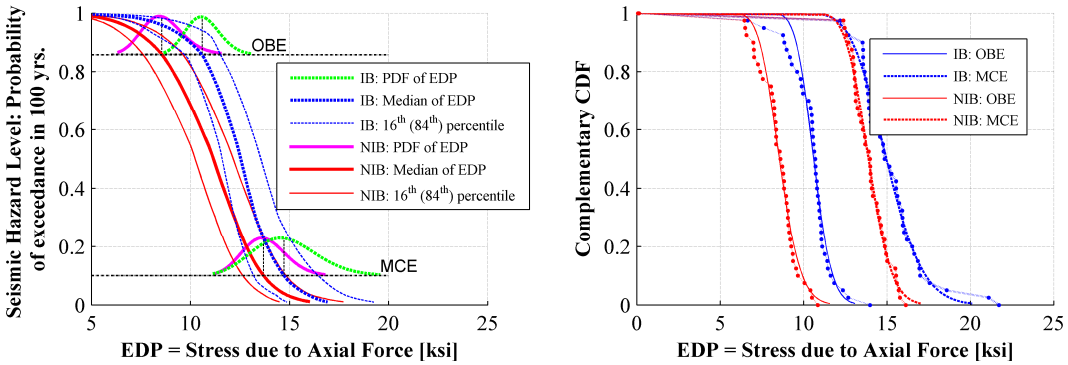

Figure 5.60: Comparison of conditional probabilistic properties of demand for all hazard levels (left) and conditional CCDF given representative hazard level (right) on rail stress at abutment expansion joint #1 due to axial force in long. dir. (x)

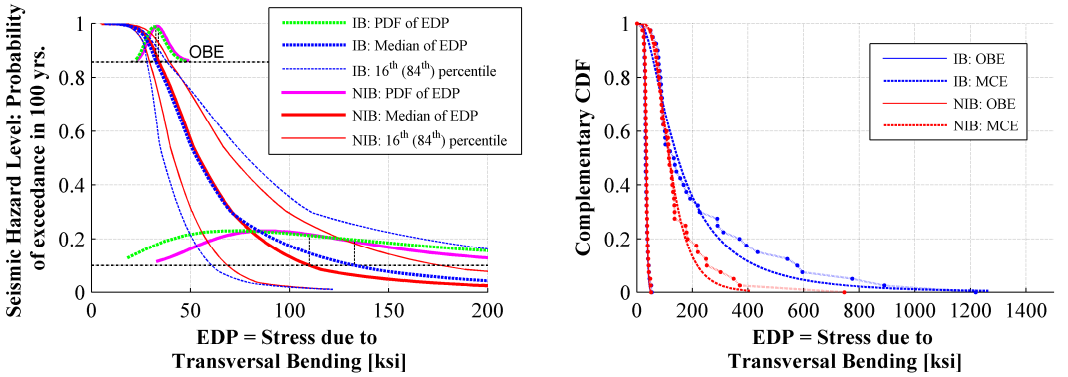

Figure 5.61: Comparison of conditional probabilistic properties of demand for all hazard levels (left) and conditional CCDF given representative hazard level (right) on rail stress at abutment expansion joint #1 due to bending in trans. dir. (y)

Figure 5.62 shows the conditional PSDHA results of rail stress at interior expansion joint #2 due to axial force in the longitudinal direction of the bridge. Figure 5.63 shows the conditional PSDHA results of the rail stress at the interior expansion joint #2 due to bending in the transverse direction of the bridge.

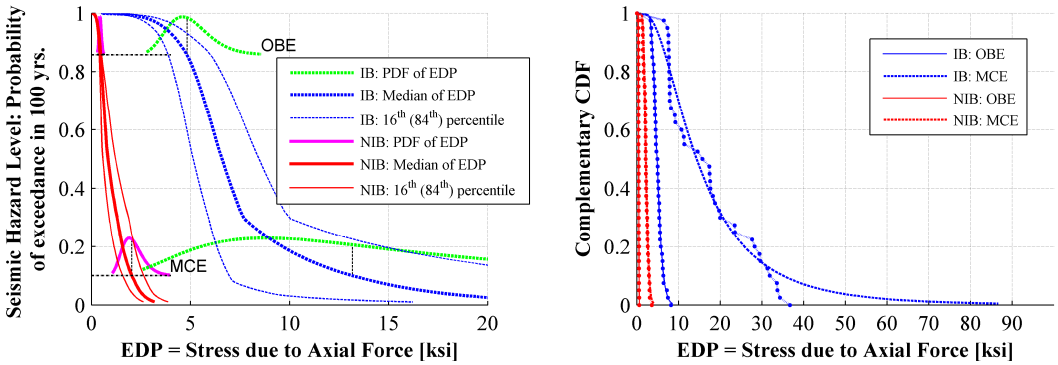

Figure 5.62: Comparison of conditional probabilistic properties of demand for all hazard levels (left) and conditional CCDF given representative hazard level (right) on rail stress at interior expansion joint #2 due to axial force in long. dir. (x)

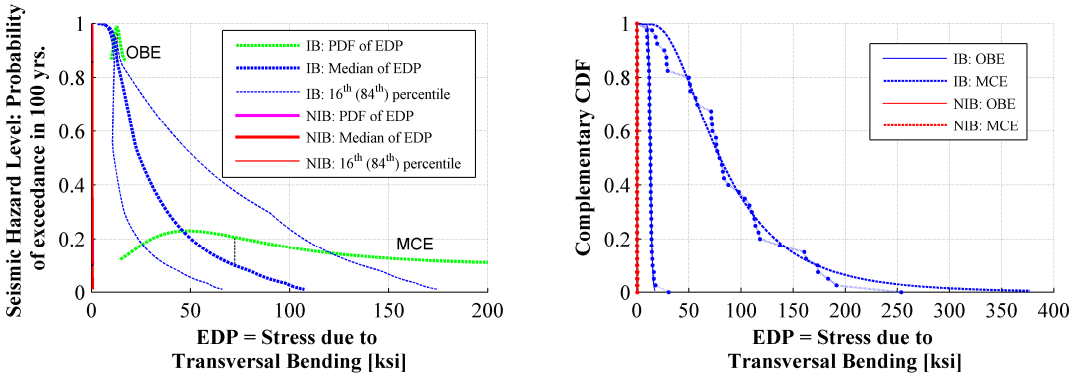

Figure 5.63: Comparison of conditional probabilistic properties of demand for all hazard levels (left) and conditional CCDF given representative hazard level (right) on rail stress at interior expansion joint #2 due to bending in trans. dir. (y)

5.4.4. Unconditional demand hazard analysis

The probabilistic seismic demand hazard curve can be obtained by the convolution of the probabilistic seismic hazard with the results of the conditional probabilistic demand. Herein the probabilistic seismic demand hazard curves, in terms of probability of exceedance in 100 years for a given EDP are presented to characterize the seismic risk of the associated demand for both IB and NIB. A de-aggregation analysis with respect to IM can estimate the

relative contribution of different IM bins for each point on the probabilistic seismic demand hazard curve. Two representative hazard points corresponding to probability of exceedance of 86% and 10% in 100 years respectively are de-aggregated for both IB and NIB.

Figure 5.64 shows the probabilistic seismic hazard curve of absolute deck acceleration over pier #5 in the longitudinal direction for both the IB and NIB. Introducing seismic isolation to the CHSR Bridge (IB) reduces the seismic risk of deck acceleration in the longitudinal direction by around 50% compared to NIB. The de-aggregation results show the relative contribution of different IM bins to the seismic demand hazard. For both IB and NIB, main contributions to the high hazard values (i.e., with RP = 950 years) are from larger intensity measure (IM) values, while main contributions to the low hazard values (i.e., with RP = 50 years) are from smaller intensity measure (IM) values. As expected the tributary IM bins of IB are smaller than the tributary IM bins of NIB. Also, the relative contribution curve of IB is narrower than that of NIB because of the narrower band of IM corresponding to longer period as seen from the uniform hazard spectrum. Similar PSDHA results for absolute acceleration in the transverse direction are shown in Figure 5.65.

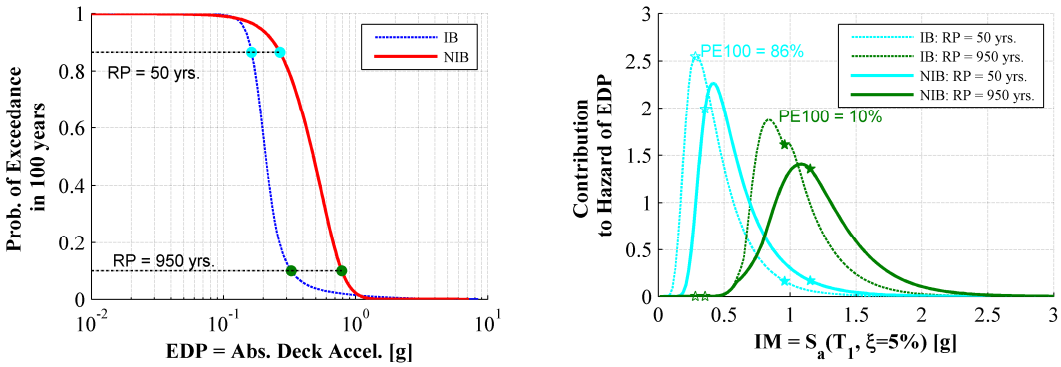

Figure 5.64: Probabilistic seismic demand hazard curve and de-aggregation of absolute deck acceleration over pier #5 in the long. dir. (x).

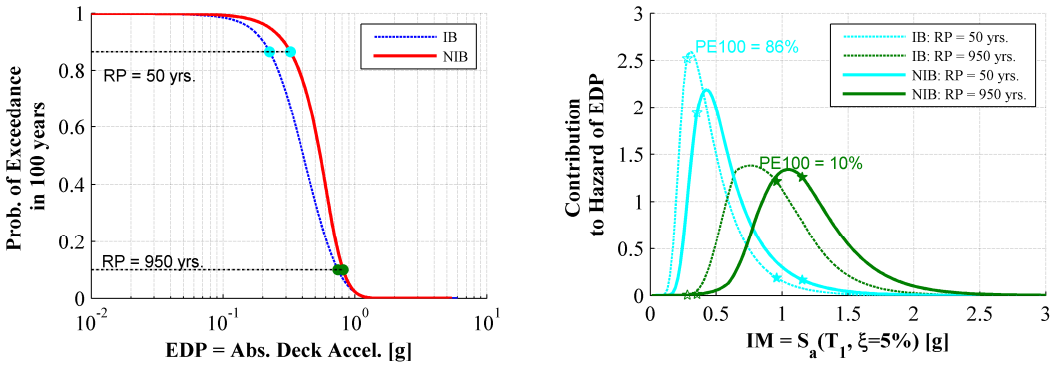

Figure 5.65: Probabilistic seismic demand hazard curve and de-aggregation of absolute deck acceleration over pier #5 in the trans. dir. (y)

Figure 5.66 present the PSDHA of the RMS of the absolute deck acceleration. The seismic isolation can reduce the RMS of the absolute deck acceleration for high hazard levels (i.e., RP = 950 years) more efficiently than low hazard levels (i.e., RP = 50 years), while this is not obvious for the maximum absolute deck acceleration demand.

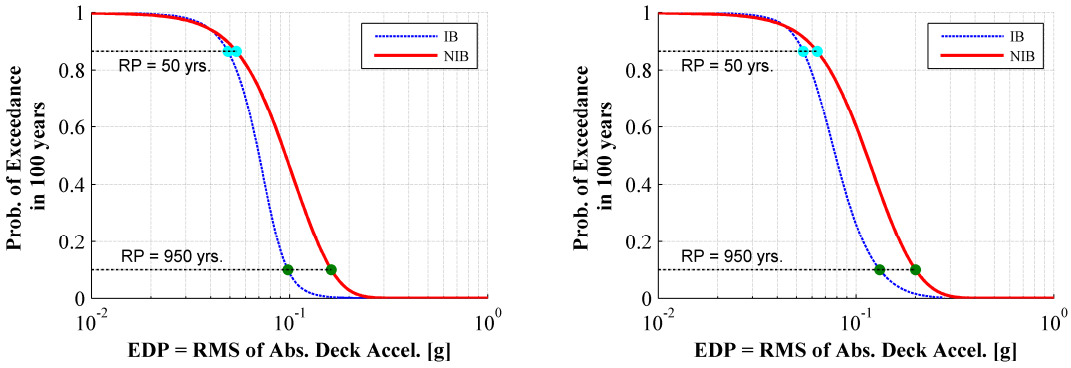

Figure 5.66: Probabilistic seismic demand hazard curve of absolute deck acceleration over pier #5 in the long. dir. (left) and in the trans. dir. (right)

The probabilistic seismic demand hazard of the relative deck displacement is shown in Figure 5.67. Consistent with the observation made from the deterministic comparison of IB and NIB, the deck displacement hazard for IB is much higher than the NIB due to period

elongation effects of the seismic isolation. Seismic isolation shifts the seismic hazard curve to the right, which implies that more seismic risk is imposed.

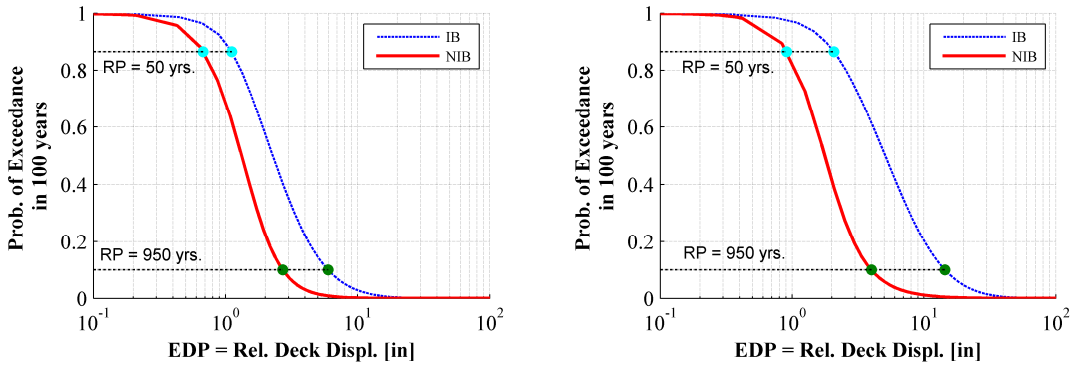

Figure 5.67: Probabilistic seismic demand hazard curve of relative deck displacement over pier #5 in the long. dir. (left) and in the trans. dir. (right)

Figure 5.68 shows the PSDHA of the lateral deformation of seismic isolator over pier #5 in both the longitudinal and transverse direction of the IB.

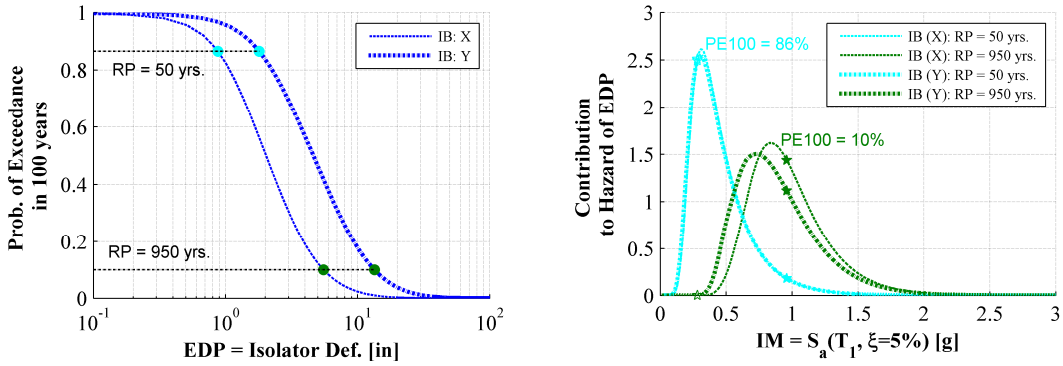

Figure 5.68: Probabilistic seismic demand hazard curve and de-aggregation of isolator deformation over pier #5

Figure 5.69 displays the PSDHA results of pier column drift relative to the pile cap. The seismic isolation pushes the seismic demand hazard curves to the left, which means seismic isolation imposes less seismic risk to pier column in terms of pier top drift with respect to the pile cap.

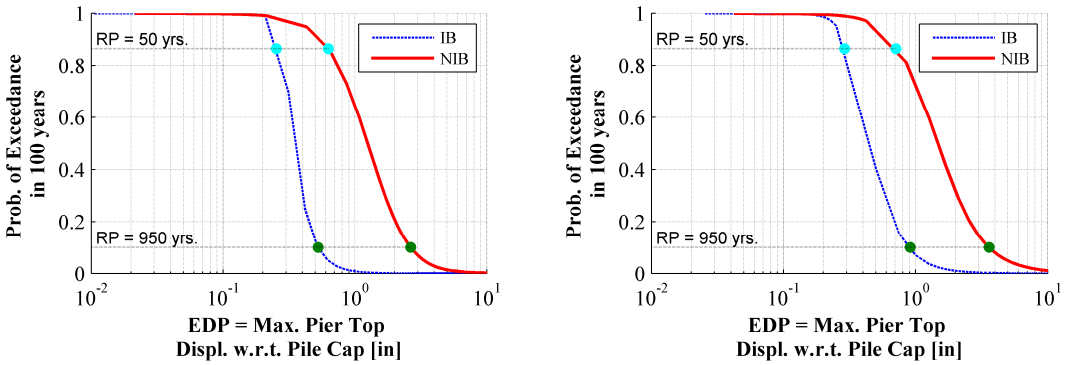

Figure 5.69: Probabilistic seismic demand hazard curve of pier column drift of pier #5 w.r.t. pile cap in the long. dir. (left) and in the trans. dir. (right)

Figure 5.70 presents the PSDHA results for column base moment at pier #5. As shown from the probabilistic seismic demand hazard curve characterized with the probability of exceedance of base moment in 100 years, the seismic isolation in IB highly mitigates the seismic risk to the base moment of the pier column in both the longitudinal and transverse directions. From the probabilistic seismic demand hazard of the bottom moment in transverse (longitudinal) direction, the probability of exceeding the cracking moment in the pier column in 100 years for IB is around 20% (2%) compared to 87% (78%) for NIB. The probability of transverse moment exceeding the first yield moment, expected moment and over-strength moment is 22%, 7%, and 3% for NIB, compared to 2%, 0.8% and 0.5% for IB. The beneficial effect of seismic isolation to the substructure is pronounced.

Figure 5.71 presents the PSDHA results of the base shear at pier column #5 in longitudinal and transverse directions of IB and NIB. The force demand reduction effect of the seismic isolation is observed as well in terms of the unconditional probabilistic demand hazard curve. The probabilistic seismic demand hazard of the total base shear force in the longitudinal and transverse directions are shown in Figure 5.72, and the corresponding results for the total horizontal reaction force in longitudinal and transverse directions is shown in Figure 5.73.

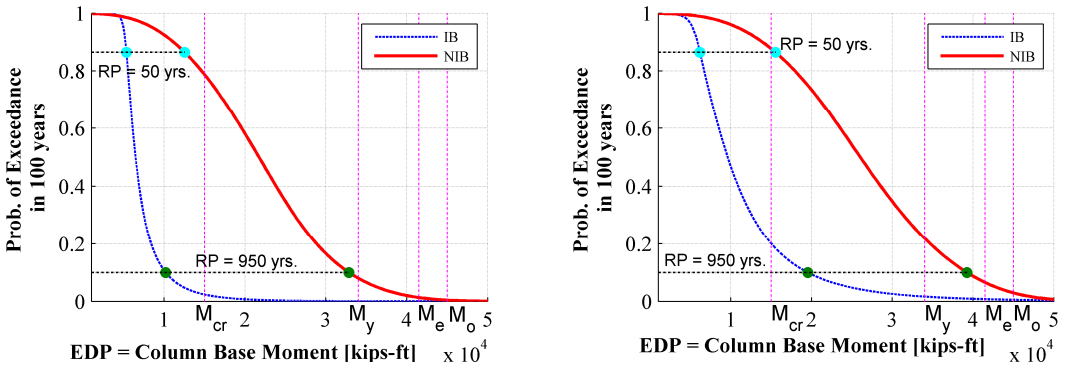

Figure 5.70: Probabilistic seismic demand hazard curve of column base moment of pier #5 in the long. dir. (left) and in the trans. dir. (right)

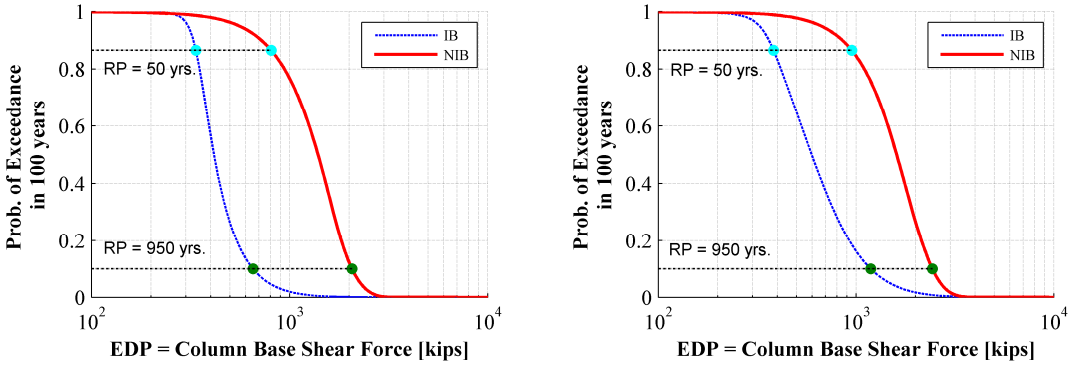

Figure 5.71: Probabilistic seismic demand hazard of column base shear force of pier #5 in the long. dir. (left) and in the trans. dir. (right)

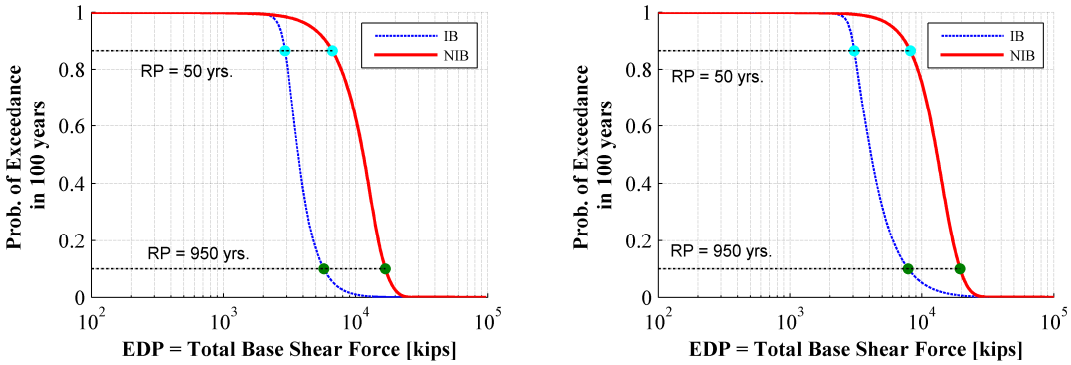

Figure 5.72: Probabilistic seismic demand hazard curve of total base shear force in the long. dir. (left) and in the trans. dir. (right)

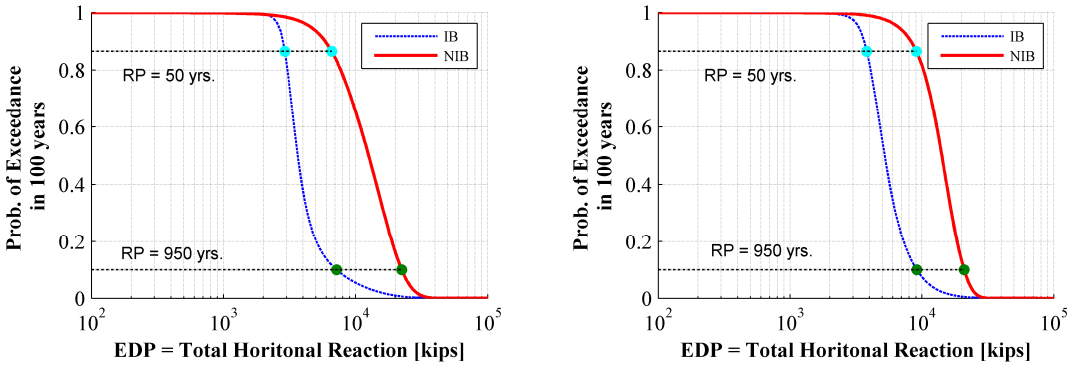

Figure 5.73: Probabilistic seismic demand hazard curve of total horizontal reaction force in the long. dir. (left) and in the trans. dir. (right)

The comparison of the seismic hazard curve of the total base shear across all columns, the total base shear including the shear force of the bearings on the abutments, and the total horizontal force (total base shear plus the pounding force after the abutment gap/shear key gap is closed) is presented in Figure 5.74 and Figure 5.75. In the longitudinal direction, the seismic isolation reduces the force demand on the system level.

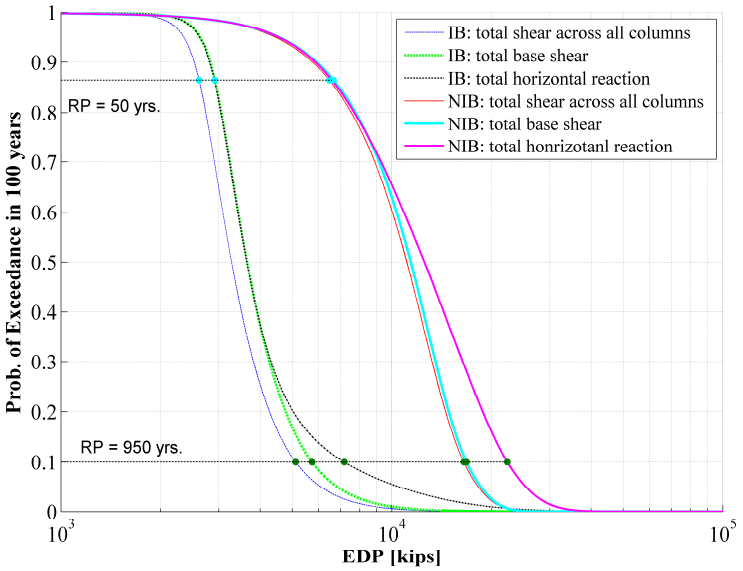

Figure 5.74: Probabilistic seismic demand hazard curve comparison between total shear force and total horizontal reaction force in longitudinal dir. (x)

The total horizontal reaction deviates from the total base shear due to the pounding force at the gaps for higher hazard levels, which occurs earlier for NIB than IB even though the seismic isolated deck in IB experience larger displacement demand. This is because of the 2in abutment gap for NIB and 4in abutment gap for IB. In the transverse direction, the deviation occurs for even smaller hazard levels due to the small abutment shear key gap of 0.5in.

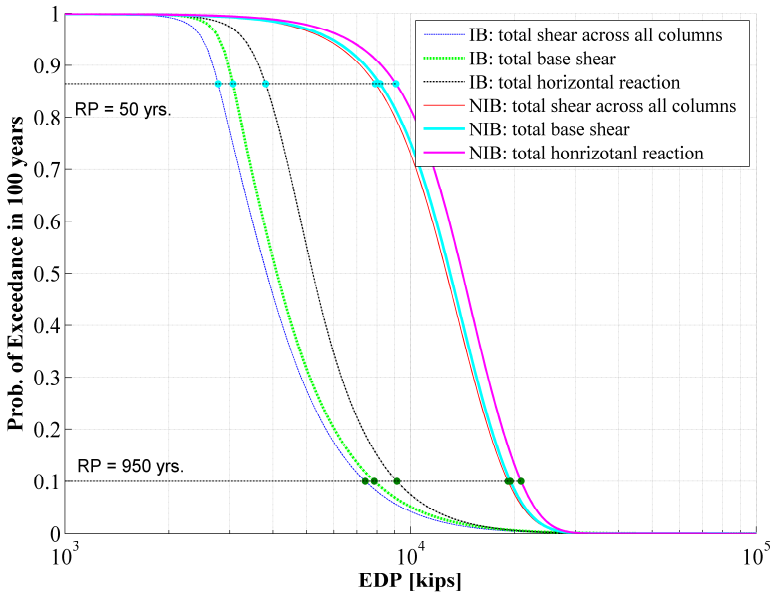

Figure 5.75: Probabilistic seismic demand hazard curve comparison between total shear force and total horizontal reaction force in transverse dir. (y)

Seismic Risk to Pile Foundation

Figure 5.76 shows the probabilistic seismic demand hazard curves and de-aggregation results of the pile cap displacement in longitudinal and transverse directions respectively. The seismic demand hazard of the normalized rotations causing pier top drift is shown in Figure 5.77. Comparing the displacement demand on the pile group foundation between IB and NIB

shows that the seismic isolation decreases the seismic risk imposed on the displacement demand over the pile group foundation.

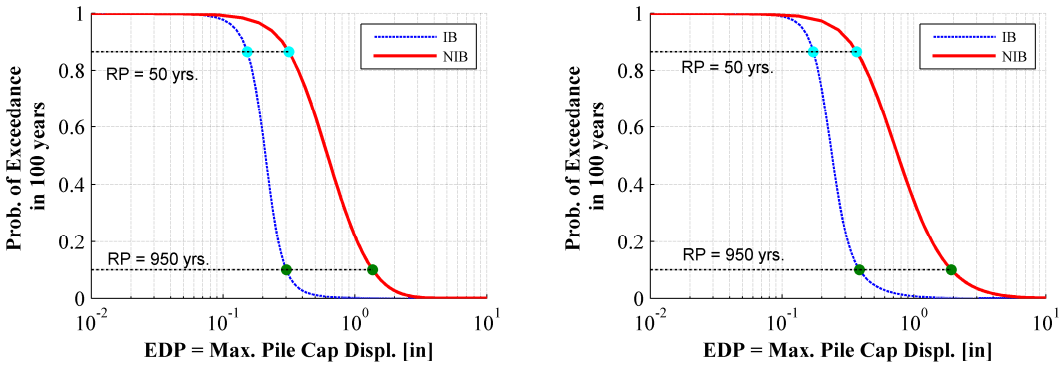

Figure 5.76: Probabilistic seismic demand hazard curve of pile cap displacement of foundation under pier #5 in the long. dir. (left) and in the trans. dir. (right)

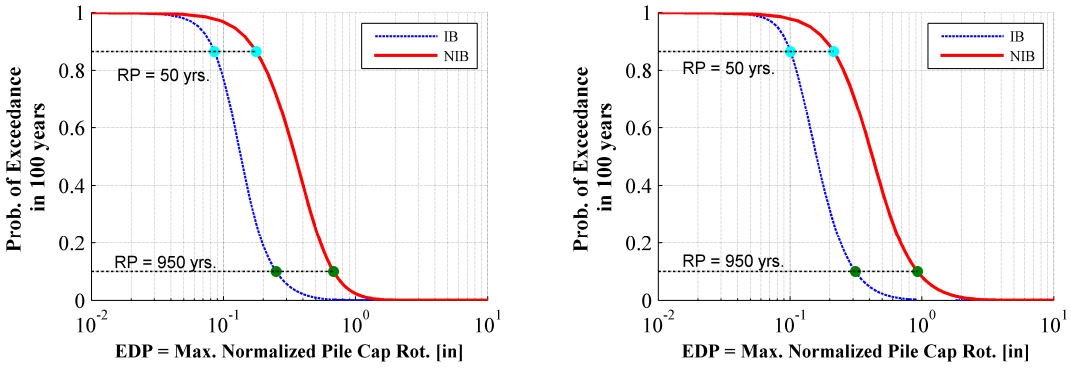

Figure 5.77: Probabilistic seismic demand hazard curve of pile cap rotation of foundation under pier #5 in the long. dir. (left) and in the trans. dir. (right)

The force demand hazard of the pile foundation in terms of maximum moment and maximum shear force in the piles under the pier column #5 is presented in Figure 5.78 for bending moment and Figure 5.79 for shear force.

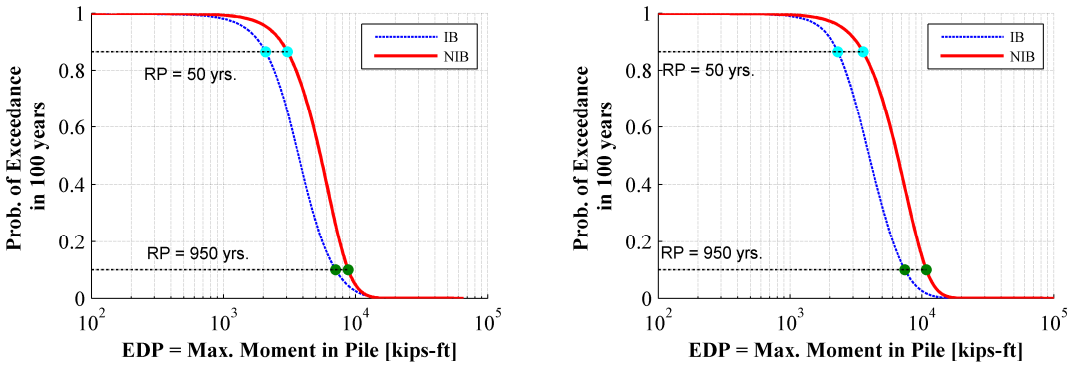

Figure 5.78: Probabilistic seismic demand hazard curve of bending moment of piles under pier #5 in the long. dir. (left) and in the trans. dir. (right)

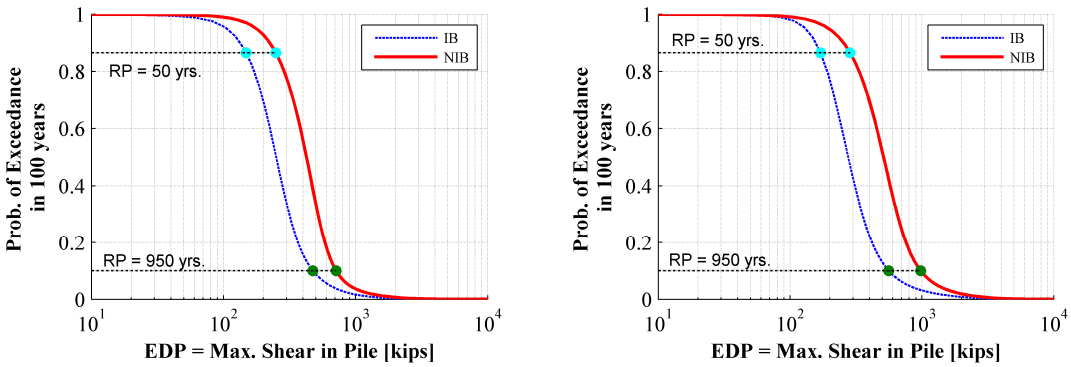

Figure 5.79: Probabilistic seismic demand hazard curve of shear force of piles under pier #5 in the long. dir. (left) and in the trans. dir. (right)

Seismic Risk to Track

Figure 5.80 displays the stress hazard of the rail at the abutment gap #1 (left end of the bridge). The seismic isolation imposed larger stresses to the rail due to the axial force in the longitudinal direction of the bridge. Regarding the stress risk due to transverse bending caused by the relative displacement of the deck at the abutment gap, the seismic hazards for IB and NIB are close at low hazard levels under the restraint of shear keys after the initial gap closure, while the stress at high hazard levels for IB is larger than NIB due to larger displacement demand on the shear keys for IB.

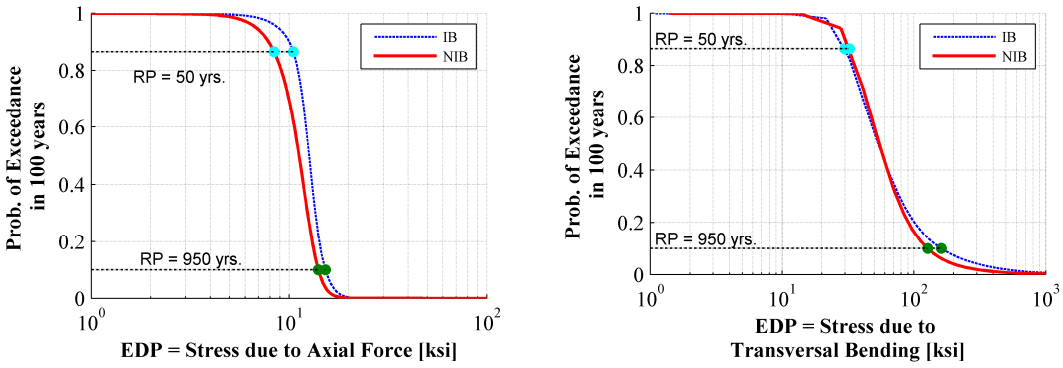

Figure 5.80: Probabilistic seismic demand hazard curve of rail stress at abutment expansion joint #1 due to axial force in the long. dir. (left) and in the trans. dir. (right)

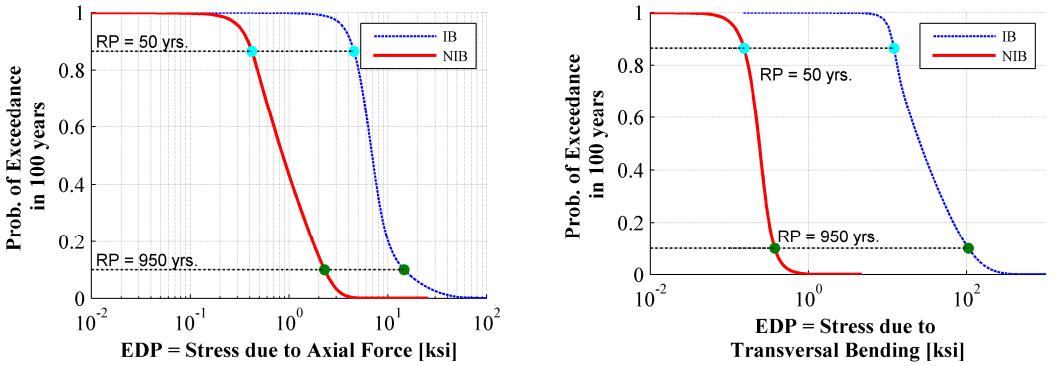

Figure 5.81: Probabilistic seismic demand hazard curve of rail stress at interior expansion joint #2 due to axial force in long. dir. (left) and bending in trans. dir. (right)

Besides the rail stress due to relative deck displacement to the abutments at the bridge ends, the relative displacement of adjacent bridge deck at interior expansion joints also leads to the detrimental effect of seismic isolation, i.e., higher risk to rail stress. The probabilistic seismic hazard of the rail stress at interior expansion joint #2 is presented in Figure 5.81. The rail stress due to axial force in the longitudinal direction of the bridge (NIB) is much smaller than that generated in IB, while stress hazard is still in the acceptable range compared to the allowable axial rail stress limit (14ksi) specified for the conditional stress demand limit under

OBE. It implies that the rail stress due to the relative displacement of adjacent bridge decks at the interior expansion joints is still under control even seismic isolation is introduced.

For the rail stress caused by relative displacement of adjacent decks in the transverse direction, the seismic isolation increases the rail stress value associated with 86% probability of exceedance from 0.5ksi in NIB to 16ksi in IB, and for a 10% probability of exceedance from 2.5ksi in NIB to 111.0ksi in IB. The predicted rail stress hazard is based on the elastic behavior assumed for the rail, which leads to unreliable stress hazard when it the yield stress is exceeded for high hazard levels. Discontinuity of deck displacement is the most critical concern when using the seismic isolation, as implied from the seismic demand hazard results of rail stress due to the transverse bending from relative deck displacement in the transverse direction.

5.5. Probabilistic Seismic Demand Hazard Analysis: Cloud Method

The cloud method employs the simplest prediction model based on linear regression analysis, which is widely used to build a mathematical model between the predictor/regressor as the input and the response as the output. In the conditional PSDHA using cloud method, the intensity measure IM (or a transformation of IM) is chosen to be the predictor, and the structural response EDPs (or a transformation of the EDPs) are chosen as the response variables. Typically, the power law, a linear relationship between the ln(IM) and ln(EDP), is utilized, which was verified between the IM and some representative EDPs, such as roof displacement, story drift ratio, pier top drift.

As a quantitative model, the cloud method rests on four principal assumptions: Linearity, Independence, Homoscedasticity (constant variance), and Normality. In contrast, the stripe method allows violation of the linearity and homoscedasticity to account for the fluctuating variance and nonlinearity of the prediction of the mean. Compared to the cloud

method, more accurate estimation of conditional demand can be achieved in stripe method if enough stripe levels with enough ground motion records at each hazard level are used at cost of computational work. As an alternative to the stripe method, the cloud method remains an important option because of its reduced computational expense (Baker, 2005) and its exemption of interpolation or extrapolation for hazard levels other than the specified stripes. Besides, another benefit of the cloud method is that the same ensemble of ground motion records can be used for all design alternatives, whereas in the stripe method, rescaling of ground motion records and de-convolution analyses must be performed multiple times. This is because different IM values are associated with each record due to the change of fundamental period for different design alternatives, leading to different scaling and thus redo of de-convolution analysis.

To reduce the computational demand involved for the probabilistic parametric/optimization analysis performed afterwards, the cloud method for the PSDHA is resorted to as a compromise between computational work and accuracy of the probabilistic performance evaluation. To assess the cloud method for seismic risk estimation in CHSR Prototype Bridge, its application is applied here first and compared with the stripe method results, in terms of conditional and unconditional probabilistic seismic demand hazard analysis.

5.5.1. Conditional PSDHA using cloud method

In this section, the conditional PSDHA results using “cloud” method are presented displaying the probabilistic performance of IB and NIB. Included are the cloud plots, the conditional demand statistics (median and percentiles) with respect to different seismic hazard levels, and the complementary CDF of two selected hazard levels (OBE and MCE).

In the cloud plot, a scatter plot for the EDP sample in the log scale is presented with the linear regressed line for the estimation of the mean of ln(EDP), i.e., the median of EDP (η_{EDP}) when lognormal distribution of EDP is assumed. The two percentiles (16^{th} percentile and 84^{th} percentile), representing one standard deviation away from the mean for normal distributed random variable ln(EDP), are also included. The fitted normal distribution for ln(EDP) conditioned on OBE and MCE hazard levels are illustrated to reflect the goal of the conditional probabilistic seismic demand analysis.

Instead of showing the cloud plots separately, the conditional statistics (median, percentiles) over a continuous range of seismic hazard levels and PDFs conditioned on OBE and MCE hazard levels are exhibited for comparison purpose with respect to the conditioned seismic hazard levels rather than the IM. The conditional PDFs on OBE and MCE hazard levels are also sketched for comparison. The complementary CDFs conditioned on those two hazard levels are displayed right after.

The results for a variety of EDPs are enclosed, including such EDPs like the absolute deck acceleration, relative deck displacement, pier column base shear/moment, pile cap translation/rotation, pile shear/moment, rail stress and so on.

Figure 5.82 to Figure 5.83 depicts the conditional demand hazard analysis results of absolute deck acceleration over pier #5 of IB and NIB in the longitudinal direction of the bridge. The introduction of seismic isolation decreased the acceleration demand hazard efficiently in terms of the mean conditional to specific hazard levels (i.e., OBE, and MCE), but the dispersion is increased, as explained by the steepness of the CCDF. A separate cluster of data points obtained from seismic simulation for IB under earthquakes with higher intensities is generated due to the pounding at the interior expansion joints.

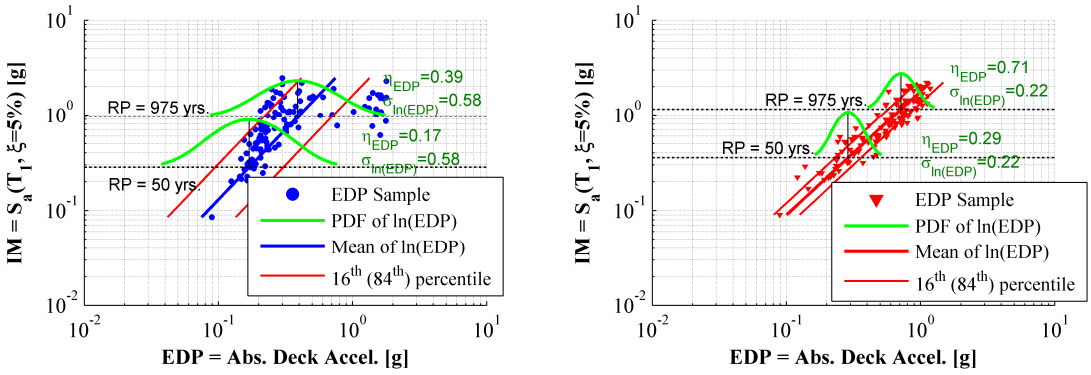

Figure 5.82: Conditional PSDHA results: conditional PDF of absolute deck acceleration over pier #5 in long. dir. (x) for IB (left) and NIB (right)

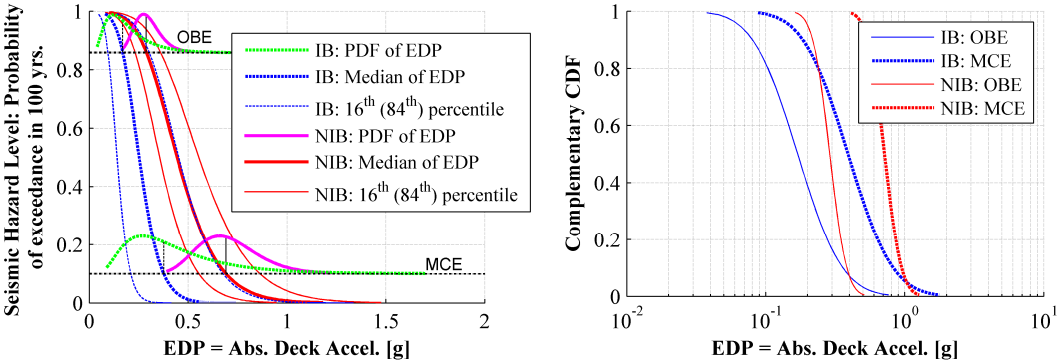

Figure 5.83: Comparison of conditional probabilistic properties of demand for all hazard levels (left) and conditional CCDF for representative hazard level (right) on the absolute deck acceleration over pier #5 in long. dir. (x).

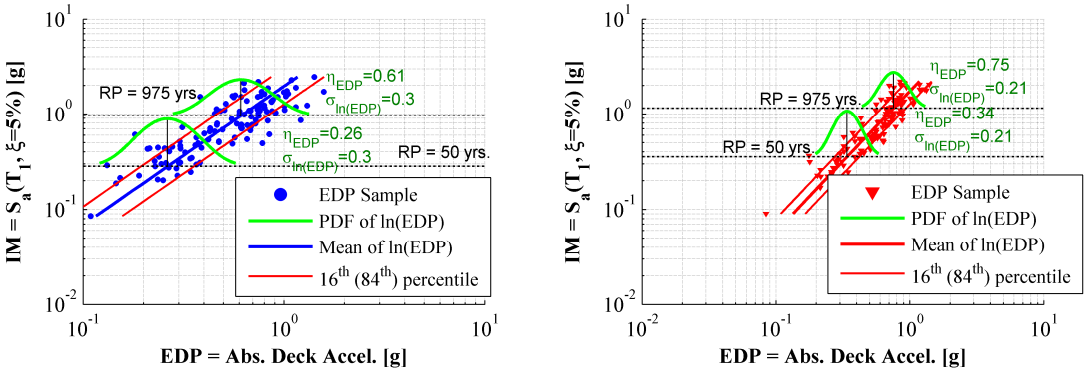

Figure 5.84: Conditional probabilistic demand hazard analysis results: conditional PDF of absolute deck acceleration over pier #5 in trans. dir. for IB (left) and NIB (right)

Figure 5.84 to Figure 5.85 shows the conditional demand hazard analysis results of absolute deck acceleration over pier #5 of IB and NIB in the transverse direction of the bridge. The seismic isolation tends to reduce the absolute deck acceleration demand conditional to specific hazard levels (i.e., OBE, and MCE).

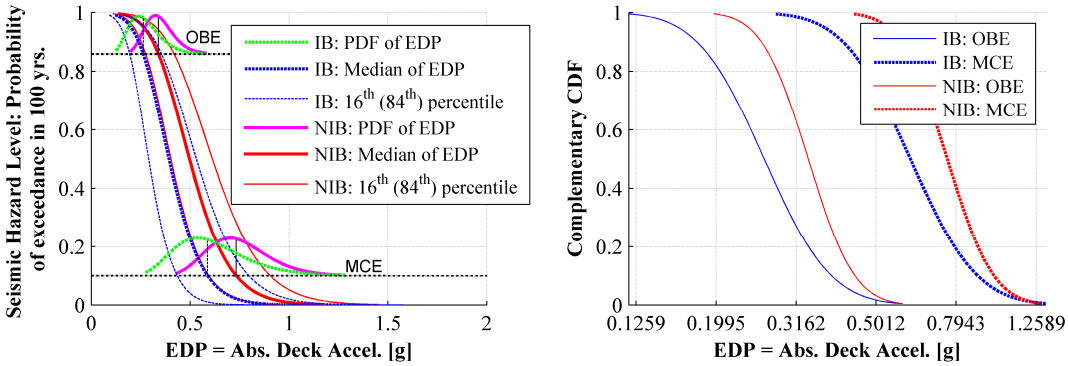

Figure 5.85: Comparison of conditional probabilistic properties of demand for all hazard levels (left) and conditional CCDF given representative hazard level (right) on absolute deck acceleration over pier #5 in trans. dir. (y)

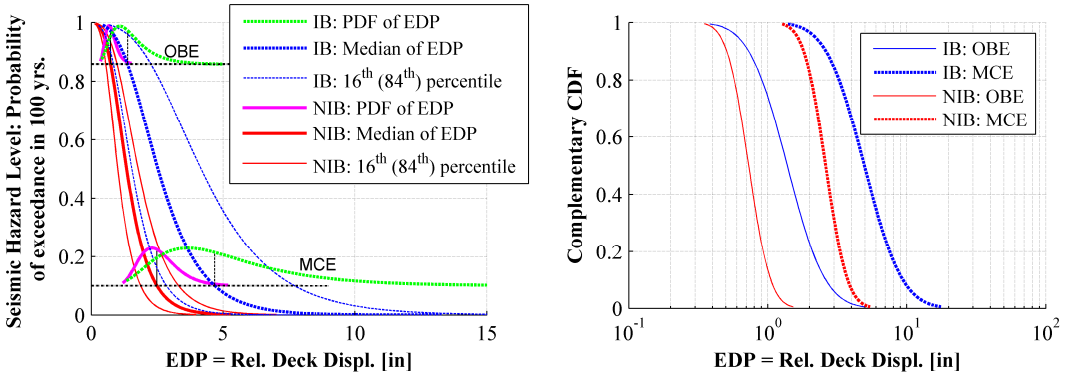

Figure 5.86: Comparison of conditional probabilistic properties of demand for all hazard levels (left) and conditional CCDF for representative hazard levels (right) on relative deck displacement over pier #5 in long. dir. (x)

Figure 5.86 shows the conditional demand hazard analysis results using the cloud method of EDP: relative deck displacement over pier #5 of IB and NIB in the longitudinal direction of the bridge. Figure 5.87 shows the comparison results of EDP: relative deck

displacement over pier #5 of IB and NIB in the transverse direction of the bridge. The conditional demand mean and variance of relative deck displacement increase for IB.

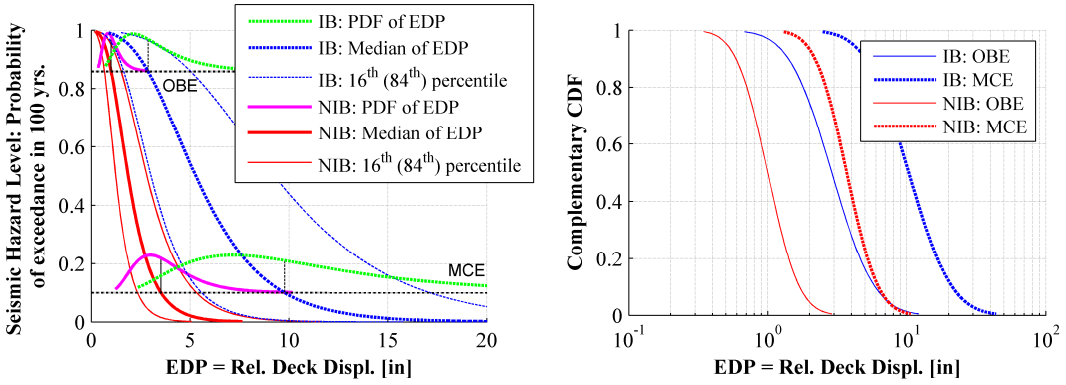

Figure 5.87: Comparison of conditional probabilistic properties of demand for all hazard levels (left) and conditional CCDF given representative hazard level (right) on relative deck displacement over pier #5 in trans. dir. (y)

Figure 5.88 to Figure 5.89 show the conditional demand hazard analysis results using cloud method for the deformation of the seismic isolator over pier #5 in both longitudinal and transverse direction of the IB.

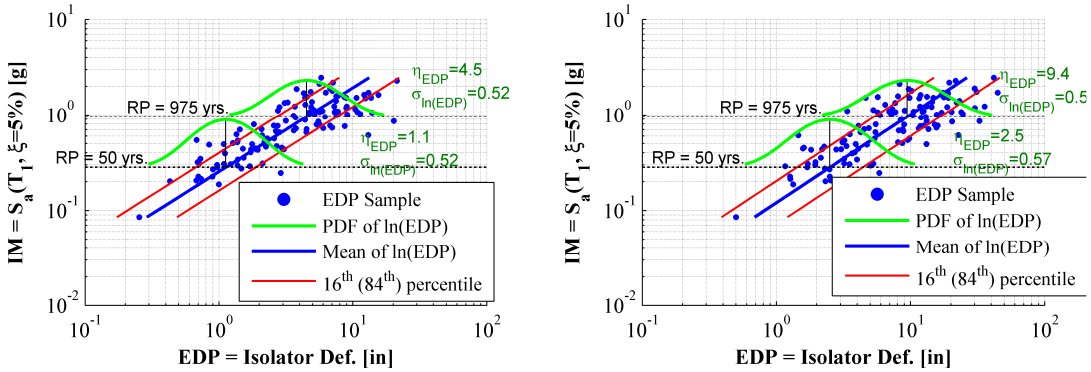

Figure 5.88: Conditional PSDHA results: conditional PDF of isolator deformation over pier #5 in long. dir. (left) and transverse dir. (right) for IB

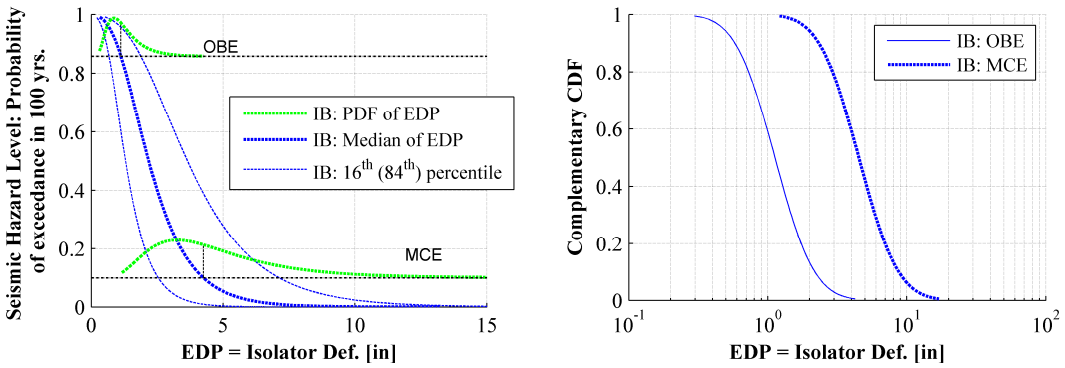

Figure 5.89: Comparison of conditional probabilistic properties of demand for all hazard levels (left) and conditional CCDF given representative hazard level (right) on isolator deformation over pier #5 in long. dir. (x)

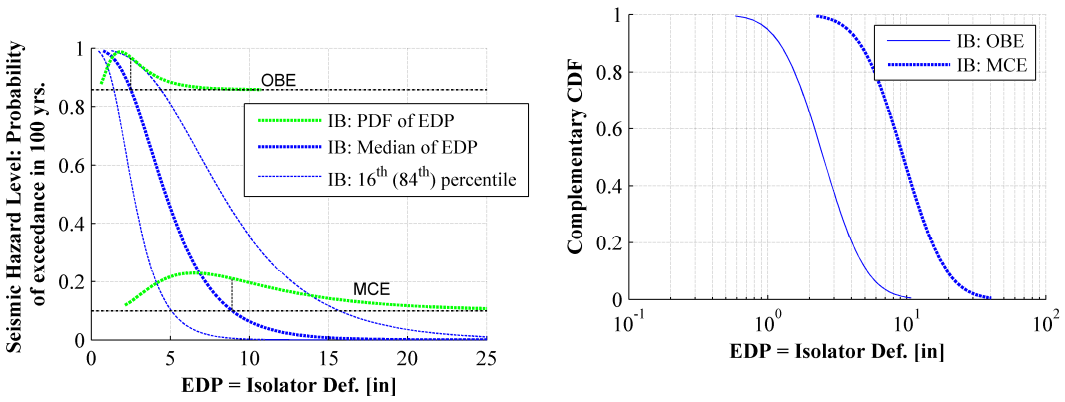

Figure 5.90: Comparison of conditional probabilistic properties of demand for all hazard levels (left) and conditional CCDF given representative hazard level (right) on isolator deformation over pier #5 in trans. dir. (y)

Figure 5.91 shows the conditional demand hazard analysis results using cloud method for column drift of pier #5 w.r.t. the pile cap of IB and NIB in the longitudinal direction of the bridge for comparison. Similar results are presented in Figure 5.92 in the transverse direction. The conditional demand hazard imposed on the pier column drift indicates that seismic isolation significantly reduced the displacement demand on the pier column. The reduction effects are more pronounced for higher than lower hazard levels.

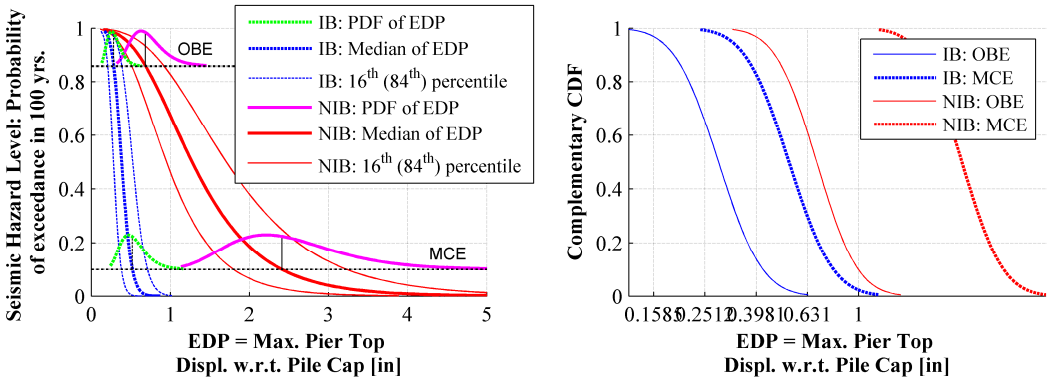

Figure 5.91: Comparison of conditional probabilistic properties of demand for all hazard levels (left) and conditional CCDF given representative hazard level (right) on pier column drift of pier #5 w.r.t. pile cap in long. dir. (x)

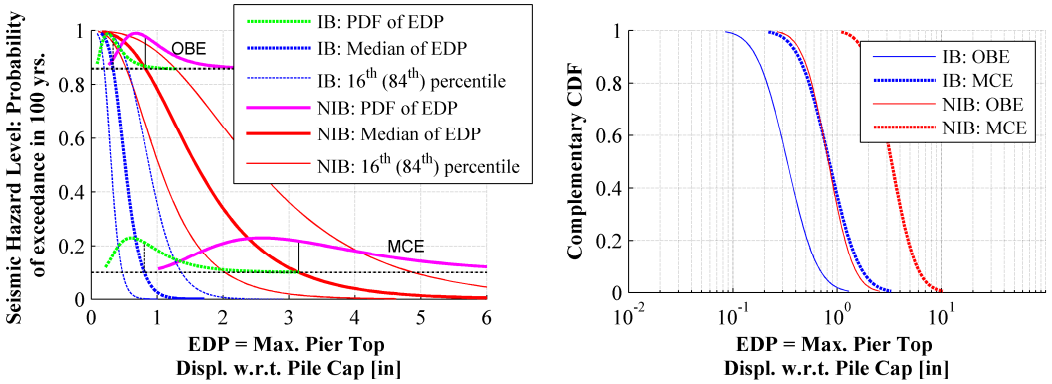

Figure 5.92: Comparison of conditional probabilistic properties of demand for all hazard levels (left) and conditional CCDF given representative hazard level (right) on pier column drift of pier #5 w.r.t. pile cap in trans. dir. (y)

The beneficial effects of seismic isolation on the demand over pier columns (base moment) are illustrated in Figure 5.93 in the longitudinal direction, Figure 5.94 in the transverse direction of the bridge.

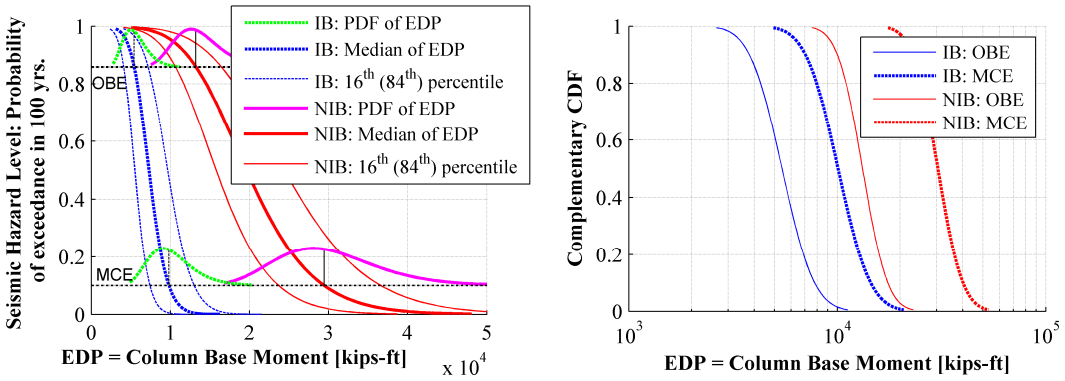

Figure 5.93: Comparison of conditional probabilistic properties of demand for all hazard levels (left) and conditional CCDF given representative hazard level (right) on column base moment of pier #5 in long. dir. (x)

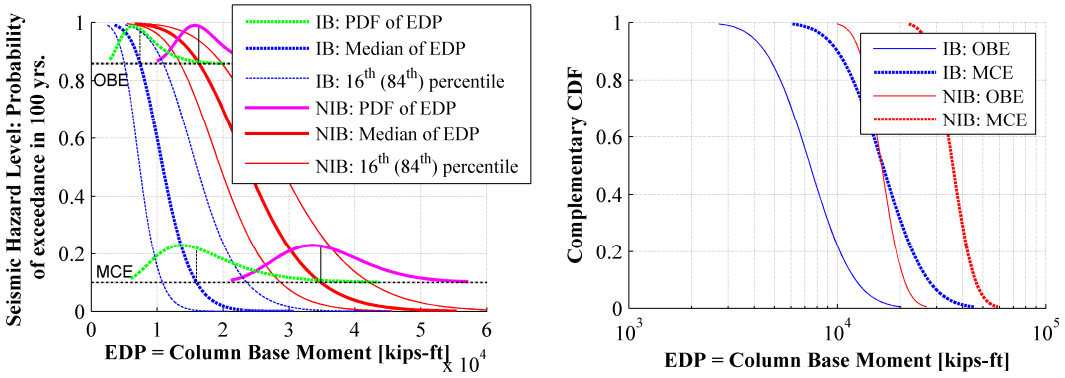

Figure 5.94: Comparison of conditional probabilistic properties of demand for all hazard levels (left) and conditional CCDF given representative hazard level (right) on column base moment of pier #5 in long. dir. (x)

Consistent with the conditional demand hazard imposed on the bottom moment of pier columns, the reduction effects of seismic isolation in the force demand in pier columns are demonstrated in Figure 5.95 with the base shear of pier column #5 in longitudinal direction and Figure 5.96 in transverse direction. Similar observations can be made from Figure 5.97 and Figure 5.98 for the total base shear force. The introduction of seismic isolation can reduce

the conditional seismic demand hazard of substructures (pier columns) in IB at the MCE hazard level to approximately the conditional demand hazard of NIB at the OBE hazard level.

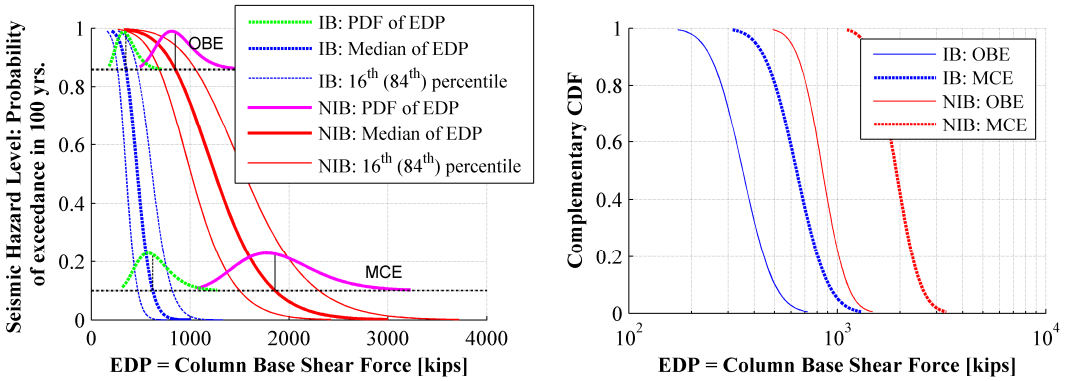

Figure 5.95: Comparison of conditional probabilistic properties of demand for all hazard levels (left) and conditional CCDF given representative hazard level (right) on column base shear force of pier #5 in long. dir. (x)

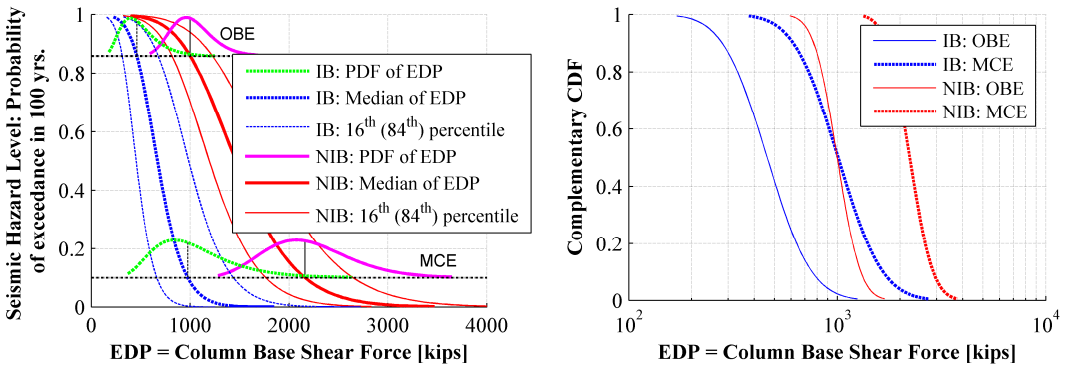

Figure 5.96: Comparison of conditional probabilistic properties of demand for all hazard levels (left) and conditional CCDF given representative hazard level (right) on column base shear force of pier #5 in trans. dir. (y)

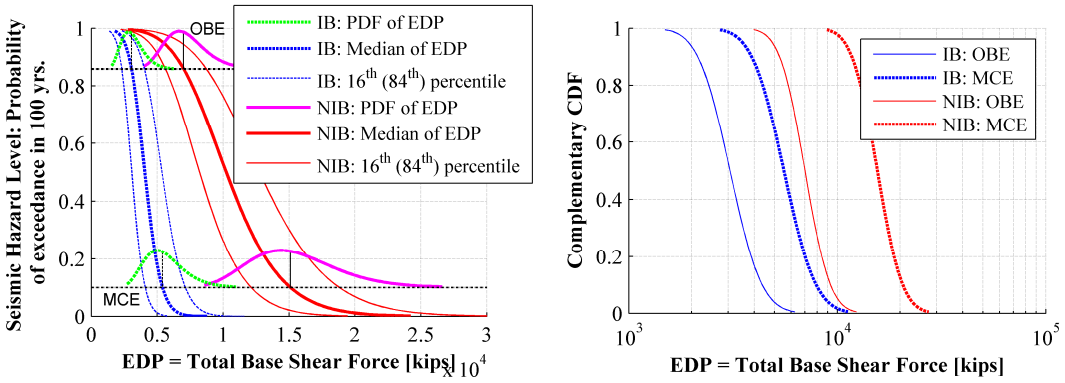

Figure 5.97: Comparison of conditional probabilistic properties of demand for all hazard levels (left) and conditional CCDF given representative hazard level (right) on total base shear force in long. dir. (x)

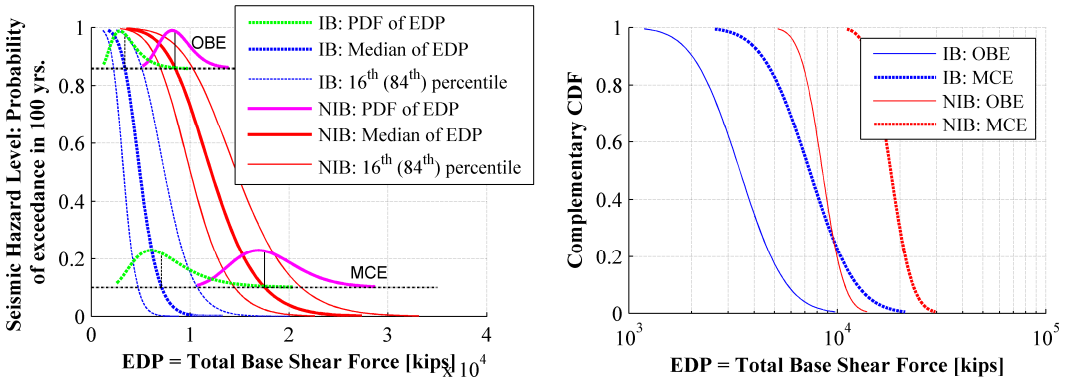

Figure 5.98: Comparison of conditional probabilistic properties of demand for all hazard levels (left) and conditional CCDF given representative hazard level (right) on total base shear force in trans. dir. (y)

Seismic Risk to Pile Group Foundation

Figure 5.99 shows the conditional seismic hazard analysis results of the pile cap displacement of the foundation under pier #5 in the longitudinal direction of IB and NIB. Figure 5.100 shows the corresponding results in the transverse direction.

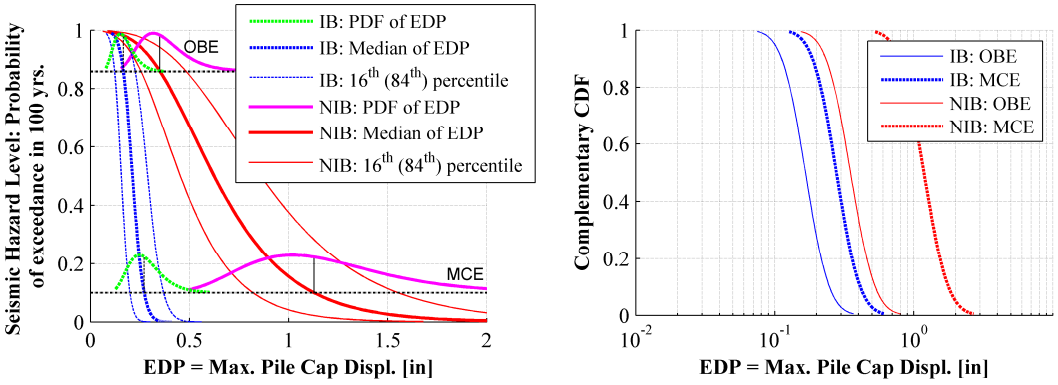

Figure 5.99: Comparison of conditional probabilistic properties of demand for all hazard levels (left) and conditional CCDF given representative hazard level (right) on pile cap displacement of foundation under pier #5 in long. dir. (x)

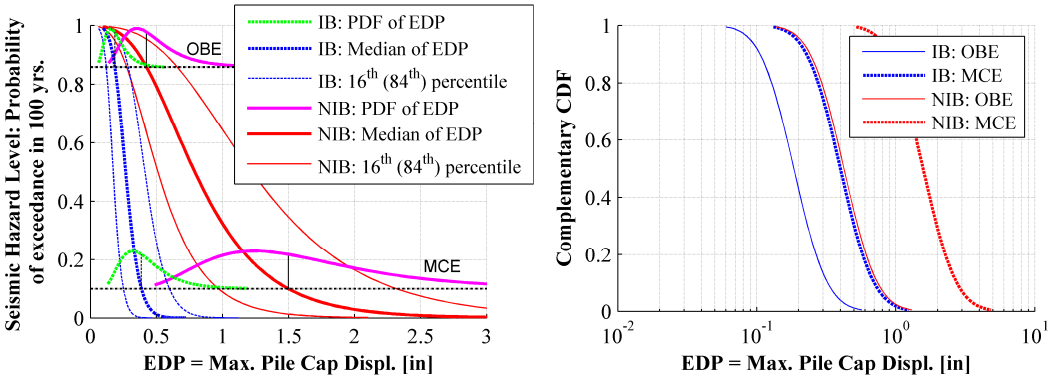

Figure 5.100: Comparison of conditional probabilistic properties of demand for all hazard levels (left) and conditional CCDF given representative hazard level (right) on pile cap displacement of foundation under pier #5 in trans. dir. (y)

Figure 5.101 shows the conditional seismic hazard analysis results of the pile cap rotation of foundation under pier #5 in the longitudinal direction of IB and NIB. Figure 5.102 shows the corresponding results for the transverse direction.

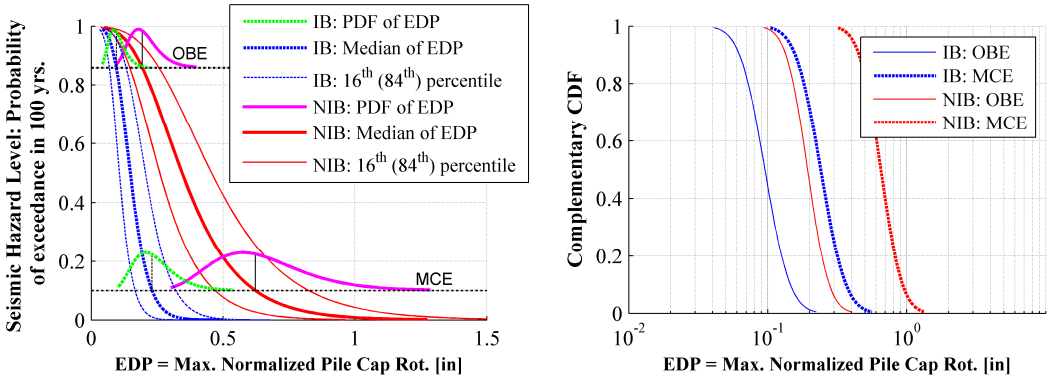

Figure 5.101: Comparison of conditional probabilistic properties of demand for all hazard levels (left) and conditional CCDF given representative hazard level (right) on pile cap rotation of foundation under pier #5 in long. dir. (x)

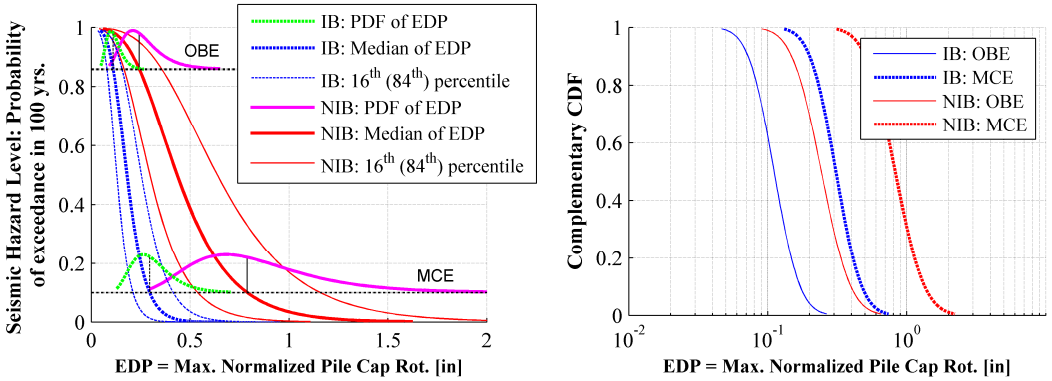

Figure 5.102: Comparison of conditional probabilistic properties of demand for all hazard levels (left) and conditional CCDF given representative hazard level (right) on pile cap rotation of foundation under pier #5 in trans. dir. (y)

Figure 5.103 shows the conditional seismic hazard analysis results of the bending moment of piles under pier #5 in the longitudinal direction of IB and NIB. Figure 5.104 shows the corresponding comparison the transverse direction.

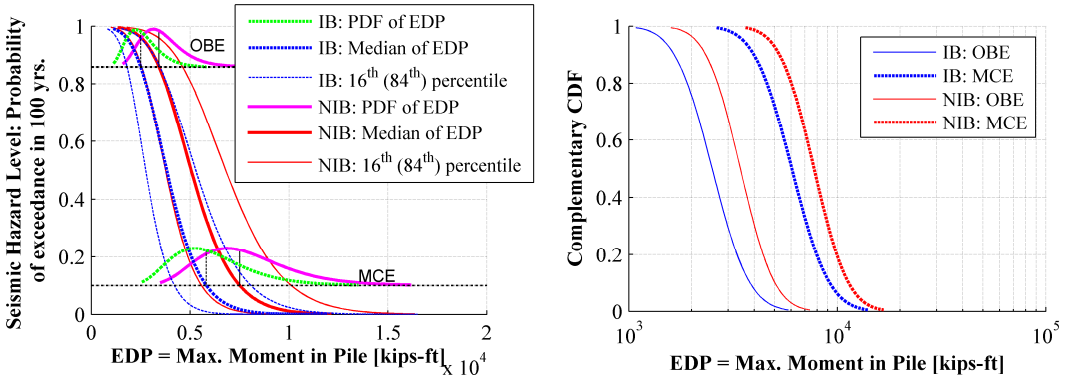

Figure 5.103: Comparison of conditional probabilistic properties of demand for all hazard levels (left) and conditional CCDF given representative hazard level (right) on bending moment of piles under pier #5 in long. dir. (x)

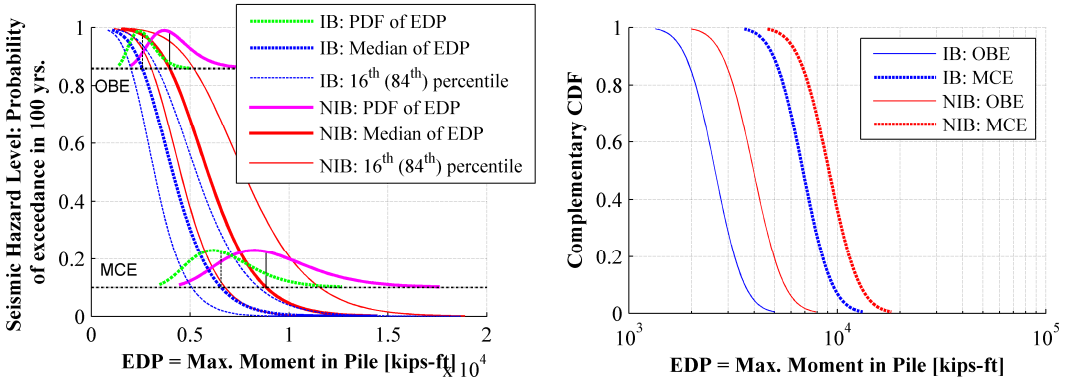

Figure 5.104: Comparison of conditional probabilistic properties of demand for all hazard levels (left) and conditional CCDF given representative hazard level (right) on bending moment of piles under pier #5 in trans. dir. (y)

Figure 5.105 shows the conditional seismic hazard analysis results of the shear force of the piles under pier #5 in the longitudinal direction of IB and NIB. Figure 5.106 shows the corresponding comparison for the transverse direction.

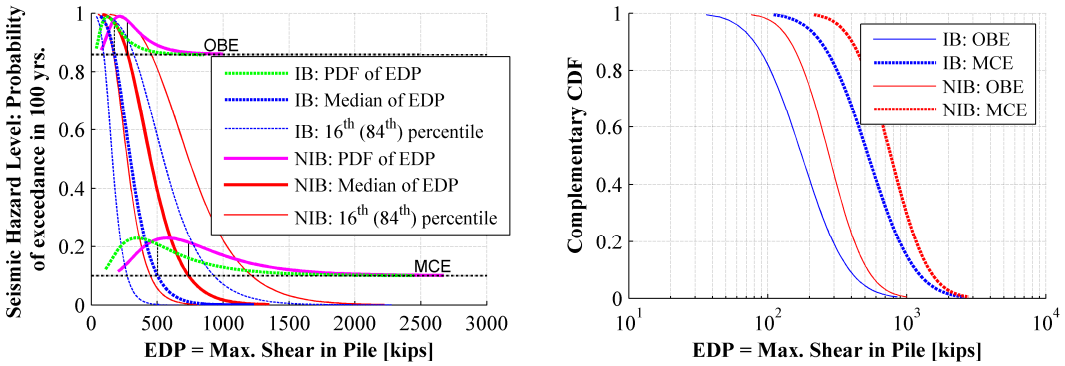

Figure 5.105: Comparison of conditional probabilistic properties of demand for all hazard levels (left) and conditional CCDF given representative hazard level (right) on shear force of piles under pier #5 in long. dir. (x)

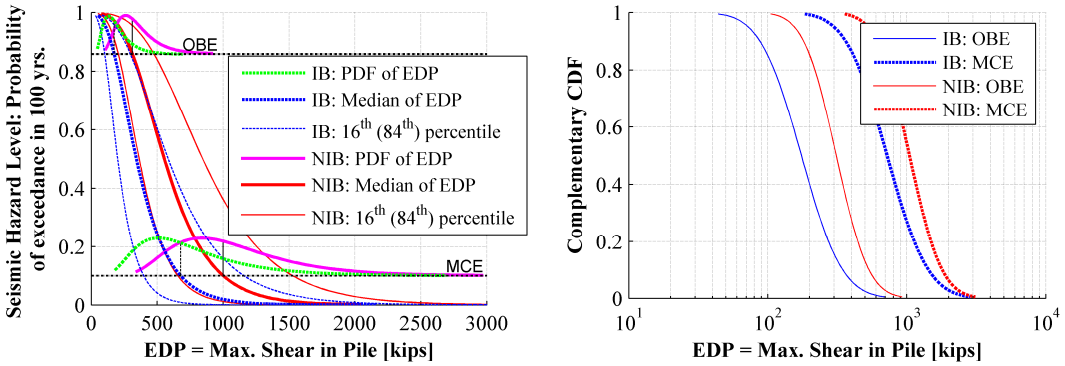

Figure 5.106: Comparison of conditional probabilistic properties of demand for all hazard levels (left) and conditional CCDF given representative hazard level (right) on shear force of piles under pier #5 in trans. dir. (y)

Seismic Risk to Track

Figure 5.107 show the conditional seismic hazard analysis results of the rail stress at the abutment expansion joint #1 due to axial force in the longitudinal direction of IB and NIB.

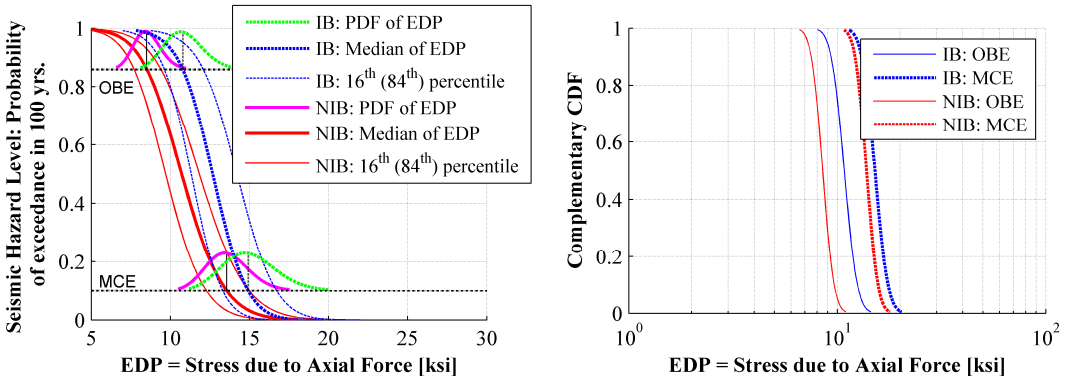

Figure 5.107: Comparison of conditional probabilistic properties of demand for all hazard levels (left) and conditional CCDF given representative hazard level (right) on rail stress at abutment expansion joint #1 due to axial force in long. dir. (x)

Figure 5.108 shows the conditional seismic hazard analysis results of the rail stress at the abutment expansion joint #1 due to bending in the transverse direction of IB and NIB for comparison.

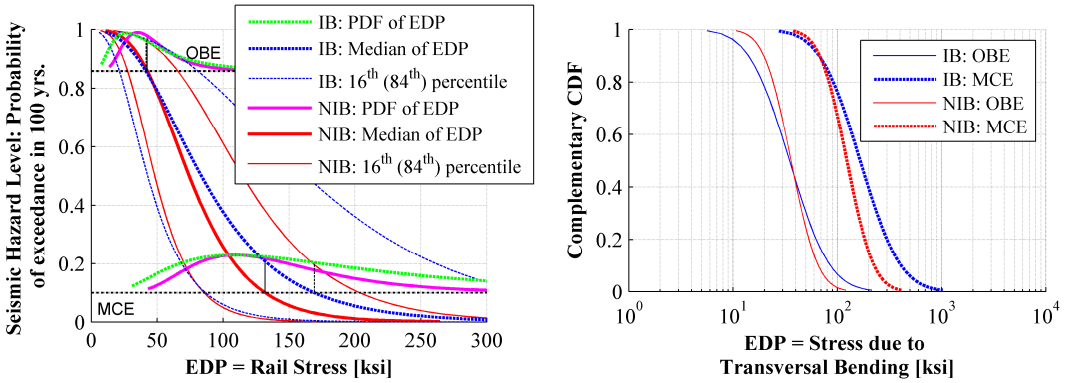

Figure 5.108: Comparison of conditional probabilistic properties of demand for all hazard levels (left) and conditional CCDF given representative hazard level (right) on rail stress at abutment expansion joint #1 due to bending in trans. dir. (y)

Figure 5.109 shows the conditional seismic hazard analysis results of the rail stress at interior expansion joint #2 due to axial force in the longitudinal direction of IB and NIB.

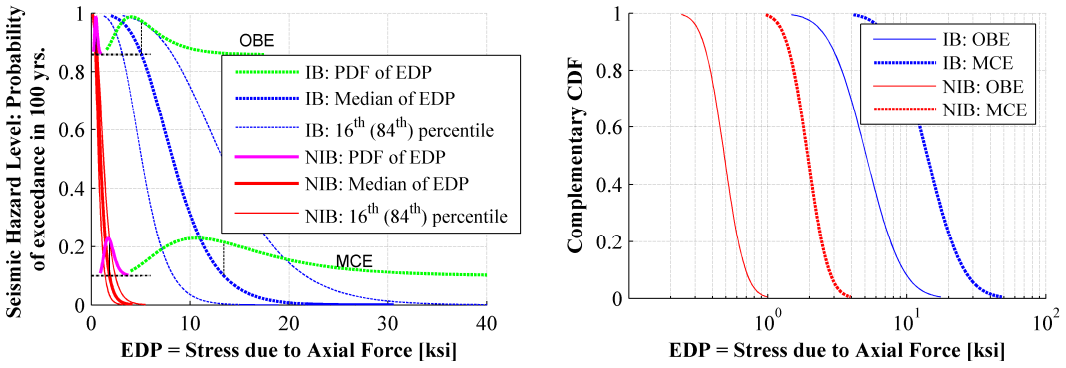

Figure 5.109: Comparison of conditional probabilistic properties of demand for all hazard levels (left) and conditional CCDF given representative hazard level (right) on rail stress at interior expansion joint #2 due to axial force in long. dir. (x)

Figure 5.110 shows the conditional seismic hazard analysis results of the rail stress at interior expansion joint #2 due to bending in the transverse direction of IB and NIB.

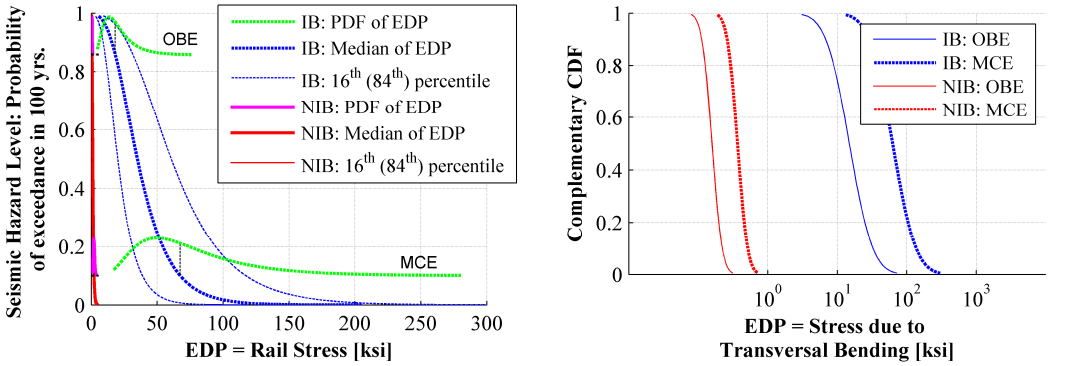

Figure 5.110: Comparison of conditional probabilistic properties of demand for all hazard levels (left) and conditional CCDF given representative hazard level (right) on rail stress at interior expansion joint #2 due to bending in trans. dir. (y)

5.5.2. Probabilistic seismic demand hazard analysis

The PSDHA results are shown in the comparison between stripe method and cloud method in next section.

5.6. Comparison between the Stripe Method and the Cloud Method

The comparison between the cloud method and the stripe method in terms of conditional and unconditional PSDHA is carried out for both IB and NIB. Some representative comparison results of typical EDPs of interest are included as follows.

The conditional PSDHA results of absolute acceleration of deck over pier #5 in the longitudinal direction of the bridge for NIB and IB are presented in Figure 5.111 and Figure 5.112. The corresponding unconditional PSDHA results are included as well in Figure 5.113. For NIB, both methods lead to similar results in terms of the conditional demand statistics and conditional probability distributions for conditional PSDHA, thus similar probabilistic seismic demand hazard curves for unconditional PSDHA. In contrast, the assumption of linear regression in cloud method (i.e., linearity, and constant variance) was not satisfied due to separate cluster of data points generated by the pounding effect at the gaps in Figure 5.82, thus the cloud method overestimates the conditional mean and variance for lower hazard levels while underestimates the mean and variance for higher hazard levels. Consequently, the cloud method leads to erroneous estimation of the probability distributions for conditional PSDHA as well as probabilistic seismic demand hazard curves for unconditional PSDHA. As a matter of fact this EDP of IB shows the worst performance of the cloud method compared to the stripe method. For other EDPs of interest for IB and NIB, the cloud method attains reliable performance evaluation results compared to the stripe method.

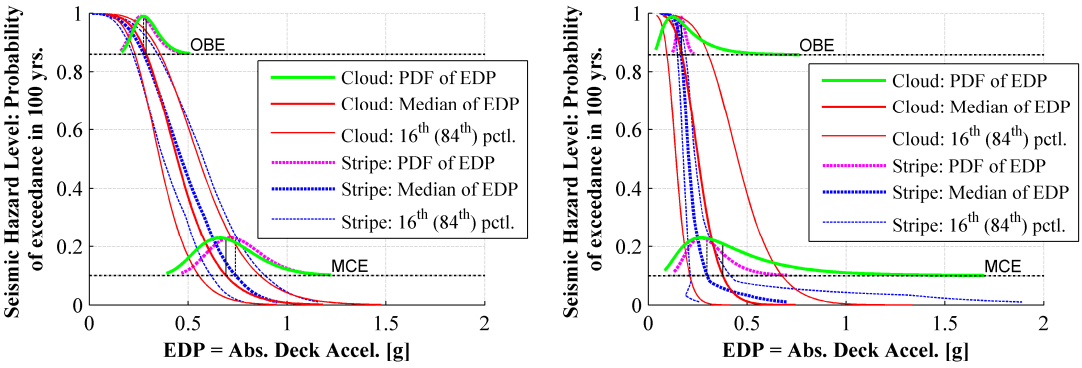

Figure 5.111: Comparison of cloud method with stripe method in terms of conditional demand statistics and PDF of absolute acceleration of deck over pier #5 in longitudinal direction for NIB (left) and IB (right)

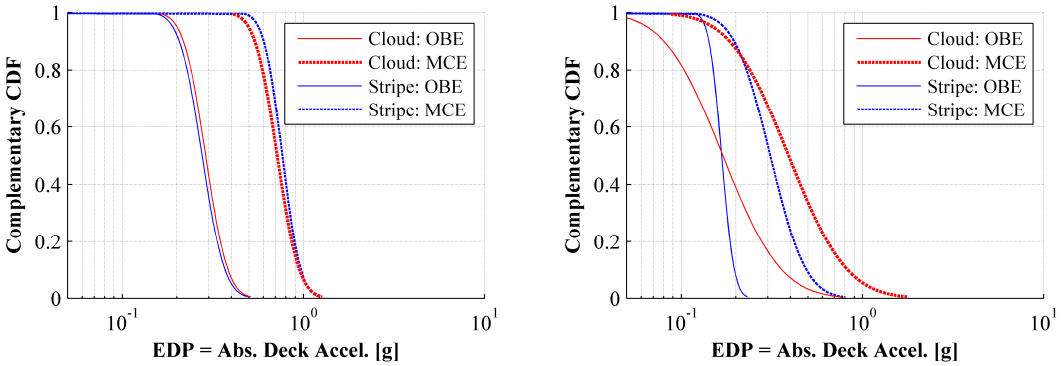

Figure 5.112: Comparison of cloud method with stripe method in terms of conditional CCDF on two hazard levels of absolute acceleration of deck over pier #5 in longitudinal direction for NIB (left) and IB (right)

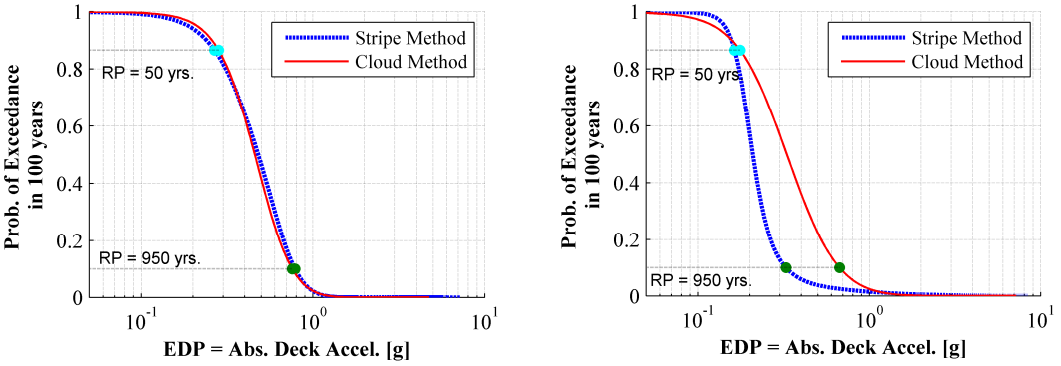

Figure 5.113: Comparison of cloud method with stripe method in terms of unconditional probabilistic seismic demand hazard of absolute acceleration of deck over pier #5 in longitudinal direction for NIB (left) and IB (right)

The conditional PSDHA results of the absolute acceleration of the deck over pier #5 in the transverse direction for NIB and IB are presented in Figure 5.114 and Figure 5.115. The corresponding unconditional PSDHA results are included in Figure 5.116. The comparison between the cloud method and the stripe method for this EDP illustrates that both lead to an approximately close probabilistic performance evaluation, characterized by conditional probabilistic statistics, conditional probability distribution, and probabilistic seismic demand hazard. Thus, the cloud method is considered to be a reliable alternative method to estimate the seismic risk to this EDP.

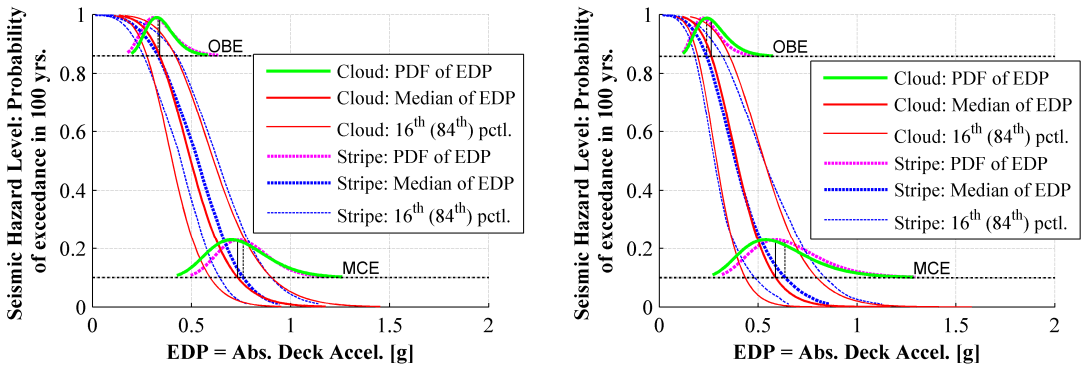

Figure 5.114: Comparison of cloud method with stripe method in terms of conditional demand statistics and PDF of absolute acceleration of deck over pier #5 in transverse direction for NIB (left) and IB (right)

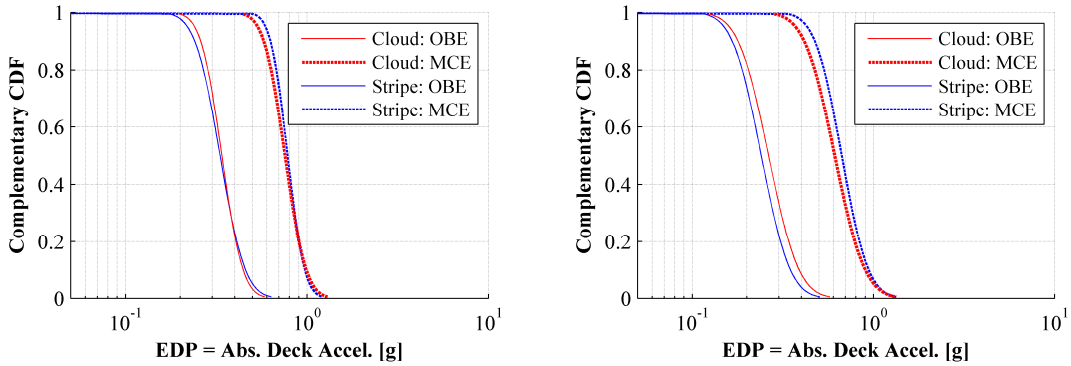

Figure 5.115: Comparison of cloud method with stripe method in terms of conditional CCDF on two hazard levels of absolute acceleration of deck over pier #5 in transverse direction for NIB (left) and IB (right)

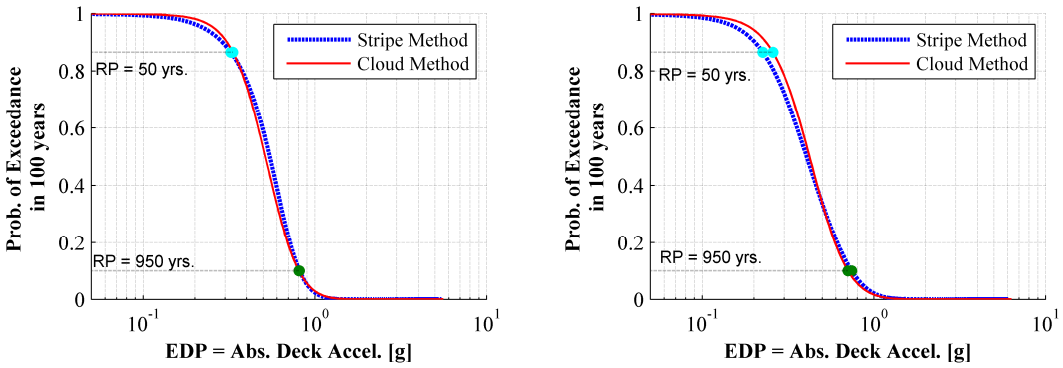

Figure 5.116: Comparison of cloud method with stripe method in terms of unconditional probabilistic seismic demand hazard of absolute acceleration of deck over pier #5 in transverse direction for NIB (left) and IB (right)

The conditional PSDHA results of relative displacement of deck over pier #5 in the longitudinal direction of the bridge for NIB and IB are presented in Figure 5.117 and Figure 5.118. The corresponding unconditional PSDHA results are included in Figure 5.119. Similar to the absolute acceleration of the deck over pier #5 in the longitudinal direction of bridge, the cloud method does not perform well in terms of the conditional variance estimation for low hazard level in IB due to the constant variance assumption inherent in linear regression, leading to discrepancies in the conditional probability distribution curve. However, the cloud method performs as well as stripe method and leads to close conditional and unconditional PSDHA results for NIB.

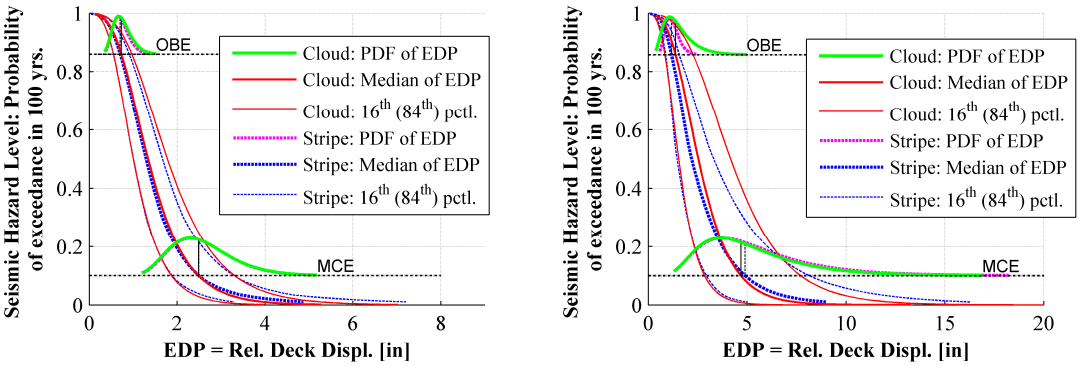

Figure 5.117: Comparison of cloud method with stripe method in terms of conditional demand statistics and PDF of relative displacement of deck over pier #5 in longitudinal direction for NIB (left) and IB (right)

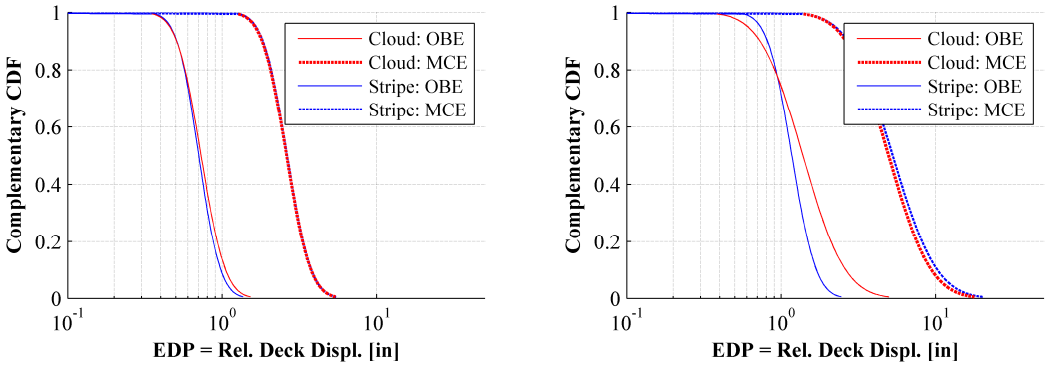

Figure 5.118: Comparison of cloud method with stripe method in terms of conditional CCDF on two hazard levels of relative displacement of deck over pier #5 in longitudinal direction for NIB (left) and IB (right)

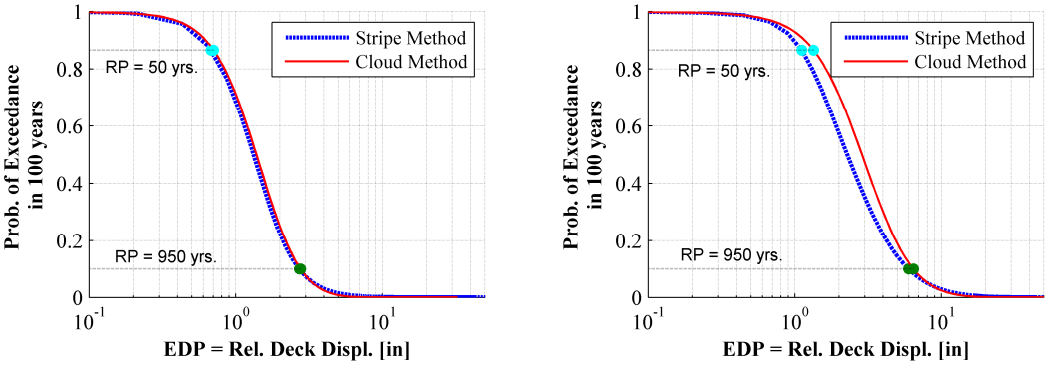

Figure 5.119: Comparison of cloud method with stripe method in terms of unconditional probabilistic seismic demand hazard of relative displacement of deck over pier #5 in longitudinal direction for NIB (left) and IB (right)

The conditional PSDHA results of the relative displacement of the deck over pier #5 in the transverse direction of bridge for NIB and IB are presented in Figure 5.120 and Figure 5.121. The corresponding unconditional PSDHA results are included as well in Figure 5.122. In the transverse direction of the bridge, with the increase of hazard levels (i.e., increase of intensities of earthquake ground motions), more nonlinearity gets involved in the seismic isolation system. The cloud method tends to underestimate the seismic response for higher hazard levels and overestimate the seismic response for lower hazard levels due to the assumptions made by this method.

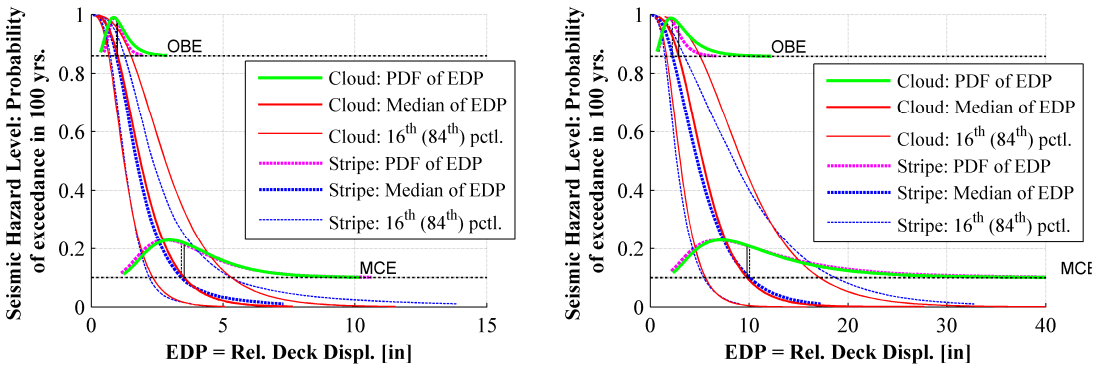

Figure 5.120: Comparison of cloud method with stripe method in terms of conditional demand statistics and PDF of relative displacement of deck over pier #5 in transverse direction for NIB (left) and IB (right)

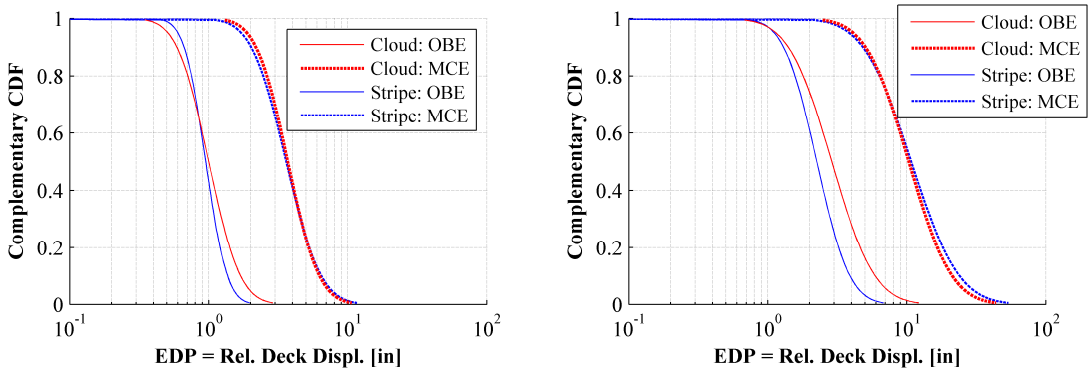

Figure 5.121: Comparison of cloud method with stripe method in terms of conditional CCDF on two hazard levels of relative displacement of deck over pier #5 in transverse direction for NIB (left) and IB (right)

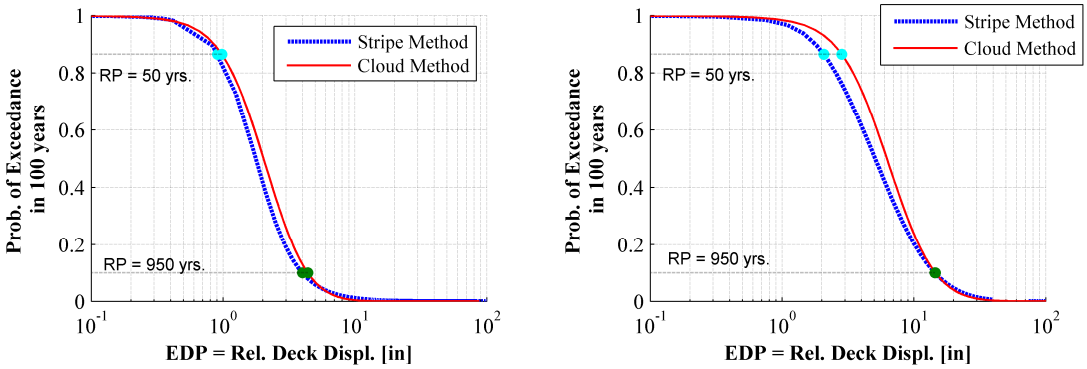

Figure 5.122: Comparison of cloud method with stripe method in terms of unconditional probabilistic seismic demand hazard of relative displacement of deck over pier #5 in transverse direction for NIB (left) and IB (right)

The conditional PSDHA results of the column base shear at pier #5 in the longitudinal direction of the bridge for NIB and IB are presented in Figure 5.123 and Figure 5.124. The corresponding unconditional PSDHA results are included in Figure 5.125.

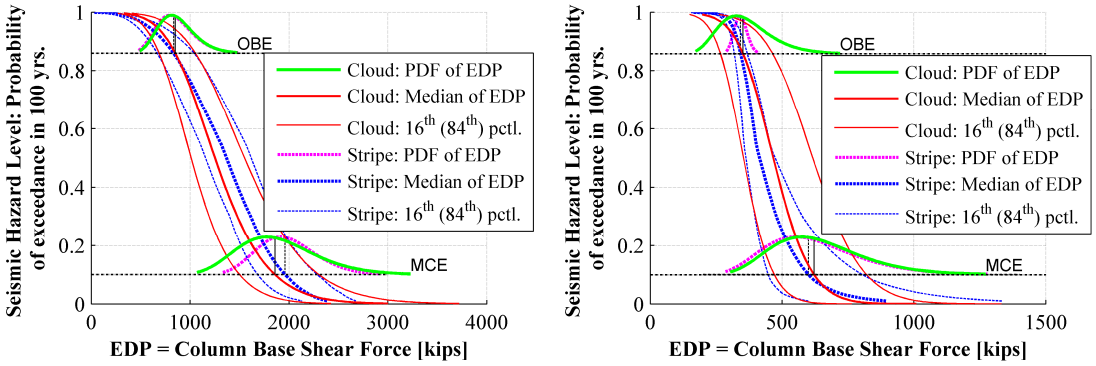

Figure 5.123: Comparison of cloud method with stripe method in terms of conditional demand statistics and PDF of column base shear of pier #5 in longitudinal direction for NIB (left) and IB (right)

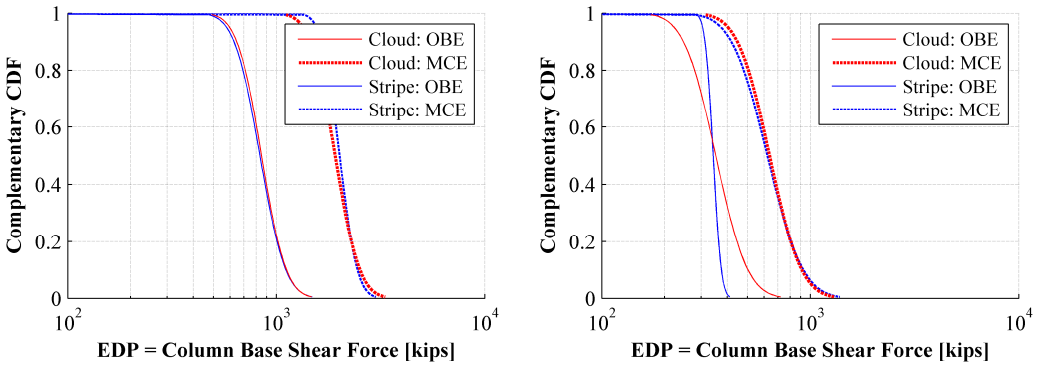

Figure 5.124: Comparison of cloud method with stripe method in terms of conditional CCDF on two hazard levels of column base shear force of pier #5 in longitudinal direction for NIB (left) and IB (right)

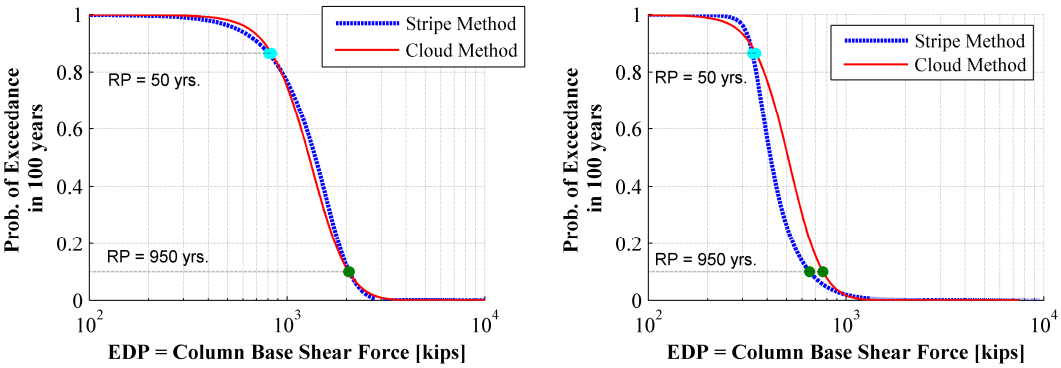

Figure 5.125: Comparison of cloud method with stripe method in terms of unconditional probabilistic seismic demand hazard of column base shear force of pier #5 in longitudinal direction for NIB (left) and IB (right)

The conditional PSDHA results of the column base shear of pier #5 in the transverse direction for NIB and IB are presented in Figure 5.126 and Figure 5.127. The corresponding unconditional PSDHA results are included in Figure 5.128.

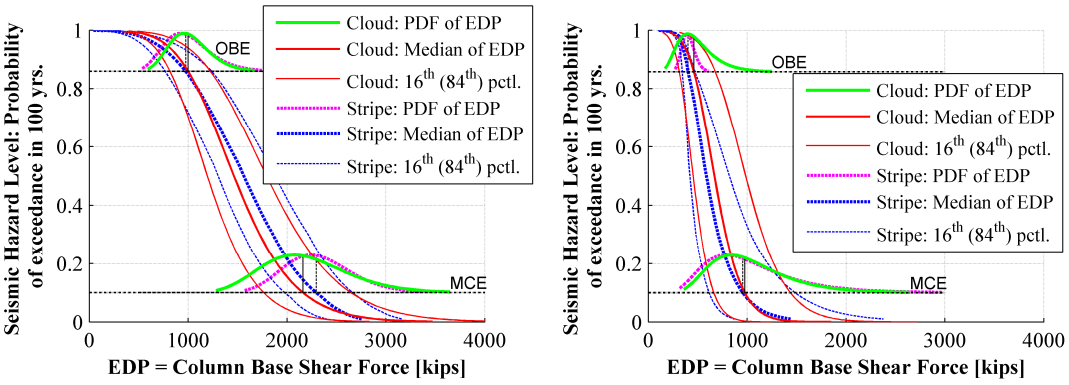

Figure 5.126: Comparison of cloud method with stripe method in terms of conditional demand statistics and PDF of column base shear force of pier #5 in transverse direction for NIB (left) and IB (right)

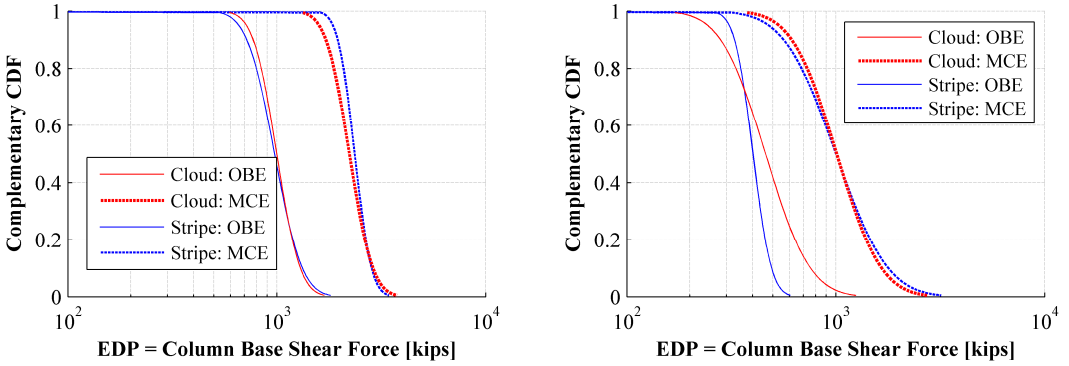

Figure 5.127: Comparison of cloud method with stripe method in terms of conditional CCDF on two hazard levels of column base shear force of pier #5 in transverse direction for NIB (left) and IB (right)

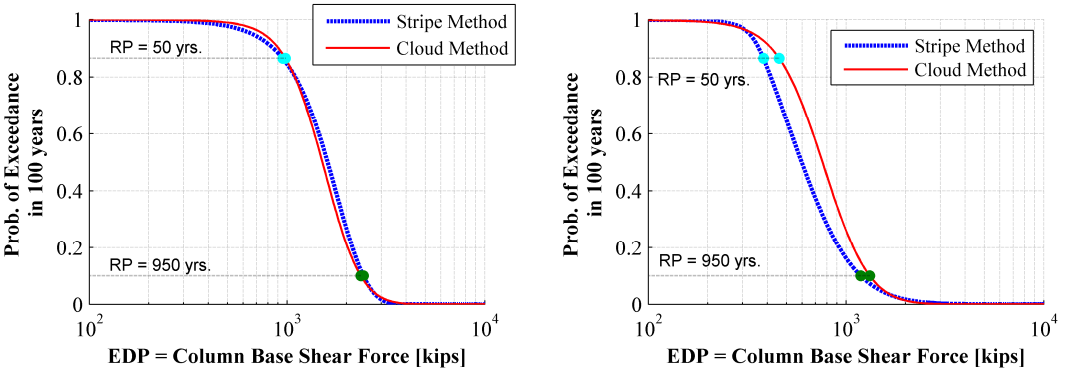

Figure 5.128: Comparison of cloud method with stripe method in terms of unconditional probabilistic seismic demand hazard of column base shear force of pier #5 in transverse direction for NIB (left) and IB (right)

The conditional PSDHA results of maximum moment of piles under pier #5 in the longitudinal direction for NIB and IB are presented in Figure 5.129 and Figure 5.130. The corresponding unconditional PSDHA results are included in Figure 5.131.

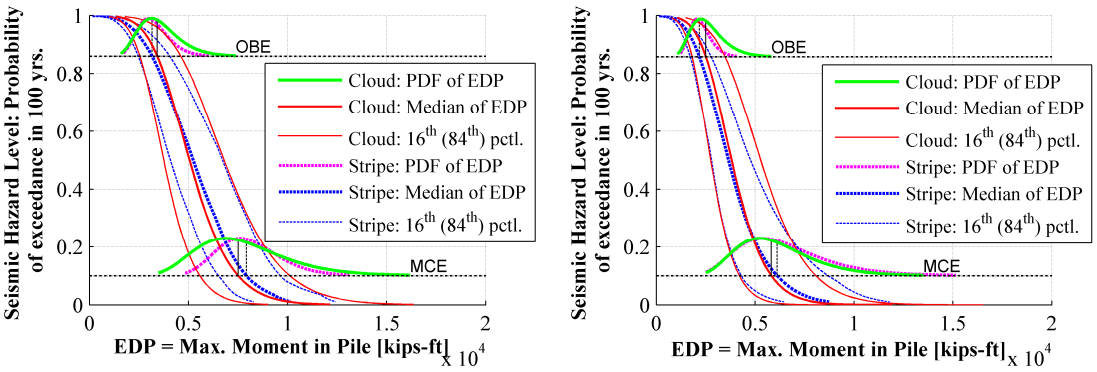

Figure 5.129: Comparison of cloud method with stripe method in terms of conditional demand statistics and PDF of maximum moment of piles under pier #5 in longitudinal direction for NIB (left) and IB (right)

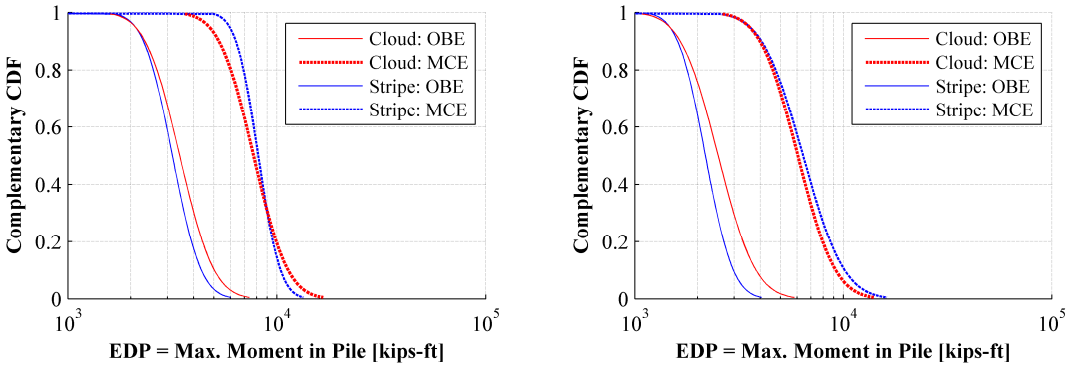

Figure 5.130: Comparison of cloud method with stripe method in terms of conditional CCDF on two hazard levels of maximum moment of piles under pier #5 in longitudinal direction for NIB (left) and IB (right)

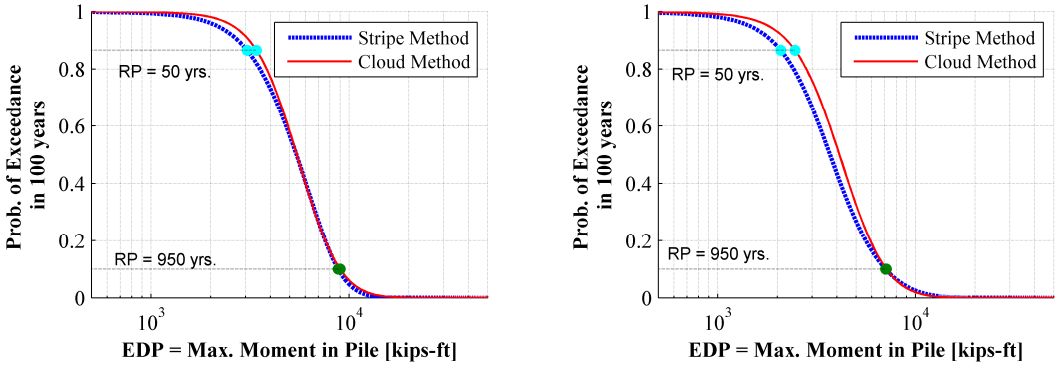

Figure 5.131: Comparison of cloud method with stripe method in terms of unconditional probabilistic seismic demand hazard of maximum moment of piles under pier #5 in longitudinal direction for NIB (left) and IB (right)

The conditional PSDHA results of maximum moment of piles under pier #5 in the transverse direction for NIB and IB are presented in Figure 5.132 and Figure 5.133. The corresponding unconditional PSDHA results are included in Figure 5.134.

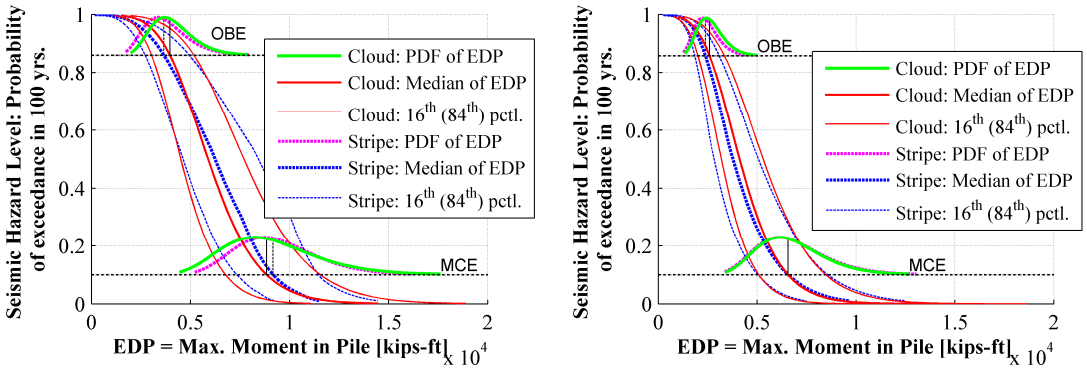

Figure 5.132: Comparison of cloud method with stripe method in terms of conditional demand statistics and PDF of maximum moment of piles under pier #5 in transverse direction for NIB (left) and IB (right)

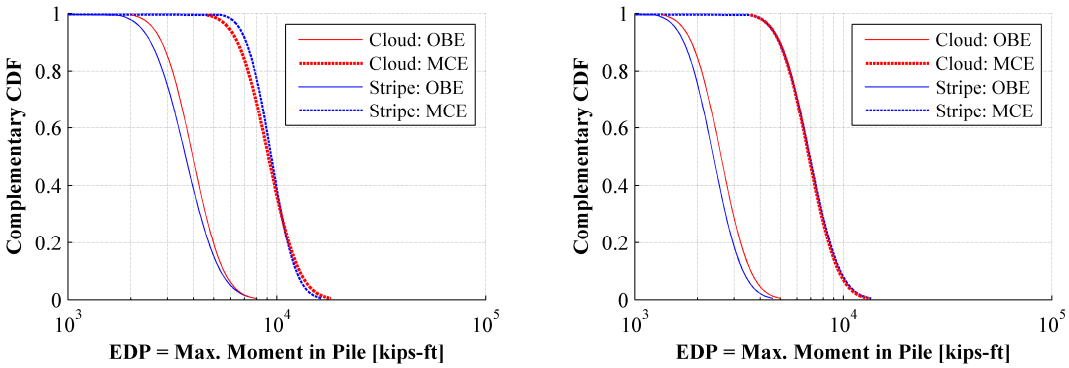

Figure 5.133: Comparison of cloud method with stripe method in terms of conditional CCDF on two hazard levels of maximum moment of piles under pier #5 in transverse direction for NIB (left) and IB (right)

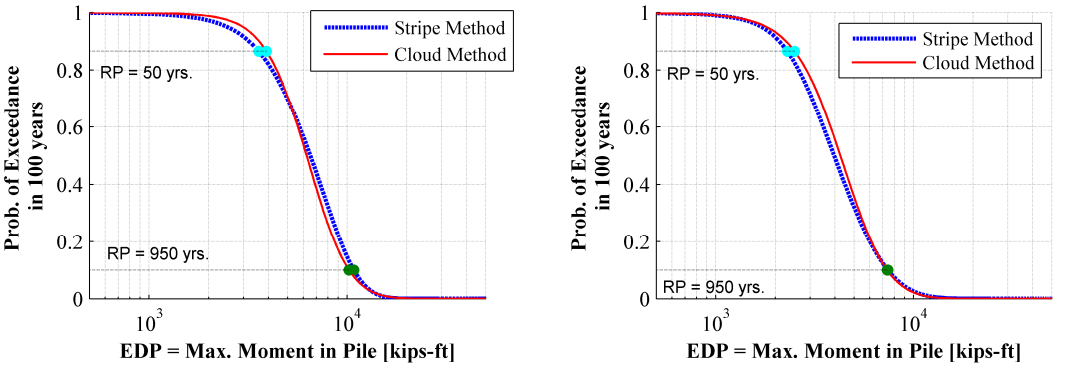

Figure 5.134: Comparison of cloud method with stripe method in terms of unconditional probabilistic seismic demand hazard of maximum moment of piles under pier #5 in transverse direction for NIB (left) and IB (right)

The above comparison results between cloud method and stripe method indicates that cloud method with restrictive assumptions attains close PSDHA results to the stripe method especially for NIB. For IB, the cloud method tends to underestimate the seismic demand conditional to higher hazard levels and to overestimate the seismic demand conditional to lower hazard levels. This is caused by the restrictive linear and constant variance assumption imposed on linear regression employed in the cloud method. The assumptions are violated

when nonlinearity is significantly increased in the structural system subjected to earthquakes from lower hazard levels to higher hazard levels, especially when a sharp change of structural mechanism, i.e., pounding due to engagement of gaps. Generally, the cloud method leads to a close approximation of the probabilistic seismic demand hazard of IB obtained with the stripe method except for the absolute acceleration of at the bridge deck. Considering the attractive advantage of less computational demand of the cloud method over the stripe method, as well as the lack of interpolation/extrapolation for other unspecified seismic hazard levels as in stripe method, the cloud method is adopted for reasonable levels of confidence.

5.7. Conclusions

Aiming to evaluate the probabilistic seismic performance of the California High-Speed Rail (CHSR) Prototype Bridges with seismic isolations, conditional probabilistic seismic demand hazard analysis (PSDHA) and unconditional PSDHA are carried out using both the stripe method and the cloud method. The beneficial and detrimental effects of seismic isolation on the CHSR prototype bridges are explored and investigated. From the probabilistic performance evaluation of IB and NIB, the conditional mean and variance of the bridge deck peak acceleration is reduced for lower hazard levels. The pounding effect increases the conditional variance of the bridge deck acceleration in the longitudinal direction. The conditional mean and variance of deck displacement increases mainly due to the seismic isolation, while the conditional mean and variance of the pier column drift decrease as a result of the earthquake protection from seismic isolation. The conditional mean of force demand on piers (i.e., pier column base shear, pier column base moment) and deformation/force demand on pile foundations (i.e., pile cap rotation, pile cap translation, maximum moments in piles, shear force in piles) are decreased with the seismic isolation system. The conditional mean and variance of the maximum stress in the rail at both abutment gaps and interior expansion joints

(i.e., stresses due to axial force in the longitudinal direction of the bridge and bending in the transverse direction of the bridge) increase significantly except for the stress at the abutment gap due to transversal bending, because the shear keys with gaps govern the transverse behavior for both IB and NIB.

From the comparison between cloud method and stripe method, the cloud method attains almost the same probabilistic performance estimation for NIB. For NIB, the cloud method leads to similar results to the stripe method, although with more discrepancy for some EDP (i.e., absolute deck acceleration in the longitudinal direction of the bridge), explained by the restrictive assumptions of linearity and constant variance being violated when strong nonlinearity is involved (i.e., seismic isolation, and especially when the occurrence of pounding is more probable). Considering the computational advantages and acceptable performance evaluation compared to the stripe method, the cloud method is selected to perform the conditional probabilistic seismic demand hazard analysis (PSDHA) and unconditional PSDHA for CHSR Prototype Bridge in the subsequent parametric and optimization analyses.

CHAPTER 6

CLOUD COMPUTING FOR PARAMETRIC PROBABILISTIC ANALYSIS & OPTIMIZATION

6.1. Background and Motivation

The emerging progress in numerical simulation technologies in the field of civil engineering has enabled large-scale high-fidelity numerical models to achieve a more realistic and detailed results. A simulation can be computationally costly, especially with a probabilistic algorithm involved. Fortunately, the rapid evolution of computing and information technologies facilitates the engineering simulation needed for the development of performance-based engineering aforementioned. Furthermore, in view of the rapidly decreasing cost of workstations and computing hardware, the future of engineering simulation is undoubtedly the scientific workflows and cloud computing using high-performance computing (HPC) and high throughput computing (HTC) technologies. Cloud computing has been widely developed and applied for scientific and engineering simulation on distant computers, owned and operated by others while connected to users' computers via the Internet.

The main goal in this research work is to promote the Probabilistic Performance-Based Optimum Seismic Design (PPBOSD) framework proposed in Chapter 2 by resolving

the problem of computational demand for large scale problems. The proposed PPBOSD framework is exercised on the CHSR Prototype Bridge, a large-scale complex soil-foundation-structure-rail interaction system, as a pilot study. To accomplish this goal, a significant amount of computational work is required as explained in depth in the next section. This implies highly powerful computational resources required to resolve simulations as complex as this makes it very unpractical to perform all computational work needed on a single commodity computer.

Nowadays, a dedicated parallel supercomputer is still expensive and not widely available. In contrast, building the high performance cluster with standard commodity hardware components and open source software is a cheap alternative thanks to rapidly decreasing cost of workstations and advances in networking hardware and software technologies. This is enhanced by the idea of HTC to exploit all available computing resources with distributed ownerships (grid computing) to build the HTC environment, aiming at maximizing the amount of resources available to scientists and engineers alike. Computational power is also achieved inexpensively with a collection of small-distributed processors than expensive single supercomputers.

In the probabilistic optimum seismic design of the CHSR Prototype Bridge, many nonlinear time history analyses are carried out for several design variations subjected to a suite of earthquake ground motions. Considering the inherent computational feature that the analysis jobs can be run independently and simultaneously, the HTC is an ideal environment for this type of research work. In view of its free availability, the Open source earthquake engineering simulation software framework (*OpenSees*) is a proper application client for the HTC environment. Thus, a cloud-based optimization (CBO) workflow is proposed for overall organization and the data manipulation, by integrating the numerical simulation tool (e.g.,

OpenSees), the job management software (e.g., HTCCondor), the probabilistic performance evaluation tool (e.g., PBEE), the optimization tool (e.g., OpenSees-SNOPT), and the grid computing resources.

The proposed CBO workflow framework explores and utilizes advanced computational resources and emerging information technologies to further develop the computational platform for parametric analysis and optimization of probabilistic seismic performance. This framework is intended for cases, when a bunch of independent nonlinear time history analyses need to be carried out for a design candidate, and when multiple design ideas can be simulated concurrently for comparison or optimization of design alternatives.

6.2. Computing Demand Involved in PPBOSD

The probabilistic performance-based optimum seismic design (PPBOSD) framework and application to the California High-Speed Rail (CHSR) Prototype Bridge is highly computationally demanding for two reasons: (1) for each function evaluation in the optimization process, which is a forward PBEE analysis, a set of nonlinear time history analyses, are carried for a suite of earthquake ground motions (e.g., around 280 jobs for the Stripe Method used previously in Chapter 2, and 120 jobs for the Cloud Method used in this research); (2) for optimization purposes, a forward PBEE analysis needs to be performed multiple times, depending on the optimization algorithm employed for the evaluation of the objective/constraint function, and the gradient estimation by finite difference method when required. For such large risk-based optimization problem using computational optimization algorithms and frameworks (e.g., *OpenSees-SNOPT*), HTC can be made use of for function evaluations in each iteration of the optimization process. Compared to optimization algorithms with the sequential iterative optimum seeking process where few design alternatives can be simulated simultaneously, parametric analysis as a “brutal force” optimization approach adds

more value to HTC with grid computing by simulating many design alternatives simultaneously.

For low dimensional optimization problems with few design variables (e.g., the optimization of seismic isolators' properties for CHSR Prototype Bridge herein), a graphic approach using parametric study, denoted as "brutal force" optimization, is adopted first instead of rigorous numerical optimization algorithms, maiking a full use of the HTC resources available. The CBO workflow using parametric analysis is implemented to reveal the appealing risk-based optimization capabilities and validate the rigorous optimization solution from *OpenSees-SNOPT* (e.g., application example in Chapter 2) and other mathematical optimization algorithms and frameworks described later on.

6.3. Development and Implementation of CBO Workflow

Workflow is defined as the sequence of industrial, administrative, or other processes through which a piece of work passes from initiation to completion. It is required for the parametric study and optimization of large-scale engineering systems in high performance/high throughput computing environment. Currently the finite element model of the CHSR Prototype Bridge is built in *OpenSees*, which utilizes the platform of TCL (Tool Command Language) as interpreter. Naturally, an ideal platform independent workflow can be constructed by integrating the finite element simulation tool (*OpenSees*), the job management software (i.e., *HTCondor*, *batchsubmit, etc.*), and TCL subscript for data post-processing (data reduction) and workflow organization, and *Matlab* (or compatible *Octave*) for data visualization after the computation work is accomplished.

Figure 6.1 schematically depicts the proposed and implemented cloud-based optimization (CBO) with specific application to probabilistic performance-based optimum seismic design. In this workflow, a job is uniquely defined by the finite element model of the

system with a different structural design labeled as “model (i)”, and the earthquake ground motion labeled as “EQ (j)” as excitation input. The main objective of the CBO workflow is to organize the all the jobs involved, including the seismic simulation and response feature extraction as data reduction in cloud for each single job, the probabilistic performance evaluation of a design, the transfer of response feature files, and comparison of various designs for the optimum designs. The core of this workflow lies in the every single job, which consists of 6 tasks as follows.

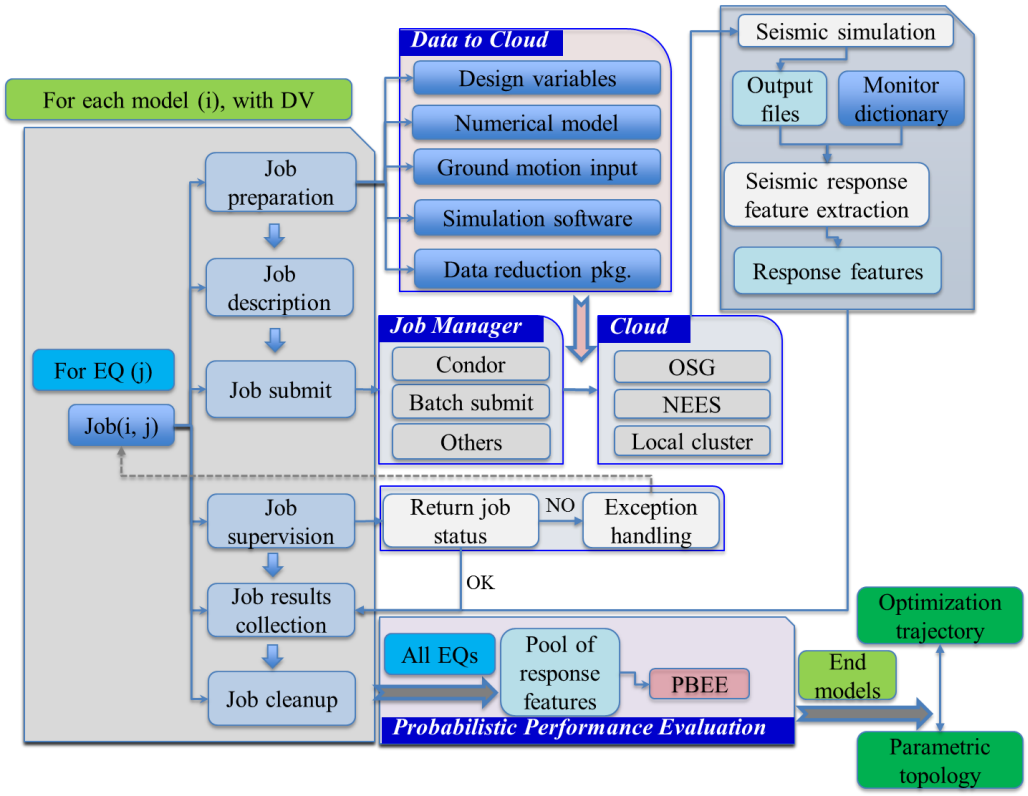

Figure 1.1: Cloud-based probabilistic optimization (CBO) workflow

Job preparation: On the job submitting node, the CBO needs to create the working directory for the job, collect and envelope all the data files needed for the seismic simulation (i.e., design variables, numerical model input files, ground motion time series files, the

simulation software, and data reduction package to extract the response features in the cloud). All these data required for seismic response simulation is sent to the cloud.

Job description: After the job preparation, the specific job description file corresponding to each job manager (i.e., Condor or HTCCondor, Batch submit, etc.) is generated. This job description file describes the executable file name, input file name for the job, the preferred computing cloud, machine requirements on which the job is to be run, etc.

Job submit: The goal of this task is to send the job to the computing cloud as described and prepared in the job description file. In the cloud, the seismic simulation is conducted first and the seismic response features of interest (i.e., the maximum base shear, the maximum pier top drift, etc.) are compiled in a monitor dictionary file extracted from the recorded simulation output files. Instead of sending back all the entire time history records (vector data), making the data transfer process the bottleneck for cloud computing, a data reduction process is carried out in the cloud to extract only the required information for probabilistic performance evaluation. This step of CBO here solves the problems of both heavy computation and data-transferring of large results files from seismic simulation of large-scale engineering system.

Job supervision: Making use of the job status inquiry capability, the CBO wraps up the job supervision task to monitor the job status in the cloud under multiple job managers. It also allows users to identify the exceptional jobs (e.g., jobs which have failed or taken too long) and resubmit them to a proper working station.

Job results collection: This task collects the seismic response feature files to be used for probabilistic performance evaluation, until the results of all seismic response features are collected in the pool of response features.

Job cleanup: To minimize the data storage taken up on the submit node, the working directory needs to be cleaned up once each job is finished, i.e., all raw data files will be removed from the job submit node.

To orchestrate complex and multi-stage scientific computations and data manipulations, the workflow is written in high-level workflow languages (e.g., script languages, directed acyclic graph, etc.). The proposed CBO workflow is implemented using TCL (Tool Command Language) as a glue language for interface between different programs, taking advantage of the existing functions and adaptability of the TCL package,. Some file manipulations in shell scripts for Linux and MS_DOS batch files are necessary to consider different platforms.

6.4. Computing Resources and Workflow Management Software used in CBO

In the CBO framework, the cloud computing resources with compatible job management system play a crucial role in the success that analysis jobs are executed in parallel on distributed resources. As brief introduction of the resources employed and integrated in the current CBO workflow is presented below, while a detailed description of them is beyond the scope of this dissertation.

6.4.1. Computing resources

This implementation of the CBO workflow in this research work integrates the accessibility to computational resources via the GlideinWMS (Igor, 2009) on the DOE (Department of Energy) Open Science Grid (OSG) cluster at the site of University of California, San Diego. OSG, as a computing infrastructure for data-intensive research, is a construction of about 80 sites (universities and national laboratories) to share across the consortium. Such examples of grid computing resources like OSG include the European Grid for E-Science (EGEE). Other computing resources, i.e., venues of Ranger, Kraken, Hansen,

Steele, NEES, the local cluster of workstation built in our research lab aforementioned, etc., can be also accessed for guaranteed and opportunistic access.

6.4.2. Job management software

The grid computing resources have proven their for the providers, but have also introduced several problems for users of the grid computing system, the three major being the complexity of job scheduling, the non-uniformity of compute resources, and the lack of good job monitoring (Igor S., 2009). To address these issues, Condor (also known as HTCondor) is an excellent choice as a mature, yet still in active development, work management system (WMS) for distributed job scheduling. Condor has been developed aiming to implement, deploy, and evaluate mechanisms and policies that support High Throughput Computing (HTC) on large collections of distributively owned computing resources, harnessing idle cycles in personal workstations (Litzkow M., et al., 1988).

GlidinWMS, working on top of HTCondor, provides a simple way to access the Grid resources with more services than Condor. Ready access to large amounts of computing power can also be enabled by Batchsubmit and Pegasus as well.

6.5. Application of CBO to 3D Parametric Study of Single Seismic Isolator

A parametric study with a relatively fine grid of the parametric space of design variables and wide range is carried out based on a single isolator model supporting equivalent bridge deck mass calibrated with the same fundamental period of the CHSR Prototype Bridge in the transversal direction. This approach is expected to eliminate the unnecessary fine mesh and improve the efficiency of parametric study of the probabilistic parametric study of the CHSR Prototype Bridge in chapter 7 therefore.

An idealized bilinear isolator model is used with the following bilinear force deformation relationship as back bone curve.

$$F = Q + K_2 D$$
$$D_y = \frac{Q}{K_1 - K_2} = \frac{Q}{K_1(1-b)} \tag{6.1}$$
$$F_y = Q\frac{K_1}{K_1 - K_2} = Q\frac{1}{1-b}$$

In which F is the lateral resisting force of the seismic isolator, Q is the characteristic strength, K_1 is the initial stiffness, K_2 is the post-yield stiffness, b is the ratio between the post-yield stiffness and the initial stiffness, D_y and F_y are the yield deformation and yield force respectively. To embody the period elongation and additional damping effects of seismic isolators, the equivalent effective stiffness K_{eff} and damping coefficient β_{eff} are estimated as follows,

$$K_{eff} = K_2 + \frac{Q}{D} \tag{6.2}$$

$$\beta_{eff} = \frac{1}{2\pi}\frac{E_{cycle}}{K_{eff}D^2} = \frac{1}{2\pi}\frac{4Q(D - D_y)}{K_{eff}D^2} \tag{6.3}$$

$$T_{eff} = 2\pi\sqrt{\frac{W}{K_{eff}g}} \tag{6.4}$$

Based on the model above, three independent parameters are used to characterize the force-deformation behavior of a specific isolator design, the yield strength, the intial stiffness, and the post-yiled stiffness ratio. In order to find the optimum combination of the three key parameters for the best performance in a probabilistic sense, a probabilistic study is performed in the parametric domain formed by these three parameters, with mesh size as $15\times15\times7$ of the parametric domain.

For the class of seismic isolators with the same post-yield stiffness ratio, such as 0.1 for typical lead rubber bearing (LRB), the seismic isolators are grouped into 4 categories conceptually illustrated in Figure 6.2, namely low yield strength with low initial stiffness

(LFLK), high yield strength with low initial stiffness (HFLK), high yield strength with high initial stiffness (HFHK), and low yield strength with high initial stiffness (LFHK). This classification will facilitate the interpretation of the analysis results later on.

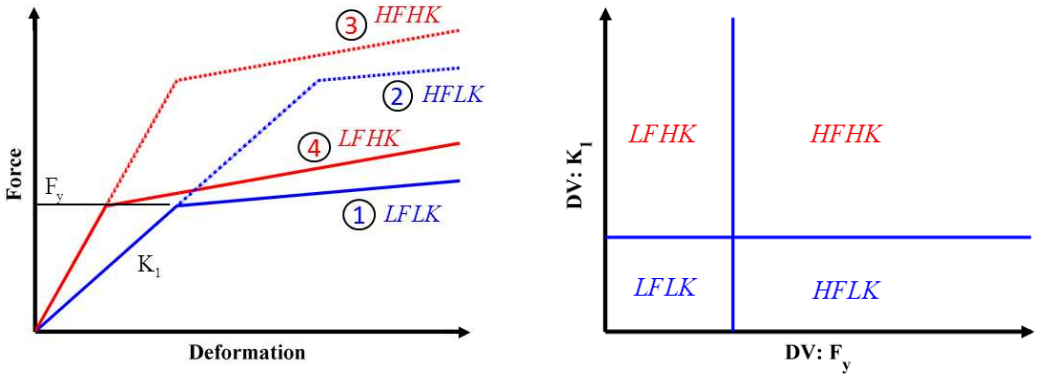

Figure 6.2: Bilinear isolator design alternatives with a fixed post-yield stiffness ratio (left) and categories (right)

The four-dimensional (4D) plot of conditional median demand level of the absolute deck acceleration on OBE hazard is presented in Figure 6.3, in which the fourth dimension is represented by color as to indicate the conditional median demand of absolute deck acceleration as a function of the three isolator parameters. Following the 4D plot, three surface plots are presented for fixed post-yield stiffness ratios (0.0, 0.05, and 0.1) in order to provide a more straight forward trend with the change of yield strength and initial stiffness, as shown in Figure 6.4, Figure 6.5, and Figure 6.6. The collection of plots implies the absolute deck acceleration demand is sensitive to the isolator parameters. The following observations can be made: (1) the lower the post yield stiffness ratio, the more efficient the reduction of absolute deck acceleration of seismic isolation; (2) when the post-yield ratio is small, the absolute deck acceleration is more sensitive to the change of yield strength than the initial stiffness; (3) when the post-yield ratio is high, the low yield strength with high initial stiffness isolators (LFHK) can lead to high acceleration demand.

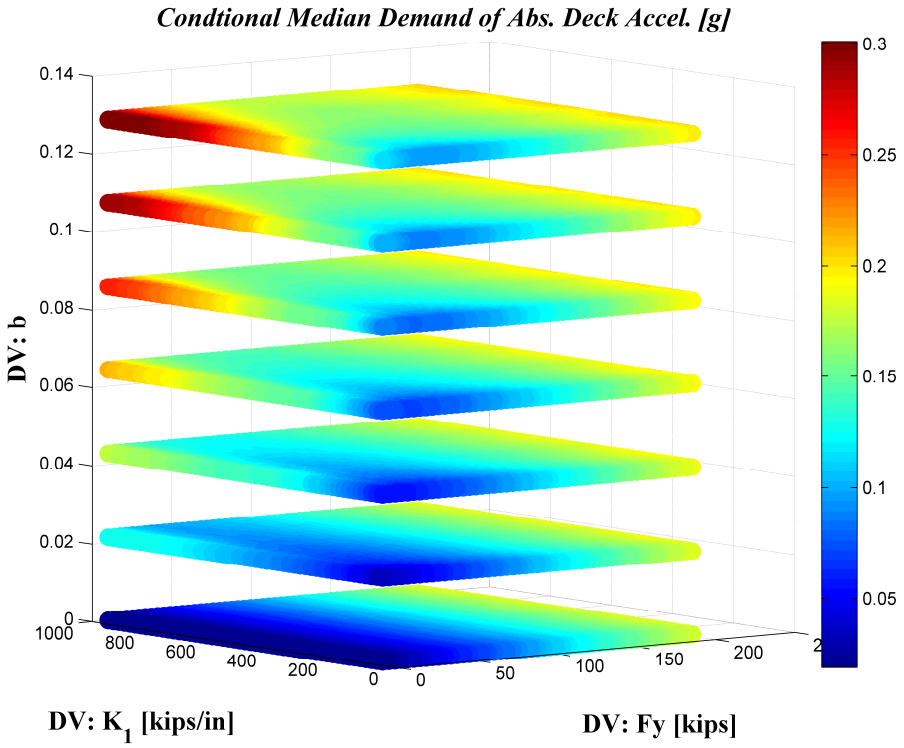

Figure 6.3: 4D plot of conditional median demand of absolute deck acceleration based on the single isolator model

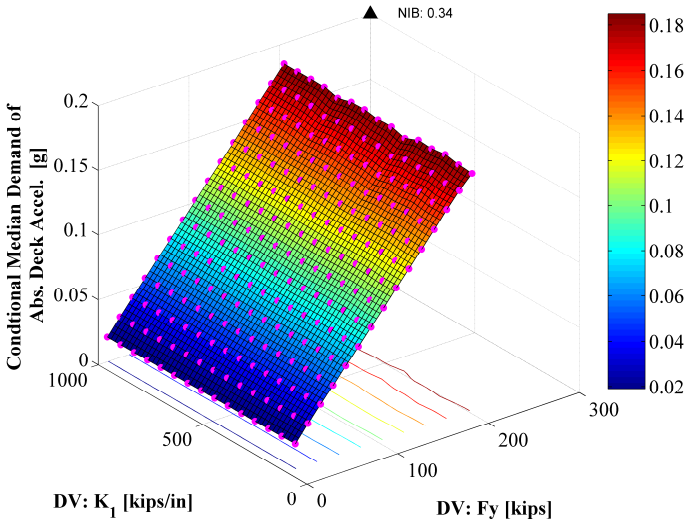

Figure 6.4: Conditional median demand of absolute deck acceleration based on the single isolator model for seismic isolator with b = 0.0

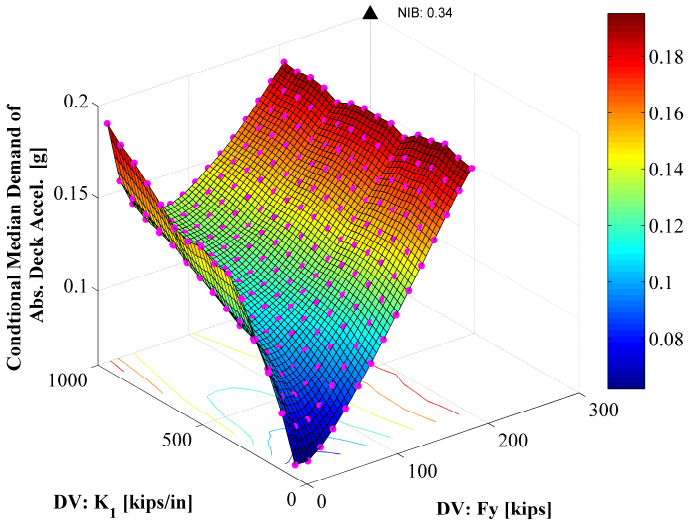

Figure 6.5: Conditional median demand of absolute deck acceleration based on the single isolator model for seismic isolator with b = 0.05

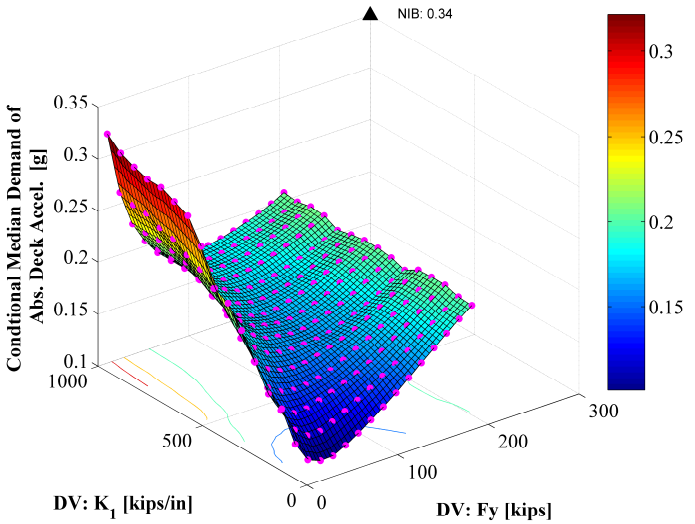

Figure 6.6: Conditional median demand of absolute deck acceleration based on the single isolator model with b = 0. 10

Regarding the deformation in the seismic isolator, the 4D plot and the three typical surface plots with fixed post-yield strength ratios are listed in Figure 6.7 to Figure 6.10. It is observed that the reduction of yield strength and initial stiffness tends to increase the isolator deformation demand. Generally, the reduction of post-yield stiffness ratio increases the isolator deformation demand except when the additional damping plays a more important role in reducing the isolator deformation. However, the change of the post-yield stiffness ratio does not change the deformation demand in the seismic isolator significantly, as seen in Figure 6.7 from the topology of the surface with respect to yield strength and initial stiffness.

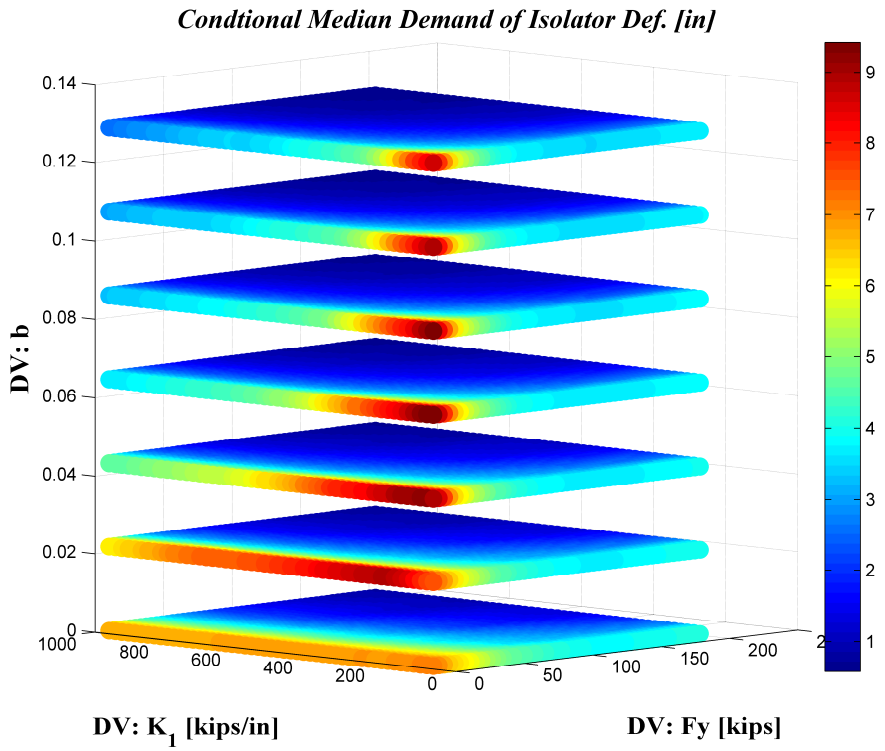

Figure 6.7: 4D plot of conditional median demand of isolator deformation based on the single isolator model

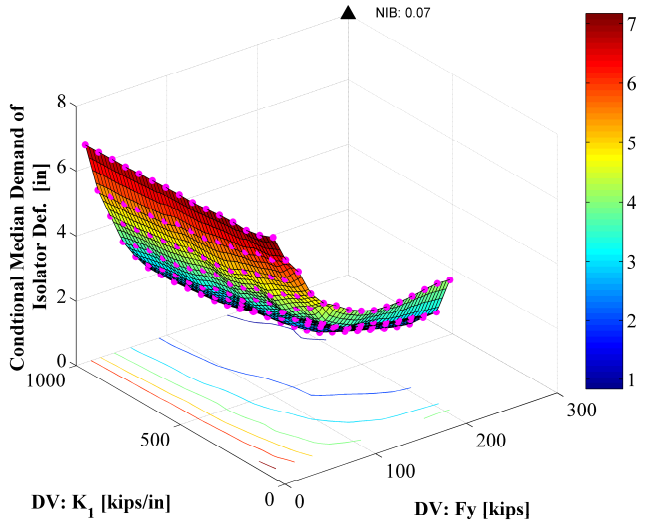

Figure 6.8: Conditional median demand of isolator deformation based on the single isolator model with b = 0.0

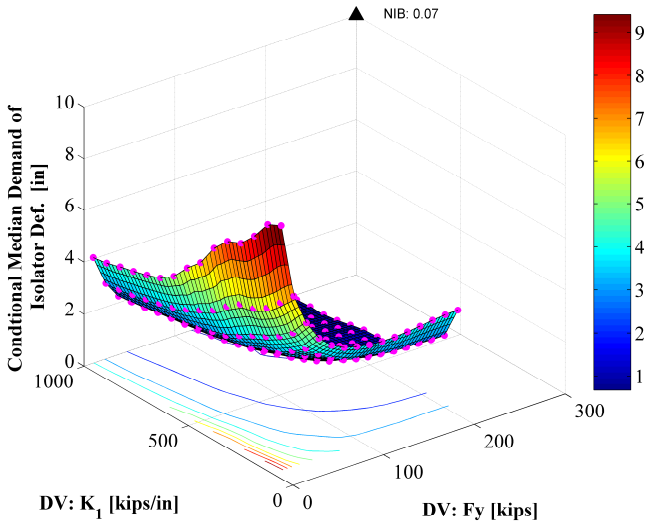

Figure 6.9: Conditional median demand of isolator deformation based on the single isolator model with b = 0.05

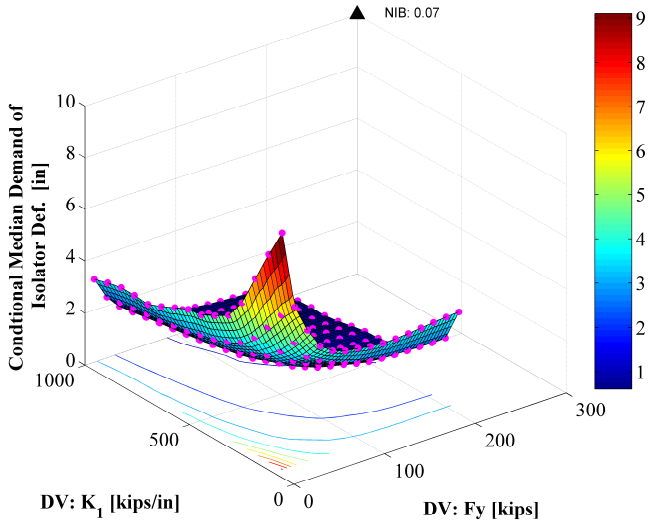

Figure 6.10: Conditional median demand of isolator deformation based on the single isolator model with b = 0. 10

Another important seismic response index is the base shear transmitted through the seismic isolator. Parallel results of parametric study for the force demand are shown in Figure 6.11 to Figure 6.14. The conditional median demand of base shear force correlates well with the conditional median demand of absolute deck acceleration supported on top of seismic isolator. It is worth noting that when the post-yield stiffness is high, the reduction of the yield strength could lead to increase of the shear force demand when the post-yield stiffness ratio is not zero.

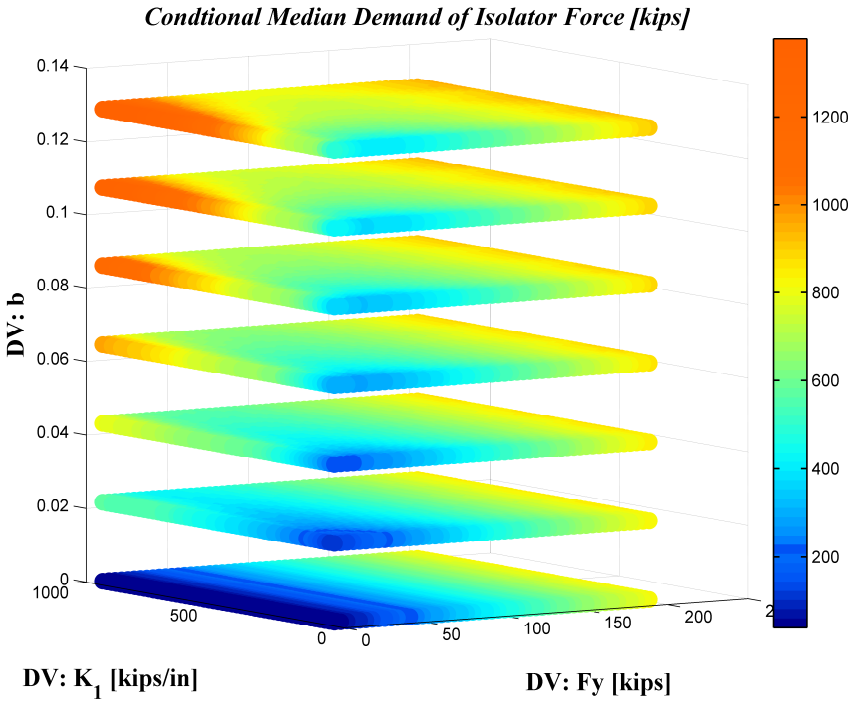

Figure 6.11: 4D plot of conditional median demand of base shear force based on the single isolator model

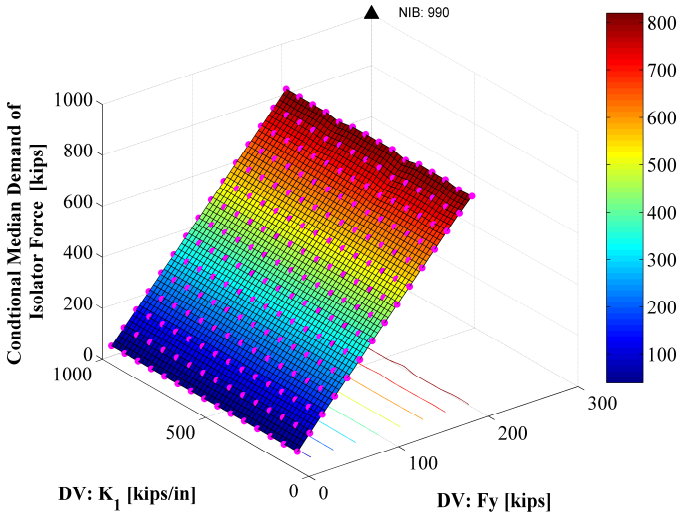

Figure 6.12: Conditional median demand of base shear force based on the single isolator model with b = 0.0

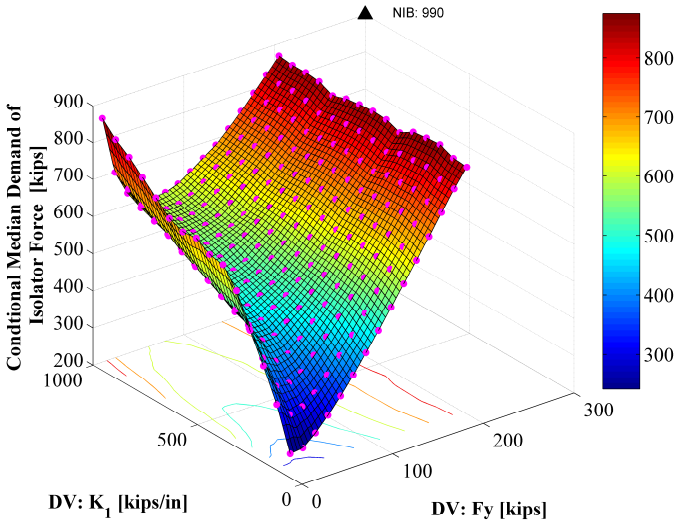

Figure 6.13: Conditional median demand of base shear force based on the single isolator model with b = 0.05

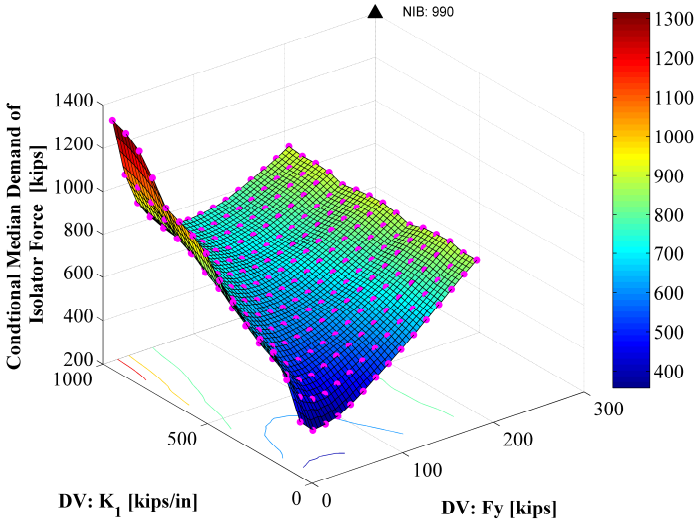

Figure 6.14: Conditional median demand of base shear force based on the single isolator model with b = 0. 10

6.6. Conclusions

To address the highly extensive computing demand involved in the probabilistic parametric analysis or optimization of large scale system (e.g., the CHSR Prototype Bridge), cloud-based optimization (CBO) workflow is developed to integrate the computing resources and platform for the purpose of high throughput computing. Using the developed platform, probabilistic parametric analysis with a refined grid of the parametric space of the design variables is carried out on probabilistic performance of a single isolator model to identify the general trend of the conditional median of absolute acceleration, isolator deformation, and base shear force at OBE hazard level. The successful implementation of CBO framework resolves the issue of computational demand in the PPBOSD framework, as demonstrated by the parametric study of the single isolator on probabilistic seismic performance, in which as many as 900 independent jobs can be run simultaneously on the DOE OSG cluster at the site of University of California, San Diego. The developed CBO workflow framework will be used as the computational platform for the parametric study of the probabilistic seismic performance of the CHSR Prototype Bridge.

References

Sfiligoi, I., Bradley, D., Burt, H., Parag, M. Sanjay, P., and Frank W.. (2009). “The pilot way to grid resources using glideinwms.” *Proc. 2009 WRI World Congress on Computer Science and Information Engineering*, Los Angeles, CA, 428–432.

Pordes, R., Petravick, D., Kramer, B., Olson, D., Livny M., Roy, A., Quick, R.. (2007) “The open science grid.” *Journal of Physics: Conference series 78(1)*, 12-57

Pordes, R., Altunay, M., Avery, P., Bejan, A., Blackburn, K., Blatecky, A., Gardner, R., Kramer, B., Livny, M., McGee, J., Potekhin, M., Quick, R., Olson, D., Roy, A., Sehgal, C., Wenaus, T., Wilde, M., and Würthwein, F. (2008) “New science on the Open Science Grid.” *Journal of Physics*, 125(1), 1-6.

Litzkow, M., Livny, M., and Mutka, M.. (1988) "Condor - A Hunter of Idle Workstations", *Proc. of the 8th International Conference of Distributed Computing System*, June, 1988, 104-111.

CHAPTER 7

PARAMETRIC PROBABILISTIC SEISMIC DEMAND ANALYSIS OF SEISMIC ISOLATED CHSR PROTOTYPE BRIDGE

7.1. Introduction

Verified by the deterministic and probabilistic performance comparisons between conventionally non-isolated bridge (NIB) and seismic isolated bridge (IB) in the previous chapters, seismic isolation is an effective earthquake protection device to reduce seismic demands on substructures and foundations. Seismic isolation can be adopted as a practical method to mitigate the seismic risk for CHSR Bridges if a proper selection of the seismic isolator properties can be sought for. Focusing on the sensitivity of probabilistic seismic response with respect to characteristic design parameters of typical force-deformation relationship of seismic isolators, a comprehensive probabilistic parametric sweeping analysis of bridges with different isolation designs is performed using the Cloud-based Probabilistic Optimization (CPO) framework introduced in last chapter.

Based on the performance of the structure expressed in terms of results obtained from probabilistic conditional (on the seismic hazard level) or unconditional demand hazard

analyses, two families of risk features are defined respectively, which can serve as objective and/or constraint functions in the optimization problem formulations presented in the next chapter.

To optimize the seismic isolation for the CHSR System in a probabilistic sense, we have explored the topology of the objective and/or constraint functions defined in terms of risk features associated with different Engineering Demand Parameters (EDPs) of the entire bridge system. Furthermore, the distribution of risk features along the bridge is investigated to study how the seismic demand will change as a function of the seismic isolator parameters.

7.2. Structural Model and Design Variables

The three-dimensional nonlinear finite element model developed in *OpenSees* for the CHSR Prototype Bridge accounting for both soil-foundation-structure interaction (SFSI) and track-structure interaction (TSI) is adopted for seismic response simulation and prediction. The seismic isolators, as the critical devices to concentrate inelastic behavior for energy dissipation and to reduce the seismic risk to the CHSR bridge system, are going to be the focus of the parametric and optimum seismic design. In the CHSR Prototype Bridge model developed in *OpenSees*, seismic isolators are modeled using a zero-length element, coupled with bilinear uniaxial materials. The yield strength and pre-yield stiffness of seismic isolators are chosen to be the design variables, with post-yield stiffness as 10% of the pre-yield stiffness as observed in elastomeric bearings and lead rubber bearings.

The design space of seismic isolation parameters is firstly estimated from the physical configurations and sizes of seismic isolators available in market and widely used in practice. In addition, the design constraints on the seismic isolators from braking and traction force under the high-speed train operation are also applied here to impose the lower bound on the isolator parameters.

7.2.1. Seismic isolator parameters based on physical configuration

Lead rubber bearings are usually characterized by bilinear force-deformation relationship, with three characteristic parameters, initial (elastic) stiffness K_1, yielded (post-yield) stiffness K_2, and characteristic strength Q or yield strength F_y. The characteristic strength Q is the intercept of the hysteresis loop in terms of force deformation relationship, and can be accurately estimated from the yield stress (1.5ksi – 2.33ksi) and the area of the lead plug. The yielded stiffness can be accurately estimated from the shear modulus of the rubber (see Table 7.1) and the bearing design. The typical values of the parameters for a wide range of DIS isolators are shown in Table 7.2. However, for specific projects, DIS Inc. can provide yielded stiffness up to three times the maximum shown in the range by limiting the displacement capacity to 2/3 of the shown values. This will serve as guidance to develop the range of bilinear isolator properties for parametric study as summarized in Table 7.3.

Table 7.1: Lead rubber bearing isolator material properties

Lead		**Rubber**	
Shear Modulus	**Shear Strength**	**Shear Modulus**	**Shear Strength**
812ksi (5.6Gpa)	1.5-2.33ksi (10.3-16Mpa)	0.055-0.102ksi (0.38-1.2MPa)	-

Table 7.2: Lead rubber bearing isolator engineering properties (from DIS Inc.)

Device Size & Configuration				**Design Properties**			
Diameter (in)	Height* (in)	# of rubber layers	Lead Diameter (in)	Yielded Stiffness (kips/in)	Characteristic Strength (kips)	Maximum Displacement (in)	Axial Load Capacity (kips)
12.0	5-11	4-14	0-4	1-2	0-15 (29)	6	100
14.0	6-12	5-16	0-4	1-2	0-15 (29)	6	150
16.0	7-13	6-20	0-5	2-3	0-25 (46)	8	200
18.0	7-14	6-20	0-5	2-4	0-25 (46)	10	250
20.5	8-15	8-24	0-7	2-4	0-40 (90)	12	300
22.5	8-15	8-24	0-7	3-5	0-40 (90)	14	400
25.5	8-15	8-24	0-8	3-6	0-50 (117)	16	600
27.5	8-17	8-30	0-8	3-8	0-50 (117)	18	700
29.5	9-18	8-30	0-9	4-9	0-60 (148)	18	800
31.5	9-20	8-33	0-9	4-9	0-60 (148)	20	900
33.5	9-21	8-35	0-10	4-10	0-80 (183)	22	1100
35.5	10-22	9-37	0-10	4-11	0-80 (183)	22	1300
37.5	10-23	10-40	0-11	4-12	0-110 (221)	24	1500
39.5	11-25	11-40	0-11	5-12	0-110 (221)	26	1700
41.5	12-26	12-45	0-12	5-12	0-130 (263)	28	1900
45.5	13-30	14-45	0-13	6-12	0-150 (309)	30	3100
49.5	14-30	16-45	0-14	7-13	0-170 (359)	32	4600
53.5	16-30	18-45	0-15	8-14	0-200 (412)	34	6200
57.1	17-30	20-45	0-16	9-14	0-230 (462)	36	7500
61.0	18-30	22-45	0-16	10-14	0-230 (462)	36	9000

* The height includes the top and bottom end plates (1.0 -2.0in thick for each plate)

7.2.2. Seismic isolator parameters bounds considering operation loads of trains

The lower bound of the isolator parameters (i.e., initial stiffness, and yield force) are determined from the design criteria specified for the braking and traction loads.

In the longitudinal direction, the rail-structure connection stiffness is 120 kips/ft per foot length of track with yield displacement of 0.02in, thus the maximum force through the bilinear fasteners transmitted from rails to a single bridge deck segment (3 spans) can be estimated as in Equation (7.6),

$$\begin{aligned} F_{rail-deck}^{\max} &= 2\times \overline{k}_{fasteners}^{per\ track} \times d_{yield} \times n_{span} \times L_{span} \\ &= 2\times 120.0 kips/\ ft/\ ft \times 0.02 in \times 3 \times 110\, ft = 132.0 kips \end{aligned} \tag{7.1}$$

Under the worst situation, a braking force on one track (1.37klf within 984.5ft) and a simultaneous traction force (2.26klf within 99.6ft) on the other track, the total force applied on track over one single segment (330ft) is larger than the maximum force through the fasteners above the bridge segment shown in Equation (7.6). This implies $F_{rail-deck}^{\max}$, the upper bound for the force transferred to bridge deck in the longitudinal direction over one bridge deck segment is a lower bound of the isolation yield force, such that operation loads of train will not lead to yield of isolators.

$$\begin{aligned} F_T^u &= 2.26klf \times \min(99.6\,ft,\ 330\,ft) = 225.1kips \\ F_B^u &= 1.37klf \times \min(985.4\,ft,\ 330\,ft) = 452.1kips \\ F_B^u + F_T^u &> F_{rail-deck}^{\max} \end{aligned} \tag{7.2}$$

In view of the 1.0in limit for the relative deck displacement at the expansion joint between segments, a lower bound for the stiffness of seismic isolator used in CHSR Prototype Bridges for parametric analysis is estimated as below:

$$K^l = \frac{F_{rail-deck}^{\max}}{d_a} = \frac{132.0kips}{1.0in} = 132.0kips/in \tag{7.3}$$

7.2.3. Grids of seismic isolator parameters for parametric study

Accounting for the available seismic isolators parameters and the basic requirement of the seismic isolator design for the braking and traction force applied from the trains, the seismic isolator bilinear properties range for parametric study are listed in Table 7.3.

Table 7.3: Properties range of bilinear isolators for parametric study

	Idealized Bilinear Properties					
	Yielded Stiffness (kips/in)	**Characteristic Strength (kips)**	**Elastic Stiffness (kips/in)**	**Max. Def. (in)**	**Yield Strength (kips)**	**Yielded/Elastic Stiffness Ratio**
LRB	6 - 42	11-230 (0.016W-0.324W)	(60)132*-4200	20-36	11.1 - 513	0.01-0.1

* Governed by the braking and traction force check

To determine the grid of seismic isolation parameters for efficient parametric study in the probabilistic framework, a relatively fine grid and wide range was first used based on a single isolator model in Chapter 6. Referring to the probabilistic parametric study of the single seismic isolator model, 16 grid points are selected for the probabilistic parametric study of the CHSR Prototype Bridge, which will be used as data sample points for interpolation.

7.3. Earthquake Selection and Scaling, and De-convolution for Cloud Method

Cloud method is employed for probabilistic parametric performance analysis at relatively lower computational cost, sacrificing the accuracy of mean response (EDP) prediction and the variance given a conditional IM. Here, the same ground motion set (40 records) is utilized as the stripe method in the previous chapter. To obtain a suite of ground motions with IM covering the range of IM of interest (i.e., the IM values employed in the Stripe Method corresponding to 7 different hazard levels), the selected ground motions are scaled uniformly by 0.4, 1.0, and 1.4 for a larger cloud size with sample size of 120. The selected ground motions' intensity distribution for initial design of seismic isolated bridge (IB) and non-isolated bridge (NIB) are shown in Figure 7.1 and Figure 7.2 respectively. Here the results for NIB are presented as well to ensure that the selected ground motions are sufficient for the parametric study of seismic isolators with higher stiffness and yield strength.

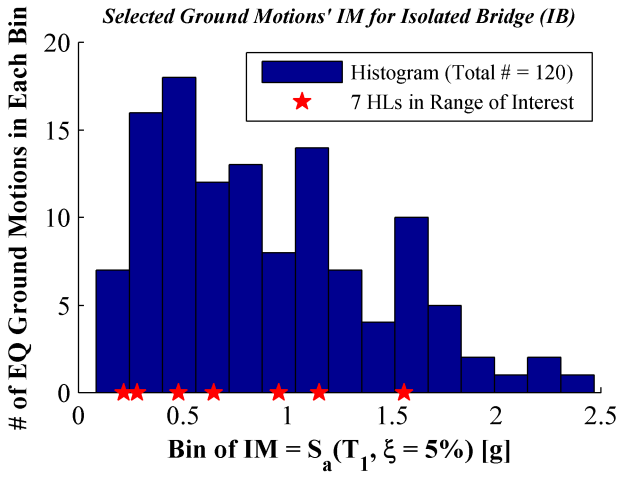

Figure 7.1: Earthquake selection and scaling for "cloud method" for the IB

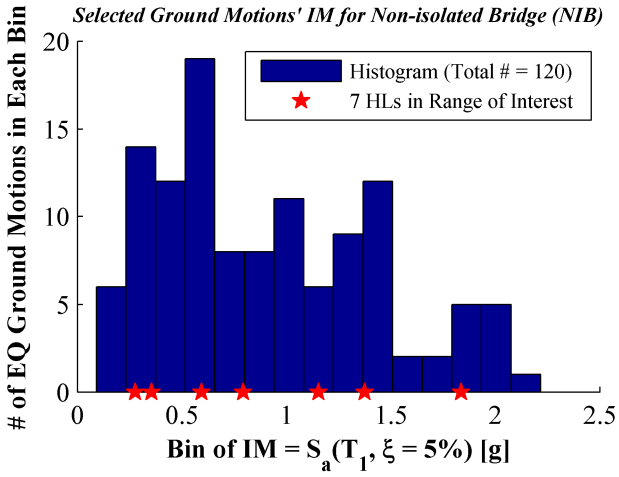

Figure 7.2: Earthquake selection and scaling for "cloud method" for the NIB

Since Soil-Pile-Structure Interaction (SPSI) is also accounted in the parametric probabilistic performance analysis of the CHSR Prototype Bridge, it is necessary to perform a de-convolution analysis for depth-varied ground motion displacements corresponding to the excitation supports of the p-y springs attached to the piles. For all these 120 ground motions,

site response analysis is carried out as a beginning step of the soil-foundation-structure analysis due to the uncoupling approach employed here.

In view of the earthquake duration of the selected earthquake ground motion pool which ranges from 18 seconds to 80 seconds (i.e., Chi-Chi Earthquake), and may take 12 to 40 hours for the complete finite element model of CHSR Prototype Bridge, it is desirable to reduce the analysis time for long-duration earthquake records to accelerate the probabilistic seismic performance evaluation. In most situations, the maximum structural response is considered to be an interested EDP for the probabilistic seismic performance evaluation. Therefore, the earthquake ground motions are cut appropriately based on the occurrence time of the peak values of various EDPs.

7.4. Probabilistic Parametric Performance Evaluation with Definition and Formulation of Risk Features

Using the developed CPO framework in Chapter 6 built on the high-throughput computing technology, a series of fully nonlinear dynamic time history analyses of CHSR Prototype Bridges is carried out considering 16 different alternative isolator designs are carried out subject to 120 earthquake ground motions respectively. The conditional and unconditional probabilistic seismic demand hazard analyses are carried out to evaluate and compare the probabilistic performance.

Referring to pattern recognition and image processing as well as big data analysis, feature extraction has been used as a special form of dimensionality reduction when the input data is too large and notoriously redundant. Likewise, corresponding to the seismic risk characterized by probabilistic conditional and unconditional probabilistic seismic demand hazard results, some features are extracted for probabilistic parametric analysis comparison purpose. They are denoted as risk features as a risk index/indicator in this research.

A risk feature is defined as an indicator of the seismic risk level to the structure as a data reduction from the risk information, which will serve as objective functions or constraint functions in the mathematical formulation of optimization problem. In the context of full PBEE analysis, the characterization of probabilistic seismic risk of structural response, damage, and loss allows us a wide variety of risk features extraction to indicate the imposed seismic risk to the bridge system. Till the second step of PBEE, basically there exits two families of risk features defined from the conditional demand hazard analysis and the probabilistic seismic demand hazard analysis respectively.

The first family includes the conditional mean, conditional median, conditional coefficient of variation, and conditional percentiles on a given seismic hazard level. The second family of risk features are the single point hazard value (i.e., the EDP value corresponding to a certain hazard level, a.k.a. unconditional percentiles), two points hazard value as a weighted average of two single point hazard values of two different hazard levels, area formed between the hazard curve and the axis, the unconditional mean, unconditional median, and unconditional coefficient of variation.

7.4.1. Risk features extracted from conditional demand hazard analysis

The conditional probabilistic demand hazard analysis yields the conditional probability of each EDP of the CHSR bridge structural system given a certain ground motion intensity measure (IM), as illustrated in Figure 7.3.

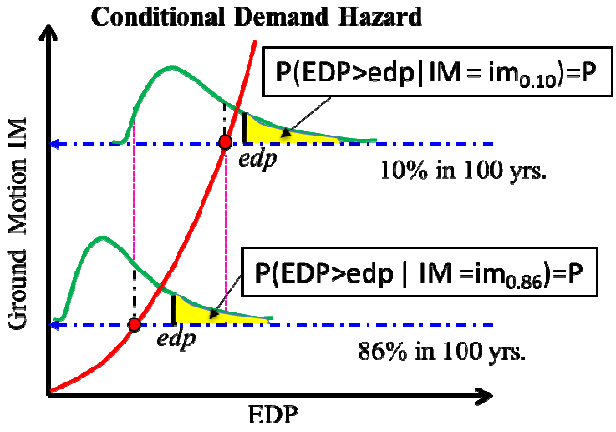

Figure 7.3: Risk feature illustration in the context of conditional demand hazard

In the performance-based design philosophy, the seismic demand conditioned on two or three seismic hazard levels is usually stated explicitly, and different performance objectives associated with specific seismic hazard levels are enforced. Consequently, the risk features can be extracted based on a certain seismic hazard level, in terms of the conditional median (i.e. exponential of the mean of logarithmic of EDP when lognormal distribution of EDP is assumed), conditional mean, variance, and percentiles, etc. Here the two hazard levels of interest in CHSR project are marked out for demonstration. However, conditional demand hazard based on other hazard levels can also be used for risk feature extraction. The risk features defined based on the conditional demand hazard are summarized as follows.

(1) Risk feature: conditional median demand

The median $\eta_{EDP|IM=im}$ of the EDP given a certain hazard level or the mean of $\ln(EDP)$ can be selected as a risk feature (also known as the conditional mean demand in the log scale in the article),

$$\eta_{EDP|IM=im} = \exp\left(E\left[\ln(EDP)\,|\,IM=im\right]\right) \tag{7.4}$$

(2) Risk feature: dispersion of conditional demand

The dispersion of the conditional demand can be characterized by the variance $\sigma_{\ln(EDP|IM=im)}$, which is assumed to be constant in the "Cloud" method, independent of the intensity measure IM.

$$\sigma_{\ln(EDP|IM=im)} = \sqrt{\mathrm{var}\left(\ln\left(EDP \mid IM = im\right)\right)},\ (\textit{for all } im's) \tag{7.5}$$

The risk feature of the variance is the second order central moment to indicate the dispersion. A dimensionless indicator is the normalized standard deviation with respect to the mean $E\left[\ln\left(EDP\right)\right]$, i.e., the coefficient of the variation, which is assumed to be constant for all hazard levels as a result of constant variance assumption in Cloud method.

$$\delta_{EDP|IM=im} = \frac{\sigma_{EDP|IM=im}}{\mu_{EDP|IM=im}} = \frac{e^{\mu_{\ln EDP|IM}+0.5\sigma_{\ln EDP|IM}}}{e^{\mu_{\ln EDP|IM}+0.5\sigma_{\ln EDP|IM}}\sqrt{e^{\sigma^2_{\ln EDP|IM}}-1}} \tag{7.6}$$

(3) Risk feature: conditional mean demand

The conditional mean demand is computed as follows from the conditional mean and variance of the ln(EDP)

$$\mu_{EDP|IM=im} = e^{\mu_{\ln EDP|IM}+0.5\sigma_{\ln EDP|IM}} \tag{7.7}$$

(4) Risk feature: conditional probability of exceedance

With a given threshold value of capacity *edp* associated with a certain limit state, the probability of EDP exceeding *edp* given a certain hazard level can be termed as

$$P^{exced}_{IM=im} = P\left[EDP > edp \mid IM = im\right] \tag{7.8}$$

(5) Risk feature: conditional probability percentile

Given a certain hazard level, the percentile (with probability of exceedance as 1-*p*) of EDP, denoted as $edp_{P^{exced}|IM}$ can serve as a risk feature as well.

$$edp_{P^{exced}|IM} = \arg_{edp}\left\{edp \mid P\left[EDP > edp \mid IM = im\right] := p\right\} \tag{7.9}$$

7.4.2. Risk features extracted from probabilistic seismic demand hazard analysis

Instead of providing the seismic demand conditioned on a given seismic hazard level, the probabilistic seismic demand hazard analysis yields the probabilistic seismic demand hazard curve of each EDP of the CHSR bridge structural system, as conceptually illustrated in Figure 7.4. The hazard can be measured in terms of annual probability of exceedance (denoted as APE), probability of exceedance in 100 years (denoted as PE100), or mean annual rate (denoted as MAR). In this thesis, the probability of exceedance in 100 years (the exposure time of the design of California high-speed rail bridge) is employed.

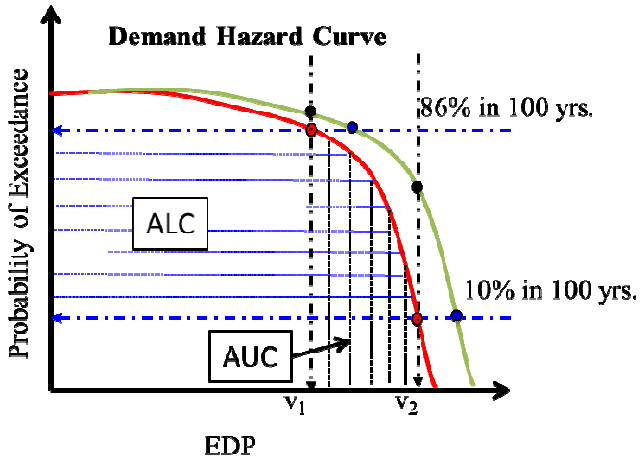

Figure 7.4: Risk feature illustration in the context of seismic demand hazard

The risk features can be extracted based on probabilistic seismic demand hazard curves in different ways, i.e., risk feature based on a single point hazard focusing on a single hazard level, risk feature based on two-points-hazard focusing the two hazard levels of interest, and the hazard over a continuous range.

(1) Risk feature: Single point hazard

The EDP value corresponding to a certain demand hazard level characterized by probability of exceedance in 100 years (PE100) can be selected as a risk feature from the seismic demand hazard curve of a certain EDP, which is actually an unconditional percentile if PE100 is considered as a complementary cumulative density function. For example, the EDP values associated with 86% and 10% probability of exceedance in 100 years respectively, corresponding to return periods of 50 years (denoted as OBE hazard level for convenience as it has the same return period as operating basis earthquakes) and 950 years (denoted as MCE hazard level for convenience as it has the same return period as maximum considered earthquakes), are the 14^{th} percentiles and 90^{th} percentile.

$$edp_{HL} = \arg_{edp}\left\{edp \mid HL\left(edp\right) := hl\right\}, \text{ where } HL : PE100 \tag{7.10}$$

Similarly, the probability of exceedance for a given threshold value *edp* can also serve as a risk feature.

$$HL = HL\left(EDP = edp\right), \text{ where } HL : PE100 \tag{7.11}$$

(2) Risk feature: Two points hazard

Multiple hazard levels are often of interest in the world of performance-based seismic design. Different weights can be imposed onto these two hazard levels, which reflect the decision maker's preference on the different importance weight low hazard level (i.e., OBE) for frequent events and high hazard level (i.e., MCE) for rare events.

$$edp_{weighted} = w_1 \times edp_{PE100=0.86} + w_2 \times edp_{PE100=0.10} \tag{7.12}$$

(3) Risk features: Hazard over a continuous range

Instead of focusing a set of finite discrete hazard levels for the seismic demand, a risk feature can also be extracted from a continuous range of hazard levels. Naturally, the area on the left side of the curve (A^{LC}) given the range of hazard of interest can be good indicator of

seismic risk to imply how far away of the seismic hazard curve is from the vertical axis. The larger of risk feature A^{LC} is, the riskier the design is.

$$A_{HL}^{LC} = \int_{hl_2}^{hl_1} EDP(hl)\, d\left(hl\right), \text{ where } \left(hl_2, hl_1\right) = \left(0.10, 0.86\right)_{PE100} \tag{7.13}$$

Alternatively, when a given EDP range of interest is prescribed, the area under the curve (A^{UC}) is also a good indicator of seismic risk as it explains how far away of the seismic hazard curve from the horizontal axis. Like the indicator of A^{LC}, the larger the risk feature A^{UC} is, the riskier the design is.

$$A_{EDP}^{UC} = \int_{edp_1}^{edp_2} HL(edp) d\left(edp\right), \text{ given } \left(edp_1, edp_2\right) \tag{7.14}$$

(4) Risk feature: unconditional statistics (median, mean, variance, and percentiles)

Based on probabilistic seismic demand hazard curve characterized by probability of exceedance in 100 years (PE100), a probability density function (PDF) of EDP can be derived as

$$f_{EDP}\left(x\right) = \frac{dF\left(x\right)}{dx} = -\frac{d\left(PE100\right)}{dx} \tag{7.15}$$

As a result, the unconditional median, mean, variance and certain percentiles can be computed as risk features to characterize the seismic risk to the demand after un-conditioning the conditional demand hazard with the probabilistic seismic hazard.

7.5. Risk Feature Exploration

Risk feature exploration is carried out to better understand how the change of design parameters for the seismic isolators will affect the probabilistic seismic performance of the bridge structure system in terms of risk features. It is essentially a probabilistic parametric study for seismic response under different seismic hazard levels, including the bridge structure response, the foundation response, and the rail response. This topology study of the risk

feature value functions will serve as reference for the mathematical formulation of the optimization problems, where the risk feature value functions can be selected to be either the objective functions or constraint functions.

In the topological plots of risk features, 16 data sample points are marked out by the solid circle, and a refined mesh using linear interpolation is employed for the surface plot. The corresponding risk feature for the NIB is marked as a solid triangular at the far corner of the 3D plot. Besides, IB with the initial design of the seismic isolators is one of the sample points marked as white solid circle with annotation X_0.

7.5.1. Risk feature exploration for conditional demand hazard analysis

To show the conditional demand hazard of various structural responses as a function of the isolator parameters, the topology of the risk feature value function as a vivid picture are displayed accordingly. The conditional mean demand at OBE and MCE hazard levels are presented first. For OBE hazard level, results for different types of EDPs are displayed. For MCE hazard level, selected results for different EDPs are included here.

Parametric conditional seismic demand hazard analysis on OBE hazard level

Figure 7.5 presents the conditional mean demand of the absolute deck acceleration over pier #5 in the longitudinal direction under earthquakes with return period of 50 years (at OBE hazard level) as a function of the isolators' yield strength and initial stiffness. As illustrated in the parametric space of interest, under low-intensity earthquakes (OBE), the mean demand on absolute deck acceleration in the longitudinal direction is decreasing with the decrease of isolators' yield strength and initial stiffness. Compared to the corresponding conditional demand in the case of NIB, as denoted by the black triangular marker with value of 0.29g, the seismic isolation can efficiently reduce acceleration demand under OBE hazard level when impact rarely occurred.

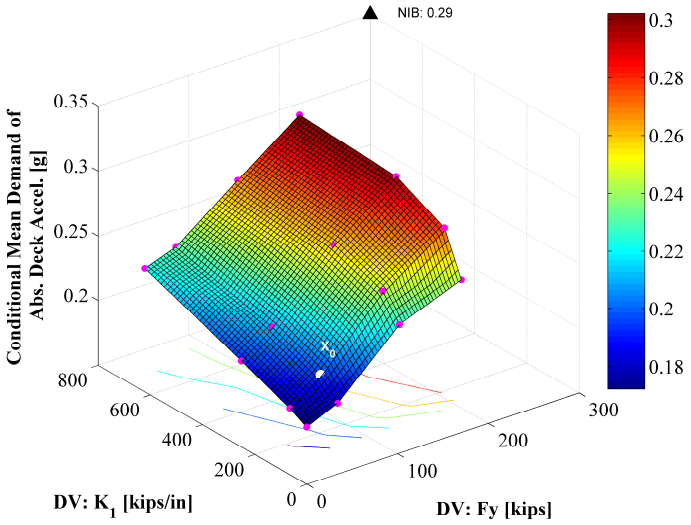

Figure 7.5: Risk feature: conditional mean demand of absolute deck acceleration over pier #5 in the longitudinal direction at OBE hazard level

Unlike in the longitudinal direction of the bridge with large gaps (4.0in), due to the existence of small gaps (0.5in) at the abutment shear keys and the tiny gaps (0.0625in) inside SHJ devices in the transverse direction of the bridge, the likely engagement of these gaps complicates the nonlinear behavior of the bridge even under OBE hazard level. Acceleration of high frequency components is introduced, while no low-pass filtering is applied to the signal when the maximum acceleration is considered as the EDP of interest here. Figure 7.6 shows the conditional mean demand of the absolute deck acceleration over pier #5 in the transverse direction under earthquakes with return period of 50 years (at OBE hazard level) as a function of the isolators' yield strength and initial stiffness. The conditional mean demand is large for isolators with high strength but low elastic stiffness (type *HFLK*) and isolators with low strength but high elastic stiffness (type *LFHK*). Acceleration demand can even be larger than the NIB case if the isolator is not properly designed.

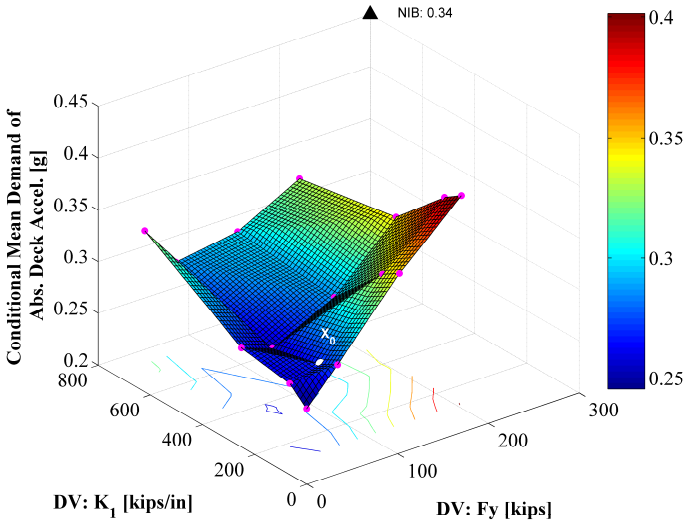

Figure 7.6: Risk feature: conditional mean demand of absolute deck acceleration over pier #5 in the transverse direction at OBE hazard level

Figure 7.7 shows the conditional mean demand of relative deck displacement of bridge deck over pier #5 in the transverse direction. It is manifested that the increasing seismic demand on bridge deck displacement comes as a cost of the introduction of the flexibility of the isolators between the bridge deck and substructures.

Compelling evidence to conclude the deck displacement demand as a cost of seismic isolation is the enlightening results of the conditional demand hazard analysis results of seismic isolator deformation. The conditional mean demand on the isolator deformation is plotted in Figure 7.8. The similarity between the deck displacement demand surface and the isolator deformation surface enhanced the conclusion about the detrimental effects of seismic isolation.

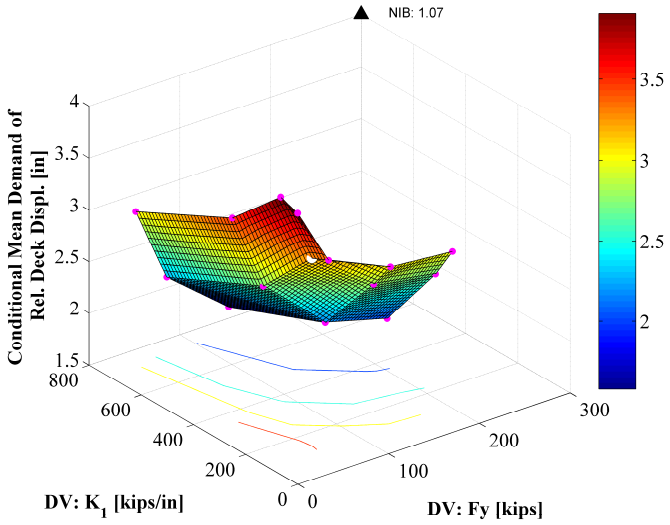

Figure 7.7: Risk feature: conditional mean demand of relative deck displacement over pier #5 in the transverse direction at OBE hazard level

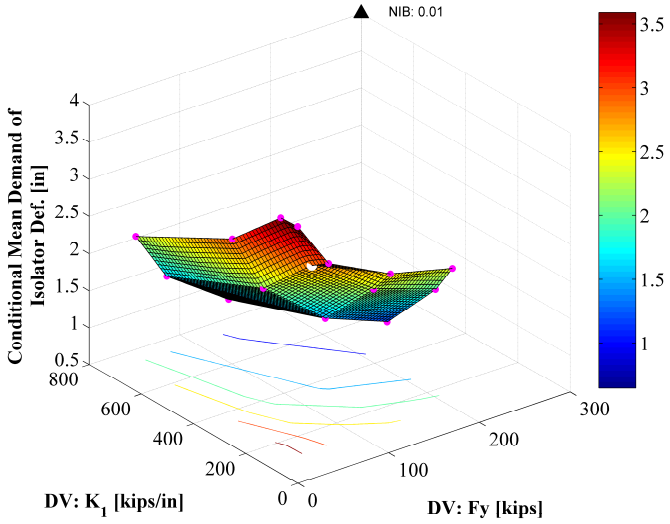

Figure 7.8: Risk feature: conditional mean demand of isolator deformation over pier #5 in the transverse direction at OBE hazard level

With the increasing deck displacement for the seismic isolation, less seismic demand on the bridge substructure will show tremendous promise on seismic isolations. Figure 7.9 and Figure 7.10 depict the topologies of the conditional mean demand on the column drift of pier #5 in both the longitudinal direction and transverse direction of the bridge. A pronounced decrease of pier column drift demand is observed with the decrease of yield strength and initial stiffness of the seismic isolators. It is worth nothing that the monotonicity for the demand in the transverse direction is broken by seismic isolators with low yield strength but high elastic stiffness (type *LYHK*), as observed in the study of single isolator case. This exception is more pronounced when the seismic intensity measure increases, as will be seen in the case of MCE.

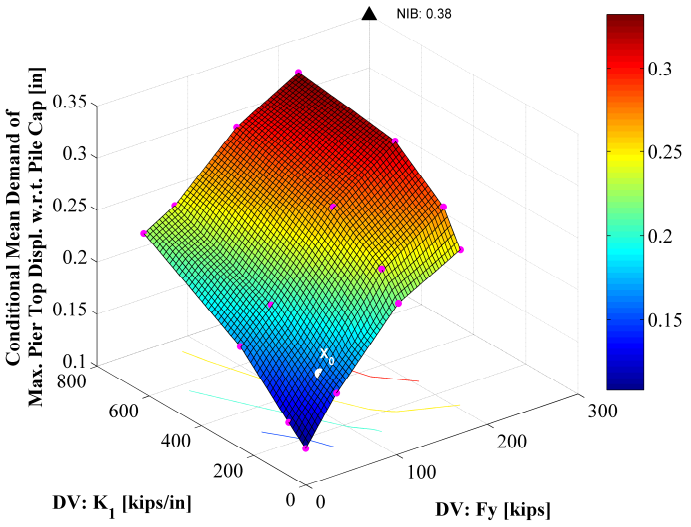

Figure 7.9: Risk feature: conditional mean demand of pier column drift of pier #5 w.r.t. pile cap in the longitudinal direction at OBE hazard level

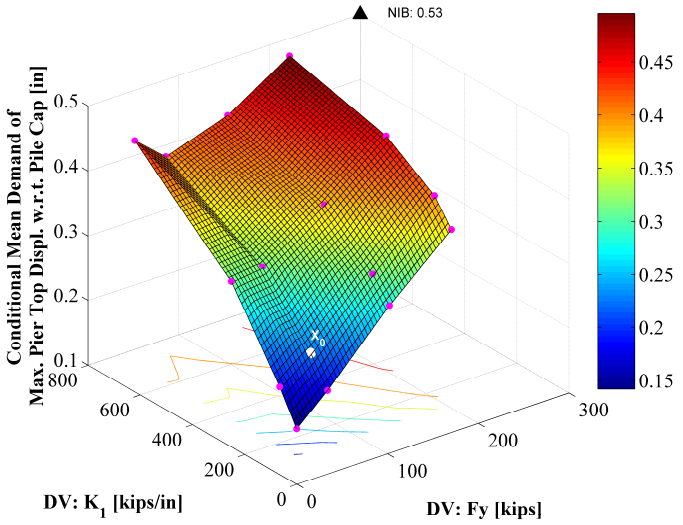

Figure 7.10: Risk feature: conditional mean demand of pier column drift of pier #5 w.r.t. pile cap in the transverse direction at OBE hazard level

Figure 7.11 and Figure 7.12 exhibit the conditional mean demand on the column base moment of pier #5. The trend of this risk feature correlates well with the conditional mean demand on the pier column drift, total shear force as shown in Figure 7.13 and Figure 7.14, pile foundation translation as shown in Figure 7.15 and Figure 7.16, pile foundation cap rotation as shown in Figure 7.17 and Figure 7.18, pile moment as shown in Figure 7.19 and Figure 7.20, and pile shear force in Figure 7.21 and Figure 7.22.

As the main stimulus for the leading beneficial effects of seismic isolation, the less demand on the substructure system are displayed in terms of the risk features on the pier column force demand and pile foundation response. The remarkable potentials as explored here imply seismic isolation can largely mitigate the seismic risk to substructure system, or reduce the financial cost on substructure system (i.e., pier and foundation) if resize is possible satisfying other non-seismic design constraints.

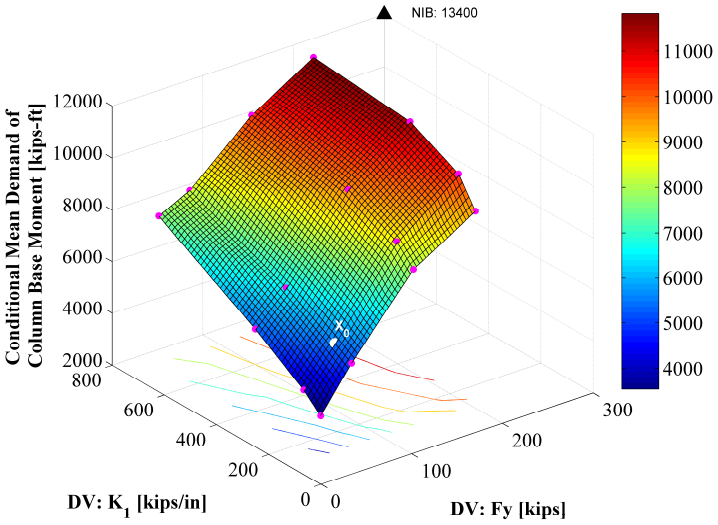

Figure 7.11: Risk feature: conditional mean demand of column base moment of pier #5 in the longitudinal direction at OBE hazard level

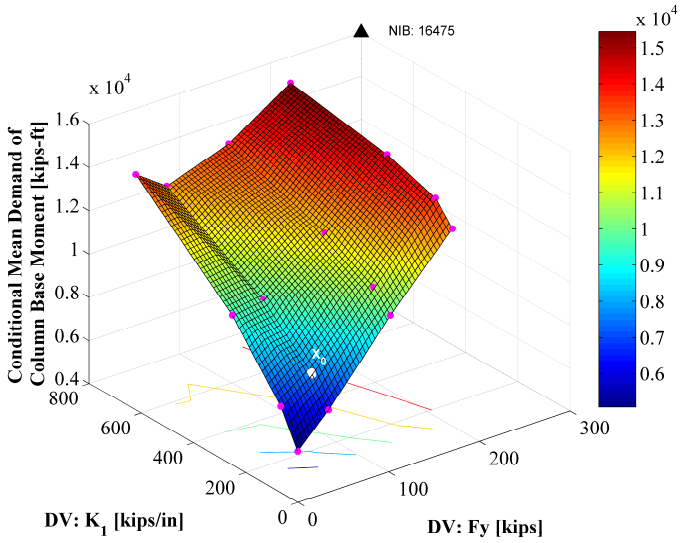

Figure 7.12: Risk feature: conditional mean demand of column base moment of pier #5 in the transverse direction at OBE hazard level

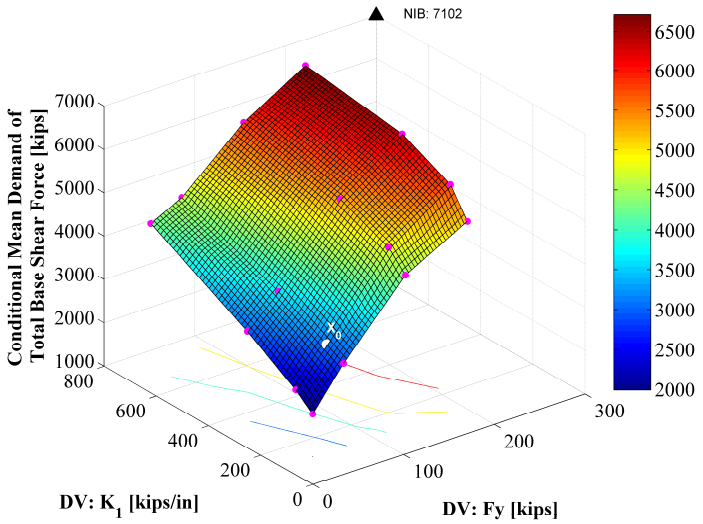

Figure 7.13: Risk feature: conditional mean demand of total base shear force in the longitudinal direction at OBE hazard level

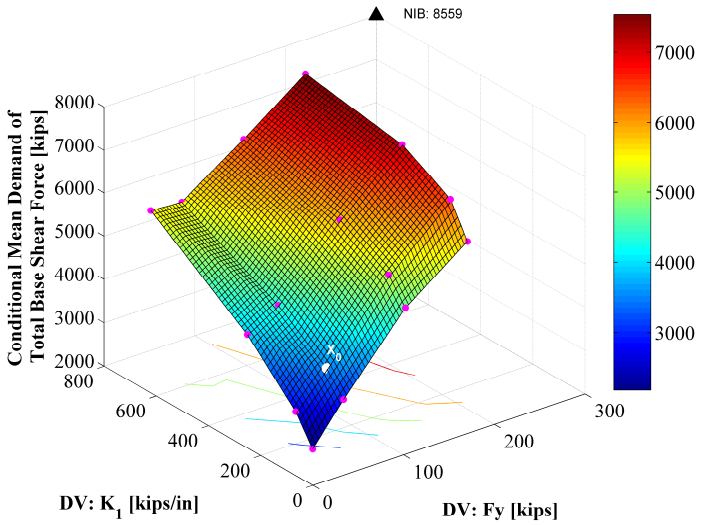

Figure 7.14: Risk feature: conditional mean demand of total base shear force in the transverse direction at OBE hazard level

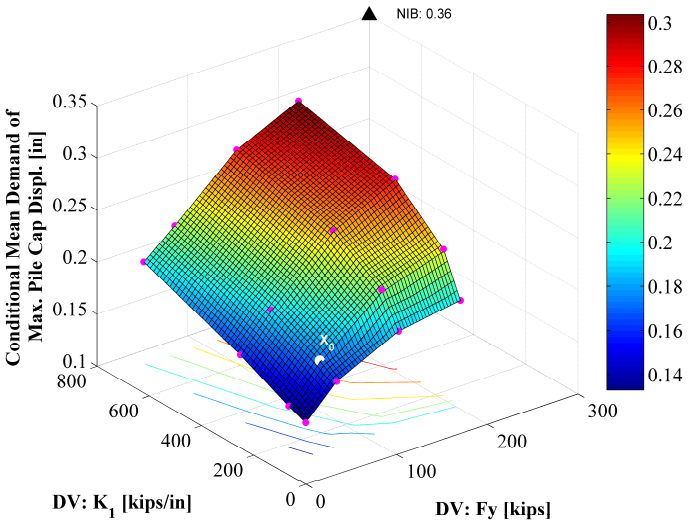

Figure 7.15: Risk feature: conditional mean demand of pile cap displacement of foundation under pier #5 in the longitudinal direction at OBE hazard level

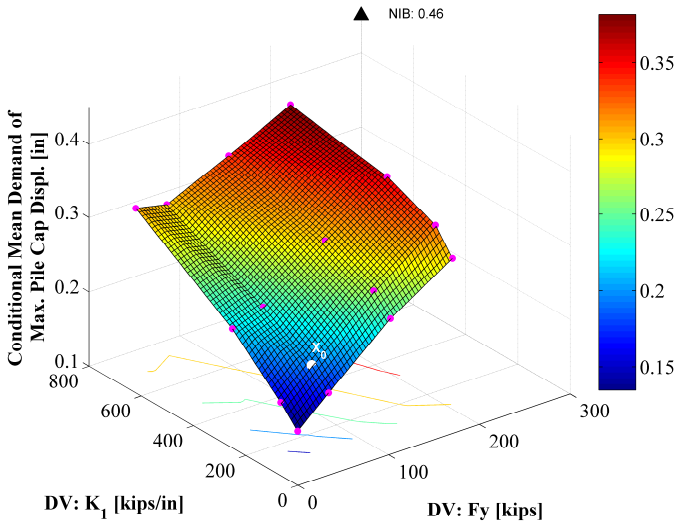

Figure 7.16: Risk feature: conditional mean demand of pile cap displacement of foundation under pier #5 in the transverse direction at OBE hazard level

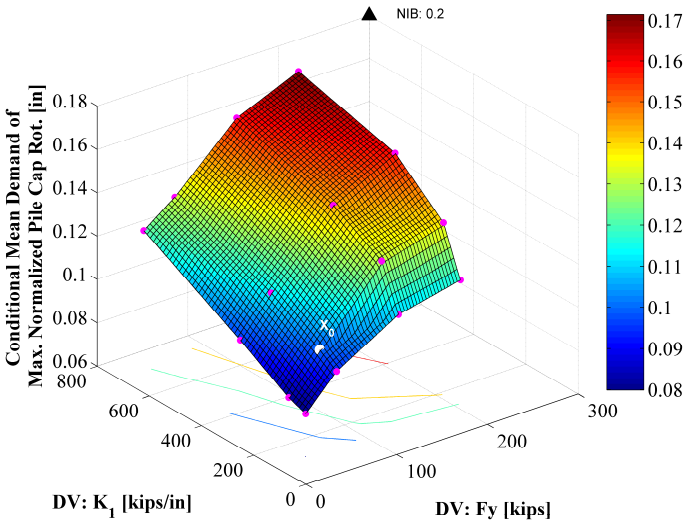

Figure 7.17: Risk feature: conditional mean demand of pile cap rotation of foundation under pier #5 in the longitudinal direction at OBE hazard level

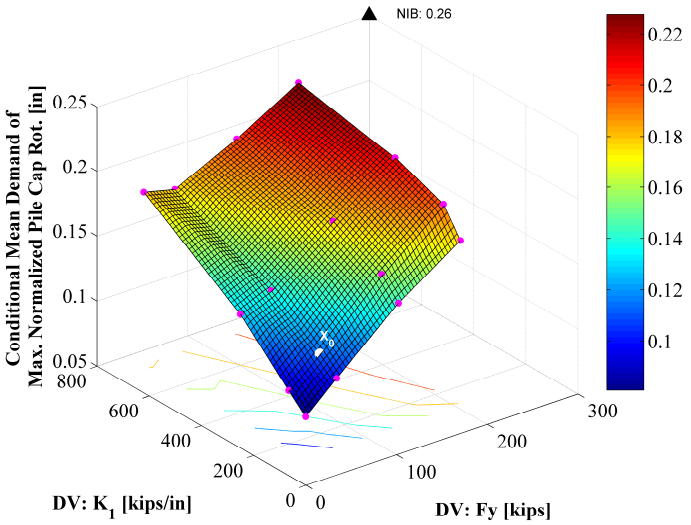

Figure 7.18: Risk feature: conditional mean demand of pile cap rotation of foundation under pier #5 in the transverse direction at OBE hazard level

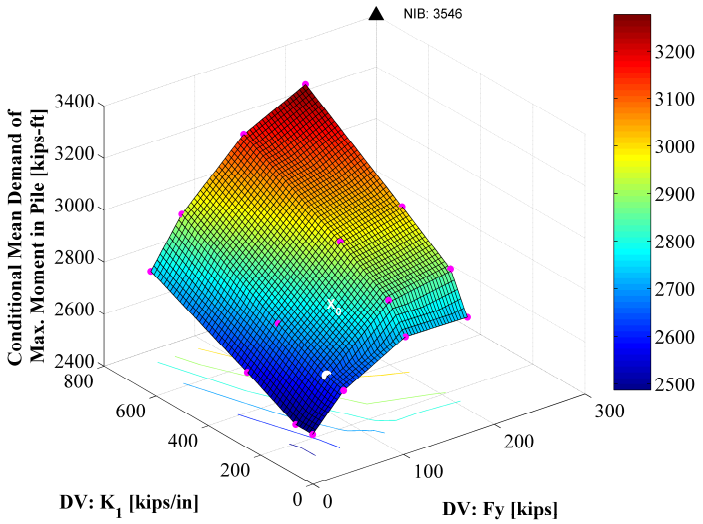

Figure 7.19: Risk feature: conditional mean demand of bending moment of piles under pier #5 in the longitudinal direction at OBE hazard level

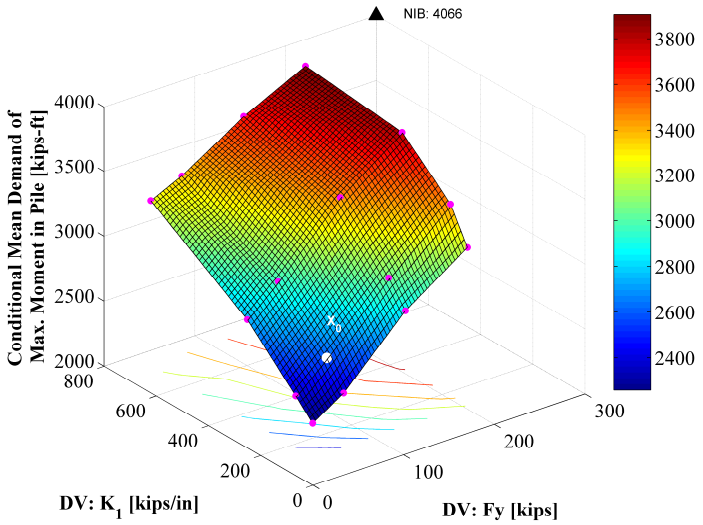

Figure 7.20: Risk feature: conditional mean demand of bending moment of piles under pier #5 in the transverse direction at OBE hazard level

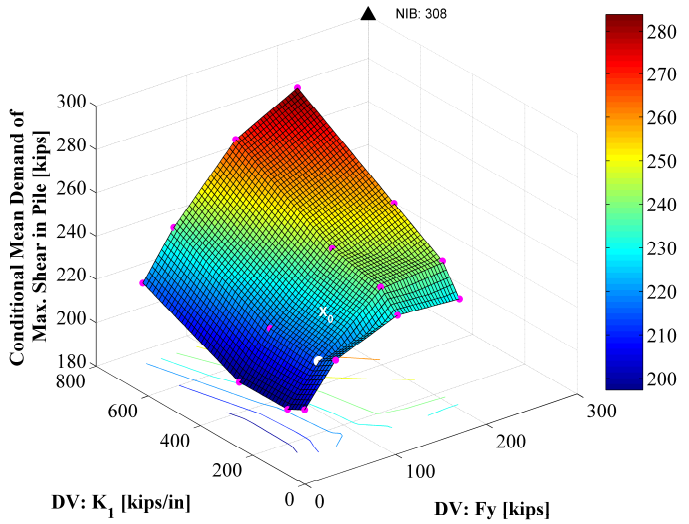

Figure 7.21: Risk feature: conditional mean demand of shear force of piles under pier #5 in the longitudinal direction at OBE hazard level

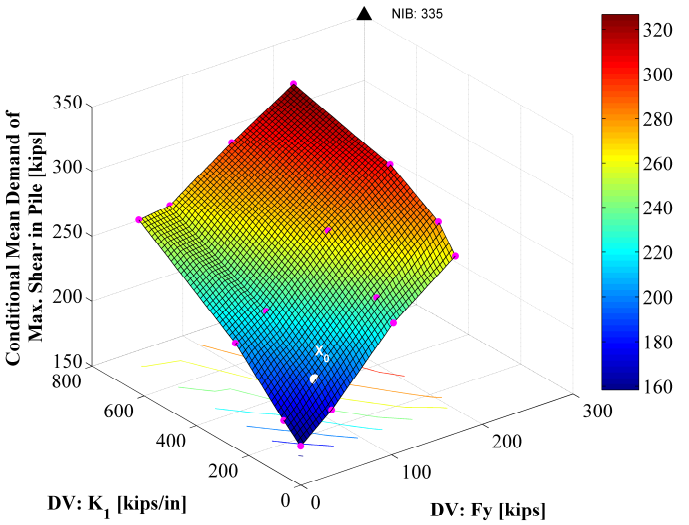

Figure 7.22: Risk feature: conditional mean demand of shear force of piles under pier #5 in the transverse direction at OBE hazard level

The relative displacements of supports to track at bridge gaps in both longitudinal direction and transverse direction of the bridge give rise to the additional rail stress. As elucidated in the parametric analysis of conditional demand hazard on deck displacements, the introduction of seismic isolation introduces or increases the relative displacement, especially at the interior expansion joints. Consequently, additional rail stresses can also be imposed as detrimental effects of seismic isolation on CHSR bridges. Exhibited in Figure 7.23 - Figure 7.26 is the maximum additional rail stresses at abutment gap #1 and interior expansion joint #2 over pier #3 resulted from the axial force in the rail and the bending in the transverse direction of bridge.

Considering the bilinear fasteners as the connection between rail-deck supports in the longitudinal direction, it helps the accommodation of relative displacement thus the additional rail stress demand. More additional axial rail stress is generated at the abutment gap as shown in Figure 7.23 compared with case of NIB. The axial rail stress at the interior expansion joint gap illustrated in Figure 7.25 implies the supported side deck segment and middle deck segment move out of phase even though they are supported on the seismic isolators of same properties, which is explained by the different boundary conditions due to possible pounding.

With respect to the rail stress due to transverse bending, the decrease of yield strength of the seismic isolators will produce more seismic demand on the additional rail stress as observed in Figure 7.24 and Figure 7.26. Compared to the rail stress at the abutment gap due to transverse bending in NIB where non-isolation bearing pads are adopted, the proper selection of isolator properties can even produce less stress demand on the rail implied in Figure 7.24. The seismic isolators with high yield strength and high elastic stiffness tends to be preferred as they lead to less demand on the bending rail stress at the abutment gap. This implies that ideal uni-directional seismic isolators are preferred by locking the transverse

deformation with stiff shear keys without gaps. Increasing the stiffness and strength at the abutment only will lead to more different dynamic characteristics of the side frame and middle frame thus result in demanding rail stress at the interior expansion joints. The design parameters of seismic isolators over the abutments should be designed differently from the other seismic isolators. Herein for the sake of simplicity, the design parameters of all seismic isolators are limited to two by neglecting the required special treatment of the seismic isolators over the abutments.

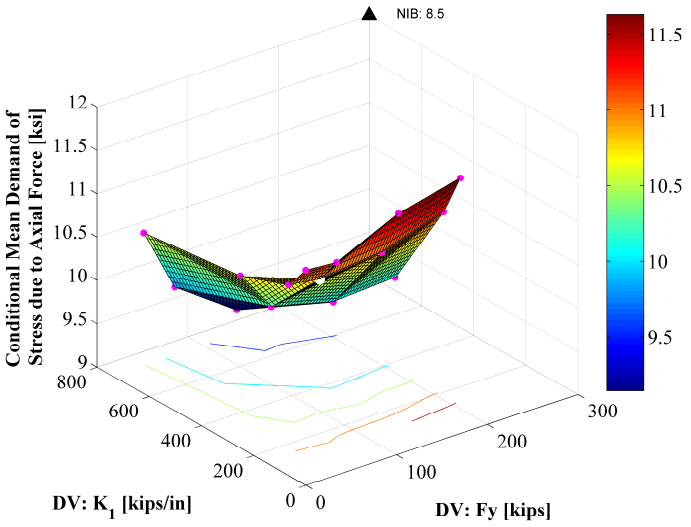

Figure 7.23: Risk feature: conditional mean demand of rail stress at abutment expansion joint #1 due to axial at OBE hazard level

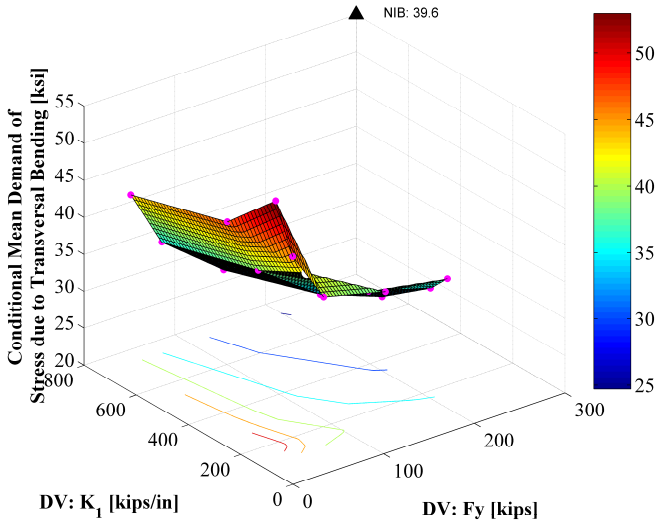

Figure 7.24: Risk feature: conditional mean demand of rail stress at abutment expansion joint #1 due to bending in the transverse direction at OBE hazard level

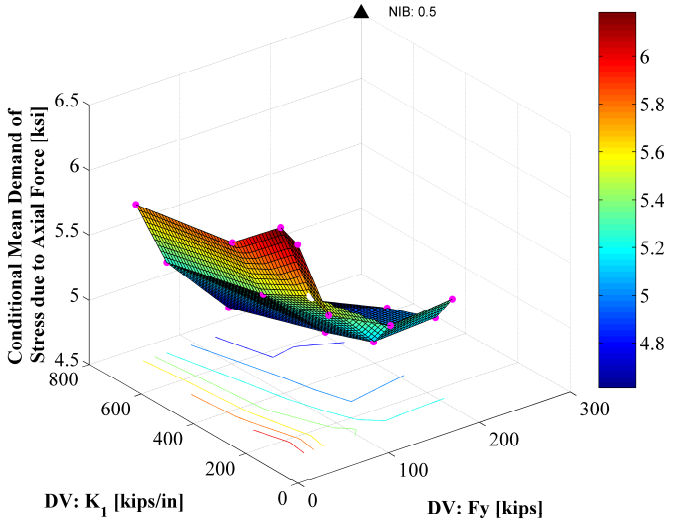

Figure 7.25: Risk feature: conditional mean demand of rail stress at interior expansion joint #2 due to axial at OBE hazard level

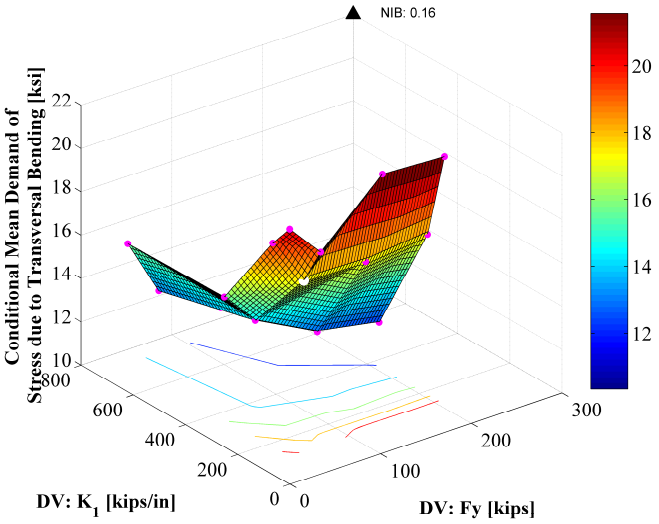

Figure 7.26: Risk feature: conditional mean demand of rail stress at interior expansion joint #2 due to bending in the transverse direction at OBE hazard level

Apart from the risk feature of the conditional mean demand, other risk features useful to quantify the conditional demand risk to the bridge structures on OBE hazard level are also explored, including the conditional median, the conditional 95th percentile, and the conditional coefficient of variation (c.o.v.). To compare with the risk feature as conditional mean demand of column base moment of pier #5 in the transverse direction shown in Figure 7.12, other risk features of the same EDP are presented in Figure 7.27, Figure 7.28, and Figure 7.30. It is found that the predicted conditional median demand is less than the conditional mean demand. While the global topology of the risk features (conditional median demand, and conditional 95th percentile) with respect to the isolator design parameters correlates well with the topology of conditional mean demand at OBE hazard level. On the contrary, the topology of the c.o.v. is conflicting with the topology of the mean demand for some isolator designs, which is due to the sensitivity of the variance to the isolator designs.

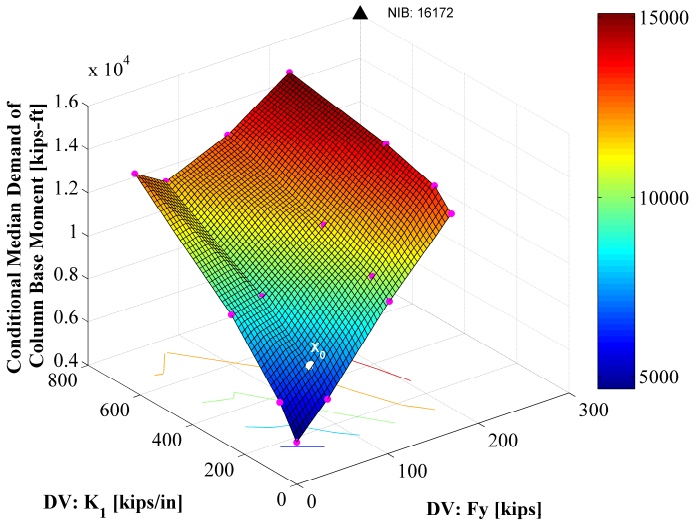

Figure 7.27: Risk feature: conditional median demand of column base moment of pier #5 in the transverse direction at OBE hazard level

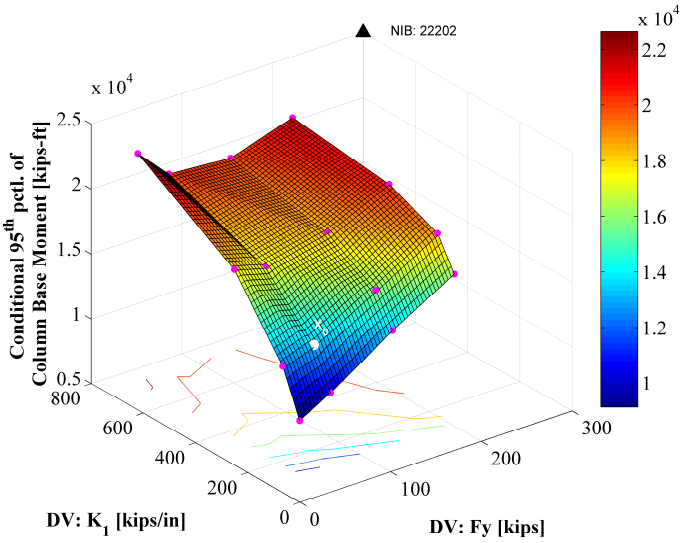

Figure 7.28: Risk feature: 95th percentile of conditional demand of column base moment of pier #5 in the transverse direction at OBE hazard level

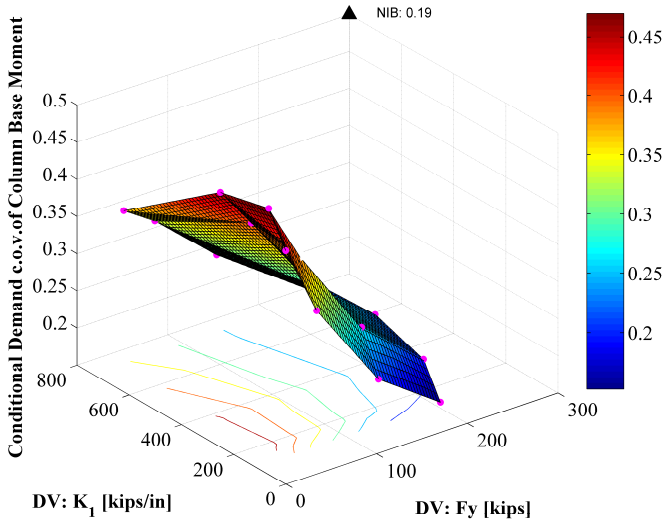

Figure 7.29: Risk feature: conditional demand c.o.v. of column base moment of pier #5 in the transverse direction at OBE hazard level

In summary, based on the parametric conditional mean demand hazard analysis on OBE hazard level, the seismic risk to the bridge highly relies on the design of seismic isolators, an optimal seismic design of seismic isolators can be achieved by maximizing the beneficial effects of seismic isolation while enforcing proper constraints to limit the detrimental effects, as illustrated in the next chapter.

Parametric conditional seismic demand hazard analysis on MCE hazard level

Under MCE hazard level earthquakes, more nonlinearity in the structural system will get involved, mainly due to the introduction of contact nonlinearities induced by pounding and more nonlinearity in seismic isolation and substructures. The pounding mainly occurs at the abutments and interior expansion joints in both longitudinal and transverse directions. The risk features of different EDPs based on the conditional seismic demand hazard analysis on the

MCE hazard level display slight difference but similar trend as a function of isolators' yield strength and initial stiffness, compared to OBE in general for most EDPs.

Figure 7.30 and Figure 7.31 presents the conditional mean demand of the absolute deck acceleration over pier #5 in the longitudinal and transverse direction at MCE hazard level. A pronounced drawback of seismic isolators with low yield strength and high elastic stiffness is exposed for deck acceleration, as discovered in deck acceleration and force demand on substructures in the transverse direction on OBE hazard level.

The conditional mean demand on the relative deck displacement over pier #5 at MCE hazard level is presented in Figure 7.32 and Figure 7.33. At OBE hazard level, risk feature is not more sensitive to either the yield strength change or the initial stiffness change in the parametric domain studied here, that is to say that no dominant dimension is observed for the mean demand surface. By contrast, the deck displacement on MCE hazard level is more sensitive to the seismic isolators' yield strength compared to the isolators' initial stiffness.

At MCE hazard level, the topology of the conditional mean demand for column base moment and total base shear force shown in Figure 7.34 to Figure 7.35 and Figure 7.36 to Figure 7.37 respectively, especially in the response in the transverse direction.

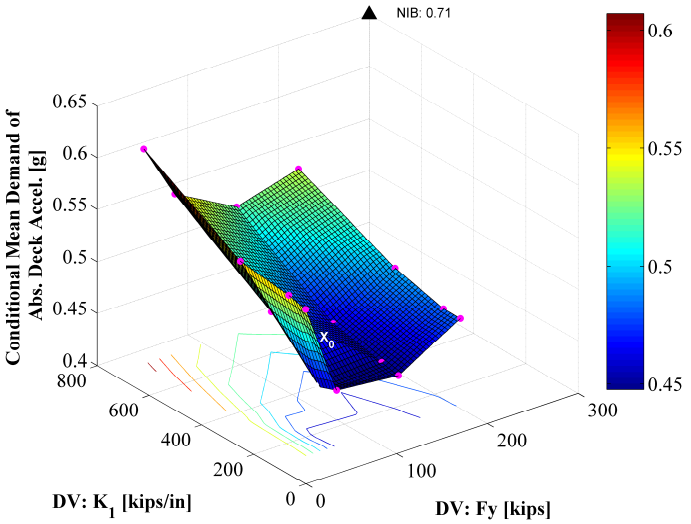

Figure 7.30: Risk feature: conditional mean demand of absolute deck acceleration over pier #5 in the longitudinal direction at MCE hazard level

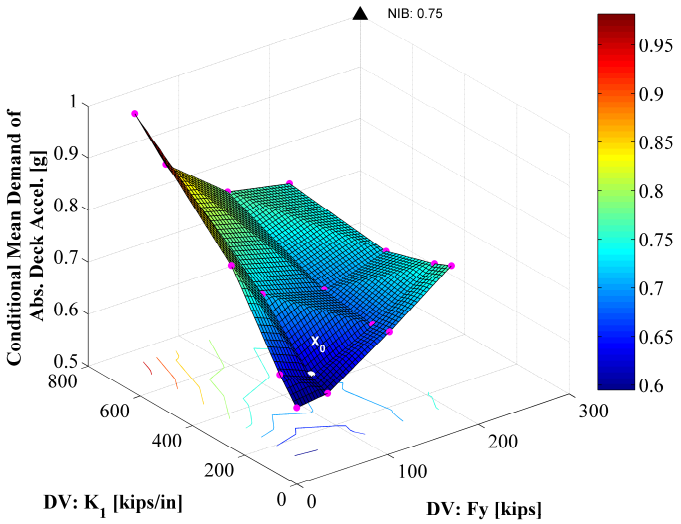

Figure 7.31: Risk feature: conditional mean demand of absolute deck acceleration over pier #5 in the transverse direction at MCE hazard level

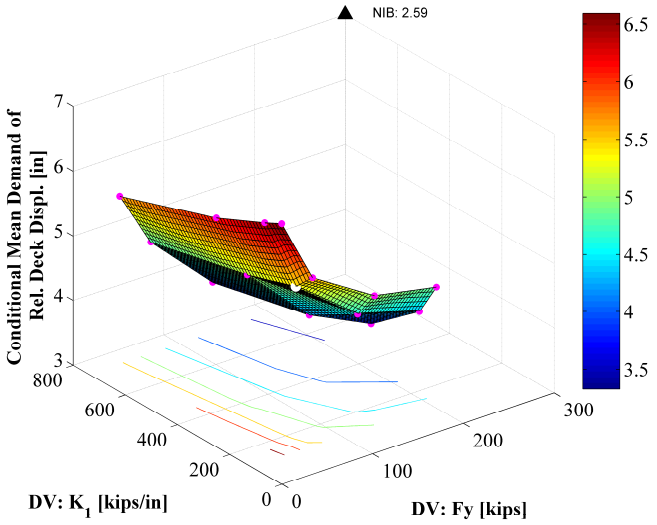

Figure 7.32: Risk feature: conditional mean demand of relative deck displacement over pier #5 in the longitudinal direction at MCE hazard level

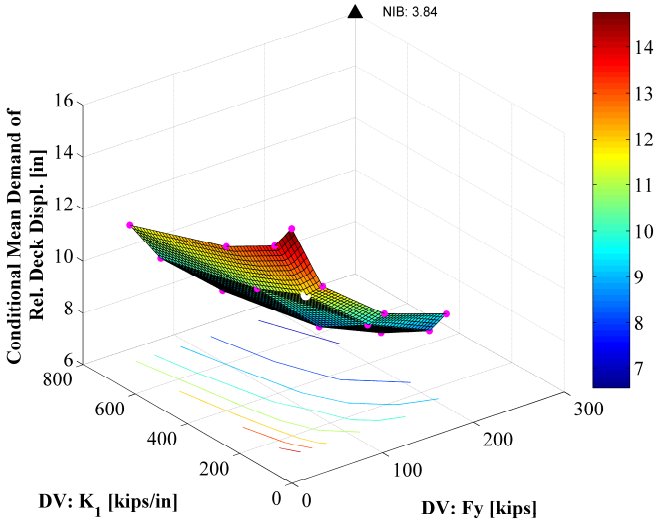

Figure 7.33: Risk feature: conditional mean demand of relative deck displacement over pier #5 in the transverse direction at MCE hazard level

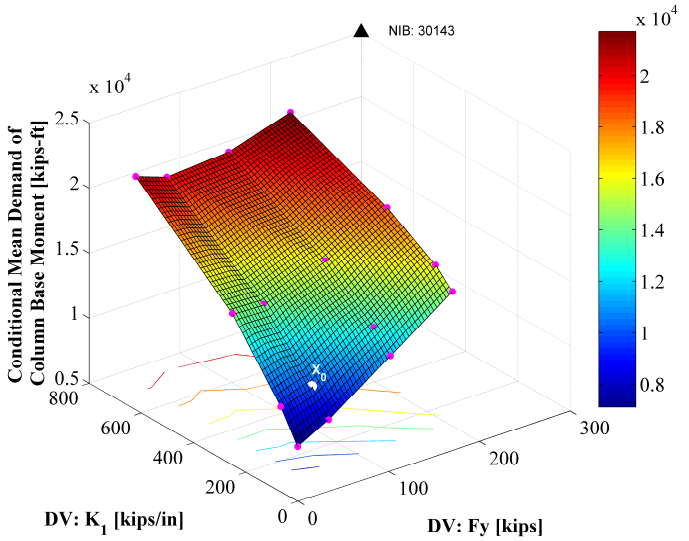

Figure 7.34: Risk feature: conditional mean demand of column base moment of pier #5 in the longitudinal direction at MCE hazard level

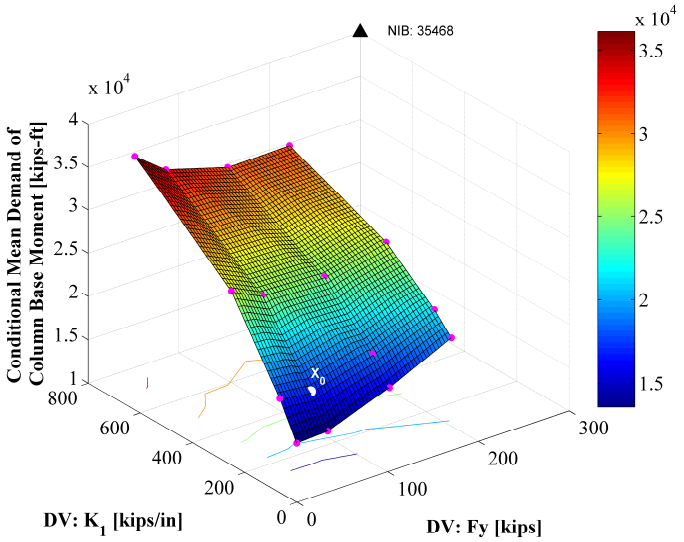

Figure 7.35: Risk feature: conditional mean demand of column base moment of pier #5 in the longitudinal direction at MCE hazard level

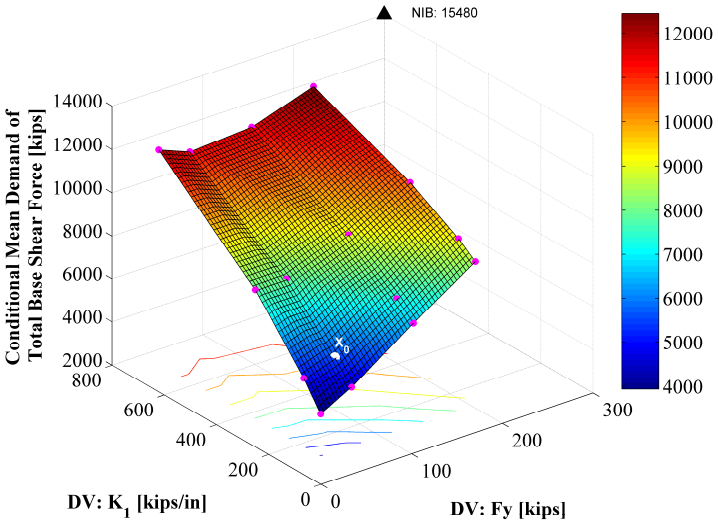

Figure 7.36: Risk feature: conditional mean demand of total base shear force in the longitudinal direction at MCE hazard level

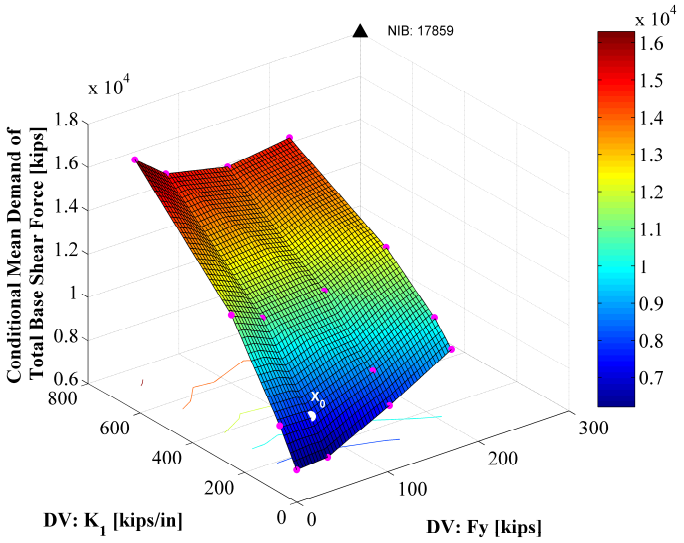

Figure 7.37: Risk feature: conditional mean demand of total base shear force in the transverse direction at MCE hazard level

The parametric study of the conditional mean demand on the pile foundations, in terms of pile cap translational displacement, pile cap rotation, maximum pile moment, and maximum pile shear force, are presented in Figure 7.38 to Figure 7.45. The decrease of seismic isolators' yield strength and initial stiffness helps reducing the demand on the pile foundations, except for certain isolator designs with inappropriate low yield strength and high initial stiffness.

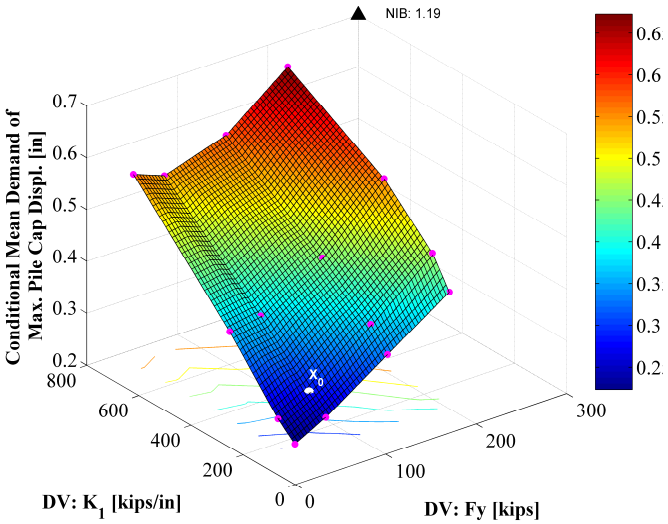

Figure 7.38: Risk feature: conditional mean demand of pile cap displacement of foundation under pier #5 in the longitudinal direction at MCE hazard level

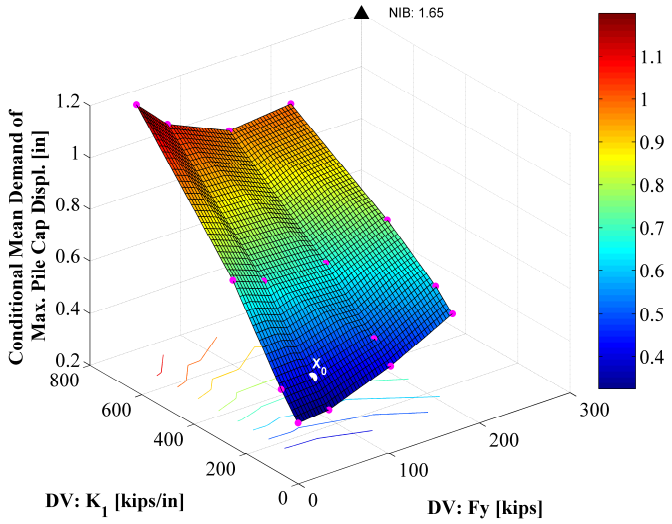

Figure 7.39: Risk feature: conditional mean demand of pile cap displacement of foundation under pier #5 in the transverse direction at MCE hazard level

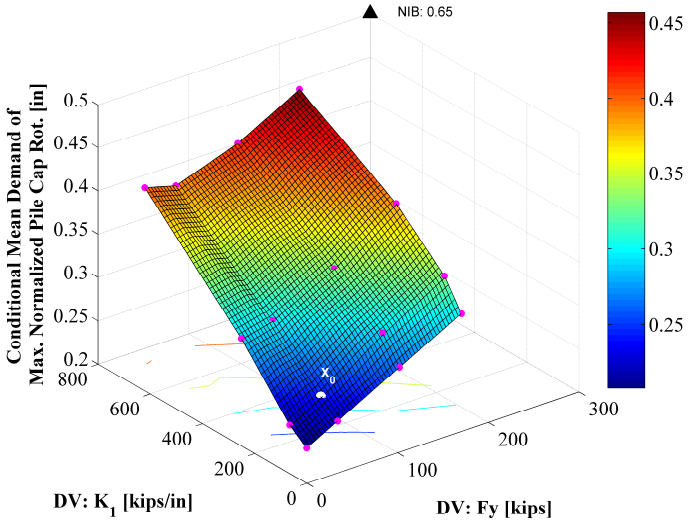

Figure 7.40: Risk feature: conditional mean demand of pile cap rotation of foundation under pier #5 in the longitudinal direction at MCE hazard level

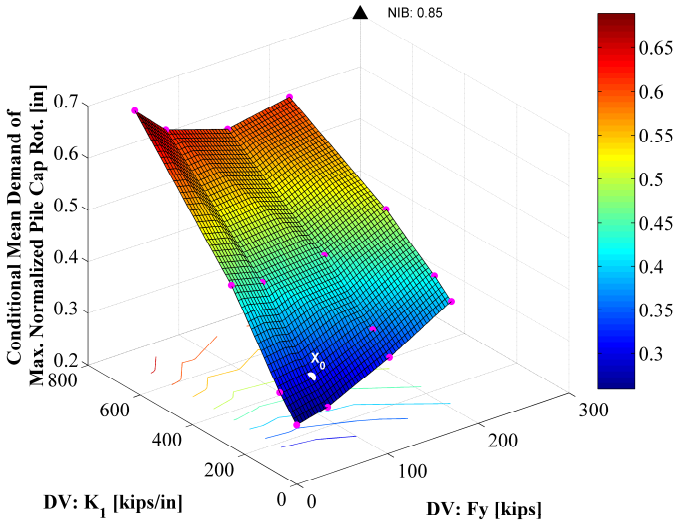

Figure 7.41: Risk feature: conditional mean demand of pile cap rotation of foundation under pier #5 in the transverse direction at MCE hazard level

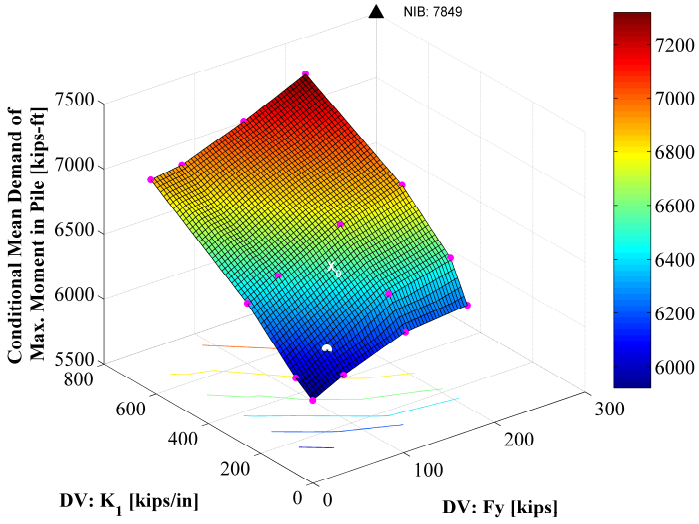

Figure 7.42: Risk feature: conditional mean demand of bending moment of piles under pier #5 in the longitudinal direction at MCE hazard level

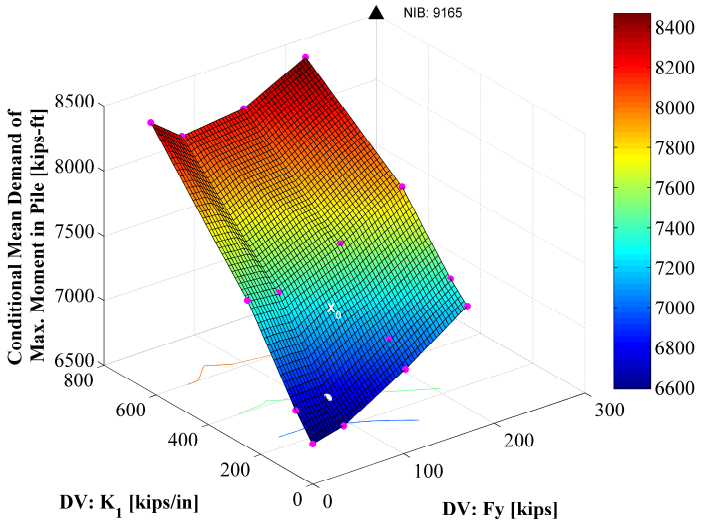

Figure 7.43: Risk feature: conditional mean demand of bending moment of piles under pier #5 in the transverse direction at MCE hazard level

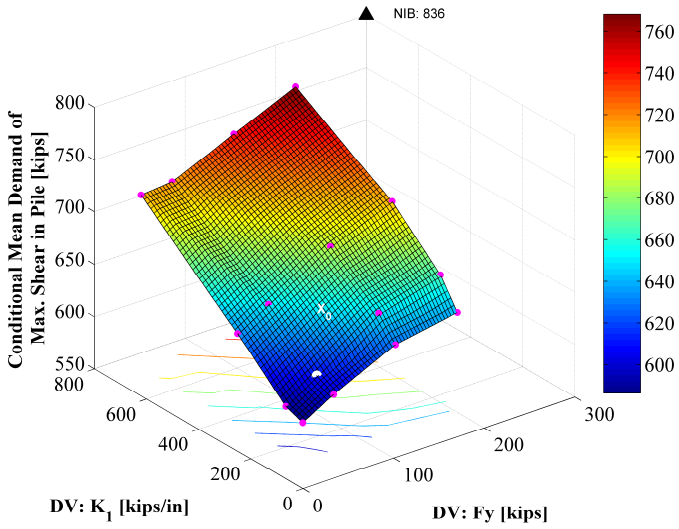

Figure 7.44: Risk feature: conditional mean demand of shear force of piles under pier #5 in the longitudinal direction at MCE hazard level

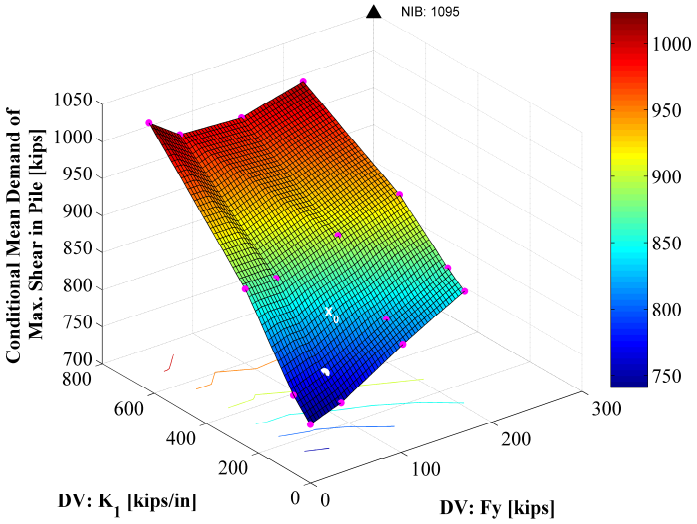

Figure 7.45: Risk feature: conditional mean demand of shear force of piles under pier #5 in the transverse direction at MCE hazard level

One feature that has persisted through all the studies of risk features as a function of isolators' yield strength and initial stiffness is the coexistence of beneficial and detrimental effects of seismic isolators. The comprehensive investigation into topologies of risk features, displayed with different trends between OBE and MCE hazard levels or even with conflicting trends among different EDPs, paves the way for the formulation of optimization problems later on. The optimization problems will be formulated concerning seismic risk to different EDPs as well as seismic risk under different hazard levels.

7.5.2. Risk feature exploration for probabilistic seismic demand hazard analysis

Probabilistic seismic demand hazard analysis, which is implemented by convolving the probabilistic seismic hazard with the conditional demand hazard for given hazard levels, yields the probabilistic seismic demand hazard curve. This section will center on the parametric study results of typical risk features defined based on the probabilistic seismic demand hazard curve, together with representative probabilistic demand hazard curves used to define those risk features.

The suite of probabilistic seismic demand hazard curves enclosed here consist of demand hazard curves for NIB and four alternative designs of IB with representative isolator parameters. The EDPs of interest include different response quantities of the bridge structure, pile foundation, and track system. The main purpose is to evaluate the how the probabilistic demand hazards change as a function of the seismic isolators' properties.

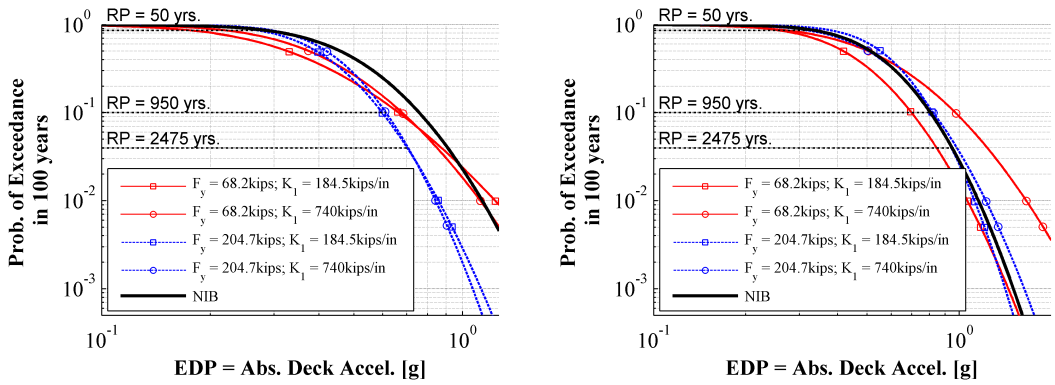

Figure 7.46: Parametric illustration of probabilistic seismic demand hazard curve of the absolute deck acceleration over pier #5 in the long. (left) and trans. (right) directions

Figure 7.46 displays the probabilistic seismic demand hazard curves of absolute deck acceleration for the NIB and IB with different seismic isolators. As observed from the probabilistic seismic demand hazard curves of absolute deck acceleration over pier #5 of the middle frame in the longitudinal direction in Figure 7.46, the introduction of seismic isolation reduces the acceleration for low hazard levels efficiently compared to the NIB case. Among the IB cases, the seismic isolators with lower yield strength are more efficient in reducing the acceleration on lower hazard levels, while the imposed acceleration demand for higher hazard levels could be as large as NIB or even larger. In the transverse direction of the bridge, the maximum absolute deck acceleration is more sensitive to the yield strength of seismic isolator when the initial stiffness is high. The seismic risk to deck acceleration can be higher than NIB

either for low hazard levels or for high hazard levels if the seismic isolators' properties are not properly selected.

Based on the definitions of risk features aforementioned, the parametric study of the risk features of the longitudinal and transverse deck acceleration are shown in Figure 7.47 to Figure 7.50. Two demand hazard levels characterized with return period of 50 years and 950 years respectively are investigated, which are referred to as OBE HL and MCE HL demand for convenience.

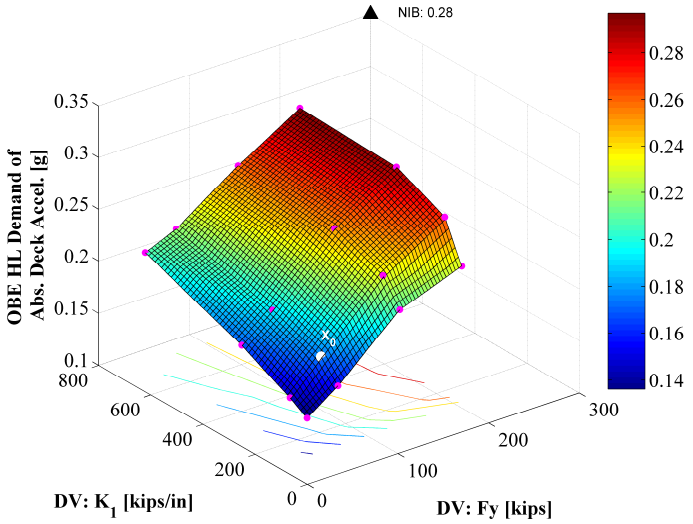

Figure 7.47: Risk feature: the unconditional demand of hazard level PE100 = 86% (i.e., RP = 50 yrs.) on the absolute deck acceleration over pier #5 in the long. dir.

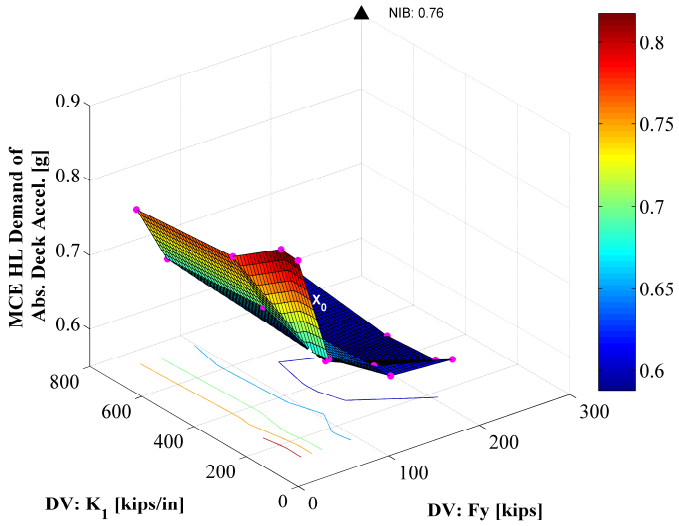

Figure 7.48: Risk feature: the unconditional demand of hazard level PE100 = 10% (i.e., RP = 950 yrs.) on the absolute deck acceleration over pier #5 in the long. dir.

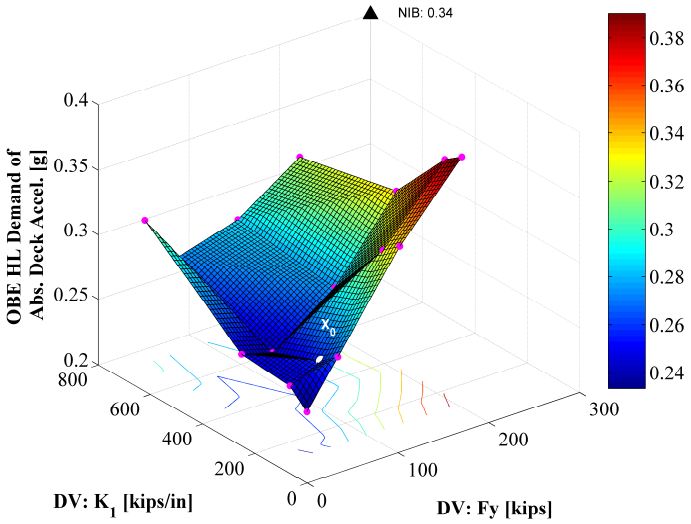

Figure 7.49: Risk feature: the unconditional demand of hazard level PE100 = 86% (i.e., RP = 50 yrs.) on absolute deck acceleration over pier #5 in the trans. dir.

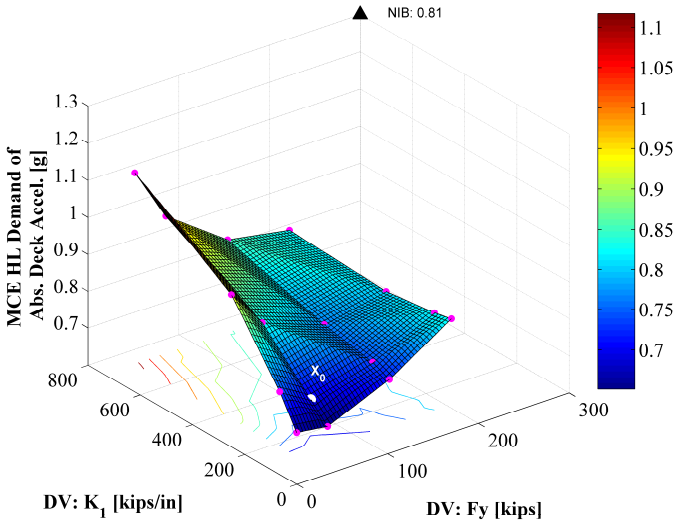

Figure 7.50: Risk feature: the unconditional demand of hazard level PE100 = 10% (i.e., RP = 950 yrs.) on absolute deck acceleration over pier #5 in the trans. dir.

A clear-cut influence of seismic isolators on deck displacement is observed from the probabilistic hazard curves shown in Figure 7.51. The unconditional single point hazards corresponding to OBE HL and MCE HL are plotted with respect to the isolators' parameters in Figure 7.52 to Figure 7.55. It is observed that the topology of the unconditional single point hazard corresponding to OBE HL and MCE HL correlates well with the topology of the conditional mean demand on OBE HL and the conditional mean demand on MCE HL respectively. The unconditional demand hazard at OBE HL is a little bit smaller than the conditional mean demand on OBE HL, while the unconditional demand hazard at MCE HL is a little bit larger than the conditional mean demand on the MCE HL.

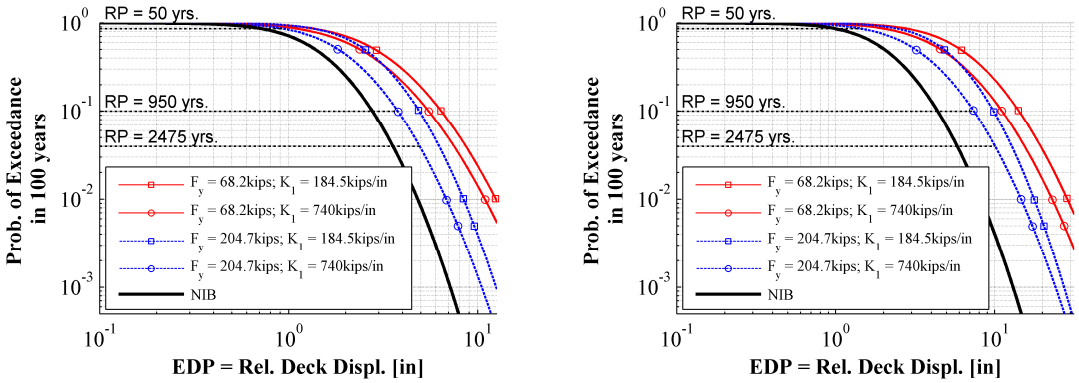

Figure 7.51: Parametric illustration of probabilistic seismic demand hazard curve of the relative deck displacement over pier #5 in the long. (left) and trans. (right) directions

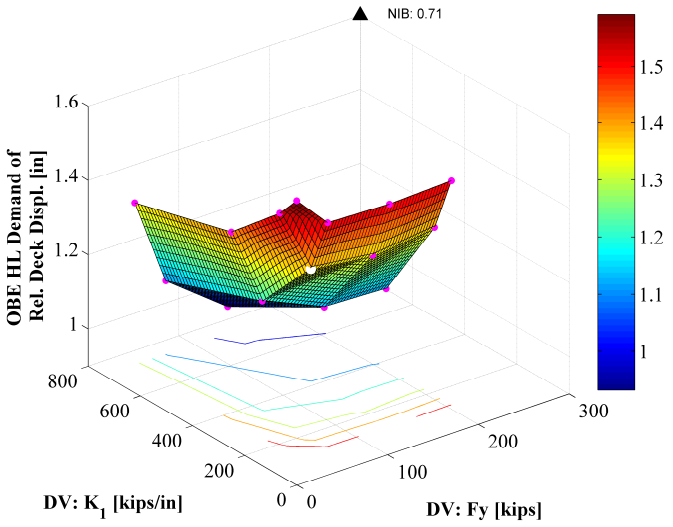

Figure 7.52: Risk feature: the unconditional demand of hazard level PE100 = 86% (i.e., RP = 50 yrs.) on relative deck displacement over pier #5 in the long. dir.

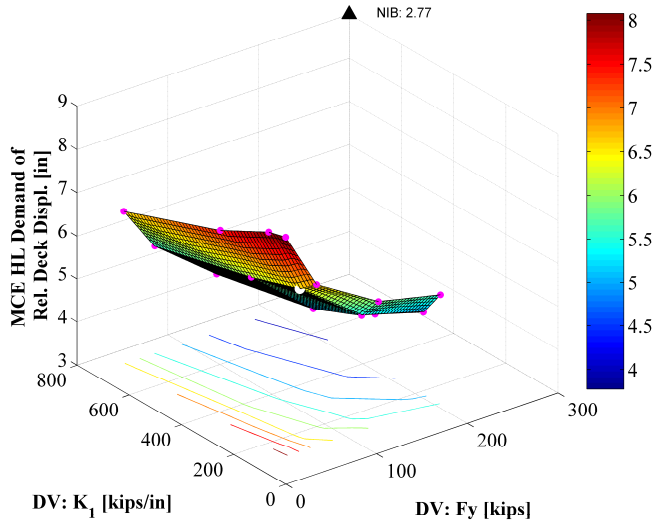

Figure 7.53: Risk feature: the unconditional demand of hazard level PE100 = 10% (i.e., RP = 950 yrs.) on relative deck displacement over pier #5 in the long. dir.

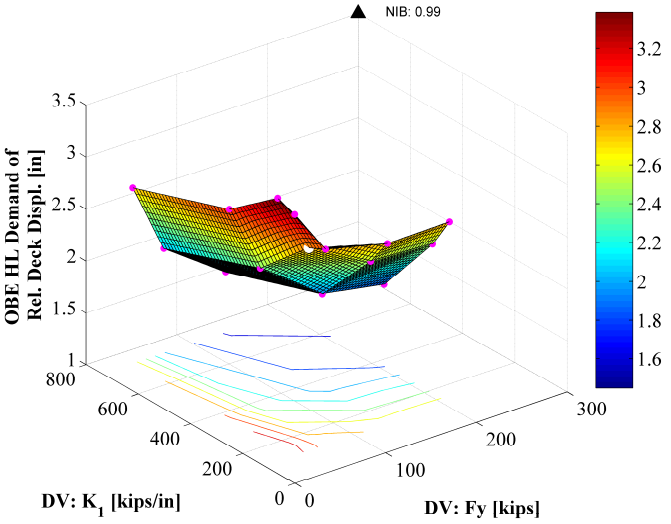

Figure 7.54: Risk feature: the unconditional demand of hazard level PE100 = 86% (i.e., RP = 50 yrs.) on relative deck displacement over pier #5 in the trans. dir.

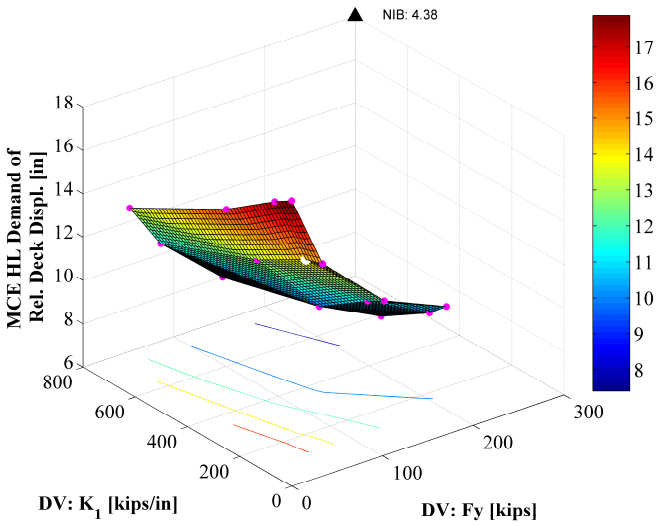

Figure 7.55: Risk feature: the unconditional demand of hazard level PE100 = 10% (i.e., RP = 950 yrs.) on relative deck displacement over pier #5 in the trans. dir.

Overall, consistent with the conclusion drawn based on the conditional demand hazard, the unconditional demand hazard of deck displacement is increased by the introduction of seismic isolators when the seismic isolators' yield strength and initial stiffness are decreased. The unconditional demand of higher hazard levels (i.e., MCE HL) is more sensitive to the change of yield strength of seismic isolators than the change of their initial stiffness.

The parametric study of the unconditional probabilistic seismic demand on the seismic isolator deformation is summarized below with the representative probabilistic demand hazard curves enclosed in Figure 7.56. The seismic demand of OBE (MCE) hazard level with PE100 = 86% (PE100 = 10%) as a function of isolators' properties are presented in Figure 7.57 and Figure 7.59 (Figure 7.58 and Figure 7.60).

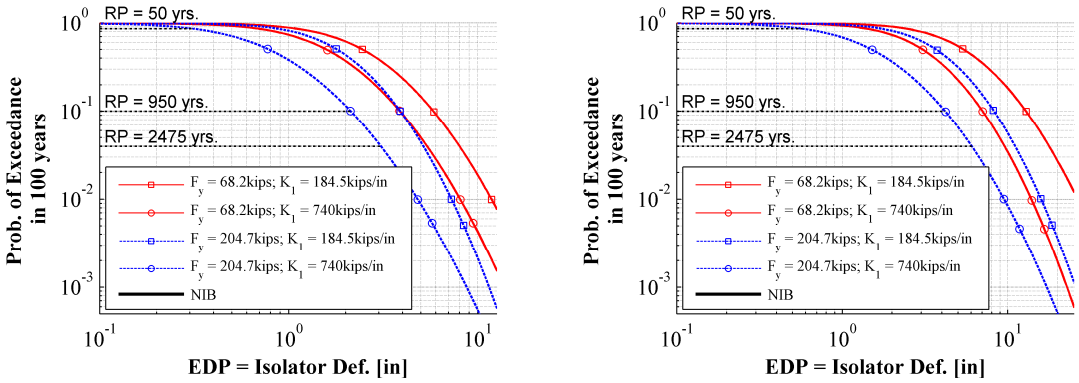

Figure 7.56: Parametric illustration of probabilistic seismic demand hazard curve of isolator deformation over pier #5 in the long. (left) and trans. (right) directions

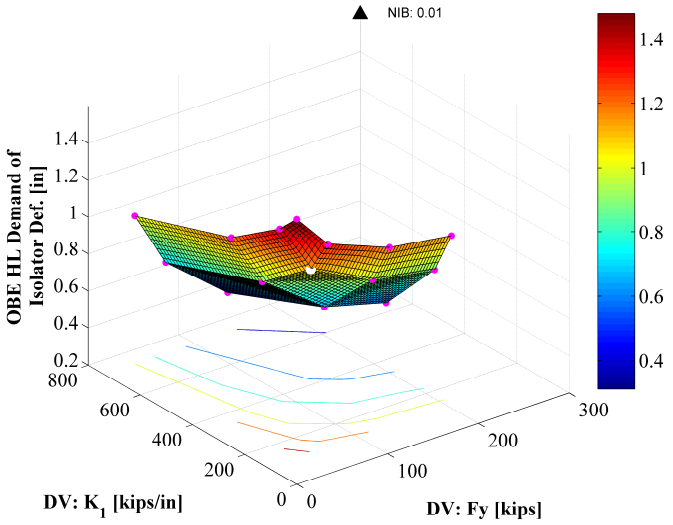

Figure 7.57: Risk feature: the unconditional demand of hazard level PE100 = 86% (i.e., RP = 50 yrs.) on isolator deformation over pier #5 in the long. dir.

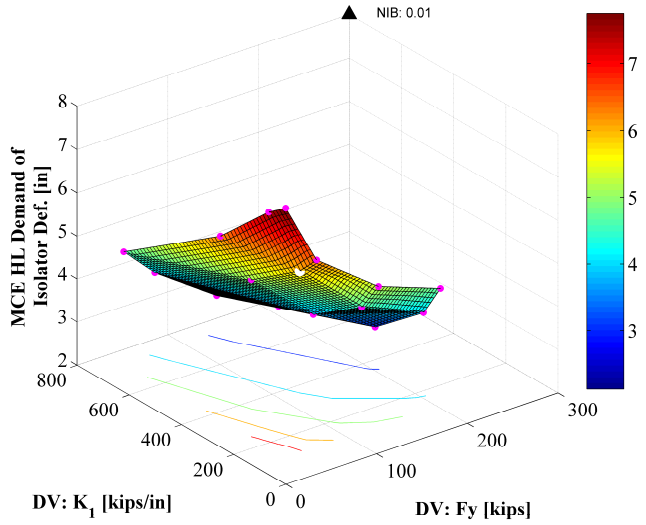

Figure 7.58: Risk feature: the unconditional demand of hazard level PE100 = 10% (i.e., RP = 100 yrs.) on isolator deformation over pier #5 in the long. dir.

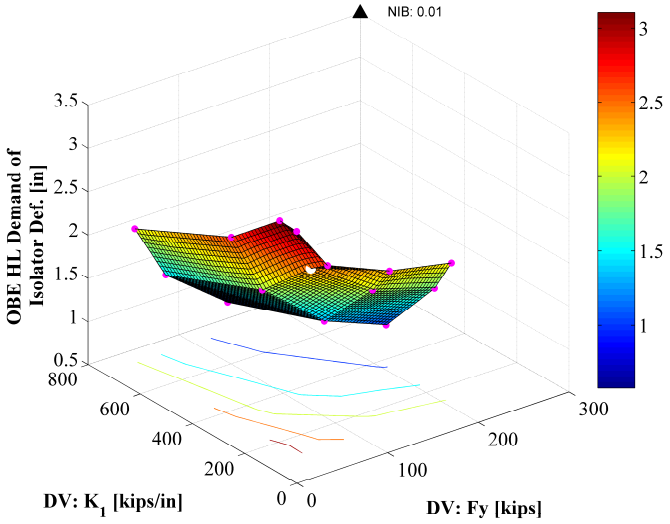

Figure 7.59: Risk feature: unconditional demand of hazard level PE100 = 86% (i.e., RP = 50 yrs.) on isolator deformation over pier #5 in the trans. dir.

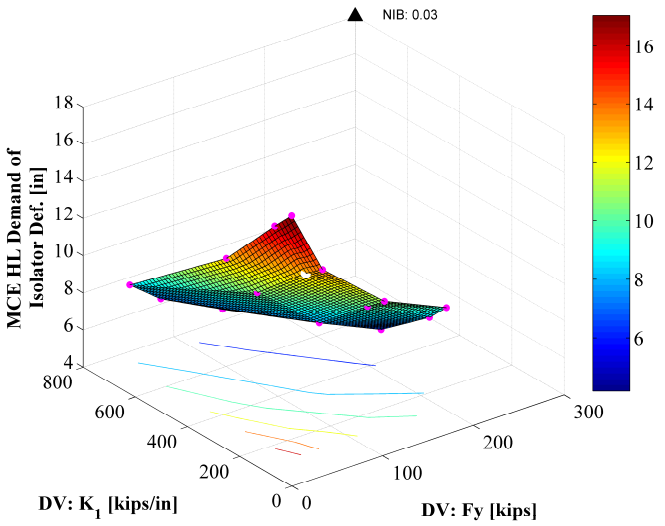

Figure 7.60: Risk feature: unconditional demand of hazard level PE100 = 10% (i.e., RP = 950 yrs.) on isolator deformation over pier #5 in the trans. dir.

Figure 7.61 shows a suite of probabilistic seismic demand hazard curves of pier column drift of pier #5 with respect to pile cap of NIB and IB with representative isolator properties. The beneficial effects of seismic isolation are not only different among different hazard levels, but different between the response in the longitudinal and transverse direction. As revealed by the topology plots of the single point hazard extracted from the probabilistic demand hazard curves, the seismic isolation's efficiency in reducing the seismic demand on pier column drift increases with the decrease of the yield strength or initial stiffness for unconditional demand of low hazard levels (e.g., OBE HL). Similar beneficial effects of seismic isolation can be observed for the unconditional demand of high hazard levels (e.g., MCE HL) except for those isolator designs with low yield strength but high initial stiffness (category *LYHK*). For higher hazard levels, an improper isolator design can even impose more demand on the substructures.

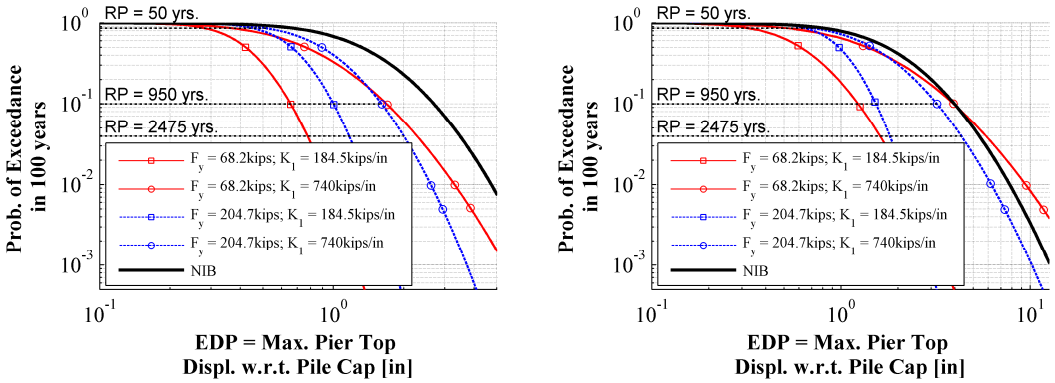

Figure 7.61: Parametric illustration of probabilistic seismic demand hazard curve of pier column drift of pier #5 w.r.t. pile cap in the long. (left) and trans. (right) directions

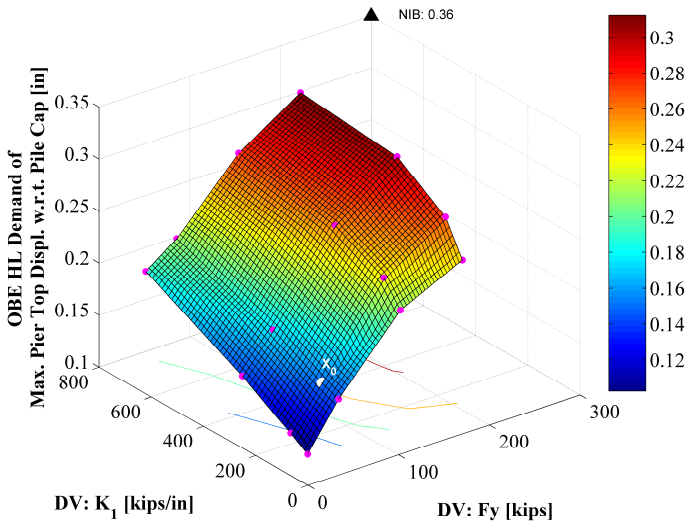

Figure 7.62: Risk feature: unconditional demand of hazard level PE100 = 86% (i.e., RP = 50 yrs.) on pier column drift of pier #5 w.r.t. pile cap in the long. dir.

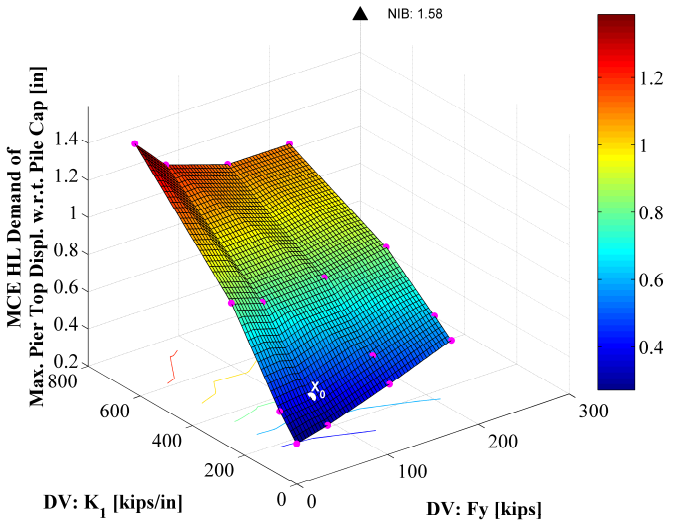

Figure 7.63: Risk feature: unconditional demand of hazard level PE100 = 10% (i.e., RP = 950 yrs.) on pier column drift of pier #5 w.r.t. pile cap in the long. dir.

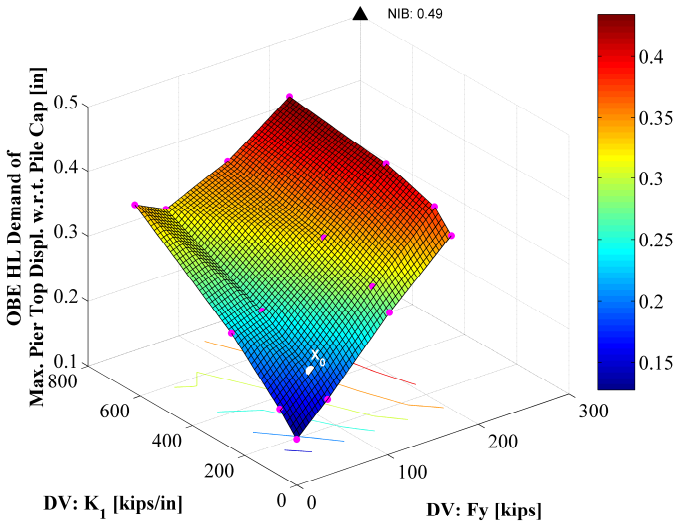

Figure 7.64: Risk feature: unconditional demand of hazard level PE100 = 86% (i.e., RP = 50 yrs.) on pier column drift of pier #5 w.r.t. pile in the trans. dir.

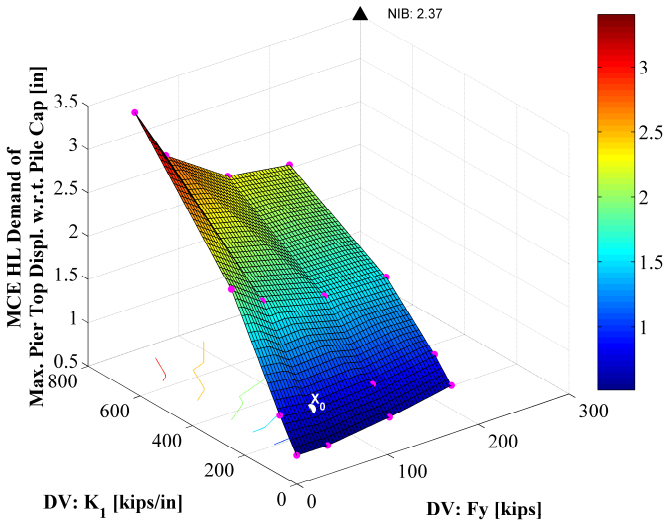

Figure 7.65: Risk feature: unconditional demand of hazard level PE100 = 10% (i.e., RP = 950 yrs.) on pier column drift of pier #5 w.r.t. pile in the trans. dir.

Parallel results on the parametric study of the unconditional probabilistic seismic demand on the pier columns and pile foundations are presented in Figure 7.66 - Figure 7.80.

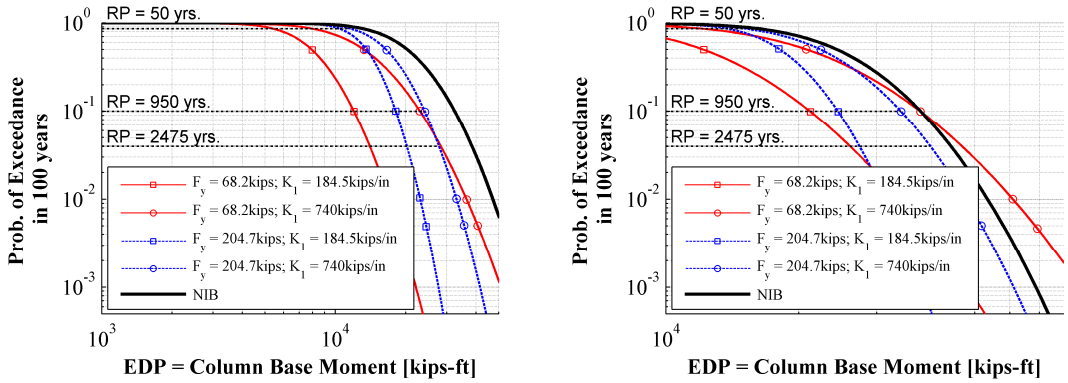

Figure 7.66: Parametric illustration of probabilistic seismic demand hazard curve of column base moment of pier #5 in the long. (left) and trans. (right) directions

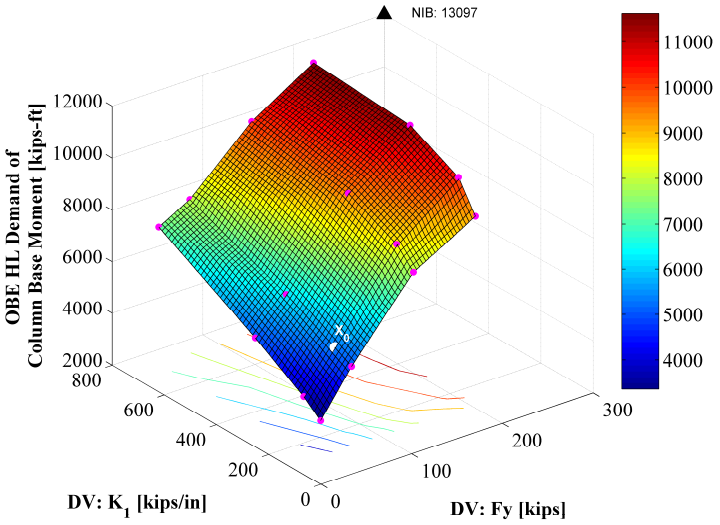

Figure 7.67: Risk feature: unconditional demand of hazard level PE100 = 86% (i.e., RP = 50 yrs.) on column base moment of pier #5 in the long. dir.

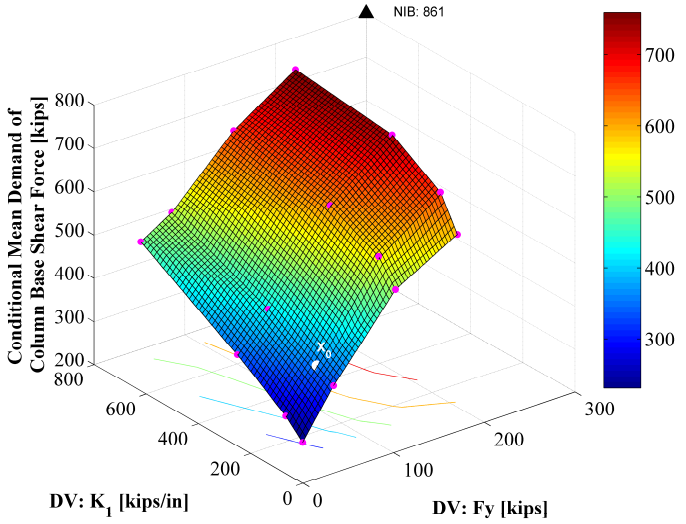

Figure 7.68: Risk feature: unconditional demand of hazard level PE100 = 10% (i.e., RP = 950 yrs.) on column base moment of pier #5 in the long. dir.

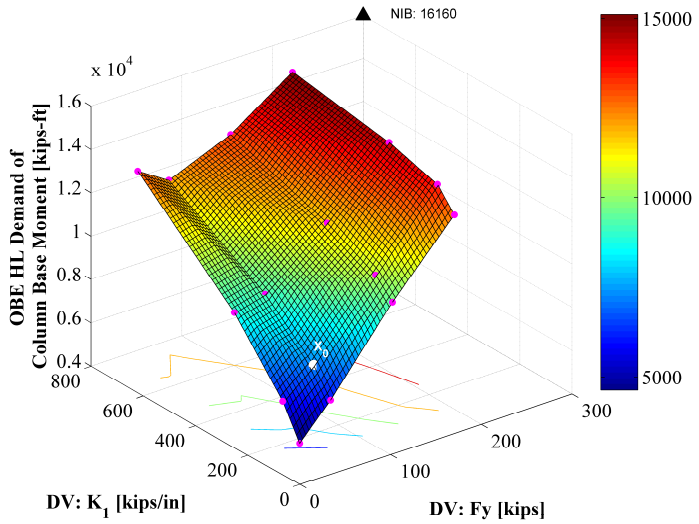

Figure 7.69: Risk feature: unconditional demand of hazard level PE100 = 86% (i.e., RP = 50 yrs.) on column base moment of pier #5 in the trans. dir.

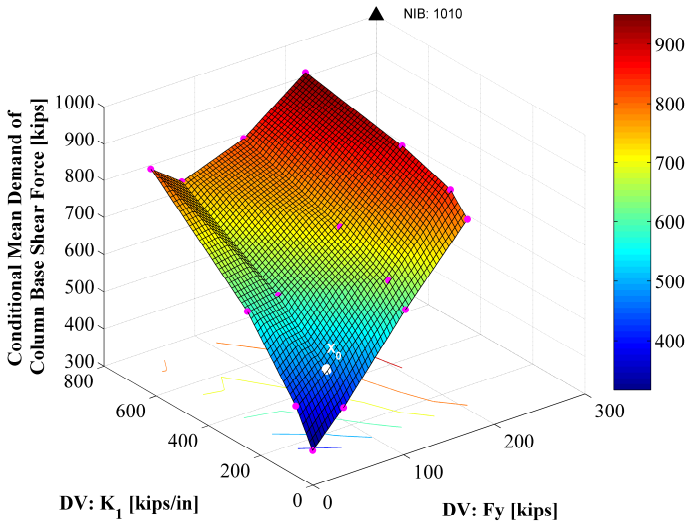

Figure 7.70: Risk feature: unconditional demand of hazard level PE100 = 86% (i.e., RP = 50 yrs.) on column base moment of pier #5 in the trans. dir.

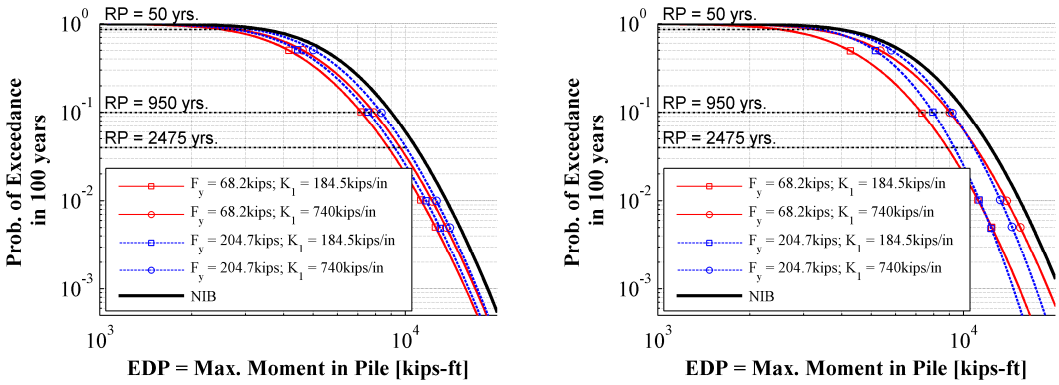

Figure 7.71: Parametric illustration of probabilistic seismic demand hazard curve of bending moment of piles under pier #5 in the long. (left) and trans. (right) directions

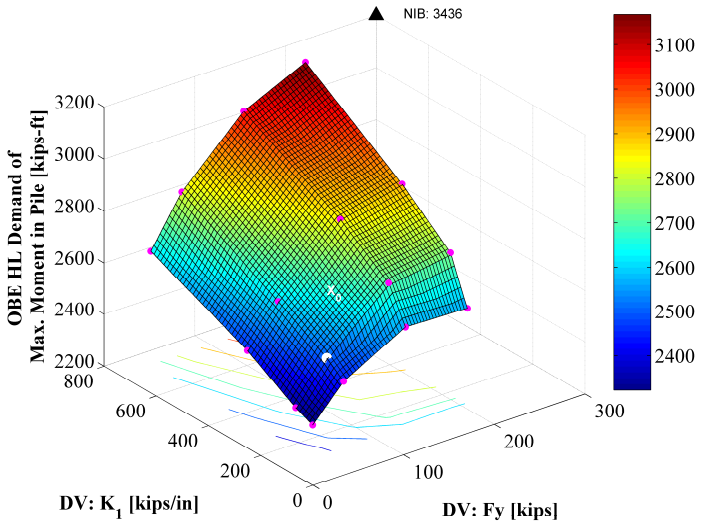

Figure 7.72: Risk feature: unconditional demand of hazard level PE100 = 86% (i.e., RP = 50 yrs.) on bending moment of piles under pier #5 in the long. dir.

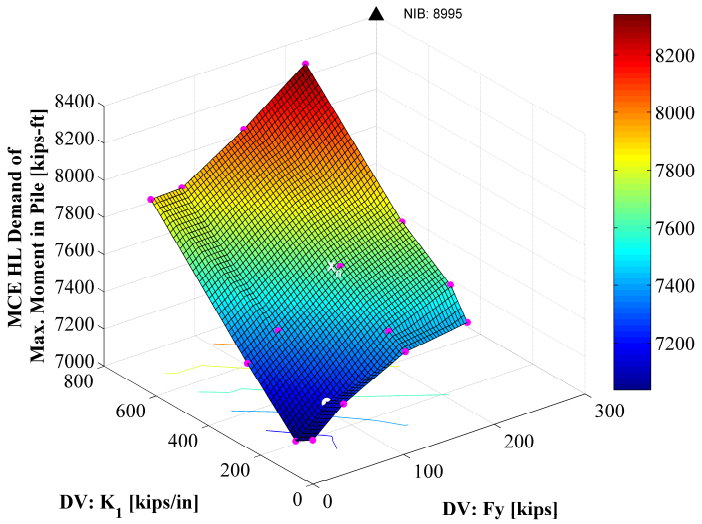

Figure 7.73: Risk feature: unconditional demand of hazard level PE100 = 10% (i.e., RP = 950 yrs.) on bending moment of piles under pier #5 in the long. dir.

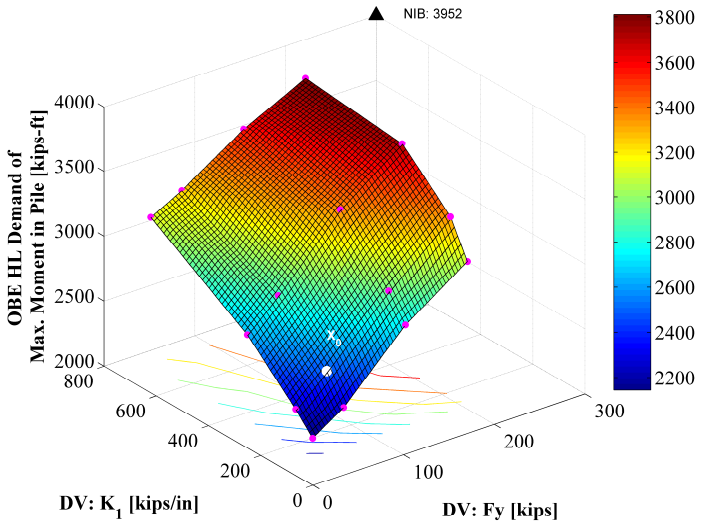

Figure 7.74: Risk feature: unconditional demand of hazard level PE100 = 86% (i.e., RP = 50 yrs.) on bending moment of piles under pier #5 in the trans. dir.

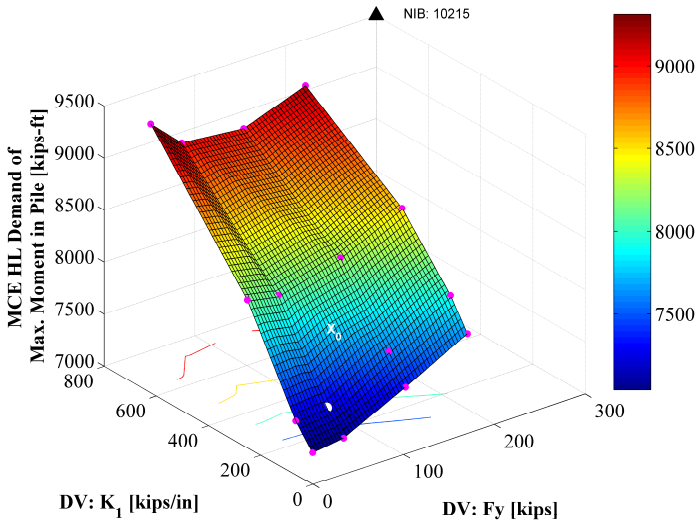

Figure 7.75: Risk feature: unconditional demand of hazard level PE100 = 10% (i.e., RP = 950 yrs.) on bending moment of piles under pier #5 in the trans. dir.

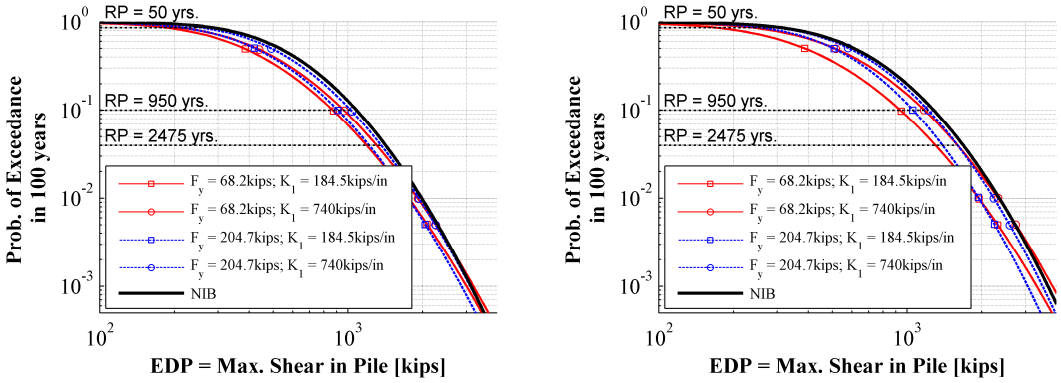

Figure 7.76: Parametric illustration of probabilistic seismic demand hazard curve of shear force of piles under pier #5 in the long. (left) and trans. (right) dir.

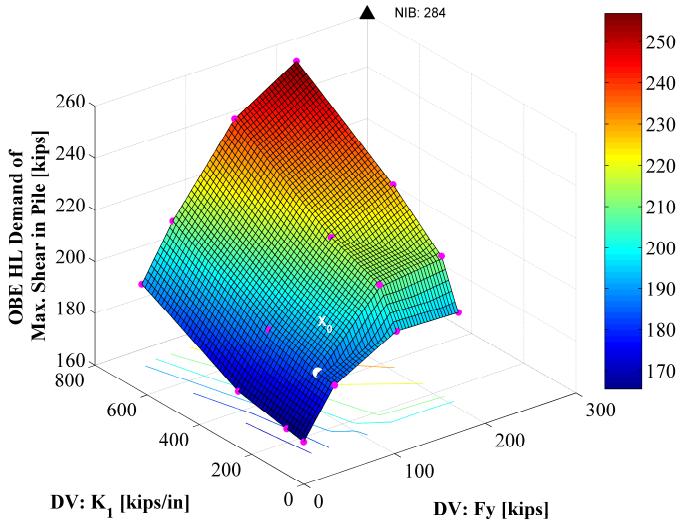

Figure 7.77: Risk feature: unconditional demand of hazard level PE100 = 86% (i.e., RP = 50 yrs.) on shear force of piles under pier #5 in the long. dir.

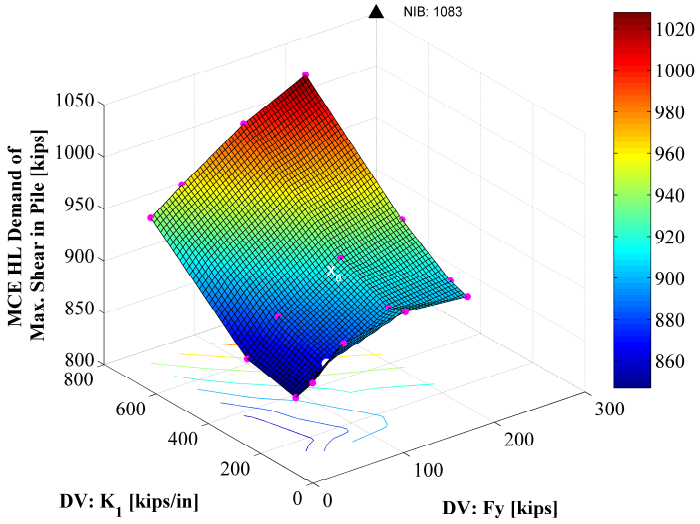

Figure 7.78: Risk feature: unconditional demand of hazard level PE100 = 10% (i.e., RP = 950 yrs.) on shear force of piles under pier #5 in the long. dir.

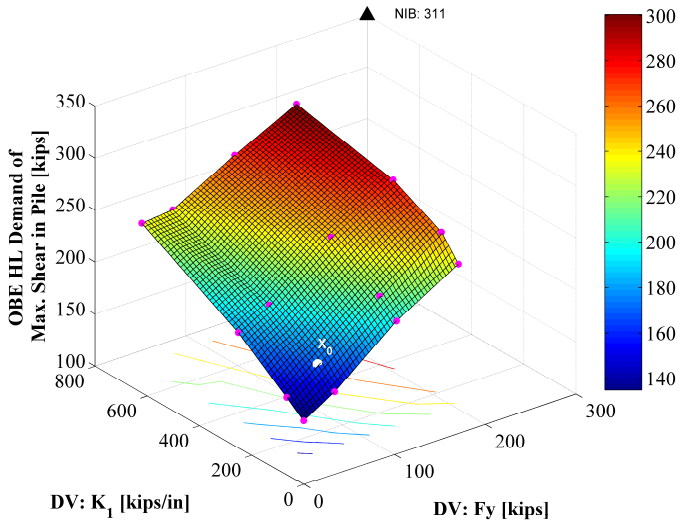

Figure 7.79: Risk feature: unconditional demand of hazard level PE100 = 86% (i.e., RP = 50 yrs.) on shear force of piles under pier #5 in the trans. dir.

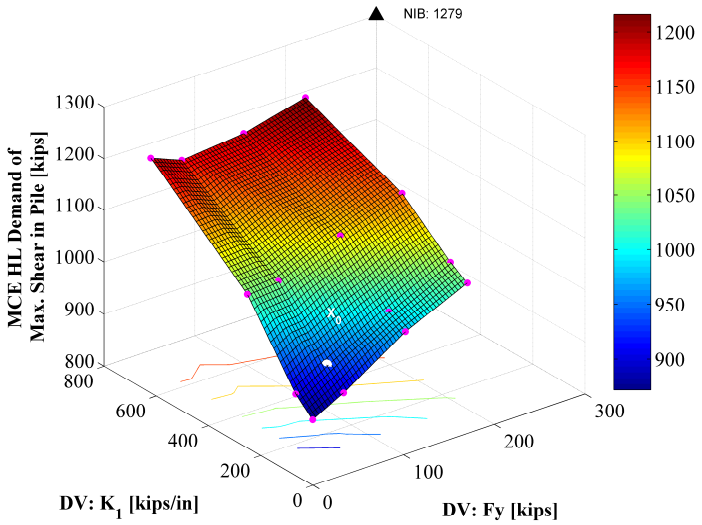

Figure 7.80: Risk feature: unconditional demand of hazard level PE100 = 10% (i.e., RP = 950 yrs.) on shear force of piles under pier #5 in the trans. dir.

The detrimental effect of seismic isolation on the rail is investigated through the parametric study of unconditional probabilistic seismic demand hazard. Figure 7.81 and Figure 7.86 illustrate how the unconditional demand hazard curves will change for different seismic isolator design alternatives.

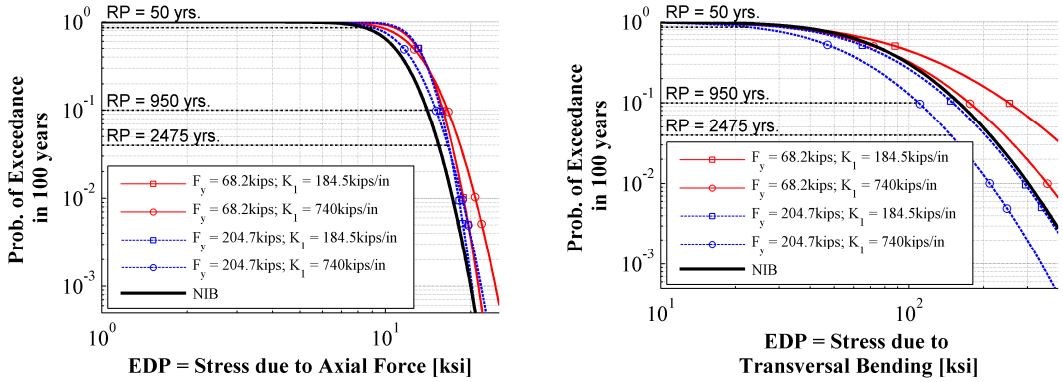

Figure 7.81: Parametric illustration of probabilistic seismic demand hazard curve for the rail stress at abutment expansion joint #1

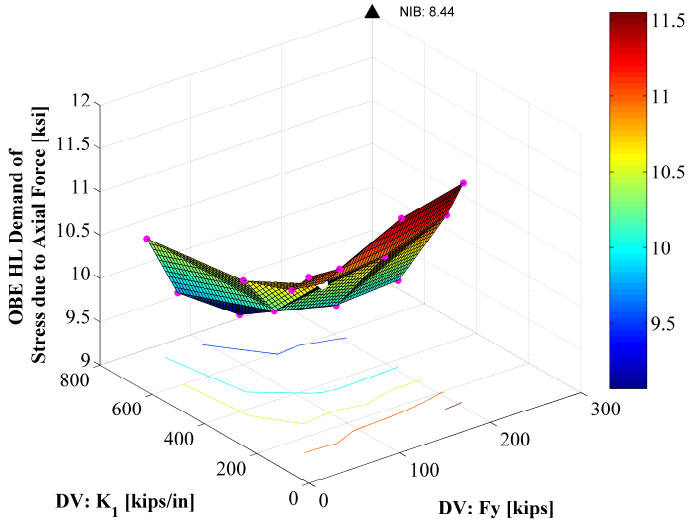

Figure 7.82: Risk feature: unconditional demand of hazard level PE100 = 86% (i.e., RP = 50 yrs.) on rail stress at abutment expansion joint #1 due to axial force

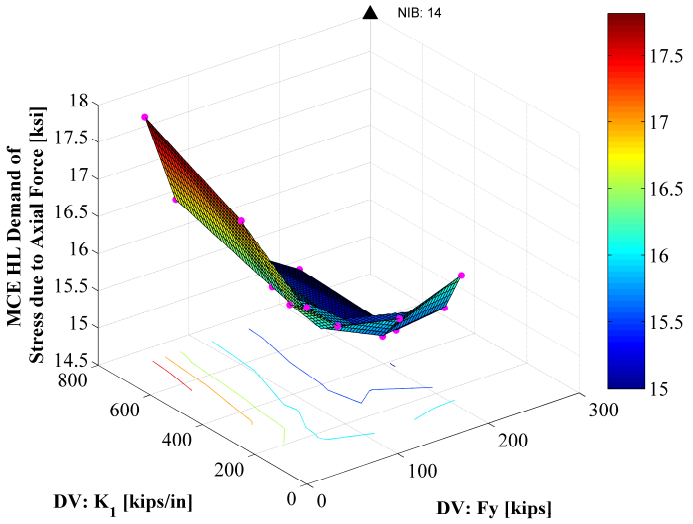

Figure 7.83: Risk feature: unconditional demand of hazard level PE100 = 10% (i.e., RP = 950 yrs.) on rail stress at abutment expansion joint #1 due to axial force

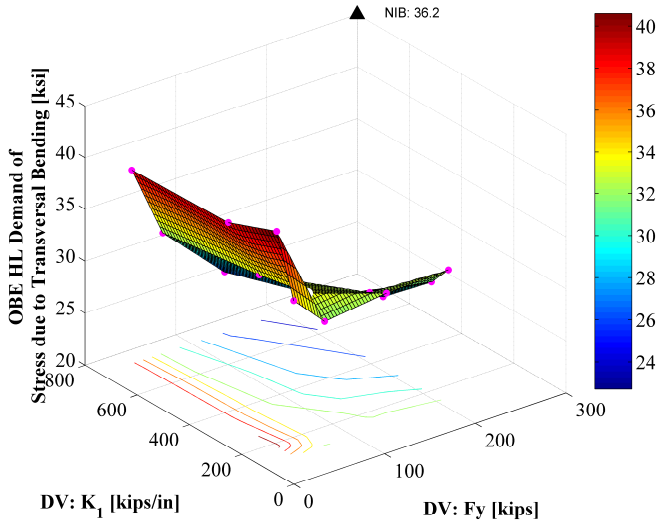

Figure 7.84: Risk feature: unconditional demand of hazard level PE100 = 86% on rail stress at abutment expansion joint #1 due to trans. bending

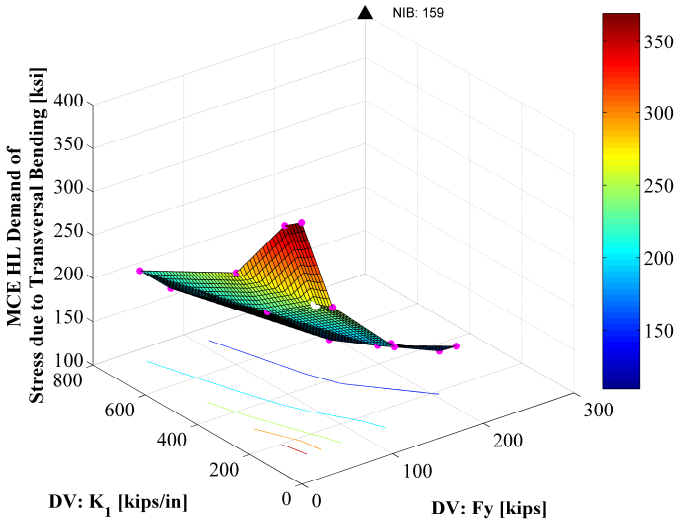

Figure 7.85: Risk feature: unconditional demand of hazard level PE100 = 10% on rail stress at abutment expansion joint #1 due to trans. bending

Figure 7.82 to Figure 7.85 show the unconditional demand, of OBE hazard level and MCE hazard level, on the rail stress around the abutment gap #1 as a function of the seismic isolator properties. The design of seismic isolators did not change of axial rail stress as much as the induced stress due to the transverse bending. Since normal rubber bearings are adopted for the traditional design of NIB, the bending stress hazard at the abutment highly depends on the design of seismic isolators, in that an isolator design with high yield strength and initial stiffness (category *HFHK*) can reduce the bending stress in rails around the abutment gap to be less than the case of NIB.

Figure 7.87 to Figure 7.90 show the parallel topology of the unconditional rail stress demand on the rails around interior expansion joint #2. The detrimental effects of seismic isolation on the additional rail stress. It is worth noting that the additional rail stress induced by the axial force changes can be controlled more efficiently by altering the yield strength of

the seismic isolators, while the additional rail stress induced by transverse bending can be controlled more efficiently by varying the initial stiffness of the seismic isolators.

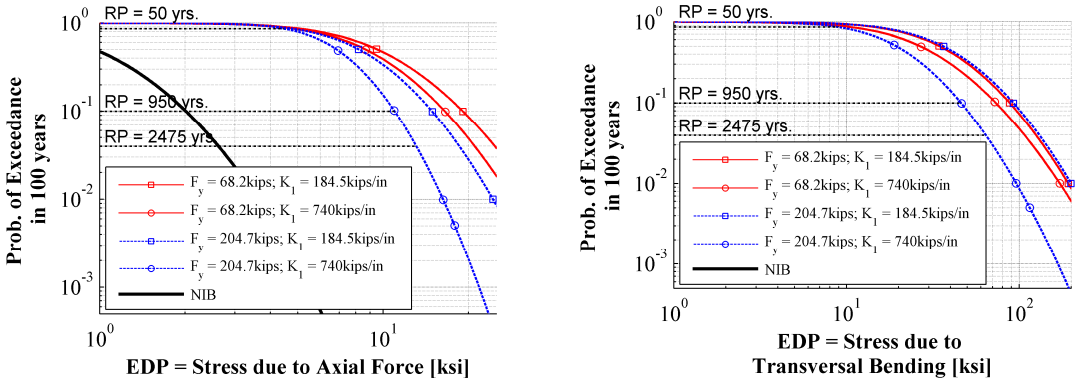

Figure 7.86: Parametric illustration of probabilistic seismic demand hazard curve of rail stress at abutment expansion joint #2

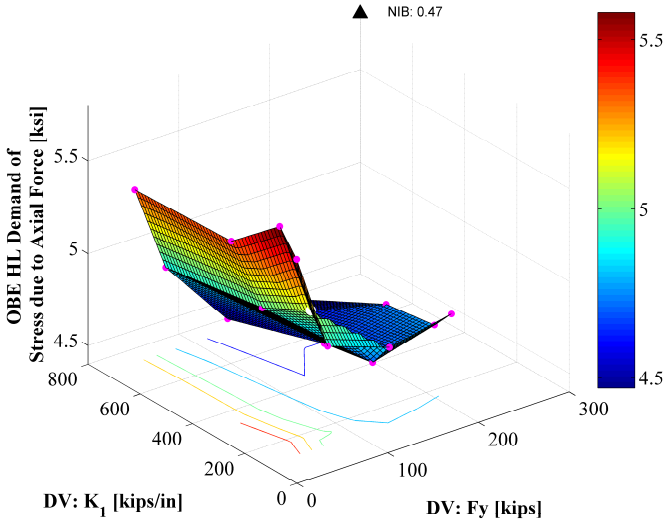

Figure 7.87: Risk feature: unconditional demand of hazard level PE100 = 86% on rail stress at interior expansion joint #2 due to axial force

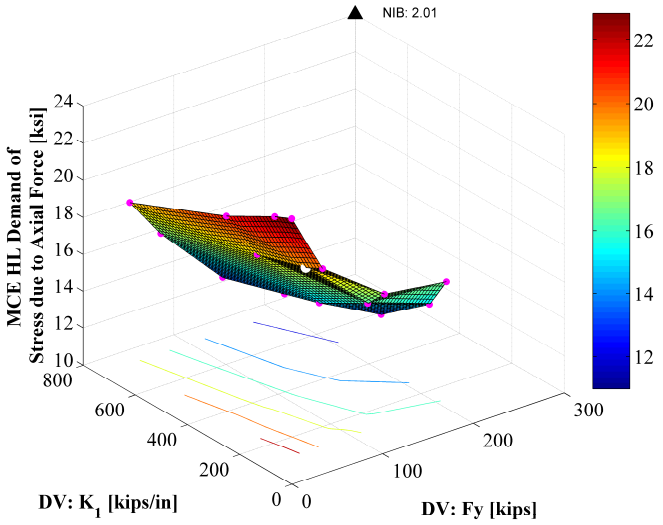

Figure 7.88: Risk feature: unconditional demand of hazard level PE100 = 10% on rail stress at interior expansion joint #2 due to axial force

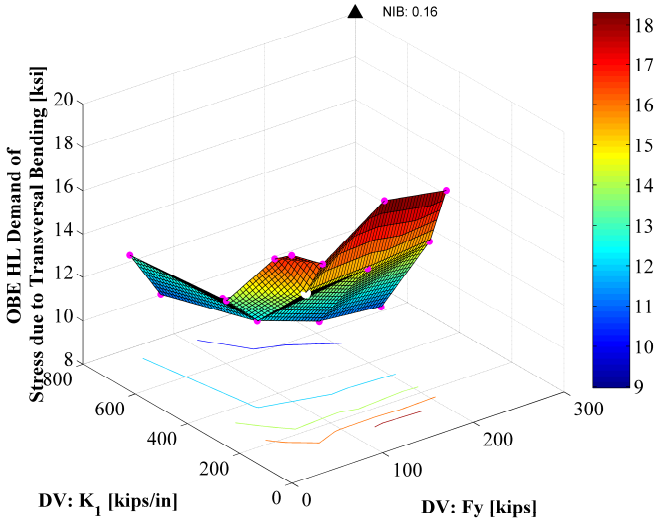

Figure 7.89: Risk feature: unconditional demand of hazard level PE100 = 86% on rail stress at interior expansion joint #2 due to trans. bending

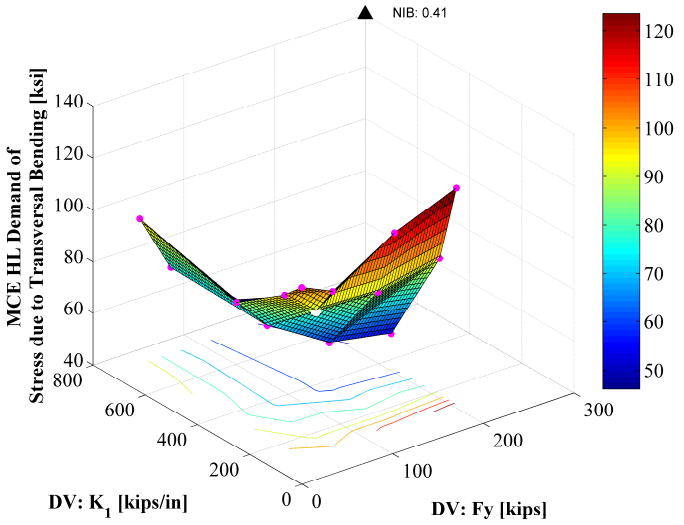

Figure 7.90: Risk feature: unconditional demand of hazard level PE100 = 10% on rail stress at interior expansion joint #2 due to trans. bending

The unconditional probabilistic seismic demand hazard curve, characterized here in terms of probability of exceedance in life exposure time of 100 years here, is essentially a complementary cumulative distribution function (CCDF). Based on the CCDF of EDP, an unconditional probability density distribution can be derived. More risk features based on the derived PDF (i.e., unconditional mean, unconditional median, unconditional coefficient of variation, and 95th percentile, namely with probability of exceedance PE100 = 5%) are investigated. The results for the three representative EDPs selected are demonstrated as below.

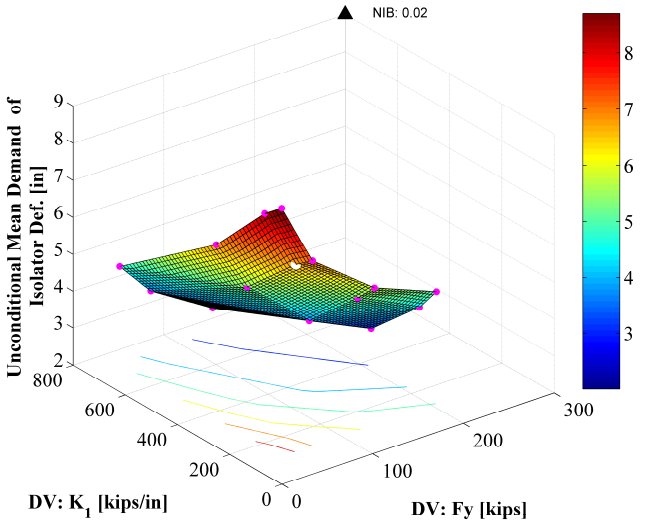

Figure 7.91: Risk feature: unconditional mean demand on isolator deformation of isolator #13 over pier #5 in the trans. dir.

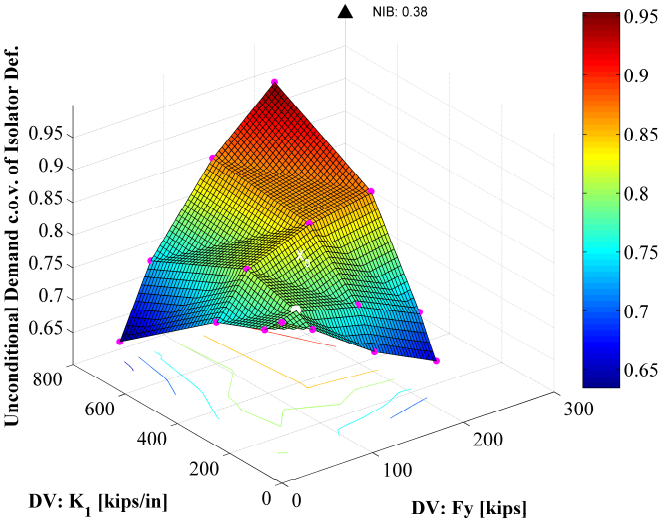

Figure 7.92: Risk feature: unconditional demand c.o.v. on isolator deformation of isolator #13 over pier #5 in the trans. dir.

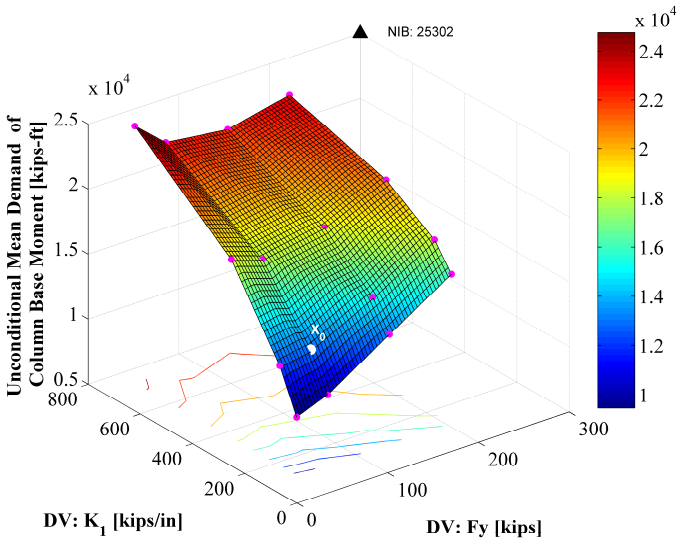

Figure 7.93: Risk feature: unconditional mean demand on column base moment of pier #5 in the trans. dir.

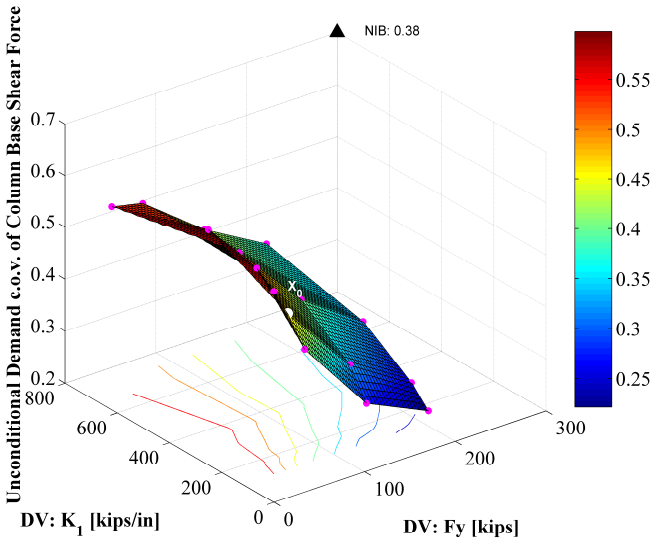

Figure 7.94: Risk feature: unconditional demand c.o.v. on column base bottom moment of pier #5 in the transverse direction

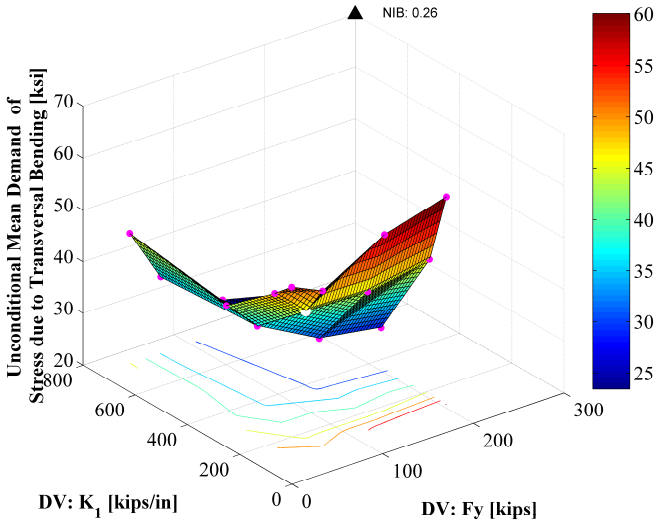

Figure 7.95: Risk feature: unconditional mean demand on rail stress due to transverse bending at interior expansion joint #2

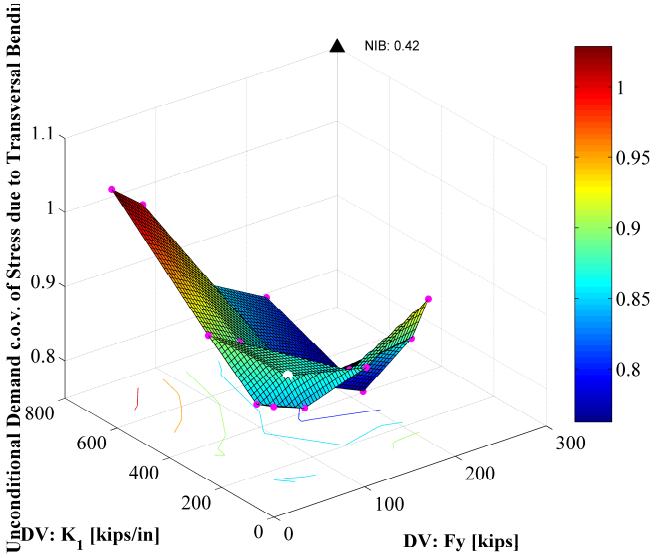

Figure 7.96: Risk feature: unconditional demand c.o.v. on rail stress due to transverse bending at interior expansion joint #2

7.5.3. Risk feature distribution along the bridge

In the previous section, the topologies of different risk features for the representative response quantities are explored comprehensively, aiming at evaluating the seismic risk when different seismic isolators are employed. To obtain a global picture of the risk features' distribution along the bridge, the risk features distribution along the bridge are investigated.

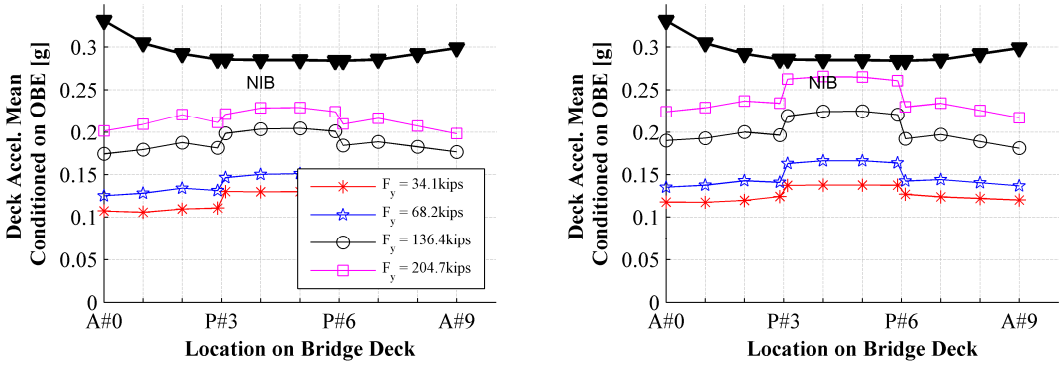

(a) K_1 = 120kips/in (b) K_1 = 184.5kips/in

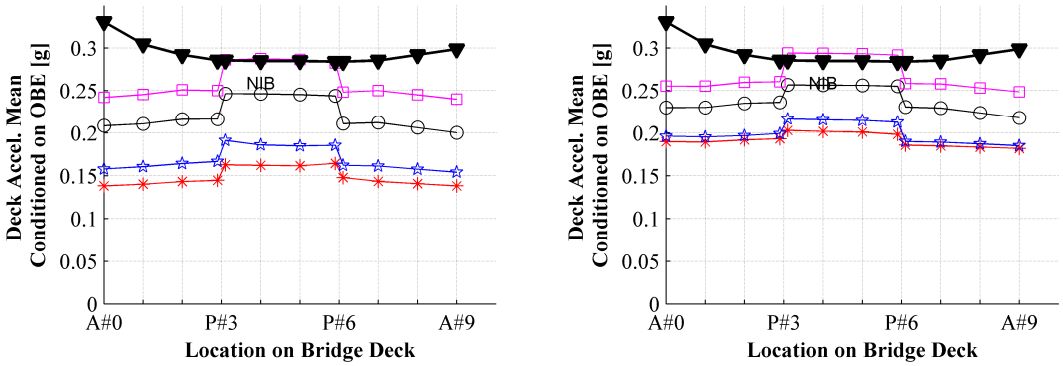

(c) K_1 = 370kips/in (d) K_1 = 740kips/in

Figure 7.97: Distribution of mean demand on absolute deck acceleration along the bridge conditioned on OBE hazard level in the longitudinal direction (x dir.) for different yield strengths of seismic isolators

Figure 7.97 shows the conditional mean demand of absolute deck acceleration in the longitudinal direction along the bridge from the left abutment A#0 to right abutment A#9 across all pier columns in between. At OBE hazard level, the dynamic mechanism of the

bridge system is relatively simple in that pounding seldom occurs in the longitudinal direction, the seismic isolation decrease the overall deck acceleration along the bridge. The more flexible the seismic isolations are, the more reduction in absolute acceleration is achieved.

Figure 7.98 displays the conditional mean demand (MCE) of absolute deck acceleration in the longitudinal direction along the bridge. Similar trends are observed as OBE hazard level, but induced increased acceleration due to the pounding effects is more pronounced.

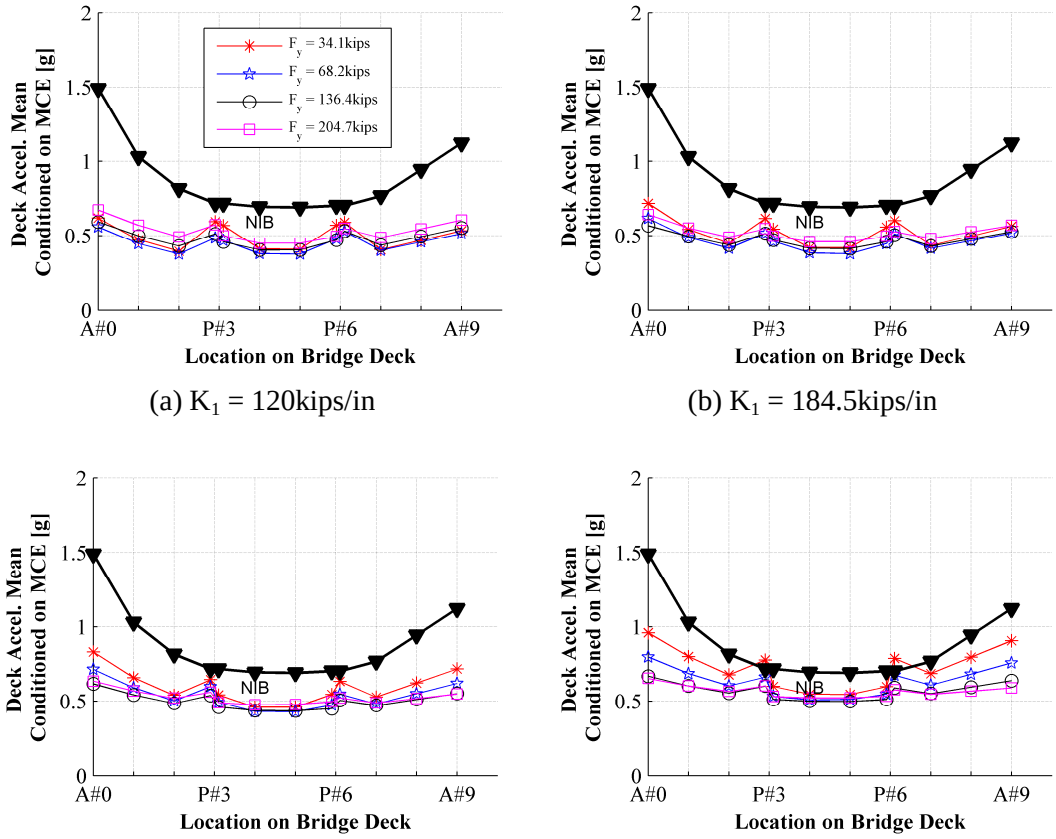

(a) K_1 = 120kips/in (b) K_1 = 184.5kips/in

(c) K_1 = 370kips/in (d) K_1 = 740kips/in

Figure 7.98: Distribution of absolute deck acceleration mean demand along the bridge conditioned on MCE hazard level in the longitudinal direction (x dir.) for different yield strengths of seismic isolators

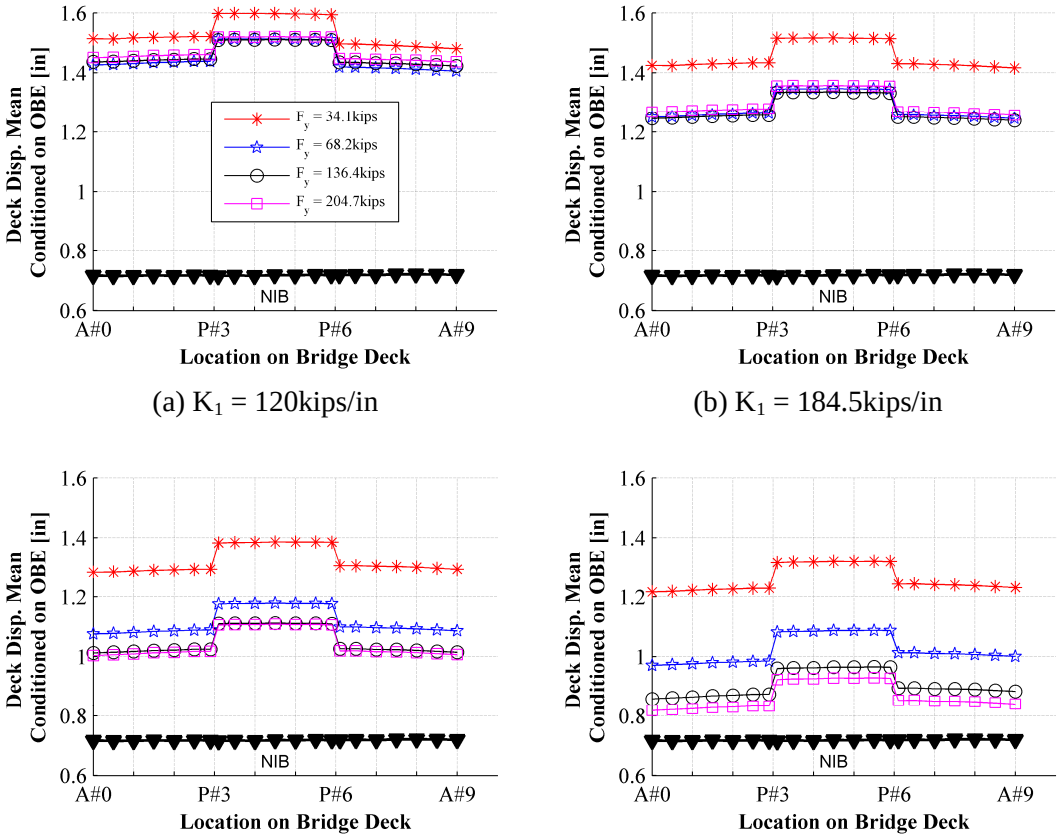

(a) K_1 = 120kips/in (b) K_1 = 184.5kips/in

(c) K_1 = 370kips/in (d) K_1 = 740kips/in

Figure 7.99: Distribution of mean demand on relative deck displacement along the bridge conditioned on OBE hazard level in the longitudinal direction (x dir.) for different yield strengths of seismic isolators

Figure 7.99 to Figure 7.100 present the conditional mean demand of the relative deck displacement in the longitudinal direction along the bridge from the left abutment A#0 to the right abutment A#9. Seismic isolation increased the seismic demand on deck displacement. Moreover, seismic isolation also introduced the relative displacement between the adjacent bridge segments. A proper combination of yield strength and initial stiffness of the seismic isolation can be achieved because the deck displacement in the longitudinal direction could be indifferent to a certain range of yield strength of the seismic isolators for OBE hazard level

when the initial stiffness is fixed (i.e., case (a) and case (b)). The change of yield strength starts to play a role when the initial stiffness increases (i.e., case (c) and case (d)), when the force demand on the isolator increases which makes the yield strength of seismic isolator plays a significant role.

Comparing Figure 7.99 with Figure 7.100, under the OBE hazard level, the deck displacement is more sensitive to the initial stiffness of the seismic isolation system when the force demand is still below the yield capacity of seismic isolators.

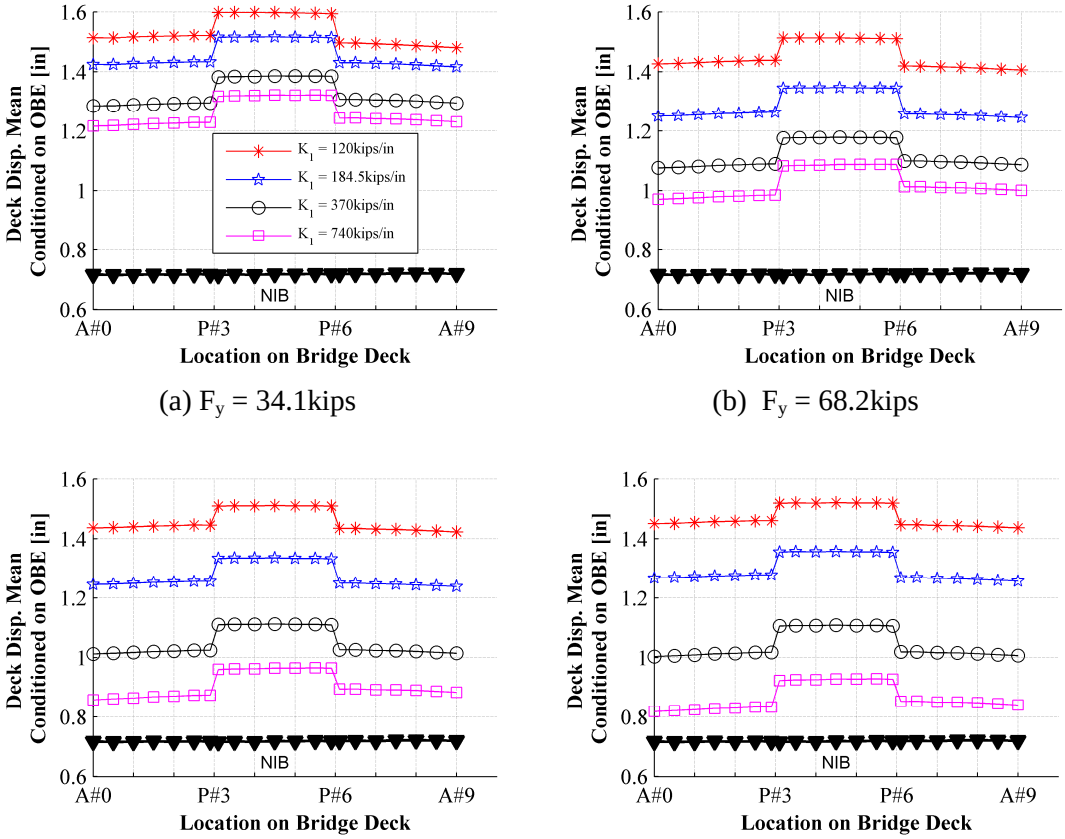

(a) F_y = 34.1kips (b) F_y = 68.2kips

(c) F_y = 136.4kips (d) F_y = 204.7kips

Figure 7.100: Distribution of mean demand on relative deck displacement along the bridge conditioned on OBE hazard level in the longitudinal direction (x dir.) for different initial stiffness's of seismic isolators

Figure 7.101 shows the conditional mean demand of relative deck displacement in the transverse direction along the bridge from the left abutment A#0 to right abutment A#9 across all pier columns in between. It is worth noting that the introduction of seismic isolation increased the seismic demand on deck center displacement by 1 to 2 times compared to the NIB model, while a stiffer isolator with bigger initial stiffness and higher yield strength could reduce the displacement of the deck close to the abutment by resorting to the abutment, which could be beneficial for the track around the abutment gap.

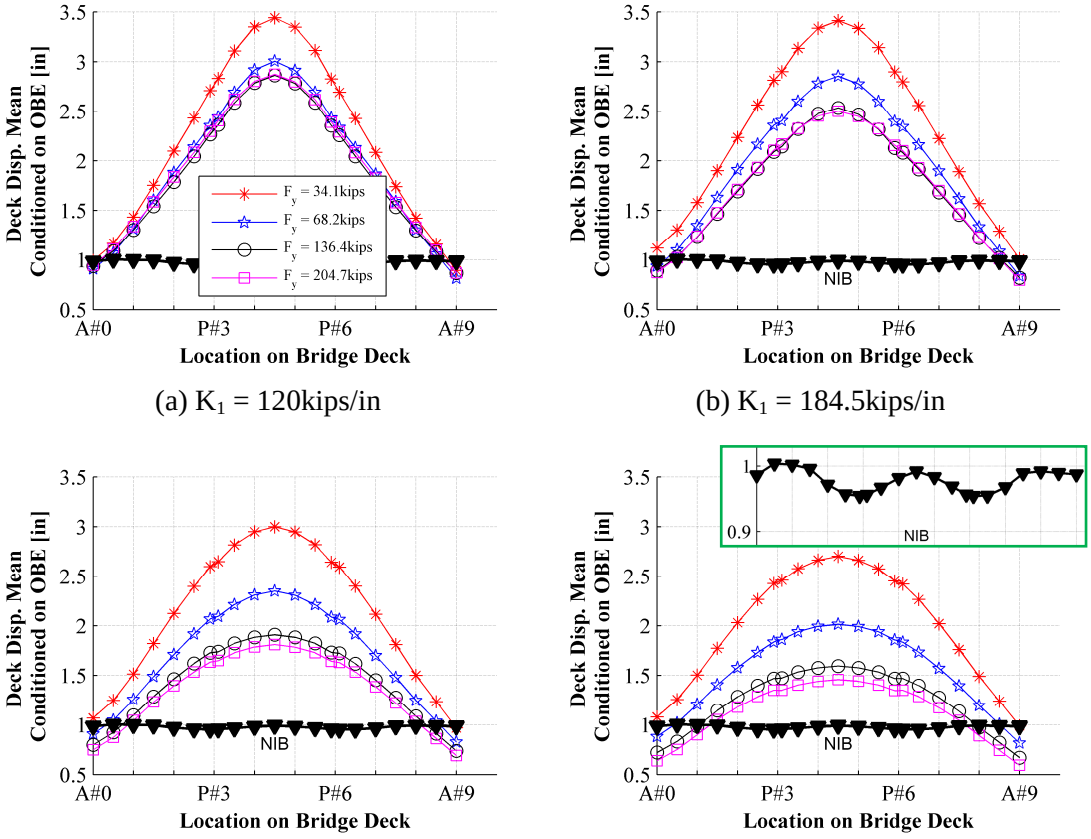

(a) K_1 = 120kips/in

(b) K_1 = 184.5kips/in

(c) K_1 = 370kips/in

(d) K_1 = 740kips/in

Figure 7.101: Distribution of mean demand on relative deck displacement along the bridge conditioned on OBE hazard level in the transverse direction (y dir.) for different yield strengths of seismic isolators

Figure 7.102 displays the conditional mean demand (MCE) for the relative deck displacement in the transverse direction along the bridge from the left abutment A#0 to right abutment A#9 across all pier columns in between. Under MCE hazard level, the distribution pattern of the mean demand for the relative deck displacement in the transverse direction (shown in the zoom in plot) is far different from the OBE hazard level due to the shear gap engagement at the abutments.

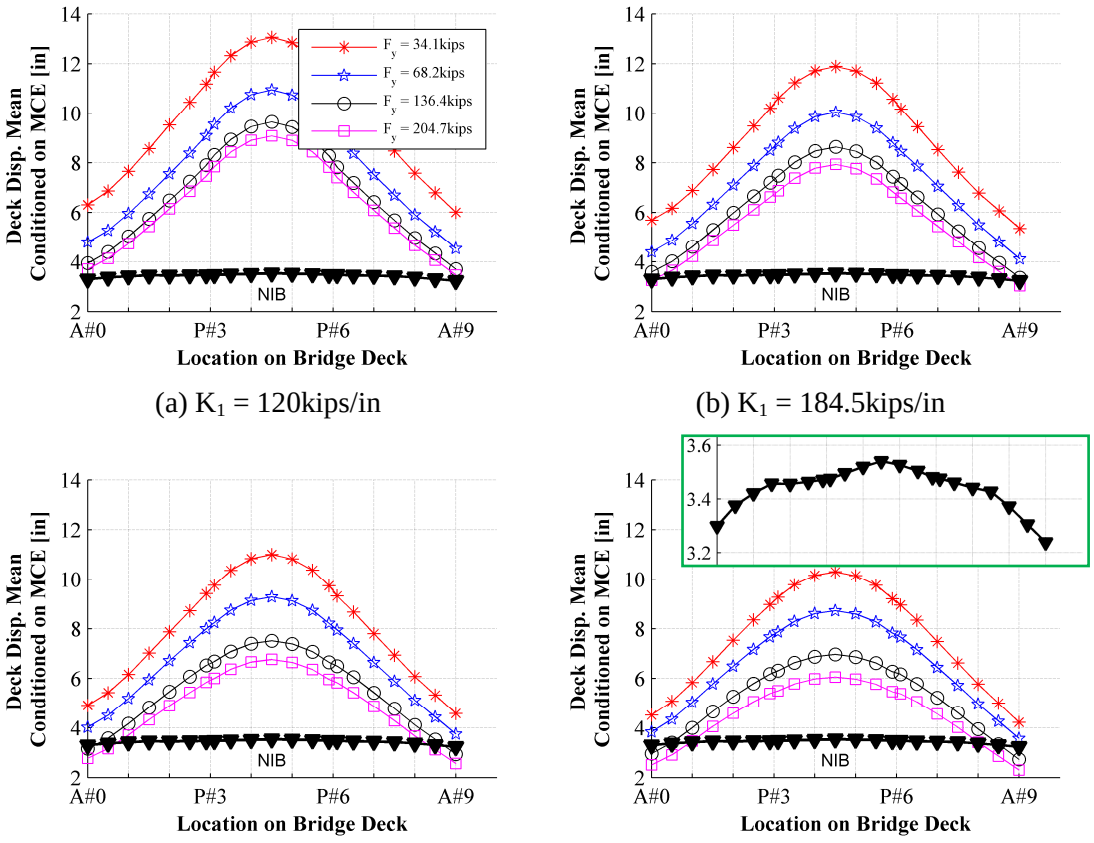

(a) K_1 = 120kips/in

(b) K_1 = 184.5kips/in

(c) K_1 = 370kips/in

(d) K_1 = 740kips/in

Figure 7.102: Distribution of mean demand on relative deck displacement along the bridge conditioned on MCE hazard level in the transverse direction (y dir.) for different yield strengths of seismic isolators

The seismic isolator deformation is obtained from the relative displacement of the top node and bottom node of seismic isolators for IB, while for NIB, the deformation of non-isolator bearing at the abutments is also extracted similarly. Figure 7.103 shows the distribution of OBE seismic demand mean on all seismic isolators' deformation in the longitudinal direction. As observed, to accommodate the compatibility of bridge deck movement, the deformation demand on bearings seated on top of the abutments is relatively large than adjacent seismic isolators on pier #1 or pier #8.

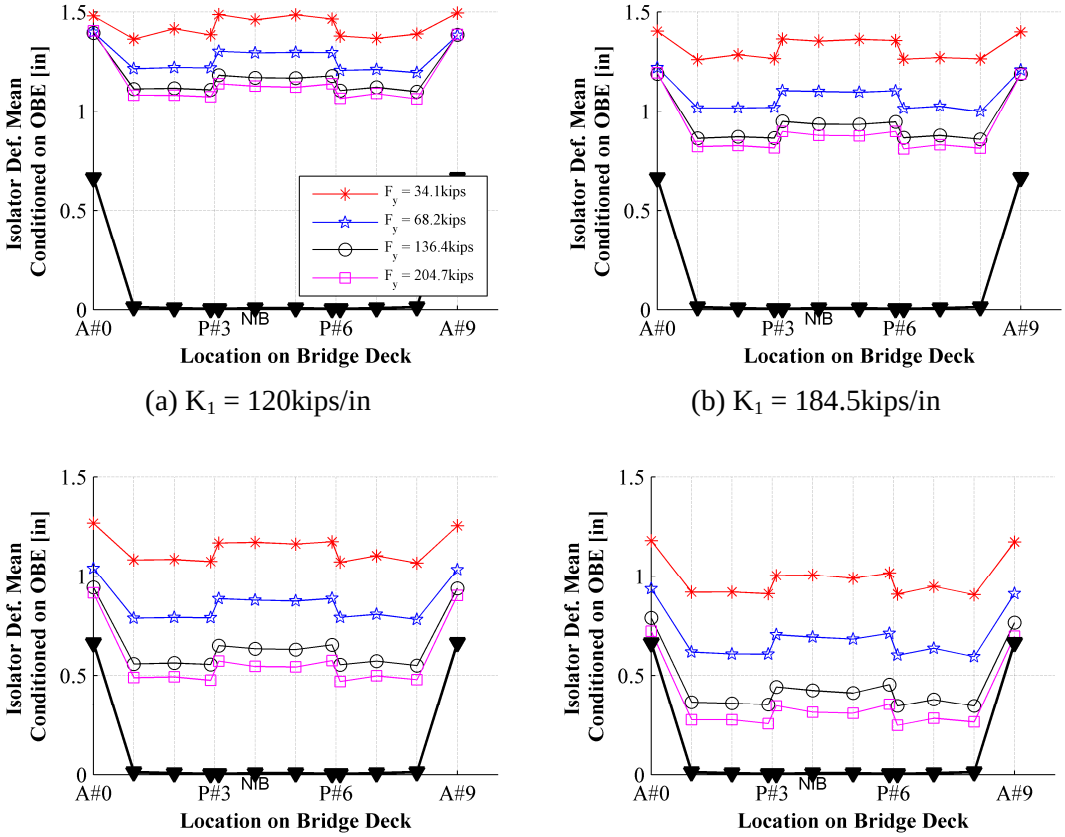

(a) K_1 = 120kips/in (b) K_1 = 184.5kips/in

(c) K_1 = 370kips/in (d) K_1 = 740kips/in

Figure 7.103: Distribution of mean demand on isolator deformation along the bridge conditioned on OBE hazard level in the longitudinal direction (x dir.) for different yield strengths of seismic isolators

Figure 7.104 shows OBE seismic demand mean on all seismic isolators' deformation in the transverse direction. It is worth noting that a stronger seismic isolator seated on top of abutments could decrease the transverse deformation concentrated at bearings over the abutments.

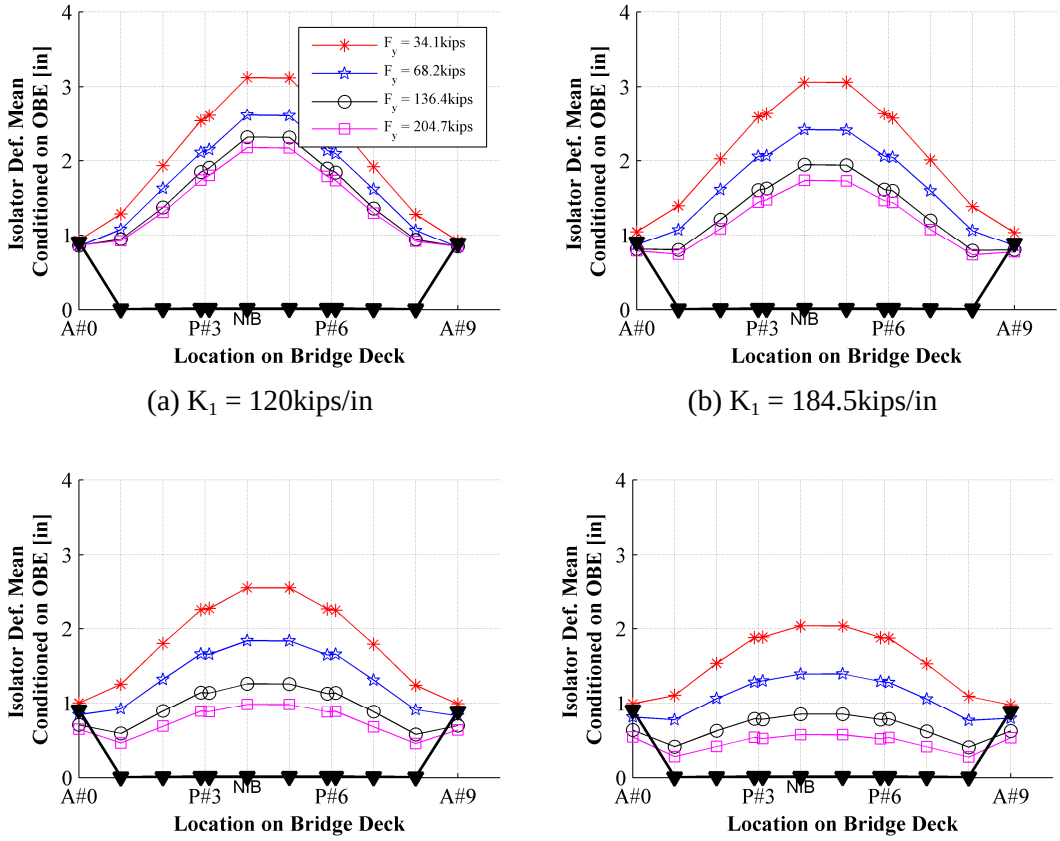

(a) K_1 = 120kips/in (b) K_1 = 184.5kips/in

(c) K_1 = 370kips/in (d) K_1 = 740kips/in

Figure 7.104: Distribution of mean demand on isolator deformation along the bridge conditioned on OBE hazard level in the transverse direction (y dir.) for different yield strengths of seismic isolators

Figure 7.105 shows the parallel results of bending moment in the transverse direction. The distribution pattern for the NIB and IB are recognized to be different in that the moment demand of pier columns for the side frames are larger than the middle frame due to the non-isolation bearing on abutments. The increase of stiffness and yield strength of the seismic

isolators for IB will lead to a lower demand on the pier columns of the side frame compared to the middle frame, which means that the seismic isolation is more efficient in reducing the force demand on the pier columns of the side frame rather than the middle one.

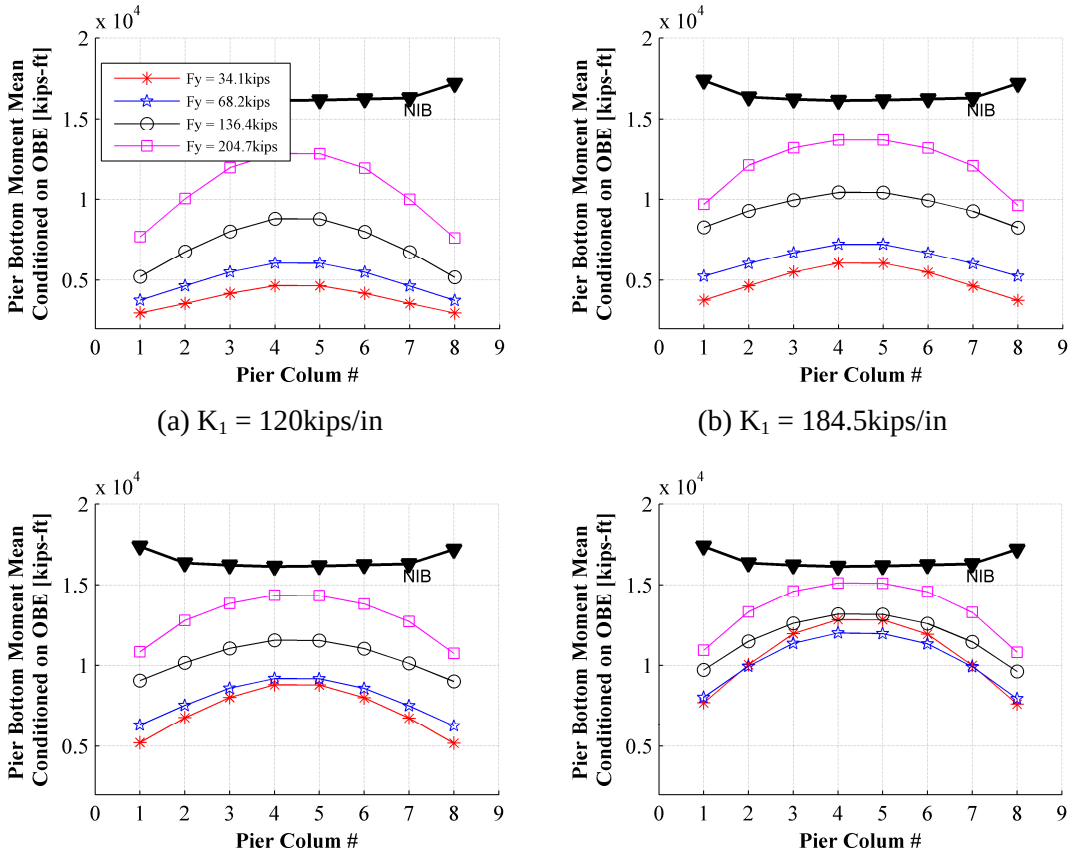

(a) K_1 = 120kips/in (b) K_1 = 184.5kips/in

(c) K_1 = 370kips/in (d) K_1 = 740kips/in

Figure 7.105: Distribution of mean demand on pier bottom bending moment along the bridge conditioned on OBE hazard level in the transverse direction (y dir.) for different yield strengths of seismic isolators

7.5.4. Summary of risk feature values

For the convenience of quantifying the range of risk features evaluated at the studied parametric domain of seismic isolators' properties, the minimum and maximum values of risk features are tabulated in this section: (1) the conditional mean demand, coefficient of variation, and 95th percentile on the OBE hazard level are summarized for different EDPs in

Table 7.4; (2) the conditional mean demand, coefficient of variation, and 95th percentile on MCE hazard level are summarized for different EDPs in Table 7.5; (3) the unconditional mean demand, coefficient of variation, and 95th percentile are summarized for different EDPs in Table 7.6.

Table 7.4: Risk feature values based on conditional demand hazard on OBE

EDP	Mean Demand		Coefficient of Variation (c.o.v.)		95th Percentile	
	Min	Max	Min	Max	Min	Max
Deck acc. in x [g]	0.13	0.294	0.243	0.866	0.412	0.454
Deck acc. in y [g]	0.236	0.394	0.177	0.421	0.376	0.556
RMS of deck acc. in x [g]	0.04	0.0686	0.191	0.287	0.0601	0.0962
RMS of deck acc. in y [g]	0.042	0.0972	0.157	0.417	0.0711	0.136
Deck disp. in x [in]	0.928	1.6	0.379	0.583	1.74	3.77
Deck disp. in y [in]	1.44	3.35	0.362	0.611	2.93	8.42
Isolator def. in x [in]	0.308	1.49	0.427	0.584	0.748	3.54
Isolator def. in y [in]	0.573	3.12	0.387	0.606	1.25	7.67
Base shear of P#5 in x [kips]	217	741	0.18	0.427	373	1.06e+03
Base shear of P#5 in y [kips]	293	926	0.15	0.469	567	1.4e+03
Total base shear (columns) in x [kips]	1.7e+03	5.59e+03	0.189	0.424	2.92e+03	8.17e+03
Total base shear (columns) in y	1.85e+03	6.57e+03	0.152	0.517	3.81e+03	9.45e+03
Total base shear in x [kips]	1.89e+03	6.55e+03	0.184	0.426	3.24e+03	9.39e+03
Total base shear in y [kips]	1.97e+03	7.35e+03	0.153	0.533	4.16e+03	1.06e+04
Total force in x [kips]	1.83e+03	6.47e+03	0.259	0.583	4.45e+03	1e+04
Total force in y [kips]	2.9e+03	7.66e+03	0.143	0.46	5.28e+03	1.09e+04
Pile moment in x [kips-ft]	2.32e+03	3.14e+03	0.294	0.382	4.13e+03	5.09e+03
Pile moment in y [kips-ft]	2.19e+03	3.81e+03	0.199	0.301	3.32e+03	5.5e+03
Pile shear in x [kips]	159	246	0.575	0.78	449	595
Pile shear in y [kips]	137	295	0.474	0.584	333	619
Pile cap disp. in x [in]	0.126	0.291	0.255	0.513	0.214	0.468
Pile cap disp. in y [in]	0.126	0.355	0.286	0.589	0.23	0.66
Pile cap rot. in x [in]	0.0744	0.164	0.292	0.498	0.139	0.268
Pile cap rot. in y [in]	0.0775	0.216	0.235	0.536	0.126	0.366
Axial rail stress at Exp. #1 [ksi]	9.07	11.6	0.102	0.153	11.2	13.7
Axial rail stress at Exp. #2 [ksi]	4.38	5.5	0.302	0.515	7.17	12.2
Axial rail stress at Exp. #3 [ksi]	4.47	5.64	0.28	0.524	7.04	12.7
Axial rail stress at Exp. #4[ksi]	9.14	11.6	0.106	0.172	11.8	14.2
Bending rail stress at Exp. #1 [ksi]	22.7	39.6	0.435	0.897	44.9	140
Bending rail stress at Exp. #2 [ksi]	8.6	18.5	0.55	0.747	23.3	47.5
Bending rail stress at Exp. #3 [ksi]	8.42	17.5	0.515	0.75	22.3	47
Bending rail stress at Exp. #4 [ksi]	22.3	39.1	0.432	0.894	44	138
Total rail stress at Exp. #1 [ksi]	29.3	46.5	0.387	0.84	54.2	155
Total rail stress at Exp. #2 [ksi]	11.1	21.9	0.475	0.618	26.5	51

Table7.4 (continued): Risk feature values based on conditional demand hazard on OBE

EDP	Mean Demand		Coefficient of Variation (c.o.v.)		95th Percentile	
	Min	Max	Min	Max	Min	Max
Total rail stress at Exp. #3 [ksi]	11	20.9	0.438	0.621	25.5	49.8
Total rail stress at Exp. #4 [ksi]	28.9	46.2	0.388	0.838	53.6	153
Pier #5 drift in x [in]	0.204	0.511	0.216	0.638	0.316	0.892
Pier #5 drift in y [in]	0.201	0.698	0.219	0.856	0.4	1.68
SHJ def. #1 [in]	0.0645	0.138	0.658	0.912	0.211	0.425
SHJ def. #2 [in]	0.0645	0.138	0.658	0.912	0.211	0.425
SHJ def. #3 [in]	0.0629	0.129	0.632	0.908	0.185	0.402
SHJ def. #4 [in]	0.0629	0.129	0.632	0.908	0.185	0.402
Shear key def. #1 [in]	0.417	0.913	0.479	0.843	0.881	3.05
Shear key def. #2 [in]	0.457	0.872	0.549	0.772	1.1	2.68
Shear key def. #3 [in]	0.41	0.904	0.478	0.848	0.865	3.03
Shear key def. #4 [in]	0.448	0.863	0.544	0.768	1.07	2.65
Pier drift resultant [in]	0.245	0.777	0.201	0.809	0.455	1.74
P#5 base moment in x [kips-ft]	3.34e+03	1.15e+04	0.179	0.411	5.88e+03	1.66e+04
P#5 base moment in y [kips-ft]	4.65e+03	1.51e+04	0.153	0.47	9.11e+03	2.26e+04
Deck drift in x [in]	0.844	1.58	0.386	0.579	1.61	3.73
Deck drift in y [in]	1.38	3.33	0.363	0.611	2.85	8.38
P#5 Bot. Ele. Rotation in x	7.16e-05	0.00026	0.231	0.992	0.000142	0.000609
P#5 Bot. Ele. Rotation in y	9.82e-05	0.000343	0.256	1.38	0.000248	0.00141
P#5 Bot. Sec. Curvature in y	0.000109	0.000385	0.252	1.43	0.000278	0.00163
P#5 Bot. Sec. Curvature in x	7.91e-05	0.000293	0.232	1.04	0.000157	0.000695
Pile torsion under P#5	0.000111	0.000325	0.248	0.448	0.000213	0.000537
Pile cap disp. w.r.t. tip in x [in]	0.126	0.291	0.255	0.513	0.214	0.468
Pile cap disp. w.r.t. tip in y [in]	0.126	0.355	0.286	0.589	0.23	0.66
Deck rotation y at Exp. #1	0.0332	0.0352	0.0441	0.0639	0.0367	0.0379
Deck rotation y at Exp. #2	8.89e-05	9.14e-05	0.0875	0.271	0.000105	0.000138
Deck rotation y at Exp. #3	8.74e-05	9.04e-05	0.0865	0.263	0.000104	0.000137
Deck rotation y at Exp. #4	0.0334	0.0352	0.0547	0.0761	0.0375	0.0385
Deck rotation z at Exp. #1	0.0185	0.0313	0.297	0.489	0.0329	0.0638
Deck rotation z at Exp. #2	3.23e-05	9.72e-05	0.264	0.409	5.77e-05	0.000177
Deck rotation z at Exp. #3	3.25e-05	9.68e-05	0.264	0.417	5.77e-05	0.000179
Deck rotation z at Exp. #4	0.0187	0.031	0.303	0.49	0.0339	0.0636
Rail centroid x at Exp. #1 [in]	0.823	1.52	0.368	0.59	1.57	3.65
Rail centroid x at Exp. #2 [in]	0.119	0.147	0.435	0.864	0.242	0.5
Rail centroid x at Exp. #3 [in]	0.118	0.15	0.402	0.878	0.228	0.515
Rail centroid x at Exp. #4 [in]	0.861	1.5	0.391	0.611	1.64	3.68
Rel. deck disp. z at Exp. #1 [in]	0.219	0.255	0.122	0.141	0.272	0.316
Rel. deck disp. z at Exp. #2 [in]	0.000625	0.00217	0.168	0.411	0.00105	0.00305
Rel. deck disp. z at Exp. #3	0.0007	0.00235	0.167	0.406	0.00122	0.00315
Rel. deck disp. z at Exp. #4 [in]	0.219	0.255	0.122	0.141	0.272	0.316
Rel. deck disp. y at Exp. #1 [in]	0.638	1.12	0.433	0.895	1.26	3.95
Rel. deck disp. y at Exp. #4 [in]	0.627	1.11	0.43	0.892	1.23	3.89
Column res. moment [kips-ft]	4.72e+03	1.63e+04	0.179	0.411	8.32e+03	2.34e+04
Isolator def. resultant [in]	0.636	3.4	0.336	0.536	1.17	7.54

Table 7.5: Risk feature values based on conditional demand hazard on MCE

EDP	Mean Demand		Coefficient of Variation (c.o.v.)		95th Percentile	
	Min	Max	Min	Max	Min	Max
Deck acc. in x [g]	0.376	0.546	0.243	0.866	0.746	1.4
Deck acc. in y [g]	0.571	0.921	0.177	0.421	0.845	1.66
RMS of deck acc. in x [g]	0.0731	0.141	0.191	0.287	0.11	0.197
RMS of deck acc. in y [g]	0.106	0.197	0.157	0.417	0.16	0.358
Deck disp. in x [in]	3.09	5.75	0.379	0.583	5.8	13.6
Deck disp. in y [in]	5.97	12.8	0.362	0.611	12.1	30.5
Isolator def. in x [in]	1.59	5.52	0.427	0.584	3.87	13.1
Isolator def. in y [in]	3.39	12.2	0.387	0.606	7.41	29.3
Base shear of P#5 in x [kips]	433	1.34e+03	0.18	0.427	744	2.25e+03
Base shear of P#5 in y [kips]	756	2.13e+03	0.15	0.469	1.34e+03	3.83e+03
Total base shear (columns) in x [kips]	3.4e+03	1.1e+04	0.189	0.424	5.74e+03	1.79e+04
Total base shear (columns) in y [kips]	5.2e+03	1.4e+04	0.152	0.517	9.52e+03	2.53e+04
Total base shear in x [kips]	3.73e+03	1.21e+04	0.184	0.426	6.42e+03	2.08e+04
Total base shear in y [kips]	5.58e+03	1.52e+04	0.153	0.533	1.05e+04	2.79e+04
Total force in x [kips]	6.01e+03	1.3e+04	0.259	0.583	1.3e+04	2.71e+04
Total force in y [kips]	6.89e+03	1.63e+04	0.143	0.46	1.14e+04	2.87e+04
Pile moment in x [kips-ft]	5.53e+03	7.01e+03	0.294	0.382	9.99e+03	1.14e+04
Pile moment in y [kips-ft]	6.38e+03	8.26e+03	0.199	0.301	9.58e+03	1.3e+04
Pile shear in x [kips]	462	665	0.575	0.78	1.41e+03	1.61e+03
Pile shear in y [kips]	640	914	0.474	0.584	1.56e+03	2e+03
Pile cap disp. in x [in]	0.213	0.646	0.255	0.513	0.36	1.11
Pile cap disp. in y [in]	0.304	1.05	0.286	0.589	0.551	2.47
Pile cap rot. in x [in]	0.194	0.437	0.292	0.498	0.361	0.781
Pile cap rot. in y [in]	0.248	0.615	0.235	0.536	0.404	1.35
Axial rail stress at Exp. #1 [ksi]	14.2	16.4	0.102	0.153	17	21
Axial rail stress at Exp. #2 [ksi]	9.05	16.3	0.302	0.515	14.7	36.2
Axial rail stress at Exp. #3 [ksi]	9.25	16.3	0.28	0.524	14.5	36.7
Axial rail stress at Exp. #4[ksi]	15	17.2	0.106	0.172	18.5	22.8
Bending rail stress at Exp. #1 [ksi]	88.9	224	0.435	0.897	176	785
Bending rail stress at Exp. #2 [ksi]	29	86.3	0.55	0.747	78.6	228
Bending rail stress at Exp. #3 [ksi]	28	75.1	0.515	0.75	74.6	196
Bending rail stress at Exp. #4 [ksi]	86.6	222	0.432	0.894	171	770
Total rail stress at Exp. #1 [ksi]	101	241	0.387	0.84	187	793
Total rail stress at Exp. #2 [ksi]	35.5	94.5	0.475	0.618	84.9	223
Total rail stress at Exp. #3 [ksi]	34.6	83	0.438	0.621	81.4	198
Total rail stress at Exp. #4 [ksi]	99.9	239	0.388	0.838	185	780
Pier #5 drift in x [in]	0.39	1.35	0.216	0.638	0.604	3.28
Pier #5 drift in y [in]	0.595	3.05	0.219	0.856	1.1	9.25

Table7.5 (continued): Risk feature values based on conditional demand hazard on MCE

EDP	Mean Demand		Coefficient of Variation (c.o.v.)		95th Percentile	
	Min	Max	Min	Max	Min	Max
SHJ def. #1 [in]	0.23	0.786	0.658	0.912	0.754	2.47
SHJ def. #2 [in]	0.23	0.786	0.658	0.912	0.754	2.47
SHJ def. #3 [in]	0.22	0.677	0.632	0.908	0.707	2.06
SHJ def. #4 [in]	0.22	0.677	0.632	0.908	0.707	2.06
Shear key def. #1 [in]	1.59	4.32	0.479	0.843	3.35	13.8
Shear key def. #2 [in]	1.92	4.4	0.549	0.772	4.62	13.1
Shear key def. #3 [in]	1.55	4.28	0.478	0.848	3.27	13.7
Shear key def. #4 [in]	1.87	4.37	0.544	0.768	4.48	12.9
Pier drift resultant [in]	0.662	3.28	0.201	0.809	1.16	9.49
P#5 base moment in x [kips-ft]	6.7e+03	2.12e+04	0.179	0.411	1.18e+04	3.56e+04
P#5 base moment in y [kips-ft]	1.25e+04	3.4e+04	0.153	0.47	2.22e+04	6.01e+04
Deck drift in x [in]	2.94	5.72	0.386	0.579	5.62	13.5
Deck drift in y [in]	5.87	12.8	0.363	0.611	12.1	30.4
P#5 Bot. Ele. Rotation in x	0.000163	0.00128	0.231	0.992	0.000323	0.00463
P#5 Bot. Ele. Rotation in y	0.000327	0.00291	0.256	1.38	0.000717	0.0139
P#5 Bot. Sec. Curvature in y	0.000365	0.00331	0.252	1.43	0.000806	0.0164
P#5 Bot. Sec. Curvature in x	0.000182	0.00144	0.232	1.04	0.00036	0.00538
Pile torsion under P#5	0.000446	0.000729	0.248	0.448	0.000851	0.00139
Pile cap disp. w.r.t. tip in x [in]	0.213	0.646	0.255	0.513	0.36	1.11
Pile cap disp. w.r.t. tip in y [in]	0.304	1.05	0.286	0.589	0.551	2.47
Deck rotation y at Exp. #1	0.0388	0.0414	0.0441	0.0639	0.0429	0.0445
Deck rotation y at Exp. #2	0.000102	0.000119	0.0875	0.271	0.000119	0.000184
Deck rotation y at Exp. #3	0.0001	0.000118	0.0865	0.263	0.000116	0.00018
Deck rotation y at Exp. #4	0.0389	0.0413	0.0547	0.0761	0.0439	0.0452
Deck rotation z at Exp. #1	0.0665	0.0942	0.297	0.489	0.113	0.191
Deck rotation z at Exp. #2	0.000133	0.000215	0.264	0.409	0.000237	0.000391
Deck rotation z at Exp. #3	0.000133	0.000216	0.264	0.417	0.000236	0.000398
Deck rotation z at Exp. #4	0.0672	0.0943	0.303	0.49	0.114	0.194
Rail centroid x at Exp. #1 [in]	2.96	5.57	0.368	0.59	5.64	13.3
Rail centroid x at Exp. #2 [in]	0.285	0.691	0.435	0.864	0.564	2.32
Rail centroid x at Exp. #3 [in]	0.288	0.685	0.402	0.878	0.545	2.37
Rail centroid x at Exp. #4 [in]	2.96	5.65	0.391	0.611	5.66	13.9
Rel. deck disp. z at Exp. #1 [in]	0.281	0.342	0.122	0.141	0.349	0.423
Rel. deck disp. z at Exp. #2 [in]	0.00134	0.00466	0.168	0.411	0.00225	0.00777
Rel. deck disp. z at Exp. #3	0.00142	0.0045	0.167	0.406	0.00247	0.0074
Rel. deck disp. z at Exp. #4 [in]	0.281	0.342	0.122	0.141	0.349	0.423
Rel. deck disp. y at Exp. #1 [in]	2.51	6.31	0.433	0.895	4.95	22
Rel. deck disp. y at Exp. #4 [in]	2.44	6.24	0.43	0.892	4.81	21.6
Column res. moment [kips-ft]	9.48e+03	3e+04	0.179	0.411	1.67e+04	5.03e+04
Isolator def. resultant [in]	3.76	13	0.336	0.536	6.89	28.9

Table 7.6: Risk features based on the derived PDF of unconditional seismic demand hazard characterized by probability exceedance in exposure time of 100 years

EDP	Mean Demand		Coefficient of Variation		95th Percentile	
	Min	Max	Min	Max	Min	Max
Deck acc. in x [g]	0.311	0.419	0.315	0.894	0.661	1.08
Deck acc. in y [g]	0.389	0.575	0.328	0.598	0.738	1.35
RMS of deck acc. in x [g]	0.0578	0.101	0.289	0.439	0.0963	0.174
RMS of deck acc. in y [g]	0.0718	0.134	0.276	0.604	0.141	0.289
Deck disp. in x [in]	1.83	3.49	0.579	0.786	4.63	10.2
Deck disp. in y [in]	3.19	7.51	0.605	0.821	9.39	22.9
Isolator def. in x [in]	0.785	3.29	0.653	0.933	2.82	9.87
Isolator def. in y [in]	1.5	7.08	0.634	0.953	5.56	21.9
Base shear of P#5 in x [kips]	341	1.05e+03	0.232	0.552	634	1.82e+03
Base shear of P#5 in y [kips]	527	1.4e+03	0.222	0.598	1.14e+03	3.13e+03
Total base shear (columns) in x [kips]	2.66e+03	8.12e+03	0.24	0.554	4.91e+03	1.45e+04
Total base shear (columns) in y [kips]	3.5e+03	9.74e+03	0.244	0.63	8.08e+03	2.06e+04
Total base shear in x [kips]	2.95e+03	9.39e+03	0.235	0.561	5.48e+03	1.68e+04
Total base shear in y [kips]	3.78e+03	1.08e+04	0.251	0.652	8.89e+03	2.26e+04
Total force in x [kips]	3.9e+03	9.83e+03	0.341	0.736	1.05e+04	2.11e+04
Total force in y [kips]	4.95e+03	1.13e+04	0.246	0.584	9.84e+03	2.35e+04
Pile moment in x [kips-ft]	3.98e+03	5.04e+03	0.428	0.497	8.27e+03	9.63e+03
Pile moment in y [kips-ft]	3.87e+03	5.83e+03	0.362	0.517	8.27e+03	1.09e+04
Pile shear in x [kips]	358	492	0.657	0.82	1.09e+03	1.27e+03
Pile shear in y [kips]	335	585	0.647	0.895	1.14e+03	1.52e+03
Pile cap disp. in x [in]	0.186	0.464	0.311	0.637	0.319	0.881
Pile cap disp. in y [in]	0.217	0.635	0.345	0.796	0.457	1.86
Pile cap rot. in x [in]	0.133	0.283	0.443	0.69	0.293	0.604
Pile cap rot. in y [in]	0.145	0.379	0.4	0.746	0.337	1.03
Axial rail stress at Exp. #1 [ksi]	11.6	13.6	0.149	0.235	15.9	19.3
Axial rail stress at Exp. #2 [ksi]	6.86	10.9	0.401	0.652	12.6	28.2
Axial rail stress at Exp. #3 [ksi]	6.9	11.2	0.393	0.645	12.5	28.7
Axial rail stress at Exp. #4[ksi]	12.1	14	0.164	0.266	17.3	20.7
Bending rail stress at Exp. #1 [ksi]	48.6	114	0.738	1.27	138	522
Bending rail stress at Exp. #2 [ksi]	19.4	45.6	0.761	1.03	59.3	164
Bending rail stress at Exp. #3 [ksi]	18.8	42.3	0.729	1.01	56.5	143
Bending rail stress at Exp. #4 [ksi]	47.5	112	0.734	1.26	134	512
Total rail stress at Exp. #1 [ksi]	58.4	127	0.655	1.17	150	538
Total rail stress at Exp. #2 [ksi]	23.4	50.9	0.686	0.92	65.2	165
Total rail stress at Exp. #3 [ksi]	22.9	47.6	0.653	0.894	62.7	147
Total rail stress at Exp. #4 [ksi]	57.7	125	0.655	1.17	148	530
Pier #5 drift in x [in]	0.164	0.574	0.304	1.02	0.314	1.87
Pier #5 drift in y [in]	0.251	1.04	0.307	1.27	0.604	4.8

Table 7.6 (continued): Risk features based on the derived PDF of unconditional seismic demand hazard characterized by probability exceedance in exposure time of 100 years

EDP	Mean Demand		Coefficient of Variation		95th Percentile	
	Min	Max	Min	Max	Min	Max
SHJ def. #1 [in]	0.161	0.391	0.912	1.22	0.559	1.69
SHJ def. #2 [in]	0.161	0.391	0.912	1.22	0.559	1.69
SHJ def. #3 [in]	0.155	0.354	0.869	1.2	0.527	1.43
SHJ def. #4 [in]	0.155	0.354	0.869	1.2	0.527	1.43
Shear key def. #1 [in]	0.9	2.47	0.721	1.05	2.58	9.75
Shear key def. #2 [in]	1.07	2.31	0.766	1.03	3.43	9.11
Shear key def. #3 [in]	0.882	2.44	0.718	1.05	2.51	9.64
Shear key def. #4 [in]	1.04	2.28	0.765	1.03	3.33	8.96
Pier drift resultant [in]	0.443	1.66	0.318	1.08	0.985	6.64
P#5 base moment in x [kips-ft]	5.3e+03	1.65e+04	0.223	0.551	1e+04	2.9e+04
P#5 bse moment in y [kips-ft]	8.52e+03	2.26e+04	0.225	0.587	1.88e+04	4.93e+04
Deck drift in x [in]	1.7	3.46	0.588	0.783	4.46	10.2
Deck drift in y [in]	3.1	7.48	0.606	0.824	9.32	22.8
P#5 Bot. Ele. Rotation in x	0.000124	0.000585	0.284	1.5	0.000267	0.003
P#5 Bot. Ele. Rotation in y	0.000215	0.00124	0.355	1.94	0.000579	0.00844
P#5 Bot. Sec. Curvature in y	0.000239	0.00145	0.356	2.05	0.00065	0.00988
P#5 Bot. Sec. Curvature in x	0.000138	0.000665	0.289	1.57	0.000297	0.00346
Pile torsion under P#5	0.000239	0.000508	0.389	0.784	0.000672	0.00109
Pile cap disp. w.r.t. tip in x [in]	0.186	0.464	0.311	0.637	0.319	0.881
Pile cap disp. w.r.t. tip in y [in]	0.217	0.635	0.345	0.796	0.457	1.86
Deck rotation y at Exp. #1	0.0366	0.0385	0.0807	0.0886	0.0416	0.0433
Deck rotation y at Exp. #2	0.000101	0.000119	0.0878	0.245	0.000116	0.000175
Deck rotation y at Exp. #3	9.94e-05	0.000119	0.0818	0.236	0.000113	0.000172
Deck rotation y at Exp. #4	0.037	0.0386	0.0842	0.0931	0.0424	0.0438
Deck rotation z at Exp. #1	0.0375	0.0582	0.477	0.745	0.0939	0.149
Deck rotation z at Exp. #2	6.88e-05	0.000162	0.434	0.717	0.000191	0.000326
Deck rotation z at Exp. #3	6.91e-05	0.000162	0.429	0.711	0.000192	0.000331
Deck rotation z at Exp. #4	0.0382	0.0581	0.477	0.752	0.0951	0.151
Rail centroid x at Exp. #1 [in]	1.68	3.36	0.577	0.801	4.47	10
Rail centroid x at Exp. #2 [in]	0.214	0.398	0.522	1.04	0.464	1.61
Rail centroid x at Exp. #3 [in]	0.21	0.404	0.514	1.05	0.448	1.65
Rail centroid x at Exp. #4 [in]	1.73	3.38	0.6	0.817	4.49	10.4
Rel. deck disp. z at Exp. #1 [in]	0.26	0.307	0.147	0.174	0.329	0.396
Rel. deck disp. z at Exp. #2 [in]	0.000998	0.00329	0.233	0.595	0.0019	0.00636
Rel. deck disp. z at Exp. #3	0.00111	0.00335	0.211	0.559	0.0021	0.00613
Rel. deck disp. z at Exp. #4 [in]	40.4	47.7	0.265	0.269	61.7	72.8
Rel. deck disp. y at Exp. #1 [in]	1.37	3.22	0.737	1.26	3.87	14.6
Rel. deck disp. y at Exp. #4 [in]	1.34	3.17	0.733	1.26	3.77	14.4
Column res. moment [kips-ft]	7.49e+03	2.33e+04	0.223	0.551	1.42e+04	4.1e+04
Isolator def. resultant [in]	1.6	7.46	0.609	0.888	5.56	21.9

7.6. Conclusions

The key objective of this chapter is to study how the probabilistic seismic performance will change as a function of seismic isolators' properties. Consequently, the probabilistic parametric analysis of the seismic performance of CHSR Prototype Bridge with various isolator designs is conducted using the cloud-based probabilistic optimization framework developed under the high-throughput computing technology. Two families of the defined risk features are extracted from the results of conditional probabilistic seismic demand analysis and the unconditional probabilistic seismic demand hazard analysis respectively. The topologies of the risk features for a variety of EDPs are presented to demonstrate the sensitivity of risk features to the isolators' yield strength and initial stiffness. And the ranges of risk features by varying the isolators' design properties are summarized to show the room of optimization of isolators' design. This comprehensive parametric study in terms of the risk features exposed the variation of beneficial and detrimental effects of seismic isolators on different hazard levels. The conflicting effect of seismic isolation on different EDPs implies the imperative need and tremendous promise of optimization to seismic isolator parameters for a trade-off in design. This need is enhanced by the different sensitivities of demand hazard on various hazard levels with respect to isolators' yield strength and initial stiffness.

CHAPTER 8

PROBABILISTIC PERFORMANCE-BASED OPTIMUM SEISMIC DESIGN OF CHSR PROTOTYPE BRIDGE

8.1. Introduction

In previous chapters, a comprehensive investigation has been carried out for seismic isolation in CHSR Prototype Bridge. It consists of the deterministic performance comparison between conventionally non-isolated bridge (NIB) and seismic isolated bridge (IB) in CHSR project in Chapter 4, the probabilistic performance evaluation of seismic in Chapter 5, and the probabilistic parametric study of seismic isolation in Chapter 7. As displayed, apart from some detrimental effects on the deck displacements and induced additional rail stress, seismic isolation is a promising effective scheme to minimize damage, reduce seismic demands on substructures, and therefore reduce foundation costs efficiently. Notably, a proper selection of seismic isolator properties must be carried out to strike a balance between the beneficial and detrimental effects after considering uncertainties in the earthquake ground motions. It is imperative to validate whether seismic isolation can be adopted as a practical method to mitigate the seismic risk for CHSR Bridges, by maximizing the beneficial effects of seismic isolation while keeping the detrimental effects of seismic isolation under an acceptable level.

Among extensive real-world problems which could benefit from structural design optimization, the feasibility and optimality of seismic isolation is investigated for a California High-Speed Rail (CHSR) prototype bridge testbed using the proposed PPBOSD framework, balancing the beneficial and detrimental effects of seismic isolation for such a bridge. Thus, probabilistic performance-based optimization problems need to be formulated and solved for an optimum design of seismic isolation for CHSR Prototype Bridge.

In the context of the proposed PPBOSD framework, the uncertainties in seismic hazard for a given site as well as record-to-record variation are addressed directly as a primary focus of this research. It is worth noting that the PPBOSD framework is largely built on the PEER PBEE methodology (i.e., forward PBEE analysis) which provides a comprehensive framework for fully probabilistic seismic performance/risk evaluation of structural-foundation system in earthquake engineering, the incorporation of other uncertainties can be implemented easily within the framework as well. While due to limited statistical database on the fragilities of the structural components for CHSR projects, only uncertainties on the seismic demand due to the uncertainties in seismic hazard for a given site as well as record-to-record variation are considered in the probabilistic performance evaluation and design.

By considering the uncertainties in the seismic input explicitly, it yields more predictable seismic performance over a range of earthquake demands. Considering the possible performance objectives for decision-makers, in terms of performance-based design objectives and acceptable damage risk constraints, several well-posed probabilistic performance-based seismic design problems for the CHSR are formulated in this Chapter, fully making use of the flexibilities of optimization problem formulation in PPBOSD framework. The proposed PPBOSD methodology can be used for single hazard level earthquakes or multiple hazard level earthquakes, as well as to embrace a continuous band of

hazard levels of earthquakes. Thus seismic performance objectives, conditioned on specific hazard levels or based on the unconditional demand hazard, can be achieved through proper design of seismic isolators for the CHSR prototype bridges. This leads to the flexibility of the formulation of the optimization problems in the proposed PPBOSD framework, as shown from the next section with some alternatives of optimization formulation in PPBOSD.

Instead of using rigorous mathematical optimization algorithms to solve the inverse problems, a grid-based graphic approach (i.e., brute-force approach) based on the cloud-based parametric analyses is adopted for the optimum solution. The probabilistic seismic performance of the optimal seismic isolated bridge is then compared with that of the isolated bridge with initial design and the non-isolated bridge aiming to verify the effectiveness of the achieved optimal design. Simultaneously, the foregoing research also contributes to expose the power of the proposed PPBOSD framework in earthquake engineering, and it implied that the grid-based graphical approach based on the cloud-based computing framework proposed in Chapter 6 for parametric sweeping analysis can be used for the practical engineering problems as adopted herein.

8.2. Alternatives of Optimization Formulations in PPBOSD

Based on the pre-defined risk features extracted from the probabilistic seismic demand hazard analysis, a wide variety of risk features can be used as objective functions or constraint functions across different EDPs, different types of risk features, different hazard levels, and different hazard analysis steps. Due to the flexibility inherent in the proposed *PPBOSD* framework, any combination of feasible constraints can actually be imposed, and the optimization objective can also be any one of them. A series of illustrative examples are presented here to show the power and flexibility of the proposed *PPBOSD* methodology. For the purpose of demonstration, the risk feature (A^{LC}) of total base shear force across all pier

columns in the transverse direction is chosen to be the objective function, aiming at minimizing the seismic risk to total base shear force. Some typical representative constraints are imposed respectively to demonstrate the alternative formulations.

8.2.1. Optimization with constraints considering different type of risk features

The following is an illustrative example to explore the capability of combining different risk features in the optimization problem formulation within the framework of PPBOSD. The underlying intention is to minimize risk to the total base shear force across all pier columns in the bridge system, subjected to the constraints that limit two different risk features of the same EDP on the same hazard level (i.e., MCE) in the conditional probabilistic seismic demand hazard analysis. The conditional median of EDP ($\eta_{EDP|IM=im}$) and the conditional 95th percentile on MCE hazard level is limited to be less than 4.0in and 10.0in respectively. That is to say, the probability of isolation deformation in the transverse direction exceeding 10.0in is constrained to be less than 5% under MCE hazard level events. The mathematical formulation is summarized in Equation (8.1).

minimize:

$A_{HL}^{LC} = \int_{hl_2}^{hl_1} EDP(hl) d(hl)$, where $(hl_2, hl_1) = (0.10, 0.86)_{PE100}$

EDP : the total base shear in trans. dir. across all pier columns

subjected to:

$(1)\ \eta_{EDP|IMCE} = \exp\left(E\left[\ln(EDP) \mid IM = im_{0.1}\right]\right) <= 4.0in$

EDP: the isolator deformation over pier #5 in trans. dir.

$(2)\ \text{Pctl.}_{EDP|MCE}^{95th} = \arg\limits_{edp}\left\{edp \mid P[EDP > edp \mid IM = im_{0.1}] := 0.05\right\} <= 10.0$

$inEDP$: the isolator deformation over pier #5 in trans. dir.

(8.1)

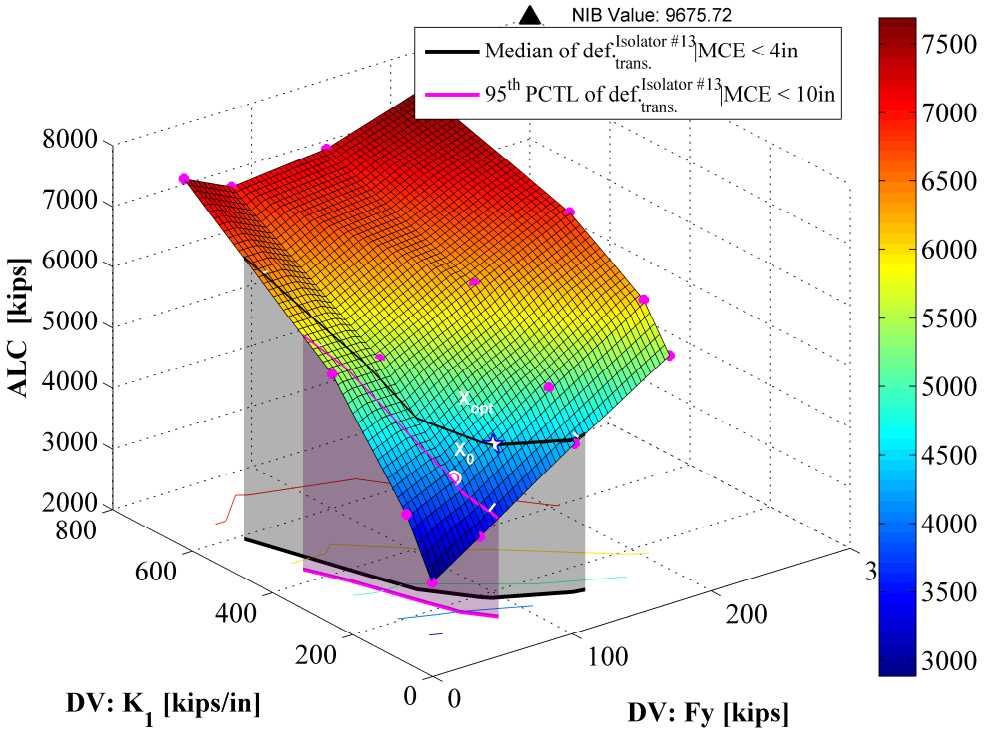

Figure 8.1: Optimization problem formulation alternative considering different risk features

The solution to the formulated optimization problem is illustrated in Figure 8.1, with the objective function plotted as the surface, intersecting with two corresponding constraint barrier walls to define the feasible domain. The optimum solution obtained lies on the boundary of the first constraint (i.e., active constraint), while the second constraint is satisfied with a certain safety margin (i.e., inactive constraint). On the contrary, the initial isolator design violated the first design constraint but activated the second design constraint.

8.2.2. Optimization with constraints across different EDPs

The second illustrative example is to show the capability of imposing constraints on different EDPs in the optimization problem formulation within the framework of PPBOSD. Two constraints are imposed on the conditional median of different EDPs on the same hazard level (i.e., OBE) in the conditional probabilistic seismic demand hazard analysis. The first

constraint is defined that the conditional median of isolator deformation in the longitudinal direction on OBE hazard level is less than the half of the abutment gap size (i.e., 2.0in), and second constraint is defined that the conditional median of the absolute deck acceleration in the transverse direction on OBE hazard level is less than 0.25g. The mathematical formulation is presented in Equation (8.2) and solved by brute-force approach shown in Figure 8.2.

minimize:

$A_{HL}^{LC} = \int_{hl_2}^{hl_1} EDP(hl)d(hl)$, where $(hl_2, hl_1) = (0.10, 0.86)_{PE100}$

EDP : the total base shear in trans. dir. across all pier columns

subjected to:

(1) $\eta_{EDP|OBE} = \exp\left(E\left[\ln(EDP) \mid IM = im_{0.86}\right]\right) <= 2.0in$

EDP: the isolator deformation over pier #5 in long. dir.

(2) $\eta_{EDP|OBE} = \exp\left(E\left[\ln(EDP) \mid IM = im_{0.86}\right]\right) <= 0.25g$

EDP: the absolute acceleration of deck over pier #5 in trans. dir.

(8.2)

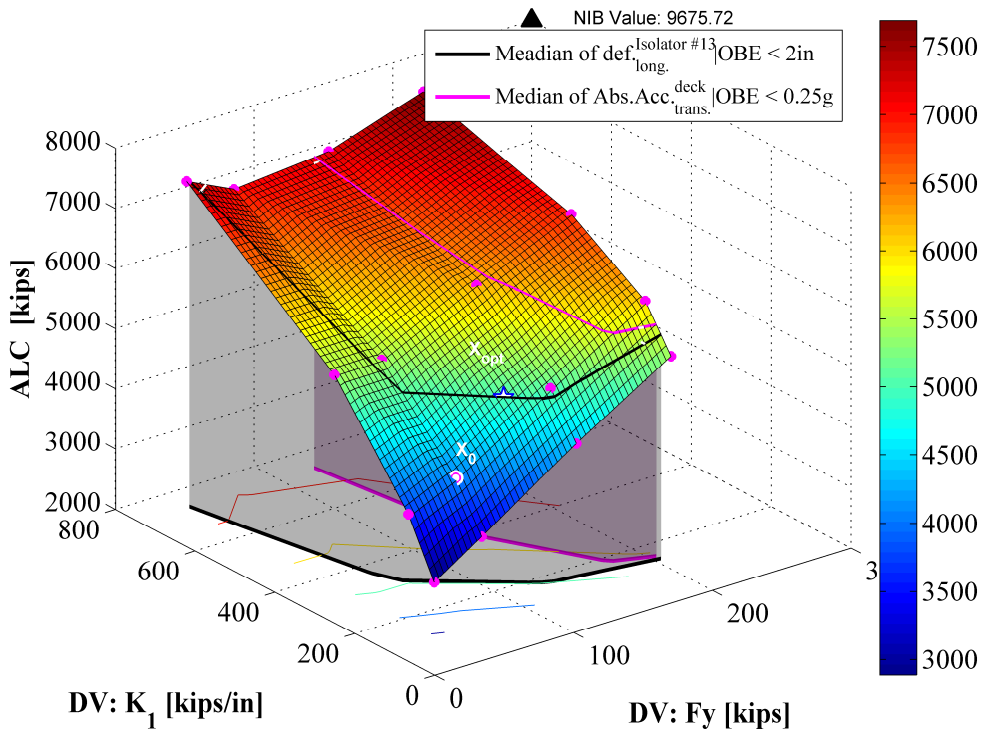

Figure 8.2: Optimization problem formulation alternative considering different EDPs

8.2.3. Optimization with constraints across different hazard levels

The third illustrative example is to show the capability of imposing constraints on different hazard levels in the optimization problem formulation within the context of PPBOSD framework. Constraints for the performance on two different hazard levels (i.e., OBE and MCE hazard level) are imposed to limit the conditional median of the EDP (i.e., isolator deformation in longitudinal direction) in the conditional probabilistic seismic demand hazard analysis. The conditional median of isolator deformation in longitudinal direction on OBE hazard level is constrained to be less than the half of the abutment gap size (i.e., 2.0in), and the conditional median of isolator deformation in longitudinal direction on MCE hazard level less than 6.0in. The optimization problem with constraints across different hazard levels is formulated in Equation (8.3) and solved in Figure 8.3.

minimize:

$A_{HL}^{LC} = \int_{hl_2}^{hl_1} EDP(hl)d(hl)$, where $(hl_2, hl_1) = (0.10, 0.86)_{PE100}$

EDP : the total base shear in trans. dir. across all pier columns

subjected to:

(1) $\eta_{EDP|\text{OBE}} = \exp\left(E\left[\ln(EDP) \mid IM = im_{0.86}\right]\right) <= 2.0in$

EDP: the isolator deformation over pier #5 in long. dir.

(2) $\eta_{EDP|MCE} = \exp\left(E\left[\ln(EDP) \mid IM = im_{0.1}\right]\right) <= 6.0in$

EDP: the isolator deformation over pier #5 in long. dir.

(8.3)

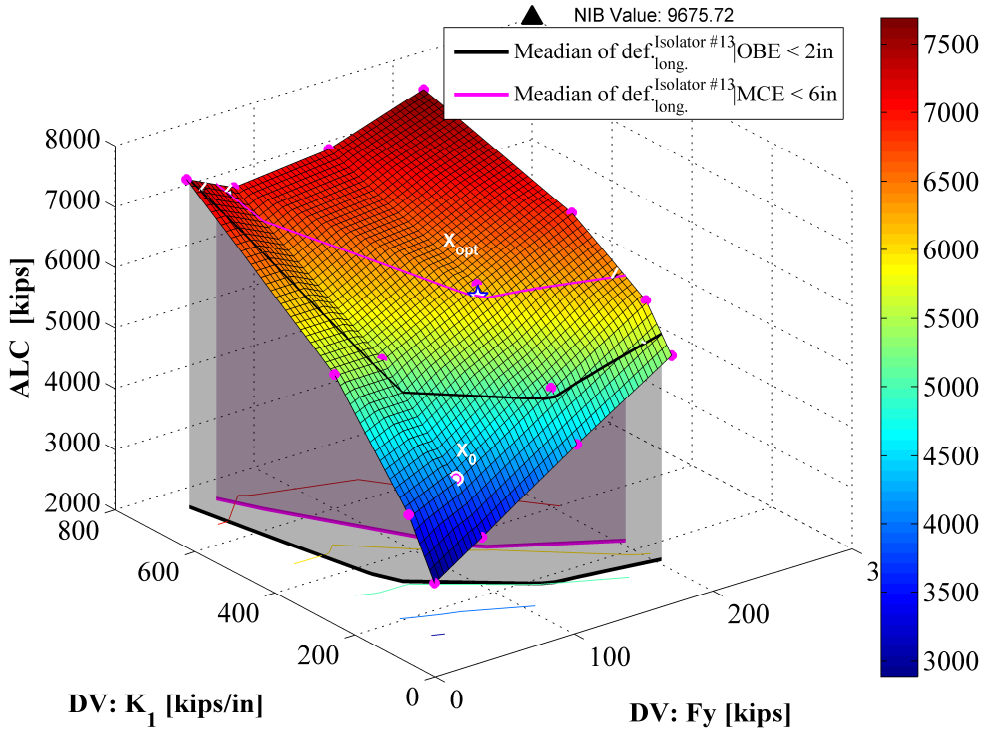

Figure 8.3: Optimization problem formulation alternative considering different hazard levels

8.2.4. Optimization with constraints across different hazard analysis steps

Apart from enforcing the constraints based on the conditional seismic demand hazard analysis, probabilistic constraints can also be defined on the unconditional seismic demand hazard analysis step of PBEE. The fourth example here intends to illustrate the capability of the proposed PPBOSD framework in imposing constraints across different hazard analysis steps. Both the unconditional 95th percentile (i.e., the value of EDP with 5% probability of exceedance on the probabilistic seismic hazard curve) and conditional 95th percentile on MCE hazard level of the bending moment at the bottom of pier column #5 in the transverse dir. are limited to be less than the expected moment of the pier column section capacity. The unconditional demand is less than the conditional demand on MCE hazard level, because the unconditional demand is between the conditional demand on OBE hazard level and MCE

hazard level as found previously. Consequently, the first constraint is satisfied automatically if the second constraint is satisfied. The optimization problem considering different hazard analysis steps is formulated in Equation (8.4) and solved in Figure 8.4. Neither of the two constraints is active when the optimum is achieved.

minimize:

$A_{HL}^{LC} = \int_{hl_2}^{hl_1} EDP(hl) d(hl)$, where $(hl_2, hl_1) = (0.10, 0.86)_{PE100}$

EDP : the total base shear in trans. dir. across all pier columns

subjected to:

$$(1)\ Pctl._{EDP}^{95th} = \arg_{edp}\{edp \mid PE100(edp) := 0.05\} <= 4.15\times10^4\ kips\text{-}ft \tag{8.4}$$

EDP: the bending moment at bottom of pier #5 in trans. dir.

$$(2)\ Pctl._{EDP|\mathrm{MCE}}^{95th} = \arg_{edp}\{edp \mid P[EDP > edp \mid IM = im_{0.1}] := 0.05\} <= 4.15\times10^4\ kips\text{-}ft$$

EDP: the bending moment at bottom of pier #5 in trans. dir.

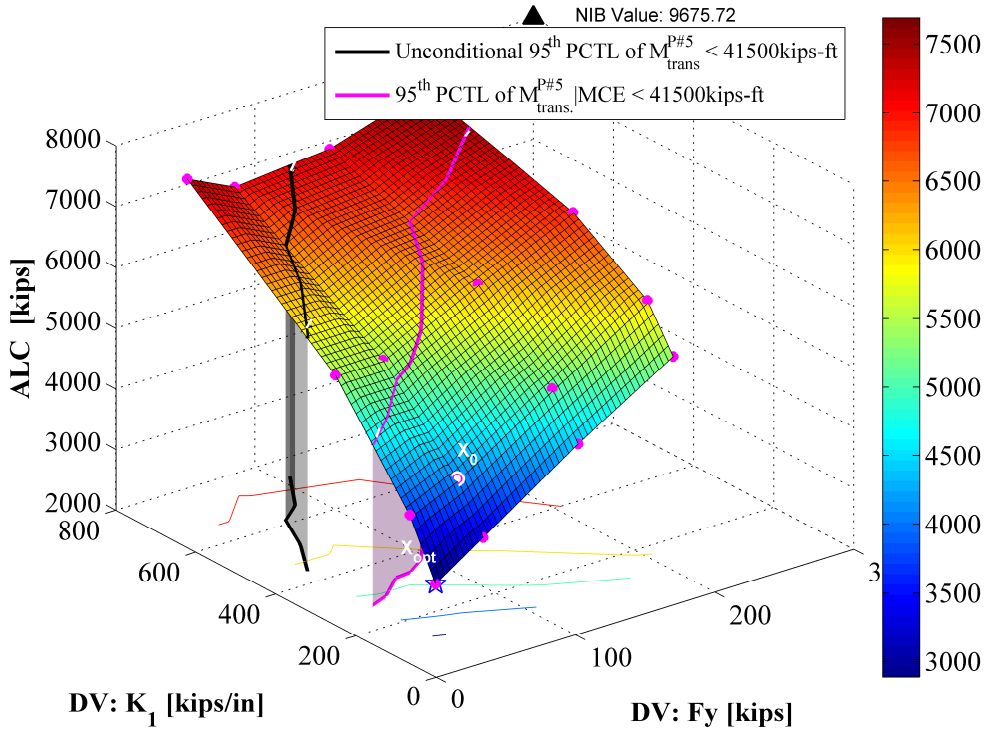

Figure 8.4: Optimization problem formulation alternative considering different hazard analysis steps

8.3. Probabilistic Performance-based Seismic Design Requirements for CHSR Bridges

Performance-based seismic design is enforced through the realization of seismic performance objectives in the seismic design criteria. It is essential to select the expected performance level of the bridge for expected probable hazard for CHSR bridges. The selection of the performance objectives/targets for the design is made by the clients and the design professionals (e.g., the engineers, stake-holders, and the policy makers) as decision-makers to reflect their expectations on the seismic performance. The performance objectives are established by coupling pairs of expected performance level or acceptable damage risk with corresponding seismic hazard levels, which is usually associated with the conditional seismic demand analysis step of PBEE analysis. In order to achieve the seismic performance goals, criteria for multiple performance levels need to be complied with. In addition, new performance objectives can also be stated in terms of the probabilistic seismic demand hazard analysis step of PBEE analysis by limiting the acceptable risk of a certain EDP exceeding limit states after accounting for all seismic hazard levels by convolution.

Probabilistic performance-based seismic design involves defining the probabilistic performance objectives and then designing the structures for the targeted performance with the probabilistic performance objectives satisfied. The performance objectives must be translated into mathematical forms to establish acceptance criteria as targets for the design, defined as limiting values in the response parameters. The probabilistic performance-based optimum seismic design (PPBOSD) is to minimize a seismic risk of interested EDP as an objective function, while satisfying the desired probabilistic constraints stated in the probabilistic objectives.

Therefore, there are three components for the probabilistic performance constraints, i.e., the associated engineering response quantity of interest (i.e., engineering demand parameter, denoted as EDP), the risk feature associated, and the limit states' threshold values as the constraint bounds.

8.3.1. EDPs of CHSR bridges used for probabilistic design constraints

Considering the safety and functionality to carry dedicated High-Speed Train Operations, the seismic performance criteria (i.e., performance level and the corresponding earthquake hazard level to evaluate the performance) established are outlined as follows (CHSRA, 2012). (1) No Collapse Performance Level (NCL): No collapse is allowed but it allows significant damage which requires extensive repair or complete replacement under MCE, the one characterized by the return period of 950 years, with 10% probability of exceedance for a design life of 100 years. (2) Operability Performance Level (OPL): No structural damage but allows CHST operate at maximum design speed and safely brake during an Operating Basis Earthquake (OBE) and short term track repairs after OBE, the one characterized by return period of 50 years, with 86% probability of exceedance for a design life of 100 years.

As specified in the CHSR design criteria (CHSRA, 2012), for OBE events, elastic structural response is required, and rocking is not allowed. OBE demands shall be verified versus force-based capacities. For MCE events, inelastic behavior is allowed within the two main fusing mechanisms for bridges, e.g., column flexural plastic hinging and foundation rocking, etc. The track system overlying on the bridge plays a significant role for the dedicate operation of train system. While during the track-structure interaction, the continuous welded rail (CWR) may serve as restrainers at the expansion joints, essentially tying adjacent frames together under seismic loading. This will definitely cause additional rail stress under

earthquakes, especially at the abutment gaps and interior expansion joint gaps, thus additional rails stress under OBE events is of significant concern when the overall system performance is evaluated.

The tendency of train to derail is often described by the L/V ratio, where L is the lateral force and V is the vertical force at the wheel-track interface (Bibel G., 2012). The probabilistic study of derailment cannot be carried out for the current model, as a full analysis model for train-rail-bridge system is required. While, the deck acceleration in the transverse direction of bare bridge (i.e., no train runs over the bridge) could also be a good indicator to the wheels and rail wear and track gauge widening like L/V, some rules of thumb limits will be specified as constraints under low hazard level earthquakes (i.e., OBE) as performance requirements.

To summarize, a wide variety of Engineering Demand Parameters (EDPs) of the entire bridge system can be used, which includes, but not limited to, peak values in the transv./long. direction of deck absolute acceleration, isolator deformation, pier deformation at the base, shear force and bending moment in pier columns and foundation piles, rotation of the foundation pile caps, peak stress in the rails, etc.. In the optimization problem formulations presented later, constraints are defined based on some of these critical EDPs of primary interest to designers of such bridges.

8.3.2. Risk features and limiting values to define probabilistic design constraints

The definition of probabilistic constraints for the design requires considerable research from the reliability theory before it can be readily applied in practice to probabilistic structural design to realize the probabilistic performance-based seismic design. To convert the usual deterministic design objectives preferred by clients to probabilistic constraints, different risk features (e.g., conditional statistics like mean, median, and percentiles, etc.) can be limited to a

reasonable performance level. For example, to be sufficiently conservative to reasonably ensure that the intended performance objectives will be achieved, the 95th percentile of the conditional demand on structural components (i.e., pier column bottom moment, pile moment, isolator deformation, etc.) are adopted, while mean or median of the conditional demand on EDPs (i.e., deck acceleration, rail stress, etc.) are used herein to define well-posed structural optimization problem. The selection of risk features also depends on the probabilistic design philosophy based on the risk control approach elaborated later.

The corresponding limit sates' values is closely related to the risk features used. Herein, referring to the "deterministic" performance criteria specified in the California High-Speed Train Project, appropriate probabilistic design constraints will proposed when seismic isolation is introduced for a higher seismic performance.

8.4. Formulations and Solutions of Structural Optimization Problems for the CHSR Prototype Bridge

The optimization problem formulation highly relies on the concerns of the decision makers in practice, which of course reflects the expectations in the design, and thus could be of various forms. Considering the flexibility of the optimization problem formulation, five different optimization problems are formulated with various intentions as below and solved using a grid-based brute-force approach herein.

8.4.1. Structural optimization for seismic performance of discretized hazard levels: conditional seismic demand hazard

Specific design provisions to control risk in terms of probability of failure P_f (i.e., damage or collapse, or exceedance of a design limit state), as the effect of extraordinary loads with uncertainties (i.e., seismic events), are developed with a probabilistic basis (Ellingwood and Leyendecker 1978, Ellingwood and Corotis 1991, and Ellingwood and Dusenberry 2005).

The computation of the probability of failure event denoted as F due to a seismic event E can be broken into the conditional probability of the failure event $P[F \mid E]$ and the probability of occurrence of event $P[E]$ as follows

$$P_f = P[F \mid E]P[E] \tag{8.5}$$

This separation technique for computing the probability of failure P_f allows us to reduce the risk management of failure event into controlling the conditional probability for the considered events given a prescribed probability. Design requirements of the structural performance corresponding to seismic events of different hazard levels are enforced usually with 2 or 3 hazard levels in the current bridge/building design codes. Operating basis earthquake hazard level (OBE) and maximum considered earthquake hazard level (MCE) are considered with corresponding requirements in the seismic design criteria for California High-speed Train Project. Aiming at reducing the foundation cost while achieving higher seismic performance for the seismic isolated CHSR Prototype Bridge, a risk feature associated with total base shear force is selected as objective function to study the potential of seismic isolation by structural optimization. Combining the design constraints explicitly specified in the design criteria and some other specific seismic performance targets for CHSR bridges with seismic isolation, structural optimization conditioned on OBE hazard level, structural optimization conditioned on MCE hazard level, and structural optimization based on mixed hazard levels are presented in this section.

Probabilistic performance-based optimization conditioned on OBE hazard level

Under OBE hazard level earthquakes with a return period of 50 years, optimal isolator design with minimum seismic risk to seismic demand on the substructure system (i.e., piers and foundations) of the current design with other components (piers and foundations) unchanged can lead to higher seismic performance or structural reliability. It also opens a door

for more room to resize the pier column and foundation for lower construction cost. The seismic demand risk to the total base shear force, measured by conditional median demand, the conditional mean demand, or conditional 95th percentile (i.e., abbreviated as Pctl.), is selected to be the objective function in the optimization problem formulation.

After observing the range of risk feature values (summarized in the previous chapter), which are evaluated for the seismic isolator designs satisfying other non-seismic design constraints (e.g., operation loads such as braking and traction), the following contributory constraints are considered:

(1) Constraints on the transverse deck acceleration

The seismic risk to transverse deck acceleration on OBE hazard level is limited in order to restrict the maintenance fees of track system as a result of possible acceleration-sensitive damage and other damage associated with the tendency of train to derail (i.e., wheels-rail wear and track gauge widening) under frequent OBE hazard level earthquakes. In view of limited statistic data on the damage correlation with transverse acceleration of bare railway bridge when train-rail-bridge interaction is not accounted, the limiting value of 0.35g is set to be upper bound of conditional mean of absolute deck acceleration in transverse direction of the bridge as a measure of seismic performance/risk. The limiting value of 0.5g is imposed on the 95th percentile of absolute deck acceleration in the transverse direction of the bridge.

$$\mu_{EDP|IM=im} = E\left[EDP \mid IM = im_{0.86}\right] <= 0.35g \tag{8.6}$$

$$Pctl.^{95th}\left[AA^{deck}_{trans.} \mid OBE\right] = \arg\underset{edp}{\left\{edp \mid P\left[EDP > edp \mid IM = im_{0.86}\right] := 0.05\right\}} <= 0.5g \tag{8.7}$$

where the EDP is the absolute deck acceleration of deck over pier #5, $AA^{deck}_{trans.}$, in the transverse direction of the bridge, $im_{0.86}$ is the intensity measure at OBE hazard level.

(2) Constraints on the force demand on the pier columns and piles

Based on the probabilistic seismic performance evaluation of the NIB of CHSR Prototype Bridge on OBE hazard level, the column is going to crack almost sure because the conditional 95th percentile of the moment demand is much higher than the cracking moment of pier column section. On the contrary, the conditional 95th percentile of the moment demand is around the first-yield moment capacity. It is worth noting that the uncertainty in capacity analysis is ignored here during the comparison. Considering the seismic safety conservativeness in the current design of the CHSR Prototype Bridge when assuming deterministic capacity, higher seismic performance criteria are expected when seismic isolation is introduced for the current substructure design. To expose the potential room to reduce the substructure sizes without jeopardizing the bridges subject to future earthquakes, an isolation design is sought for that the pier column will not even crack under OBE hazard level earthquakes. Thus the following constraint is imposed to the bottom bending moment of pier column #5, in terms of the 95th percentile of transverse bending moment less than the cracking moment capacity of 15000kips-ft. For similar reasoning, another constraint on the maximum bending moment of all piles under pier #5 is enforced to be less than the cracking moment capacity of 5000kips-ft. The mathematical definition of these two constraints is stated as follows:

$$\begin{aligned}&\text{Pctl.}^{95th}\left[M_{trans.}^{P\#5} \mid IM\right] = \\ &\quad \arg_{edp}\left\{edp \mid P\left[EDP > edp \mid IM = im_{0.86}\right] := 0.05\right\} <= 15000 kips\text{-}ft\end{aligned} \tag{8.8}$$

in which the EDP is the transverse bending moment of pier column #5, $M_{trans.}^{P\#5}$;

$$\begin{aligned}&\text{Pctl.}^{95th}\left[M_{trans.}^{piles,\,P\#5} \mid IM\right] = \\ &\quad \arg_{edp}\left\{edp \mid P\left[EDP > edp \mid IM = im_{0.86}\right] := 0.05\right\} <= 5000 kips\text{-}ft\end{aligned} \tag{8.9}$$

in which the EDP is the maximum bending moment of piles under pier column #5, $M_{trans.}^{piles,\,P\#5}$, in the transverse direction of the bridge.

(3) Constraints on the stress state of the rails at expansion joint gaps

The axial rail stress of continuously welded rails, which are attached to the bridge deck across track-slab by direct fixation fasteners, is of crucial concern to engineers for high-speed railway bridges under OBE hazard level earthquakes, especially when seismic isolation and seismic gap is introduced into railway bridges. This concern has been in the way for promoting the application of seismic isolation in railway bridges to a degree. The additional axial rail stress due to OBE events is limited to 14.0ksi for stress due to axial force in rails in the deterministic design criteria. Thus the predicted 95th percentile of axial rail stress at abutment gap is enforced to be less than 12.5ksi considering a resistance factor of 0.9 in view of the full-section loading condition.

$$\begin{aligned} &\text{Pctl.}^{95th}\left[\sigma_P^{rail,\ \text{abut.}} \mid \text{OBE}\right] = \\ &\qquad \arg\underset{edp}{\left\{edp \mid P\left[EDP > edp \mid IM = im_{0.86}\right] := 0.05\right\}} <= 12.5ksi \end{aligned} \tag{8.10}$$

in which the EDP is the 95th percentile of axial rail stress at the left abutment gap, $\sigma_P^{rail,\ \text{abut.}}$, under OBE hazard level earthquakes.

As observed from the additional bending stress due to the transverse discontinuity at the abutment in the transverse direction, the bending stress in rails of IB and NIB is relatively large around the same magnitude due to the minimum construction gap 0.5in is left for shear keys. It implies the limitation of the seat-type abutment, which may calls for transverse lock with as small as possible gap size to realize the concept of unidirectional seismic isolator over abutments or integral abutment type for railway bridges with overlying track system of CWR. The conditional mean demand of total rail stress due to both bi-directional bending moment and axial force is enforced to be less than 42.5ksi as follows

$$E\left[\sigma_{P+M}^{rail,\ \text{abut.}} \mid OBE\right] = \mu_{EDP|IM=im_{0.86}} <= 42.5ksi \tag{8.11}$$

in which EDP is the conditional mean demand of total rail stress at left abutment gap, $\sigma_{P+M}^{rail,\ \text{abut.}}$, due to both bi-directional bending moment and axial force on OBE hazard level earthquakes.

In summary, the mathematic formulation of the probabilistic performance-based optimization problem conditioned on OBE hazard level is presented in Equation (8.12).

$$
\begin{aligned}
&\underset{\substack{34.1kips \le F_y \le 204.7kips \\ 120kips/in \le K_1 \le 740kips/in}}{\textbf{\textit{Minimize}}} \quad \text{conditional median: } \eta\left[F_{trans.}^{\text{TBS, all columns}} \,|\, OBE\right] \\
&(1)\ E\left[AA_{trans.}^{deck} \,|\, OBE\right] \le 0.35g \\
&(2)\ Pctl.^{95th}\left[AA_{trans.}^{deck} \,|\, OBE\right] \le 0.5g \\
&(3)\ Pctl.^{95th}\left[M_{trans.}^{P\#5} \,|\, OBE\right] \le M_{cr}^{pier}(1.5\times10^4\, kips\text{-}ft) \\
&(4)\ Pctl.^{95th}\left[M_{trans.}^{piles,\ P\#5} \,|\, OBE\right] \le M_{cr}^{pile}(5.3\times10^3\, kips\text{-}ft) \\
&(5)\ Pctl.^{95th}\left[\sigma_{P}^{rail,\ \text{abut.}} \,|\, OBE\right] \le 12.5ksi \\
&(6)\ \eta\left[\sigma_{P+M}^{rail,\ \text{abut.}} \,|\, OBE\right] \le 42.5ksi
\end{aligned}
\tag{8.12}
$$

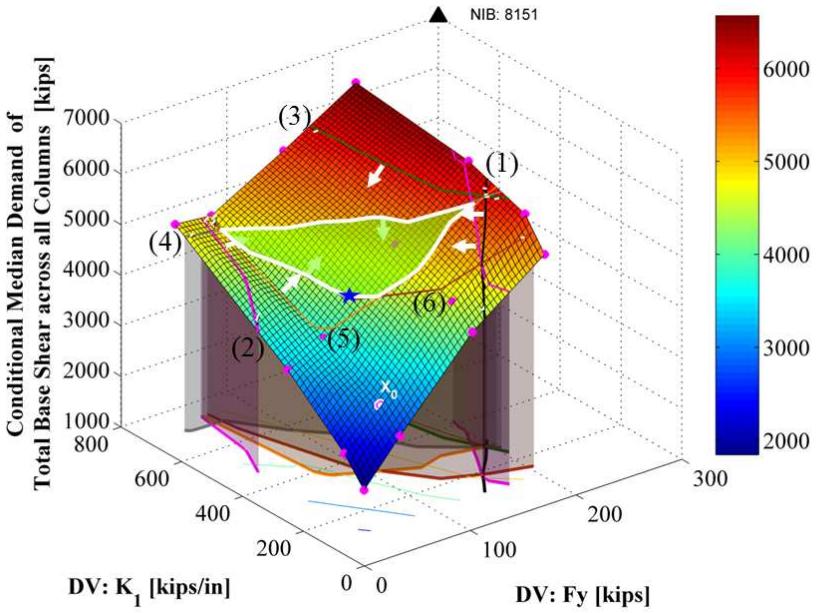

Figure 8.5: Structural optimization solution to the optimization problem formulated for probabilistic performance-based design on given seismic hazard level (i.e., OBE)

The formulated optimization is solved using the grid-based graphic approach demonstrated in Figure 8.5. As seen from the feasible domain defined by the constraints (1) and (2) on the transverse acceleration of bridge deck, the isolator design alternatives of high elastic stiffness with low yield strength and low elastic stiffness with high yield strength are eliminated. It indicates that a proper combination of initial stiffness and yield strength of bilinear isolation is beneficial to the absolute deck acceleration. The force demand constraints (3) and (4) eliminate the design alternatives of seismic isolators with high yield strength and high initial stiffness, because a flexible isolation layer is more beneficial to the force demand on the substructures (i.e., pier columns and foundation system). On the contrary, the imposed constraints (5) and (6) on rail stress avoid inappropriate seismic isolator designs by limiting the detrimental effects of seismic isolation on rail stress. All these imposed constraints lead to the reduced feasible design domain.

The obtained optimum design of seismic isolator is marked out by the pentagram with yield strength 95.54kips and initial stiffness 330.8kips/in, which lies on the intersection of boundaries of the constraints on the axial rail stress and total rail stress. Notably, the beneficial effects of seismic isolation are fully made use of, meanwhile satisfying the design constraints and expected performance requirements by limiting the detrimental effects of seismic isolation Thus the following observations can be made: (1). It indicates the applicability of seismic isolation to railway bridges, with the dominated rail stress constraints. (2). Higher-level seismic performance on substructures is reached, which implies that the substructure can be resized when seismic isolation is introduced. (3). Under the probabilistic constraints imposed, the conditional median demand on total base shear force across all columns on OBE hazard level is minimized to be 4327.4kips (0.12W, where W is the total weight of the bridge

superstructure), compared to 8151.2kips (0.228W) for NIB and 3062.4kips (0.09W) for IB with initial isolation design which violated the probabilistic constraints on the rail stress.

Under OBE hazard level, other objective functions can be defined based on the conditional mean demand and the conditional 95th percentile of total base shear in the transverse direction under OBE hazard level. The solutions to these two optimization problems as well as the former optimization problem with the same constraints imposed are summarized in Table 8.1.

Table 8.1: Summary of optimization results comparison with different objective functions for probabilistic performance-based design conditioned on OBE hazard level

Objective	**Conditional median**		**Conditional mean**		**Conditional 95th percentile**	
Optimal solution	DV $F_y(kips)$ $K_1(kips/in)$	Objective function	DV $F_y(kips)$ $K_1(kips/in)$	Objective function	DV $F_y(kips)$ $K_1(kips/in)$	Objective function
Optimal design	(95.54, 330.8)	4327.4kips (0.12W)	(95.54, 380.4)	4619.9kips (0.13W)	(109.2, 330.8)	7707kips (0.22W)
IB with initial design	(68.225, 184.54)	3062.4kips (0.09W)	(68.225, 184.54)	3302kips (0.093W)	(68.225, 184.54)	5799kips (0.17W)
NIB	-	8151.2kips (0.228W)	-	8306.1kips (0.233W)	-	11215kips (0.32W)

The optimal solutions obtained depend on the formulation of the optimization problems, i.e., the selection of the optimization problem herein. However, a consistent trend for the optimal isolator design is observed that a seismic isolator design with higher yield strength and higher initial stiffness is obtained, and objective function value is increased compared to the initial isolator design. This implies that higher shear force demand is imposed due to the design constraints limiting the detrimental effects. When comparing the optimal solution with the counterparts for NIB, the total base shear force demand is reduced, e.g., the

conditional median of the total base shear force demand is reduced by 47% (i.e., from 0.228W to 0.12W); or the conditional mean of the total base shear force demand is reduced by 44% (i.e., from 0.233W to 0.13W); or the conditional 95th percentile of the total base shear force demand is reduced by 31% (i.e., from 0.32W to 0.22W).

Probabilistic performance-based structural optimization conditioned on MCE hazard level

Under MCE hazard level earthquakes with a return period of 950 years referred to as rare seismic events, the displacement demand needs to be checked in the deterministic seismic design criteria for the California High-speed Rail Project. Herein, apart from the probabilistic constraints on the displacement/deformation demand with higher seismic performance criteria for less damage risk, some extra force demand constraints are also enforced to keep the demand conditioned on MCE hazard level below the expected capacity when seismic isolation is introduced. Similar objective functions are selected for the MCE hazard level. Regarding to the probabilistic constraints, the following constraints are considered.

(1) Constraints on plastic deformation on pier columns

The maximum relative end rotation of the last element of pier column #5 is monitored as an EDP to characterize the seismic damage of the pier columns, and probabilistic seismic demand hazard is achieved in terms of this EDP. Constraints on the risk features of this relative rotation is enforced with limiting values referred to the normalized curvature capacity of pier column section (i.e., multiplied by the element length). The relative end rotation is limited to be less than $2\kappa_e^{section}\ell_{element} = 7.1\kappa_y^{section}\ell_{element} = 1.126\%$ for a higher performance objective for the IB to expose the beneficial effects of seismic isolation, as follows

$$Pctl.^{95th}\left[\Theta_{trans.}^{P\#5} \mid MCE\right] = \arg_{edp}\left\{edp \mid P\left[EDP > edp \mid IM = im_{0.10}\right] := 0.05\right\} <= 1.126\% \quad (8.13)$$

in which the EDP is the maximum relative end rotation of the last element of pier column #5, $\Theta_{trans.}^{P\#5}$, due to the transverse deformation. This implies under seismic isolation, the section ductility of the pier column is limited to be 7.1 under MCE hazard level earthquakes, where the ductility is defined as

$$\mu_{\kappa} = \frac{\kappa}{\kappa_y} \tag{8.14}$$

in which κ_y is the curvature when the tension reinforcement first reaches the expected yield strength, corresponding to the first-yield moment capacity in the capacity analysis of the pier column section.

(2) Constraint on deformation in seismic isolators

The maximum deformation in the seismic isolators must be constrained to avoid instability and therefore unseating of railway bridges, considering the seismic isolation deformation capacity limit seen from the capacity of the DIS lead rubber bearings. Since the unseating of railway bridge will be catastrophic, and uncertainty of the seismic isolator properties are not considered here, the seismic isolation deformation is limited to 20in with 95% confidence, i.e.,

$$\begin{aligned} &Pctl.^{95th}\left[disp._{trans.}^{Isolator\#13} \mid MCE\right] = \\ &\qquad \arg_{edp}\left\{edp \mid P\left[EDP > edp \mid IM = im_{0.10}\right] := 0.05\right\} <= 20in \end{aligned} \tag{8.15}$$

in which the EDP is the lateral isolation deformation of seismic isolator #13 on the pier column #5, $disp._{trans.}^{Isolator\#13}$, in the transverse direction of the bridge.

(3) Constraints on the force demand on pier columns and piles

The conditional moment demands on pier columns and piles are enforced to be less than the expected moment capacities respectively on MCE hazard level, in order to protect the substructure system with higher seismic performance and higher reliability for seismic isolated

bridge. Meanwhile, it will expose the potential for further resizing of piers and foundation system if substructure system is designed to be fully with limited displacement capacity specified in traditional design bridges on MCE hazard level earthquakes. Thus, the following constraints are imposed for the structural optimization based on the probabilistic performance conditioned on MCE hazard level:

$$\begin{aligned}&\text{Pctl.}^{95th}\left[M_{trans.}^{P\#5} \mid \text{MCE}\right] = \\ &\quad \arg_{edp}\left\{edp \mid P\left[EDP > edp \mid IM = im_{0.10}\right] := 0.05\right\} <= 41500 kips\text{-}ft\end{aligned} \tag{8.16}$$

in which the EDP is the maximum bending moment of pier column #5 in the transverse direction of the bridge, $M_{trans.}^{P\#5}$,

$$\begin{aligned}&\text{Pctl.}^{95th}\left[M_{trans.}^{pile,P\#5} \mid \text{MCE}\right] = \\ &\quad \arg_{edp}\left\{edp \mid P\left[EDP > edp \mid IM = im_{0.10}\right] := 0.05\right\} <= 12000 kips\text{-}ft\end{aligned} \tag{8.17}$$

in which the EDP is the maximum bending moment of piles under pier column #5, $M_{trans.}^{piles,P\#5}$, in the transverse direction of the bridge.

The mathematic formulation of probabilistic performance-based structural optimization problem conditioned on MCE hazard level is presented in Equation (8.18) with objective function chosen as the 95th percentile of total base shear force demand. The solutions to the formulated optimization problem as well as other two optimization problems with different objective functions are summarized in Table 8.2. Similar observation is made to the probabilistic performance-based structural optimization problems conditioned on OBE hazard level. When comparing the optimal solution with the counterparts for NIB, the total base shear force demand is reduced more significantly than the OBE case, e.g., the conditional 95th percentile of the total base shear force demand is reduced by 59% (i.e., from 0.663W to 0.27W); or the conditional mean of the total base shear force demand is reduced by 64% (i.e.,

from 0.50W to 0.182W); or the conditional median of the total base shear force demand is reduced by 64% (i.e., from 0.482W to 0.175W).

$$\underset{\substack{34.1kips \le F_y \le 204.7kips \\ 120kips/in \le K_1 \le 740kips/in}}{\textbf{\textit{Minimize}}} \quad \text{conditional } 95^{th} \text{ Percentile: } Pctl.^{95th}\left[F_{trans}^{\text{TBS, all columns}} \mid \text{MC}\,E\right]$$

$$\begin{aligned}
&(1)\ Pctl.^{95th}\left[\Theta_{trans.}^{P\#5} \mid MCE\right] \le 1.3\% \\
&(2)\ Pctl.^{95th}\left[disp._{trans.}^{Isolator\#13} \mid MCE\right] \le 20in \\
&(3)\ Pctl.^{95th}\left[M_{trans.}^{P\#5} \mid MCE\right] \le M_e^{pier}(4.15\times10^4\, kips\text{-}ft) \\
&(4)\ Pctl.^{95th}\left[M_{trans.}^{piles,\,P\#5} \mid MCE\right] \le M_e^{pile}(1.2\times10^4\, kips\text{-}ft)
\end{aligned} \tag{8.18}$$

Table 8.2: Summary of optimization results comparison with different objective functions for probabilistic performance-based design conditioned on MCE hazard level

Objective	**95th percentile**		**mean**		**median**	
Optimal solution	DV $F_y(kips)$ $K_1(kips/in)$	Objective function	DV $F_y(kips)$ $K_1(kips/in)$	Objective function	DV $F_y(kips)$ $K_1(kips/in)$	Objective function
Optimal design	(105.78, 120.8)	9596 (0.27W)	(105.78, 120.8)	6479.3 (0.182W)	(105.78, 120.8)	6254.8 (0.175W)
Initial design	(68.225, 184.54)	12500 (0.35W)	(68.225, 184.54)	7117.6 (0.20W)	(68.225, 184.54)	6601.1 (0.185W)
NIB	Infinity	23682.27 (0.663W)	Infinity	17539.43 (0.50W)	Infinity	17212.48 (0.482W)

Probabilistic performance-based structural optimization with constraints conditioned on two seismic hazard levels (i.e., OBE and MCE)

The probabilistic performance-based optimum design problem can also be formulated to account for the probabilistic design constraints associated with the conditional demand on both OBE and MCE hazard levels, i.e., the two hazard levels as specified in the seismic design criteria for CHST Project. Four more design constraints on the MCE hazard level are included in the optimization problem formulated in Equation (8.19) in addition to the other six design constraints on the OBE hazard level. The solution of this optimization problem is illustrated in

Figure 8.6, to minimize the conditional mean demand of the total base shear force across all columns in transverse direction on OBE hazard level while satisfying all the ten constraints defined on two discretized hazard levels.

It is observed that with the introduction of seismic isolation, high performance objectives on the beneficial effects of the seismic isolation are achieved, while the possible detrimental effect of seismic isolation is limited via satisfying the probabilistic design constraints as well. Under the seismic isolation obtained by structural optimization, the pier columns and piles can be maintained un-cracked under OBE hazard level and only slightly damaged under MCE hazard level. Here slight damage to pier column means the moment demand on pier column is less than the expected moment capacity, which is defined as the moment corresponding to extreme unconfined concrete fiber reaching strain of -0.004 or extreme tensile longitudinal bar reaching strain of 1%. The conditional mean demand on MCE of the total base shear force in the transverse direction is reduced to be 9473kips (0.27W) compared to 17539.43kips (0.49W) for traditional bridge design without seismic isolation. The initial isolator design is excluded as it violates the isolation deformation constraint and rail stress constraints imposed.

$$\underset{\substack{34.1kips \le F_y \le 204.7kips \\ 120kips/in \le K_1 \le 740kips/in}}{\textbf{\textit{Minimize}}} \quad \text{conditional mean: } E\left[F_{trans.}^{\text{TBS, all columns}} \mid OBE\right]$$

$$(1)\ E\left[AA_{trans.}^{deck} \mid OBE\right] \le 0.35g$$

$$(2)\ Pctl.^{95th}\left[AA_{trans.}^{deck} \mid OBE\right] \le 0.5g$$

$$(3)\ Pctl.^{95th}\left[M_{trans.}^{P\#5} \mid OBE\right] \le M_{cr}^{pier}(1.5\times10^{4}kips\text{-}ft)$$

$$(4)\ Pctl.^{95th}\left[M_{trans.}^{piles,\ P\#5} \mid OBE\right] \le M_{cr}^{pile}(5.3\times10^{3}kips\text{-}ft)$$

$$(5)\ Pctl.^{95th}\left[\sigma_{P}^{rail,\ \text{abut.}} \mid OBE\right] \le 12.5ksi \qquad (8.19)$$

$$(6)\ \eta\left[\sigma_{P+M}^{rail,\ \text{abut.}} \mid OBE\right] \le 42.5ksi$$

$$(7)\ Pctl.^{95th}\left[\Theta_{trans.}^{P\#5} \mid MCE\right] \le 1.3\%$$

$$(8)\ Pctl.^{95th}\left[disp._{trans.}^{Isolator\#13} \mid MCE\right] \le 20in$$

$$(9)\ Pctl.^{95th}\left[M_{trans.}^{P\#5} \mid MCE\right] \le M_{e}^{pier}(4.15\times10^{4}kips\text{-}ft)$$

$$(10)\ Pctl.^{95th}\left[M_{trans.}^{piles,\ P\#5} \mid MCE\right] \le M_{e}^{pile}(1.2\times10^{4}kips\text{-}ft)$$

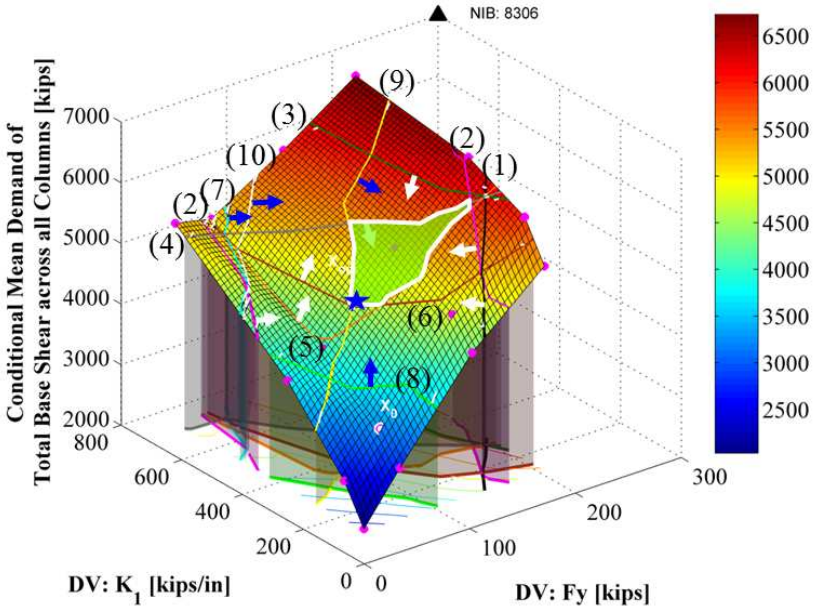

Figure 8.6: Structural optimization solution to the optimization problem formulated for probabilistic performance-based design with constraints on OBE & MCE

8.4.2. Structural optimization for seismic performance of continuous hazard levels: the unconditional seismic demand hazard

Instead of controlling the conditional probability for seismic demand under the considered events given a prescribed hazard level (e.g., OBE, MCE) as usually specified in the current design codes, direct seismic risk management on the seismic demand hazard is another alternative. The probabilistic seismic demand hazard is quantified by the second step of PBEE analysis, convolving the conditional seismic demand hazard with the probabilistic seismic hazard of seismic events.

Herein, a structural optimization problem is formulated in the stage of probabilistic seismic demand hazard analysis with the following constraints enforced for an expected probabilistic seismic performance.

$$E\left[AA_{trans.}^{deck}\right]=\mu_{EDP} <= 0.5g \tag{8.20}$$

$$Pctl.^{95th}\left[AA_{trans.}^{deck}\right]=\arg_{edp}\left\{edp \mid P\left[EDP>edp\right]:=0.05\right\} <= 1.0g \tag{8.21}$$

in which the EDP is the maximum absolute deck acceleration of bridge deck over pier column #5 in the transverse direction of the bridge, $AA_{trans.}^{deck}$.

$$Pctl.^{95th}\left[disp._{trans.}^{Isolator\#13}\right]=\arg_{edp}\left\{edp \mid P\left[EDP>edp\right]:=0.05\right\} <= 20.0in \tag{8.22}$$

in which the EDP is the maximum isolator deformation of seismic isolator over pier column #5 in the transverse direction of the bridge, $disp._{trans.}^{Isolator\#13}$.

$$E\left[\sigma_P^{rail,\ abut.}\right]=\mu_{EDP} <= 12.5ksi \tag{8.23}$$

in which the EDP is the maximum axial rail stress at the left abutment gap, $\sigma_P^{rail,\ abut.}$.

$$Pctl.^{95th}\left[\Theta_{trans.}^{P\#5}\right]=\arg_{edp}\left\{edp \mid P\left[EDP>edp\right]:=0.05\right\} <= 0.0015 \tag{8.24}$$

in which the EDP is the maximum relative end rotation of bottom element in pier column #5 in the transverse direction of the bridge, $M_{trans.}^{P\#5}$.

$$Pctl.^{95th}\left[M_{trans.}^{P\#5}\right] = \arg_{edp}\left\{edp \mid P\left[EDP > edp\right] := 0.05\right\} <= 41500 kips\text{-}ft \tag{8.25}$$

in which the EDP is the maximum bottom bending moment of pier column #5 , $M_{trans.}^{P\#5}$, in the transverse direction of the bridge.

The risk feature ALC defined in Chapter 7 is a good indicator of the overall demand risk measure over a continuous range of demand hazard levels. Thus, the ALC between the 100-year probability of exceedance 86% (i.e., 14th percentile) and 10% (i.e., 90th percentile) for the probabilistic seismic hazard curve of total base are used for the objective function. The formulated optimization problem is:

$$\begin{aligned}
&\underset{\substack{34.1kips \le F_y \le 204.7kips \\ 120kips/in \le K_1 \le 740kips/in}}{\textbf{\textit{Minimize}}} \quad ALC_{PE100=0.1}^{PE100=0.86}\left[F_{trans.}^{\text{TBS, all columns}}\right] \\
&(1)\ E\left[AA_{trans.}^{deck}\right] \le 0.5g \\
&(2)\ Pctl.^{95th}\left[AA_{trans.}^{deck}\right] \le 1.0g \\
&(3)\ Pctl.^{95th}\left[disp._{trans.}^{Isolator\#13}\right] \le 20in \\
&(4)\ E\left[\sigma_P^{rail,\ \text{abut.}}\right] \le 12.5ksi \\
&(5)\ Pctl.^{95th}\left[\Theta_{trans.}^{P\#5}\right] \le 0.15\% \\
&(6)\ Pctl.^{95th}\left[M_{trans.}^{P\#5}\right] \le M_e^{pier}(4.15\times10^4 kips\text{-}ft)
\end{aligned} \tag{8.26}$$

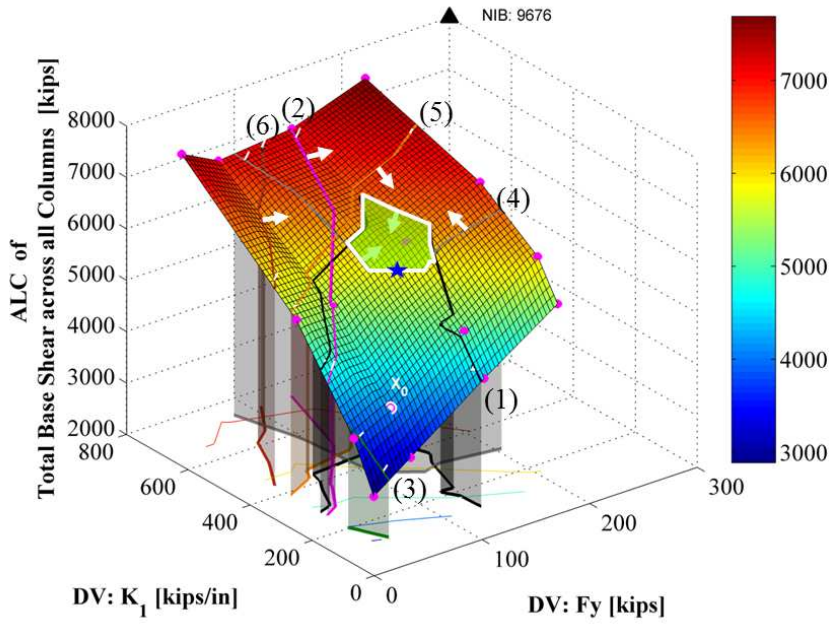

Figure 8.7: Structural optimization solution to the problem formulated for continuous hazard levels based on the unconditional seismic demand hazard with the objective function as the ALC of total base shear in the trans. dir. of the CHSR prototype bridge

The solution to optimization problem formulated with this objective function is illustrated in Figure 8.7. It shows that all the probabilistic design constraints are satisfied here with the optimizers lying on the boundary of constraint imposed on axial rail stress. The probabilistic design constraints plays a significant role on the optimal design in that the objective function selected is almost linear, which leads to the optimum occurs on the active constraints boundaries.

8.4.3. Structural optimization for seismic performance based on the mean demand and variance demand

Mean-variance optimization (MVO) in financial engineering, devised by economist Harry M. Markowitz with his famous Markowitz's modern portfolio theory (MPT), has been widely used as a quantitative tool in portfolio selection by assessing the trade-off between risk

and return in order to maximizing the return while minimizing the risk (with the standard deviation as the risk metric). An optimization problem based on the mean and the variance of seismic demand could be formulated to guide the decision makers with different utilities (i.e., risk averse and risk adverse). Naturally, for decision makers in the structural design practice, a structural design is expected to experience smaller seismic demand that carries the same or fewer uncertainties in terms of coefficient of variation. Here optimization problems are formulated in such a way that the mean demand is to be minimized with or without other probabilistic design constraints besides the constraints on the coefficient of variation of the seismic demand.

Probabilistic performance-based optimization on conditional mean with constraints on the conditional variance

While optimizing the seismic demand risk to the EDP (total base shear force in the transverse direction of the bridge) in terms of the conditional mean demand on OBE hazard level, the conditional variance of the EDP is also constrained to be less than 30% of the mean demand for seismic risk management (i.e., coefficient of variation, c.o.v., less than 0.3):

$$c.o.v.\left[F_{trans.}^{\text{TBS, } all\ columns} \mid OBE \right] \le 0.3 \tag{8.27}$$

As shown in the solution illustrated in Figure 8.8, the additional constraint on the conditional variance of the EDP could eliminate some design alternatives, which implies the conflicting behavior of the mean demand and the c.o.v..

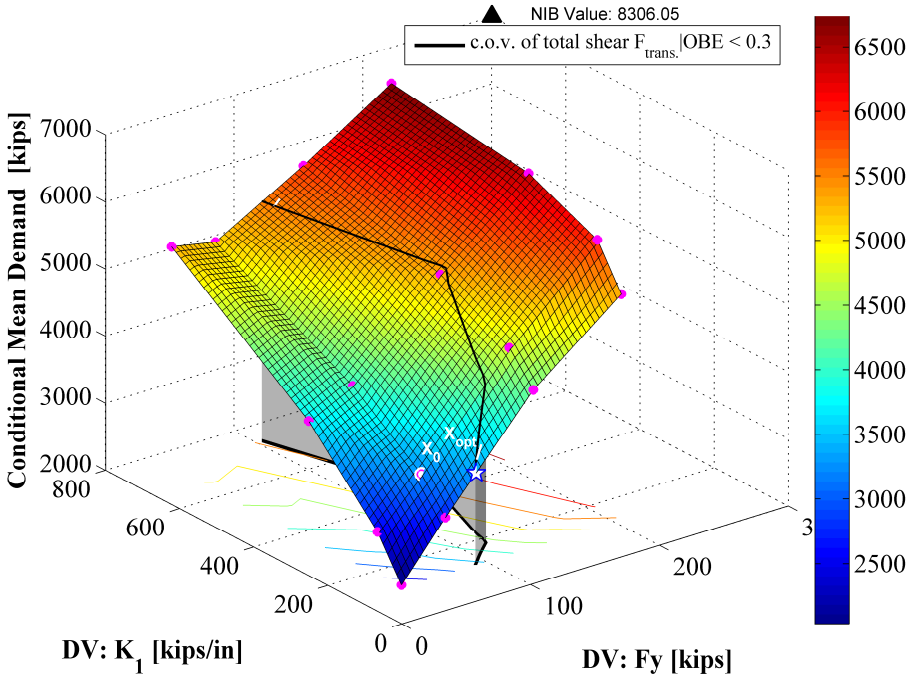

Figure 8.8: Structural optimization solution to the problem formulated to minimize the conditional mean demand with the constraints on conditional demand variance on OBE hazard level

Therefore, in the probabilistic performance-based structural optimization problem presented previously to minimize the conditional mean demand on the total base shear force in the transverse direction, an additional constraint on the conditional variance can be imposed for more robust design, other than the probabilistic design constraints specified. Compared to the previous optimum design when no constraint is imposed on the variance, the optimum objective function is increased a little bit as a sacrificial result after enforcing the additional constraint on the variance of the EDP used for objective function, as shown in Figure 8.9.

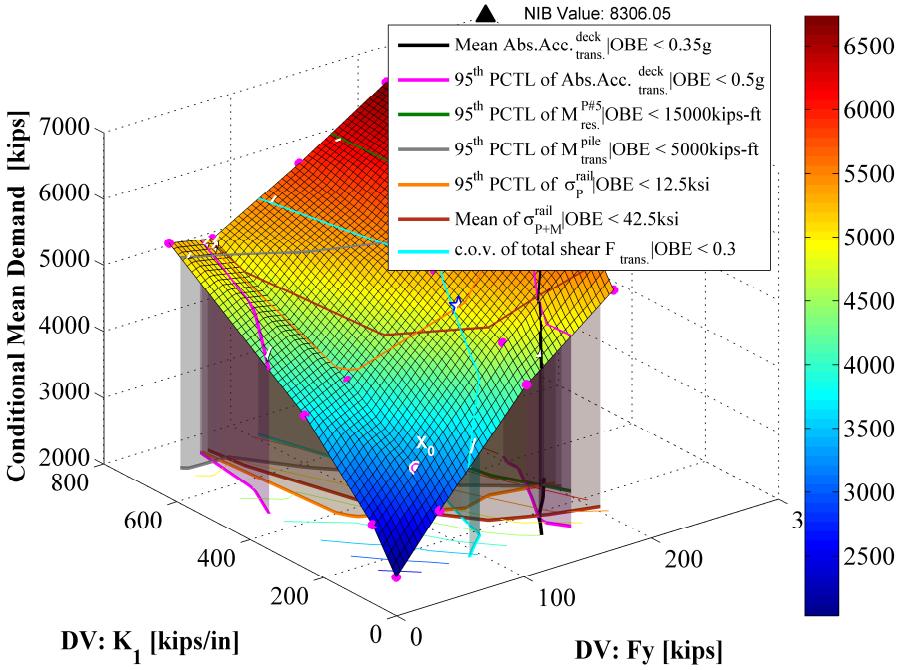

Figure 8.9: Structural optimization solution to the problem formulated to minimize the conditional mean demand with the constraints on conditional demand variance on OBE hazard level and other constraints

Probabilistic performance-based optimization on unconditional mean with constraints on the unconditional variance

In the probabilistic performance-based structural optimization carried out on unconditional seismic demand hazard to minimize the unconditional mean of EDP (i.e., total base shear of the bridge in the transverse direction), an additional constraint on the unconditional variance of the EDP can be enforced,

$$c.o.v.\left[F_{trans.}^{\text{TBS, all columns}}\right] \le 0.4 \tag{8.28}$$

and the solution is demonstrated in Figure 8.10, which implies the conflicting behavior of the mean demand and the c.o.v..

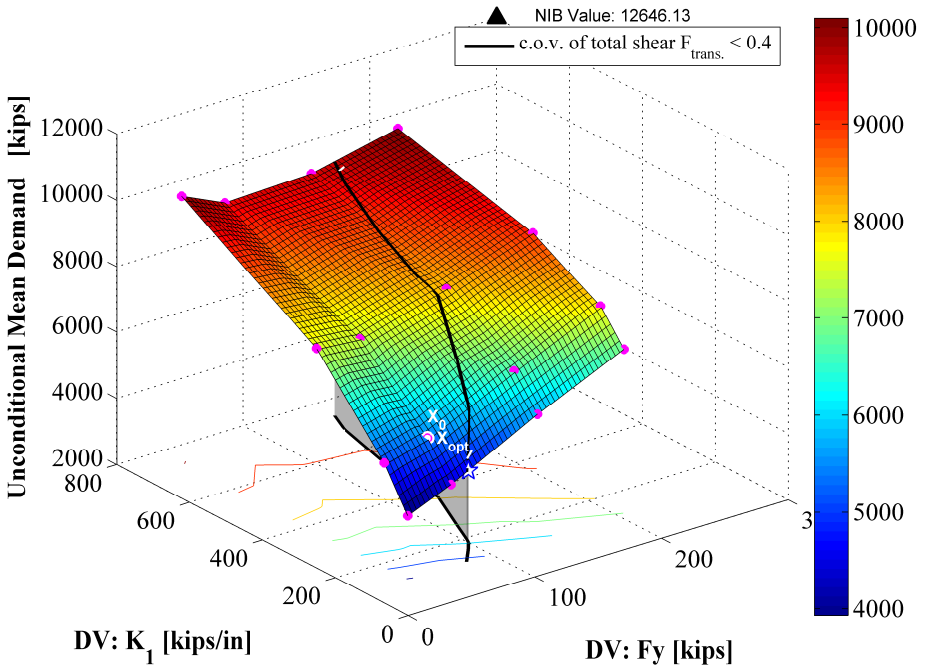

Figure 8.10: Structural optimization solution to the problem formulated to minimize the unconditional mean demand with the constraints on unconditional demand variance hazard level and other constraints

This additional constraint can also be applied to the optimization problem formulated with some other probabilistic constraints defined earlier on the unconditional probabilistic seismic demand hazard. The solution to the optimization problem is illustrated in Figure 8.11, which shows that the constraint actually did not change the optimum solution.

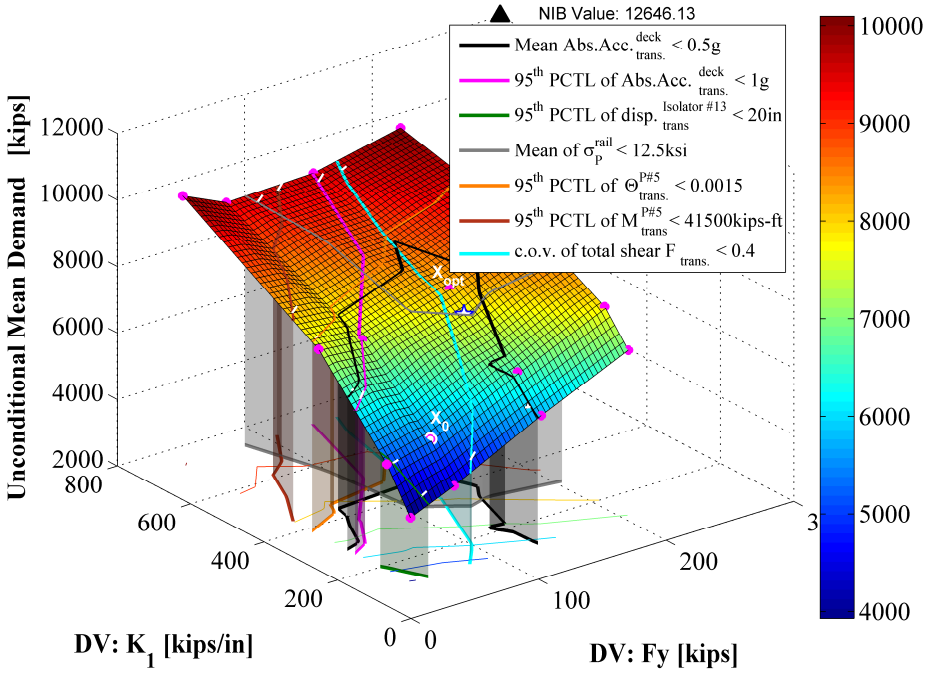

Figure 8.11: Structural optimization solution to the problem formulated to minimize the unconditional mean demand with the constraints on unconditional demand variance and other constraints

8.5. Optimum Design Evaluation

To make sure that the PPBOSD methodology yields structures with predictable optimal seismic performance, a probabilistic seismic demand analysis is followed for the optimum design obtained when minimizing the conditional mean demand of total base shear on OBE with constraints prescribed on OBE and MCE hazard levels. Probabilistic seismic demand hazard analysis is performed for the CHSR Prototype Bridge with the optimum seismic isolator with yield strength 98.95kips and initial yield stiffness of 368.0kips/in. The probabilistic seismic demand analysis results for some representative EDPs for the IB with optimum isolator design are compared with the counterpart for the NIB and the IB with initial design as follows.

Figure 8.12 to Figure 8.13 summarizes the comparison in terms of conditional and unconditional probabilistic seismic demand hazard for the EDP: the absolute deck acceleration over pier #5 in transverse direction of the bridge. They are the conditional median demand, conditional PDF of seismic demand with 95th percentiles marked on OBE and MCE hazard levels, conditional CCDF of demand on OBE and MCE hazard levels, and the probabilistic seismic demand hazard curves. It is observed that the optimization process drove the conditional median demand curve (Figure 8.12: left) and the unconditional seismic demand curve (Figure 8.13: right) to the right with higher risk, but still far away left to the NIB case. This implies the optimum isolator design did reduce the acceleration demand compared to the NIB effectively, but compared to the IB with initial isolator design, the optimization process sacrifice the reduction effect slightly, especially for high seismic hazard levels for conditional demand (Figure 8.12: right, Figure 8.13: left) and high demand hazard levels for unconditional demand (Figure 8.13: right).

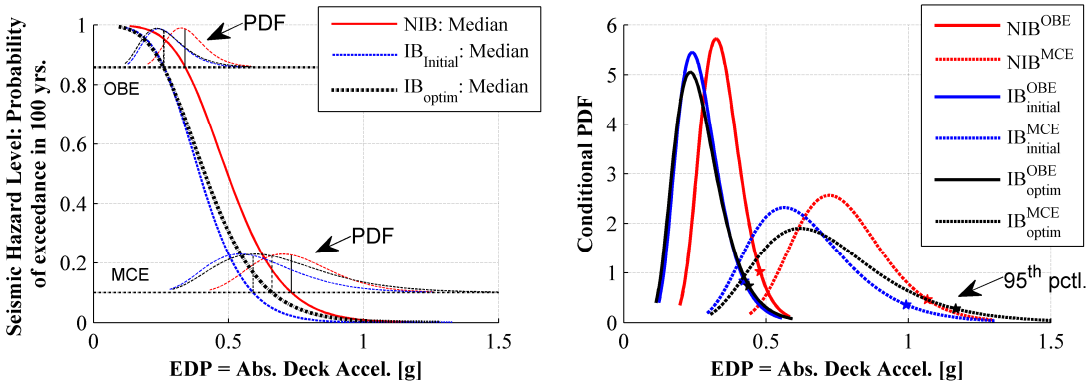

Figure 8.12: Conditional median demand on all continuous seismic hazard levels (left) and conditional PDF of demand on OBE and MCE hazard level (right) for the EDP of the absolute acceleration at deck over pier #5 in the transverse direction

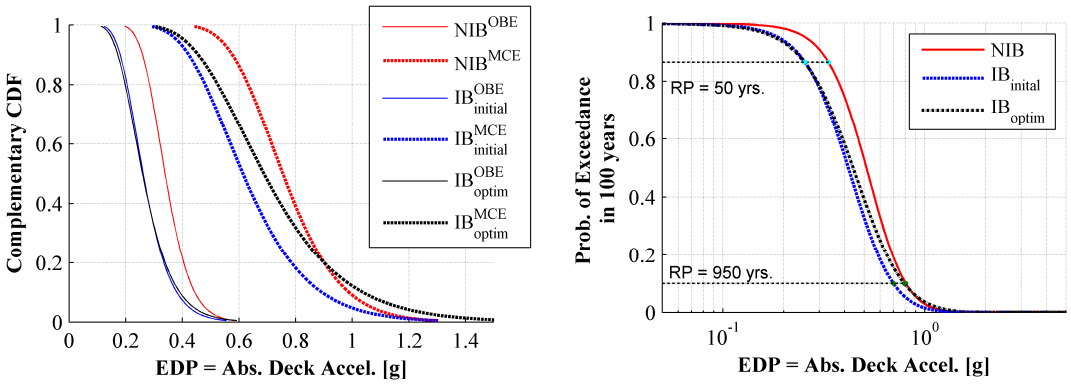

Figure 8.13: Conditional CCDF of demand on OBE and MCE hazard level (left) and unconditional probabilistic seismic demand hazard curves for the EDP of the absolute acceleration at deck over pier #5 in the trans. dir.

Figure 8.14 to Figure 8.15 presents the conditional and unconditional probabilistic seismic demand hazard for the EDP: the maximum deformation of isolator over pier #5 in the longitudinal direction of the bridge. The conditional and unconditional probabilistic seismic demand hazard for the EDP: the maximum deformation of isolator over pier #5 in the transverse direction of the bridge is presented in Figure 8.16 to Figure 8.17.

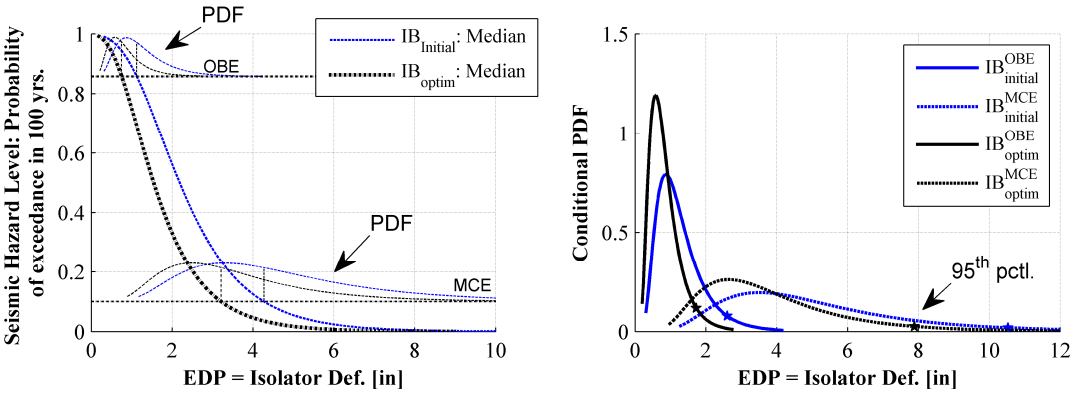

Figure 8.14: Conditional median demand on all continuous seismic hazard levels (left) and conditional PDF of demand on OBE and MCE hazard level (right) for the EDP of the maximum deformation in the isolator over pier #5 in the long. dir.

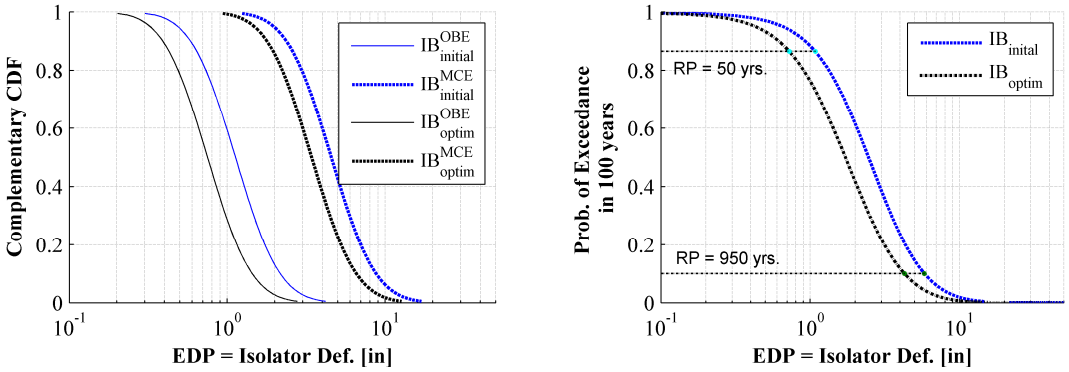

Figure 8.15: Conditional CCDF of demand on OBE and MCE hazard level (left) and unconditional probabilistic seismic demand hazard curves for the EDP of the maximum deformation in the isolator over pier #5 in the long. dir.

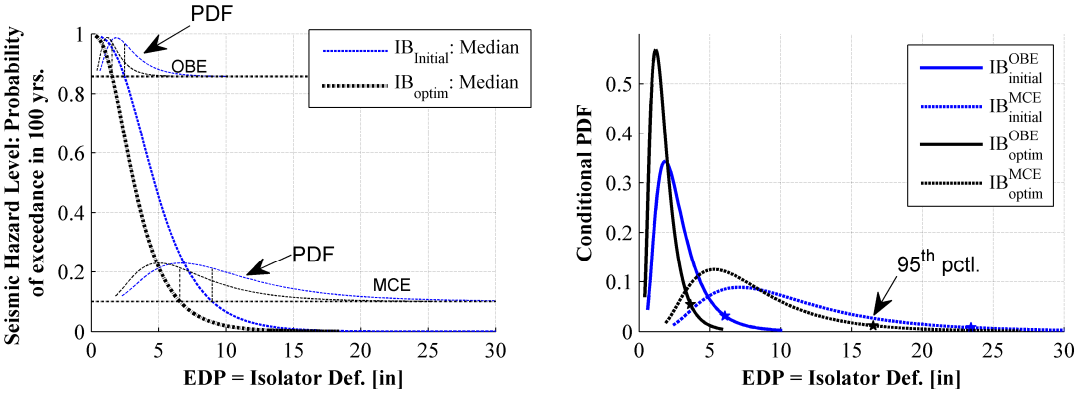

Figure 8.16: Conditional median demand on all continuous seismic hazard levels (left) and conditional PDF of demand on OBE and MCE hazard level (right) for the EDP of the maximum deformation in the isolator over pier #5 in the trans. dir.

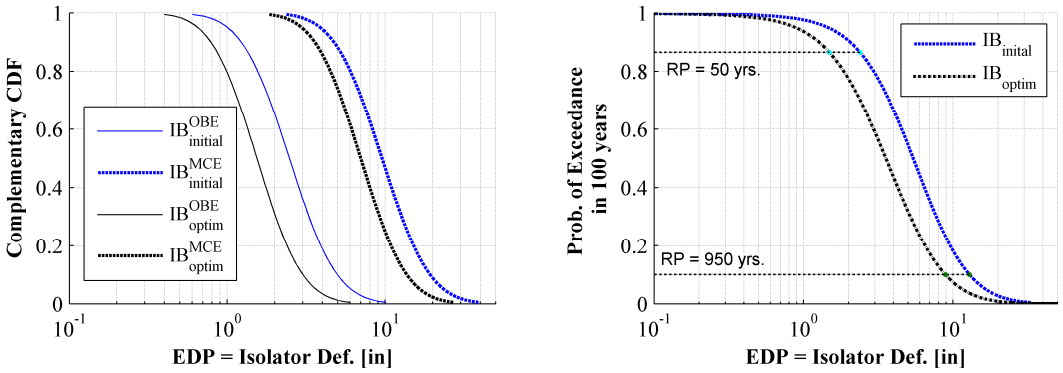

Figure 8.17: Conditional CCDF of demand on OBE and MCE hazard level (left) and unconditional probabilistic seismic demand hazard curves for the EDP of the maximum deformation in the isolator over pier #5 in the trans. dir.

The difference in the probabilistic seismic demand in terms of isolator deformation is shown to compare the optimal seismic isolator design with the initial isolator design. To achieve the probabilistic performance stated in the optimization problem formulation, see Equation (8.19), a relative stiffer seismic isolator with less deformation demand is desired.

Figure 8.18 to Figure 8.19 shows the comparison in terms of conditional and unconditional probabilistic seismic demand hazard for the EDP: the maximum column base moment of pier #5 in the transverse direction. Higher seismic demand risk to this EDP is imposed on the optimum design compared with the initial design of seismic isolators, while much lower seismic risk is imposed compared with the NIB in terms of all these probabilistic measures. Significant benefits are observed by seismic isolation, which reduced the conditional seismic hazard on MCE hazard level to the conditional seismic hazard on MCE hazard level in NIB in terms of the median demand, but with larger conditional variance.

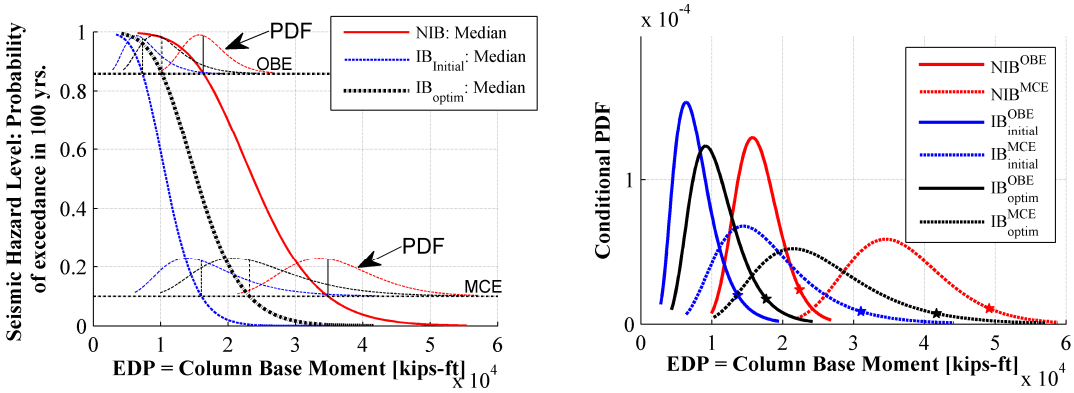

Figure 8.18: Conditional median demand on all continuous seismic hazard levels (left) and conditional PDF of demand on OBE and MCE hazard level (right) for the EDP of the maximum bottom moment of pier #5 in the trans. dir.

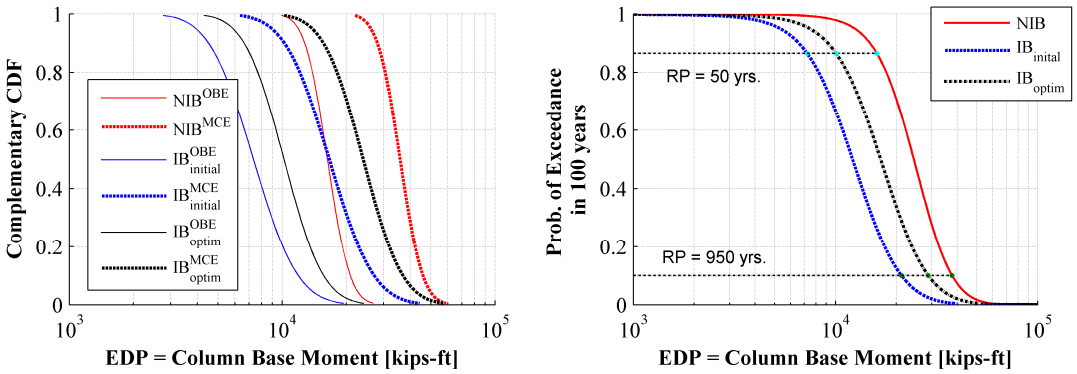

Figure 8.19: Conditional CCDF of demand on OBE and MCE hazard level (left) and unconditional probabilistic seismic demand hazard curves for the EDP of the maximum bottom moment of pier #5 in the trans. dir.

Figure 8.20 to Figure 8.21 shows the comparison in terms of conditional and unconditional probabilistic seismic demand hazard for the EDP: the relative end rotation of bottom element of pier #5 in the transverse direction. Similar observation can be made related to the results of the bottom moment above.

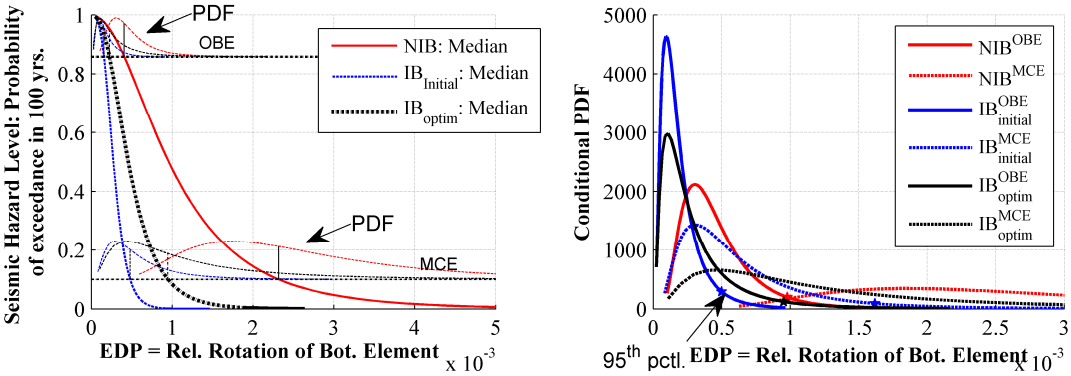

Figure 8.20: Conditional median demand on all continuous seismic hazard levels (left) and conditional PDF of demand on OBE and MCE hazard level (right) for the EDP of the maximum relative end rotation of bottom element of pier #5 in the trans. dir.

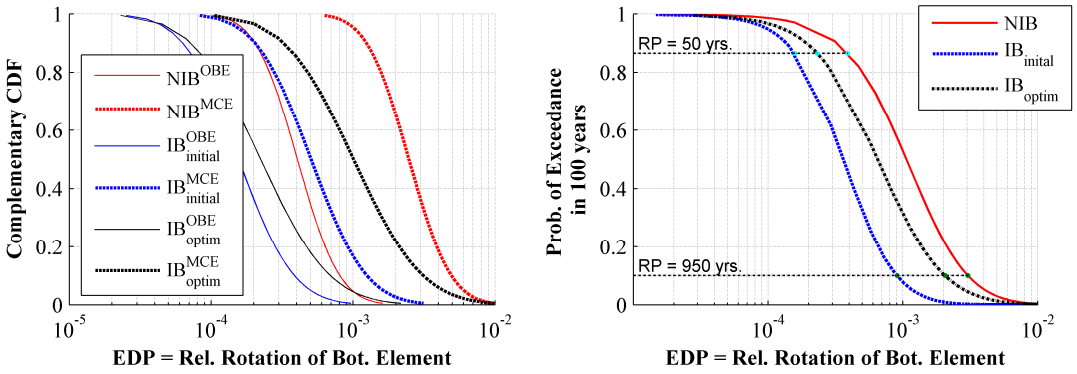

Figure 8.21: Conditional CCDF of demand on OBE and MCE hazard level (left) and unconditional probabilistic seismic demand hazard curves for the EDP of the maximum relative element end rotation of bottom of pier #5 in the trans. dir.

Figure 8.22 to Figure 8.23 shows the comparison in terms of conditional and unconditional probabilistic seismic demand hazard for the EDP: the maximum total base shear across all columns in the longitudinal direction of the bridge. Significant benefit of seismic isolation can be observed with the optimum seismic design to strike a trade-off, thus the seismic hazard sitting between the seismic hazards of NIB and initial IB.

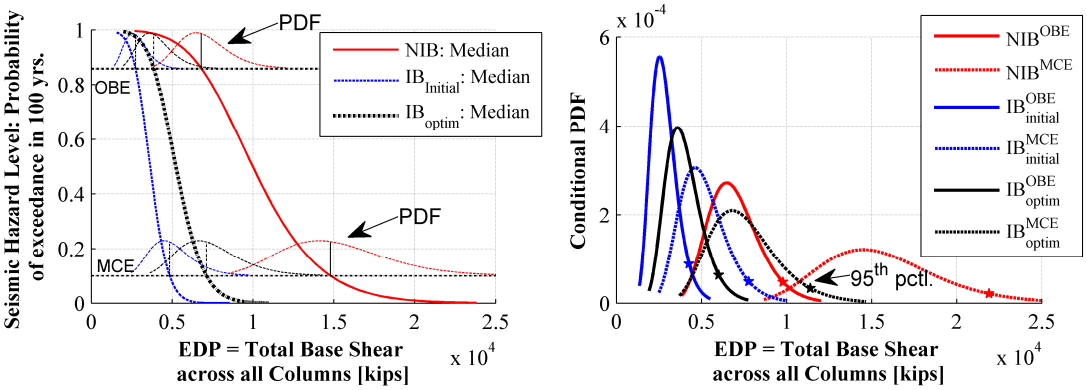

Figure 8.22: Conditional median demand on all continuous seismic hazard levels (left) and conditional PDF of demand on OBE and MCE hazard level (right) for the EDP of the maximum total base shear across all columns in long. dir.

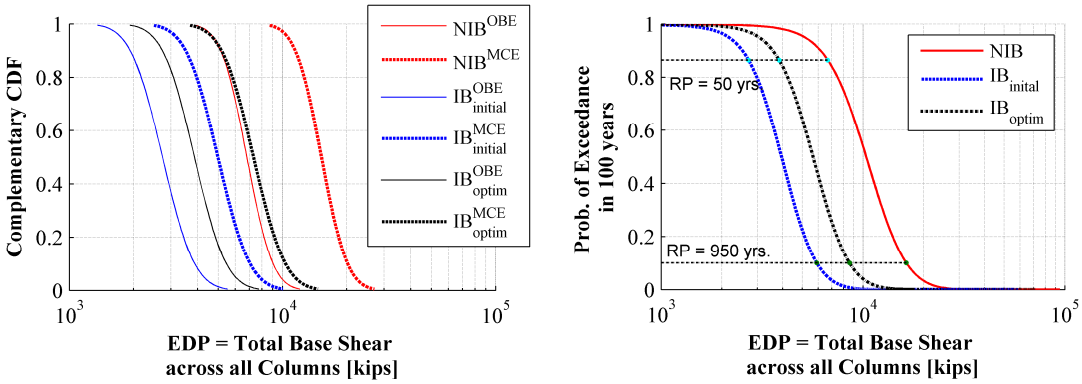

Figure 8.23: Conditional CCDF of demand on OBE and MCE hazard level (left) and unconditional probabilistic seismic demand hazard curves for the EDP of the maximum total base shear across all columns in longitudinal direction

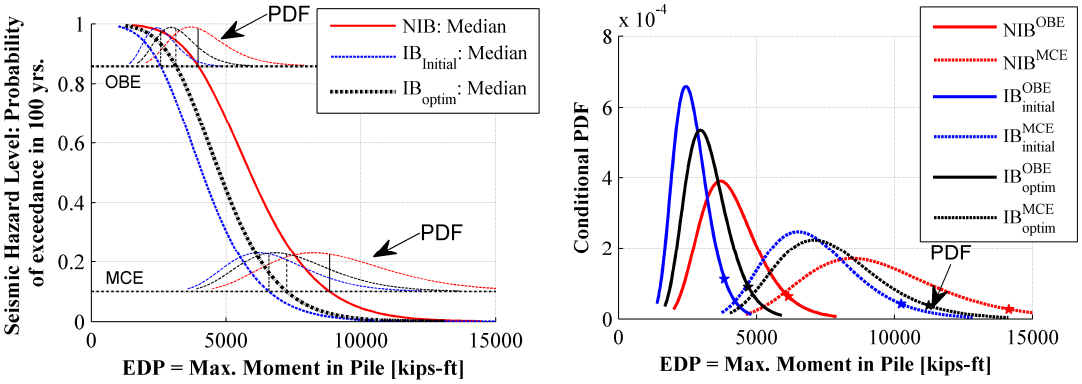

Figure 8.24: Conditional median demand on all continuous seismic hazard levels (left) and conditional PDF of demand on OBE and MCE hazard level (right) for the EDP of pile moment under pier #5 in the trans. dir.

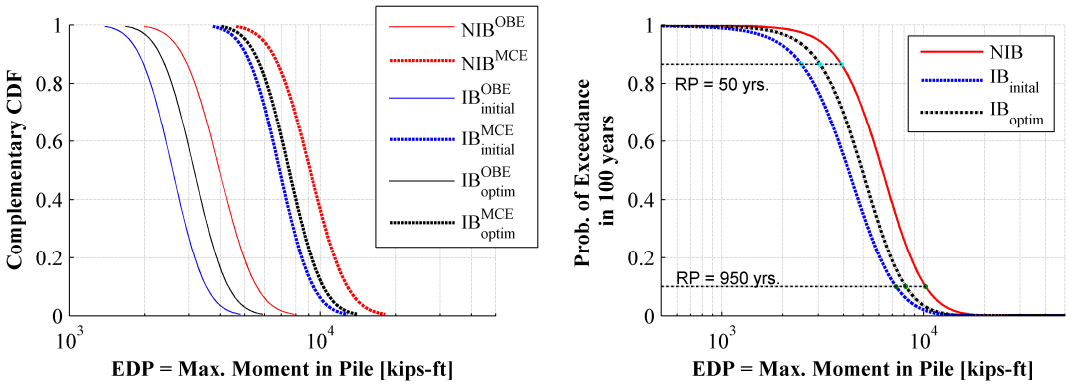

Figure 8.25: Conditional CCDF of demand on OBE and MCE hazard level (left) and unconditional probabilistic seismic demand hazard curves for the EDP of pile moment under pier #5 in the trans. dir.

Figure 8.24 to Figure 8.25 shows the comparison in terms of conditional and unconditional probabilistic seismic demand hazard for the EDP: the maximum pile moment under pier #5 in the transverse direction of the bridge. Similar to the seismic demand hazard to total base shear across all columns and bottom moment of pier columns, the optimum design is imposed with higher seismic demand risk than initial design, but lower seismic demand risk than NIB. In contrast, the seismic risk mitigation effect of seismic isolation on piles is not as efficient as in reducing the seismic demand on pier columns above. This is explained that the reduction of seismic isolation on force demand for pier columns more than piles with a more complex effects including inertial effect and kinematic effects.

Figure 8.26 to Figure 8.27 shows the comparison in terms of conditional and unconditional probabilistic seismic demand hazard for the EDP: the maximum rail stress at abutment gap #1 due to axial force and bending moments, to reflect the improve of rail stress demand hazard compared to the initial design of seismic isolation.

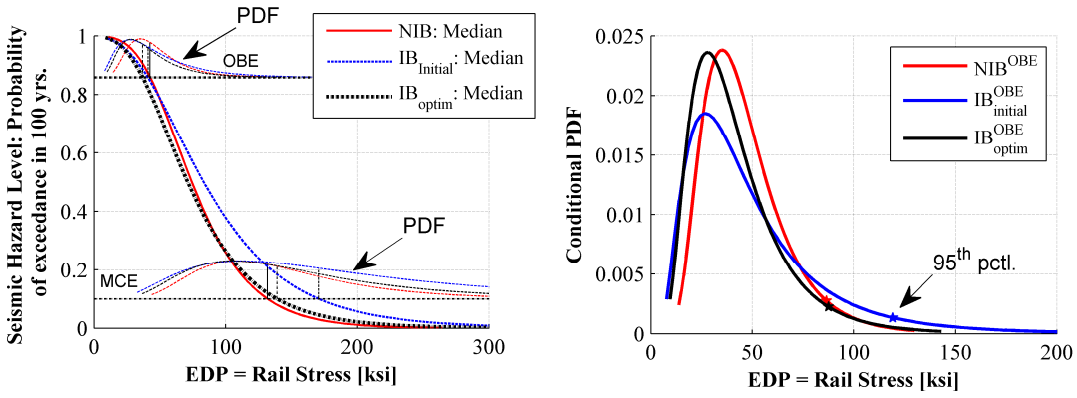

Figure 8.26: Conditional median demand on all continuous seismic hazard levels (left) and conditional PDF of demand on OBE and MCE hazard level (right) for the EDP of rail stress at abutment gap #1 due to axial force and bending moments

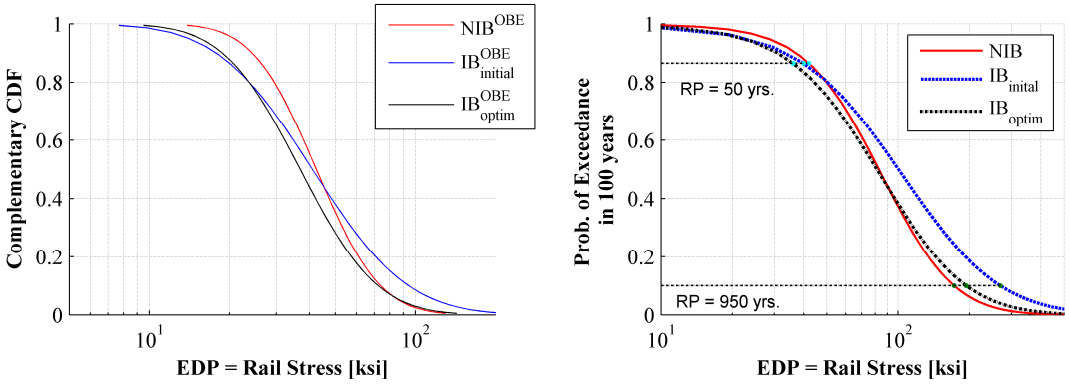

Figure 8.27: Conditional CCDF of demand on OBE and MCE hazard level (left) and unconditional probabilistic seismic demand hazard curves for the EDP of rail stress at abutment gap #1 due to axial force and bending moments

8.6. Conclusions

This chapter mainly focused on the formulations and solutions of the PPBOSD problems for seismic isolators in the California High-Speed Rail (CHSR) Prototype Bridge. A significant flexibility in the formulation of the PPBOSD problems addressing various design needs are explored, which allows considering various performance objectives. The performance objectives can be established across various EDPs, various risk features (e.g., mean, median, percentiles, probability exceeding a certain EDP value, weighted hazard values, area under the hazard curve, etc.), multiple seismic hazard levels, different performance evaluation stages (e.g., conditional probabilistic seismic demand analysis, unconditional probabilistic seismic demand analysis). Several candidates of the possible optimization problems are formulated for the CHSR Prototype Bridge to resolve the conflicts in the beneficial and detrimental effects of seismic isolation. As an alternative to avoid the demanding computational work for large-scale engineering problem, the solution of the PPBOSD problem is collapsed into two steps in this chapter: step (1) is using grid-based "brute-force" (i.e., parametric graphic approach) to find the optimum design; step (2) is

evaluate the optimum design by the comparison between the optimum design and the initial design as well as the NIB. The evaluation of the optimum design shows that higher seismic demand risk of substructures and pile foundations is imposed compared to the initial design of IB, while limiting the detrimental effects of seismic isolation (i.e., additional rail stresses). The improvement in maximizing the beneficial effects of seismic isolation in the optimum seismic design under PPBOSD is still significant compared to the NIB.

References

California High-speed Rail Authority (CHSRA). (2012). *California High-speed Train Project Design Criteria*, San Francisco, California.

Ellingwood, B. R., and Leyendecker, E. V. (1978). "Approaches for design against profressive collapse." *J. Struct. Div.*, 104(3), 413-423.

Ellingwood, B. R., and Corotis, R. B. (1991). "Load combinations for buildings exposed to fires." *Engineering Journal*, ASIC, 28(1), 37-44.

Ellingwood, B. R., and Dusenberry, D. O. (2005). "Building design for abnormal loads and profressive collapse." Computer-Aided Civil and Infrastruct. Engrg. 20(5), 194-205.

Bibel G.. (2012). *Train wreck, the forensics of rail disasters*, The Johns Hopkins University Press, http://www.scientificamerican.com/article/the-physics-of-disaster/

CHAPTER 9

CONCLUSIONS AND FUTURE WORK

9.1. Summary of Research Work

Building on the PEER Performance-based Earthquake Engineering (PBEE) methodology, this dissertation proposes a probabilistic performance-based optimum seismic design (PPBOSD) methodology and applies it to a California high-speed rail (CHSR) prototype bridge system. The following research objectives were accomplished:

(i) implementation of the PEER PBEE methodology, which is at the heart of the proposed PPBOSD framework;

(ii) formulation and implementation of the proposed PPBOSD framework and application to a nonlinear single-degree-of-freedom (SDOF) system for illustration, verification and validation purposes;

(iii) design and detailed modeling of a CHSR prototype bridge considering track-structure-interaction (TSI) and soil-foundation-structure-interaction (SFSI);

(iv) investigation and performance evaluation of seismic isolation for a CHSR prototype bridge in a deterministic and probabilistic setting, respectively;

(v) a parametric probabilistic study of the seismic isolated CHSR prototype bridge using cloud-based high throughput computing platform to investigate the topology of the objective and constraint functions and of the feasible

domain in the design parameter space for various risk-based performance metrics;

(vi) formulation of well-posed optimization problems for the seismic isolation design of a CHSR prototype bridge using the proposed PPBOSD framework.

This research project addressed key needs for advancing the application of the PBEE methodology to probabilistic performance-based optimum seismic design aiming at reducing the seismic risk of civil infrastructure systems. The major components and accomplishments of this research project are outlined below.

9.1.1. Implementation of PEER performance-based earthquake engineering (PBEE) methodology

To develop a robust probabilistic performance evaluation tool requires several components. Thus, a PBEE package is implemented in MATLAB by integrating probabilistic seismic hazard analysis, probabilistic seismic demand hazard analysis, probabilistic seismic damage hazard analysis, and probabilistic seismic loss hazard analysis. These analysis steps consist of assessing probabilistically the earthquake intensity measure (IM), the structural response, the structural damage, and the loss (e.g., death, repair/replacement cost, and downtime). A PBEE analysis was performed on a nonlinear SDOF bridge model (deduced from a detailed nonlinear FE model of an actual bridge) to illustrate the various steps and the functionality of the implemented PBEE methodology. The PBEE software package is an essential ingredient of the proposed PPBSOD framework.

9.1.2. Formulation and implementation of the proposed PPBOSD framework and application to a nonlinear SDOF system for illustration, verification and validation

Traditional PBEE methodology, which will heretofore be referred to as a "PBEE analysis", has been widely accepted as a probabilistic seismic performance evaluation approach. To extend this framework for "performance-based design" purposes, an inverse PBEE analysis was proposed by integrating the forward PBEE analysis with an optimization layer, resulting in a probabilistic performance-based optimum seismic design (PPBOSD) methodology. The supporting software framework integrates a FE analysis software (e.g., OpenSees), and an optimization tool (e.g., SNOPT), and the PBEE analysis software developed in Matlab. For illustration purposes, a nonlinear inelastic SDOF structural system (representing the longitudinal seismic response behavior of an actual bridge system) was optimized iteratively so as to yield a target loss hazard curve. The PPBOSD software framework was validated by its successful application to the nonlinear SDOF bridge model. This simple example illustrates the power of the proposed PPBOSD methodology in designing civil infrastructure systems for risk-based performance objectives.

9.1.3. Design, modeling, and seismic response simulation of CHSR prototype bridge considering track-structure interaction (TSI) and soil-foundation-structure-interaction (SFSI)

A CHSR prototype bridge was selected as a test-bed to show the potential of applying the proposed PPBOSD methodology to a real-world structure. A 9-span CHSR prototype isolated bridge was designed according to the code for the California High-Speed Train Project in collaboration with senior engineers at Parsons Brinckerhoff and Bridge Seismic Specialist Roy A. Imbsen from Earthquake Protection Systems, Inc. A detailed three-

dimensional FE model of the bridge system was developed in OpenSees, which accounts for track-structure-interaction (TSI) and soil-foundation-structure-interaction (SFSI). SFSI was modeled using the dynamic *p-y* approach, which was validated by centrifuge tests conducted at the University of California, Davis.

Pertinent nonlinear modeling and dynamic analysis techniques (e.g., multiple-support-excitation with a Rayleigh damping model) were investigated theoretically and numerically. Since *p-y*/*t-z*/*q-z* springs were used to capture SFSI effects, multiple-support-excitation (MSE) was required for the seismic response simulation of the proposed CHSR prototype bridge. A sufficient and necessary condition was derived for the damping model to produce the same seismic response under the uniform excitation and multiple-support-excitation formulations. The mass proportional part of the Rayleigh damping model does not satisfy that condition. However, in the case of the CHSR prototype bridge analyzed herein, when using the Rayleigh damping model (with both mass and stiffness proportional terms), the difference in seismic response of the bridge between the uniform excitation and multiple-support-excitation formulations is negligible.

For realistic and reliable seismic response simulation under earthquake ground motions of a wide range of intensities, it is important to account for soil-pile-structure interaction. The seismic response of a sub-structure of the bridge consisting of a bridge pier (with lumped mass at its top) and a pile group foundation was analyzed with and without SFSI (i.e., pier fixed at the bottom in one model and soil-pile-pier subsystem modeled using the p-y approach). The SFSI effects were found to be significant. It was also found that the effect of the variation with depth of the multiple support (*p-y* spring) excitations, especially for large intensity free-field ground motion records, on the bridge response can be significant. Large

force demands were observed in the deeper part of piles under MCE events due to the kinematic effect of SFSI.

9.1.4. Deterministic and probabilistic performance evaluation of seismic isolation for the CHSR prototype bridge system

Seismic isolation was incorporated in the numerical model developed for the CHSR prototype bridge in order to investigate its beneficial and detrimental effects on the performance of the bridge system and the track system connected to it. Both far-field and near-field earthquake ground motions were considered in a deterministic investigation at two hazard levels (OBE and MCE) under a single earthquake scenario. The beneficial and detrimental effects of incorporating seismic isolation are summarized below. When incorporating seismic isolation,

(1) the deck acceleration decreases significantly especially for large-magnitude earthquakes if acceleration spikes due to pounding are not considered;

(2) the pier drift decreases and the horizontal deck displacement (relative to the pile cap) increases, which is due to the deformation of the seismic isolators;

(3) the seismic demands on the substructure (e.g., bottom moments of pier columns, total base shear across all bridge piers) are reduced by more than 50%, especially for large (e.g., MCE) earthquakes, thus decreasing correspondingly the seismic demand on the foundations; and

(4) the maximum stresses in the rail (especially the bensing stress caused by the transverse displacement of the bridge) increase due to the larger deck displacement. The critical locations of rail failure are located in the neighborhood of the abument gaps and interior expansion joints.

A probabilistic performance evaluation of seismic isolation was conducted for the CHSR prototype bridge system considered by computing the demand hazard curves for both the isolated and the non-isolated bridges (IB and NIB). The findings in the probabilistic performance evaluation are consistent with the observations obtained from the deterministic comparative study on the beneficial and detrimental effects of seismic isolation. Furthermore, they show that seismic isolation increases significantly the conditional or unconditional mean/median demand on maximum deck displacement (relative to the pile cap), the maximum stress in the rails at both abutment gaps and interior expansion joints except for the stress at the abutment gap due to transverse bending, because the shear keys with gaps govern the rail stress due to transverse behavior for both the IB and NIB. In the contrast, it shows that seismic isolation reduces significantly the conditional and unconditional mean/median demand (i.e., force and displacement) on bridge substructure (i.e., piers, pile foundations).

9.1.5. Cloud-based parametric probabilistic analysis and optimization framework

As discussed above, investigation of the advantages and drawbacks of seismic isolation for the CHSR prototype bridge system required a parametric probabilistic performance evaluation of the seismic isolation system. Probabilistic optimum seismic design problems were formulated to strike a balance between the beneficial and detrimental effects (expressed in the objective and constraint functions) of seismic isolation for the CHSR prototype bridge. The probabilistic performance-based optimization of the bridge system was computationally highly intensive due to the complexity of the bridge model. The optimization process included probabilistic analysis of structural system performance, which included some or all the steps of the PBEE methodology, and parametric probabilistic studies (over a grid in the design variable space for brute-force optimization) or iterations of the optimization

algorithm in the design variable space. Thus, a high-performance distributed computing strategy was adopted.

A Condor cluster, administrated by a specialized workflow management system for computationally intensive tasks, was implemented and used for the probabilistic performance optimization of an inelastic SDOF structural system. The Condor cluster is managed by a central manager on a Linux Machine and consists of a 60-core heterogeneous cluster from eight local machines in the local computer laboratory.

For the optimization of the bridge system, GlideinWMS, another workflow management system which builds on top of Condor, was also employed in this project to provide a simple and effective way to access the grid resources for parameter sweeping and optimization. A cloud-based probabilistic optimization (CBO) workflow platform was developed using distributed computing in Open Science Grid (OSG) and NEESHub. This CBO workflow platform minimized the required knowledge for using cloud computing technologies and platforms, and maximized the computational capacity (e.g., over 950 time-history-analysis jobs can be run simultaneously using the OSG cluster at the University of California, San Diego).

9.1.6. Probabilistic performance-based optimization of seismic isolation for the CHSR prototype bridge

Feasibility and optimization of seismic isolation for the CHSR prototype bridge were investigated, considering the seismic performance of the combined bridge and track system under multiple hazard levels. In order to determine the optimal force-deformation characteristics of the seismic isolators, a comprehensive parametric probabilistic analysis was performed using the CBO workflow platform described above. Based on conditional probabilistic seismic demand hazard analysis and unconditional probabilistic seismic demand

hazard analysis, two families of seismic risk features were defined. The topology of the selected risk features with respect to the isolator design parameters shows the efficiency of seismic isolation in decreasing the seismic demand risk to the bridge substructure (i.e., piers and pile foundations) at the expense of increasing the horizontal displacement of the bridge deck and seismic demand risk to the rails. However, seismic isolators with low yield strength and high initial stiffness may even result in increasing the seismic demand risk to the bridge substructure as compared to the non-isolated bridge design.

Several well-posed optimization problems were formulated with objective and constraint functions expressed in probabilistic terms to show the versatility of the proposed PPBOSD framework in determining the optimal design for a wide range of risk-based performance-based metrics included in either the objective or the constraint functions. It is shown that various risk-based performance objectives can be reached by optimum seismic design of bridge structures using the framework of PPBOSD developed herein.

9.2. Limitations of this Research Work

9.2.1. Pertinent sources of uncertainty to be considered in probabilistic performance evaluation

The first limitation lies in the pertinent sources of uncertainty to be considered in the probabilistic performance evaluation of civil infrastructure systems such as the CHSR prototype bridge considered here; only the uncertainties associated with the seismic hazard (at the assumed site with given soil conditions) and the record-to-record variability were considered herein. The uncertainties associated with the computational bridge model (modeling uncertainty), structural and soil material properties, and the various capacity terms used to define the limit-states of interest were not considered, mainly based on the premise that the uncertainties associated with the seismic hazard and the record-to-record variability

are the predominant sources of uncertainty. However, the proposed PPBOSD framework can be readily extended to take into account other sources of epistemic and aleatory uncertainty to predict more accurately the reliability or seismic risk of structures.

9.2.2. Definition of risk-based performance metrics in the context of the PEER PBEE methodology

The second limitation lies in the stage of the PEER PBEE methodology at which the risk-based performance metrics are defined for the application of the proposed PPBOSD framework. In this research, for the real-world CHSR prototype bridge testbed, these metrics were defined in terms of the demand hazard analysis results (both conditional on IM and unconditional after accounting for all IMs by convolution). However, the proposed PPBOSD framework can readily accommodate risk-based performance metrics defined at other stages of the PEER PBEE methodology, such as damage hazard analysis and decision variable (i.e., loss) hazard analysis. The performance metrics can also be defined across different PEER PBEE analysis stages.

9.2.3. Scalar intensity measure in probabilistic seismic hazard analysis and scalar EDP for demand hazard analysis and limit-state function formulation

The third limitation is that: (1) the intensity measure used to characterize probabilistically the seismic loading is reduced to a scalar intensity measure (IM), and (2) the seismic demand is characterized by scalar EDPs at the demand hazard analysis stage and in the formulation of the limit-state functions (i.e., each limit-state function is characterized by a single EDP). As already recognized by other researchers, vector intensity measures (i.e., set of statistically correlated IMs) are often needed to better characterize the seismic loading for real-world civil infrastructure systems, i.e., increase the efficiency and sufficiency of existing IMs. Examples of such vector IMs consist of spectral accelerations at multiple periods and along

different directions (e.g., longitudinal and transversal). Limit-states involving more than one EDP and considering the statistical correlation between EDPs need to be accommodated in the PEER PBEE methodology and therefore the proposed PPBOSD framework. Thus, a joint probability distribution function (PDF) of a vector of EDPs must be used for characterizing the seismic demand and limit-state functions commonly used in engineering practice.

9.2.4. Probabilistic seismic hazard accounting explicitly for near-fault ground motions

The fourth limitation also lies in the probabilistic seismic hazard characterization. Current probabilistic seismic hazard analysis results used in this research do not account explicitly for near-fault effects, even though near-fault ground motions may impose significant demand on seismic-isolated structures. This implies that, by not incorporating explicitly near-fault effects in the probabilistic seismic hazard analysis, the seismic risk predicted by the current PEER PBEE methodology may be inaccurate to some degree.

9.2.5. Optimization for probabilistic optimum seismic design of seismic isolation for CHSR prototype bridge

The formulation and solution of well-posed optimization problems for the CHSR prototype bridge considered the seismic isolator parameters only as the design variables to be optimized, without considering any of the bridge substructure parameters (e.g., diameter and steel reinforcement ratio of bridge piers, geometry and size of pile foundations). Ideally, the optimization of seismic isolators and other bridge system parameters should be performed jointly to achieve an optimum design of the whole system. In the real-world application example of a CHSR prototype bridge considered, the solution of the optimization problems formulated did not resort to computational optimization algorithms as in the case of the nonlinear inelastic SDOF structural model due to the prohibitive computational cost. A compromise in the level of complexity of the computational model of the system to be

optimized is necessary to solve the optimization problems using state-of-the-art computational optimization algorithms.

Furthermore, because it is impractical to apply the proposed PPBOSD framework to any structural system for design purposes in engineering practice due to its complexity, simplified probabilistic PBD methods need to be developed, calibrated, and validated using the PPBOSD framework developed.

9.2.6. Finite element modeling and simulation

(1) Consideration of the vertical excitation component of earthquake ground motions is necessary for a comprehensive performance evaluation of seismic isolation for the CHSR prototype bridge considered herein. This will require a more advanced seismic isolator model able to capture the coupling effects between axial and lateral (flexural and shear) behavior.

(2) Vehicle-track-structure-interaction (VTSI) analysis is of interest to decision makers (e.g., government officials) as the tool required to estimate the probability of derailment due to earthquakes. Thus, seismic response simulation of the bridge-vehicle system considering VTSI needs to be investigated.

(3) Hybrid seismic protection systems (e.g., combination of seismic isolation and passive energy dissipation such as seismic dampers) should be considered as another strategy to mitigate seismic risk to CHSR bridges.

(4) A comparative study of the SFSI effects for the seismic isolated versus non-isolated CHSR prototype bridge is of interest.

(5) The fidelity of detailed nonlinear FE models of bridges such as the one developed herein for the CHSR bridge prototype needs to be evaluated. This can be achieved through correlation studies between numerical response predictions and measured experimental/field response of bridge structures subjected to earthquakes of varying intensities. Validated high-

fidelity FE models of bridge systems can then be used to derive systematically (e.g., using sensitivity analysis) and validate simplified bridge models suited for the PPBOSD framework using computational optimization (e.g., OpenSees-SNOPT).

9.3. Recommendations for Future Research Work

The development of the newly proposed probabilistic performance-based optimum seismic design framework in the context of the PEER PBEE methodology requires further research in the following areas:

1. Appropriate selection of performance objectives (1) based on the damage hazard and loss hazard analysis results of the PEER PBEE methodology, and (2) associated with resilience (i.e., damage resistance to earthquakes) and sustainability (e.g., life cycle costs) of civil infrastructure systems.

2. Calibration of acceptable risk levels (both conditional on the seismic hazard level and unconditional) for the proposed PPBOSD methodology.

3. Experimental and/or field validation of detailed FE models of bridge systems such as the one developed for the CHSR prototype bridge considered herein. Ideally, this validation must be performed over a wide range of earthquake intensity.

4. The current PEER PBEE methodology, which is at the heart of the proposed PPBOSD framework, needs to be further extended to include both vector-valued ground motion intensity measures and vector-valued engineering demand parameters, in order to increase the accuracy of the probabilistic seismic performance estimates.

5. The epistemic and aleatory uncertainties in the computational (FE) model, model parameters, and capacity terms of the bridge system, must be accounted for in the probabilistic performance assessment in addition to the uncertainties associated with the seismic loading, in order to achieve more accurate and reliable results.

6. The major challenge in the application of the proposed PPBOSD framework to large and complex real-world structures is the very high computational cost, which is associated with the ensembles of nonlinear time history analyses based on the detailed nonlinear FE model of the structural system. This challenge can be tackled in two different ways. The first alternative is to use highly efficient computational optimization algorithms in conjunction with a simplified but sufficiently accurate nonlinear computational model of the structural system. The other alternative is to use brute-force optimization through parametric probabilistic performance evaluations, based on the detailed nonlinear FE model, over a grid in the design variable space using high-performance cloud-computing resources. Ideally, a hybrid version of these two approaches balancing their advantages and disadvantages is desirable. In the future, emphasis should be placed on solving real-world (i.e., exact) problems with approximate methods as opposed to solving idealized (i.e., approximate) real-world problems with exact methods, which has often been the trend in the past in the area of structural optimization.

APPENDIX A PASSIVE PRESSURE THEORY FOR ESTIMATING PILE CAP RESISTANCE AND ABUTMENT WALL RESISTANCE

The passive pressure against the embedded pile cap as well as the earth resistance against the abutment back-wall or stem wall plays a significant role in soil-structure-interaction for bridge structures. The soil resistance is a function of the movement displacement of the structure, the soil properties of the surrounding soil, and the friction or adhesion on the interface between the structure and soil. The resistance behavior has been systematically studied (Duncan and Mokwa 2001), by comparing the well-known Rankine Theory (Rankine 1857), Coulomb Theory (Coulomb 1776), and Log Spiral Theory (Terzaghi 1943, Terzaghi et al. 1996) for the maximum passive pressure with field test results, leading to a rational method to estimate the force displacement behavior of soil resistance, i.e., the Log Spiral (LS) numerical method using the LS theory with corrected 3D effects implemented in PYCAP (Mokwa 1999). The LS method assumes the failure surface consist of the Prandtl zone bounded by logarithmic spiral and the Rankine zone. This method provides an adequate accurate means of estimating the passive resistance for a wide range of conditions, especially when the interface friction angle is greater than 40% of the internal friction angle, under which the Coulomb theory assuming the plane sliding surface will over predict the resistance. The

Rankine theory, as the simplest method, assumes the interface friction angle as the inclination of the ground surface with limitations. In this research, the p-y curve for the passive pressure resistance is estimated using the LS theory to characterize the force displacement behavior of the surround soil against the pile cap, abutment back-wall and stem wall, respectively.

The abutment backfill in the CHSR prototype bridge is 3% cemented (by weight) well-graded gravel with low permeability and is modeled as soil with zero friction angle and increased cohesion c = 50psi after Abramson (2001). Since the surrounding soil of a pile cap in the California High-speed Rail (CHSR) prototype bridge considered here is clay, the estimation of the soil resistance to pile cap falls into the situation of cohesive soil with zero friction angles. These are the soil properties utilized to estimate the passive resistance parameters to characterize the p-y curve in the CHSR prototype bridge considered in this research.

For cohesive soils with zero friction angles, the formulation using the LS theory in PYCAP (see Equation (A1)), which ignores the side cohesion resistance, predicts close results with the approach developed by Reese (2007) for modeling the failure zone in front of a laterally loaded pile as a failure wedge with plane failure surface, especially for the cases with small values for the friction angle.

$$P_{ult}{}^{p} = \frac{1}{2} c B_{cap} H_{cap} \left(4 + 2\alpha + \frac{\gamma H_{cap}}{c} + \frac{0.25 H_{cap}}{B_{cap}} \right) \tag{A1}$$

$P_{ult}{}^{p}$: ultimate soil resistance

c : cohesion of cohesive soil

B_{cap} : pile cap or stem wall width

H_{cap} : pile cap or stem wall height

$\alpha = \frac{c_a}{c}$: percentage of the front interface cohesion c_a with respect to the soil cohesion c

γ: soil weight density

The passive soil resistance for the back wall estimated based on the LS theory is also used to verify the physically parameterized backbone curves for passive response of abutment walls with homogeneous backfills proposed by Khalili-Tehrani et al. (2010).

A nonlinear spring that accounts for the bridge abutment-backfill resistance is calibrated explicitly accounting for the physical properties of soil and geometrical dimensions of abutment wall, using the closed-form relationship for the Generalized Hyperbolic Force-Displacement (GHFD) back bone curve prediction proposed by Khalili-Tehrani et al. (2010). The generalized predictive model is regressed after performing extensive parametric studies for abutment wall with backfill with a previously validated Extended HFD model based on 3D numerical modeling and field tests results by Shamsabadi et al. (2010), and validated using published measurements from several field and laboratory tests (i.e., two full-scaled field tests performed by Rollins K. M. et al. (2006), and the centrifuge test at Rensselaer Polytechnic Institute by Gadre A. D. (1998)).

$$\bar{F}(y) = \frac{a_r y}{\hat{H} + b_r y}\hat{H}^n,\ \hat{H} = \frac{H}{H_r} \tag{A2}$$

$$\begin{aligned} a_r &= \frac{1}{\beta}(\eta - 1)\alpha,\ b_r = \frac{1}{\beta}(\eta - 2) \\ \alpha &= \frac{F_{ult}}{\hat{H}^n},\ \beta = \frac{y_{\max}}{\hat{H}},\ and\ \eta = \frac{y_{\max}}{y_{50}} \end{aligned} \tag{A3}$$

$\bar{F}(y)$: abutment resisting force per unit width of the wall developed at abutment displacement of y

y_{50}: displacement corresponding the 50% of the ultimate force capacity

$y_{\max}$: displacement capacity

H : abutment back-wall height

$\hat{H}$: reference height

a_r : parabolic parameter as shape factor for the HFD curve

b_r : parabolic parameter as shape factor for the HFD curve

α : height normalized factor for back fill force capacity

β : wall displacement factor at displacement capacity

η : shape factor for the HFD curve

n: exponent factor for the height effect on the capacity

Considering the possibility that the soil parameters used in CHSR for the abutment back-wall resistance backbone curve may fall outside the feasible range for usual highway bridge abutments, it may not be appropriate to be used here with acceptable prediction error. Thus, the formulation for passive soil pressure in PYCAP is used herein as verification and validation for the backbone curve relationship for backfill resistance.

For the soil resistance against a pile cap, the estimation approach utilized in Zhao (2011) as below is adopted, appropriate accounting for the contribution from different mechanisms, including side resistance.

$$P_{ult}{}^{p} = P_{ult}{}^{front} + P_{ult}{}^{bot} + P_{ult}{}^{side} \tag{A4}$$

$$P_{ult}{}^{front} = \frac{1}{2}\left(4c\sqrt{K_p} + \gamma H_{cap} K_p\right) B_{cap} H_{cap} \tag{A5}$$

$$P_{ult}{}^{bot} = 0.25 c_a B_{cap} L_{cap} \tag{A6}$$

$$P_{ult}{}^{side} = 2 c_a H_{cap} L_{cap} \tag{A7}$$

K_p : passive pressure coefficient

References

Abramson, L. W., Lee, T. S., Sharma S., and Boyce, G. M. (2001). *Slope Stability and Stabilization Methods*. Wiley, 2d Edition. New York.

Columb, C. A. (1776). "Essai sur une application des regles des maximas et minmas a quelques problemes de statique relatifs a l'architecture." *Mem. Acad. Roy. Pres. Divers savanta*, 7, Paris (in French).

Duncan, J. M., and Mokwa, R. L. (2001). "Passive earth pressures: theories and tests." *Journal of Geotechnical and Geoenvironmental Engineering*, 127(3), 248-257.

Gadre, A. D. and Dobry, R. (1998). "Centrifuge modeling of cyclic lateral response of pile cap systems and seat-type abutments in dry sand." *Rep. MCEER-98-0010*, Rensselaer Institute, Civil Engineering Dept., Troy, N.Y.

Khalili-Tehrani P., Taciroglu E., and Shamsabadi A. (2010) "Backbone Curves for Passive Lateral Response of Abutment Walls with Homogeneous Backfills." *Soil Foundation Structure Interaction*, 149-154.

Khalili-Tehrani P., Shamsabadi A., Stewart J. P., and Taciroglu E. (2012) "Physically Parameterized Backbone Curves for Passive Lateral Response of Abutment Walls with Homogeneous Backfills." *To be submitted to ASCE Journal of Geotechnical and Geoenvironmental Engineering*.

Mokwa, R. L. and Duncan, J. M. (2001). "Experimental evaluation of lateral-load resistance of pile caps." *Journal of Geotechnical and Geoenvironmental Engineering*, 127 (2), 185-192.

Mokwa, R. L. (1999). "Investigation of the resistance of pile caps to lateral loading." Ph.D. dissertation, Virginia Polytechnic Institute and State University, Blacksburg, Virginia.

Rankine, W. J. M. (1857). "On the stability of loose earth." *Philosophical Trans. Royal Soc.*, London.

Rollins, K. M. and Cole, R. T., (2006). "Cyclic Lateral Load Behavior of a Pile Cap and Backfill" *J. Geotechnical and Geoenv. Engrg.*, 132 (9), 1143-1153.

Reese, L. C., Isenhower W. M., and Wang S. T. (2007). *Analysis and Design of Shallow and Deep Foundations*. John Wiley & Sons, Inc. New York.

Shamsabadi, A., Rollins, K. M., and Kapuskar, M. (2007). "Nonlinear soil-abutment-bridge structure interaction for seismic performance-based design." *Journal of Geotechnical and Geoenvironmental Engineering*, 133(6), 707-720.

Terzaghi, K. (1943). *Theoretical soil mechanics*, Wiley, New York.

Terzaghi, K., Peck, R. B., and Mezri, G. (1996). *Soil mechanics in engineering practice*, 3rd Edition., Wiley, New York.

Zhao, M. X. (2011). “Response of bridges to lateral spreading and earthquake shaking.” Ph.D., dissertation, University of California, Los Angeles, California.

APPENDIX B SOIL SPRING (p-y, t-z, q-z) FORMULATION SUMMARY AND PROPERTIES SPECIFICATION PROCEDURE

The methods based on the theory of elasticity are widely in early design practice of pile foundations, in which it is assumed that the soil is uniform and isotropic elastic material characterized with a Yong's modulus and a Poisson's ratio. These methods use Mindlin's (Mindlin 1936) equations for stress and deformation at any point in the interior of semi-infinite, elastic, and isotropic solids resulting from a force applied at another point in the solids. While the actual ground conditions rarely, if ever, satisfy the basic assumption made in the elasticity-based methods. To avoid over-simplification, the load transfer method (commonly referred to as the *p-y, t-z, Q-z* method) are used under the Winkler assumption.

The acquisition of load-transfer curves from a load test requires that the pile be instrumented along the depth. Commonly-accepted theories and empirical formulas based on test results will be employed to estimate the soil spring properties. Based on the analysis of the results from full-scale experiments and centrifuge tests with instrumented piles, the commonly used formulation of the *p-y* spring is presented here (Boulanger et al., 1999; Curras et al., 2001), followed by recommendations for the specification of the properties of soil springs to compute the ultimate soil resistance (Boulanger et al., 1999; Curras et al., 2001, Brandenberg 2005; Huo 2011; Zhao 2011; Reese 2001; Reese 2007).

Soil Springs' (p-y, t-z, and q-z) Formulation

As identified from the experimental and field test results, the backbone curve for p-y spring first depends on the soil type defined to approximate the specific backbone curve shape (e.g., soft or silt clay model developed based on the Matlock (1970), stiff clay based on Reese's (1975), and sand model based on API (1993)). The other four parameters to define the force-displacement behavior are:

p_{ult} : ultimate capacity of the soil resistance;

y_{50} : the displacement corresponding to 50% of the ultimate capacity mobilized during monotonic loading;

C_d : drag resistance ratio of the drag force with respect to the ultimate capacity when a full gap is formed, a reasonable suggested value could be 0.3 for clay based on the back-calculated p-y curves from the centrifuge experiments (Wilson 1998);

c_{dash} : viscous damping term on the far field component (in parallel with the elastic component) to approximate the radiation damping.

As shown in Figure B.1, the resistance behavior (p-y) from the soil medium surrounding the pile is conceptualized as three components in series, consisting of a gap component (a closure spring denoted as $p^c - y^g$ in parallel with a drag spring denoted as $p^d - y^g$), a plastic component (denoted as $p - y^p$), and an elastic component (an elastic spring denoted as $p^e - y^e$ in parallel with a dashpot denoted as $p^r - \dot{y}^e$). Each component is elaborated as below.

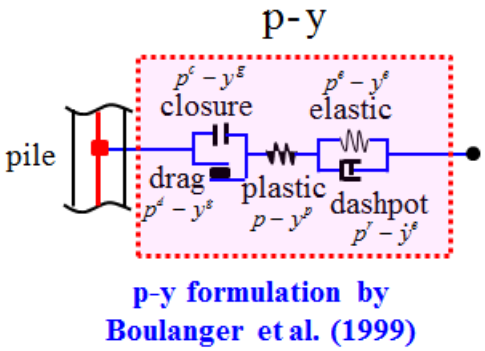

Figure B.1: p-y Spring Formulation

The gap component is defined by the following three equations, in which y_0^+ and y_0^- are the memory terms for the maximum past positive and negative side of the gap respectively. y_0^g and p_0^d are y^g and p^d respectively at the start of the current loading cycle.

$$p\left(y_p\right) = p^c\left(y_p\right) + p^d\left(y_p\right) \tag{B1}$$

$$p^c\left(y^g\right) = 1.8 p_{ult}\left[\frac{y_{50}}{y_{50} + 50\left(y_0^+ - y^g\right)} - \frac{y_{50}}{y_{50} - 50\left(y_0^- - y^g\right)}\right] \tag{B2}$$

$$p^d\left(y^g\right) = C_d\, p_{ult} - \left(C_d\, p_{ult} - p_0^d\right)\left[\frac{y_{50}}{y_{50} + 2\left|y^g - y_0^g\right|}\right] \tag{B3}$$

The plastic spring is considered as rigid inside the rigid zone and defined by the following equation outside the region zone, in which c and n are the shape parameters. (e.g., for drained sand, defaulted c = 0.5, n = 2, and Cr = 0.2; for soft clay, defaulted c = 10, n = 5, and Cr = 0.35).

$$p\left(y_p\right) = p_{ult} - \left(p_{ult} - p_0\right)\left[\frac{cy_{50}}{cy_{50} + \left|y_p - y_0^p\right|}\right]^n \tag{B4}$$

The p-y behavior for clay was based on the relations presented by Matlock (1970), in the shape defined as

$$p(y) = 0.5 p_{ult} \left(\frac{y}{y_{50}} \right)^{\frac{1}{3}} \quad \text{(B5)}$$

This material is also well calibrated with experimental results (Matlock 1970) for soft clay, capturing the gapping effects and cyclic degradation reasonably well (Boulanger et al. 2003).

The formulation of t-z spring to represent the vertical soil friction resistance against piles is similar to the lateral p-y spring except that there is no gap component. The backbone curve of the resistance behavior is following the recommended one for drilled shafts in clay by Reese and O'Neill's (1987) and Mosher's (1984) for axially loaded piles in sand.

The formulation of q-z spring to represent the pile tip resistance is similar to the lateral p-y spring except for the different behaviors in compression versus uplift. The resistance behavior backbone curve is following the recommended one for drilled shafts in clay by Reese and O'Neill's (1987), and Vijayvergiya's (1977) for axially loaded piles in sand.

Soil Spring (p-y) Properties Specification

Piles in Clay:

$$\begin{aligned} p_{ult} &= \bar{p}_{ult} d_{tributary} \\ \bar{p}_{ult} &= c_u b N_p \\ N_p &= \min\left(3 + \frac{\gamma' z}{c_u} + \frac{Jz}{b}, 9 \right) \\ y_{50} &= 2.5 b \varepsilon_{50} \end{aligned} \quad \text{(B6)}$$

In which:

b = the pile diameter

N_p = lateral bearing capacity factor

γ' = the average buoyant unit weight

z = soil spring depth from the ground surface

c_u = the undrained shear strength

ε_{50} = strain corresponding to 50% of the ultimate stress in a laboratory stress-strain curve, typical value of 0.005. J is 0.5 for soft clay and 0.25 for medium clay according to Matlock's recommendations (1970), but 0.5 is frequently used in practice.

It is worth noting that the modification to the static p-y curve to consider the cyclic degradation for clay is not appropriate for pile foundation subjected to earthquake loading, because the modification was proposed for the case of wave loads against offshore foundations where hundreds of thousands loading cycles occur.

Pile in Sand: API ("Recommended" 1993, not liquefiable)

The estimate of ultimate resistance in the sand is based on the following equations:

$$\begin{aligned} p_{ult} &= \bar{p}_{ult} d_{tributary} \\ \bar{p}_{ult} &= A_s \bar{p}_u = A_s \min\left(\bar{p}_{st}, \bar{p}_{sd}\right) \end{aligned} \tag{B7}$$

$$\bar{p}_{st} = \gamma' z \left[\begin{array}{l} \dfrac{K_0 z \tan\phi \sin\beta}{\tan(\beta-\phi)\cos\alpha} + \dfrac{\tan\beta}{\tan(\beta-\phi)}\left(b + z\tan\beta\tan\alpha\right) + \\ K_0 z \tan\beta\left(\tan\phi\sin\beta - \tan\alpha\right) - K_a b \end{array} \right] \tag{B8}$$

$$\bar{p}_{sd} = K_a b\gamma z\left(\tan^8\beta - 1\right) + K_0 b\gamma z \tan\phi \tan^4\beta \tag{B9}$$

$$\alpha = \frac{\phi}{2}; \beta = 45^o + \frac{\phi}{2}; K_0 = 0.4; K_a = \tan^2\left(45^o - \frac{\phi}{2}\right) \tag{B10}$$

ϕ = friction angle for sand

K_0 = the coefficient of lateral earth pressure at rest, taken as representative value of 0.4

K_a = the coefficient of active lateral earth pressure

γ' = the average buoyant unit weight

b = pile diameter

z = soil spring depth from the ground surface

b = pile diameter

$\bar{p}_{st}$ = the ultimate resistance for per unit length of pile in sand based on the wedge shaped mechanism

$\bar{p}_{sd}$ = the ultimate resistance for per unit length of pile in sand based on the horizontal plane strain failure mechanism

A_s = the shape factor

p_{ult} = the ultimate capacity for the soil spring representing the soil resistance corresponding the tributary depth $d_{tributary}$

Also, based on API (1987) recommendations, p-y curves are described using Hyperbolic functions as below,

$$p(y) = p_{ult} \tanh\left(\frac{k^c z}{p_{ult}} y\right) \tag{B11}$$

which can be used to estimate the y_{50} inversely proportional to the depth

$$y_{50} = \tanh^{-1}(0.5)\frac{p_{ult}}{k^c z} \tag{B12}$$

in which,

$$k^c = c_\sigma k = \begin{cases} 1 \cdot k & \text{(API)} \\ \sqrt{\dfrac{\sigma_{ref}'}{\sigma_v'}} k & \text{(Boulanger et al. (2003))} \end{cases} \tag{B13}$$

k = initial modulus of subgrade reaction based on API for sand

c_σ = correction factor for overburden effects

σ_{ref}' =reference stress at which k was calibrated, taken as 50kPa

k^c = modulus of subgrade reaction after correction for overburden effects by Boulanger (2003) considering the fact that elastic modulus of sand approximately increases with the square root of confining stress instead of in proportion with the confining stress.

Soil Properties Specification for t-z Spring against Drilled Shafts (CIDH)

Piles in Clay:

Several studies on the load-transfer curves for side resistance in cohesive soil can be found in the literature (Coyle and Reese 1966; Vijayvergiya 1977; Kraft et al. 1981a, 1981b, and 1981c; Reese and O'Neill 1988). The backbone curve formulated based on Reese and O'Neill (1988) is used, and the ultimate transfer load is estimated as below,

$$\begin{aligned} t_{ult} &= \overline{t}_{ult} d_{tributary} \\ \overline{t}_{ult} &= c_a \pi b = \alpha c_u \pi b \end{aligned} \tag{B14}$$

In which friction force is estimated by α method (Stas C. V., 1984)

$$\alpha = \min\left(0.21 + 0.26 \frac{p_{atm}}{c_u},\ 1.0 \right) \tag{B15}$$

The displacement z_{50}, corresponding to 50% of the resistance capacity, is estimated to be 0.1% of the pile diameter based on the normalized curves showing load transfer in side resistance versus settlement for drilled shafts in clay in Reese and O'Neill (1988).

Piles in Sand:

The transfer load in skin friction (side resistance) of axially loaded piles in sand was can be found in the literature (Coyle and Sulaiman 1967; Vijayvergiya 1977; Mosher 1984; O'Neill and Reese 1999). The backbone for the load transfer curve is formulated after Vijayvergia (1977), and the ultimate transfer load is estimated as below,

$$t_{ult} = K_0 \sigma_v' \pi b \delta \tag{B16}$$

In which,

K_0 : the coefficient of lateral earth pressure at rest, taken as representative value of 0.4

δ: the interface friction angle between soil and pile, taken as $\delta = 0.8\phi$ to be representative of a smooth precast concrete pile after Kulhawy et al. (1991).

Based on the t-z curve of the shape recommended by Mosher (1984), the deformation corresponding to 50% of the ultimate capacity is estimated as

$$z_{50} = \frac{t_{ult}}{k_f} \tag{B17}$$

where the initial tangent based on friction angle can be estimated based on Mosher (1984).

Soil Properties Specification for Q-z Spring

Piles in Sand:

The ultimate tip bearing capacity q_{ult} in sandy soil deposit can be estimated as follows (Mayerhof 1976):

$$q_{ult} = N_q \sigma_v' \tag{B18}$$

$$N_q = \frac{1+2K_0}{3-\sin\phi} e^{\left(\frac{\pi}{2}-\phi\right)\tan\phi} \tan^2\left(\frac{\pi}{4}+\frac{\phi}{2}\right) I_r^{\frac{4\sin\phi}{3(1+\sin\phi)}}$$
$$where:\ K_0 = 1-\sin\phi,\ I_r = \frac{G_s}{\sigma_v' \tan\phi} \tag{B19}$$

in which N_q is bearing capacity factor, ϕ is the fiction angle, G_s is the soil shear modulus, σ_v' is the effective overburden stress at the pile tip, and K_0 is the lateral earth pressure coefficient. The

ultimate resistance of the bearing Q_{ult} is computed based on the effective pile tip area A_{tip} as follows.

$$Q_{ult} = q_{ult} A_{tip} \tag{B20}$$

Based on Q-z curve of the form (Vijayvergiya 1977)

$$q(z) = q_{ult}\left(\frac{z}{z_c}\right)^{\frac{1}{3}} \tag{B21}$$

in which z_c is the critical tip deflection given as a range from 3% to 9% of the pile diameter at the pile tip, here 5% is taken as a representative value, z_{50} can be estimated as:

$$z_{50} = 0.125 z_c \tag{B22}$$

Radiation dashpot values in p-y and t-z springs

The magnitude of the radiation damping depends on the mode of oscillation, the frequency of excitation, the geometry of the soil-foundation system, soil profiles, and the stress-strain characteristics. A simple model (Gazetas et al. 1984) is proposed to account for the radiation damping in single pile embed in soil, with the horizontal and vertical dashpot values presented in Figure B.2, which was shown to match well with the available tests results. Here, the lower bound value of the radiation dashpot value for conservation and simplicity without frequency dependency considered is employed.

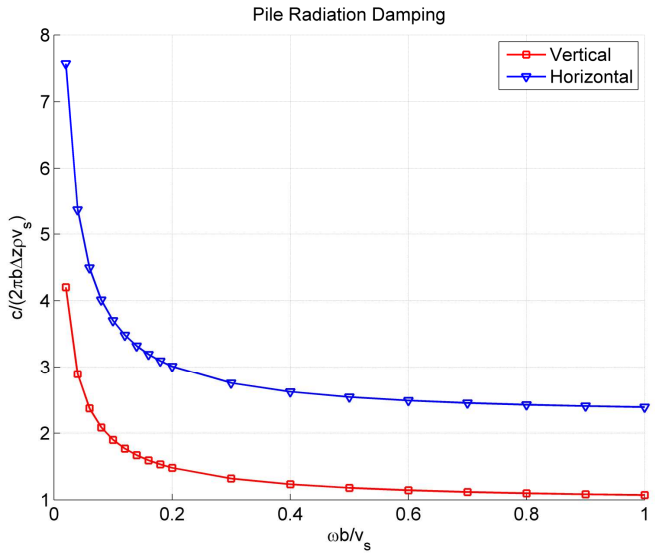

Figure B.2: Pile Radiation Damping Estimation (after Gazetas et al., 1984)

References

American Petroleum Institute (API) (1993). *Recommended practice for planning, designing and constructing fixed offshore platforms – Working stress design*. 20th Edition, American Petroleum Institute, Washington, DC.

Boulanger, R. W., Curras, C. J., Kutter, B. L., Wilson, D. W., and Abghari, A. (1999). "Seismic soil-pile-structure interaction experiments and analysis." *Journal of Geotechnical and Geo-environmental Engineering*, 125(9), 750-759.

Boulanger, R. W., Kutter, B. L., Brandenberg S. J., Singh P., Chang D. (2003). "Pile foundations in liquefied and laterally spreading ground during earthquakes: centrifuge experiments and analyses." *Rep. No. UCD/CGM-03/01*, Center for Geo-technique Modeling, Dept. of Civil and Environmental Engineering, University of California, Davis, California.

Brandenberg, S. J. (2005). "Behavior of Pile Foundations in Liquefied and Laterally Spreading Ground." Ph.D. dissertation. University of California, Davis, California.

Brinch Hansen, J. (1961). "The ultimate resistance of rigid piles against transversal forces." *Bulletin No. 12*, Geoteknisk Institute, Copenhagen, 59.

Coyle, H. M. and Sulaiman I. H. (1967). "Skin friction for steel piles in sand." *Journal of Soil Mechanics and Foundations Division*, ASCE 93(SM6, 5590), 261-278.

Coyle, H. M. and Reese, L. C. (1966). "Load Transfer for Axially Loaded Piles in Clay." *Journal of the soil Mechanics and Foundations Division*, ASCE 92(SM2, 4702), 1-26.

Curras, C., Boulanger, R., Kutter, B. L., and Wilson, D. W. (2001). “Dynamic experiments and analyses of a pile-group-supported structure.” *Journal of geotechnical and Geoenvironmental Engineering*, 585–596.

Gazetas, G., and Dobry, R. (1984). “Simple Radiation Damping Model for Piles and Footings.” *Journal of Engineering Mechanics*, 110(6), 937–956.

Gazetas, G., and Dobry, R. (1984). “Horizontal Response of Piles in Layered Soils.” *Journal of Geotechnical Engineering*, 110(1), 20–40.

Huo, Y. L. (2011). “Highway Bridge Seismic Assessment and Improvement Analysis with Fragility Function Method.” Ph.D., dissertation, University of California, Los Angeles, California.

Kraft, L. M., Cox, W. R., and Verner, E. A. (1981a). “Pile Load Test: Cyclic Loads at Varing Load Rates.” *Journal of Geotechnical Engineering*, 107(11), 1-19.

Kraft, L. M., Focht, J. A., and Amerasinghe, S. F. (1981b). “Friction Capacity of Piles in Driven into Clay.” *Journal of Geotechnical Engineering*, 107(11), 1521-1541.

Kraft, L. M., Ray, R. P. and Kagawa, T. (1981c). “Theoretical t-z Curves.” *Journal of Geotechnical Engineering*, 107(11), 1543-15601.

Kulhawy, F. H. (1984). “Limiting Tip and Side Resistance: Fact or Fallacy? Analysis and Design of Pile Foundation.” *ASCE Symp.*, 80-98.

Kulhawy, F. H. (1991). “Drilled shaft foundations.” *Foundation engineering handbook, 2nd Ed.*, Chap 14, H.-Y. Fang ed., Van Nostrand Reinhold, New York.

Kulhawy, F. H. and Mayne, P. W. (1990). Manual on Estimating Soil Properties for Foundation Design. Electrical Power Research Institute. *EPRI EL-6800, Project 1493-6 Final Report*.

Matlock, H. (1970). “Correlations for design of laterally loaded piles in soft clay.” *Proceedings of the 2nd Annual Offshore Technology Conference*, Houston, Texas, 577-594.

Mcgann, C. R., Arduino, P., Asce, M., & Mackenzie-helnwein, P. (2012). *Simplified Procedure to Account for a Weaker Soil Layer in Lateral Load Analysis of Single Piles*, September, 1129–1137.

Meyerhof G. G. (1976). “Bearing capacity and settlement of pile foundations.” *J. Geotech. Eng. Div.*, 102(3), 195-228.

Mindlin, R. D. (1936). “Force at a Point in the Interior of a Semi-infinite Solid.” *Physics*, 7(5), 195-202.

Mosher, R. L. (1984). *Load transfer criteria for numerical analysis of axial loaded piles in sand*. U.S. Army Engineering and Waterways Experimental Station, Automatic Data Processing Center, Vicksburg, Miss.

O'Neill M. W. and Reese L. C. (1999). "Drilled Shafts: Construction Procedure and Design Methods." *FHWA Report No. IF-99-025*.

Reese, L. C., Isenhower W. M., and Wang S. T. (2007). *Analysis and Design of Shallow and Deep Foundations*. John Wiley & Sons, Inc. New York.

Reese, L. C. and Van Impe, W. F. (2001), *Single Piles and Pile Groups under Lateral Loading*. A.A. Balkema, Rotterdam, Netherlands.

Resse, L. C. and O'Neill, M. W. (1988). "Filed Load Test of Drilled Shaft." *Proceedings, International Seminar on Deep Foundations on Bored and Auger Piles,* Van Impe (ed.), Balkema, Rotterdam, 145-192.

Stas, C. V. and Kulhawy, F. H. (1984). "Critical evaluation of design methods for foundations under axial uplift and compression loading." *EPRI Report EL-3771*, Research Project 1493-1, Electric Power Research Institute, Palo Alto, California.

Vijayvergiya, V. N. (1977). "Load-movement characteristics of piles." *Proc., Ports 77 Conf.*, ASCE, New York.

Wilson, D. W. (1998). "Soil-pile-superstructure interaction in soft clay and liquefiable sand." *Rep. No. UCD/CGM-98/04*, Center for Geo-technique Modeling, Department of Civil and Environmental Engineering, University of California, Davis, California.

Zhao, M. X. (2011). "Response of bridges to lateral spreading and earthquake shaking." Ph.D., dissertation, University of California, Los Angeles, California.